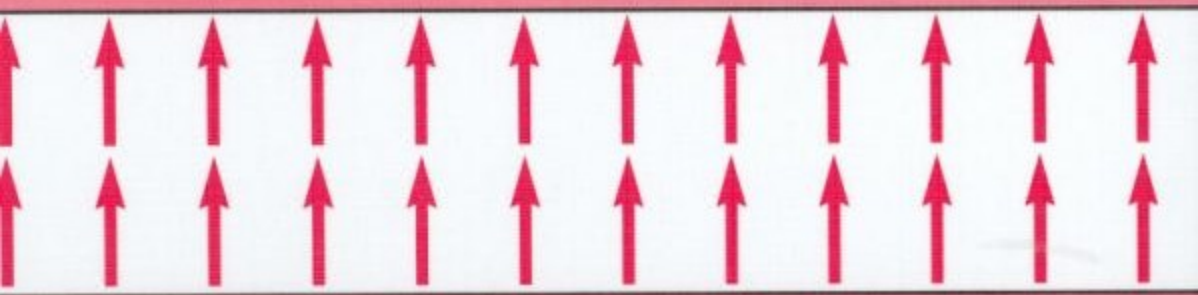
Handbook of Magnetic Materials

Edited by

K.H.J. Buschow

VOLUME

12



North - Holland

ELSEVIER SCIENCE B.V.
Sara Burgerhartstraat 25
P.O. Box 211, 1000 AE Amsterdam, The Netherlands

© 1999 Elsevier Science B.V. All rights reserved.

This work is protected under copyright by Elsevier Science, and the following terms and conditions apply to its use:

Photocopying
Single photocopies of single chapters may be made for personal use as allowed by national copyright laws. Permission of the Publisher and payment of a fee is required for all other photocopying, including multiple or systematic copying, copying for advertising or promotional purposes, resale, and all forms of document delivery. Special rates are available for educational institutions that wish to make photocopies for non-profit educational classroom use.

Permissions may be sought directly from Elsevier Science Rights & Permissions Department, PO Box 800, Oxford OX5 1DX, UK; phone: (+44) 1865 843830, fax: (+44) 1865 853333, e-mail: permissions@elsevier.co.uk. You may also contact Rights & Permissions directly through Elsevier's home page (http://www.elsevier.nl), selecting first 'Customer Support', then 'General Information', then 'Permissions Query Form'.

In the USA, users may clear permissions and make payments through the Copyright Clearance Center, Inc., 222 Rosewood Drive, Danvers, MA 01923, USA; phone: (978) 7508400, fax: (978) 7504744, and in the UK through the Copyright Licensing Agency Rapid Clearance Service (CLARCS), 90 Tottenham Court Road, London W1P 0LP, UK; phone: (+44) 171 631 5555; fax: (+44) 171 631 5500. Other countries may have a local reprographic rights agency for payments.

Derivative Works
Tables of contents may be reproduced for internal circulation, but permission of Elsevier Science is required for external resale or distribution of such material.
Permission of the Publisher is required for all other derivative works, including compilations and translations.

Electronic Storage or Usage
Permission of the Publisher is required to store or use electronically any material contained in this work, including any chapter or part of a chapter.

Except as outlined above, no part of this work may be reproduced, stored in a retrieval system or transmitted in any form or by any means, electronic, mechanical, photocopying, recording or otherwise, without prior written permission of the Publisher.
Address permissions requests to: Elsevier Science Rights & Permissions Department, at the mail, fax and e-mail addresses noted above.

Notice
No responsibility is assumed by the Publisher for any injury and/or damage to persons or property as a matter of products liability, negligence or otherwise, or from any use or operation of any methods, products, instructions or ideas contained in the material herein. Because of rapid advances in the medical sciences, in particular, independent verification of diagnoses and drug dosages should be made.

First edition 1999

Library of Congress Cataloging in Publication Data
A catalog record from the Library of Congress has been applied for.

ISBN Vol. 12: 0 444 50249 1
ISBN Set: 0 444 85313 8

♾ The paper used in this publication meets the requirements of ANSI/NISO Z39.48-1992 (Permanence of Paper).
Printed in The Netherlands.

PREFACE TO VOLUME 12

The Handbook series Magnetic Materials is a continuation of the Handbook series Ferromagnetic Materials. When Peter Wohlfarth started the latter series, his original aim was to combine new developments in magnetism with the achievements of earlier compilations of monographs, producing a worthy successor to Bozorth's classical and monumental book *Ferromagnetism*. This is the main reason that *Ferromagnetic Materials* was initially chosen as title for the Handbook series, although the latter aimed at giving a more complete cross-section of magnetism than Bozorth's book.

In the last few decades magnetism has seen an enormous expansion into a variety of different areas of research, comprising the magnetism of several classes of novel materials that share with truly ferromagnetic materials only the presence of magnetic moments. For this reason the Editor and Publisher of this Handbook series have carefully reconsidered the title of the Handbook series and changed it into *Magnetic Materials*. It is with much pleasure that I can introduce to you now Volume 12 of this Handbook series.

The giant magnetoresistance or GMR is a prominent example of such expansion of magnetism. The giant magnetoresistance effect is found in heterostructures and was discovered only recently. The GMR of multilayers is induced by the variation of the angle between the magnetization of consecutive magnetic layers, and its discovery was preceded by the discovery of exchange coupling between magnetic layers across a non-magnetic metal layer. Under certain circumstances the coupling is antiferromagnetic and induces an antiparallel alignment of the magnetization of adjacent magnetic layers. When an external magnetic field aligns the magnetization of all magnetic layers in parallel, there is a giant decrease of the resistance of the multilayer. The discovery of interlayer exchange and GMR has lead to an enormous proliferation of experimental and theoretical studies on multilayers and more generally on magnetic nanostructures. GMR effects have been observed not only in exchange coupled magnetic multilayers but also in uncoupled multilayers, spin valve structures, multilayered nanowires and granular systems.

At present the giant magnetoresistance effect is used in various types of device such as sensors, read heads and magnetic RAM. Apart from the giant magnetoresistance effect and its applications, research on GMR has revealed a new class of magnetotransport phenomena which can be obtained in magnetic nanostructures by making use of the spin polarisation of carriers. This is a new field of research which is frequently referred to as spin electronics. Examples of emerging directions of research with important potential applications in this area are spin injection spin dependent tunnelling and magneto-Coulomb

blockade. The review presented in Chapter 1 of this Volume is focused on GMR in magnetic multilayers. It includes an experimental overview of results obtained on conventional multilayers, spin valves, multilayers on grooved substrates and multilayered nanowires. The review comprises also theoretical models and employs the experimental data to discuss the current understanding of GMR and the underlying physics.

A key aspect of the study of the properties of thin magnetic films and multilayers is the relationship between the structural and magnetic properties of the material, which has become one of the most active areas of research in magnetism in recent years. Nuclear magnetic resonance (NMR) is a well-known technique that offers the possibility to obtain experimental information on atomic scale properties in systems with reduced dimensionality. A review of the results obtained by NMR on the latter systems is presented in Chapter 2 of this Volume. Because of its high sensitivity this method has the additional advantage that it provides not only experimental information on the nature of the magnetic and non-magnetic layers but also information on the nature of the interfaces. The Chapter is written in a tutorial style so that it can be helpful for many a scientist familiar with the preparation and properties of thin magnetic films but having little knowledge of the NMR of ferromagnetic materials.

Among the intermetallic rare-earth compounds with 3d transition metals, those that exhibit a magnetic instability of the 3d-subsystem are of particular interest. In combination with large magnetovolume effects, these compounds exhibit a number of characteristic properties that make them suitable for checking various physical theories. In the third Chapter of this Volume the attention is focused on such compounds, in which the d-electron subsystem is neither non-magnetic, nor carries a stable magnetic moment. Prominent examples of this group are the RCo_2 Laves phase compounds in which the hybridised itinerant 3d–5d electron subsystem leads to exchange enhanced Pauli paramagnetism. Particular interest is paid to systems that undergo a metamagnetic transition, i.e. a field-induced magnetic phase transition from the paramagnetic to the ferromagnetic state under an external magnetic field exceeding a certain critical value. The chapter deals with basic concepts of the theory of itinerant-electron magnetism. It includes magnetic properties of the systems consisting of both itinerant electrons and localised spins, and discusses the effects of spin fluctuations on the magnetic behavior, heat capacity and magnetoresistance. Apart from metamagnetism, a comprehensible description is given of magnetovolume effects and spin fluctuations in the nearly ferromagnetic compounds. The itinerant-electron metamagnetism and the spin fluctuations are interesting not only in themselves. By studying these phenomena it is possible to understand more deeply some aspects of the theory of itinerant-electron metamagnetism and open up the possibilities incorporated in this theory for describing different unusual effects observed in experiments.

Magnetic refrigeration is a promising technology that can be used is quite a broad range of applications. It is based on the magnetocaloric effect associated with the entropy change occurring when a magnetic materials is isothermally subjected to a changing magnetic field and the temperature change when the field is changed adiabatically. Refrigeration can be achieved by using the magnetocaloric effect of ferromagnets in repeated magnetization-demagnetization cycles under adiabatic and isothermal conditions. Research on magnetocaloric materials has received new impetus because of the need to realise room temperature magnetic refrigeration without the use of chlorofluorocarbons that are considered have

a destructive impact on the ozone layer. The last decade has witnessed quite a strong development in magnetic cooling technology and research activities in this field have been extended to a variety of magnetocaloric materials, including amorphous alloys, nanocomposites, intermetallic compounds and perovskite type oxides. The many materials, their magnetocaloric efficiency as well as the physical principles behind it are reviewed in the last Chapter of this Volume.

Volume 12 of the Handbook on the Properties of Magnetic Materials, as the preceding volumes, has a dual purpose. As a textbook it is intended to be of assistance to those who wish to be introduced to a given topic in the field of magnetism without the need to read the vast amount of literature published. As a work of reference it is intended for scientists active in magnetism research. To this dual purpose, Volume 12 of the Handbook is composed of topical review articles written by leading authorities. In each of these articles an extensive description is given in graphical as well as in tabular form, much emphasis being placed on the discussion of the experimental material in the framework of physics, chemistry and material science.

The task to provide the readership with novel trends and achievements in magnetism would have been extremely difficult without the professionalism of the North Holland Physics Division of Elsevier Science B.V., and I wish to thank Jonathan Clark and Wim Spaans for their great help and expertise.

K.H.J. Buschow

CONTENTS

Preface to Volume 12 v

Contents ix

Contents of Volumes 1–11 xi

List of Contributors xv

1. Giant Magnetoresistance in Magnetic Multilayers
   A. BARTHÉLÉMY, A. FERT and F. PETROFF 1
2. NMR of Thin Magnetic Films and Superlattices
   P.C. RIEDI, T. THOMSON and G.J. TOMKA 97
3. Formation of 3d-Moments and Spin Fluctuations in Some Rare-Earth–Cobalt Compounds
   N.H. DUC and P.E. BROMMER 259
4. Magnetocaloric Effect in the Vicinity of Phase Transitions
   A.M. TISHIN 395

Author Index 525

Subject Index 559

Materials Index 565

CONTENTS OF VOLUMES 1–11

Volume 1

1. Iron, Cobalt and Nickel, *by E. P. Wohlfarth* 1
2. Dilute Transition Metal Alloys: Spin Glasses, *by J. A. Mydosh and G. J. Nieuwenhuys* 71
3. Rare Earth Metals and Alloys, *by S. Legvold* 183
4. Rare Earth Compounds, *by K. H. J. Buschow* 297
5. Actinide Elements and Compounds, *by W. Trzebiatowski* 415
6. Amorphous Ferromagnets, *by F. E. Luborsky* 451
7. Magnetostrictive Rare Earth–Fe_2 Compounds, *by A. E. Clark* 531

Volume 2

1. Ferromagnetic Insulators: Garnets, *by M. A. Gilleo* 1
2. Soft Magnetic Metallic Materials, *by G. Y. Chin and J. H. Wernick* 55
3. Ferrites for Non-Microwave Applications, *by P. I. Slick* 189
4. Microwave Ferrites, *by J. Nicolas* 243
5. Crystalline Films for Bubbles, *by A. H. Eschenfelder* 297
6. Amorphous Films for Bubbles, *by A. H. Eschenfelder* 345
7. Recording Materials, *by G. Bate* 381
8. Ferromagnetic Liquids, *by S. W. Charles and J. Popplewell* 509

Volume 3

1. Magnetism and Magnetic Materials: Historical Developments and Present Role in Industry and Technology, *by U. Enz* 1
2. Permanent Magnets; Theory, *by H. Zijlstra* 37
3. The Structure and Properties of Alnico Permanent Magnet Alloys, *by R. A. McCurrie* 107
4. Oxide Spinels, *by S. Krupička and P. Novák* 189
5. Fundamental Properties of Hexagonal Ferrites with Magnetoplumbite Structure, *by H. Kojima* 305
6. Properties of Ferroxplana-Type Hexagonal Ferrites, *by M. Sugimoto* 393
7. Hard Ferrites and Plastoferrites, *by H. Stäblein* 441
8. Sulphospinels, *by R. P. van Stapele* 603
9. Transport Properties of Ferromagnets, *by I. A. Campbell and A. Fert* 747

Volume 4

1. Permanent Magnet Materials Based on 3d-rich Ternary Compounds, *by K. H. J. Buschow* 1
2. Rare Earth–Cobalt Permanent Magnets, *by K. J. Strnat* 131

3. Ferromagnetic Transition Metal Intermetallic Compounds, *by J. G. Booth* 211
4. Intermetallic Compounds of Actinides, *by V. Sechovský and L. Havela* 309
5. Magneto-Optical Properties of Alloys and Intermetallic Compounds, *by K. H. J. Buschow* . . . 493

Volume 5

1. Quadrupolar Interactions and Magneto-Elastic Effects in Rare-Earth Intermetallic Compounds, *by P. Morin and D. Schmitt* 1
2. Magneto-Optical Spectroscopy of f-Electron Systems, *by W. Reim and J. Schoenes* 133
3. INVAR: Moment-Volume Instabilities in Transition Metals and Alloys, *by E. F. Wasserman* . . . 237
4. Strongly Enhanced Itinerant Intermetallics and Alloys, *by P. E. Brommer and J. J. M. Franse* . . . 323
5. First-Order Magnetic Processes, *by G. Asti* 397
6. Magnetic Superconductors, *by Ø. Fischer* 465

Volume 6

1. Magnetic Properties of Ternary Rare-Earth Transition-Metal Compounds, *by H.-S. Li and J. M. D. Coey* 1
2. Magnetic Properties of Ternary Intermetallic Rare-Earth Compounds, *by A. Szytula* 85
3. Compounds of Transition Elements with Nonmetals, *by O. Beckman and L. Lundgren* 181
4. Magnetic Amorphous Alloys, *by P. Hansen* 289
5. Magnetism and Quasicrystals, *by R. C. O'Handley, R. A. Dunlap and M. E. McHenry* 453
6. Magnetism of Hydrides, *by G. Wiesinger and G. Hilscher* 511

Volume 7

1. Magnetism in Ultrathin Transition Metal Films, *by U. Gradmann* 1
2. Energy Band Theory of Metallic Magnetism in the Elements, *by V. L. Moruzzi and P. M. Marcus* 97
3. Density Functional Theory of the Ground State Magnetic Properties of Rare Earths and Actinides, *by M. S. S. Brooks and B. Johansson* 139
4. Diluted Magnetic Semiconductors, *by J. Kossut and W. Dobrowolski* 231
5. Magnetic Properties of Binary Rare-Earth 3d-Transition-Metal Intermetallic Compounds, *by J. J. M. Franse and R. J. Radwański* 307
6. Neutron Scattering on Heavy Fermion and Valence Fluctuation 4f-systems, *by M. Loewenhaupt and K. H. Fischer* 503

Volume 8

1. Magnetism in Artificial Metallic Superlattices of Rare Earth Metals, *by J. J. Rhyne and R. W. Erwin* 1
2. Thermal Expansion Anomalies and Spontaneous Magnetostriction in Rare-Earth Intermetallics with Cobalt and Iron, *by A. V. Andreev* 59
3. Progress in Spinel Ferrite Research, *by V. A. M. Brabers* 189
4. Anisotropy in Iron-Based Soft Magnetic Materials, *by M. Soinski and A. J. Moses* 325
5. Magnetic Properties of Rare Earth–Cu_2 Compounds, *by Nguyen Hoang Luong and J. J. M. Franse* 415

Volume 9

1. Heavy Fermions and Related Compounds, *by G.J. Nieuwenhuys* 1
2. Magnetic Materials Studied by Muon Spin Rotation Spectroscopy, *by A. Schenck and F.N. Gygax* . 57

3. Interstitially Modified Intermetallics of Rare Earth and 3d Elements, *by H. Fujii and H. Sun* . . . 303
4. Field Induced Phase Transitions in Ferrimagnets, *by A.K. Zvezdin* 405
5. Photon Beam Studies of Magnetic Materials, *by S.W. Lovesey* 545

Volume 10

1. Normal-State Magnetic Properties of Single-Layer Cuprate High-Temperature Superconductors and Related Materials, *by D.C. Johnston* 1
2. Magnetism of Compounds of Rare Earths with Non-Magnetic Metals, *by D. Gignoux and D. Schmitt* 239
3. Nanocrystalline Soft Magnetic Alloys, *by G. Herzer* 415
4. Magnetism and Processing of Permanent Magnet Materials, *by K.H.J. Buschow* 463

Volume 11

1. Magnetism of Ternary Intermetallic Compounds of Uranium, *by V. Sechovský and L. Havela* . . 1
2. Magnetic Recording Hard Disk Thin Film Media, *by J.C. Lodder* 291
3. Magnetism of Permanent Magnet Materials and Related Compounds as Studied by NMR, *by Cz. Kapusta, P.C. Riedi and G.J. Tomka* 407
4. Crystal Field Effects in Intermetallic Compounds Studied by Inelastic Neutron Scattering, *by O. Moze* 493

chapter 1

GIANT MAGNETORESISTANCE IN MAGNETIC MULTILAYERS

A. BARTHÉLÉMY, A. FERT and F. PETROFF

Unité Mixte de Physique CNRS–Thomson CSF
LCR, Domaine de Corbeville
91404 Orsay

and

Université Paris Sud
91405 Orsay
France

Handbook of Magnetic Materials, Vol. 12
Edited by K.H.J. Buschow
© 1999 Elsevier Science B.V. All rights reserved

CONTENTS

1. Introduction 3
2. Overview of experimental results 4
3. Simple picture of GMR 17
3.1. Two-current model for the conduction in ferromagnets 17
3.2. Simple picture of GMR 19
4. Physics of GMR: theoretical models and comparison with experimental data 20
4.1. Introduction to physics of GMR and theoretical models 20
4.2. Theoretical models of the CIP-GMR 23
4.3. Theoretical models of the CPP-GMR, spin accumulation effects 29
4.4. Quantitative analysis of GMR data 34
4.5. Discussion of the microscopic mechanism of the GMR 41
4.6. Thickness dependence and scaling length in CIP 49
4.7. Thickness dependence and scaling length in CPP 51
4.8. Temperature dependence 55
4.9. Angular dependence 57
5. Guide to experimental data 58
References 85

1. Introduction

Magnetoresistance (MR) is the change in electric resistance of a conductor by a magnetic field. In nonmagnetic conductors, for example in metals like copper or gold, the MR is due to the Lorentz force that a magnetic field exerts on moving electrons; in general, it is relatively low. In magnetic conductors, for example, in ferromagnetic metals, the spin polarization of the electrons generates other contributions to the MR; for a review, see Campbell and Fert (1982).

A first well-known property of ferromagnetic conductors induced by spin–orbit coupling, is the dependence of resistance on the angle between magnetization and electric current; when a magnetic field is applied, it modifies this angle and thereby the resistance; this is called anisotropic magnetoresistance or AMR. The AMR of ferromagnets does not exceed a few percents at room temperature; however, it is used in a number of applications because the magnetization of a soft ferromagnet can be easily rotated by very small fields. Another type of MR in ferromagnets comes from the so-called spin disorder contribution to the resistivity. Spin disorder at the atomic scale increases the resistivity; by reducing the spin disorder with an applied field, one generates a negative and isotropic MR. This MR is generally low in ferromagnetic transition metals and alloys, but can be very high in other types of ferromagnetic materials, for example, in some mixed valence Mn oxides. Discovered in 1994, the MR of these Mn oxides has been called colossal magnetoresistance or CMR; for a review, see Coey et al. (1999).

The giant magnetoresistance or GMR is another type of MR, existing in heterostructures and discovered in 1988 in Fe/Cr multilayers (Baibich et al. 1988; Binasch et al. 1989). The GMR of multilayers is induced by the variation of the angle between the magnetizations of consecutive magnetic layers. The discovery of the GMR was preceded by the discovery of exchange coupling between magnetic layers across a nonmagnetic metal layer. This interlayer exchange coupling was found in 1986 in Fe/Cr/Fe trilayers (Grünberg et al. 1986), in Gd/Y (Majkrzak et al. 1986) and in Dy/Y (Salamon et al. 1986) multilayers. In Fe/Cr/Fe trilayers or Fe/Cr multilayers, there are ranges of thickness of the Cr layers where the coupling is antiferromagnetic and induces an antiparallel alignment of the magnetizations of adjacent Fe layers. When a magnetic field aligns all the magnetizations in parallel, the resistance of the multilayer decreases dramatically, this was called giant magnetoresistance or GMR.

The discovery of interlayer exchange and GMR has triggered extensive experimental and theoretical studies on multilayers and more general magnetic nanostructures. GMR effects have been observed not only in exchange coupled magnetic multilayers but also in uncoupled multilayers, spin valve structures, multilayered nanowires and granular systems. In multilayers, GMR has been studied not only for current in the plane (CIP) but

also with current perpendicular to the plane of the layers (CPP-geometry). The CPP-GMR has revealed interesting spin accumulation effects which have formed the basis for further developments.

Today GMR is used in various types of device such as sensors, read heads and magnetic RAM. These devices generally operate at very small fields; the interest in multilayers is that only very small fields are required to rotate the magnetization of a soft ferromagnetic layer. While comparable low fields can activate AMR and GMR devices, the amplitude of GMR is larger. On the other hand, the amplitude of the CMR can be much larger, however, its drawback for applications comes from the relatively high field required to alter the magnetization of a ferromagnetic above its spontaneous value.

Beyond GMR of magnetic multilayers and its applications, research on GMR has revealed a new class of magnetotransport phenomena which can be obtained in magnetic nanostructures by making use of the spin polarization of carriers. This is a new field of research which is called "spin electronics". Examples of emerging directions of research with important potential applications in this area are: spin injection effects (Johnson 1993; Berger 1996; Slonczewski 1996; Vasko et al. 1997; Tsoi et al. 1998), spin dependent tunneling (Moodera et al. 1995) and magneto-Coulomb blockade (Barnas and Fert 1998).

The present review is focused on GMR in magnetic multilayers. In section 2, we present an experimental overview which gathers results on conventional multilayers, spin valves, multilayers on grooved substrates and multilayered nanowires. In section 3, we summarize the two-current model of conduction in ferromagnets and present a simple picture of GMR. The physics of GMR is discussed in section 4. We review the theoretical models and make use of selected experimental data to discuss the current understanding of GMR. Section 5 is a guide to experimental data. The related problem of interlayer exchange is not in the scope of this chapter; the reader is referred to the review article of Grünberg et al. (1999) in this series, and also to Rhyne and Erwin (1995) for the special case of rare earth multilayers. For the general problems of preparation and characterization of thin films and multilayers, and also for an earlier review of interlayer exchange and GMR, the reader is referred to Heinrich and Bland (1994).

2. Overview of experimental results

Giant magnetoresistance (GMR) was discovered in 1988 by Baibich et al. (1988) on Fe/Cr (0 0 1) superlattices and by Binasch et al. (1989) on Fe/Cr/Fe (0 0 1) trilayers, in both cases on samples grown by MBE. In fig. 1, we show the variation of the resistance as a function of the magnetic field for Fe/Cr superlattices at 4.2 K. The resistance drops as the configuration of the magnetizations in neighbor Fe layers goes from antiparallel to parallel. Arrows indicate the saturation field H_s, that is the field required to overcome the antiferromagnetic interlayer coupling between the Fe layers and align the magnetizations of consecutive layers. It turns out that aligning the magnetizations reduces significantly the resistivity of the Fe/Cr superlattices, this is called GMR. The magnetoresistance ratio, defined as the ratio of resistivity change to the resistivity in the parallel configuration,

$$\mathrm{MR} = \frac{\rho_{\mathrm{AP}} - \rho_{\mathrm{P}}}{\rho_{\mathrm{P}}},$$

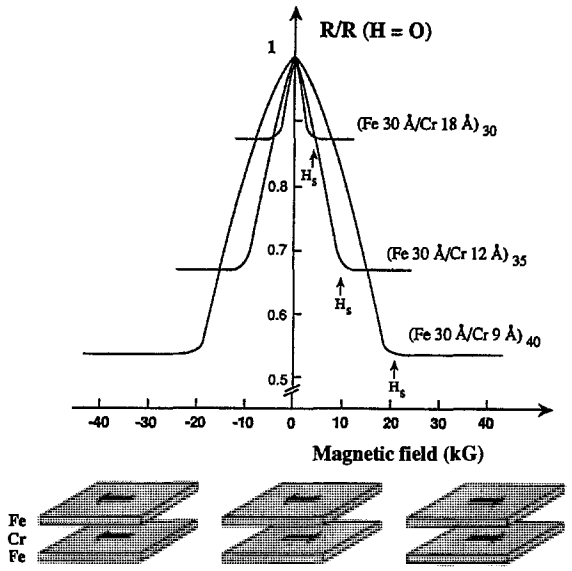


Fig. 1. Magnetoresistance curves at 4.2 K of (Fe/Cr) multilayers. From Baibich et al. (1988).

reaches 79% at 4.2 K, for the sample with 9 Å thick Cr layers shown in fig. 1 (and still 20% at room temperature); note in fig. 1, an alternate definition of the MR is used where the denominator is the resistance at zero field. A record MR ratio of 220% has been obtained in 1994 by Schad et al. (1994a, 1994b) again on Fe/Cr multilayers.

The results of Baibich et al. (1988) and Binasch et al. (1989) were obtained on samples grown epitaxially by MBE. In 1990, Parkin et al. succeeded in reproducing similar GMR effects with Fe/Cr, Co/Ru and Co/Cr multilayers deposited by sputtering, that is with polycrystalline samples. In the perspective of applications, this was of definite interest because sputtering is a simple and fast deposition technique. In addition, Parkin et al. (1990) could explore very broad thickness ranges and find the oscillatory variation of the magnetoresistance which reflects the oscillations of the interlayer exchange coupling as a function of the spacer thickness. GMR effects exist in the thickness ranges where the coupling is antiferromagnetic (AF) and vanish when the coupling is ferromagnetic, as shown in fig. 2 for Fe/Cr.

A more extensively studied system presenting GMR oscillations, found in 1991 (Mosca et al. 1991a; Parkin et al. 1991a), is Co/Cu. As shown in fig. 3, the variation of the MR ratio as a function of the thickness of Cu exhibits three well defined maxima associated with three ranges of antiferromagnetic coupling. The height of the maxima is a decreasing function of the Cu thickness. For thicknesses larger than about 45 Å, the oscillatory behavior disappears and the GMR ratio decreases continuously with the thickness of Cu. In this thickness range, the exchange coupling is weaker than the coercive forces, the magnetic arrangement at a low field is approximately random and the GMR is due to the crossover of the magnetic configuration from random to parallel.

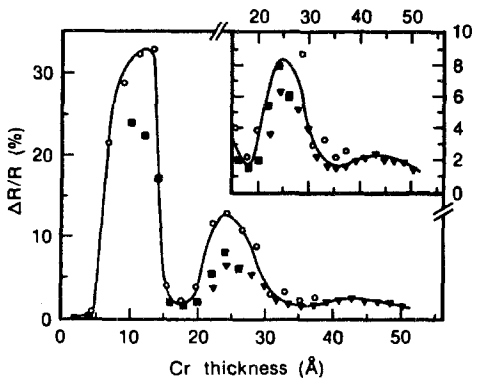


Fig. 2. Transverse saturation magnetoresistance (4.5 K) versus Cr thickness for three series of structures of the form Si(1 1 1)/Cr(100Å)/[Fe(20Å)/Cr(t_{Cr})]$_N$/Cr(50Å), deposited at temperature of ▼, ■ – 40°C (N = 30); ○ – 125°C (N = 20). From Parkin et al. (1990).

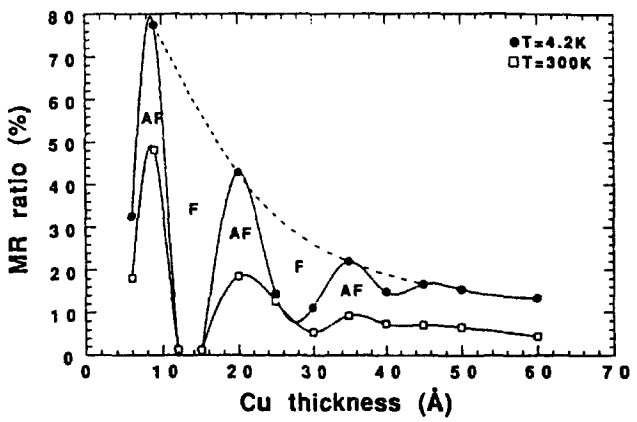


Fig. 3. Variation of the MR ratio as a function of the thickness of Cu for [Co(15Å)/Cu(t_{Cu})]$_{30}$ multilayers. The black circles and squares are for data at 4.2 and 300 K, respectively. The solid lines are guides for the eyes. The dashed line is the envelope of the MR peaks. From Mosca et al. (1991a).

GMR oscillations have been found in a large number of systems but the typical variation as a function of the spacer thickness illustrated in fig. 2 and fig. 3 is not always observed. It frequently occurs that, at small thicknesses of the spacer layer, the AF exchange coupling is reduced (or even reversed) by ferromagnetic coupling by pinholes or defects. Therefore, in some systems, the first GMR peak has a reduced height, as illustrated in fig. 4, or even disappears. Co/Ag is a typical example of a system in which bridging by pinholes suppresses GMR at small thickness of Ag. However, the GMR can be restored when the Co layers are broken into small islands to reduce the deleterious effects of the coupling by pinholes. This can be obtained by depositing only very small thicknesses of Co (Araki et

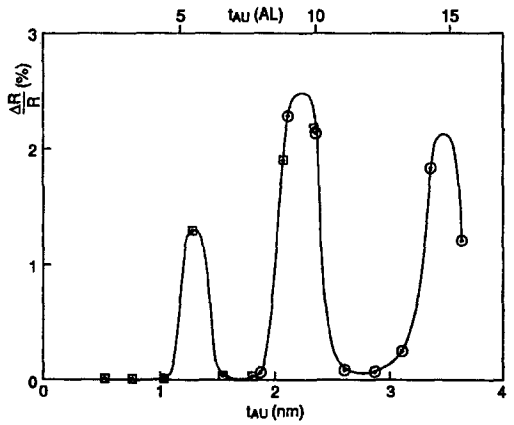


Fig. 4. Magnetoresistance versus gold spacer thickness t_{Au} at room temperature for Au/Co/Au/Co/Au(1 1 1) samples with two Co layers of equal thickness 1.2 nm. The different symbols correspond to two different stepped-wedge samples, each one with eight different gold spacer thicknesses t_{Au}. From Grolier et al. (1993).

al. 1991; Loloee et al. 1995), depositing the Co at low temperature (Rodmacq et al. 1993) or annealing the multilayers (Hylton et al. 1993).

GMR requires that an antiparallel configuration of the magnetizations in the multilayers can be switched into parallel by applying a magnetic field, but AF interlayer exchange is not the only way to obtain an antiparallel configuration. GMR effects can also be obtained with multilayers combining hard and soft magnetic layers (Barnas et al. 1990; Shinjo and Yamamoto 1990; Dupas et al. 1990). As the switching of the magnetizations of the hard and soft magnetic layers occurs at different fields, there is a field range in which they are antiparallel and the resistance is higher, as illustrated in fig. 5 and fig. 6.

The best known structure in which interlayer exchange is not used to obtain an AF configuration and GMR, is the spin valve structure, introduced by Dieny et al. (1991a). A spin valve structure, in its simplest form shown in fig. 7, consists of a magnetically soft layer separated by a nonmagnetic layer from a second magnetic layer, which has its magnetization pinned by an exchange biasing interaction with an antiferromagnetic (FeMn) or ferrimagnetic layer. The nonmagnetic layer is thick enough to minimize the magnetic coupling between the ferromagnetic layers. The operation of the spin valve can be understood from the magnetization and magnetoresistance curves in fig. 8. One of the permalloy layers has its magnetization pinned by the FeMn in the negative direction. When the magnetic field is increased from negative to positive values, the magnetization of the free layer reverses in a small field range close to $H = 0$, whereas the magnetization of the pinned layer remains fixed in the negative direction. Consequently, the resistance increases steeply in this small field range. Only by applying a large positive field can the exchange biasing interaction be overcome; then the pinned permalloy layer switches too and the resistance comes back to its initial value. The steep slope of the resistance variation in a small positive field is now used for many low field applications (sensors, read heads, MRAM).

Several types of spin valve structures have been developed and fig. 7 represents what is called a simple exchange-biased spin valve. Copper is generally used for the nonmagnetic

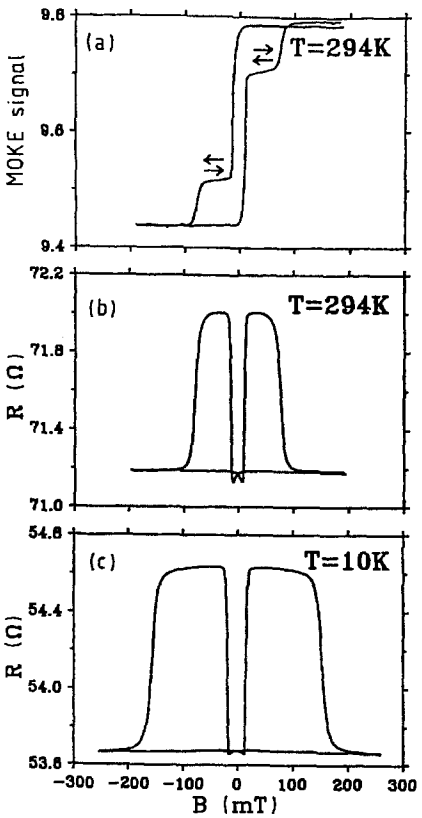


Fig. 5. (a) Moke signal and (b) and (c) resistance of a Co/Au/Co structure with Co film thickness $d = 100$ Å and Au interlayer thickness $d_0 = 60$ Å. The field ranges in which the magnetizations of the two Co layers are antiparallel are indicated by arrows. From Barnas et al. (1990).

layer and the ferromagnetic layers can be layers of permalloy ($Ni_{80}Fe_{20}$), cobalt or NiFeCo alloys. An ultrathin layer of Co can be inserted between permalloy and Cu to enhance the GMR ratio (Parkin et al. 1993). The pinning layer can be an antiferromagnetic compound such as FeMn, a ferrimagnetic alloy of Tb and Co (Freitas et al. 1994a, 1994b) or an antiferromagnetic oxide such as NiO (Anthony et al. 1994; Swagten et al. 1996; Egelhoff et al. 1997b). The highest GMR ratios have been obtained with magnetic layers of Co and NiO for the pinning layer. The advantage of NiO comes from the increased specularity of the reflections of electrons at the metal/oxide interface. A GMR ratio of 15% at room temperature has been obtained by Swagten et al. (1996) with a NiO/Co/Cu/Co/Cu/NiO structure in which the bottom NiO layer is the pinning layer while a NiO over-layer is introduced to improve the specularity of reflections at the top surface. Recently there have been made efforts to further improve the specularity of the reflections and enhance GMR. For example, as shown by Egelhoff et al. (1997a), growth in the presence of a partial pressure of O_2 (acting as a surfactant) creates surfaces and interfaces that scatter the electrons

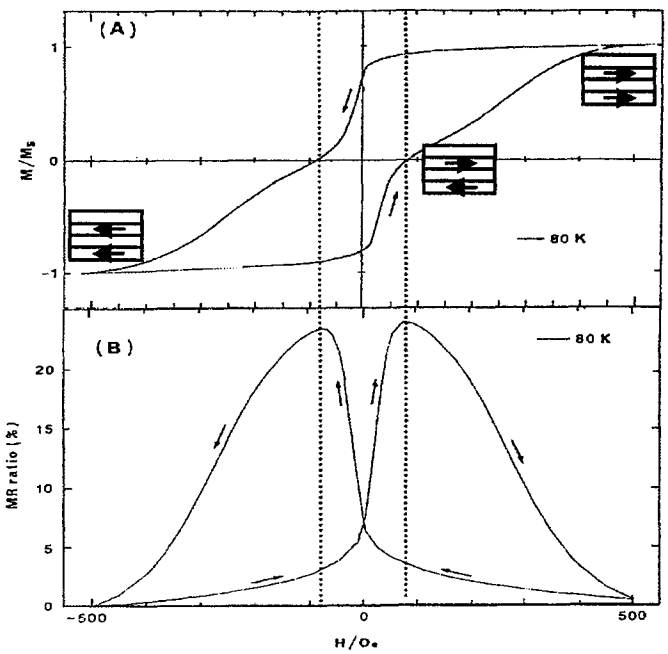


Fig. 6. Magnetic hysteresis (A) and magnetoresistance (B) curves of a [Cu(50Å)/Co(30Å)/Cu(50Å)/NiFe(30Å)]$_{15}$ multilayer. Arrows indicate successive orientations of the magnetizations in Co and NiFe layers as the field increases. From Yamamoto et al. (1991).

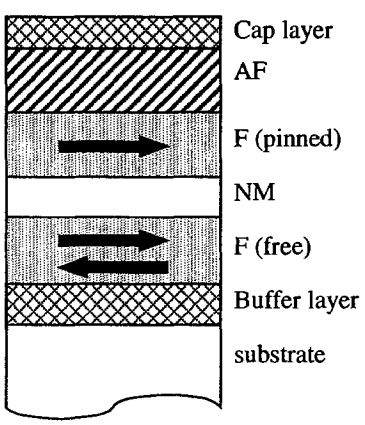


Fig. 7. Schematic cross-section of a "simple" exchange-biased spin-valve layered structure.

more specularly, and also reduce the ferromagnetic bridging across the copper layer. In this way GMR ratios of 19% at room temperature have been obtained (Egelhoff et al. 1997b).

For applications at a very low field, spin valves with permalloy give the best results. In fig. 9, we show an example of GMR curves for $Ni_{80}Fe_{20}$/Cu/$Ni_{80}Fe_{20}$/$Fe_{50}Mn_{50}$

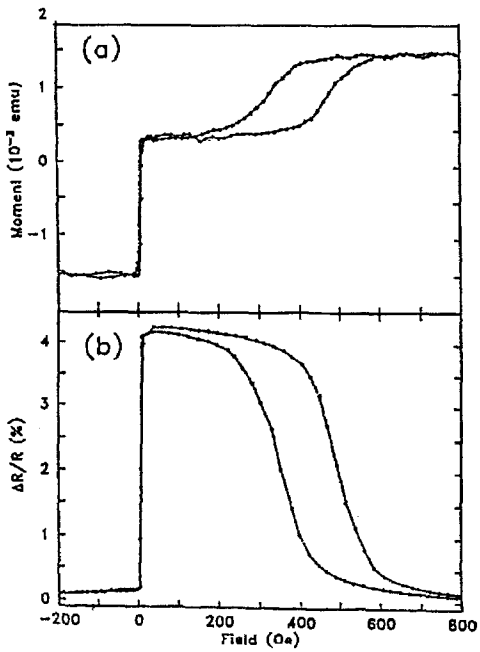


Fig. 8. Hysteresis loop (a) and magnetoresistance (b) of a spin valve [NiFe(60Å)/Cu(22Å)/NiFe(40Å)/FeMn(70Å)] structure at room temperature. The field is swept between ±1 kOe along the easy axis. From Dieny (1993).

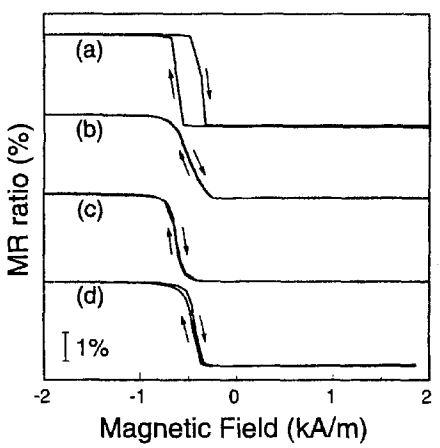


Fig. 9. Low field magnetoresistance of [$Ni_{80}Fe_{20}$(80Å)/Cu(30Å)/$Ni_{80}Fe_{20}$(60Å)/$Fe_{50}Mn_{50}$(80Å)] spin valves with (a) parallel anisotropies, (b) crossed anisotropies field induced during sputtering, and (c) crossed anisotropies induced by annealing (160°C), (d) crossed anisotropies induced during sputtering and by additional thermal treatment. From Rijks et al. (1994).

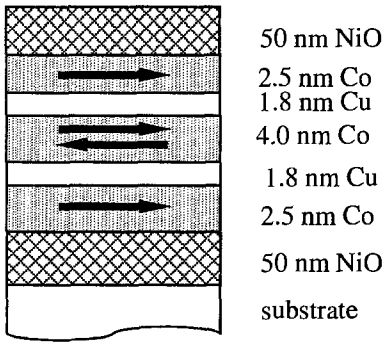


Fig. 10. Typical layer structure of the symmetric spin-valve studied by Egelhoff et al. (1995).

spin valves prepared by sputtering in a magnetic field so as to induce a uniaxial magnetic anisotropy. When the anisotropy directions of the two permalloy layers are parallel (fig. 9(a)), the field sensitivity, defined as $(1/R)(\mathrm{d}R/\mathrm{d}H)$ at the steepest point of the GMR curve, reaches 33%/(A/m); however a drawback for applications is a relatively large hysteresis (0.3 kA/m). In fig. 9(b) with crossed anisotropies obtained by rotating the magnetic field before sputtering the second permalloy layer, the hysteresis is negligible and the sensitivity is still 8%/(kA/m). Curves (c) and (d) are for samples that have been annealed in an applied field, the hysteresis is small and the sensitivity is 18%/(kA/m).

An alternative to the spin valve structure of fig. 7 is the symmetric spin valve of fig. 10 with three magnetic layers. The central magnetic layer is free; the bottom and top magnetic layers are pinned by an exchange biasing interaction. With five metallic layers instead of three in the simple spin valve structure of fig. 7, the proportion of "inactive" electron scattering by the lower and upper surfaces is reduced and a higher GMR ratio is obtained. For example, by growing symmetric spin valves with NiO pinning layers in the presence of a partial pressure of O_2, Egelhoff et al. (1997a) have reached a GMR ratio of 24.8% at room temperature.

All the measurements described above were made with the electric current parallel to the plane of the layers, what is called the Current In Plane or CIP geometry. GMR effects can also be obtained with the Current Perpendicular to the Plane of the layers, that is, in the so-called CPP geometry.

The first measurements in the CPP geometry have been performed at Michigan State University (MSU) by Pratt et al. (1991) by sandwiching multilayers between two superconducting layers of niobium. The geometry of the sample is shown in fig. 11. A bottom strip of Nb is first deposited through a mechanical mask, then the multilayer is deposited through a second mask, and finally the top Nb strip is laid through a third mask. The experiments are performed at 4.2 K by applying a current between e and h and measuring the voltage between g and f. Owing to the superconducting properties of the Nb contacts, a uniform distribution of the current can be realized in the square region where the Nb strips overlap. The difficulty comes from the very low voltage drop between the two Nb strips. With a square area of 1 mm^2, a total thickness of 12 μm for the multilayer, a current

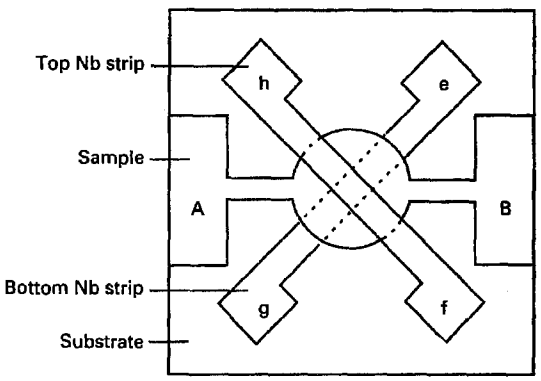


Fig. 11. CPP-MR sample geometry. The CPP MR is measured with the current injected at e and removed at h; the voltage is measured between g and f. The CIP MR is measured by applying current between A and B and measuring voltage between A and B. From Pratt et al. (1991).

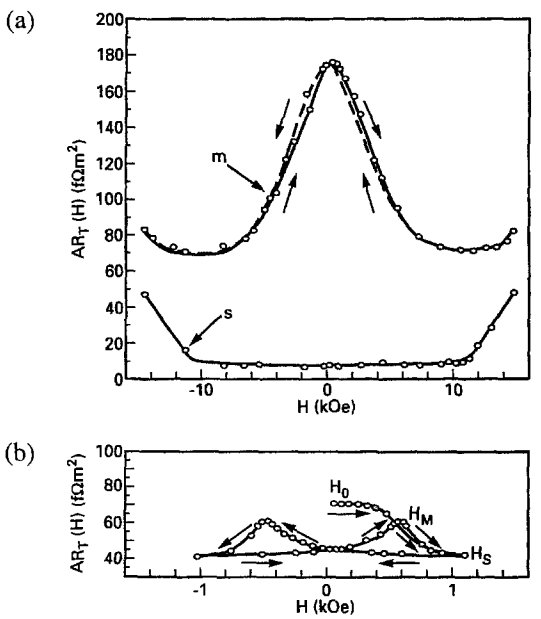


Fig. 12. (a) Resistance versus applied field curve for antiferromagnetically coupled Co/Cu multilayers (d_{Co} = 1.5 nm and d_{Cu} = 0.9 nm, with a 5 nm Fe buffer layer) (curve m), and for a Nb/Co/Nb sandwich (d_{Co} = 9 nm) (curve s). (b) Resistance versus applied field curve for an uncoupled Co/Cu multilayer (d_{Co} = 1.5 nm and d_{Cu} = 4.0 nm). From Pratt et al. (1993a).

of 10^{-2} A and a resistivity of the order of 10^{-8} Ω m, the voltage drop is of the order of 10 nV and a SQUID-based technique was used by Pratt et al. (1991) to measure this small voltage.

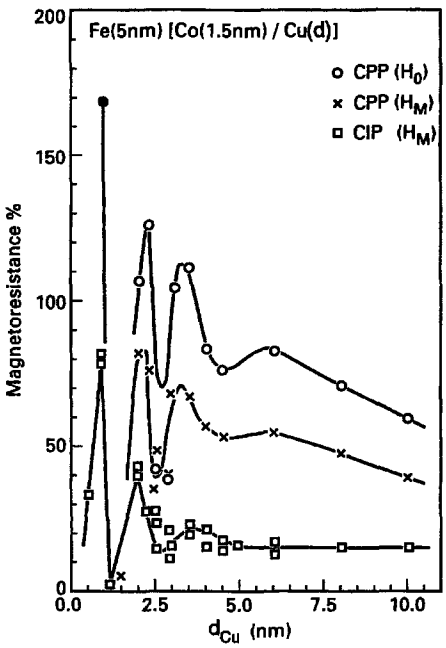


Fig. 13. CPP MR determined from the resistance at zero field (H_0) in the virgin state (○) and at the field H_M corresponding to the MR peak (x) and CIP MR at field H_M (□) against Cu layer thickness d_{Cu} for Co(1.5nm)/Cu(d_{Cu}) multilayers. See the difference between the virgin state and the peak resistance in fig. 12. From Schroeder et al. (1993a, 1993b).

The technique using superconducting contacts and SQUID has been applied at MSU to extensive series of multilayers (Pratt et al. 1993a, 1993b; 1997; Yang et al. 1994a; Bass et al. 1995, 1998) and also at the University of Leeds (List et al. 1995a, 1995b). In fig. 12, we show examples of the magnetoresistance curve recorded at MSU for Co/Cu.

A comparison between the amplitude of the CIP and CPP-GMR for a series of Co/Cu multilayers can be seen in fig. 13. It turns out that the GMR is definitely higher in the CPP geometry. We will also see in sections 4.4 and 4.7 that, in the CPP geometry, GMR effects subsist for much thicker layers than in CIP and can even be observed for individual layer thicknesses in the micron range. It can also be seen in figs 12 and 13 that the resistance of the virgin state (H_0) is higher than the resistance maximum (H_M) obtained by cycling the magnetic field. This difference has been generally observed in the measurements of the MSU group on uncoupled samples and, although not well understood, indicates that the magnetic configuration is different for the virgin state and the "peak" states. As it will be seen in section 4.3, in the long spin diffusion length (SDL) limit of the CPP-GMR, the maximum magnetoresistance is expected not only for antiparallel configurations but also for any configuration for which the magnetization is zero within a volume of the order of the cube of the SDL. The Michigan State University group (Schroeder et al. 1993a, for example) has demonstrated that such a configuration is realized in the virgin state of uncoupled samples, the main argument being that the experimental points for this virgin

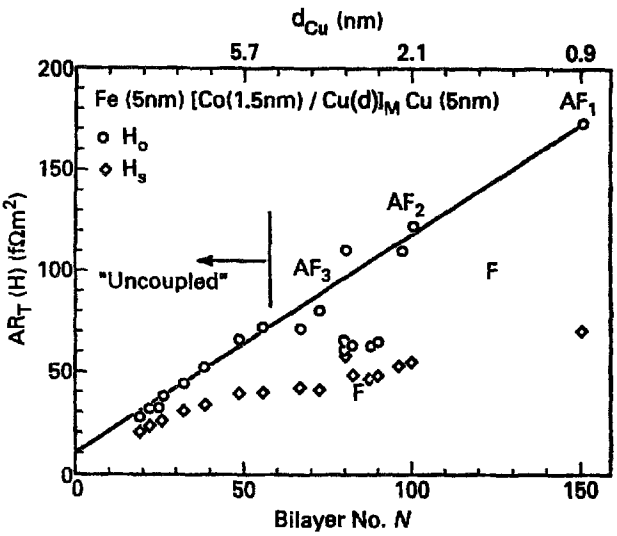


Fig. 14. Resistance in the virgin state (○) and at saturation (✧) against bilayer number N for Co(1.5nm)/Cu(d_{Cu}) multilayers grown on 5 nm Fe buffer layers with fixed total thickness. The data demonstrate the continuous behavior from uncoupled (small N) to antiferromagnetically coupled (AF_1, AF_2, AF_3 refer to the first three AF peaks of the variation with Cu thickness) multilayers. From Schroeder et al. (1993a).

state lie on the same straight line as those corresponding to the antiferromagnetic coupling peaks in plots similar to that of fig. 14. The comparison between CPP measurements on multilayers and spin valves has also confirmed that the virgin state can be taken as a state with zero mean magnetization within the SDL (Steenwyck et al. 1997).

The technique developed at MSU has the advantage of a relatively simple sample preparation. However, measurements can be performed only below the critical temperature of Nb. Several other methods without superconducting contacts have been developed for measurements at higher temperatures and also to avoid the drawbacks of measuring very low signals. Some of these methods are based on lithography and microfabrication techniques. "Pillar"-like samples for CPP-GMR measurements have been fabricated by several groups (Gijs et al. 1993a, 1993b, 1994a, 1994b; Vavra et al. 1995). The fabrication technique by photolithography developed by Gijs et al. (1993a, 1993b) is shown in fig. 15 and leads to pillars with a typical diameter of a few μm and about 1 μm for their height. However, experiments with such structures are not at all straightforward, first, because the measured signal includes significant and not well known contributions from contacts and lead resistances; secondly, because, with the typical dimension quoted above, the current lines are not strictly perpendicular to the planes of the layers. Experiments on pillars have been used to obtain the first data on the temperature dependence of the CPP-GMR (Gijs et al. 1993b; Vavra et al. 1995).

Another technique, developed by Ono and Shinjo (1995), Gijs et al. (1995a, 1995b), Oeps et al. (1996), Maeda at al. (1997), is based on the deposition of multilayers on prestructured substrates. In figs 16(a) and (b), we show a schematic diagram of the surface

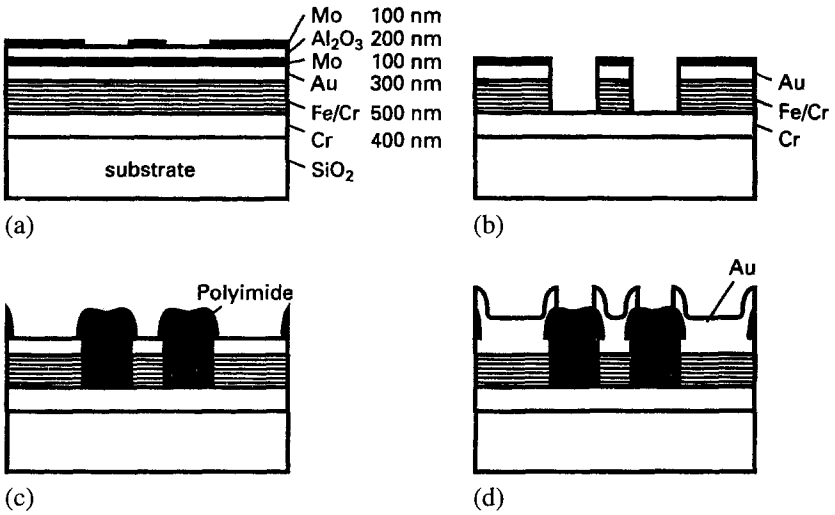


Fig. 15. Schematic diagram of different processing steps in the pillar structuring and contact fabrication. From Gijs et al. (1993c, 1994b).

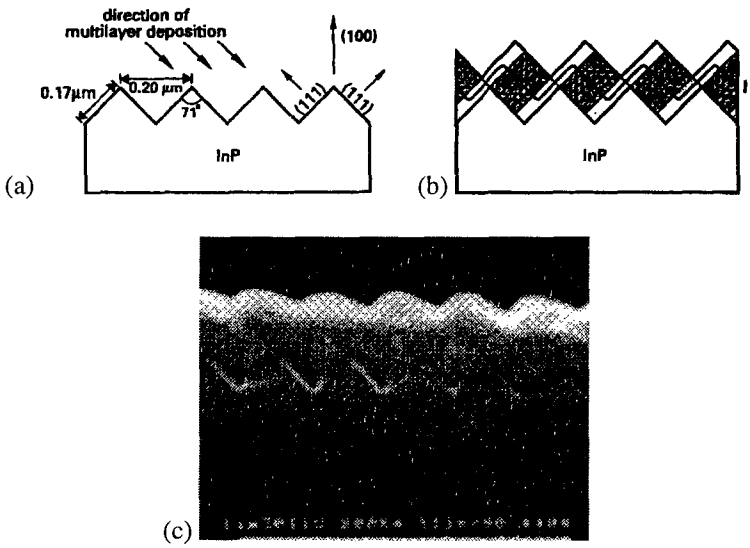


Fig. 16. Schematic diagram of (a) the grooved InP-substrate surface and (b) a multilayer evaporated under an angle with indication of the current flow for the CPP-like case. (c) Scanning electron microscopy picture of the cross-section of the complete structure. From Gijs et al. (1995a).

of an InP grooved substrate and the preparation of a structure for CPP-GMR by oblique deposition of a multilayer (Gijs et al. 1995a, 1995b; Oeps et al. 1996). The CPP-GMR is studied with the current perpendicular to the grooves, while the CIP-GMR can also be

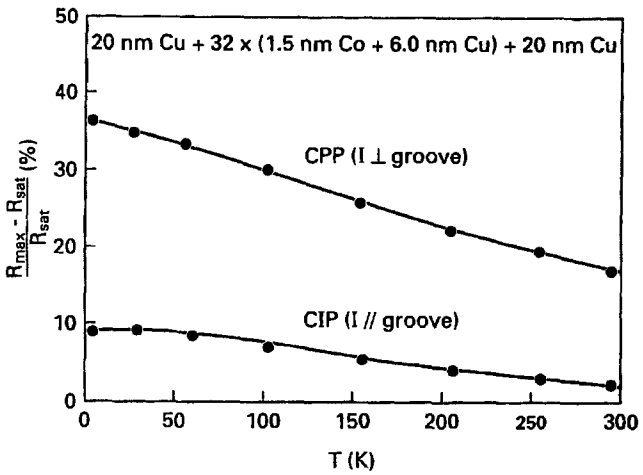


Fig. 17. Temperature dependence of the CPP and CIP MRs of a Cu(20nm)/[Co(1.5nm)/Cu(6.0nm)]$_{32}$/Cu(20 nm) multilayer measured in the CPP-like geometry (I ⊥ groove) and CIP-like geometry (I ∥ groove). From Gijs et al. (1995a).

measured with the same sample when the current is parallel to the grooves. An example of experimental result obtained by Gijs et al. (1995a, 1995b) with this structure is shown in fig. 17. Ono and Shinjo (1995), Maeda et al. (1997) have also used V-grooved substrates to prepare structures in which, when the current is perpendicular to the grooves, it makes an angle intermediate between 0 and 90° with the layer planes, this is the so-called CAP geometry. Its GMR effects are intermediate between CIP and CPP. Sussiau et al. (1997) have also obtained GMR effects intermediate between CIP and CPP by depositing multilayers on silicon substrates prestructured by step bunching.

Finally, the CPP-GMR has also been studied in multilayered nanowires electrodeposited into the pores of nuclear track-etched polycarbonate membranes (Blondel et al. 1994; Piraux et al. 1994, 1996a, 1996b; Liu et al. 1995; Voegeli et al. 1995; Dubois et al. 1997a, 1997b), as illustrated in fig. 18. The very high aspect ratio, with a length of 20–40 mm for a diameter in the range 30–100 nm, guarantees that the current is perpendicular to the layers; also, the relatively large resistance cannot be affected by spurious contact resistances. On the other hand, it is not generally possible to know the number of nanowires that are contacted in parallel (even if Voegeli et al. (1995) succeeded in determining this number in some experiments). Consequently, the measurements can only determine the magnetoresistance ratio and not the absolute value of the resistance of individual wires.

Most experiments on multilayered nanowires have been performed on Co/Cu and NiFe/Cu systems. Except in the earliest experiments, the GMR ratios obtained with nanowires are very similar to those measured with conventional multilayers in the CPP geometry, at least for layers thicker than a couple of nm. This indicates the good quality of multilayers obtained by the electrodeposition technique, in agreement with the results of structure characterization (Piraux et al. 1998 and Maurice et al. 1998, for example). An example of the experimental GMR curve for nanowires is shown in fig. 18(b).

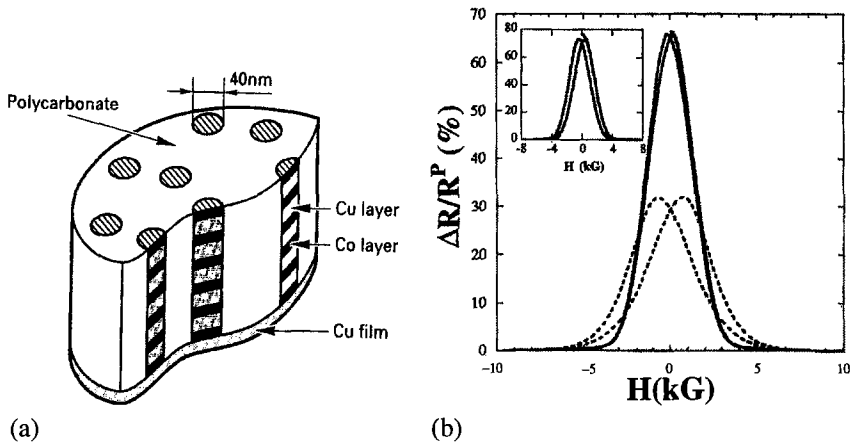


Fig. 18. (a) Schematic representation of the array of nanowires in an insulating polymer matrix. From Piraux et al. (1994) and (b) Magnetoresistance versus applied field parallel to the layers at $T = 77$ K for NiFe(12nm)/Cu(4nm) (—) and Co(10nm)/Cu(5nm) (- - -) multilayered nanowires; inset: same plot at 4.2 K for the NiFe/Cu sample. From Dubois et al. (1997a).

GMR effects can be obtained not only in multilayers but also in granular systems (Berkowitz et al. 1992; Xiao et al. 1992). Although the physics in both types of the system is very similar, we will limit our review to multilayers. We simply mention that some structures are really intermediate between multilayers and granular alloys, e.g., multilayers with discontinuous magnetic layers that can be viewed as layers of clusters (Hylton et al. 1993; Loloee et al. 1995), and also "hybrid structures" combining continuous magnetic layers and layers of magnetic clusters, with large GMR effects can be obtained at a very low field (Holody et al. 1994).

3. Simple picture of GMR

3.1. Two-current model for the conduction in ferromagnets

The GMR is related to the spin dependence of the conduction in ferromagnetic metals and alloys (Mott 1936; Fert and Campbell 1968, 1976; Farrel and Greig 1970; Loegel and Gautier 1971; Dorleijn and Miedema 1976; Campbell and Fert 1982). At low temperature ($T \ll T_c$), when the spin flip scattering of the conduction electrons by magnons is frozen out, the spin mixing rate is much lower than the momentum relaxation rate and there is conduction in independent parallel channels by the spin-↑ (majority) and spin-↓ (minority) electrons. The resistivity of the ferromagnet is then expressed as

$$\rho = \frac{\rho_\uparrow \rho_\downarrow}{\rho_\uparrow + \rho_\downarrow}, \tag{1}$$

where $\rho_\uparrow$ ($\rho_\downarrow$) is the resistivity of the spin-↑ (-↓) channel. In a given channel σ, the parameter ρ_σ includes the contributions from s, d, and s–p or s–d hybridized electrons and from

various scattering processes. The asymmetry between the two channels is characterized by spin asymmetry coefficients:

$$\alpha = \rho_{\downarrow}/\rho_{\uparrow}, \tag{2}$$

or, alternatively,

$$\beta = \frac{(\rho_{\downarrow} - \rho_{\uparrow})}{(\rho_{\downarrow} + \rho_{\uparrow})} = \frac{\alpha - 1}{\alpha + 1}. \tag{3}$$

There are several origins for the difference between $\rho_{\uparrow}$ and $\rho_{\downarrow}$. Schematically, the resistivity ρ_{σ} can be written as a function of the number n_{σ}, effective mass m_{σ}, relaxation time, τ_{σ} and density of states (DOS) at the Fermi level $n_{\sigma}(E_{\mathrm{F}})$ of spin σ electrons in the following way

$$\rho_{\sigma} = \frac{n_{\sigma} e^2}{m_{\sigma} \tau_{\sigma}}. \tag{4}$$

For a given type of scattering potential characterized by its matrix elements V_{σ} and in the Born approximation

$$\tau_{\sigma}^{-1} \sim |V_{\sigma}|^2 n_{\sigma}(E_{\mathrm{F}}). \tag{5}$$

There are intrinsic origins of the spin dependence of ρ_{σ} that are related to the spin dependence of n_{σ}, m_{σ}, or $n_{\sigma}(E_{\mathrm{F}})$ in the host metal. For example, in Ni and Co, the spin-$\uparrow$ DOS at the Fermi level comes from only s–p electrons and is definitely smaller than the spin-$\downarrow$ DOS (s–p + d); consequently, there is a tendency to have $\rho_{\uparrow} < \rho_{\downarrow}$ in Ni and Co-based systems. Actually, the ratio α can exceed 10 for many Ni and Co based alloys (Campbell and Fert 1982; Mertig et al. 1993).

On the other hand, there are also extrinsic origins of the spin dependence of ρ_{σ} related to some spin dependence of the impurity or defect potential V_{σ}. We take the well known example of Ni containing Cr impurities (Campbell and Fert 1982; Mertig et al. 1993). The magnetic moment of Cr impurity is opposite to that of the Ni atoms, which indicates there is a strong repulsive potential for the spin-$\uparrow$ d-electrons. The hybridization of the d$\uparrow$ states of Cr with the band d$\uparrow$ of Ni is replaced by the hybridization with the s$\uparrow$ band of Ni to form a virtual bound state and to a strong scattering in the spin-$\uparrow$ channel in agreement with the experimental result of a coefficient $\alpha < 1$.

The ratio α has been derived from resistivity measurements for many Ni-, Co- and Fe-based alloys (see Campbell and Fert (1982) for extensive tables of experimental data, Mertig et al. (1993, 1994), Irkhin and Irkhin (1996) for their interpretation).

Away from the low temperature limit it is necessary to take into account the transfer of momentum between the two channels of conduction by spin-flip electron–magnon scattering. Spin-$\uparrow$ (spin-$\downarrow$) electrons are scattered to spin-$\downarrow$ (spin-$\uparrow$) states by annihilating (creating) a magnon and the transfer of momentum from the fast to the slow channel – the

so-called spin-mixing effect – tends to equalize the two currents. In this case the general expression of the resistivity is

$$\rho = \frac{\rho_\uparrow \rho_\downarrow + \rho_{\uparrow\downarrow}(\rho_\uparrow + \rho_\downarrow)}{\rho_\uparrow + \rho_\downarrow + 4\rho_{\uparrow\downarrow}}, \tag{6}$$

where $\rho_{\uparrow\downarrow}$ is the spin mixing resistivity term (Fert and Campbell 1976).

3.2. Simple picture of GMR

In fig. 19(a) we illustrate the mechanism of GMR. In the parallel configuration, the electrons of the spin '+' and spin '−' channels are, respectively, majority and minority electrons in all the magnetic layers, and this gives different resistances r_+ and r_- for the two channels. The final resistance is

$$r_P = \frac{r_+ r_-}{r_+ + r_-}. \tag{7}$$

If, for example, r_+ is much lower than r_-, the current is shorted by the spin '+' channel of fast electrons and $r_P \approx r_+$ (throughout the article, our notation is '+' and '−' for the spin directions corresponding to $s_z = +1/2$ and $s_z = -1/2$, z being an absolute axis, and $\uparrow$ and $\downarrow$ for the majority and minority spin directions inside a ferromagnet). In the antiparallel configuration, electrons of both channels are alternatively majority and

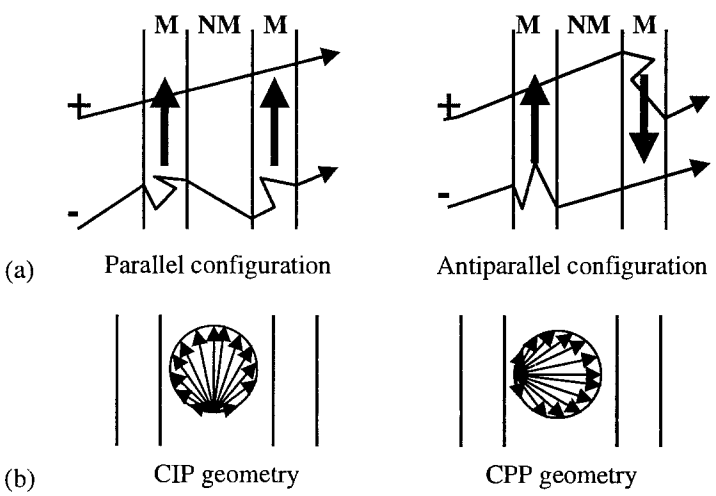


Fig. 19. (a) Schematic picture of the GMR mechanism. The electron trajectories between two scatterings are represented by straight lines and the scatterings by abrupt changes in direction. The signs + and − are for spins $s_z = +1/2$ and $-1/2$, respectively. The arrows represent the majority spin direction in the magnetic layers. (b) Schematic picture of the current distribution in k space for CIP and CPP geometries.

minority spin electrons and the shorting by one of the channels disappears. The resistance is $(r_+ + r_-)/2$ for both channels and the final resistance is

$$r_{AP} = \frac{r_+ + r_-}{4} > r_P. \tag{8}$$

If r_+ is much lower than r_-, $r_{AP} \approx r_-/4$ is much higher than $r_P \approx r_+$. This gives a GMR ratio of

$$\text{GMR} = \frac{r_{AP} - r_P}{r_P} = \frac{(r_- - r_+)^2}{4r_+r_-}. \tag{9}$$

The above simple picture holds for both the CIP and CPP geometries. However, as illustrated in fig. 19(b), the current is distributed differently among the electron wave vectors for CIP and CPP; even in the limit of uniform spatial averaging we are considering for this simple picture, the averaging in k-space is different in the two geometries. In general, this can give different CIP and CPP values for the ratio r_-/r_+ entering eq. (9) and different MR ratios in CIP and CPP. This point will be discussed in section 4.5.

The above simple picture no longer holds when the thickness of the layers becomes larger than the electron MFP (typically 10 nm in nonmagnetic layers, a few nm in a ferromagnetic layer), at least in CIP. For example, when the thickness of the nonmagnetic layers, t_N, becomes larger than the MFP in these layers, λ, there is no overlap between the respective effects of two consecutive magnetic layers on the electron distribution function, and the GMR decreases as $\exp(-t_N/\lambda_N)$. This is discussed in section 4.6. In the CPP geometry, due to spin accumulation effects, the scaling length becomes the spin diffusion length l_{sf}, as shown in section 4.3. The spin diffusion length (SDL) is related to spin flip scattering and can be much larger than the MFP. It is only when the thickness t_N of the nonmagnetic layers exceeds the spin diffusion length l_{sf}^N in the nonmagnetic material that the CPP-GMR decreases as $\exp(-t_N/l_{sf}^N)$. The thickness dependence in CPP is discussed in sections 4.3 and 4.7.

4. Physics of GMR: theoretical models and comparison with experimental data

4.1. Introduction to physics of GMR and theoretical models

Several types of theoretical models have been developed for GMR; some of them focus on spin dependent scattering of the electrons, others on the dependence of the band structure on the magnetic configuration. We sketch the potential landscape for conduction electrons in fig. 20. The potential for electrons can be separated into intrinsic potential of the multilayered structure and extrinsic scattering potentials due to defects.

(i) The intrinsic potential is a potential of perfect structure. It is periodic for periodic multilayers; its period is equal to the chemical period of the multilayer for the parallel (P) configuration (figs 20(a) and (b)) and to twice the chemical period for the antiparallel (AP) configuration (fig. 20(c)). In fig. 20, the intrinsic potential is represented by a Kronig–Penney potential. The exchange splitting of band structures in the ferromagnetic

layer is depicted by different heights of the steps of the Kronig–Penney potential in the spin '+' (fig. 20(a)) and spin '−' (fig. 20(b)) channels for the P configuration. In the AP configuration (fig. 20(c)), low and high steps alternate.

(ii) The scattering potentials are random extrinsic potentials associated with defects (impurities, structural defects, interface roughness) and are represented by spikes in fig. 20. In a first approximation, the interface scattering potentials can be viewed as an excess or deficit potential due to some modulation of the steps by roughness. They are obviously spin-dependent since the steps are at the interfaces between magnetic and nonmagnetic metals. The scattering potentials of impurities and defects within the magnetic layers are also spin dependent, as it is well known from experiments on bulk materials (Fert and Campbell 1976).

Both, the intrinsic potential (the steps in fig. 20) and the scattering potentials (spikes in fig. 20) generate GMR for CIP as well as for CPP geometry.

The GMR generated by spin dependent scattering has been introduced in the earliest models (Camley and Barnas 1989) and can be described very simply. For example, it is clear that, with the small scattering potentials in the spin − channel of fig. 20(b), there will be a short circuit effect by this channel with weak scattering and this will give a smaller resistivity for the P configuration.

The mechanism of GMR generated by intrinsic potentials can also be understood straightforwardly. The simplest case to consider is that of a superlattice with a low concentration of defects so that the MFP is much larger than the period of the superlattice.

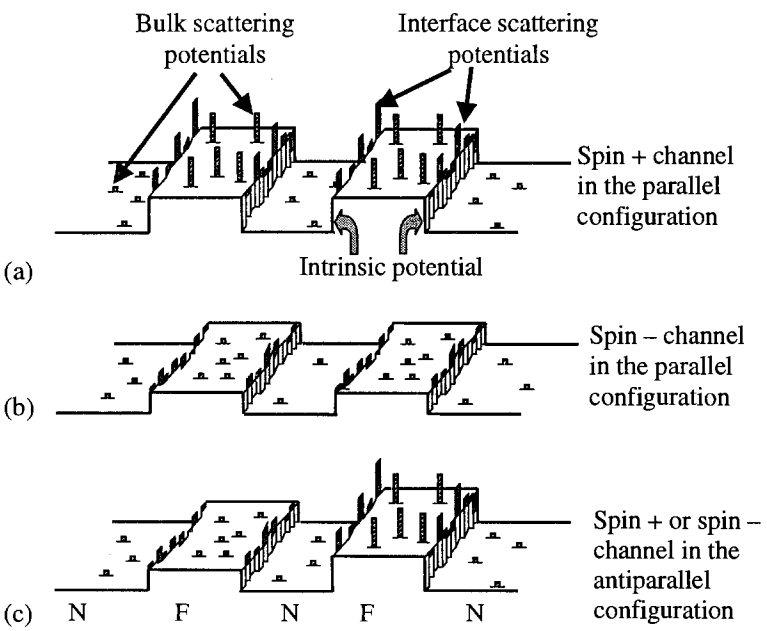


Fig. 20. Potential landscape for spin + and spin − conduction electrons in the parallel and antiparallel configurations. The intrinsic potential is represented by a periodic array of steps (Kronig–Penney-like potential); the bulk and interface scattering potentials are represented by spikes.

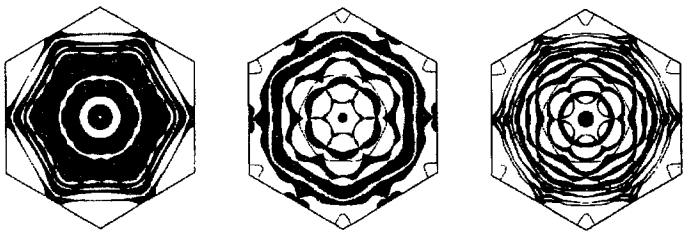


Fig. 21. Projections inside the first Brillouin zone of different Fermi surfaces for a (1 1 1) oriented Co_3/Cu_3 multilayer on a plane parallel to the interfaces. (a) Majority spin and (b) minority spin in the parallel configuration, (c) either spin in the antiparallel configuration. From Schep et al. (1998).

Then, the periodic intrinsic potential determines Bloch functions for the superlattice; these functions, as well as the Fermi surfaces and Fermi velocities, are different for the periodic potentials of fig. 20(a), (b) and (c). In fig. 21, we show an example of Fermi surfaces calculated for a Co_3/Cu_3 superlattice. Conduction in parallel by the spin '+' Fermi surface of fig. 21(a) and spin '−' Fermi surface of fig. 21(b) for the P configuration is not equivalent to conduction by the spin '+' and spin '−' Fermi surfaces of fig. 21(c) for the AP configuration. This gives rise to GMR effects even with only spin independent scatterings.

If the MFP is not much larger than the period (as in many real multilayers), the fine gap structure of fig. 21 is blurred out and a superlattice approach becomes less appropriate. In this regime the contribution from the intrinsic potential to the GMR is more appropriately described by taking into account specular reflections of electrons of metal A at the interface with metal B and neglecting the interference between reflections at successive interfaces that builds the superlattice Bloch functions. In this layer by layer approach for the CPP geometry, the effect of the intrinsic potential is expressed by a spin dependent interface resistance, see section 4.3.

The possible twofold contribution to GMR from scattering and intrinsic potentials initially leads to theoretical models which focused on one or the other mechanisms. Progressively, theorists have tried to take into account both mechanisms within the same models. But as it will be seen below, treating both mechanisms on equal footing is not an easy task. We will also see from the analysis of experimental results that, although the GMR strongly depends on spin-dependent scattering effects, the influence of the intrinsic potential is also fairly important and cannot be neglected.

Apart from the microscopic origin of the GMR discussed above, another important problem for theory is that of the scaling lengths governing the decrease and collapse of GMR as the thickness of the layers increases. Experimentally GMR decreases much more rapidly with the thickness of the layers in the CIP than in the CPP geometry; this is due to the different scaling lengths governing the thickness dependence in CIP and CPP. Scaling lengths will be discussed more in detail in sections 4.3, 4.6 and 4.7. We will see that the scaling length involved in CIP is a relatively short MFP, whereas spin accumulation effects make the scaling length in CPP a much longer spin diffusion length (SDL).

4.2. Theoretical models of the CIP-GMR

GMR has triggered a large number of theoretical approaches that we summarize in this paragraph. The reader can also look at the excellent review by Levy (1994).

The first models of CIP-GMR were based on the picture of free electrons scattered by a distribution of spin-dependent scatterers that depend on the magnetic configuration of the multilayer. These models – *semi-classical* or *quantum mechanical* – focus on *spin-dependent scattering* effects and neglect the influence of the *intrinsic potential* of the multilayer.

Since 1992, the *intrinsic potential* has been progressively introduced into the models in addition to the *scattering potentials*. In the case where the MFP is comparable to the layer thickness or smaller, the interference of reflections by steps at different interfaces is unimportant. This justifies a *layer by layer* approach taking into account specular reflections by interfaces, but neglecting the interference between reflections from different interfaces. When the MFP is much larger than the period of the multilayer, the coherent scattering by successive interfaces builds *superlattice bands*. This leads to a different type of model in which the *superlattice band structure* (or the quantum well band structure if the system is not periodic) is first calculated before introducing the *scattering* in a second step. *Ab initio* models have been developed in this way, ab initio referring to only the first part of the calculation in which the band structure is calculated before introducing scattering effects.

The main difficulty with a theoretical approach to GMR is that real systems are generally *intermediate* between the situations described by the *layer by layer* and *superlattice* models. The effects of scattering that are always present can blur out a great part of the features predicted by superlattice models; on the other hand, layer by layer models a priori neglect any quantum interference effects.

4.2.1. Semi-classical models

The first model of GMR was the semi-classical model of Camley and Barnas (1989). This model is based on the picture of free electrons scattered by a distribution of spin dependent scatterers that depends on the magnetic configuration of the multilayer, and uses a Boltzmann equation formalism. Bulk scattering is taken into account by introducing spin dependent (spin independent) relaxation times in the magnetic (nonmagnetic) layers. Interface scattering is described by introducing boundary conditions at the interfaces, that is, by assuming that a proportion T_σ of the spin σ electrons is transmitted without scattering, while the proportion $(1 - T_\sigma)$ is diffusely scattered (a probability of specular reflection can also be introduced). The major success of this model was that it predicted the thickness dependence of the GMR. It shows that the influence of the spin-dependent scattering on the electron distribution function does not extend further than about the MFP inside the nonmagnetic layers, so that the resistance becomes independent of the relative orientation of consecutive magnetic layers when they are apart by more than the MFP.

The semi-classical approach of Camley and Barnas (1989) has been further developed in a large number of papers, and extensively applied to the interpretation of experimental data (Binasch et al. 1989; Dieny et al. 1992a, 1992b; Ustinov and Kravtsov 1995). Analytical expressions of the GMR have been derived by Barthélémy and Fert (1991) in the simple case where only interface scattering is spin dependent. It is found that, in the limit of a thick layer, the MR ratio depends on the nonmagnetic layer thickness t_N as $\exp(-t_N/\lambda_N)$,

where λ_N is the MFP in the spacer, while the variation as t_F^{-1} at large values of t_F reflects the progressive dilution of the spin dependent interface scattering.

A difficulty with the approach of Camley and Barnas (1989) is that the interface and bulk scatterings are not treated on an equal footing. To overcome this difficulty, Johnson and Camley (1991) represented the strong scattering by the disorder at the interface by an interfacial layer in which is a short MFP. This approach allowed Johnson and Camley (1991) and Duvail et al. (1994) to give a more physical interpretation of experimental data.

All the models described above focus on scattering effects and neglect the influence of the multilayer intrinsic potential. To take this into account, Hood and Falicov (1992) studied the effect of specular reflections from potential steps introduced into the semi-classical model of Camley and Barnas (1989). For thick enough layers superlattice coherence effects can be neglected and this layer by layer approach can, in principle, reasonably describe the influence of potential steps. However, the number of free parameters in such a phenomenological approach becomes so large that the model of Hood and Falicov (1992) cannot be really used for quantitative interpretations.

4.2.2. Kubo formalism

The first quantum mechanical model of the GMR was introduced by Levy et al. (1990a). The model uses the Kubo formalism to calculate the conductivity of free electrons scattered by spin-dependent potentials:

$$V(\vec{r}, \hat{\sigma}) = (v + j\hat{M} \cdot \hat{\sigma})(\vec{r} - \vec{r}_a), \tag{10}$$

where the operator $\hat{\sigma}$ represents the Pauli spin matrix, and $\vec{M}$ is a unit vector in the direction of magnetization. The scattering centers $\vec{r}_a$ are randomly distributed in the layers and in the plane of the interfaces, with $v = v_N$, $j = 0$ in the nonmagnetic layers, $v = v_M$, $j = j_M$ in the magnetic layers, $v = v_S$, $j = j_S$ at the interfaces. The model of Levy et al. (1990a) uses the Kubo formalism in momentum space. Other models have been worked out with the Kubo formalism in the real space to describe the same problem of free electrons scattered by spin-dependent potentials of the form of eq. (10) (Vedyayev et al. 1992; Camblong and Levy 1992; Camblong et al. 1993; Camblong 1995). Models of this type based on the Kubo formalism have been applied to interpret the thickness dependence of the GMR in several systems (Levy et al. 1990a, 1990b; Gijs and Okada 1992; Vedyayev et al. 1992; Zhang et al. 1992). Zhang and Butler (1994) reviewed several of the above models and, for the simple case of a metallic film, compared their results with those of another approach also based on the Kubo formalism but under the assumption of uniformly distributed scattering rates (instead of uniformly distributed scattering centers).

All the above early models using the Kubo formalism assume free electrons and do not introduce the intrinsic potential of the multilayer (step in fig. 20). Since 1993, this intrinsic potential has been progressively introduced into most models (Zhang and Levy 1993a; Vedyayev et al. 1993; Barnas 1994; Bulka and Barnas 1995). In fig. 22, we show some results of Zhang and Levy (1993a) on the variation of the GMR with the parameter U which characterizes the step height for the majority spin direction introduced in the Kronig–Penney intrinsic potential of the model. The conclusion of the authors is that the introduction of a spin-dependent intrinsic potential can enhance or reduce the GMR significantly

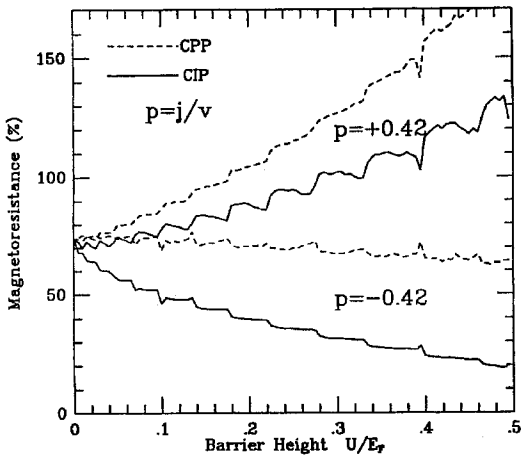


Fig. 22. The CIP and CPP magnetoresistance as a function of barrier height U for the majority spin direction with fixed $p = p_S = p_M = 0.42$. The barrier height is zero for the minority spin direction. p_S (p_M) represents the ratio j/v of the j and v terms of eq. (10) for interface (bulk) scattering. From Zhang and Levi (1993a).

if U is not much smaller than the Fermi energy. However, a quantitative prediction is difficult with only a phenomenological one band model. Very different values of the exchange splitting U are expected for the s and d electrons and, without additional information on the s and d contributions to the current, it is difficult to introduce a realistic value of U into the model. The limit of phenomenological models appears at this stage.

In addition to the above approaches based on the Kubo formalism, another type of quantum mechanical model has been worked out by Barnas and Bruynseraede (1995, 1996). In this model, developed for (ferromagnetic/spacer/ferromagnetic) trilayers, the method introduced by Calecki (1989, 1991) is used to describe the scattering of quantum well states by impurities and interface roughness. The model presents another interesting example of interplay between effects, respectively, due to the intrinsic potential (the well) and defect potentials. It also predicts quantum size oscillations of the GMR for ultrathin layers.

4.2.3. Ab initio models

Most ab initio models start with first-principle calculation of the electronic structure for a perfect superlattice. The results on the superlattice band structure are then used to describe the transport properties in various ways, generally by introducing relaxation times in the transport equations to take into account the scattering effects. The change of band structure induced by scattering is not generally taken into account, which means that most ab initio models only aim at describing the limit of very perfect superlattices (the opposite limit is that of the layer by layer models). Also, ab initio models generally introduce global relaxation times for the whole system and, therefore, cannot describe the reduction of the contribution from spin-dependent scattering to GMR when the layer spacing is larger than the MFP. Consequently, the ab initio models are generally appropriate for the interpretation of GMR effects in the limit of very thin layers with a small concentration of

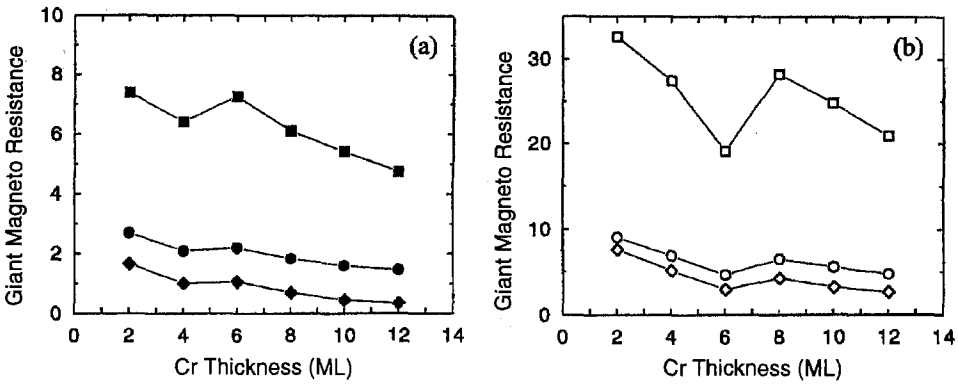


Fig. 23. Calculated GMR ratio for Fe_3/Cr_n as a function of the Cr layer thickness from 2 to 12 monolayers (ML). The results assuming Cr defects in Fe layers are indicated by squares ($\beta = 0.11$). Dots mark the results for spin independent scattering ($\beta = 1$) and diamonds for the value of β which minimizes the GMR. (a) CIP geometry (closed symbols). (b) CPP geometry (open symbols). From Zahn et al. (1995).

defects. However, in this limit, they are the only models able to give a realistic description of the GMR.

Zahn et al. (1995) have calculated the electronic structure of Fe/Cr superlattices by using the spin density functional theory within the framework of an optimized LCAO scheme. They also calculate from first principles the spin-dependent relaxation times for the scattering by Cr impurities in bulk Fe. Both, the results of the band structure calculation (Fermi surface and velocities) and the relaxation times are introduced into a Boltzmann equation model of transport. In fig. 23, we show the GMR ratio calculated for $Fe_3/Cr_n(0\,0\,1)$ superlattices. The GMR found with a spin-independent, i.e., $\beta = 1$, relaxation rate reflects only the influence of the magnetic configuration on the band structure. Its maximum value is 220%. When spin-dependent relaxation rates calculated for Cr impurities in Fe (with $\beta = 0.11$) are introduced into the calculation, the GMR is much higher and reaches the maximum value of 750%. It turns out that, as in many ab initio calculations, the GMR ratios are higher than the experimental ones. This is not really surprising, first, because the band structure contribution is certainly reduced by imperfections in the superlattices, and, second, because it would be necessary to know all the scattering processes (impurities, structural defects, interface roughness) to derive the spin asymmetry of the total scattering in a realistic way. Also, most models do not take into account the spin–orbit coupling which is expected to reduce the spin asymmetry.

Ab initio calculations of the type described above have been also applied by the Dresden group to Co/Cu and Fe/Cu/Co multilayers (Binder et al. 1997). In recent publications (Binder et al. 1998), the theory has been improved by calculating the contribution of defects of different types located at different positions in the multilayer.

Ab initio models have also been worked out for Co/Cu, Fe/Cr, Ni/Cu and $Ni_{80}Fe_{20}$/Cu multilayers by Nesbet (1994, 1996), Butler et al. (1993, 1995), Kai et al. (1998), Moser et al. (1998) and Blaas et al. (1998). In the models developed by Butler et al., the interface disorder in Co/Cu and the structural disorder of permalloy layers are treated in the Coherent

Potential Approximation (CPA) to obtain average Green functions and the conductivity is calculated using the Kubo formalism. This is an appropriate approach to take into account the influence of imperfections on the band structure. The difficulty still comes from the poor knowledge of imperfections of the real systems. This certainly explains that, again, the calculated GMR ratios are much higher than the experimental ones.

Finally, an interesting approach is that developed by Stiles (1996) with ab initio calculations of transmission and reflection coefficients for Ag/Fe, Au/Fe, Cu/Co and Cu/Ni interfaces. Interestingly, these coefficients can be used to understand both the GMR and oscillatory exchange coupling; also, they can be used to calculate interface resistances in the CPP-geometry. Bruno (1995) presents a similar calculation for Co/Cu interfaces based on a tight binding LMTO model.

4.2.4. Mesoscopic models

While the layered structures in which GMR has been observed up till now are in the regime of diffuse transport, there have been at least two calculations of the GMR in the mesoscopic limit, i.e., when there are so few impurities so that the nature of the wave functions over the entire structure dominates the transport.

In a series of papers Maekawa's group has considered the magnetoresistance of nanostructures containing isolated scatterers (Oguri et al. 1992; Asano et al. 1993). In their approach they calculate the wave functions of the entire structure in the presence of a specific distribution of these scatterers. With these functions they calculate the conductance for the distribution of impurities by using either the Kubo linear response formalism or, equivalently, the Landauer formula. They repeat the calculation of the wave functions and ensuing conductance for a large number of different realizations for the distributions of impurities, and finally take the average of conductances as the "conductance" one would observe for a macroscopic sample. For magnetic multilayers they repeat these calculations for both the parallel and antiparallel aligned configurations of the magnetic layers and thereby obtain the GMR. A great difference of calculations done in the diffuse regime is that in the mesoscopic regime the conductance is calculated for a given distribution of impurities and this is subsequently averaged over different realizations of the distribution of impurities; in the diffuse regime one can take a "short cut" and calculate the conductance by using impurity averaged propagators, i.e., those which have been averaged over a random distribution of impurities or, equivalently, propagators for a fictitious medium in which the impurities are uniformly distributed over the lattice. The drawback of this mesoscopic approach is that one is limited in the size of systems one can study by one's computational resources.

Bauer and coworkers (Bauer 1992; Schep et al. 1998; Asano et al. 1993) go to the ballistic limit where there is no impurity scattering at all and determine the GMR that ensues solely from the changes in the electronic band structure when a magnetic multilayer goes from parallel to antiparallel alignment of its magnetic layers. In this approach, they calculate the band structure (Bloch state wave functions) of a superlattice (they assume periodicity of the multilayer) for the ferromagnetic and antiferromagnetic configurations of the magnetic layers. They calculate the conductivity either by using the Landauer–Buttiker formalism for the conductance, or by calculating the current across a small cross section, as one does in the kinetic theory of gases. Their derivation of the ballistic conductance "... is analogous to the calculation of molecular diffusion of a dilute gas through a small hole in

response to a pressure gradient". With their treatment they were able to demonstrate the importance of s–d hybridization in producing the spin polarization of the itinerant electrons on the Fermi surface. Their results show that the GMR produced by changes of the band structure is high; their results are applicable to systems where the transport is ballistic. This is not the case for the systems in which GMR has been observed until now; however, there are attempts underway to achieve ballistic transport in magnetic multilayers through either point contacts or nanostrictions.

More recently Mathon and coworkers have focused on the oscillations in the GMR that can be found in the ballistic regime (Mathon et al. 1995; Mathon 1997). The most important result is that, independently of the oscillations of coupling, there are additional oscillations which come from the difference between the potential of the different layers.

4.2.5. Calculations of spin-dependent scattering

The spin dependent scattering terms introduced in most models above can arise from various scattering sources, structural defects or impurities inside the layers, rough or interdiffused interfaces, etc. Calculations have been developed to understand the spin dependence of these various scattering processes.

The spin dependence of scattering by impurities in magnetic layers is already well documented from previous experimental works on bulk materials (see Campbell and Fert (1982) for a review) and from calculations worked out to understand the experimental data. In addition to early virtual bound state models (Friedel 1967), we can refer to recent ab initio calculations by Drittler et al. (1989), Mertig et al. (1993, 1994), Irkhin and Irkhin (1996). The results of Mertig et al. (1993) for impurities in Ni are shown in fig. 24. Zahn et al. (1998) have also calculated the scattering by impurities located at various positions in Co/Cu multilayers. This calculation shows that the spin asymmetry of the scattering by a given impurity, compared to its value in a bulk metal or a thick layer, can be enhanced or reduced depending on its position in the multilayer.

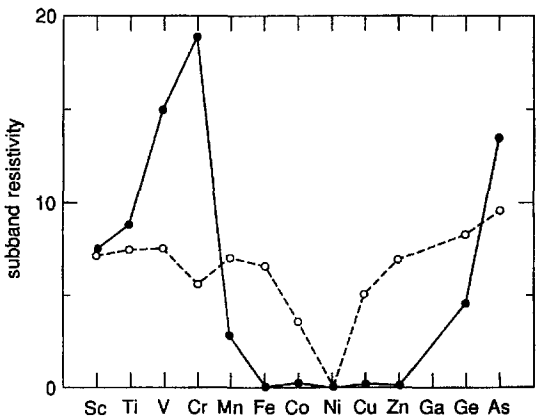


Fig. 24. Calculated subband resistivities $\rho_\uparrow$ (solid line) and $\rho_\downarrow$ (broken line) in $\mu\Omega$ cm/at% for 3d and 4sp impurities in Ni. From Mertig et al. (1993).

The Coherent Potential Approximation (CPA) has been used to determine the amount of scattering that comes from substitutional disorder out of the low defect concentration limit. This method is particularly appealing as one can simultaneously treat the intrinsic potential as well as the scattering by disorder. Calculations of resistivity and GMR of magnetic multilayers based on CAP have been done by Butler et al. (1993), Itoh et al. (1995), Inoue (1996).

In the early years of GMR, models of virtual bound state type similar to those for impurities have been also applied to describe the spin dependence of interface scattering (Inoue and Maekawa 1991; Coehoorn 1995). Now the spin dependence of interface scattering has also been obtained in a number of ab initio calculations, for example, by Butler et al. (1993, 1995) and Nesbet (1994) for scattering by rough interfaces in Fe/Cr.

It is interesting to compare the spin asymmetry of the scattering by the roughness of an interface A/B with that by an impurity B in the ferromagnetic metal A. There is some similarity in a number of systems. For example, the spin-↑ electrons are scattered less in Co doped with Cu (Binder et al. 1997) and at Co/Cu interfaces (Nesbet et al. 1994), while they are scattered more in Fe doped with Cr (Mertig et al. 1993) and at Fe/Cr interfaces (Nesbet 1996).

Most calculations of interfacial scattering are based on a simple picture of an interface with atoms A diluted in the first layer of B and vice versa. However, several publications have tried to discuss the different effects expected from different types of roughness. For example, geometrical roughnesses (i.e., non-planar interfaces) can have different length scales which leads to different effects on interface scattering (Hood et al. (1994)). An example of a quantum mechanical approach to a similar problem is presented by Zhang and Levy (1996) and Gu et al. (1997) who have shown that correlated scattering from pairs of interdiffused impurities can produce enhanced spin-dependent scattering.

4.3. Theoretical models of the CPP-GMR, spin accumulation effects

Compared to GMR in the CIP geometry, the CPP-GMR presents a *disadvantage* and an *advantage* for the theorist.

The *disadvantage* is that it is necessary to introduce spin relaxation (i.e., spin-flip scattering) to describe how the CPP-GMR depends on the layer thickness. This has been recognized for the first time by Zhang and Levy (1991a) who showed that, without spin relaxation and, consequently, with current conservation in each spin channel, the CPP-GMR remains finite when the layer thickness increases to infinity. Valet and Fert (1993) have shown that this non-physical result disappears when spin relaxation is taken into account and found that the spin diffusion length becomes the scaling length governing the decrease of the CPP-GMR at large layer thickness. However, the difficulty for a theorist is that spin-flip and spin-relaxation are difficult to introduce in most theoretical treatments and, up till now, have been taken into account only in Boltzmann equation models.

The *advantage* of the CPP-GMR is that, on one condition, the effect of the multilayer intrinsic potential (steps in fig. 20) can be simply expressed by introducing a spin-dependent interface resistance. The condition is that the mean free path (taking into account both bulk and interface scatterings) is not much larger than the period of the multilayer. This makes that the electron reflected by different interfaces does not interfere coherently with forming superlattice Bloch functions and justifies a layer by layer approach instead of a superlattice

model. In this situation, which is the most frequent in experiments, the intrinsic contribution to GMR is expressed by a spin dependent interface resistance; more precisely, the interface resistance includes contributions from both the intrinsic potential (interface steps in fig. 20) and the random scattering potentials giving rise to diffuse scattering at the interface (spikes in fig. 20). Interface resistances have been calculated for several types of interface potentials, i.e., for the step of a perfect Kronig–Penney potential by Barnas and Fert (1994a), Dieny et al. (1995), for the step of a Kronig–Penney potential with random defects by Barnas and Fert (1994b), Dugaev and Litvinov (1995), Ustinov and Kravtsov (1995), Zhang and Levy (1996) and for perfect interfaces in the ab initio model of Co/Cu by Schep et al. (1997).

In this limit of low potential steps and weak diffuse scattering by interface defects, the intrinsic contribution and the contribution from diffuse scattering to the interface resistance are simply additive (Barnas and Fert (1994b)). However, Zhang and Levy (1998) have shown that perturbative treatments for the calculation of interface resistance are not really appropriate and have found that the contributions from diffuse scattering and intrinsic potential should not be simply additive. In fact, interface diffuse scattering can enhance as well as reduce the intrinsic interface resistance. In addition, Schep et al. (1997) have shown that the intrinsic interface resistance also depends on the amount of scattering within the layers between two interfaces and becomes constant only in the limit of "diffuse bulk propagation". This limit seems relevant for the interpretation of experiments, not only because it allows Schep et al. (1997) to obtain a reasonable agreement for the spin dependent resistances of Co/Cu interfaces, but also since, in a number of systems, the interface resistances and their spin dependence appear to be nearly independent of the layer thickness and impurity concentration (Pratt et al. 1993a, 1993b; Lee et al. 1995, see fig. 27).

4.3.1. Theoretical models with spin relaxation

It is important in the CPP geometry to take into account spin relaxation because perpendicular transport in magnetic multilayers generates spin accumulations that must be balanced by spin relaxation, as described by Valet and Fert (1993) or Fert et al. (1994).

Suppose, for example, the situation illustrated in fig. 25(a), that is two semi-infinite ferromagnetic layers with opposite magnetizations separated by a thin nonmagnetic layer. We consider a flux of electrons going from left to right. If, for example, the conductivity in the ferromagnetic material is larger for the majority spin electrons, the incoming flux is carried in a large part by the spin '+' electrons, while the outgoing flux is carried by the spin '−' electrons. This implies that the spin '+' electrons must accumulate in the central region before flipping and thus being able to continue across the zone in the spin '−' channel. Because the spin life time is relatively long and much longer than the momentum life time, the spin '+' accumulation diffuses and spreads faraway from the central region; in fact, as far as the spin diffusion length (SDL, defined below). It goes without saying that charge neutrality leads to a symmetric depression of the spin '−' electrons. Spin '+' accumulation and spin '−' depression imply a splitting of the spin '+' and spin '−' chemical potentials (Fermi energies), as illustrated in fig. 25(b). The damping length governing the decrease of this splitting is the SDL of the corresponding material. The gradient of the spin dependent chemical potentials gives rise to spin dependent pseudo-electric fields that slow down the faster electrons, accelerate the slower ones and, on the whole, increase the effective

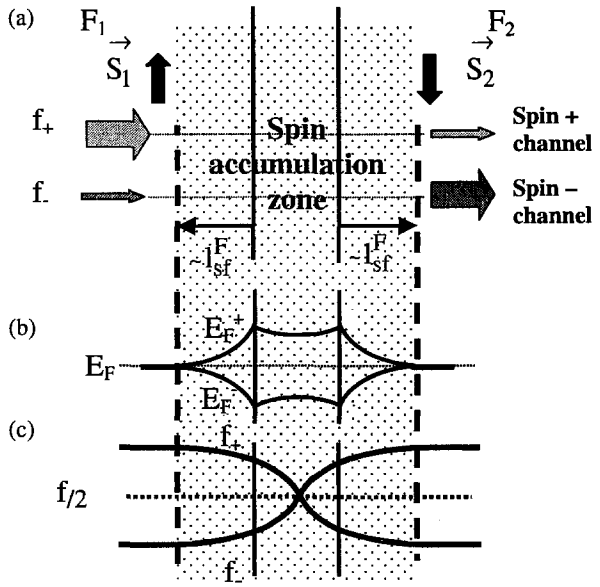


Fig. 25. (a) Illustration of spin accumulation effects in the case of two semi-infinite layers (F_1, F_2) with opposite spin directions ($\vec{S}_1$, $\vec{S}_2$) separated by a thin nonmagnetic layer (N with $t_N < l_{sf}^N$). There is an electron flux from left to right. Far from N in F_1, the incoming spin '+' flux, f_+, is larger than the incoming spin '−' flux, f_-, whereas far from N in F_2, $f_+ < f_-$. The resulting accumulation of spin '+' electrons (and the depletion of spin '−') extends to about a distance l_{sf}^F from N on both sides of N. (b) In the spin accumulation zone, the chemical potential is split into E_F^+ and E_F^-. In (c) we show the variation of the electron flux in each spin channel (f is the total flux).

resistivity for the broad spin accumulation region. The net result, when one compares the resistivity of the parallel and antiparallel configurations, will be a large magnetoresistance that subsists for layers as thick as the SDL (which is much larger than the mean free path).

The model of Valet and Fert (1993) is a Boltzmann equation-type model in which a modified Boltzmann equation describes not only the displacement of the electron distribution function associated with the current but also the spin splitting of the chemical potential due to spin accumulation. In addition to the usual relaxation term for the momentum, the Boltzmann equation of Valet and Fert also includes a spin-lattice relaxation term describing the relaxation of spin accumulation by spin-flip scattering. In the limit where the momentum relaxation times $\tau_\uparrow$ and $\tau_\downarrow$, are much shorter than the spin-lattice relaxation times τ_{sf}, a simple solution can be found by taking terms of first order in $\tau_{\uparrow(\downarrow)}/\tau_{sf}$. The following notation is generally used in the calculation of the magnetoresistance of a multilayer:

$$\rho_{\uparrow(\downarrow)}^F = 2\rho_F^*[1 - (+)\beta], \tag{11}$$

$$\rho_{\uparrow(\downarrow)}^N = 2\rho_N^*, \tag{12}$$

$$r_{\uparrow(\downarrow)} = 2r_b^*[1 - (+)\gamma], \tag{13}$$

for, respectively, the spin-↑ and spin-↓ resistivities of the ferromagnetic metal, $\rho_{\uparrow}^{F}$ and $\rho_{\downarrow}^{F}$, the (equal) spin-↑ and spin-↓ resistivities of the nonmagnetic metal, $\rho_{\uparrow}^{N}$ and $\rho_{\downarrow}^{N}$, and the interface resistances per unit area, $r_{\uparrow}$ and $r_{\downarrow}$. β and γ are, respectively, the bulk and interface scattering spin asymmetry coefficients. Equations (40)–(42) of Valet and Fert (1993) give general expressions for the resistance in the parallel (P) and antiparallel (AP) configurations, R^{P} and R^{AP}, as a function of

$$\rho_{F}^{*}, \quad \rho_{N}^{*}, \quad r_{b}^{*}, \quad \beta \quad \text{and} \quad \gamma;$$

$$t_{N}/l_{sf}^{N} \quad \text{and} \quad t_{F}/l_{sf}^{F},$$

where t_N (t_F), l_{sf}^{N} (l_{sf}^{F}) are, respectively, the thickness and SDL of the nonmagnetic (ferromagnetic) layers. The SDL in the ferromagnetic layers is related to the mean free paths $\lambda_{\uparrow} = v_F\tau_{\uparrow}$ and $\lambda_{\downarrow} = v_F\tau_{\downarrow}$, and to the spin mean free path $\lambda_{sf} = v_F\tau_{sf}$ by the relation:

$$l_{sf}^{F} = \left[\frac{\lambda_{sf}}{3(1/\lambda_{\uparrow} + 1/\lambda_{\downarrow})}\right]^{1/2}. \tag{14}$$

In the nonmagnetic layers, eq. (14) becomes

$$l_{sf}^{N} = \left[\frac{\lambda_{sf}\lambda}{6}\right]^{1/2}. \tag{15}$$

We do not reproduce here the general expressions of R^{P} and R^{AP} of the Valet–Fert (VF) model but only simple expressions obtained in several limits.

In the long SDL limit, when the individual layer thicknesses are much smaller than the SDL, i.e., $t_N \ll l_{sf}^{N}$, $t_F \ll l_{sf}^{F}$, the VF model predicts simple expressions that are equivalent to those derived by the phenomenological resistor series model of Lee et al. (1992). There are several ways of writing down these expressions:

$$\left[\left(R^{AP} - R^{P}\right)R^{AP}\right]^{1/2} = \beta\,\frac{t_F L}{t_F + t_N}\,\rho_F^{*} + 2N\gamma r_b^{*}, \tag{16a}$$

$$\left[\left(R^{AP} - R^{P}\right)R^{AP}\right]^{1/2} = N\left[\beta\rho_F^{*}t_F + 2\gamma r_b^{*}\right], \tag{16b}$$

$$\left(\frac{R^{AP} - R^{P}}{R^{AP}}\right)^{-1/2} = \frac{\rho_F^{*}t_F + 2r_b^{*}}{\beta\rho_F^{*}t_F + 2\gamma r_b^{*}} + \frac{\rho_N^{*}t_N}{\beta\rho_F^{*}t_F + 2\gamma r_b^{*}}, \tag{17}$$

$$R^{AP} = N\left[\rho_F^{*}t_F + \rho_N^{*}t_N + 2r_b^{*}\right]. \tag{18}$$

R^{P} and R^{AP} are the resistances of a unit area of the multilayer, N is the number of periods, $L = N(t_N + t_F)$ is the total thickness.

Equation (16a) has been frequently used at Michigan State University (Pratt et al. 1993a, 1993b, for example) to account for experimental data on multilayers with constant L,

$t_N = t_F$ and variable N. It predicts a linear variation as a function of N with a slope proportional to γ and an intercept with the axis $N = 0$ proportional to β. For constant L and constant t_F, eq. (16b) predicts a proportionality to N with the slope depending on the value of t_F. Finally eq. (17) predicts a linear variation of $(\Delta R/R^{AP})^{-1/2}$ with t_N, with all the straight lines obtained for different values of t_F crossing at a single point whose vertical coordinate is β^{-1}.

Although in the initial VF model (Valet and Fert 1993), expressions of the type of eqs (16)–(18) have been derived in the simple case where R^P and R^{AP} are the resistances of parallel and antiparallel configurations, it can be shown (Fert et al. 1995a) that, in the long SDL limit, the resistance has the same maximum value R^{AP} for a true antiparallel configuration and for a state with zero net magnetization in a volume of the order of the cube of the cube of the SDL; the equivalence of AP and random configurations has also been demonstrated by Zhang and Levy (1993a) in a similar limit.

Simple limits of the VF expressions can also be obtained when the layer thicknesses are much larger than the SDL. For $t_N \gg l_{sf}^N$ with $t_F \ll l_{sf}^F$, the magnetoresistance ratio is expected to decrease as $\exp(-t_N/l_{sf}^N)$. In the opposite situation of a very thick ferromagnetic layer, i.e., for $t_F \gg l_{sf}^F$ with $t_N \ll l_{sf}^N$, the GMR ratio (Piraux et al. 1996a, 1996b, 1998) is given by

$$\frac{(R^{AP} - R^P)}{R^P} = \frac{2p\beta^2 l_{sf}^F}{(1-\beta^2)t_F}, \tag{19}$$

where p is the proportion of antiparallel configurations between consecutive magnetic layers ($p = 1$ for a perfect AP configuration). Equation (19) expresses that only a depth l_{sf}^F on both sides of a magnetic layer is "active" in this limit.

Extensions of the VF expressions to structures other than the simple F/N multilayers have also been worked out by several authors (Steenwyck et al. 1997; Dubois et al. 1999).

4.3.2. Models without spin relaxation

Although models without spin relaxation lead to the unphysical result of a finite GMR for an infinite layer thickness (Zhang and Levy 1991a), these models are interesting to describe the limit where the spin relaxation can be ignored (thin layer limit) and to discuss the validity of the approximations of the model with spin relaxation presented in the preceding paragraph (VF model).

In the Kubo formalism, Zhang and Levy (1993a) compared the CIP and CPP-GMR predicted by a model taking into account both an intrinsic superlattice potential of the Kronig–Penney type and some amount of spin-dependent scattering. Their results are presented in fig. 22. The oscillations are superlattice effects. It is interesting to notice that, without the intrinsic potential (i.e., for $U = 0$), the same GMR ratio is found for CIP and CPP. When the intrinsic potential is introduced (i.e., for $U \neq 0$), the CIP and CPP-GMR are different (the CPP-GMR is larger), which illustrates the different role of the intrinsic potential in CIP and CPP. This appears also in a layer by layer approach; in CPP, the intrinsic potential gives rise to an interface resistance (see, for example, Schep et al. 1997), whereas there is nothing like in CIP; in contrast, as emphasized in section 4.5, the intrinsic potential gives rise to important channeling effects in CIP; out of the thin layer limit, the difference in

scaling length, MFP and SDL, respectively, also contribute to the difference between CIP and CPP.

The difference between CIP and CPP-GMR has also been discussed in several models using the Kubo formalism by Asano et al. (1993), Itoh et al. (1995), Vedyayev et al. (1997a) and in the semi-classical approach by Ustinov and Kravtsov (1995). Ab initio calculations have been developed by Butler et al. (1993) and Mertig and coworkers (Zahn et al. 1995). Results of Zahn et al. (1995) for the CIP and CPP-GMR of Fe/Cr superlattices are presented in fig. 23. The ballistic limit has been treated by Mathon et al. (1997) and Schep et al. (1998).

Finally, Mathon (1996, 1997) has discussed the case of multilayers with a fluctuating layer thickness and predicted an enhancement of the GMR by Anderson localization-like effects in pseudo random-structures.

4.4. Quantitative analysis of GMR data

4.4.1. CIP-GMR

The first analysis of CIP-GMR data was done with models based on spin-dependent scattering in Boltzmann or Kubo formalism. An example is shown in fig. 26; Gijs and Okada (1992) fitted their data on Fe/Cr multilayers with the model of Levy et al. (1990a) based on the scattering potential of eq. (10). However, they could not determine unambiguously all the parameters in eq. (10); their only definite conclusion was that a large value of the interface spin asymmetry p_s is needed to account for the steep decrease of the GMR with the thickness of Cr. As a matter of fact, there are always difficulties for a quantitative analysis of experimental data of CIP-GMR. First, the thickness dependence can be

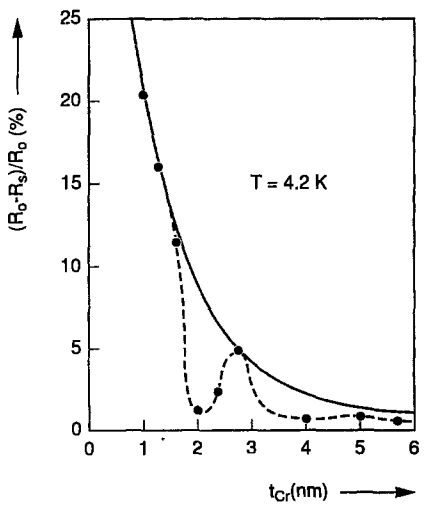


Fig. 26. GMR ratio for Fe(30Å)/Cr multilayers versus Cr thickness. The experimental data (black dots) are obtained at 4.2 K. The solid lines are calculated within the quantum model of Levy et al. (1990a). From Gijs and Okada (1992).

due to several independent effects, i.e., (i) the progressive decoupling of the scattering in neighbor magnetic layers as the ratio t_{Cr}/λ_{Cr} varies, (ii) the variation of the proportion of interface and bulk scattering, and (iii) the decrease of the degree of antiparallel ordering as the interlayer coupling decreases (in fig. 26, Gijs and Okada have implicitly assumed a perfect AP configuration at the first and second maxima and a reduced one at the third maximum). Secondly, models based on the assumption of free electrons are approximate and, in particular, ignore the additional effects due to the intrinsic potential of the multilayer. In summary, the large number of free parameters, the uncertainty in the degree of antiparallel ordering when the thickness varies in the nanometer range, the uncertainty resulting from the approximations, all conspire to make it difficult to quantitatively analyze CIP-GMR data with this type of model.

As we have described in section 4.2, the first generation of models based only on spin-dependent scattering of free electrons, have been improved by introducing the intrinsic potential in a phenomenological way (Hoods and Falicov 1992; Zhang and Levy 1993a, 1993b; Vedyayev et al. 1993; Barnas 1994). However, in this type of model, the number of free parameters becomes so large that they can be hardly used for a realistic and quantitative analysis of experimental results.

The comparison between ab initio predictions and experimental data also presents important difficulties. First most ab initio calculations have been worked out for layers containing a very small number of atomic planes, a thickness range which is often out of the reach of current experiments. The interest in ab initio models is thus generally limited to the interpretation of the limit of the GMR ratio at a very small thickness. The main problem is that most ab initio calculations predict GMR ratios that are much larger than the experimental ones. This can be seen on the data of fig. 23 (Zahn et al. 1995) and from the calculations performed for Co/Cu, NiFe/Cu or Fe/Cr by Butler et al. (1993, 1995) or Nesbet (1994, 1996). This discrepancy is mainly due to the difficulties that theorists encounter when they leave the ab initio approach and introduce phenomenological parameters to represent the scattering by imperfections. It is necessary to introduce the scattering by imperfections, first, because ignoring the scattering effects leads to overestimates of the contribution of the superlattice effects (intrinsic potential), secondly, because the spin dependence of the scattering also contributes to the GMR. The spin dependence of the scattering depends on the type of defect and a realistic prediction would require a precise knowledge of the proportion of different defects.

4.4.2. CPP-GMR

The quantitative analysis of experimental data in the CPP-geometry is much easier than in the CIP-geometry. As described in section 4.3, for the most frequent situation encountered, with negligible effects arising from quantum interferences between reflections from many successive interfaces, the main advantage of the CPP-GMR is that the influence of the intrinsic potential can be described by its contribution to the spin dependent interface resistance. In CPP, this interface resistance is an essential parameter, summing up contributions from both the intrinsic potential of the multilayer and the interface scattering potentials (Barnas and Fert 1994b; Dugaev and Litvinov 1995; Zhang and Levy 1998).

The second advantage of the CPP-geometry is that the resistance and magnetoresistance can be expressed by analytical expressions as a function of a relatively small number of

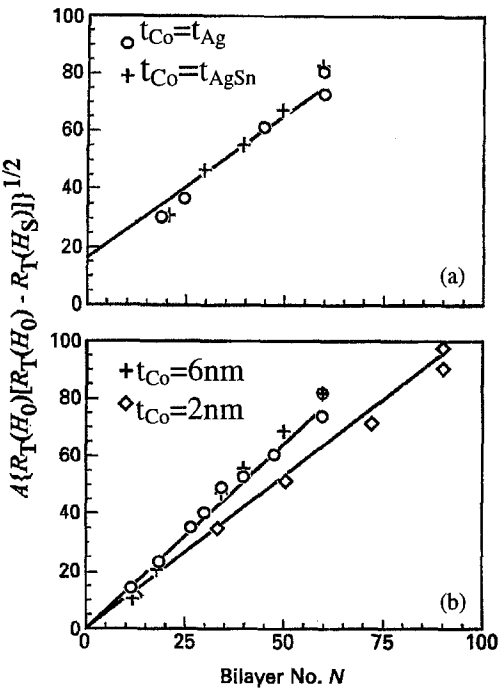


Fig. 27. $A[R_T(H_0)[R_T(H_0) - R_T(H_s)]]^{1/2}$, where A is the sample area, $R_T(H_0)$ the resistance in the virgin state and $R_T(H_S)$ the resistance at saturation, against N for Ag/Co and AgSn/Co multilayers with a fixed total thickness, $L = 0.72$ μm and (a) $t_{Co} = t_{Ag} = t_{AgSn}$ and (b) $t_{Co} = 6$ nm and 2 nm with t_{Ag} varying. The resistivities of the Ag and AgSn layers are, respectively, 1 μΩ cm and 18 μΩ cm. From Pratt et al. (1993a).

parameters (ρ_F^*, ρ_N^*, r_b^*, β, γ, l_{sf}^N, l_{sf}^F, in the notation of section 4.3.1). In addition, in a very broad range of thickness corresponding to the long SDL limit ($t_F \ll l_{sf}^F$, $t_N \ll l_{sf}^N$), these expressions become very simple and relate the resistance and magnetoresistance to only five parameters (ρ_F^*, ρ_N^*, r_b^*, β, γ), as it can be seen in eqs (16)–(18).

Most measurements of CPP-GMR performed at Michigan State University (Pratt et al. 1993a, 1993b; Schroeder et al. 1993a, 1993b; Lee et al. 1995; Bass et al. 1998) on Co/Cu, Co/Ag, $Ni_{80}Fe_{20}$/Cu and $Ni_{80}Fe_{20}$/Ag multilayers have been fit with expressions of the type of eqs (16) and (18). For $t_F = t_N$, L = constant and varying N, eq. (16a) predicts a linear variation of $(\Delta R\, R^{AP})^{1/2}$ with N, as observed in the experimental results of fig. 27(a) for Co/Ag multilayers. Once the values of ρ_F^*, ρ_N^*, r_b^* have been derived from independent fits of R^{AP} with eq. (18), the slope of the linear variation of $(\Delta R\, R^{AP})^{1/2}$ with N gives the interface scattering spin asymmetry coefficient γ and the coordinate of the intercept with the axis $N = 0$ gives the bulk spin asymmetry coefficient β.

In the same way, for constant L and t_F, eq. (16b) predicts that $(\Delta R\, R^{AP})^{1/2}$ is proportional to N, with different slopes for different values of t_N, as illustrated by the experimental results of fig. 27(b) for Co/Ag. We also note that the experimental data of fig. 27(a) for pure Ag ($\rho_{Ag}^* = 1$ μΩ cm) and an AgSn alloy ($\rho_{AgSn}^* = 18.5$ μΩ cm) lie on the same straight line. This is in agreement with eq. (16b), where ρ_N^* does not appear. This also

means that the parameters r_b^* and γ are insensitive to a great variation of the scattering rate inside the layers, or, in other words, that r_b^* and γ have reached their value of the completely diffuse plateau (Schep et al. 1997) even with layers of pure Ag and thicknesses in the nanometer range. Finally, it can also be pointed out that the ΔR of fig. 27 is the difference between the resistance of the virgin state and the resistance of the parallel configuration at saturation. As noted in section 4.3.1, eqs (16)–(18) hold when AP refers to a strictly antiparallel configuration or, at least, a configuration of zero total magnetization for a volume of the order of the SDL. Such a zero total magnetization turns out to be realized in the virgin state of the multilayers studied at Michigan State University (see fig. 14 and our comment in section 2), and this justifies the use of eqs (16)–(19) for a quantitative analysis of the experimental data.

The Michigan State University group has also performed measurements on samples including two types of magnetic materials, Co/Cu/$Ni_{80}Fe_{20}$, and the results have been analyzed in the same resistor series model corresponding to the long SDL limit of the Valet–Fert model (Yang et al. 1995). A good fit is obtained by using the parameters ρ^*_{Cu}, ρ^*_{Co}, β_{Co}, ρ^*_{NiFe}, β_{NiFe}, $r^*_{Co/Cu}$, $\gamma_{Co/Cu}$, $r^*_{NiFe/Cu}$, $\gamma_{NiFe/Cu}$ determined independently of the previous experiments on Co/Cu and $Ni_{80}Fe_{20}$/Cu multilayers. This analysis demonstrates that, once the above parameters have been derived for various materials and interfaces, it is possible to predict the GMR properties of more complicated structures including these materials and interfaces.

Extensive measurements of CPP-GMR on Co/Cu and $Ni_{80}Fe_{20}$/Cu multilayered nanowires have also been analyzed by using eq. (17). An example of experimental results on Co/Cu at 77 K is shown in fig. 28(a). The linear variation of $(\Delta R/R^{AP})^{-1/2}$ as a function of t_{Cu}, with different straight lines for different thicknesses of t_{Co} is well observed. Since eq. (17) predicts that the straight lines corresponding to different values of t_{Co} cross at the vertical coordinate β^{-1}, the intercept of the straight lines of fig. 28(a) gives directly $\beta = 0.36$. The other parameters are obtained by an independent determination of ρ^*_{Cu} and by a fit of eq. (18) to the straight lines in fig. 28(a). A similar linear variation of $(\Delta R/R^{AP})^{1/2}$ has also been reported for $Ni_{80}Fe_{20}$/Cu nanowires (Dubois et al. 1997a, 1999).

A quantitative analysis of CPP-GMR data has also been performed out of the long SDL limit. In the VF model (Valet and Fert 1993) for $t_N \gg l^N_{sf}$ and t_F still much smaller than l^F_{sf}, the MR ratio is expected to decrease as $\exp(-t_N/l^N_{sf})$. This behavior is illustrated by experimental data on Co/Cu nanowires in fig. 28(b). When t_{Cu} exceeds about 120 nm, the variation of $(\Delta R/R^{AP})^{1/2}$ with t_{Cu} departs from linearity and its upturn can be accounted for by an exponential variation with $l^{Cu}_{sf} = 140$ nm.

For SDL exceeding 100 nm in nonmagnetic layers of Cu or Ag, the limit $t_N \gg l^N_{sf}$ is hard to reach in conventional multilayers. However, the SDL of nonmagnetic layers can be shortened to the nanometer range by doping them with paramagnetic impurities, i.e., Mn, or nonmagnetic impurities with strong spin–orbit scattering (Pt). This allowed the Michigan State University group (Bass et al. 1994; Yang et al. 1994b; Hsu et al. 1996) to determine the SDL in Cu or Ag doped with Mn, Pt or Ni impurities. This will be discussed in section 4.7.

Another simple limit, outside of the long SDL limit, is for $t_F \gg l^F_{sf}$ with $t_N \ll l^N_{sf}$. From eq. (19), one expects a linear variation of $R^P/\Delta R$ as a function of t_F, at least if

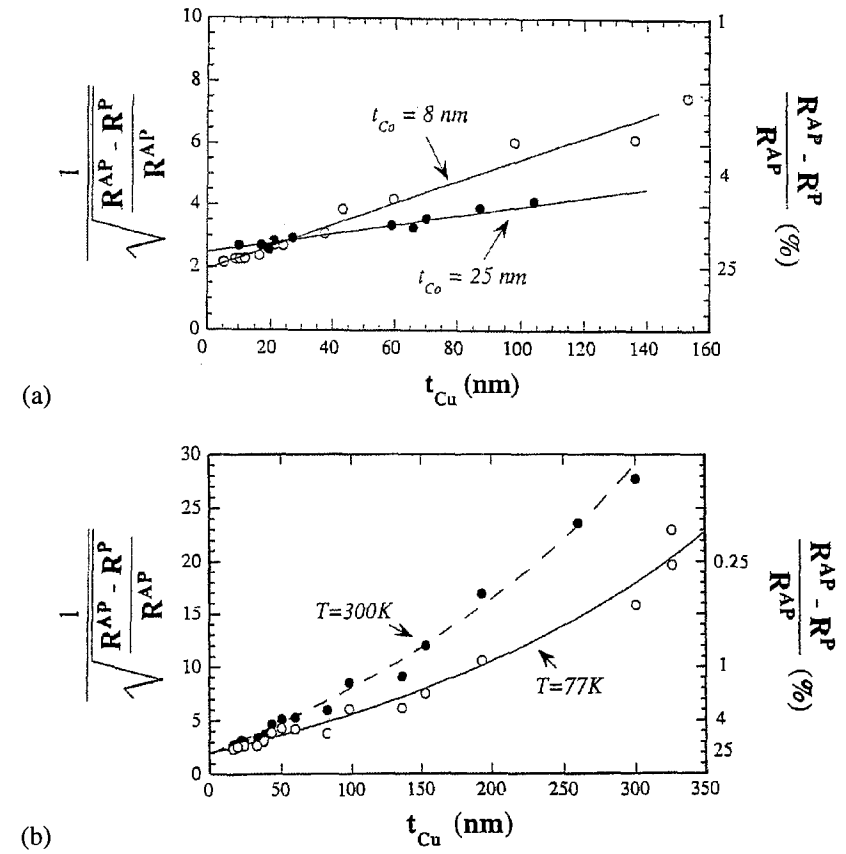


Fig. 28. Plot of $(\Delta R/R_{AP})^{-1/2}$ as a function of t_{Cu} for Co(t_{Co})/Cu(t_{Cu}) multilayered nanowires (a) in the long SDL regime, i.e., for $t_{Cu} < 120$ nm, and at 77 K, with two straight lines corresponding to two different Co thicknesses and (b) in an extended thickness range for $t_{Co} = 8$ nm, at two different temperatures. Corresponding MR values (in percent) are also given on the right-hand side scale (From Piraux et al. 1998).

the parameter p characteristic of the proportion of AP configuration between consecutive layers is independent of t_F. Such a linear variation is illustrated by experimental results shown in fig. 29 for Co/Cu nanowires with $t_{Co} > 80$ nm (Piraux et al. 1998). We note that, in agreement with eq. (19), $R^P/\Delta R$ is not only proportional to t_{Co} but also independent of t_{Cu} (data for $t_{Cu} = 8$ nm and 15 nm lie on the same straight line). With the value of β derived from the analysis of the long SDL limit and the value of p found from MFM measurements on the nanowires, the fit of the experimental data of fig. 29 with eq. (19) leads to $l_{sf}^{Co} = 59 \pm 18$ nm (at 77 K).

In the most general case, that is, for t_F (t_N) in the range of l_{sf}^F (l_{sf}^N) or just above, the expressions for the MR derived from the VF model are more complex and cannot be reduced to simple exponential or linear variations. An example of fit of experimental data in the general case is shown in fig. 30 for $Ni_{80}Fe_{20}$/Cu/$Ni_{80}Fe_{20}$ spin valves at 4.2 K (Steenwyck et al. 1997). The saturation of ΔR in the limits of large t_F corresponds to the linear varia-

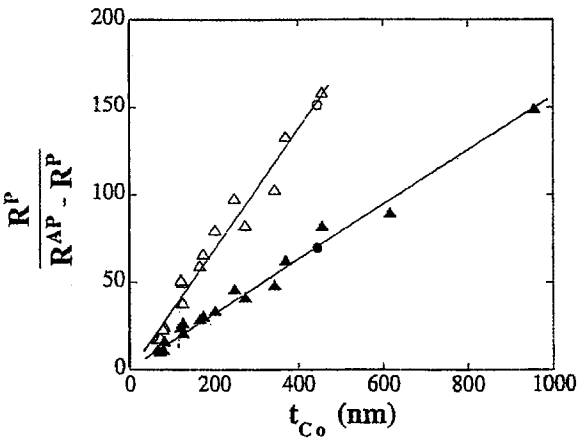


Fig. 29. Linear variation of the inverse of the magnetoresistance versus Co thickness for Co(t_{Co})/Cu(8nm) multilayered nanowires at $T = 77$ K (filled symbols) and $T = 300$ K (open symbols). The circles refer to data obtained on a Co(435nm)/Cu(15nm) sample. From Piraux et al. (1998).

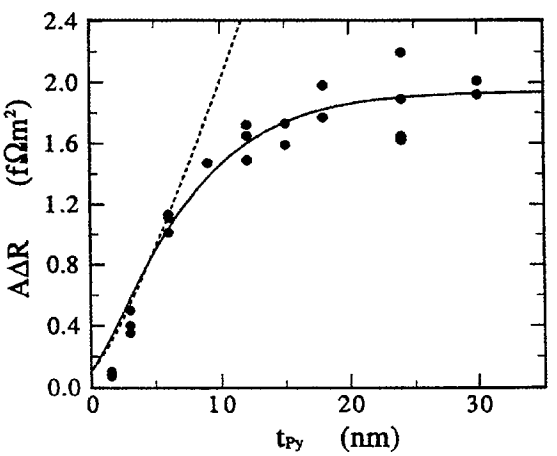


Fig. 30. A ΔR vs. t_{NiFe} for $Ni_{80}Fe_{20}(t_{NiFe})$/Cu(20nm)/$Ni_{80}Fe_{20}(t_{NiFe})$ exchange-biased spin-valve. A is the area of the sample and ΔR the resistance change between parallel and antiparallel configurations. The dots represent experimental data, the dashed curve is calculated in the VF model for $l_{sf}^{NiFe} = \infty$ and the solid curve is for $l_{sf}^{NiFe} = 5.5$ nm, from Steenwyck et al. (1997).

tion of $\Delta R/R$ with t_F^{-1} in eq. (19). The fit of fig. 30 leads to a very short SDL in $Ni_{80}Fe_{20}$ (permalloy or Py), $l_{sf}^{Py} = 5.5$ nm, in agreement with the result found for Py/Cu nanowires, 3.3 nm $< l_{sf}^{Py} <$ 5.3 nm (Dubois et al. 1999).

The parameters derived from CPP-GMR measurements at low temperature (4.2–77 K) on various types of Co/Cu, Py/Cu and Co/Cu/Py/Cu multilayers are presented in table 1.

TABLE 1

Best fit parameters derived from CPP-GMR measurements at low temperature (4.2–77 K) on Co/Cu, Py/Cu and Co/Cu/Py/Cu multilayers. The two last lines indicate also the threshold thickness t^* above which the contribution from bulk scattering to the square root of the GMR exceeds the interface contribution, i.e., $t^* = 2\gamma r_b^*/\beta\rho_F^*$. The first column displays the parameters derived at Michigan State University on multilayers prepared by sputtering. Most data come from a global fit of measurements on series of Co/Cu, Py/Cu and Co/Cu/Py/Cu multilayers (Yang et al. 1995; Pratt et al. 1996). However, for β_{Py}, $\gamma_{Py/Cu}$ and l_{sf}^{Py}, we have taken values derived by the same group from measurements on Py/Cu/Py spin valves and an improved analysis taking into account the finite value of the SDL in Py (Steenwyck et al. 1997). The data of the second column have been obtained on Co/Cu multilayers deposited on a grooved substrate (Oeps et al. 1996). The 3rd and 4th columns display the parameters derived from measurements on multilayered nanowires prepared by electrodeposition. The data of the 3rd column come from Piraux et al. (1996a, 1998) for Co/Cu, and from Dubois et al. (1999) for Py/Cu. The data of the 4th column come from Doudin et al. (1996). These authors present results on two series of samples prepared under different conditions and we have kept only the results for one of these series. Doudin et al. (1996) have also estimated the SDL in Co but, according to their discussion, the value of this SDL turns out to depend strongly on some assumptions of their analysis and is not reported in the table. Most of the parameters of this table have also been derived by Lee et al. (1995) for Co/Ag multilayers: $\rho_{Ag}^* = 1 \times 10^{-8}\ \Omega\,m$, $\rho_{Co}^* = 10.7 \times 10^{-8}\ \Omega\,m$, $\beta_{Co} = 0.48$, $r_{Co/Ag}^* = 0.56 \times 10^{-15}\ \Omega\,m^2$ and $\gamma_{Co/Ag} = 0.85$.

	MSU (multilayers)	Eindhoven (grooved substrates)	Louvain–Orsay (nanowires)	Lausanne (nanowires)
ρ_{Cu}^* ($10^{-8}\ \Omega\,m$)	0.45	0.36	3.1	1.3–3.3
ρ_{Cu}^* ($10^{-8}\ \Omega\,m$)	8.1	5.7	18 ± 2	51–57
β_{Co}	0.51	0.27	0.36 ± 0.02	0.46 ± 0.05
$r_{Co/Cu}^*$ ($10^{-15}\ \Omega\,m^2$)	0.52	0.2	0.3 ± 0.15	0.3–1.1
$\gamma_{Co/Cu}$	0.76	0.52	0.85 ± 0.15	0.55 ± 0.07
ρ_{Py}^* ($10^{-15}\ \Omega\,m$)	15.9		26.3	
β_{Py}	0.73		0.8 ± 0.1	
$r_{Py/Cu}^*$ ($10^{-15}\ \Omega\,m^2$)	0.54			
$\gamma_{Py/Cu}$	0.70		0.8 ± 0.1	
l_{sf}^{Cu} (nm)			140 ± 20	
l_{sf}^{Co} (nm)			59 ± 18	
l_{sf}^{Py} (nm)	5.5		4.3 ± 1	
t_{Co}^* (nm)	19	13.5	7.9	
t_{Py}^* (nm)	6.5			

The table includes the results obtained on conventional multilayers sandwiched between superconducting contacts (first column), multilayers deposited on grooved substrates (second column) and multilayered nanowires prepared by electrodeposition (third and fourth columns). Different methods of preparation lead to different concentrations of defects and therefore to different resistivities (ρ_F^* or ρ_N^*) but, in contrast, the scattering spin asymmetry coefficients β and γ and the interface resistance r_b^* do not depend much on the preparation.

For Co/Cu, whatever the method of preparation, $\gamma_{Co/Cu}$ is larger than β_{Co}. In this system, the contribution to the GMR from interface scattering (see term in $2\gamma r_b^*$ in eq. (16) or in the inverse of eq. (17)) is definitely larger than the contribution from bulk scattering (term in

$\beta\rho_F^* t_F$ in eq. (16) or in the inverse of eq. (17)) for thicknesses of a few nm. The contribution from bulk scattering in $(\Delta R\, R^{AP})^{1/2}$ or $(\Delta R/R^{AP})^{1/2}$ becomes preponderant only for Co layers larger than a threshold thickness t_{Co}^* of the order of 10 nm (t_{Co}^* varies from 8 nm in the results of column 3 to 19 nm in those of column 1). For Py/Cu, β and γ always have very similar values in the range 0.7–0.8 and this leads to a threshold thickness t_{Py}^* of the order of 6 nm.

We want to emphasize that the consistent analysis of CPP-GMR measurements on extensive series of multilayers with a simple set of parameters has important implications for the interpretation of GMR. The interpretation of series of measurements with a single couple of parameters for each metal (ρ^*, β) and each type of interface (r_b^*, γ), independently of the layer thicknesses, is a characteristic feature of a layer by layer approach in the limit of completely diffuse propagation (as defined, for example, by Schep et al. (1997). Such a layer-by-layer approach is at the basis of the VF model and therefore, in the long SDL limit, leads to the resistor series picture (Valet and Fert 1993; Lee et al. 1992). The relevance of this layer-by-layer approach is, of course, not surprising for multilayers with relatively thick or impure layers (even more for the layers of a very resistive AgSn alloy with thicknesses above 15 nm in the data of fig. 27(a)) for which superlattice effects and deviations from diffuse propagation can be ruled out. But an interesting result is that the same analysis with the same parameters extends down to the nanometer range, as this appears, for example, for the existence of a unique straight line in fig. 27(a) for both samples with thin layers of pure Ag and thick layers of AgSn. This shows that a layer by layer approach in the limit of "diffuse bulk propagation" can also describe correctly the experimental results obtained with only a few nm thick layers.

An important theoretical challenge is now to understand how far are the predictions of superlattice and layer-by-layer approaches and how the introduction of scattering effects from the beginning in superlattice models can bring the two approaches closer.

It also remains to discuss the microscopic origin of the spin asymmetry coefficients derived from the above quantitative analysis of CPP-GMR data, e.g., in table 1, and also to understand what makes the CIP-GMR more complex and its quantitative analysis much more difficult. This is the subject of the next section. In sections 4.6 and 4.7 we will also come back to the problem of the scaling lengths governing the thickness dependence, MFP in CIP and SDL in CPP.

4.5. Discussion of the microscopic mechanism of the GMR

As described in section 4.1, both the intrinsic potential of the multilayer (the spin-dependent steps in fig. 20) and the extrinsic scattering potentials due to defects at interface or in the bulk (the spin-dependent spikes in fig. 20) generate GMR effects. Owing mainly to the difficulty in introducing a realistic distribution of defects into a model, the proportion of intrinsic and extrinsic contributions cannot be really predicted by theory. However, some information on the relative importance of the two contributions can be derived from experiments on multilayers in which the concentration of defects or impurities is changed in a controlled way.

In the CIP-geometry, a number of authors have shown the influence of defects or impurities on the GMR. For example, it is well known that doping the magnetic layers with

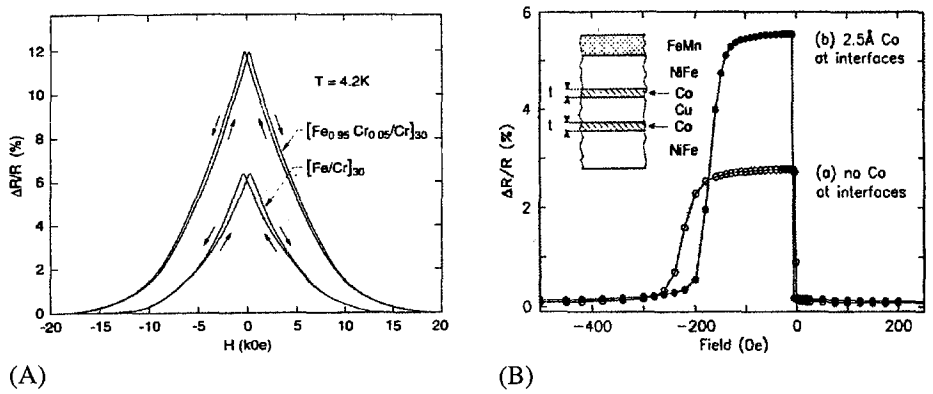


Fig. 31. Magnetoresistance curves for (A) Fe/Cr and $Fe_{0.95}Cr_{0.05}$/Cr multilayers. From Chen et al. (1993). (B) (a) Spin valves $Ni_{80}Fe_{20}$(53Å)/Cu(32Å)/$Ni_{80}Fe_{20}$(22Å)/FeMn(90Å)/Cu(10Å) and (b) the same structure with 2.5 Å thick Co layers added at each $Ni_{80}Fe_{20}$/Cu interface. From Parkin (1993).

impurities – that is, introducing bulk scattering centers – can enhance, reduce or even reverse the GMR (Chen et al. 1993; George et al. 1994; Daniels and Clemens 1995b; Renard et al. 1995; Kubota et al. 1997). An example of such an effect is shown in fig. 31(A). In the same way, GMR can be strongly affected by doping the interfaces (see fig. 31(B)) with a third element (Baumgart et al. 1991; Parkin 1993; Dieny et al. 1993). However, it is always difficult to separate what is really due to some change of the interface scattering and what results from changes in the degree of antiparallel ordering or in the interface spin fluctuations.

The influence of interface roughness on the CIP-GMR is also discussed in a number of publications but most results are only qualitative. In the case of Co/Cu multilayers, Willekens et al. (1995a) find that intermixing at the interfaces decreases the GMR. In contrast, for Fe/Cr, an increase of GMR with roughness is generally found. Colino et al. (1996) report that a moderate annealing of Fe/Cr(1 1 0) multilayers prepared by sputtering induces an increase of the GMR (an increase of both $\Delta\rho$ and $\Delta\rho/\rho$) due to "a less correlated interface roughness and/or a moderate interdiffusion". The most quantitative analysis is presented by Schad et al. (1999) on Fe(28Å)/Cr(11Å)(0 0 1) superlattices of a very high epitaxial quality (so that bulk scattering is weak and, for the layer thickness of the sample, GMR is dominated by interface scattering). Schad et al. make use of anomalous X-ray diffraction, STM, and AFM to determine the vertical roughness amplitude, η, and the lateral and vertical correlation lengths of the roughness, ξ_x and ξ_y, respectively. The enhancement of the GMR by annealing can be explained by an increase of both $\Delta\rho$ and $\Delta\rho/\rho$ with the density of roughness, i.e., the parameter η/ξ_x, as shown in fig. 32.

Clearer information on the respective roles of intrinsic and extrinsic effects, and also on the relative importance of bulk and interface scattering, can be derived from CPP-GMR experiments. As this has been emphasized in section 4.4, the main advantage of the CPP geometry is that the experimental data can be analyzed quantitatively. The analysis yields interface parameters $r_\uparrow$ and $r_\downarrow$ (or, equivalently, r_b^* and γ) which include contributions from both the multilayer intrinsic potential and the interface scattering potentials, and bulk

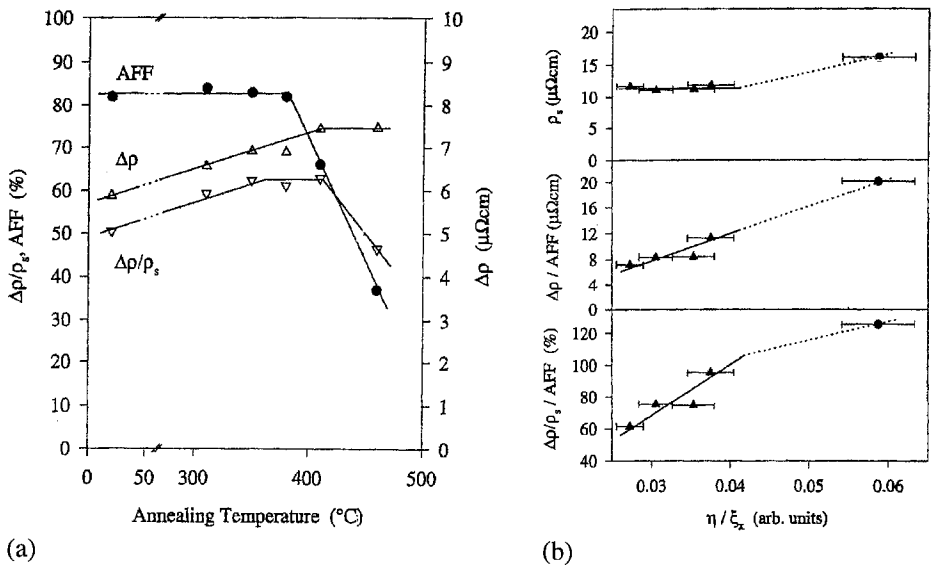


Fig. 32. (a) variation of $\Delta\rho$, $\Delta\rho/\rho_S$ and antiferromagnetic fraction AFF with annealing temperature for Fe/Cr(0 0 1) superlattices (AFF is defined by 100 AFF $= 1 - M_f/M_s$, where M_f and M_s are, respectively, the remanent and saturation magnetization), (b): variation of the resistivity at saturation ρ_s, $\Delta\rho$/AFF, $\Delta\rho/\rho_S$ AFF as a function of η/ξ_x (η is the roughness amplitude, ξ_x is the lateral correlation length of the roughness). The triangles correspond to samples with constant η and ξ_x varying. From Schad et al. (1999).

parameters, ρ_N^*, ρ_F^*, β, reflecting mainly the scattering rates within the layers. As we will see below, CPP measurements on multilayers doped with selected impurities clearly show how extrinsic effects strongly influence the parameters ρ^* and β, and, consequently, GMR. In particular, it turns out that, depending on the type of impurity added in the magnetic layers, both positive and negative values of β can be obtained. The same type of experiments shows that the interface spin asymmetry coefficient γ can also be positive or negative. Although experiments on doped multilayers demonstrate the strong influence of extrinsic scattering effects on GMR, we will also see that the influence of the intrinsic potential cannot be ignored, in particular, to understand the differences between CPP and CIP experiments.

The most spectacular examples of impurity effects on GMR are obtained when impurities are added to induce spin asymmetries either with opposite signs in consecutive layers (this inverse the GMR as explained in fig. 33) or with opposite and competing signs at interfaces and in the bulk. A typical example with these two effects is presented in fig. 34 for $Ni_{0.95}Cr_{0.05}$/Cu/Co/Cu multilayers in which Ni layers are doped with 5 at% of Cr impurities. Cr impurities in Ni scatter more strongly the majority of spin electrons (Fert et al. 1976; Mertig et al. 1995; Irkhin and Irkhin 1996), which makes that the bulk scattering spin asymmetry coefficient $\beta_{\underline{Ni}Cr}$ is negative and, for thick enough layers, also the global spin asymmetry of the $\underline{Ni}Cr$ layers is negative. In contrast, as predicted by all the theoretical models, β_{Co} and $\gamma_{Co/Cu}$ are positive for the Co layers.

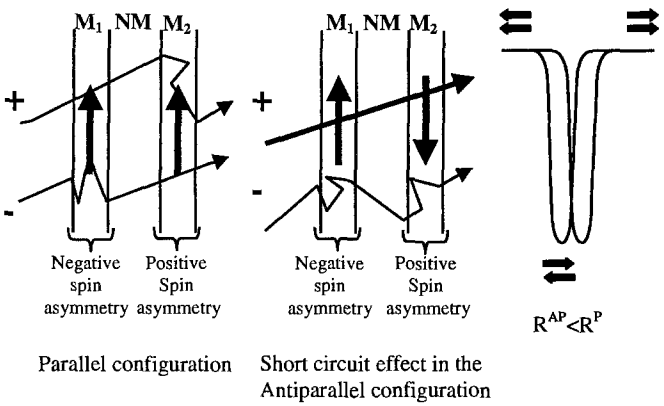


Fig. 33. Schematic picture of the inverse GMR effect. The signs '+' and '−' are for spins $s_z = +1/2$ and $-1/2$, respectively. The arrows represent the majority spin direction in the magnetic layers. The electron trajectories between two scatterings are represented by straight lines and the scattering by abrupt changes in direction. When M_1 and M_2 are two different magnetic materials having opposite spin asymmetries, one of the spin directions (the spin '+' direction, for example) is weakly scattered everywhere in the antiparallel configuration. This gives rise to a short circuit effect and a lower resistance in this antiparallel configuration, and, consequently, to an inverse GMR effect.

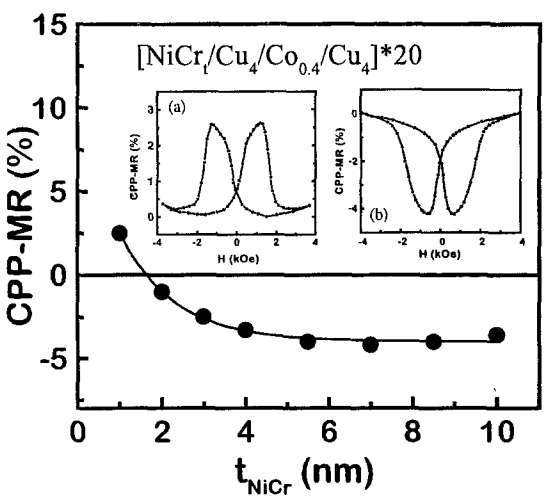


Fig. 34. Variation of the CPP-GMR as a function of the thickness of the $Ni_{0.95}Cr_{0.05}$ layers in NiCr/Cu/Co/Cu multilayers. The competition between the bulk scattering (characterized by $\beta_{NiCr} < 0$) and interface scattering (with $\gamma_{NiCr/Cu} > 0$) gives rise to a compensation thickness t^*_{NiCr} at which they cancel each other (t^*_{NiCr} is determined by $\beta_{NiCr}\rho^*_{NiCr}t^*_{NiCr} + 2\gamma_{NiCr/Cu}r^*_{NiCr/Cu} = 0$). Below this compensation thickness t^*_{NiCr}, the interface scattering is predominant, the global spin asymmetry of the NiCr layer is positive as that of the Co layer (characterized by $\beta_{Co} > 0$ and $\gamma_{Co/Cu} > 0$) and the effect is normal (see insert (a)). Above t^*, the bulk scattering in NiCr becomes predominant so that the global asymmetry of the NiCr layers is negative. Consequently, with alternating spin asymmetries for the NiCr and Co layers, the effect is inverse (see insert (b)). From Vouille et al. (1999).

With opposite spin asymmetries in the NiCr and Co layers, the current is shorted in the antiparallel magnetic configuration by the electrons which are successively majority and minority spin electrons in consecutive magnetic layers. This explains the inverse GMR seen in fig. 34 for $t_{\underline{\mathrm{NiCr}}} = 7$ nm (insert (a)) and more generally, for $t_{\underline{\mathrm{NiCr}}} > 1.8$ nm (Vouille et al. 1997, 1999). However, the GMR in fig. 34 is normal for $t_{\underline{\mathrm{NiCr}}} < 1.8$ nm because, with $\gamma_{\underline{\mathrm{NiCr}}/\mathrm{Cu}}$ positive, the GMR is reversed only when the NiCr bulk scattering with negative spin asymmetry overcomes the interface scattering with positive spin asymmetry. The change from normal to inverse GMR occurs at $t^*_{\underline{\mathrm{NiCr}}} = 1.8$ nm, which is the compensation thickness between bulk and interface scatterings. The compensation condition (Hsu et al. 1997; Vouille et al. 1997, 1999) is:

$$\beta_{\underline{\mathrm{NiCr}}}\rho^*_{\underline{\mathrm{NiCr}}}t^*_{\underline{\mathrm{NiCr}}} + 2\gamma_{\underline{\mathrm{NiCr}}/\mathrm{Cu}}r^*_{\underline{\mathrm{NiCr}}/\mathrm{Cu}} = 0.$$

A similar behavior has been observed in a large number of multilayers of the type A/Cu/Co/Cu where A can be Ni doped with Cr impurities, Co doped with Cr and Fe doped with Co or V. The inversion of the GMR above a compensation thickness t^*_{A} is always a signature of the competition between a positive $\gamma_{\mathrm{A/Cu}}$ and a negative β_{A} (Hsu et al. 1997; Vouille et al. 1997, 1999). The concentration of impurities required to obtain the inversion can be as low as 2.5% in the case of NiCr, which is enough to obtain the negative asymmetry for bulk scattering. In contrast, when A is simply a pure ferromagnetic metal, Ni, Co or Fe, or an alloy of Ni with Fe (permalloy) or Cu, or Co with Fe impurities, the absence of inversion indicates that both β_{A} and $\gamma_{\mathrm{A/Cu}}$ are positive.

The type of experiment illustrated by fig. 34 demonstrates that scattering effects do contribute significantly to the GMR and allow one to easily tailor the GMR by selectively doping the magnetic layers with impurities. Extensive series of experiments of this type have been analyzed by Hsu et al. (1996) and Vouille et al. (1997, 1999) to determine the bulk scattering spin asymmetry coefficient β for a large number of metals and alloys, see examples in table 2. Compared to the previous results obtained in bulk alloys (Fert et al. 1976;

TABLE 2

Bulk scattering spin asymmetry parameter β deduced from CPP-inverse GMR measurements. From Hsu et al. (1997), Vouille et al. (1997, 1999), Steenwyck et al. (1997) and Reilly et al. (1999).

System	β
$Ni_{95}Cr_5$	−0.13
$Fe_{90}Cr_{10}$	−0.16
$Fe_{70}Cr_{30}$	−0.28
$Fe_{85}V_{15}$	−0.11
$Co_{90}Cr_{10}$	−0.12
Pure Co	+0.51
$Co_{90}Fe_{10}$	+0.65
$Ni_{80}Fe_{20}$	+0.73
$Ni_{70}Cu_{30}$	+0.19

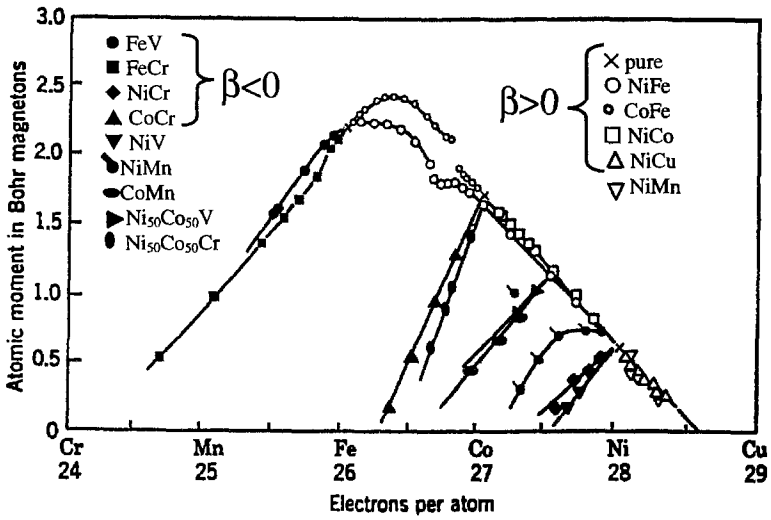


Fig. 35. Slater–Pauling plot for alloys of 3d metals and scattering spin asymmetry: the spin asymmetry coefficient β is positive for the pure metals, Fe, Co, and Ni and their alloys located in the slope at $-45°$, i.e., NiCu, NiCo, NiFe, CoFe; β is negative on the branches at $+45°$, i.e., for FeV, FeCr, CoCr, NiCr alloys.

Dorleijn and Miedema 1976, 1977) and calculations (Mertig et al. 1995 or Irkhin and Irkhin 1996) the signs of β are the same but the numerical values are only in rough agreement. As in previous studies the magnitude of β is generally much smaller when it is negative. This partly explains why the MR ratio generally remains small in systems with inverse GMR.

The sign of β in transition metal alloys is clearly related to the location of the alloy on the classical Slater–Pauling curve. We see in fig. 35 that β is positive for pure metals, Co and Ni, and their alloys located on the slope at $-45°$ of the Slater–Pauling curve, from CoFe to NiCu. In contrast, negative values of β have been found for alloys on the branches going down from Fe (FeCr, FeV), Co (CoCr) or Ni (NiCr). This can be explained by the electronic structure (Mertig et al. 1995; Irkhin and Irkhin 1996). The positive values of β are associated with a higher density of states (DOS) at the Fermi level for the minority spin direction in the pure metals or on the impurity sites. In contrast, for Cr or V impurities in Fe or Cr impurities in Co or Ni, the d levels of the impurity are well above the host d band for the majority spin direction and cannot be hybridized with the d band states. The resulting resonant scattering of spin-$\uparrow$ s–p electrons with empty d states of the impurity just above the Fermi level accounts for the high spin-$\uparrow$ resistivity and for the negative sign of β; alternatively one can say that the formation of a virtual bound state leads to a high spin-$\uparrow$ DOS at the Fermi level on the impurity site.

In fig. 36, we present an example of an experiment aimed at determining the sign and magnitude of the interface spin asymmetry coefficient γ. The samples are $[\mathrm{Co}(t)/\mathrm{Cr}(0.9\mathrm{nm})/\mathrm{Py}(7\mathrm{nm})/\mathrm{Cr}(0.9\mathrm{nm})]_N$ multilayers, with a thickness of Cr corresponding to the first peak of AF coupling. The change of sign of the GMR at a compensation thickness, $t^*_{\mathrm{Co}} = 4$ nm, is due to the competition between the positive β_{Co} of the Co layers and the

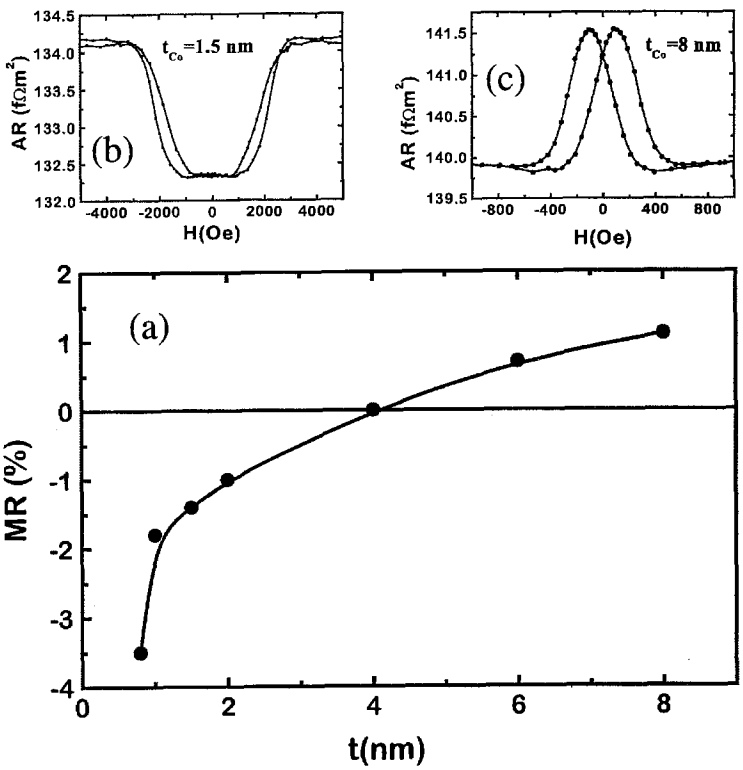


Fig. 36. (a) Variation of the CPP-GMR ratio as a function of the Co thickness in [Co(t)/Cr(0.9nm)/Py(7nm)/Cr(0.9nm)]$_N$ multilayers. The inversion and zero GMR at t = 4 nm results from the competition between negative interface and positive bulk spin asymmetries, i.e., $\gamma_{Co/Cr} < 0$ and $\beta_{Co} > 0$. (b) Below the compensation thickness, the global spin asymmetry of the Co layers is negative, which, combined with the positive spin asymmetry of the Py layers, gives rise to inverse GMR. (c) Above the compensation thickness, the global spin asymmetry of the Co layers is positive and the GMR is normal. From Vouille et al. (1999).

negative $\gamma_{Co/Cr}$ of the Co/Cr interfaces. As there is a predominant positive spin asymmetry from bulk scattering for the 7 nm thick Py layer, one obtains an inverse GMR when $|2\gamma_{Co/Cr}r^*_{Co/Cr}|$ exceeds $\beta_{Co}\rho^*_{Co}t_{Co}$ for $t_{Co} < t^*_{Co} = |2\gamma_{Co/Cr}r^*_{Co/Cr}/(\beta_{Co}\rho^*_{Co}t_{Co})|$ and a normal GMR for $t_{Co} > t^*_{Co}$.

Negative values of γ are found for Co/Cr and Fe/Cr interfaces, while γ is positive for most interfaces of Fe, Co, Ni or Py with noble metals, Cu, Ag or Au. The negative sign of γ for Fe/Cr and its positive sign for Co/Cu are in agreement with theoretical predictions (Nesbet 1996; Butler et al. 1997). For the systems investigated till now, the same sign is generally found for the coefficient β of an alloy AB and the coefficient γ of the A/B interface. This indicates some similarity between the problems of impurity scattering and electron reflections at interfaces (similarity probably related to the role of the separation between the d levels of A and B in both problems) but this should not be a strict rule.

A general conclusion from the interpretation of CPP-GMR data is that extensive series of measurements on various systems can be accounted for by a set of parameters β and γ which characterize each ferromagnetic material F and each F/N interface, and can be positive or negative. Both the bulk and interface contributions are important, with a larger bulk (interface) contribution above (below) a characteristic thickness t^*. The most spectacular situation occurs when opposite signs of β and γ lead to zero GMR at t^*.

The bulk spin asymmetry coefficient β results from the spin asymmetry of the scattering process and, as expressed by eqs (4) and (5), reflects both the intrinsic dependence of the DOS in the ferromagnetic metal and the specific spin dependence of the scattering by extrinsic defects or impurities. In practice, β can be easily tuned by doping with selected impurities. Its maximum values are obtained with Ni and Co doped with Fe ($\beta_{\underline{\mathrm{NiFe}}} = 0.73$, $\beta_{\underline{\mathrm{CoFe}}} = 0.65$). The interface contribution associated with r_b^* and γ can, in principle, include an intrinsic contribution due to specular reflections and an extrinsic one associated with the imperfections at the interface. The relative importance of these intrinsic and extrinsic interface effects is not well known. Experiments on multilayers with doped or intentionally mixed interfaces could clarify the problem but few CPP-measurements on such multilayers have been performed up till now.

The CIP-GMR is more complex and cannot be analyzed in terms of a small number of parameters, like the parameters ρ^*, β, r_b^* and γ used for the interpretation of the CPP-GMR. The main advantage of the CPP-geometry is that the influence of the intrinsic potential can be expressed by its contributions to the interface resistance and appears in r_b^* and γ. On the contrary, in the CIP-geometry, specular reflections of electrons by the multilayer intrinsic potential do not contribute directly to resistance terms because momentum along the current direction is conserved by specular reflections in CIP. However, the intrinsic potential indirectly affects conduction by channeling the electrons inside some of the layers. Binder et al. (1998) have described this complex situation, where the current is partly carried by delocalized electrons and partly by electrons more or less confined in normal or magnetic layers. The main result is that the confined electrons differentially probe the scattering potentials in different parts of the multilayered structure. This is in sharp contrast with the situation of the CPP-geometry in which the current is carried by delocalized electrons which successively probe the scattering potentials in all layers. The influence of channeling effect is also described in the model of Brown et al. (1998).

The different role of the intrinsic potential in CIP and CPP probably explains some experimental results which seem puzzling at a first view. For example, when CIP measurements are performed on systems presenting an inverse CPP-GMR, a great part of them exhibit only a normal CIP-GMR (Hsu et al. 1997; Vouille et al. 1997, 1999). This can be explained in the following way. Let us consider, for example, a system like $\underline{\mathrm{Ni}}_{0.95}\mathrm{Cr}_{0.05}$/Cu/Co/Cu for which the inversion in CPP is due to the negative β of $\underline{\mathrm{NiCr}}$. If a significant part of the CIP current is carried by electrons partly confined in the Cu layers, these electrons will be more affected by the scattering at the F/N interfaces than by bulk scattering within the ferromagnetic layers; consequently, the contribution to the GMR of the negative β will be reduced in the CIP-geometry.

In addition to the "quantum channeling" of the electron waves by the intrinsic potential, another source of channeling in CIP comes from the damping of the electron distribution function with the mean free path (MFP) as scaling length (see next paragraph on the scaling

lengths). In ferromagnetic layers, the MFP does not generally exceed a few nanometers; when the layer thickness is larger, only a depth of the order of the MFP along both interfaces contributes to the CIP-GMR. On the other hand, the conduction in the inner part of the ferromagnetic layer is insensitive to the orientation of the magnetization in the neighboring layers and this inner part forms an independent channel. This type of channeling, as well as the "quantum channeling" effects by the intrinsic potential, leads to an inhomogeneous weighting of the scattering potentials and, in general, to some reduction of the bulk scattering contribution for CIP.

To sum up, the different role of the intrinsic potential in CIP and CPP is an important point for the understanding of the GMR.

In CPP, the intrinsic potential appears only through its contribution to the interface resistance r_b^* and γ. This leads to a simple quantitative analysis in terms of the bulk, ρ_N^*, ρ_F^* and β, and interface, r_b^* and γ, parameters (out of the long SDL regime, the SDL also enters the analysis). All these parameters can be derived from experimental data. The bulk parameters reflect the scattering of the electrons within the layers and can be tailored by doping them with impurities. The interpretation of the interface parameters is not completely clear yet because it remains to understand what is due, respectively, to the specular reflections by intrinsic potential of the multilayer and to diffuse scattering by interface imperfections.

In CIP, the intrinsic potential induces channeling effects which make that the carriers differentially probe the scattering potentials at the interfaces and in the magnetic or nonmagnetic layers. This gives entwined intrinsic and extrinsic contributions and, together with the shortness of the scaling length for the damping of the electron distribution function, complicates greatly the possibility of a quantitative analysis in the CIP-geometry.

4.6. Thickness dependence and scaling length in CIP

The thickness dependence of the CIP-GMR is expected to be governed by:

(a) The exponential damping of the electron distribution function with a characteristic length equal to the mean free path (MFP);
(b) The variation of the proportion of different scattering processes (at the interfaces, within the magnetic layers, and within the nonmagnetic layers).

The MFP appears as the scaling length for the thickness dependence of the CIP-GMR in the exponential terms of the semi-classical model of Camley and Barnas (1989). Barthélémy and Fert (1991) have applied the semi-classical approach of Camley and Barnas to the simplest case with a spin independent MFP λ in all the layers and only spin dependent scattering at the interfaces. As a function of the thickness of the nonmagnetic layers, t_N, they find asymptotic decreases of the MR ratio driven by the exponential factor $\exp(-t_N/\lambda)$. This factor expresses the progressive decoupling of the electron distribution functions on both sides of a nonmagnetic layer. As a function of the thickness of the magnetic layer t_F, the asymptotic variation as $1/t_F$ expresses the variation of the proportion of interface scattering (dilution effect). When the bulk scattering is spin dependent so that its contribution to GMR becomes predominant for thick magnetic layers, the active part of the magnetic layers is limited to a depth λ along both interfaces for $t_F > \lambda$, and this leads also to an asymptotic decrease as λ/t_F.

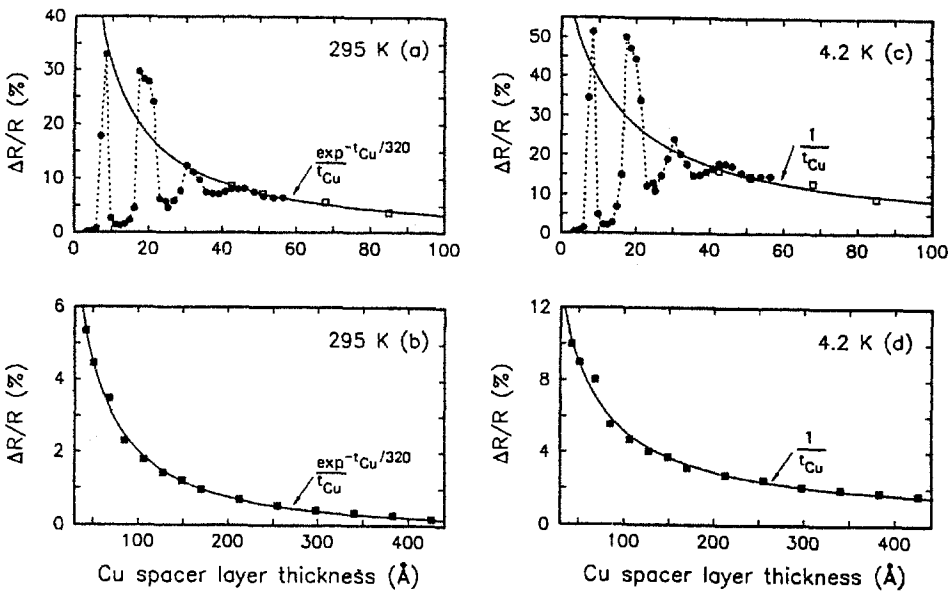


Fig. 37. Saturation magnetoresistance versus Cu spacer layer thickness for several series of $[Co(11Å)/Cu(t_{Cu})]_N$ multilayers. The number of Co/Cu periods, N, is 20 (solid circles) and 6 (open and closed squares). Data are shown for temperatures of (a) and (b) 295 K, and (c) and (d) 4.2 K. The $N = 6$ data (in (a) and (c)) have been scaled by an empirical factor of 1.6 to perform the comparison with $N = 20$. From Parkin et al. (1993).

The thickness dependence of the CIP-GMR is relatively difficult to characterize experimentally. For layer thickness of a few nm, the intrinsic variation described above is mixed with other effects related to the oscillatory decrease of the antiferromagnetic coupling and to the crossover to an uncoupled regime with a lower degree of antiparallel ordering. A careful analysis of magnetization data can be used to single out the intrinsic variation (Gijs et al. 1992). For thick enough spacer layers, the interlayer coupling can be neglected but the small amplitude of the MR limits the accuracy of the determination of its thickness dependence.

In fig. 37, we show the variation of the GMR of Co/Cu multilayers as a function of the thickness of Cu (Parkin et al. 1993). Below about 5 nm, the intrinsic variation cannot be separated from what is due to the variation of the interlayer coupling. Above 5 nm, i.e., in the uncoupled regime, and at 295 K the experimental MR varies approximately as $\exp(-t_{Cu}/\lambda)/t_{Cu}$ with 32 nm for the MFP λ in Cu (fig. 37(b)). The exponential factor expresses the damping of the electron distribution in the Cu layers. The factor $1/t_{Cu}$ comes from the progressive dilution of spin dependent scattering as the thickness of the Cu layers increases. At 4.2 K, fig. 37(d), the variation is roughly proportional to $1/t_{Cu}$. This means that, with a longer MFP at low temperature, the exponential regime is not reached in the experimental thickness range and only the variation as $1/t_{Cu}$ subsists.

The exponential variation as a function of a ratio of the type t/λ in approximate expressions of the GMR has been sometimes used to determine the MFP. For Co layers, Gurney et al. (1993) find that the ratio $\lambda_\uparrow/\lambda_\downarrow$ is large (greater than 5), whereas Swagten et al. (1996)

and Strijkers et al. (1996) conclude that the MFP in Co layers should be weakly spin dependent. This divergence may be due to the inaccuracy of the approximate expressions used in this type of analysis. We also want to point out that the interest of the parameters $\lambda_\uparrow$ and $\lambda_\downarrow$ is limited to the problem of the scaling length for the thickness dependence. The GMR is not directly related to the ratio $\lambda_\uparrow/\lambda_\downarrow$. The condition for the existence of a contribution from bulk scattering to GMR is that the resistivities $\rho_\uparrow$ and $\rho_\downarrow$ are different, i.e., $\beta \neq 0$ in the conventional notation. This is the condition for a shorting of the current by one of the channels in the antiparallel configuration. To a first approximation, ρ_σ can be written:

$$\rho_\sigma = \frac{m_\sigma v_F^\sigma}{n_\sigma e^2} \frac{1}{\lambda_\sigma},$$

where m_σ, n_σ, v_F^σ are, respectively, the effective mass, number, and Fermi velocity of electrons with spin σ. It can be seen that the dependence of ρ_σ on σ can be due not only to some dependence of λ_σ on σ but also to the dependence of m_σ, v_F^σ or n_σ. In other words, $\lambda_\uparrow = \lambda_\downarrow$ does not mean a zero bulk contribution to GMR; conversely $\lambda_\uparrow \neq \lambda_\downarrow$ can coexist with a zero bulk contribution to GMR.

4.7. Thickness dependence and scaling length in CPP

In CPP, the interpretation of the thickness dependence is easier than in CIP for two main reasons:

(a) The CPP-GMR can be described by analytical expressions (Lee et al. (1992) for the long SDL limit, Valet and Fert (1993) for the general regime).

(b) The much larger scaling length for the thickness dependence in CPP (the SDL instead of the MFP in CIP) means that there is a much broader range in which the layer thickness can be much smaller than the scaling length. In this long SDL limit, the variation of the CPP-GMR in eqs (16)–(18) reflects only the variation of the proportion of the different scattering processes (dilution effects). The dependence of the CPP-GMR on the ratio of the thickness to SDL appears only out of the long SDL regime, so that the contribution from the dilution and SDL effects can be separated easily.

In the long SDL limit, i.e., for $t_N \ll l_{sf}^N$ and $t_F \ll l_{sf}^F$, the resistance and magnetoresistance are given by eqs (16)–(18). As the SDL in nonmagnetic layers, l_{sf}^N, is generally very long, the linear variations with t_N predicted by these equations can be followed through a broad range of t_N. This is illustrated by the linear variation of $(\Delta R/R^{AP})^{-1/2}$ with t_{Cu} in the experimental results for Co/Cu nanowires in fig. 28(a). A departure from linearity is observed only above 100 nm in fig. 28(b). A fit to experimental data above this threshold thickness has been used to estimate that the SDL in Cu layers equals 140 nm (Piraux et al. 1996a). In most measurements on conventional multilayers, for example, in those of fig. 27, the thickness of the layers remains smaller than the SDL, so that it is impossible to see departures from the long SDL limit and to determine l_{sf}^N.

Examples of variations with t_F are shown in fig. 27(a) and fig. 30. In fig. 27(a), for Co/Ag multilayers in which t_{Co} does not exceed 20 nm, only the linear variation of the long SDL limit, eq. (16), can be seen. In fig. 30, ΔR is plotted as a function of the thickness of permalloy (Py) for Py/Cu/Py spin valve structures in which the thickness of Cu is constant

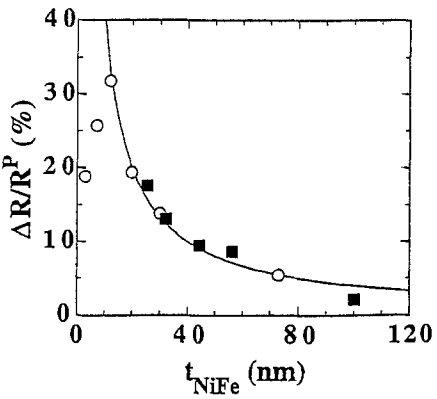


Fig. 38. CPP-GMR versus $Ni_{80}Fe_{20}$ layer thickness at $T = 77$ K for [$Ni_{80}Fe_{20}(t_{NiFe})$/Cu(10nm)/$Ni_{80}Fe_{20}(t_{NiFe})$/Cu(100nm)] (open circles) and [$Ni_{80}Fe_{20}(t_{NiFe})$/Cu(10nm)/$Ni_{80}Fe_{20}(t_{NiFe})$/Cu(500nm)] (closed squares) multilayered nanowires. The solid line represents a variation as $1/t_{NiFe}$. From Dubois et al. (1999).

and small ($t_{Cu} = 10$ nm $\ll l_{sf}^{Cu}$). After a roughly linear variation corresponding to the regime $t_{Py} < l_{sf}^{Py}$, ΔR saturates when t_{Py} becomes much larger than l_{sf}^{Py}. The fit with theoretical expressions derived from the model of Valet and Fert (1993) is indicated by a solid line; it has been obtained with $l_{sf}^{Py} = 5.5 \pm 1$ nm. Almost complete saturation is obtained when t_{Py} is 5 or 6 times larger than l_{sf}^{Py}; the maximum of $\Delta R/R$ is reached when t_{Py} is 3 times larger than l_{sf}^{Py}, at about 15 nm. The interpretation of the saturation of ΔR for $t_F \gg l_{sf}^{F}$ is that only thicknesses of the order of l_{sf}^{F} along each interface of the magnetic layer contribute to ΔR. Increasing more the thickness of the layer does not bring any additional contribution to ΔR. We point out that, since R becomes proportional to t_F in the limit of very thick magnetic layers, the saturation of ΔR is equivalent to the variation of $\Delta R/R^P$ as $1/t_F$ predicted by eq. (18). Examples of variation of $\Delta R/R^P$ as $1/t_F$ in the limit of large t_F are shown in fig. 29 and fig. 38 and have been used to determine the SDL in Co, $l_{sf}^{Co} = 59 \pm 18$ nm, and in Py, $l_{sf}^{Py} = 4.3 \pm 1$ nm at 77 K. The results for Py also confirm a very low value of the SDL in Py found from the fit in fig. 30 by Steenwyck et al. (1997) and Pratt et al. (1997).

An important question is the origin of the spin-flip processes involved in the SDL. The SDL, eqs (14)–(15), is proportional to $(\lambda\lambda_{sf})^{1/2}$ where $\lambda_{sf} = \tau_{sf}v_F$ is the spin mean free path associated with the spin lattice relaxation time τ_{sf} controlling the relaxation of spin accumulations. The experimental results of the Michigan State University group have given unambiguous information on the main spin-flip processes involved in τ_{sf}. Yang et al. (1994b) and Bass et al. (1994) have shown that the SDL of Cu or Ag layers can be dramatically shortened by doping these layers with Pt or Mn impurities. In fig. 39, this shortening of the SDL accounts for the strong reduction of the GMR and definite deviation from the linear variation of the long SDL limit. The shortening of the SDL can be explained by the spin-flip scattering associated with the strong spin–orbit interactions on Pt sites (transfer of spin accumulation to the lattice) and by the exchange scattering by

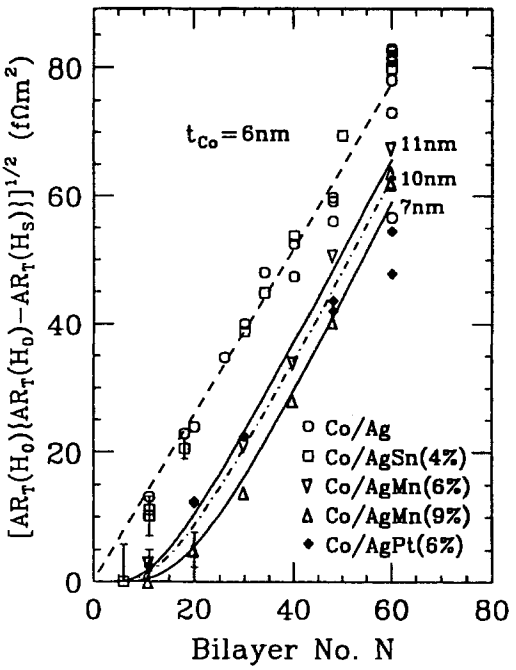


Fig. 39. $\{AR_T(H_0)[AR_T(H_0) - AR_T(H_S)]\}^{1/2}$ versus the number of bilayer N for Co/Ag, Co/AgSn(4%), Co/AgMn(6%), Co/AgMn(9%) and Co/AgPt(6%), where A is the sample area, $R_T(H_0)$ and $R_T(H_S)$ are the resistances at a zero field and saturation field, respectively. From Bass et al. (1994).

paramagnetic Mn impurities (transfer of spin accumulation to the Mn system and then to the lattice). In contrast, as seen in fig. 27, nonmagnetic impurities with only small spin–orbit interactions (Sn) do not affect the GMR. Similarly Hsu et al. (1996) have shown that the SDL in Cu layers can be strongly reduced by nonmagnetic Ni impurities and that this reduction can also be accounted for by spin–orbit scattering.

The origin of the SDL in multilayers has been discussed by Fert et al. (1995a). In the case of spin–orbit scattering by transition metal impurities, the spin-flip rate is expected to be proportional to the square of the spin–orbit constant λ_d and therefore is expected to be particularly high for 5d impurities like Pt, as this has already been found in ESR experiments on doped metals (Monod and Schultz 1982). By estimating the spin-flip scattering by Pt impurities from ESR data, Fert et al. (1995a) find a SDL of 6.8 nm for Cu with 6 at% Pt, in reasonable agreement with the SDL of 8 nm derived from experiments of Bass et al. (1994). The shortening of the SDL by spin–orbit scattering on Ni impurities in Cu layers can also be accounted for by estimating the corresponding spin-flip rate from ESR data (Hsu et al. 1996). The SDL in Cu doped with Mn has also been estimated from data on the exchange interaction between conduction electrons and Mn impurities (Fert et al. 1995a) and is in good agreement with the SDL found in CPP-GMR experiments.

The SDL in pure metal layers can also be attributed mainly to spin–orbit scattering by imperfections, that is structural defects or impurities. The much shorter SDL in magnetic

layers of 3d elements compared to the SDL of Cu or Ag layers can be explained by the stronger spin–orbit interaction when the d character of the carriers is stronger and also by the generally higher resistivity, and concomitantly shorter MFP, of transition metal layers (the total scattering rate is given by the resistivity, while the spin–orbit coupling determines the proportion of spin-flip scattering in the scattering rate). However, it remains to explain the relatively broad range of SDL found in ferromagnetic layers, from 59 nm in Co to approximately ten times lower values in permalloy ($Ni_{80}Fe_{20}$) or $Ni_{97}Cr_3$ (Dubois et al. 1999; Pratt et al. 1997; Park et al. 1999). This difference can be qualitatively understood by writing eq. (14) as:

$$l_{sf}^{F} = \left[\frac{\lambda_{sf}\lambda}{6(1-\beta)^2}\right]^{1/2},$$

where $\lambda = (\lambda_\uparrow + \lambda_\downarrow)/2$ is the spin averaged value of the MFP. In an approximate free electron model, λ is related to the resistivity ρ by $\lambda\rho = k_F/(ne^2)$. Although the spin–orbit coupling is roughly the same in Fe, Co, and Ni, the shorter SDL in permalloy or $Co_{90}Fe_{10}$ in comparison to Co can be explained by: (i) stronger structural disorder and thus higher scattering rate, and shorter λ and λ_{sf} in permalloy and $Co_{90}Fe_{10}$, (ii) higher values of β in permalloy and $Co_{90}Fe_{10}$, $\beta \approx 0.65$–0.73, as compared to $\beta \approx 0.3$–0.5 in Co (see table 1). A quantitative discussion of the short SDL in permalloy has been presented by Dubois et al. (1999).

The SDL data discussed above are those obtained from measurements at low temperatures. A contribution from exchange scattering has not been considered in our discussion because the spin-flip exchange scattering is frozen at low temperature in ferromagnets. However, one can ask whether the spin-flip exchange scattering by spin fluctuations contribute to spin-lattice relaxation at higher temperatures and thereby reduce the SDL as temperature increases. In fact, we will see in the next paragraph that the SDL of Co layers is moderately reduced at room temperature. It decreases from 69 nm at 77 K to only 38 nm at 300 K. It has been argued that electron–magnon scattering conserves the total spin of the electron system (s–p + d). Therefore, it should not contribute directly to the spin-lattice relaxation; rather it equalizes the spin accumulation over the Fermi surface (Fert et al. 1995a; Piraux et al. 1998). Experiments on spin wave emission by spin injection can clear up the question of the interaction between spin waves and spin accumulation (Tsoi et al. 1998).

It is important to distinguish the spin-lattice relaxation rate involved in the SDL, τ_{sf}^{-1}, from the spin mixing relaxation rate, $\tau_{\uparrow\downarrow}^{-1}$, which characterizes the momentum transfer between the spin-$\uparrow$ and spin-$\downarrow$ channels in the two-current model (Fert and Campbell 1976). The main contribution to $\tau_{\uparrow\downarrow}^{-1}$ comes from electron–magnon scattering which is able to transfer momentum between the two currents; this explains the strong temperature dependence of the spin mixing parameter $\rho_{\uparrow\downarrow}$ in ferromagnets. In comparison, the contribution to $\tau_{\uparrow\downarrow}^{-1}$ from elastic spin–orbit scattering is generally almost negligible. On the other hand, electron–magnon scattering is not a direct mechanism for spin-lattice relaxation and τ_{sf}^{-1} is due primarily to spin–orbit scattering. It has been shown that, if the experimental values of $\rho_{\uparrow\downarrow}$ (of the order of 10^{-7} Ω m) were used to estimate τ_{sf}^{-1}, the SDL in ferromagnetic metals would be shortened to a couple of nm and the CPP-GMR would be dramatically reduced at room temperature (Piraux et al. 1998).

4.8. Temperature dependence

Several effects contribute to the variation of the GMR with temperature:

(a) Inelastic scattering processes by phonons or magnons (including interface phonons and magnons) add up to elastic scattering processes by imperfections. As the spin asymmetry is generally different for different scattering processes, the GMR is necessarily changed. For example, if the inelastic scatterings are spin independent, they contribute to R but not to ΔR and the GMR ratio is reduced.

(b) Electron–magnon scattering with spin-flip also transfers momentum between the spin-$\uparrow$ and spin-$\downarrow$ currents. This is the well-known spin-mixing effect characterized by the spin mixing resistivity $\rho_{\uparrow\downarrow}$ in ferromagnetic materials (Fert and Campbell 1976). Spin mixing equalizes the two currents and reduces the GMR.

(c) As the global scattering rate increases with temperature, the scaling lengths governing the decrease of the GMR at increasing thickness, MFP in CIP and SDL in CPP, are shortened and the variation of the GMR with thickness is more pronounced.

Including all these effects into a theoretical model is a difficult task and necessarily involves a relatively high number of adjustable parameters. The contribution from spin fluctuations has been introduced into theoretical models by Hasegawa (1993, 1996) and Zhang and Levy (1991c). A more empirical approach has been used by Petroff et al. (1991b) and Duvail et al. (1994) by introducing spin dependent terms in semi-classical models. In their calculation based on the semi-classical approach of Johnson and Camley (1991), Duvail et al. (1994) introduce parameters derived from bulk materials for the temperature dependent resistivity terms $\delta\rho_\sigma(T)$ and the spin mixing term $\rho_{\uparrow\downarrow}(T)$, and included a temperature-dependent interface scattering term as a free parameter. A good fit is obtained for the temperature dependence of the CIP-resistivity and magnetoresistance of a series of Co/Cu multilayers.

However, this is again in the CPP-geometry that the modeling of the temperature dependence is easier and the interpretation of experimental results can be more quantitative.

When spin mixing is neglected, the CPP-resistance and magnetoresistance in the long SDL limit are still given by eqs (16)–(18) where now ρ_F^*, ρ_N^*, r_b^*, β, and γ are replaced by temperature-dependent parameters $\rho_F^*(T)$, $\rho_N^*(T)$, $r_b^*(T)$, $\beta(T)$ and $\gamma(T)$, taking into account both the elastic and inelastic contributions to the scattering. The experimental results of Oeps et al. (1996) on Co/Cu multilayers deposited on grooved substrates (see fig. 17) have been analyzed in this way. This leads to the temperature dependence of the resistivity and interface parameters shown in fig. 40. The interface resistance parameters $r_b^*(T)$ and its spin asymmetry coefficient $\gamma(T)$, are weakly temperature-dependent. This means that, up to room temperature, the main contribution to the interface resistances still comes from elastic scattering (specular and diffuse), with a relatively small contribution from inelastic scattering. The increase of the resistivities $\rho_F^*(T)$ and $\rho_N^*(T)$ by more than a factor of two between 4.2 K and 300 K reflects the additional inelastic scattering by phonons and magnons. However, the spin asymmetry coefficient of the resistivity in the Co layers is almost temperature-independent, which suggests that the spin asymmetry is about the same for elastic and inelastic scattering in Co; this is in agreement with the results from measurements on bulk Co alloys by Loegel and Gautier (1971).

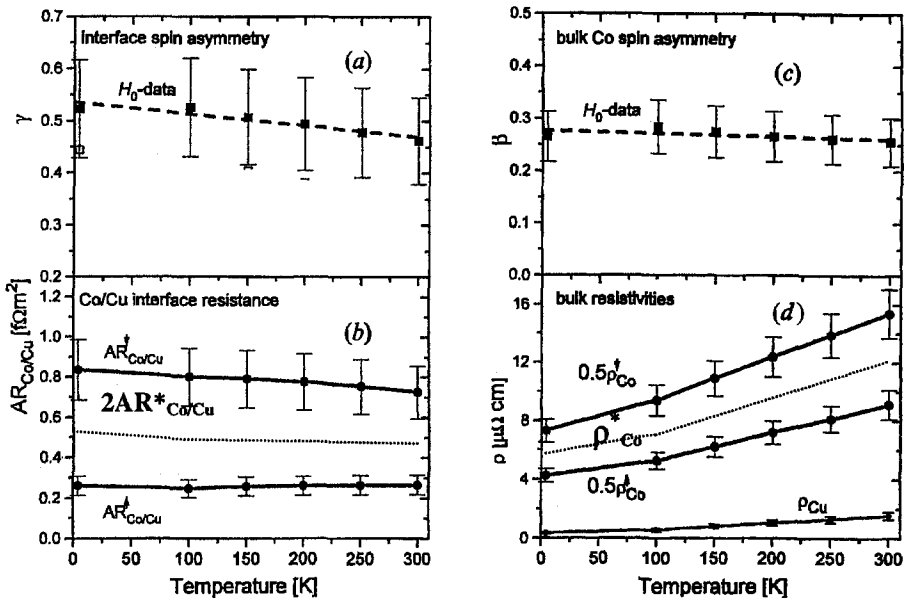


Fig. 40. Temperature dependence of the spin asymmetry parameter at the interface γ (a) and within the bulk β (c), of the resistance at the Co/Cu interface (b) and of the resistivity of Co and Cu layers (d). From Oeps et al. (1996).

When spin mixing is taken into account, it has been shown (Piraux et al. 1998 and references therein) that, in the expression for the GMR, eq. (18), $\rho^{*}_{F}(T)$, $\beta(T)$, $r^{*}_{b}(T)$ and $\gamma(T)$ should be replaced by the following effective parameters:

$$\rho^{F}_{eff}(T) = \rho^{*}_{F}(T) + \rho_{\uparrow\downarrow}(T), \tag{20}$$

$$\beta_{eff}(T) = \frac{\beta(T)}{[1 + \rho_{\uparrow\downarrow}(T)/\rho^{*}(T)]}, \tag{21}$$

$$r^{b}_{eff}(T) = r^{*}_{b}(T) + r_{\uparrow\downarrow}(T), \tag{22}$$

$$\gamma_{eff}(T) = \frac{\gamma(T)}{[1 + r_{\uparrow\downarrow}(T)/r^{*}_{b}(T)]}, \tag{23}$$

where $\rho_{\uparrow\downarrow}(T)$ is the spin mixing parameter of the two current model, and $r_{\uparrow\downarrow}(T)$ is a similar parameter introduced to express the spin mixing at interfaces.

The analysis of CPP-GMR data on Co/Cu multilayered nanowires with the above model by Piraux et al. (1998) confirms the results of Oeps et al. (1996) on the weak temperature dependence of the spin asymmetry coefficient in Co layers; $\beta_{eff}(T)$ decreases from 0.36 to 0.31 between 77 K and 300 K, and this decrease can be accounted for by the increase of the term in $\rho_{\uparrow\downarrow}(T)$ in the denominator of eq. (21). Ono et al. (1997) have also analyzed the temperature dependence of the CPP-GMR data on Py/Cu/Co/Cu multilayers in a model taking into account the spin mixing in the SDL limit and have been able to derive both, the bulk and interface spin mixing terms, $\rho_{\uparrow\downarrow}(T)$ and $r_{\uparrow\downarrow}(T)$.

Spin mixing can also be taken into account outside of the long SDL limit. For example, in the limit of very thick magnetic layers (with thin nonmagnetic layers), eq. (19) becomes:

$$\frac{\Delta R}{R^{\mathrm{P}}} = \frac{2p\beta_{\mathrm{eff}}^2(T)}{(\rho_{\mathrm{F}}^*(T)/\rho_{\mathrm{eff}}^{\mathrm{F}}(T) - \beta_{\mathrm{eff}}^2(T))} \frac{l_{\mathrm{sf}}^{\mathrm{F}}}{t_{\mathrm{F}}}. \tag{24}$$

Equation (24) has been used by Piraux et al. (1998) to analyze the room temperature data of fig. 29 on Co/Cu multilayered nanowires and to derive the SDL in Co at 300 K, $l_{\mathrm{sf}}^{\mathrm{Co}}(300\ \mathrm{K}) \approx 38 \pm 12$ nm.

As pointed out in the preceding paragraph, a moderate reduction of the SDL between 77 K (59 nm) and 300 K indicates that the SDL is mainly controlled by elastic spin–orbit scattering on imperfections and has no important contribution from electron–magnon scattering.

4.9. Angular dependence

In most theoretical descriptions of the GMR, only parallel and antiparallel orientations of the magnetization in consecutive layers are considered and only a few publications have addressed the question of the variation with the angle γ between the magnetizations.

In CIP geometry and in the simple case with only spin-dependent scattering (no potential barriers between the layers), the resistance is found to vary as (Zhang et al. 1992):

$$R(\gamma) = R^{\mathrm{P}} + \Delta R \sin^2(\gamma/2), \tag{25}$$

where γ is the angle between the magnetizations of consecutive magnetic layers. On the other hand, the calculations of Vedyayev et al. (1994) for a simplified structure composed of only two magnetic layers find a linear variation of the conductance as $\sin^2(\gamma/2)$ when only spin-dependent scattering is taken into account and very large departures from this variation when a spin-dependent potential step is introduced. Barnas et al. (1997) have calculated the angular dependence in a semi-classical model as well as in a quantum mechanical approach. In the quasi-classical limit, they find that the resistance of a multilayer varies approximately linearly with $\sin^2(\gamma/2)$, even when interface potentials (i.e., specular reflections) are taken into account. On the other hand, in the quantum limit, the linear variation of eq. (25) occurs only when the structure is symmetrical also with spin-independent intrinsic potential. Finally, Vedyayev et al. (1997) have calculated the angular dependence of the GMR in the CPP geometry and also expect deviations from eq. (25) when the intrinsic potential is spin-dependent and larger.

There are also few experimental results on the angular dependence of the GMR. In conventional multilayers, the angle γ varies as the field H is applied, but there is generally some uncertainty in the relation between γ and H; it can occur that the angle γ is not uniformly distributed over the sample, and this makes a precise determination of the angular dependence difficult. However, Chaiken et al. (1990) have carefully analyzed GMR experiments on Fe/Cr multilayers and found a reasonable agreement with eq. (25).

Other studies of the angular dependence have been performed on structures in which the magnetization of some layers can be rotated, while the magnetization of the neighbor layers is pinned by their coercivity or by their interaction with an antiferromagnetic

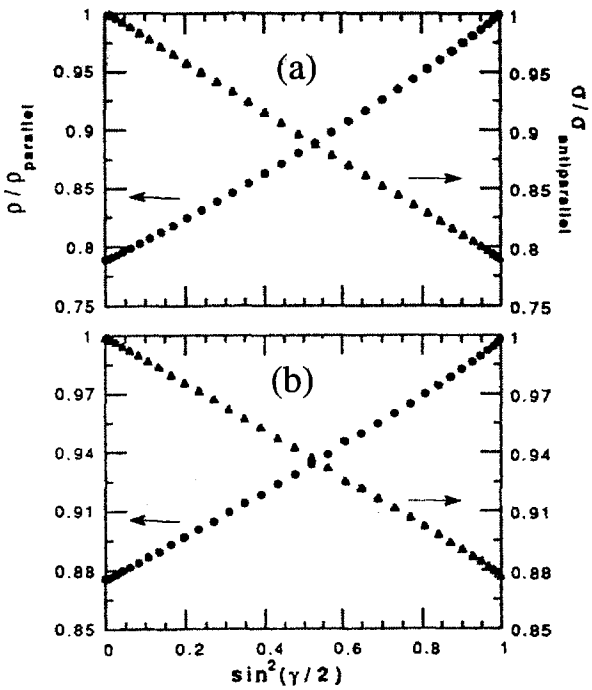


Fig. 41. Resistivity (•) and conductivity (▲) as a function of $\sin^2(\gamma/2)$ for (a) [Co(4Å)/Ag(40Å)/NiFe(40Å)/Ag(40Å)]$_{15}$ and [Co(5Å)/Cu(60Å)/NiFe(40Å)/Cu(60Å)]$_{15}$. From Steren et al. (1995a, 1995b).

layer. Measurements have been performed on (NiFe/Cu/NiFe/FeMn) spin valves (Dieny et al. (1991a) and on multilayers alternating soft and hard magnetic layers, NiFe/Cu/Co/Cu and NiFe/Ag/Co/Ag (Shinjo 1993; Steren et al. 1995a). Various tricks have been used to correct the results for the contribution from AMR and for some effects due to the residual coupling between the soft and hard layers. None of these measurements could evidence clearly some deviation from eq. (25). An example of variation for a multilayer alternating very soft NiFe layers and hard layers composed of Co clusters is shown in fig. 41. The variation of the resistance is almost linear in $\sin^2(\gamma/2)$. The absence of significant deviation from eq. (25) could be interpreted by the predominance of spin-dependent scattering effects in the multilayers in which the angular dependence has been studied. But one can also argue that the angular dependence has been studied only in samples with a relatively thick spacer layer (to avoid any coupling between the magnetic layers) and reflects the quasi-classical regime described by Barnas et al. (1997). It might be that some deviation from eq. (25) can be observed only for multilayers with much thinner layers.

The angular dependence has been studied in the CPP geometry too (Dauguet et al. 1996a; Vedyayev et al. 1997b). The deviations from eq. (25) are more pronounced than in CIP measurements but remain relatively small.

5. Guide to experimental data

See table 3.

TABLE 3

Publications reporting experimental work on GMR are listed in chronological order by year, and in alphabetic order for a given year. The first column refers to the reference list. The last column indicates the investigated system(s). The other columns indicate the geometry of the measurements (CIP, CPP or CAP) and the characteristic features of reported work.

Reference	Geometry	Characteristic 1	Characteristic 2	System
Baibich et al. (1988)	CIP		Nonmagn. thickness dep.	Fe/Cr
Binasch et al. (1989)	CIP			Fe/Cr
Takahata et al. (1989)	CIP		Magn. thickness dep.	Co/Au
Barnas et al. (1990)	CIP	Dependence on the number of layers Different coercivities		Fe/Cr Co/Au
Barthélémy et al. (1990)	CIP		Nonmagn. thickness dep. Magn. thickness dep. T-dependence	Fe/Cr
Chaiken et al. (1990)	CIP	Angular dependence		Fe/Cr
Dieny et al. (1990)	CIP			Spin valve (FeMn) NiFe/Cu
Dupas et al. (1990)	CIP			Co/Au
Gurney et al. (1990)	CIP	Planar doping (Au or Ag at interface)		Fe/Cr
Parkin et al. (1990)	CIP		Nonmagn. thickness dep.	Co/Ru, Co/Cr Fe/Cr
Shinjo and Yamamoto (1990)	CIP			Co/Cu/NiFe
Araki et al. (1991)	CIP		Nonmagn. thickness dep. Magn. thickness dep.	Co/Ag
Baumgart et al. (1991)	CIP	Planar doping (V, Mn, Ge, Ir, Al at interface)	Dependence with the thickness of the doping layer	Fe/Cr
Brubaker et al. (1991)	CIP			Fe/Mo
Chaiken et al. (1991a)	CIP		T-dependence	Fe/Cr
Chaiken et al. (1991b)	CIP		Magn. thickness dep. (t_{Fe})	Fe/Cu/Co
Chaiken et al. (1991c)	CIP		Magn. thickness dep. (t_{Co})	Fe/Cu/Co

TABLE 3 (Continued)

Reference	Geometry	Characteristic 1	Characteristic 2	System
Dieny et al. (1991a)	CIP	Angular dependence		Spin valve (FeMn) Co/Cu/NiFe
Dieny et al. (1991b)	CIP		Nonmagn. thickness dep. Magn. thickness dep.	Spin valve (FeMn) NiFe/Cu, Co/Cu Co/Cu/NiFe, Co/Ag/NiFe Co/Au/NiFe, Ni/Cu/NiFe
Dos Santos et al. (1991)	CIP			Ag/Ni
Freitas et al. (1991)	CIP		Nonmagn. thickness dep.	Gd/Y
Gurney et al. (1991)	CIP	Planar doping (V, Cr, Mn, Ir, Al, Ge at interface)	Dependence on the thickness of the planar doping layer	Fe/Cr
Mosca et al. (1991a)	CIP		Nonmagn. thickness dep.	Co/Cu
Mosca et al. (1991b)	CIP		Nonmagn. thickness dep. Magn. thickness dep.	Co/Cu, Co/Ag
Parkin et al. (1991a)	CIP			Co/Cu
Parkin et al. (1991b)	CIP	Influence buffer and overlayer		Co/Cu
Petroff et al. (1991a)	CIP		Nonmagn. thickness dep.	Co/Cu, Fe/Cu
Petroff et al. (1991b)	CIP		Nonmagn. thickness dep. T-dependence	Fe/Cr
Pratt et al. (1991)	CPP, CIP		Nonmagn. thickness dep.	Co/Ag
Yamamoto et al. (1991)	CIP		Nonmagn. thickness dep. T-dependence Effect. number of period	Co/Cu/NiFe
Dieny et al. (1992b)	CIP		Magn. thickness dep. T-dependence	Spin valve (FeMn) Co/Cu/NiFe Ni/Cu/NiFe NiFe/Cu/NiFe

TABLE 3 (Continued)

Reference	Geometry	Characteristic 1	Characteristic 2	System
Dieny et al. (1992a)	CIP		T-dependence	Spin valve (FeMn) Co/Cu/NiFe
Edwards et al. (1992)	CIP		Nonmagn. thickness dep. Magn. thickness dep.	Co/Cu
Fert and Bruno (1992)	CIP			Review paper
Fert et al. (1992)	CIP		Nonmagn. thickness dep.	Fe/Cr Co/Cu Fe/Cu
Folkerts et al. (1992)	CIP			Fe/Cr
Freitas et al. (1992)	CIP		Nonmagn. thickness dep.	Co/Re
Fullerton et al. (1992)	CIP	Influence of roughness (sputtering pressure)	Nonmagn. thickness dep.	Fe/Cr
Gijs and Okada (1992)	CIP		Nonmagn. thickness dep. T-dependence	Fe/Cr
Giron et al. (1992)	CIP		Nonmagn. thickness dep.	Co/Cu
Huai and Cochrane (1992)	CIP		Nonmagn. thickness dep. T-dependence	Co/Re
Jacob et al. (1992)	CIP	Influence of roughness	Magn. thickness dep.	Fe/Cr
Kamijo and Igarashi (1992a)	CIP			Fe/Cr
Kamijo and Igarashi (1992b)	CIP	Influence of interface roughness		Fe/Cr
Lee et al. (1992)	CPP	Scattering parameters		Co/Ag
Mattson et al. (1992)	CIP		Nonmagn. thickness dep.	Fe/Nb
Obi et al. (1992)	CIP	Effect of roughness (sputtering pressure)	Nonmagn. thickness dep.	Fe/Cr
Okuyama et al. (1992)	CIP	Angular dependence		Co/Cu/NiFe

TABLE 3 (Continued)

Reference	Geometry	Characteristic 1	Characteristic 2	System
Parkin (1992a)	CIP	Planar doping (Co at interfaces)	Nonmagn. thickness dep.	NiFe/Cu
Parkin (1992b)	CIP	Effect of annealing	Nonmagn. thickness dep. T-dependence	NiFe/Cu
Parkin et al. (1992)	CIP		Nonmagn. thickness dep. T-dependence	Co/Cu
Piraux et al. (1992)	CIP	Correlation between thermopower and GMR		Co/Cu Fe/Cu Fe/Cr
Pizzini et al. (1992)	CIP	Correlation GMR-structure	Nonmagn. thickness dep.	Fe/Cu, Co/Cu
Renard et al. (1992)	CIP		T-dependence	Co/Cu
Rodmacq et al. (1992)	CIP		Nonmagn. thickness dep.	Ni/Ag
Saito et al. (1992)	CIP	Influence of concentration of alloy effect on growth condition (Ar acceleration voltage)	Nonmagn. thickness dep.	Co_xFe_{1-x}/Cu
Schelp et al. (1992)	CIP	Effect of annealing		Co/Ag
Shinjo et al. (1992)	CIP	Angular dep. of influence buffer	Nonmagn. thickness dep.	Co/Cu/NiFe Co/Ag/NiFe Co/Au/NiFe
Tomlinson et al. (1992)	CIP	Effect of Fe buffer	Nonmagn. thickness dep.	Co/Cu
Vélu et al. (1992)	CIP		T-dependence	Fe/Au Co/Au
Alper et al. (1993)	CIP	Electrodeposited multilayers		CoNiCu/Cu
Aoki et al. (1993)	CIP		Nonmagn. thickness dep.	Fe/Cr
Araki (1993)	CIP	Discontinuous layer	Nonmagn. thickness dep. Magn. thickness dep.	Co/Ag
Araki and Narumiya (1993)	CIP	Influence of microstructure	Nonmagn. thickness dep.	Co/Ag
Avdi et al. (1993)	CIP	Correlation of thermopower and GMR	Nonmagn. thickness dep.	Pillar structures Co/Cu

TABLE 3 (Continued)

Reference	Geometry	Characteristic 1	Characteristic 2	System
Bauer et al. (1993)	CPP			Fe/Cr
Bian et al. (1993)	CIP		T-dependence Nonmagn. thickness dep.	NiCo/Cu
Chaiken et al. (1993)	CIP	Influence of the Co concentration		CoFe/Ag/Fe
Chen et al. (1993)	CIP	Influence of alloying	Nonmagn. thickness dep. T-dependence	$Fe_{1-x}Cr_x$/Cr
Childress et al. (1993)	CIP	Control of coercivity		Fe/Pd/Cu/Co/Cu Fe/Pd/Ag/Fe/Ag
Chubing et al. (1993)	CIP		Nonmagn. thickness dep.	NiFe/Cr
Coehoorn and Duchateau (1993)	CIP	Effect of composition of the magnetic layer		FeCoNi/Cu
Dei et al. (1993)	CIP	Effect buffer layer (roughness and texture)	Nonmagn. thickness dep.	NiFe/Cu
Dieny et al. (1993)	CIP	Planar doping Interface scattering Scattering parameters		Spin valve (FeMn) NiFe/Cu/Co NiFe/Cu, NiFe/Cu/Fe
Doi et al. (1993)	CIP		Nonmagn. thickness dep.	Fe/Cu
Dorner et al. (1993)	CIP	Effect of Fe buffer	Nonmagn. thickness dep.	Co/Cu
Fullerton et al. (1993a)	CIP	Influence of orientations (1 0 0) and (2 1 1)	Nonmagn. thickness dep. Magn. thickness dep.	Fe/Cr
Fullerton et al. (1993b)	CIP		Nonmagn. thickness dep.	Fe/Cr
George et al. (1993)	CIP	Planar doping		
Gijs et al. (1993a)	CPP			Pillar structures Fe/Cr

TABLE 3 (Continued)

Reference	Geometry	Characteristic 1	Characteristic 2	System
Gijs et al. (1993b)	CIP, CPP	Determination of scattering parameters		Pillar structures Fe/Cr
Gijs et al. (1993c)	CPP, CIP		T-dependence	Pillar structures Fe/Cr
Grolier et al. (1993)	CIP		Nonmagn. thickness dep.	Co/Au
Grundy et al. (1993)	CIP	Effect of buffer layer		Co/Cu
Gurney et al. (1993)	CIP	Filter layer: determination of the spin up and down mean free path in Co, Fe, NiFeCu, AuCu		Spin valve (FeMn) Fe/NiFe/Cu/NiFe Cu/NiFe/Cu/NiFe Co/NiFe/Cu/NiFe AuCu/NiFe/Cu/NiFe
Hall et al. (1993a)	CIP	Effect of annealing		Co/Cu
Hall et al. (1993b)	CIP	Effect of annealing	Nonmagn. thickness dep.	Co/Cu
Harp et al. (1993)	CIP	Effect of roughness (growth temperature)	Nonmagn. thickness dep.	Co/Cu
Honda et al. (1993)	CIP	Effect of texture, roughness	Nonmagn. thickness dep.	Co/Cu
Huang et al. (1993)	CIP	Influence of roughness (dependence on annealing temperature)		Spin valve (FeMn) NiFe/Cu
Inomata and Hashimoto (1993)	CIP	Effect of sputtering voltage (roughness)	Nonmagn. thickness dep. Magn. thickness dep.	NiFe/Cu/Co
Inomata and Saito (1993)	CIP	Effect of composition of the magnetic layer	Magn. thickness dep. Nonmagn. thickness dep.	CoFe/Cu
Inomata et al. (1993)	CIP	Effect of growth condition Effect of composition of the magnetic layer	Nonmagn. thickness dep.	NiFe/Cu Co_xFe_{1-x}/Cu
Jimbo et al. (1993a)	CIP	Effect of buffer	Nonmagn. thickness dep.	NiFeCo/Cu

TABLE 3 (Continued)

Reference	Geometry	Characteristic 1	Characteristic 2	System
Jimbo et al. (1993b)	CIP	Effect buffer layer	Nonmagn. thickness dep.	NiFeCo/Cu
Kano et al. (1993a)	CIP	Influence of roughness (growth temperature)		Co/Cu
Kano et al. (1993b)	CIP	Effect of composition of the magnetic layer	Magn. thickness dep.	CoFe/Cu CoNi/Cu
Kataoka et al. (1993a)	CIP	Effect of composition of the magnetic layer	Nonmagn. thickness dep.	$CoFe/Cu/Co_xFe_{1-x}$
Kataoka et al. (1993b)	CIP	Effect of composition of the magnetic layer		CoMn/Cu CoCr/Cu CoNi/Cu Co_xFe_{1-x}/Cu
Kobayashi et al. (1993)	CIP		Magn. thickness dep. Nonmagn. thickness dep.	Co/Cu
Kubota et al. (1993)	CIP	Effect of composition of the magnetic layer	Nonmagn. thickness dep.	Ni_xCo_{1-x}/Cu
Le Dang et al. (1993)	CIP	Influence of buffer		Co/Cu
Lee et al. (1993)	CPP	Scattering parameters		Co/Ag Co/AgSn
Lottis et al. (1993)	CIP		Nonmagn. thickness dep. Magn. thickness dep.	NiFe/Cu/Co
Mattheis et al. (1993)	CIP		Nonmagn. thickness dep.	Co/Cu
Melo et al. (1993a)	CIP	Planar doping at interface (Fe, Ni, Co, Cr)	Magn. thickness dep. Nonmagn. thickness dep.	Co/Re
Melo et al. (1993b)	CIP		Magn. thickness dep. Nonmagn. thickness dep.	Co/Cu
Miyauchi and Araki (1993)	CIP			NiFe/Cu/Co
Nakatani et al. (1993)	CIP	Effect of texture (1 0 0) or (1 1 1)	Nonmagn. thickness dep.	NiFe/Cu

TABLE 3 (Continued)

Reference	Geometry	Characteristic 1	Characteristic 2	System
Nozières et al. (1993)	CIP	Effect of annealing (roughness)	Magn. thickness dep.	Spin valves (FeMn) NiFe/Cu
Oomi et al. (1993)	CIP	Effect pressure	Nonmagn. thickness dep.	Fe/Cr
Parkin (1993)	CIP	Planar doping Interface scattering	Variation with thickness and position of the inserted Co layer	Spin valve (FeMn) NiFe/Cu
Parkin and York (1993)	CIP	Influence structure perfection (deposition temperature)		Fe/Cr
Parkin et al. (1993)			Nonmagn. thickness dep.	Co/Cu
Plaskett and McGuire (1993)	CIP		Number of layer dep.	Co/Cu
Pratt et al. (1993a)		Scattering param.		Co/Cu Co/Ag
Pratt et al. (1993b)	CPP	Scattering param.		Co/Ag Co/AgSn
Rensing et al. (1993)	CIP	Effect growth condition (roughness)	Nonmagn. thickness dep.	Fe/Cr
Rodmacq et al. (1993)	CIP	Effect of annealing	Nonmagn. thickness dep.	NiFe/Ag
Rupp and Schuster (1993)	CIP	Effect of substrate and growth conditions Correlation of GMR–AF coupling	Magn. thickness dep. Nonmagn. thickness dep.	Co/Cu
Saito et al. (1993)	CIP	Effect of growth condition (roughness)		Co/Cu
Sakakima and Satomi (1993a)	CIP		Effect of number of period	Spin valve (FeMn) NiFeCo/Cu NiCo/Cu CoFe/Cu
Sakakima and Satomi (1993b)	CIP		Nonmagn. thickness dep.	Spin valve (FeMn) NiFeCo/Cu NiFeCo/Cu/Co
Sato et al. (1993)	CIP	Effect of buffer layer Effect of composition of the magnetic layer	Magn. thickness dep.	Ni_xFe_{1-x}/Cu

TABLE 3 (Continued)

Reference	Geometry	Characteristic 1	Characteristic 2	System
Satomi and Sakakima (1993)	CIP	Effect of annealing		NiFeCo/Cu NiFe/Cu/Co
Schroeder et al. (1993a)				
Schroeder et al. (1993b)	CPP	Scattering parameters	Nonmagn. thickness dep.	Co/Cu, Co/Ag
Sdaq et al. (1993)	CIP		Nonmagn. thickness dep.	Co/Cu
Shinjo (1993)	CIP			Co/Cu/NiFe
Shintaku et al. (1993)	CIP	Influence of orientations (1 0 0) and (1 1 1)	Nonmagn. thickness dep.	Fe/Au
Shintaku et al. (1993)	CIP		Nonmagn. thickness dep.	Fe/Au
Speriosu et al. (1993)	CIP	Effect of annealing	Nonmagn. thickness dep. Magn. thickness dep.	Spin valve (FeMn) NiFe/Cu
Suzuki and Taga (1993)	CIP	Effect of intermixing at interface (roughness)		Co/Cu
Suzuki et al. (1993)	CIP	Effect of buffer (texture, roughness)		Co/Cu
Tosin et al. (1993)	CIP	Effect of annealing (roughness)		Co/Ag
Tsunashima et al. (1993)	CIP		Nonmagn. thickness dep.	NiFeCo/Cu
Valet et al. (1993)	CIP			NiFe/Cu/Co
Yamamoto et al. (1993)	CIP	Planar doping at interface (Cr, Mn, Fe, Co, NiFe)		NiFe/Cu/Co
Alper et al. (1994)	CIP	Electrodeposition	Nonmagn. thickness dep.	CoNiCu/Cu
Bass et al. (1994)	CPP	Doped layer: influence of impurities on the lsf		Co/Ag, Co/Ag(Mn), Co/Ag(Sn) Co/Cu Co/Cu(Mn), Co/Cu(Sn)
Bian et al. (1994)	CIP	Influence of concentration of alloy	Nonmagn. thickness dep.	Ni_xCo_{1-x}/Cu

TABLE 3 (Continued)

Reference	Geometry	Characteristic 1	Characteristic 2	System
Blondel et al. (1994)	CPP			Nanowires Co/Cu
Chen et al. (1994)	CIP	Influence of concentration of alloy	Nonmagn. thickness dep.	$Fe_{1-x}Cr_x$/Cr
Clarke et al. (1994)	CIP	Paramagn. impurities at the interface	Nonmagn. thickness dep.	Co/Cu
Dieny (1994)				Review paper
Dinia et al. (1994)	CIP		Nonmagn. thickness dep. T-dependence	Co/Ru
Duvail et al. (1994)	CIP		T-dependence	Co/Cu
Eckl et al. (1994)	CIP	Correlation growth–GMR	Nonmagn. thickness dep.	Co/Cu
Farrow et al. (1994)	CIP	Effect of annealing and growth temperature		NiFeAg/Ag
Freitas et al. (1994a)	CIP			Spin valve (TbCo) NiFe/Cu
Freitas et al. (1994b)	CIP			Spin valve (TbCo) NiFe/Co/Cu/Co/NiFe
Gangopadhyay et al. (1994)	CIP	Effect of composition of the magnetic layer		NiFeCo/Cu
George et al. (1994)	CIP	Inverse GMR		Fe/Cu/Fe(Cr)
Gijs et al. (1994a)	CPP		T-dependence	Pillar structure Co/Cu
Gijs et al. (1994b)	CPP CIP		T-dependence	Pillar structure Fe/Cr
Hahn et al. (1994)	CIP	Effect of annealing Correlation GMR–AF coupling		Fe/Cr
Holody et al. (1994)	CIP			Hybrid structures NiFe/Ag/Co
Hossain et al. (1994)	CIP	Influence of annealing	Co concentration dependence	NiFeCo/Cu

TABLE 3 (Continued)

Reference	Geometry	Characteristic 1	Characteristic 2	System
Hua et al. (1994)	CIP		Nonmagn. thickness dep.	CoNiCu/Cu
Huai et al. (1994)	CIP		Nonmagn. thickness dep.	Co/Re
Inomata et al. (1994)	CIP		Magn. thickness dep.	CoFe/Cu
Kubota et al. (1994)	CIP	Effect of composition of the magnetic layer	Nonmagn. thickness dep.	NiCo/Cu Co/Cu Ni/Cu
Kubota et al. (1994)	CIP	Effect of composition of the magnetic layer	Nonmagn. thickness dep.	Ni_xCo_{1-x}/Cu
Leal et al. (1994)	CIP		Nonmagn. thickness dep.	Co/Re
Lenczowski et al. (1994)	CIP	Correlation GMR–AF coupling	Nonmagn. thickness dep. T-dependence	Co/Cu
Liou et al. (1994)	CIP			Co/Cr
McGuire and Plaskett (1994a)	CIP	Effect of thin Co layer inserted in Cu	Nonmagn. thickness dep.	Spin valves (CoO) Co/Cu
McGuire and Plaskett (1994b)	CIP			Spin valve (NiCoO) NiCo/Cu
McGuire et al. (1994)	CIP	Effect of annealing	Nonmagn. thickness dep.	Co/Cu
Min and Joo (1994)	CIP		Magn. thickness dep.	Co/Cu
Modak et al. (1994)	CIP	Influence of microstructure		Co/Cu
Naoe et al. (1994)	CIP		Nonmagn. thickness dep.	NiFe/Cu
Parkin et al. (1994)	CIP		Nonmagn. thickness dep.	NiFe/Au NiFeAu/Au
Patel et al. (1994)	CIP		T-dependence	Spin valve (CoO) NiFe/Cu/Co
Piraux et al. (1994)	CPP			Nanowires Co/Cu
Rijks et al. (1994)	CIP	Crossed anisotropy		Spin valve (FeMn) NiFe/Cu

TABLE 3 (Continued)

Reference	Geometry	Characteristic 1	Characteristic 2	System
Sato et al. (1994)	CIP		Nonmagn. thickness dep.	Ni/Cu
Schad et al. (1994a)	CIP		Magn. thickness dep.	Fe/Cr
Schad et al. (1994b)	CIP	Influence of biquadratic coupling	Nonmagn. thickness dep.	Fe/Cr
Schroeder et al. (1994)	CPP, CIP	Comparison between maximum and zero applied field resistances		Co/Cu NiFe/Cu Co/Ag
Schuhl et al. (1994a)	CIP	Control coercivity		(Fe/Co/Pd)/(Cu/Co/Cu)
Schuhl et al. (1994b)	CIP	Concentration dependence		Ni_xFe_{1-x}/Pd/Fe/Pd/Fe
Shukh et al. (1994)	CIP		Magn. thickness dep.	Co/Cu
Sousa et al. (1994)	CIP		T-dependence	Co/Re
Watanabe et al. (1994)	CIP		Nonmagn. thickness dep.	NiFeCo/Cu/Co
Wellock et al. (1994)	CIP	Effect of Au impurities at interface		Co/Cu
Yang et al. (1994b)	CPP	Determination of spin diff. length		Co/AgMn, Co/CuMn Co/AgPt, Co/CuPt
Zhang et al. (1994)	CIP	Effect of annealing		Co/Cu
Attenborough et al. (1995a)	CPP		Nonmagn. thickness dep	Nanowires CoNiCu/Cu
Attenborough et al. (1995b)	CIP			NiFeCu/Cu
Bass et al. (1995)	CPP	Determination of spin asymmetry coefficients		Co/Cu/NiFe/Cu
Blondel et al. (1995)	CPP			Nanowires CoNi/Cu
Bobo et al. (1995)	CIP		Nonmagn. thickness dep.	Co/CuGe Co/CuNi
Cheng et al. (1995)	CIP	Effect of stress		Co/Cu/Fe
Cros et al. (1995)	CIP			CoPd/Ag
Czapkiewicz and Stobiecki (1995)	CIP		Magn. thickness dep.	Co/Zr, Fe/Zr

TABLE 3 (Continued)

Reference	Geometry	Characteristic 1	Characteristic 2	System
Daniels and Clemens (1995a)	CIP	Effect of doped magn. layer		$Fe_{1-x}Cr_x$/Cr $Co_{1-x}Cu_x$/Cu
Daniels and Clemens (1995b)	CIP	Effect of doping (concentration dependence)		Fe_xCr_{1-x}/Cr
Dieny et al. (1995)	CIP			Spin valves (FeMn) NiFe/Cu/Co
Dinia and Ounadjela (1995)	CIP		Nonmagn. thickness dep. T-dependence	Co/Ru
Dinia et al. (1995)	CIP		Effect of number of period Nonmagn. thickness dep.	Co/Ru
Duvail et al. (1995)	CPP CIP	Angular dependence Influence of T-growth	Nonmagn. thickness dep. Magn. thickness dep.	Hybrid structure Co/Ag/NiFe Co/Cu/NiFe
Egelhoff et al. (1995)	CIP		Magn. thickness dep. T-dependence	Spin valve (NiO) Co/Cu
Fert et al. (1995b)	CPP CIP			Review paper
Fujimoto et al. (1995)	CIP		T-dependence	Co/Cu/NiFe
Gijs et al. (1995a)	CAP CIP		T-dependence	V grooves Co/Cu
Gijs et al. (1995b)	CPP CIP		T-dependence	Pillar structures Fe/Cr, Co/Cu
Gillies et al. (1995)	CIP			Spin valves (FeMn) NiFe/Cu/NiFe
Hylton et al. (1995)	CIP			Dots NiFe/Ag
Jimbo et al. (1995)	CIP	Amorphous layers		CoFeB/Cu/Co
Jin et al. (1995)	CIP		Nonmagn. thickness dep.	Co/Al

TABLE 3 (Continued)

Reference	Geometry	Characteristic 1	Characteristic 2	System
Kano et al. (1995)	CIP	Low field effects		NiFeCo(Cu)/Cu
Kawawake and Sakakima (1995)	CIP			NiFe/Cu/Co NiFe/Cu/Ag/Cu/Co
Kim and Sanders (1995)	CIP	Effect of annealing		NiFe/Ag
Korenivski et al. (1995)	CIP	Effect of roughness (irradiation, annealing)		Fe/Cr
Kubota et al. (1995)	CIP	Influence of composition of the magnetic layer	T-dependence	NiCo/Cu NiFe/Cu CoFe/Cu
Lee et al. (1995)	CPP			
Lenczowski et al. (1995a)	CIP	Scattering parameters	Magn. thickness dep. Nonmagn. thickness dep.	NiFe/Cu Co/Cu
Lenczowski et al. (1995b)	CIP	Effect of growth conditions (electrodeposition)	Nonmagn. thickness dep.	Co/Cu
List et al. (1995a)	CPP, CIP		Nonmagn. thickness dep.	Co/Cu
List et al. (1995b)	CPP, CIP		Nonmagn. thickness dep.	Co/Cu
Liu et al. (1995)	CPP	Determination of spin diff. length	T-dependence	Nanowires Co/Cu
Loloee et al. (1995)	CPP		Magn. thickness dep. Nonmagn. thickness dep.	Co/Ag
McMichael et al. (1995)	CIP	Thermal stability		Spin valve (NiO) Co/Cu
Meguro et al. (1995)	CIP	Effect of composition of the magnetic layer		NiFeCo/Cu
Mulloy et al. (1995a)	CIP		Magn. thickness dep.	Co/Au
Mulloy et al. (1995b)	CIP	Dependence on the number of layers		Co/Au

TABLE 3 (Continued)

Reference	Geometry	Characteristic 1	Characteristic 2	System
Ono and Shinjo (1995)	CAP CIP			V grooves Co/Cu/NiFe
Pollard et al. (1995a)	CIP	Correlation GMR–growth conditions (texture)		Co/Cu
Pollard et al. (1995b)	CIP	Initial GMR curve		Co/Cu
Pollard et al. (1995c)	CIP	Effect of growth conditions (ion beam energy)		Co/Cu
Redon et al. (1995)	CIP			CoFe/Ag
Renard et al. (1995)	CIP	Inverse GMR	T-dependence	FeV/Au/Co
Saito et al. (1995)	CIP	Effect of roughness (effect of sputtering of Ar acceleration voltage, effect of annealing)		NiFe/Cu/Co
Sakakima et al. (1995)	CIP			NiFeCo/Cu
Schad et al. (1995)	CIP	Effect of growth condition (interface roughness)		Fe/Cr
Steren et al. (1995a)	CIP	Angular dependence		Hybrid structures Co/Ag/NiFe
Steren et al. (1995b)	CIP	Angular dependence	Nonmagn. thickness dep.	Hybrid structures Co/Ag/NiFe
Uwatoko et al. (1995)	CIP	Effect of pressure		Co/Cu
Van Alphen and De Jonge (1995)	CIP	Effect of discontinuous layers, effect of annealing	Magn. thickness dep. Nonmagn. thickness dep.	Co/Ag
Vas'kovskij et al. (1995)	CIP		T-dependence	NiFe/Cu NiFe/Cr NiFe/TiN

TABLE 3 (Continued)

Reference	Geometry	Characteristic 1	Characteristic 2	System
Vavra et al. (1995)	CPP	Size effect		Lithography NiFeCo/Cu/Co
Voegeli et al. (1995)	CPP		Magn. thickness dep. Nonmagn. thickness dep.	Nanowires Co/Cu
Wellock et al. (1995)	CIP	Planar doping (Au, Ge, Cu at interface)		Co/Cu
Willekens et al. (1995a)	CIP	Effect of interface mixing		Spin valves (Co/Ru/Co) Co/Cu/Co
Willekens et al. (1995b)	CIP	Effect of interface mixing		Spin valve (FeMn) and antiferro-coupled) Co/Cu
Yang and Scheinfein (1995)	CIP		Nonmagn. thickness dep.	Co/Cu
De Azevedo et al. (1996)	CIP		Nonmagn. thickness dep.	Co/CuAu
Coehoorn (1996)	CIP			Review paper on spin valves
Colino et al. (1996)	CIP	Effect of annealing (roughness)		Fe/Cr
Cross and Kos (1996)	CIP	Relaxation effect		NiFe/Ag
Cross et al. (1996)	CIP	Size effect		Spin valves (FeMn) NiFe/Cu
Dauguet et al. (1996a)	CPP	Hybrid structure Angular dependence		Co/Ag/NiFe
Dauguet et al. (1996b)	CPP	Hybrid structure		Co/Ag/NiFe
Dieny et al. (1996)	CPP, CIP	Angular dependence	Magn. thickness dep. Nonmagn. thickness dep.	Spin valves (FeMn) NiFe/Cu/Co, NiFe/Ag
Doudin et al. (1996)	CPP	Scattering parameters	Magn. thickness dep. Nonmagn. thickness dep.	Nanowires Co/Cu

TABLE 3 (Continued)

Reference	Geometry	Characteristic 1	Characteristic 2	System
Egelhoff et al. (1996a)	CIP	Comparison of bottom and symmetric spin valves	Magn. thickness dep. Nonmagn. thickness dep.	Spin valves (NiO) Co/Cu
Egelhoff et al. (1996b)	CIP	Effect of temperature growth		Spin valves (FeMn) NiFe/Co/Cu/Co/NiFe
Egelhoff et al. (1996c)	CIP	Effect of roughness (in surfactant)		Spin valves (FeMn) NiFe/Cu/Co
Faini et al. (1996)	CIP	Determination of magn. reversal	Size effect	Dots Co/Cu/Co particule
Farrow et al. (1996)	CIP	Effect of roughness (annealing)	Nonmagn. thickness dep.	NiFe/Au NiFeAu/Au
Gangopadhyay et al. (1996)	CIP	Effect of sputtering condition (roughness) and annealing	Nonmagn. thickness dep.	CoFe/Cu
Hosoito et al. (1996)	CIP	Correlation GMR–AF ordering		Fe/Cr Fe/Au Co/Cu/NiFe
Hossain et al. (1996)	CIP	Effect of annealing	Magn. thickness dep.	NiFeCo/Cu
Huang et al. (1996)	CIP			Co/Cu
Imada et al. (1996)	CIP	Effect of buffer layer Effect of annealing		NiFeCo/Cu
Inoue (1996)	CIP	Effect of concentration		Co_xNi_{1-x}/Cu
Jimbo et al. (1996)	CIP		Magn. thickness dep. (CoFeB)	CoFeB/Cu/Co
Kamiguchi et al. (1996)	CIP	Effect of substrate		Spin valves (FeMn) CoFe/Cu/CoFe CoNbZr/NiFe/CoFe/Cu/CoFe
Kawawake et al. (1996)	CIP			Co/Cu/NiFe Co/Cu/Ag/Cu/NiFe

TABLE 3 (Continued)

Reference	Geometry	Characteristic 1	Characteristic 2	System
Kief et al. (1996)	CIP		Effect of number of period Nonmagn. thickness dep.	NiFe/Cu/Co
Kirschenbaum et al. (1996)	CIP			NiFe/Ag
Kitakami et al. (1996)	CIP			Spin valves (NiO) Co/Cu, NiFe/Cu
Kobayashi et al. (1996)	CIP			Co/Cu(Mn)
Kolb et al. (1996)	CIP	Hybrid structure	T-dependence	Co/Au
Krebs et al. (1996)	CPP			Pillar structures Co/Cu/NiFeCo
Kubinski and Holloway (1996a)	CIP	Effect of islanding	Nonmagn. thickness dep.	Co/Cu
Liou et al. (1996)	CIP			Co/Cr
Lucinski et al. (1996)	CIP	Effect of annealing (paramagnetic region at interface)		Fe/Cr
Mao et al. (1996)	CIP			Spin valves (NiMn) NiFe/Co/Cu/Co/NiFe
Matsuyama et al. (1996)	CIP			Strips Co/Cu/NiFe
Mibu et al. (1996)	CIP		Nonmagn. thickness dep.	Spin valve (CoSm) Co/Cu/NiFe
Min et al. (1996)	CIP		Magn. thickness dep. Nonmagn. thickness dep.	Co/Cu NiFeCo/Cu NiFe/Cu
Mosca et al. (1996)	CIP	Effect of seed layer		Fe/Cu
Nabiyouni and Scharzacher (1996)	CIP	Effect of texture	Nonmagn. thickness dep.	CoNiCu/Cu
Nagamachi et al. (1996)	CIP	Ion beam direct deposition method	Nonmagn. thickness dep.	Co/Cu
Nishioka et al. (1996)	CIP			Spin valves (FeMn) CoFe/Cu

TABLE 3 (Continued)

Reference	Geometry	Characteristic 1	Characteristic 2	System
Oeps et al. (1996)			T-dependence	Co/Cu
Oomi et al. (1996)	CIP	Effect of pressure		Co/Cu Fe/Cu Fe/Cr
Parkin (1996)	CIP	Effect of substrate	Magn. thickness dep. Nonmagn. thickness dep.	Spin valves (FeMn) NiFe/Cu NiFe/Co/Cu/Co/NiFe
Parkin and Rabedeau (1996)	CIP		Nonmagn. thickness dep.	NiFe/Au
Persat et al. (1996a)	CIP	Planar doping at the interface with Ag	Nonmagn. thickness dep.	Co/Cu
Persat et al. (1996b)	CIP		Nonmagn. thickness dep.	Co/Cu
Piraux et al. (1996a)	CPP	Scattering parameters lsf	Magn. thickness dep. Nonmagn. thickness dep.	Nanowires Co/Cu
Piraux et al. (1996b)	CPP	Scattering parameters	Nonmagn. thickness dep. Magn. thickness dep.	Nanowires Co/Cu
Pratt et al. (1996)	CPP	Scattering parameters	Variation with number of period	Co/Cu/NiFe Co/Ag/NiFe
Renard et al. (1996)	CIP	Inverse GMR	Magn. thickness dep. (FeV) T-dependence	FeV/Au/Co
Rensing et al. (1996)	CIP	Dependence on concentration Effect of thin Cr layer in Fe		$Fe_{1-x}Cr_x$/Cr
Sanders et al. (1996)	CIP	Effect of stripe width		NiFe/Ag
Schad et al. (1996a)	CIP	Effect of roughness		Fe/Cr
Schad et al. (1996b)	CIP		Magn. thickness dep.	Fe/Cr
Shinjo and Ono (1996)	CAP CIP		Nonmagn. thickness dep. T-dependence	V grooves Co/Cu/NiFe
Strijkers et al. (1996)	CIP	Determination of mean free path		Spin valves (Co/Ru/Co) Co/Cu

TABLE 3 (Continued)

Reference	Geometry	Characteristic 1	Characteristic 2	System
Swagten et al. (1996)	CIP	Planar doping with Ru in the magnetic layer		Spin valve (AF coupling) Co/Cu
Tsutsumi et al. (1996a)	CIP	Effect of growth condition (gas)	Nonmagn. thickness dep.	Co/Cu
Tsutsumi et al. (1996b)	CIP	Influence of sputtering conditions (gas: Ar, Kr)	Nonmagn. thickness dep.	Co/Cu
Ueda et al. (1996a)	CIP	Influence of composition of the magnetic layer	Nonmagn. thickness dep.	Co_xCu_{1-x}/Cu
Ueda et al. (1996b)	CIP	Influence of composition of the magnetic layer	Nonmagn. thickness dep.	Fe_xCr_{1-x}/Cr
Ustinov et al. (1996a)	CIP	Determination of scattering parameters		Fe/Cr
Ustinov et al. (1996b)	CIP	Correlation of GMR and biquadratic coupling		Fe/Cr
Vas'kovskij and Svalov (1996)	CIP			Spin valves (FeMn) NiFe/Cu
Young et al. (1996)	CIP			Strips NiFe/Ag
Zeltser and Smith (1996)	CIP	Effect of annealing	Magn. thickness dep. Nonmagn. thickness dep.	NiFe/Cu NiFeCo/Cu
Zeng and Wong (1996)	CIP	Effect of roughness (discharge pressure)		Ni/Ag
De Azevedo et al. (1997)	CIP		Nonmagn. thickness dep.	Co/CuAu
Aliev et al. (1997)	CIP			Co/Cr/Ag/Co
Almeida et al. (1997)	CIP	Influence of growth techn.	Temperature-dependence of the resistivity	Fe/Cr
Ando et al. (1997)	CIP	Correlation with AF coupling	Nonmagn. thickness dep.	NiFe/Cu

TABLE 3 (Continued)

Reference	Geometry	Characteristic 1	Characteristic 2	System
Blondel et al. (1997)	CPP	Scattering parameters	T-dependence	Nanowires Co/Cu
Bouat et al. (1997)	CIP	Effect of annealing		NiFe/Ag
Bouziane et al. (1997)	CIP		Nonmagn. thickness dep. Magn. thickness dep.	Co/Cu, CoZr/Cu CoZr/Co/CoZr/Cu Co/CoZr/Co/Cu
Burkett et al. (1997)	CIP	Effect of the pinned layer thickness		Spin valves (FeMn) CoNiFe/Cu NiFe/Cu CoFe/Cu
Butler et al. (1997)	CIP		Magn. thickness dep.	Spin valves FeMn Co/Cu
Caballero et al. (1997)	CIP	Half metallic	Nonmagn. thickness dep.	NiMnSb/Cu NiMnSb/Ag
Caulet et al. (1997)	CIP			Dots Co/Au
Chiang et al. (1997a)	CPP	Effect of pseudo-random fluctuation		Co/Cu
Chiang et al. (1997b)	CPP CIP	Effect of sequencing lsf		$(Co/Ag/NiFe)_n$ $(Co/Ag)_n/(NiFe/Ag)_n$
Chopra et al. (1997)	CIP	Effect of Pb layer (roughness)		Spin valves (NiO) Co/Cu
Corno et al. (1997)	CIP	Effect of Au coverage (during growth)		Co/Au
Cros et al. (1997)	CIP	Detect. of magnetization reversal via GMR	Size dependence	Dots Co/Cu/Co Co/Cu/NiFe
Diao et al. (1997)	CIP	Effect of buffer (roughness)		NiFeCo/Cu
Dinia et al. (1997)	CIP	Inverse GMR		Co/Ru/CoRu

TABLE 3 (Continued)

Reference	Geometry	Characteristic 1	Characteristic 2	System
Dubois et al. (1997a)	CPP	Scattering parameters	Nonmagn. thickness dep. Magn. thickness dep.	Nanowires NiFe/Cu Co/Cu
Dubois et al. (1997b)	CPP	Influence of dipolar coupling on moment		Nanowires NiFe/Cu
Egelhoff et al. (1997b)	CIP	Influence of specular reflections at the top surface (Au, Ag, Cu)		Spin valve (NiO) Co/Cu/Co
Encinas et al. (1997)	CAP CIP			Step bunching NiFe/Co/Cu
Fang et al. (1997a)	CIP	Influence of growth conditions	Magn. thickness dep. Nonmagn. thickness dep.	NiFe/Cu/Co
Fang et al. (1997b)	CIP	Influence of substrate temperature during growth	Nonmagn. thickness dep. Magn. thickness dep.	NiFe/Cu/Co
Fettar et al. (1997)	CIP	Influence of continuity	Nonmagn. thickness dep.	CoFe/Ag
Fujita et al. (1997)	CIP	Effect of annealing		Spin valve (FeMn) CoFeB/Cu/CoFeB/NiFe
Fuke et al. (1997)	CIP	Effect of annealing	Magn. thickness dep. (pinned CoFe layer)	Spin valve (IrMn) CoFe/Cu/CoFe/NiFe/CoZrNb
Gijs et al. (1997)	CPP	Scattering parameters	T-dependence	V grooves Co/Cu
Guarisco et al. (1997)	CIP		Nonmagn. thickness dep.	Spin valve (NiO) NiFe/Co/Cu/Co/NiFe
Hall et al. (1997)	CIP	Effect of annealing correlation on GMR-F coupling		Co/Cu
Han et al. (1997)	CIP	Influence of surface/interface roughness		Spin valve (NiO) NiFe/CoFe/Cu/Co/NiFe Co/Cu/Co
Hsu et al. (1997)	CPP	Inverse GMR scattering parameters	Magn. thickness dep. (FeV)	FeV/Cu/Co

TABLE 3 (Continued)

Reference	Geometry	Characteristic 1	Characteristic 2	System
Imada et al. (1997)	CIP		Nonmagn. thickness dep.	FeCoNi/Cu
Jarratt et al. (1997)	CIP	Effect of annealing		CoFe/Ag
Kawawake and Sakakima (1997)	CIP	Influence of Ag capping	Magn. thickness dep.	NiFe/Cu/Co
Kikuchi et al. (1997)	CIP	Effect of pinholes	Nonmagn. thickness dep.	Co/Cu
Kim et al. (1997)	CIP	Tilt Si substrate		NiFeCo/Cu/Co
Kos et al. (1997)	CIP	Device size dependence Current density dependence	T-dependence	Spin valve (FeMn) NiFe/Cu
Kubinski and Holloway (1997a)	CIP		Magn. thickness dep.	Co/Cu
Kubinski and Holloway (1997b)	CIP	Concentration dependence	Magn. thickness dep. Nonmagn. thickness dep.	$Co_{1-x}Cu_x$/Cu
Kubota et al. (1997)	CIP		Nonmagn. thickness dep. T-dependence	Ni/Cu NiCo/Cu NiFe/Cu
Lai et al. (1997)	CIP		T-dependence	Spin valve (NiO) NiFe/Cu
Liou et al. (1997)	CIP	Nonmagn. thickness dep.		Co/Cr
Maeda et al. (1997)	CAP CIP			V grooves Co/Cu
Mao et al. (1997)	CIP		Magn. thickness dep.	Co/Cu
Marrows et al. (1997)	CIP	Effects of impurity at interface or in bulk		Co/Cu
Miyamoto et al. (1997)	CIP	Effect of ion bombardment at the interface		NiFe/Cu
Miyazaki et al. (1997)	CIP		Concentration dependence	FeCoNi/Cu

TABLE 3 (Continued)

Reference	Geometry	Characteristic 1	Characteristic 2	System
Nakatani et al. (1997a)	CIP	Effect of buffer (texture)		NiFeCo/Cu
Nakatani et al. (1997b)	CIP	Dependence on concentration	Nonmagn. thickness dep.	NiFe/Cu_xNi_{1-x} Co/Cu_xNi_{1-x}
Oeps et al. (1997)	CPP	Scattering parameters Influence of growth techn.	Nonmagn. thickness dep.	V grooves Co/Cu
Ono et al. (1997)	CAP CIP	Scattering parameters	Magn. thickness dep. Nonmagn. thickness dep. T-dependence	V grooves Co/Cu/NiFe
Park and Shin (1997)	CIP	Effect of Ar pressure during sputtering		Spin valve (FeMn) NiFeCo/Cu
Pettit et al. (1997)	CIP			NiFe/Cu
Piraux et al. (1997)	CPP			Nanowires Co/Cu NiFe/Cu
Portier et al. (1997a)	CIP	Correlation GMR–magnetization		Spin valve (MnNi) NiFe/Co/Cu/Co/NiFe
Portier et al. (1997b)	CIP	Correlation GMR–magnetization		Spin valve (MnNi) NiFe/Cu/Co/NiFe
Pratt et al. (1997)	CPP	lsf in NiFe	Magn. thickness dep. Number of layer dep	Spin valve (FeMn) NiFe/Ag NiFe/Cu NiFe/Cu/Co
Rogers et al. (1997)	CIP			NiFe/Ag
Sakakima et al. (1997)	CIP		Magn. thickness dep.	Spin valve (CoO) CoMnB/Co/Cu/Co CoMnB/Fe/Cu/Fe
Schmeusser et al. (1997)	CIP	Effect of deposition conditions (impurity, roughness)		Co/Cu
Schwarzacher et al. (1997)	CPP		Nonmagn. thickness dep.	Nanowires CoNiCu/Cu

TABLE 3 (Continued)

Reference	Geometry	Characteristic 1	Characteristic 2	System
Steenwyck et al. (1997)	CPP	lsf in NiFe		Spin valve (FeMn) NiFe/Cu
Strijkers et al. (1997)	CIP	Interface scattering	Dependence on the magn. thickness of the probe layer	Spin valve (NiO) Co/Cu NiFe/Cu
Szucs et al. (1997)	CIP		T-dependence	Spin valve (FeMn) NiFe/Co/Cu/Co/NiFe NiFe/Cu/NiFe
Tanaka et al. (1997)	CIP			Spin valve (PdPtMn) NiFe/CoFe/Cu/Co/NiFe
Tsoukatos et al. (1997)	CIP		Nonmagn. thickness dep.	NiFe/Au
Tsunashima et al. (1997)	CIP		Magn. thickness dep.	Spin valve (NiO) CoFeB/Cu/Co CoFeB/Cu/CoFeB
Vouille et al. (1997)	CPP, CIP	Inverse GMR scattering parameters	Magn. thickness dep.	NiCr/Cu/Co
Wang et al. (1997)	CIP	Effect of annealing	Magn. thickness dep.	CoFe/Cu
Yan et al. (1997)	CIP		Nonmagn. thickness dep. T-dependence	Fe/Mo
Yanagihara et al. (1997)	CIP			Co/Ir
Yasuna et al. (1997)	CPP, CIP	Preparation: press rolling	T-dependence	Fe/Ag
Yu et al. (1997)	CIP		T-dependence	$Fe_{1-x}Co_x/Cr$
Christides et al. (1998)	CIP	Effect of magnetostatic interactions, effect of buffer		Co/Cu
Du et al. (1998) Dubois et al. (1999)	CIP			NiCo/Cu
Ge et al. (1998)	CIP	Effect of roughness		Fe/Mo
Hase et al. (1998)	CIP	Effect of roughness		Co/Cu

TABLE 3 (Continued)

Reference	Geometry	Characteristic 1	Characteristic 2	System
Holloway and Kubinski (1998)	CIP	Resistance loss after exposure to magnetic field		Co/Cu
Hwang et al. (1998)	CIP	Effect of buffer (roughness)		Spin valve (NiO) NiFe/Cu
Kools et al. (1998)	CIP			Spin valve (NiO) CoFe/Cu/CoFe/NiFeCo
Leal and Kryder (1998)	CIP	Comparison between the two pinning layers	T-dependence	Spin valves (Co/Ru/Co and FeMn) NiFe/Cu/Co/NiFe
Ono et al. (1998)	CIP	Determination of magnetization state via GMR		NiFe/Cu
Piraux et al. (1998)	CPP	Temperature dependence (spin mixing, phonon)		Nanowires Co/Cu
Reiss et al. (1998)	CIP	Effect of growth technique (roughness)		NiFe/Cu
Sakakima et al. (1998)	CIP	Effect of capping layer (Cu/Ag)		NiFe/Cu/Co
Sato et al. (1998)	CIP	Effect of specular reflection by NiO cover layer		Spin valves (NiO) NiFe/Cu/NiFe
Schad et al. (1998a)	CIP	Correlation GMR–interface roughness		Fe/Cr
Shinjo and Ono (1998)	CPP, CAP CIP			V grooves Co/Cu NiFe/Cu NiFe/Cu/Co
Ustinov et al. (1998)	CIP	Correlation GMR–microwave frequency		Fe/Cr
Velez and Schuller (1998)	CIP	Effect of roughness (sputtering Ar pressure)		Fe/Cr
Zoll et al. (1998)	CIP	Correlation of growth techn. and GMR	Nonmagn. thickness dep.	Co/Ru

References

Aliev, F.G., E. Kunnen, K. Temst, K. Mae, G. Verbanck, J. Barnas, V.V. Moshchalkov and Y. Bruynseraede, 1997, Phys. Rev. Lett. **78**, 134.

Almeida, B.G., V.S. Amaral, J.B. Sousa, J. Colino, I.K. Schuller, R. Schad, V.V. Moshchalkov and Y. Bruynseraede, 1997, J. Appl. Phys. **81**, 5194.

Alper, M., K. Attenborough, R. Hart, S.J. Lane, D.S. Lashmore, C. Younes and W. Schwarzacher, 1993, Appl. Phys. Lett. **63**, 2144.

Alper, M., K. Attenborough, V. Baryshev and D.S. Lashmore, 1994, J. Appl. Phys. **75**, 6543.

Ando, Y., H. Koizumi and T. Miyazaki, 1997, J. Magn. Magn. Mater. **166**, 75.

Anthony, T.C., J.A. Brug and S. Zhang, 1994, IEEE Trans. Magn. **30**, 3819.

Aoki, Y., H. Sato, Y. Kobayashi, K. Honda, T. Kumano, S. Hashimoto, T. Yokoyama, T. Hanyu, T. Kaneko and R. Yamamoto, 1993, J. Magn. Magn. Mater. **126**, 448.

Araki, S., 1993, J. Appl. Phys. **73**, 3910.

Araki, S., and Y. Narumiya, 1993, J. Magn. Magn. Mater. **126**, 521.

Araki, S., K. Yasui and Y. Narumiya, 1991, J. Phys. Soc. Japan **60**, 2827.

Asano, Y., A. Oguri and S. Maekawa, 1993, Phys. Rev. B **48**, 6192.

Attenborough, K., R. Hart, W. Schwarzacher, J.Ph. Ansermet, A. Blondel, B. Doudin and J.P. Meier, 1995a, in: Magnetic Ultrathin Films, Multilayers and Surfaces, MRS Symp. Proc., Vol. 384 (MRS, Pittsburg, Pennsylvania) p. 384.

Attenborough, K., R. Hart, S.J. Lane, M. Alper and W. Scharzacher, 1995b, J. Magn. Magn. Mater. **148**, 335.

Avdi, E., J. Hickey, D. Greig, M.A. Howson, M.J. Hall, J. Xu, M.J. Walker, N. Wiser and P. de Groot, 1993, J. Appl. Phys. **73**, 5521.

Baibich, M.N., J.M. Broto, A. Fert, F. Nguyen Van Dau, P. Etienne, G. Creuzet, A. Friederich and J. Chazelas, 1988, Phys. Rev. Lett. **61**, 2472.

Barnas, J., 1994, J. Magn. Magn. Mater. **131**, L14.

Barnas, J., and Y. Bruynseraede, 1995, Europhys. Lett. **32**, 167.

Barnas, J., and Y. Bruynseraede, 1996, Phys. Rev. B **53**, 5449.

Barnas, J., and A. Fert, 1994a, Phys. Rev. B **49**, 12835.

Barnas, J., and A. Fert, 1994b, J. Magn. Magn. Mater. **136**, 260.

Barnas, J., and A. Fert, 1998, Phys. Rev. Lett. **80**, 1058.

Barnas, J., A. Fuss, R.E. Camley, P. Grünberg and W. Zinn, 1990, Phys. Rev. B **42**, 8110.

Barnas, J., O. Baksalary and A. Fert, 1997, Phys. Rev. B **56**, 6079.

Barthélémy, A., and A. Fert, 1991, Phys. Rev. B **43**, 13124.

Barthélémy, A., A. Fert, M.N. Baibich, S. Hadjoudj, F. Petroff, P. Etienne, R. Cabanel, S. Lequien and G. Creuzet, 1990, J. Appl. Phys. **67**, 5908.

Bass, J., Q. Yang, S.F. Lee, P. Holody, R. Loloee, P.A. Schroeder and W.P. Pratt Jr., 1994, J. Appl. Phys. **75**, 6699.

Bass, J., P.A. Schroeder, W.P. Pratt, S.F. Lee, Q. Yang, P. Holody, L.L. Henry and R. Loloee, 1995, Mater. Sci. Eng. B **31**, 77.

Bass, J., W.P. Pratt and P.A. Schroeder, 1998, Comments Cond. Mater. Phys. **18**, 223.

Bauer, G.E.W., 1992, Phys. Rev. Lett. **69**, 1676.

Bauer, G.E.W., M.A.M. Gijs, S.K.J. Staszek, K.J. Lenczowski and J.B. Giesberg, 1993, J. Magn. Magn. Mater. **126**, 454.

Baumgart, P., B.A. Gurney, D.R. Wilhoit, B. Dieny and V.S. Speriosu, 1991, J. Appl. Phys. **69**, 4792.

Berger, L., 1996, Phys. Rev. B **54**, 9353.

Berkowitz, A.E., J.R. Mitchell, M.J. Carey, A.P. Young, S. Zhang, F.E. Spada, F.T. Parker, A. Hutten and G. Thomas, 1992, Phys. Rev. Lett. **68**, 3745.

Bian, X., J.O. Ström-Olsen, Z. Altounian, Y. Huai and R.W. Cochrane, 1993, Appl. Phys. Lett. **62**, 3525.

Bian, X., J.O. Ström-Olsen, Z. Altounian, Y. Huai and R.W. Cochrane, 1994, J. Appl. Phys. **75**, 7064.

Binasch, G., P. Grünberg, F. Saurenbach and W. Zinn, 1989, Phys. Rev. B **39**, 4828.

Binder, J., and I. Mertig, 1998, to be published.

Binder, J., P. Zahn and I. Mertig, 1997, J. Magn. Magn. Mater. **165**, 100.

Blaas, C., P. Weinberger, L. Szunyogh, P.M. Levy and C.B. Sommers, 1998, Philos. Mag. **78**, 549.

Blondel, A., J.P. Meier, B. Doubin and J.Ph. Ansermet, 1994, Appl. Phys. Lett. **65**, 3019.

Blondel, A., J. Meier, B. Doudin, J.Ph. Ansermet, K. Attenborough, P. Evans, R. Hart, G. Nabiyouni and W. Schwarzacher, 1995, J. Magn. Magn. Mater. **148**, 317.

Blondel, A., B. Doudin and J.Ph. Ansermet, 1997, J. Magn. Magn. Mater. **165**, 34.

Bobo, J.F., L. Hennet and M. Piecuch, 1995, J. Magn. Magn. Mater. **140–144**, 587.

Bouat, S., B. Rodmacq and P. Auric, 1997, in: Magnetic Ultrathin Films, Multilayers and Surfaces, MRS Symp. Proc., Vol. 475 (MRS, Pittsburg, Pennsylvania) p. 291.

Bouziane, K., J. Ben Youssef, M. El Harfaoui, O. Koshkina, H. Le Gall, J.M. Desvignes, M. El Yamani and A. Fert, 1997, J. Magn. Magn. Mater. **165**, 284.

Brown, R.H., D.M.C. Nicholson, W.H. Butler, X.G. Zhang, W.A. Shelton, T.C. Schulthess and J.M. MacLaren, 1998, Phys. Rev. B **58**, 11146.

Brubaker, M.E., J.E. Mattson, C.H. Sowers and S.D. Bader, 1991, Appl. Phys. Lett. **58**, 2306.

Bruno, P., 1995, Phys. Rev. B **52**, 411.

Bulka and J. Barnas, 1995, Phys. Rev. B **51**, 6348.

Burkett, S.L., J.C. Lusth, J.L. Bresowar and M.R. Parker, 1997, J. Magn. Magn. Mater. **168**, L233.

Butler, W.H., J.M. MacLaren and X.G. Zhang, 1993, Mater. Res. Soc. Symp. Proc. **313**, 59.

Butler, W.H., X.G. Zhang, D.M.C. Nicholson and J.M. MacLaren, 1995, J. Magn. Magn. Mater. **151**, 354.

Butler, W.H., X.G. Zhang, T.C. Schulthess, D.C. Nicholson, J.M. MacLaren, V.S. Speriosu and B.A. Gurney, 1997, Phys. Rev. B **56**, 14574.

Caballero, J.A., F. Petroff, A. Cabbibo, Y.D. Park and J.R. Childress, 1997, in: Magnetic Ultrathin Films, Multilayers and Surfaces, MRS Symp. Proc., Vol. 475 (MRS, Pittsburg, Pennsylvania) p. 175.

Calecki, D., 1989, Phys. Rev. Lett. **62**, 1302.

Calecki, D., 1991, Phys. Rev. B **43**, 581.

Camblong, H.E., 1995, Phys. Rev. B **51**, 1855.

Camblong, H.E., and P.M. Levy, 1992, Phys. Rev. Lett. **69**, 2835.

Camblong, H.E., S. Zhang and P.M. Levy, 1993, Phys. Rev. B **47**, 4735.

Camley, R.E., and J. Barnas, 1989, Phys. Rev. Lett. **63**, 664.

Campbell, I.A., and A. Fert, 1982, in: Ferromagnetic Materials, ed. E.P. Wohlfarth (North-Holland, Amsterdam) p. 769.

Caulet, J., B. Bartenlian, V. Kottler, C. Chappert, A. Anane and P. Veillet, 1997, J. Magn. Magn. Mater. **165**, 349.

Chaiken, A., G.A. Prinz and J.J. Krebs, 1990, J. Appl. Phys. **67**, 4892.

Chaiken, A., T.M. Tritt, D.J. Gillespie, J. Jkrebs, P. Lubitz, M.Z. Harford and G.A. Prinz, 1991a, J. Appl. Phys. **69**, 4798.

Chaiken, A., P. Lubitz, J.J. Krebs, G.A. Prinz and M.Z. Harford, 1991b, J. Appl. Phys. **70**, 5864.

Chaiken, A., P. Lubitz, J.J. Krebs, G.A. Prinz and M.Z. Harford, 1991c, Appl. Phys. Lett. **59**, 240.

Chaiken, A., C.J. Guttierrez, J.J. Krebs and G.A. Prinz, 1993, J. Magn. Magn. Mater. **125**, 228.

Chen, L.H., T.H. Tiefel, S. Jin, R.B. van Dover, E.M. Gyorgy and R.M. Fleming, 1993, Appl. Phys. Lett. **63**, 1279.

Chen, L.H., S. Jin, T.H. Tiefel, R.B. van Dover, E.M. Gyorgy and R.M. Fleming, 1994, J. Appl. Phys. **75**, 7052.

Cheng, S.F., M. Wun-Fogle, J.B. Restorff, J.P. Teter and K.B. Hathaway, 1995, J. Magn. Magn. Mater. **148**, 344.

Chiang, W.C., R. Loloee, W.P. Pratt and J. Bass, 1997a, in: Magnetic Ultrathin Films, Multilayers and Surfaces, MRS Symp. Proc., Vol. 475 (MRS, Pittsburg, Pennsylvania) p. 451.

Chiang, W.C., Q. Yang, W.P. Pratt, R. Loloee and J. Bass, 1997b, J. Appl. Phys. **81**, 4570.

Childress, J.R., O. Durand, A. Schuhl and J.M. George, 1993, Appl. Phys. Lett. **63**, 1996.

Chopra, H.D., B.J. Hockey, P.J. Chen, W.F. Egelhoff, M. Wuttig and S.Z. Hua, 1997, Phys. Rev. B **55**, 8390.

Christides, C., S. Stavroyiannis, N. Boukos, A. Travlos and D. Niarchos, 1998, J. Appl. Phys. **83**, 3724.

Chubing, P., D. Chen and D. Daosheng, 1993, J. Magn. Magn. Mater. **126**, 400.

Clarke, R., D. Barlett, F. Tsui, B. Chen and C. Uher, 1994, J. Appl. Phys. **75**, 6174.

Coehoorn, R., 1996, Magnetic Thin Films and Multilayer Systems: Physics, Analysis and Industrial Applications, Springer Series in Materials Science, ed. U. Hartmann.

Coehoorn, R., and J.P.W.B. Duchateau, 1993, J. Magn. Magn. Mater. **126**, 390.

Coehoorn, R., 1995, J. Magn. Magn. Mater. **151**, 341.

Coey, J.M.D., M. Viret and S. von Molnar, 1999, Adv. Phys. **48**, 167.

Colino, J.M., I.K. Schuller, V. Koreniski and K.V. Rao, 1996, Phys. Rev. B **54**, 13030.

Corno, J., M. Galtier and D. Renard, 1997, J. Magn. Magn. Mater. **174**, L10.

Cros, V., J.L. Duvail, A. Barthélémy, O. Durand, F. Petroff, L.B. Steren, A. Schuhl and A. Fert, 1995, J. Magn. Magn. Mater. **140–144**, 611.

Cros, V., S.F. Lee, G. Faini, A. Cornette, A. Hamzic and A. Fert, 1997, J. Magn. Magn. Mater. **165**, 512.

Cross, R.W., and A.B. Kos, 1996, J. Appl. Phys. **79**, 5820.

Cross, R.W., Y.K. Kim, J.O. Oti and S.E. Russek, 1996, Appl. Phys. Lett. **69**, 3935.

Czapkiewicz, M., and T. Stobiecki, 1995, J. Magn. Magn. Mater. **148**, 333.

Daniels, B.J., and B.M. Clemens, 1995a, in: Magnetic Ultrathin Films, Multilayers and Surfaces, MRS Symp. Proc., Vol. 384 (MRS, Pittsburg, Pennsylvania) p. 347.

Daniels, B.J., and B.M. Clemens, 1995b, Appl. Phys. Lett. **66**, 520.

Dauguet, P., P. Grandit, J. Chaussy, S.F. Lee, A. Fert and P. Holody, 1996a, Phys. Rev. B **54**, 1083.

Dauguet, P., P. Grandit and J. Chaussy, 1996b, J. Appl. Phys. **79**, 5823.

De Azevedo, M.M.P., V.S. Amaral, J.B. Sousa and P.P. Freitas, 1996, J. Magn. Magn. Mater. **157–158**, 276.

De Azevedo, M.M.P., B.G. Almeida, J.B. Sousa and P.P. Freitas, 1997, J. Magn. Magn. Mater. **173**, 155.

Dei, T., R. Nakatani, K. Hoshino and Y. Sugita, 1993, J. Magn. Magn. Mater. **126**, 489.

Diao, Z.T., S. Goto, K. Meguro, S. Tsunashima and M. Jimbo, 1997, J. Appl. Phys. **81**, 2327.

Dieny, B., 1992a, J. Phys. Cond. Matter **4**, 8009.

Dieny, B., 1992b, Europhys. Lett. **17**, 261.

Dieny, B., 1994, J. Magn. Magn. Mater. **36**, 335.

Dieny, B., V.S. Speriosu, S. Mertin, S.S.P. Parkin, B.A. Gurney, P. Baumgart and D.R. Wilhoit, 1990, J. Appl. Phys. **69**(8), 4774.

Dieny, B., V.S. Speriosu, S.S.P. Parkin, B.A. Gurney, D.R. Wilhoit and D. Mauri, 1991a, Phys. Rev. B **43**, 1297.

Dieny, B., V.S. Speriosu, S. Metin, S.S.P. Parkin, B.A. Gurney and P. Baumgart, 1991b, J. Appl. Phys. **69**, 4774.

Dieny, B., J.P. Nozières, V.S. Speriosu, B.A. Gurney and D.R. Wilhoit, 1992a, Appl. Phys. Lett. **61**, 2111.

Dieny, B., P. Humbert, V.S. Speriosu, S. Metin, B.A. Gurney, P. Baumgart and H. Lefakis, 1992b, Phys. Rev. B **45**, 806.

Dieny, B., V.S. Speriosu, J.P. Nozières, B.A. Gurney, A. Vedyayev and N. Ryzhanova, 1993, in: Proc. Nato ARW on Structure and Magnetism in Systems of Reduced Dimensions, NATO ASI Series B: Physics, Vol. 309 (Plenum Press, New York) p. 279.

Dieny, B., A. Granovsky, A. Vedyayev, N. Ryzhanova, C. Cowache and L.G. Pereira, 1995, J. Magn. Magn. Mater. **151**, 378.

Dieny, B., C. Cowache, A. Nossov, P. Dauguet, J. Chaussy and P. Grandit, 1996, J. Appl. Phys. **79**, 6370.

Dinia, A., and K. Ounadjela, 1995, J. Magn. Magn. Mater. **146**, 66.

Dinia, A., S. Zoll and K. Ounadjela, 1994, J. Appl. Phys. **75**, 6548.

Dinia, A., S. Zoll and K. Ounadjela, 1995, J. Magn. Magn. Mater. **148**, 327.

Dinia, A., K. Rahmouni, N. Persat and K. Ounadjela, 1997, in: Magnetic Ultrathin Films, Multilayers and Surfaces, MRS Symp. Proc., Vol. 475 (MRS, Pittsburg, Pennsylvania) p. 481.

Doi, M., T. Kanbe and M. Matsui, 1993, J. Magn. Magn. Mater. **126**, 443.

Dorleijn and Miedema, 1976, AIP Conf. Proc. **34**, 50.

Dorleijn and Miedema, 1977, J. Phys. F **7**, 23.

Dorner, C., M. Haidi and H. Hoffmann, 1993, J. Appl. Phys. **74**, 5886.

Dos Santos, C.A., B. Rodmacq, M. Vaezzadeh and B. George, 1991, Appl. Phys. Lett. **59**, 126.

Doudin, B., A. Blondel and J.Ph. Ansermet, 1996, J. Appl. Phys. **79**, 6092.

Drittler, B.N.S., S. Blügel, R. Zeller and P.H. Dederich, 1989, Phys. Rev. B **40**, 8203.

Du, J., L.N. Tong, M. Lu, K. Xia, M.H. Pan, J. Wu, D. Feng, H.R. Zhai, L.Y. Chen, X.F. Jin and H. Xia, 1998, Appl. Phys. Lett. **72**, 3371.

Dubois, S., J.M. Beuken, L. Piraux, J.L. Duvail, A. Fert, J.M. George and J.L. Maurice, 1997a, J. Magn. Magn. Mater. **165**, 30.

Dubois, S., C. Marchal, J.M. Beuken, L. Piraux, J.L. Duvail, A. Fert, J.M. George and J.L. Maurice, 1997b, Appl. Phys. Lett. **70**, 396.

Dubois, S., L. Piraux, J.M. George, K. Ounadjela, R. Ferre, J.L. Duvail and A. Fert, 1999, Phys. Rev. B **60**, 477.

Dugaev, V.K., V.I. Litvinov and P.P. Petrov, 1995, Phys. Rev. B **52**, 5306.

Dupas, C., P. Beauvillain, C. Chappert, J.P. Renard, F. Trigui, P. Veillet, E. Velu and D. Renard, 1990, J. Appl. Phys. **67**(9), 5680.

Duvail, J.L., A. Fert, L.G. Pereira and D.K. Lottis, 1994, J. Appl. Phys. **75**, 7070.

Duvail, J.L., A. Barthélémy, L.B. Steren, R. Morel, F. Petroff, M. Sussiau, M. Wiedmann, A. Fert, P. Holody, R. Loloee and P.A. Schroeder, 1995, J. Magn. Magn. Mater. **151**, 324.

Eckl, Th., G. Reiss, H. Brückl and H. Hoffmann, 1994, J. Appl. Phys. **75**.

Edwards, D.M., J. Mathon, R.B. Muniz and S.S.P. Parkin, 1992, J. Magn. Magn. Mater. **114**, 252.

Egelhoff, W.F., T. Ha, R.D.K. Misra, Y. Kadmon, J. Nir, C.J. Powell, M.D. Stiles, R.D. McMichael, C.-L. Lin, J.M. Sivertsen, J.H. Judy, K. Takano, A.E. Berkowitz, T.C. Anthony and J.A. Brug, 1995, J. Appl. Phys. **78**, 273.

Egelhoff, W.F., P.J. Chen, C.J. Powell, M.D. Stiles, R.D. McMichael, C.L. Lin, J.M. Sivertsen, J.H. Judy, K. Takano, A.E. Berkowitz, T.C. Anthony and J.A. Brug, 1996a, J. Appl. Phys. **79**, 5277.

Egelhoff, W.F., P.J. Chen, R.D.K. Misra, T. Ha, Y. Kadmon, C.J. Powell, M.D. Stiles, R.D. McMichael, C.L. Lin, J.M. Sivertsen and J.H. Judy, 1996b, J. Appl. Phys. **79**, 282.

Egelhoff, W.F., P.J. Chen, C.J. Powell, M.D. Stiles and R.D. McMichael, 1996c, J. Appl. Phys. **79**, 2491.

Egelhoff, W.F., P.J. Chen, C.J. Powell, M.D. Stiles, R.D. McMichael, J.H. Judy, K. Takano, A.E. Berkowitz, 1997a, J. Appl. Phys. **82**, 6142.

Egelhoff, W.F., P.J. Chen, C.J. Powell, M.D. Stiles, R.D. McMichael, J.H. Judy, K. Takano, A.E. Berkowitz and J.M. Daughton, 1997b, IEEE Trans. Magn. **33**, 3580; J. Appl. Phys. **82**, 6142.

Encinas, A., F. Nguyen Van Dau, M. Sussiau, A. Schuhl and P. Galtier, 1997, Appl. Phys. Lett. **71**, 3299.

Faini, G., A. Cornette, V. Cros, S.F. Lee, A. Barthélémy, F. Petroff and A. Fert, 1996, Microelectr. Eng. **30**, 483.

Fang, R., T. Chen, H. Wan and D. Dai, 1997a, IEEE Trans. Magn. **33**, 3571.

Fang, R., T. Chen, Y. Yu and D. Dai, 1997b, J. Appl. Phys. **82**, 3957.

Farrel, T., and D. Greig, 1970, J. Phys. C **3**, 138.

Farrow, R.F.C., R.F. Marks, T.A. Rabedeau, M.F. Toney, D. Dobbertin, R. Beyers and S.S.P. Parkin, 1994, J. Appl. Phys. **76**, 3688.

Farrow, R.F.C., S.S.P. Parkin, R.F. Marks, M. Krishnan and Thangaraj, 1996, Appl. Phys. Lett. **69**, 1963.

Fert, A., and P. Bruno, 1992, Ultrathin Magnetic Structures (Springer-Verlag, Berlin).

Fert, A., and I.A. Campbell, 1968, Phys. Rev. Lett. **21**, 1190.

Fert, A., and I.A. Campbell, 1976, J. Phys. F **6**, 849.

Fert, A., A. Barthélémy, P. Etienne, S. Lequien, R. Loloee, D.K. Lottis, D.H. Mosca, F. Petroff, W.P. Pratt and P.A. Schroeder, 1992, J. Magn. Magn. Mater. **104–107**, 1712.

Fert, A., T. Valet and J. Barnas, 1994, J. Appl. Phys. **75**, 6693.

Fert, A., J.L. Duvail and T. Valet, 1995a, Phys. Rev. B **52**, 6513.

Fert, A., P. Grünberg, A. Barthélémy, F. Petroff and W. Zinn, 1995b, J. Magn. Magn. Mater. **140–144**, 1.

Fettar, F., L.B. Steren, A. Barthélémy, R. Morel, A. Fert, J.A. Barnard and J.D. Jarratt, 1997, J. Magn. Magn. Mater. **165**, 316.

Folkerts, W., W. Hoving and W. Coene, 1992, J. Appl. Phys. **71**, 362.

Freitas, P.P., M. From, L.V. Melo and T.S. Plaskett, 1991, J. Appl. Phys. **69**, 4532.

Freitas, P.P., L.V. Melo, I. Trindade and M. From, 1992, Phys. Rev. B **45**, 2495.

Freitas, P.P., J.L. Leal, T.S. Plaskett, L.V. Melo and J.C. Soares, 1994a, J. Appl. Phys. **75**, 6480.

Freitas, P.P., J.L. Leal, L.V. Melo, N.J. Oliveira, L. Rodrigues and A.T. Sousa, 1994b, Appl. Phys. Lett. **65**, 493.

Friedel, 1967, in: Rendicenti della Scuola Intern di Fisica Enrico Fermi XXXVII, Corso (Academic Press, New York).

Fujimoto, T., M. Patel, E. Gu, C. Daboo and J.A.C. Bland, 1995, J. Magn. Magn. Mater. **148**, 323.

Fujita, M., K. Yamano, A. Maeda, T. Tanuma and M. Kume, 1997, J. Appl. Phys. **81**, 4909.

Fuke, H.N, K. Saito, Y. Kamiguchi, H. Iwasaki and M. Sahashi, 1997, J. Appl. Phys. **81**, 4004.

Fullerton, E.E., D.M. Kelly, J. Guimpel, I.K. Schuller and Y. Bruynsereade, 1992, Phys. Rev. Lett. **68**, 859.

Fullerton, E., M.J. Conover, J.E. Mattson, C.H. Sowers and S.D. Bader, 1993a, Phys. Rev. B **48**, 15755.

Fullerton, E., M.J. Conover, J.E. Mattson, C.H. Sowers and S.D. Bader, 1993b, Appl. Phys. Lett. **63**, 1699.

Gangopadhyay, G., S. Hossain, J. Yang, J.A. Barnard, M.T. Kief, H. Fujiwara and M.R. Parker, 1994, J. Appl. Phys. **76**, 6522.

Gangopadhyay, S., M.T. Kief, J.A. Barnard and M.R. Parker, 1996, J. Magn. Magn. Mater. **161**, 43.

Ge, S.H., Z.Z. Zhang, W.J. Ku, K. Westerholt, Th. Muhge, H. Zabel, M.L. Yan, W.Y. Lai and R.J. Gan, 1998, J. Magn. Magn. Mater. **177–181**, 1179.

George, J.M., A. Barthélémy, O. Durand, J.L. Duvail, A. Fert, P. Galtier, O. Heckmann, L.G. Pereira, F. Petroff and T. Valet, 1993, Mater. Res. Soc. Symp. Proc. **13**, 737.

George, J.M, L.G. Pereira, A. Barthélémy, F. Petroff, L.B. Steren, J.L. Duvail, A. Fert, R. Loloee and P.A. Schroeder, 1994, Phys. Rev. Lett. **72**, 408.

Gijs, M.A.M., and M. Okada, 1992, Phys. Rev. B **46**, 2908; J. Magn. Magn. Mater. **113**, 105.

Gijs, M.A.M., J.B. Giesberg, S.K.J. Lenczowski and H.H.J.M. Janssen, 1993a, Appl. Phys. Lett. **63**, 111.

Gijs, M.A.M., S.K.J. Lenczowski and J.B. Giesbers, 1993b, Phys. Rev. Lett. **70**, 3343.

Gijs, M.A.M., S.K.J. Lenczowski and J.B. Giesberg, 1993c, in: Magnetic Ultrathin Films, Multilayers and Surfaces. Interfaces and Characterization. Materials Research Soc. Symp. Proc., Vol. 384 (MRS, Pittsburg, Pennsylvania) p. 329.

Gijs, M.A.M., S.K. Lenczowski, R.J.M. van de Veerdonk, J.B. Giesbers, M.T. Johnson and J.B.F. aan de Stegge, 1994a, Phys. Rev. B **50**, 16733.

Gijs, M.A.M., J.B. Giesbers, M.T. Johnson, J.B.F. aan de Stegge, S.K.J. Lenczowski, R.J.M. van de Veerdonk and W.J.M. de Jonge, 1994b, J. Appl. Phys. **75**, 6709.

Gijs, M.A.M., M.T. Johnson, A. Reinders, P.E. Huisman, R.J.M. van de Veerdonk, S.K.J. Lenczowski and R.M.J. Gansewinkel, 1995a, Appl. Phys. Lett. **66**, 1839.

Gijs, M.A.M., S.K.J. Lenczowski, J.B. Giesbers, R.J.M. van de Veerdonk, M.T. Johnson, R.M. Jungblut, A. Reinders and R.M.J. van Gansewinkel, 1995b, J. Magn. Magn. Mater. **151**, 333.

Gijs, M.A.M., A. Reinders, R.M. Jungblut, W. Oepts and W.J.M. de Jonge, 1997, J. Magn. Magn. Mater. **165**, 17.

Gillies, M.F., J.N. Chapman and J.C.S. Kools, 1995, J. Appl. Phys. **78**, 5554.

Giron, F., P. Boher, Ph. Houdy, F. Pierre, P. Beauvillain, C. Chappert, K. Le Dang and P. Veillet, 1992, J. Appl. Phys. **72**, 4710.

Grolier, V., D. Renard, B. Bartenlian, P. Beauvillain, C. Chappert, C. Dupas, J. Ferré, M. Galtier, E. Kolb, M. Mulloy, J.P. Renard and P. Veillet, 1993, Phys. Rev. Lett. **71**, 3023.

Grünberg P., R. Schreiber, Y. Pang, M.B. Brodsky and H. Soweis, 1986, Phys. Rev. Lett. **57**, 2442.

Grünberg et al., 1999, in preparation for the Handbook of Ferromagnetic Materials.

Grundy, P.J., R.J. Pollard and M.E. Tomlinson, 1993, J. Magn. Magn. Mater. **126**, 516.

Gu, R.Y., L. Sheng, D.Y. Xing and J. Dong, 1997, Phys. Rev. B **55**, 14450.

Guarisco, D., E. Kay and S.X. Wang, 1997, IEEE Trans. Magn. **33**, 3595.

Gurney, B.A., D.R. Wilhoit, V.S. Speriosu and I.L. Sanders, 1990, IEEE Trans. Magn. **26**, 2747.

Gurney, B.A., P. Baumgart, D.R. Wilhoit, B. Dieny and V.S. Speriosu, 1991, J. Appl. Phys. **70**, 5867.

Gurney, B.A., V.S. Speriosu, J.P. Nozières, H. Lefakis, D.R. Wilhoit and O.U. Need, 1993, Phys. Rev. Lett. **71**, 4023.

Hahn, W., M. Loewenhaupt, G.P. Felcher, Y.Y. Huang and S.S.P. Parkin, 1994, J. Appl. Phys. **75**, 3564.

Hall, M.J., B.J. Hickey, M.A. Howson, M.J. Walker, D. Greig and N. Wiser, 1993a, J. Magn. Magn. Mater. **121**, 421.

Hall, M.J., B.J. Hickey, M.A. Howson, M.J. Walker, J. Xu, D. Greig and N. Wiser, 1993b, Phys. Rev. B **47**, 12785.

Hall, M.J., D.B. Jardine, J.E. Evetts, J.A. Leake and R.E. Somekh, 1997, J. Magn. Magn. Mater. **173**, 253.

Han, D.H., J.-G. Zhu, J.H. Judy and J.M. Sivertsen, 1997, IEEE Trans. Magn. **33**, 3550.

Harp, G.R., S.S.P. Parkin, R.F.C. Farrow, R.F. Marks, M.F. Toney, Q.H. Lam, T.A. Rabedeau and R.J. Savoy, 1993, Phys. Rev. B **48**, 8721.

Hase, T.P.A., I. Pape, B.K. Tanner, H. Laidler, P. Ryan and B.J. Hickey, 1998, J. Magn. Magn. Mater. **177–181**, 1164.

Hasegawa, H., 1993, Phys. Rev. B **47**, 15073.

Hasegawa, H., 1996, J. Appl. Phys. **79**, 6376.

Heinrich, B., and J.A.C. Bland, 1994, Ultrathin Magnetic Structures I and II (Springer-Verlag, Berlin, Heidelberg).

Holloway, H., and D.J. Kubinski, 1998, J. Appl. Phys. **83**, 2705.

Holody, P., L.B. Steren, R. Morel, A. Fert, R. Loloee and P.A. Schroeder, 1994, Phys. Rev. B **50**, 12999.

Honda, S., S. Ohmoto, R. Imada and M. Nawate, 1993, J. Magn. Magn. Mater. **126**, 419.

Hood, R.Q., and L.M. Falicov, 1992, Phys. Rev. B **46**, 8287.

Hood, R.Q., L.M. Falicov and D.R. Penn, 1994, Phys. Rev. B **49**, 368.

Hosoito, N., K. Mibu, T. Ono, T. Emoto and T. Shinjo, 1996, J. Magn. Magn. Mater. **156**, 325.

Hossain, S., D. Seale, G. Qiu, J. Jarratt, J.A. Barnard, H. Fujiwara and M.R. Parker, 1994, J. Appl. Phys. **75**, 7067.

Hossain, S.A., B.H. Pirkle and M.R. Parker, 1996, J. Magn. Magn. Mater. **156**, 303.

Hsu, S.Y., P. Holody, R. Loloee, J.M. Rittner, W.P. Pratt and P.A. Schroeder, 1996, Phys. Rev. B **54**, 9027.

Hsu, S.Y., A. Barthélémy, P. Holody, R. Loloee, P.A. Schroeder and A. Fert, 1997, Phys. Rev. Lett. **78**, 2652.

Hua, S.Z., D.S. Lashmore, L. Salamanca-Riba, W. Schwarzacher, L.J. Swartzenber, R.D. McMichael and L.H. Bennett, 1994, J. Appl. Phys. **76**, 6519.

Huai, Y., and R.W. Cochrane, 1992, J. Appl. Phys. **72**, 2523.

Huai, Y., R.W. Cochrane, X. Bian and M. Sutton, 1994, J. Appl. Phys. **75**, 6554.

Huang, T.C., J.P. Nozières, V.S. Spériosu, B.A. Gurney and H. Lefakis, 1993, Appl. Phys. Lett. **62**, 1478.

Huang, J.C.A., Y.H. Lee, Y.M. Hu and T.C. Chang, 1996, J. Appl. Phys. **79**, 6276.

Hwang, D.G., S.S. Lee and C.M. Park, 1998, Appl. Phys. Lett. **72**, 2162.

Hylton, T.L., K.R. Coffrey, M.A. Parker and J.K. Howard, 1993, Science **261**, 1021.

Hylton, T.L., M.A. Parker, K.R. Coffey, J.K. Howard, R. Fontana and C. Tsang, 1995, Appl. Phys. Lett. **67**, 1154.

Imada, R., I. Maruyama, M. Jimbo and S. Tsunashima, 1996, J. Magn. Magn. Mater. **156**, 367.

Imada, R., Y. Fujiwara, S. Tsunashima, M. Jimbo and M. Matsuura, 1997, J. Appl. Phys. **81**, 5191.

Inomata, K., and S. Hashimoto, 1993, J. Appl. Phys. **74**, 4096.

Inomata, K., and Y. Saito, 1993, J. Magn. Magn. Mater. **126**, 425.

Inomata, K., Y. Saito and S. Hashimoto, 1993, J. Magn. Magn. Mater. **121**, 350.

Inomata, K., Y. Saito and R.J. Highmore, 1994, J. Magn. Magn. Mater. **137**, 257.

Inoue, J., 1996, J. Magn. Magn. Mater. **164**, 273.

Inoue, J., and S. Maekawa, 1991, Prog. Theor. Phys. **106**, 187.

Irkhin, V.Y., and Y.P. Irkhin, 1996, J. Magn. Magn. Mater. **164**, 1191.

Itoh, H., J. Inoue and S. Maekawa, 1995, Phys. Rev. B **51**, 342.

Johnson, M., 1993, Phys. Rev. Lett. **70**, 2142.

Johnson, B.L., and R.E. Camley, 1991, Phys. Rev. B **44**, 9997.

Jacob, M., G. Reiss, H. Brückl and H. Hoffmann, 1992, Phys. Rev. B **46**, 11208.

Jarratt, J.D., T.J. Klemmer and J.A. Barnard, 1997, in: Magnetic Ultrathin Films, Multilayers and Surfaces, MRS Symp. Proc., Vol. 475 (MRS, Pittsburg, Pennsylvania) p. 351.

Jimbo, M., S. Tsunashima, T. Kanda, S. Goto and S. Uchiyama, 1993a, J. Appl. Phys. **74**, 3341.

Jimbo, M., T. Kanda, S. Goto, S. Tsunashima and S. Uchiyama, 1993b, J. Magn. Magn. Mater. **126**, 422.

Jimbo, M., K. Komiyama, H. Matue, S. Tsunashima and S. Uchiyama, 1995, Jap. J. Appl. Phys. **34**, L112.

Jimbo, M., K. Komiyama and S. Tsunashima, 1996, J. Appl. Phys. **79**, 6237.

Jin, Q.Y., M. Lu, Q.S. Bie, Y.B. Xu, H.R. Zhai and Y.H. Shen, 1995, J. Magn. Magn. Mater. **140–144**, 565.

Kai, T., Y. Ohashi and K. Shiiki, 1998, J. Magn. Magn. Mater. **183**, 292.

Kamaguchi, Y., K. Saito, H. Iwasaki, M. Sahashi, M. Ouse and S. Nakamura, 1996, J. Appl. Phys. **79**, 6399.

Kamijo, A., and H. Igarashi, 1992a, J. Appl. Phys. **71**, 2455.

Kamijo, A., and H. Igarashi, 1992b, J. Appl. Phys. **72**, 3497.

Kano, H., K. Kagawa, A. Suzuki, A. Okabe, K. Hayashi and K. Aso, 1993a, Appl. Phys. Lett. **63**, 2839.

Kano, H., Y. Iwasaki, K. Hayashi and K. Aso, 1993b, J. Magn. Magn. Mater. **126**, 445.

Kano, H., A. Okabe, K. Kagawa, A. Suzuki, T. Yaoi, Y. Negoro and K. Hayashi, 1995, J. Magn. Magn. Mater. **148**, 329.

Kataoka, N., K. Saito and H. Fujimori, 1993a, J. Magn. Magn. Mater. **126**, 508.

Kataoka, N., K. Saito and H. Fujimori, 1993b, J. Magn. Magn. Mater. **121**, 383.

Kawawake, Y., and H. Sakakima, 1995, J. Magn. Magn. Mater. **149**, L255.

Kawawake, Y., and H. Sakakima, 1997, IEEE Trans. Magn. **33**, 3538.

Kawawake, Y., H. Sakakima, Y. Irie and M. Satomi, 1996, J. Appl. Phys. **79**, 6231.

Kief, M.T., J. Bresowar and Q. Leng, 1996, J. Appl. Phys. **79**, 4766.

Kikuchi, H., J.F. Bobo and R.L. White, 1997, IEEE Trans. Magn. **33**, 3583.

Kim, Y.K., and S.C. Sanders, 1995, Appl. Phys. Lett. **66**, 1009.

Kim, H.J., B.I. Lee and S.K. Joo, 1997, J. Appl. Phys. **81**, 3995.

Kirschenbaum, L.S., C.T. Rogers, P.D. Beale, S.E. Russek and S.C. Sanders, 1996, Appl. Phys. Lett. **68**, 3099.

Kitakami, O., H. Takashima and Y. Shimida, 1996, J. Magn. Magn. Mater. **164**, 43.

Kobayashi, Y., Y. Aoki, H. Sato, A. Kamijo and M. Abe, 1993, J. Magn. Magn. Mater. **126**, 501.

Kobayashi, Y., H. Sato, Y. Aoki, R. Loloee and W.P. Pratt, 1996, J. Magn. Magn. Mater. **156**, 362.

Kolb, E., M.J. Walker, E. Vélu, M.A. Howson, P. Veillet, D. Greig, J.P. Renard and C. Dupas, 1996, J. Magn. Magn. Mater. **156**, 377.

Kools, J.C.S., S. Lardoux and F. Roozeboom, 1998, Appl. Phys. Lett. **72**, 611.

Korenivski, V., K.V. Rao, D.M. Kelly, I.K. Schuller, K.K. Larsen and J. Bottiger, 1995, J. Magn. Magn. Mater. **140–144**, 549.

Kos, A.B., S.E. Russek, Y.K. Kim and R.W. Cross, 1997, IEEE Trans. Magn. **33**, 3541.

Krebs, J.J., W. Vavra, G.A. Prinz, S.F. Cheng and A. Fink, 1996, J. Appl. Phys. **79**, 6084.

Kubinski, D.J., and H. Holloway, 1996a, J. Appl. Phys. **79**, 1662.

Kubinski, D.J., and H. Holloway, 1996b, J. Appl. Phys. **79**, 7090.

Kubinski, D.J., and H. Holloway, 1997a, J. Magn. Magn. Mater. **165**, 104.

Kubinski, D.J., and H. Holloway, 1997b, J. Appl. Phys. **82**, 322.

Kubota, H., S. Ishio and T. Miyazaki, 1993, J. Magn. Magn. Mater. **126**, 463.

Kubota, H., S. Ishio, T. Miyazaki and Z.M. Stadnik, 1994, J. Magn. Magn. Mater. **129**, 383.

Kubota, H., M. Sato and T. Miyazaki, 1995, Phys. Rev. B **52**, 343.

Kubota, H., M. Sato and T. Miyazaki, 1997, J. Magn. Magn. Mater. **167**, 12.

Lai, C.H., T.J. Regan, R.L. White and T.C. Anthony, 1997, Appl. Phys. **81**, 5191.

Le Dang, K., P. Veillet, E. Velu, S.S.P. Parkin and C. Chappert, 1993, Appl. Phys. Lett. **63**, 108.

Leal, J.L., and P.P. Freitas, 1994, J. Appl. Phys. **75**, 6449.

Leal, J.L., and M.H. Kryder, 1998, J. Appl. Phys. **83**, 3720.

Lee, S.F., W.P. Pratt Jr., R. Loloee, P.A. Schroeder and J. Bass, 1992, Phys. Rev. B **46**, 548.

Lee, S.F., W.P. Pratt Jr., Q. Yang, P. Holody, R. Loloee, P.A. Schroeder and J. Bass, 1993, J. Magn. Magn. Mater. **118**, L1.

Lee, S.F., Q. Yang, P. Holody, R. Loloee, J.H. Hetherington, S. Mahmood, B. Ikegami, K. Vigen, L.L. Henry, P.A. Schroeder, W.P. Pratt and J. Bass, 1995, Phys. Rev. B **52**, 15426.

Lenczowski, S.K.J., M.A.M. Gijs, J.B. Giesbers, R.J.M. van de Veerdonk and W.J.M. de Jonge, 1994, Phys. Rev. B **50**, 9982.

Lenczowski, S.K.J., M.A.M. Gijs, R.J.M. van de Veerdonk, J.B. Giesbers and W.J.M. de Jonge, 1995a, in: Magnetic Ultrathin Films, Multilayers and Surfaces, MRS Symp. Proc., Vol. 384 (MRS, Pittsburg, Pennsylvania) p. 341.

Lenczowski, S.K.J., C. Schönenberger, M.A.M. Gijs and W.J.M. de Jonge, 1995b, J. Magn. Magn. Mater. **148**, 455.

Levy, P.M., 1994, Solid State Phys. **47**, 367.

Levy, P.M., S. Zhang and A. Fert, 1990a, Phys. Rev. Lett. **65**, 1643.

Levy, P.M., K. Ounadjela, S. Zhang, Y. Wang, C.B. Sommers and A. Fert, 1990b, J. Appl. Phys. **67**, 5914.

Liou, Y., J.C.A. Huang, Y.D. Yao, C.H. Lee, K.T. Wu, C.L. Lu, S.Y. Liao, Y.Y. Chen, N.T. Liang, W.T. Yang, C.Y. Chen and B.C. Hu, 1994, J. Appl. Phys. **76**, 6516.

Liou, Y., J.C.A. Huang, Y.D. Yao, W.T. Yang, S.Y. Liao and C.P. Chang, 1996, J. Appl. Phys. **79**, 6282.

Liou, Y., C.R. Chang, C.K. Lo, P. Chang, Y.D. Yao and I. Klik, 1997, IEEE Trans. Magn. **33**, 3652.

List, N.J., W.P. Pratt Jr., M.A. Howson, J. Xu, M.J. Walker, B.J. Hickey and D. Greig, 1995a, in: Magnetic Ultrathin Films, Multilayers and Surfaces, MRS Symp. Proc., Vol. 384 (MRS, Pittsburg, Pennsylvania) p. 329.

List, N.J., W.P. Pratt Jr., M.A. Howson, J. Xu, M.J. Walker and D. Greig, 1995b, J. Magn. Magn. Mater. **148**, 342.

Liu, K., K. Nagodawithana, P.C. Searson and C.L. Chien, 1995, Phys. Rev. B **51**, 7381.

Loegel, B., and F. Gautier, 1971, J. Phys. Chem. Solids **32**, 2723.

Loloee, R., P.A. Schroeder, W.P. Pratt, J. Bass and A. Fert, 1995, Physica B **204**, 274.

Lottis, D., A. Fert, R. Morel, L.G. Pereira, J.C. Jacquet, P. Galtier, J.M. Coutellier and T. Valet, 1993, J. Appl. Phys. **73**, 5515.

Lucinski, T., D. Elefant, G. Reiss and P. Verges, 1996, J. Magn. Magn. Mater. **162**, 29.

Maeda, A., T. Tanuma, M. Kume, R. Shimizu and A. Doi, 1997, IEEE Trans. Magn. **33**, 3535.

Majkrzak, C.F., J.W. Cable, J. Kwo, M. Hong, D.B. McWhan, Y. Yafet, J.W. Waszczak and C. Vettier, 1986, Phys. Rev. Lett. **56**, 2700.

Mao, S., S. Gangopadhyay, N. Amin and E. Murdock, 1996, Appl. Phys. Lett. **69**, 3593.

Mao, M., M. Gibbons, B. Law, F. Grabner, S.P. Vernon and C. Cerjan, 1997, IEEE Trans. Magn. **33**, 3532.

Marrows, C.H., B.J. Hickey, M. Malinowska and C. Mény, 1997, IEEE Trans. Magn. **33**, 3673.

Mathon, J., 1996, Phys. Rev. B **54**, 55.

Mathon, J., 1997, Phys. Rev. B **55**, 960.

Mathon, J., M. Villeret and H. Itoh, 1995, Phys. Rev. B **52**, R6983.

Matsuyama, K., H. Asada, S. Ikeda and I. Chida, 1996, J. Magn. Magn. Mater. **156**, 301.

Mattheis, R., W. Andra, L. Fritzsch, A. Hubert, M. Rührig and F. Thrum, 1993, J. Magn. Magn. Mater. **121**, 424.

Mattson, J.E., C.H. Sowers, A. Berger and S.D. Bader, 1992, Phys. Rev. Lett. **68**, 3252.

Maurice, J.L., D. Imhoff, P. Etienne, S. Dubois, L. Piraux, J.M. George, P. Galtier and A. Fert, 1998, J. Magn. Magn. Mater. **184**, 1.

McGuire, T.C., and T.S. Plaskett, 1994a, J. Appl. Phys. **76**, 4734.

McGuire, T.R., and T.S. Plaskett, 1994b, J. Appl. Phys. **75**, 6537.

McGuire, T.R., J.M. Harper, C. Cabral and T.S. Plaskett, 1994, J. Appl. Phys. **76**, 6601.

McMichael, R.D., W.F. Egelhoff and M. Ha, 1995, Magnetic Ultrathin Films, Multilayers and Surfaces, MRS Symp. Proc., Vol. 384 (MRS, Pittsburg, Pennsylvania) p. 397.

Meguro, K., S. Hirano, M. Jimbo, S. Tsunshima and S. Uchiyama, 1995, J. Magn. Magn. Mater. **140–144**, 601.

Melo, L.V., P. Monteiro and P.P. Freitas, 1993a, J. Magn. Magn. Mater. **121**, 390.

Melo, L.V., I.G. Trindade, M.M. Godinho and P.P. Freitas, 1993b, J. Magn. Magn. Mater. **121**, 395.

Mertig, I., R. Zeller and P.H. Diederich, 1993, Phys. Rev. B **47**, 16178.

Mertig, I., R. Zeller and P.H. Diederich, 1994, Phys. Rev. B **49**, 11767.

Mertig, I., P. Zahn, H. Eschrig and P.H. Diederich, 1995, J. Magn. Magn. Mater. **151**, 363.

Mibu, K., T. Nagahama and T. Shinjo, 1996, J. Magn. Magn. Mater. **156**, 299.

Min, K.I., and S.K. Joo, 1994, J. Appl. Phys. **75**, 4632.

Min, K.I., S.K. Joo and K.H. Shin, 1996, J. Magn. Magn. Mater. **156**, 375.

Miyamoto, Y., K. Watanabe, S. Nakagawa and M. Naoe, 1997, IEEE Trans. Magn. **33**, 3523.

Miyauchi, D., and S. Araki, 1993, Appl. Phys. Lett. **636**, 1702.

Miyazaki, T., J. Kondo, H. Kubota and J. Inoue, 1997, J. Appl. Phys. **81**, 5187.

Modak, A.R., S.S.P. Parkin and D.J. Smith, 1994, J. Magn. Magn. Mater. **129**, 415.

Monod, P., and S. Schultz, 1982, J. Physique (Paris) **43**, 393.

Moodera, J.S., L.R. Kinder, T.M. Wong and R. Meservry, 1995, Phys. Rev. Lett. **74**, 3273.

Mosca, D.H., F. Petroff, A. Fert, P.A. Schroeder, W.P. Pratt and R. Loloee, 1991a, J. Magn. Magn. Mater. **94**, L1.

Mosca, D.H., A. Barthélémy, F. Petroff, A. Fert, P.A. Schroeder, W.P. Pratt, R. Loloee and R. Cabanel, 1991b, J. Magn. Magn. Mater. **93**, 480.

Mosca, D.H., N. Mattoso, E.M. Kakuno, W.H. Schreiner, I. Mazzaro and S.R. Teixeira, 1996, J. Magn. Magn. Mater. **156**, 391.

Moser, A., U. Krey, A. Paintner and B. Zellermann, 1998, J. Magn. Magn. Mater. **183**, 272.

Mott, 1936, Proc. Roy. Soc. **156**, 368.

Mulloy, M., E. Kolb, C. Dupas, M. Galtier, D. Renard, J.P. Renard and E. Vélu, 1995a, J. Magn. Magn. Mater. **148**, 337.

Mulloy, M., E. Vélu, C. Dupas, M. Galtier, E. Kolb, D. Renard and J.P. Renard, 1995b, J. Magn. Magn. Mater. **147**, 177.

Nabiyouni, G., and W. Scharzacher, 1996, J. Magn. Magn. Mater. **156**, 355.

Nagamachi, S., M. Ueda, H. Sakakima, M. Satomi and J. Ishikawa, 1996, J. Appl. Phys. **80**, 4217.

Nakatani, R., T. Dei and Y. Sugota, 1993, J. Appl. Phys. **73**, 6375.

Nakatani, R., K. Hoshino, H. Hoshiya and Y. Sugita, 1997a, J. Magn. Magn. Mater. **170**, 74.

Nakatani, R., K. Hoshino, H. Hoshiya and Y. Sugita, 1997b, J. Magn. Magn. Mater. **166**, 261.

Naoe, M., Y. Miyamoto and S. Nakagawa, 1994, J. Appl. Phys. **75**, 6525.

Nesbet, R.K., 1994, J. Phys. C **6**, L449.

Nesbet, R.K., 1996, J. Magn. Magn. Mater. **159**, L17.

Nishioka, K., T. Iseki, H. Fujiwara and M.R. Parker, 1996, J. Appl. Phys. **79**, 4970.

Nozières, J.P., V.S. Speriosu, B.A. Gurney, B. Dieny, H. Lefakis and T.C. Huang, 1993, J. Magn. Magn. Mater. **121**, 386.

Obi, Y., K. Takanashi, Y. Mitani, N. Tsuda and H. Fujimori, 1992, J. Magn. Magn. Mater. **104–107**, 1747.

Oeps, W., M.A.M. Gijs, A. Reinders, R.M. Jungblut, R.M.J. van Gansweinkel and W.J.M. de Jonge, 1996, Phys. Rev. B **53**, 14024.

Oeps, W., M.A.M. Gijs, A. Reinders, R.M. Jungblut, J.M. Kerkhof, A.M.A. van Zon and W.J.M. de Jonge, 1997, J. Magn. Magn. Mater. **165**, 356.

Oguri, A., Y. Asano and S. Maekawa, 1992, J. Phys. Soc. Japan **61**, 2652.

Okuyama, T., H. Yamamoto and T. Shinjo, 1992, J. Magn. Magn. Mater. **113**, 79.

Ono, T., and T. Shinjo, 1995, J. Phys. Soc. Japan **64**, 363.

Ono, T., Y. Sugita, K. Shigeto, K. Mibu, N. Hosoito and T. Shinjo, 1997, Phys. Rev. B **55**, 14457.

Ono, T., H. Miyajima, K. Shigeto and T. Shinjo, 1998, Appl. Phys. Lett. **72**, 1116.

Oomi, G., Y. Uwatoko, Y. Obi, K. Takanashi and H. Fujimori, 1993, J. Magn. Magn. Mater. **126**, 513.

Oomi, G., Y. Uwatoko, T. Sakai, K. Takanashi and H. Fujimori, 1996, J. Magn. Magn. Mater. **156**, 402.

Park, C.M., and K.H. Shin, 1997, Appl. Phys. Lett. **70**, 776.

Park, W., R. Loloee, J. Caballero, W.P. Pratt, P.A. Schroeder, J. Bass, A. Fert and C. Vouille, 1999, J. Appl. Phys. **85**, 4542.

Parkin, S.S.P., 1992a, Appl. Phys. Lett. **61**, 1358.

Parkin, S.S.P., 1992b, Appl. Phys. Lett. **60**, 512.

Parkin, S.S.P., 1993, Phys. Rev. Lett. **71**, 1641.

Parkin, S.S.P., 1996, Appl. Phys. Lett. **69**, 3092.

Parkin, S.S.P., and T. Rabedeau, 1996, Appl. Phys. Lett. **68**, 1162.

Parkin, S.S.P., and B.R. York, 1993, Appl. Phys. Lett. **62**, 1842.

Parkin, S.S.P., N. More and K.P. Roche, 1990, Phys. Rev. Lett. **64**, 2304.

Parkin, S.S.P., R. Bhadra and K.P. Roche, 1991a, Phys. Rev. Lett. **66**, 2152.

Parkin, S.S.P., Z.G. Li and D.J. Smith, 1991b, Appl. Phys. Lett. **58**, 2710.

Parkin, S.S.P., R.F. Marks, R.F.C. Farrow, G.R. Harp, Q.H. Lam and R.J. Savoy, 1992, Phys. Rev. B **46**, 9262.

Parkin, S.S.P., A. Modak and D.J. Smith, 1993, Phys. Rev. B **47**, 9136.

Parkin, S.S.P., R.F.C. Farrow, R.F. Marks, A. Cebollada, G.R. Harp and R.J. Savoy, 1994, Phys. Rev. Lett. **72**, 3718.

Patel, M., T. Fujimoto, E. Gu, C. Daboo and J.A.C. Bland, 1994, J. Appl. Phys. **75**, 6528.

Persat, N., A. Dinia, J.P. Jay, C. Mény and P. Panissod, 1996a, J. Magn. Magn. Mater. **156**, 335.

Persat, N., A. Dinia, J.P. Jay, C. Mény and P. Panissod, 1996b, J. Magn. Magn. Mater. **164**, 37.

Petroff, F., A. Barthélémy, D.H. Mosca, D.K. Lottis, A. Fert, P.A. Schroeder, W.P. Pratt Jr, R. Loloee and S. Lequien, 1991a, Phys. Rev. B **44**, 5355.

Petroff, F., A. Barthélémy, A. Hamzic, A. Fert, P. Etienne, S. Lequien and G. Creuzet, 1991b, J. Magn. Magn. Mater. **93**, 95.

Petroff, F., A. Barthélémy, A. Fert, P. Etienne and S. Lequien, 1992, J. Magn. Magn. Mater. **104–107**, 1712.

Pettit, K., S. Gilder, S.S.P. Parkin and M.B. Salamon, 1997, Phys. Rev. B **56**, 7819.

Piraux, L., A. Fert, P.A. Schroeder, R. Loloee and P. Etienne, 1992, J. Magn. Magn. Mater. **110**, L247.

Piraux, L., J.M. George, J.F. Despres, C. Leroy, E. Ferain, R. Legras, K. Ounadjela and A. Fert, 1994, Appl. Phys. Lett. **65**, 2484.

Piraux, L., S. Dubois and A. Fert, 1996a, J. Magn. Magn. Mater. **159**, L287.

Piraux, L., S. Dubois, C. Marchal, J.M. Beuken, L. Filipozzi, J.F. Despres, K. Ounadjela and A. Fert, 1996b, J. Magn. Magn. Mater. **156**, 317.

Piraux, L., S. Dubois, J.L. Duvail, K. Ounadjela and A. Fert, 1997, J. Magn. Magn. Mater. **175**, 127.

Piraux, L., S. Dubois, A. Fert and L. Belliard, 1998, Europhys. J. B **4**, 413.

Pizzini, S., F. Baudelet, D. Chandesris, A. Fontaine, H. Magnan, J.M. George, A. Barthélémy, A. Fert, R. Loloee and P.A. Schroeder, 1992, Phys. Rev. B **46**, 1253.

Plaskett, T.S., and T.R. McGuire, 1993, J. Appl. Phys. **74**, 6378.

Pollard, R.J., M.J. Wilson and P.J. Grundy, 1995a, J. Magn. Magn. Mater. **151**, 139.

Pollard, R.J., M.J. Wilson and P.J. Grundy, 1995b, J. Magn. Magn. Mater. **148**, L375.

Pollard, R.J., M.J. Wilson and P.J. Grundy, 1995c, J. Magn. Magn. Mater. **146**, L1.

Portier, X., A.K. Petford-Long, R.C. Doole, T.C. Anthony and J.A. Brug, 1997a, IEEE Trans. Magn. **33**, 3574.

Portier, X., A.K. Petford-Long, R.C. Doole, T.C. Anthony and J.A. Brug, 1997b, Appl. Phys. Lett. **71**, 2032.

Pratt, W.P., S.F. Lee, J.M. Slaughter, R. Loloee, P.A. Schroeder and J. Bass, 1991, Phys. Rev. Lett. **66**, 3060.

Pratt, W.P., S.F. Lee, P. Holody, Q. Yang, R. Loloee, J. Bass and P.A. Schroeder, 1993a, J. Magn. Magn. Mater. **126**, 406.

Pratt, W.P., S.F. Lee, Q. Yang, P. Holody, R. Loloee, P.A. Schroeder and J. Bass, 1993b, J. Appl. Phys. **73**, 5326.

Pratt, W.P., Q. Yang, L.L. Henry, P. Holody, W.C. Chiang, P.A. Schroeder and J. Bass, 1996, J. Appl. Phys. **79**, 5811.

Pratt Jr., W.P., S.D. Steenwyk, S.Y. Hsu, W.C. Chiang, A.C. Schaefer, R. Loloee and J. Bass, 1997, IEEE Trans. Magn. **33**, 3505.

Redon, O., J. Pierre, B. Rodmacq, B. Mevel and B. Dieny, 1995, J. Magn. Magn. Mater. **149**, 398.

Reilly, A.C., W. Park, R. Slater, B. Ouaglal, R. Loloee, W.P. Pratt and J. Bass, 1999, to be published.

Reiss, G., L. van Loyen, T. Lucinski, D. Elefant, H. Brückl, N. Mattern, R. Rennekamp and W. Ernst, 1998, J. Magn. Magn. Mater. **184**, 280.

Renard, J.P., P. Beauvillain, C. Dupas, K. Le Dang, P. Veillet, E. Vélu, C. Marlière and D. Renard, 1992, J. Magn. Magn. Mater. **115**, L147.

Renard, J.P., P. Bruno, R. Mégy, B. Bartenlian, P. Beauvillain, C. Chappert, C. Dupas, E. Kolb, M. Mulloy, P. Veillet and E. Velu, 1995, Phys. Rev. B **51**, 12821.

Renard, J.P., P. Bruno, R. Megy, B. Bartenlian, P. Beauvillain, C. Chappert, C. Dupas, E. Kolb, M. Mulloy, J. Prieur, P. Veillet and E. Vélu, 1996, J. Appl. Phys. **79**, 5270.

Rensing, N.M., and B.M. Clemens, 1994, J. Appl. Phys. **76**, 6617.

Rensing, N.M., A.P. Payne and B.M. Clemens, 1993, J. Magn. Magn. Mater. **121**, 436.

Rensing, N.M., B.M. Clemens and D.L. Williamson, 1996, J. Appl. Phys. **79**, 7757.

Rhyne, J.J., and R.W. Erwin, 1995, in: Handbook of Magnetic Materials, Vol. 8, ed. K.H.J. Buschow (Elsevier, Amsterdam) p. 1.

Rijks, Th.G.S.M., W.J.M. de Jonge, W. Folkerts, J.C.S. Kools and R. Coehoorn, 1994, Appl. Phys. Lett. **65**, 916.

Rodmacq, B., B. George, M. Vaezzadeh and Ph. Mangin, 1992, Phys. Rev. B **46**, 1206.

Rodmacq, B., G. Palumbo and Ph. Gerard, 1993, J. Magn. Magn. Mater. **118**, L11.

Rogers, C.T., L.S. Kirschenbaum, P.D. Beale, S.E. Russek and S.C. Sanders, 1997, Phys. Rev. B **56**, R8503.

Rupp, G., and K. Schuster, 1993, J. Magn. Magn. Mater. **121**, 416.

Saito, Y., S. Hashimoto and K. Inomata, 1992, Appl. Phys. Lett. **60**, 2436.

Saito, Y., K. Inomata, A. Goto and H. Yasuoka, 1993, J. Magn. Magn. Mater. **126**, 466.

Saito, Y., K. Inomata, K. Yusu, A. Goto and H. Yasuoka, 1995, Phys. Rev. B **52**, 6500.

Sakakima, H., and M. Satomi, 1993a, Jpn. J. Appl. Phys. **32**, L1441.

Sakakima, H., and M. Satomi, 1993b, J. Magn. Magn. Mater. **121**, 374.

Sakakima, H., M. Satomi, K. Onaka and S. Yamamoto, 1995, J. Magn. Magn. Mater. **155**, L268.

Sakakima, H., M. Satomi, Y. Irie and Y. Kawawake, 1997, J. Magn. Magn. Mater. **165**, 108.

Sakakima, H., E. Hirota and Y. Kawawake, 1998, J. Magn. Magn. Mater. **184**, 49.

Salamon, M.B., S. Sinha, J.J. Rhyne, J.E. Cunningham, R.W. Erwin and C.P. Flyn, 1986, Phys. Rev. Lett. **56**, 259.

Sanders, S.C., R.W. Cross, S.E. Russek, A. Roshko and J.O. Oti, 1996, J. Appl. Phys. **79**, 6240.

Sato, M., S. Ishio and T. Miyazaki, 1993, J. Magn. Magn. Mater. **126**, 460.

Sato, H., T. Matsudai, W. Abdul-Razzaq, C. Fierz and P.A. Schroeder, 1994, J. Phys. Cond. Mater **6**, 6151.

Sato, H., S. Miya, Y. Kobayashi, Y. Aoki, H. Yamamoto and M. Nakada, 1998, J. Appl. Phys. **83**, 5927.

Satomi, M., and H. Sakakima, 1993, J. Magn. Magn. Mater. **126**, 504.

Schad, R., C.D. Potter, P. Beliën, G. Verbanck, V.V. Moshchalkov and Y. Bruynseraede, 1994a, Appl. Phys. Lett. **64**, 3500.

Schad, R., C.D. Potter, P. Beliën, G. Verbanck, V.V. Moshchalkov, Y. Bruynseraede, M. Schäfer, R. Schäfer and P. Grünberg, 1994b, J. Appl. Phys. **76**, 6604.

Schad, R., C.D. Potter, P. Beliën, G. Verbanck, J. Dekoster, G. Langouche, V.V. Moshchalkov and Y. Bruynseraede, 1995, J. Magn. Magn. Mater. **148**, 331.

Schad, R., J. Barnas, P. Beliën, G. Verbanck, C.D. Potter, H. Fischer, S. Lefebvre, M. Bessiere, V.V. Moshchalkov and Y. Bruynseraede, 1996a, J. Magn. Magn. Mater. **156**, 339.

Schad, R., P. Beliën, J. Barnas, G. Verbanck, C.D. Potter, G. Gladyszewski, V.V. Moshchalkov and Y. Bruynseraede, 1996b, J. Magn. Magn. Mater. **156**, 341.

Schad, R., P. Beliën, G. Verbanck, C.D. Potter, H. Fischer, S. Lefebvre, M. Bessiere, V.V. Moshchalkov and Y. Bruynseraede, 1998a, Phys. Rev. B **57**, 13692.

Schad, R., P. Beliën, G. Verbanck, K. Teenst, V.V. Moshchalkov, Y. Bruynseraede, J. Dekoster and G. Langouche, 1998b, Europhys. Lett. **44**, 379, and private communication.

Schad, R., P. Beliën, G. Verbanck, V.V. Moshchalkov, Y. Bruynseraede, H.E. Fischer, S. Lefebvre and M. Bessiere, 1999, Phys. Rev. B **59**, 1242.

Schelp, L.F., G. Tosin, M. Carara, M.N. Baibich, A.A. Gomes and J.E. Schmidt, 1992, Appl. Phys. Lett. **61**, 1858.

Schep, K.M., J.B.A.N. van Hoof, P.J. Kelly, G.E. Bauer and J.E. Inglesfield, 1997, Phys. Rev. B **56**, 10805.

Schep, K.M., P.J. Kelly and G.E.W. Bauer, 1998, Phys. Rev. B **57**, 8907.

Schmidt, M., 1997, J. Magn. Magn. Mater. **174**, 192.

Schmeusser, S., G. Rupp and A. Hubert, 1997, J. Magn. Magn. Mater. **166**, 267.

Schroeder, P.A., J. Bass, P. Holody, S.F. Lee, R. Loloee, W.P. Pratt Jr. and Q. Yang, 1993a, in: Magnetic Ultrathin Films, Multilayers and Surfaces. Interfaces and Characterization. Materials Research Soc. Symp. Proc., Vol. 313 (MRS, Pittsburg, Pennsylvania) p. 47.

Schroeder, P.A., J. Bass, P. Holody, S.F. Lee, R. Loloee, W.P. Pratt Jr. and Q. Yang, 1993b, in: Proc. Nato ARW on Structure and Magnetism in Systems of Reduced Dimensions, NATO ASI Series B: Physics, Vol. 309 (Plenum Press, New York) p. 129.

Schroeder, P.A., S.F. Lee, P. Holody, R. Loloee, Q. Yang and W. Pratt, 1994, J. Appl. Phys. **76**, 6610.

Schuhl, A., O. Durand, J.R. Childress, J.M. George and L.G. Pereira, 1994a, J. Appl. Phys. **75**, 7061.

Schuhl, A., P. Galtier, O. Durand, J.R. Childress and R. Kergoat, 1994b, Appl. Phys. Lett. **65**, 913.

Schwarzacher, W., K. Attenborough, A. Michel, G. Nabiyouni and J.P. Meier, 1997, J. Magn. Magn. Mater. **165**, 23.

Sdaq, A., J.M. Broto, H. Rakoto, J.C. Ousset and B. Raquet, 1993, J. Magn. Magn. Mater. **121**, 409.

Shinjo, T., 1993, in: Proc. Nato ARW on Structure and Magnetism in Systems of Reduced Dimensions, NATO ASI Series B: Physics, Vol. 309 (Plenum Press, New York) p. 323.

Shinjo, T., and T. Ono, 1996, J. Magn. Magn. Mater. **156**, 11.

Shinjo, T., and T. Ono, 1998, J. Magn. Magn. Mater. **177–181**, 31.

Shinjo, T., and H. Yamamoto, 1990, J. Phys. Soc. Japan **59**, 3061.

Shinjo, T., H. Yamamoto, T. Anno and T. Okuyama, 1992, Appl. Surf. Sci. **60**, 798.

Shintaku, K., Y. Daitoh and T. Shinjo, 1993a, Phys. Rev. B **47**, 14584.

Shintaku, K., N. Hosoito and T. Shinjo, 1993b, J. Magn. Magn. Mater. **121**, 413.

Shukh, A.M., D.H. Shin and H. Hoffmann, 1994, J. Appl. Phys. **76**, 6507.

Slonczewski, J.C., 1996, J. Magn. Magn. Mater. **159**, 1.

Sousa, J.B., R.P. Pinto, B. Almeida, M.E. Braga, P.P. Freitas, L.V. Melo and I.G. Trindade, 1994, J. Magn. Magn. Mater. **137**, 73.

Speriosu, V.S., J.P. Nozières, B.A. Gurney, B. Dieny, T.C. Huang and H. Lefakis, 1993, Phys. Rev. B **47**, 11579.

Steenwyck, S.D., S.Y. Hsu, R. Loloee, J. Bass and W.P. Pratt, 1997, J. Magn. Magn. Mater. **170**, L1.

Steren, L.B., A. Barthélémy, J.L. Duvail, A. Fert, R. Morel, F. Pétroff, P. Holody, R. Loloee and P.A. Schroeder, 1995a, Phys. Rev. B **51**, 292.

Steren, L.B., R. Morel, A. Barthélémy, F. Pétroff, A. Fert, P. Holody, R. Loloee and P.A. Schroeder, 1995b, J. Magn. Magn. Mater. **140–144**, 495.

Stiles, M.D., 1996, J. Appl. Phys. **79**, 5805.

Strijkers, G.J., M.M.H. Willekens, H.J.M. Swagten and W.J.M. de Jonge, 1996, Phys. Rev. B **54**, 9365.

Strijkers, G.J., H.J.M. Swagten, A.H.M. Mettler, M.M.H. Willekens and W.J.M. de Jonge, 1997, in: Magnetic Ultrathin Films, Multilayers and Surfaces, MRS Symp. Proc., Vol. 475 (MRS, Pittsburg, Pennsylvania) p. 99.

Sussiau, M., F. Nguyen Van Dau and P. Galtier, 1997, Mater. Res. Soc. Symp. Proc. **475**, 195.

Suzuki, M., and Y. Taga, 1993, J. Appl. Phys. **74**, 4660.

Suzuki, M., Y. Taga, A. Goto and H. Yasuoka, 1993, J. Magn. Magn. Mater. **126**, 495.

Swagten, H.J.M., G.J. Strijkers, M.M.H. Willekens and W.J.M. de Jonge, 1996, J. Magn. Magn. Mater. **156**, 329.

Szucs, J., T. O'Brien and D.K. Lottis, 1997, J. Appl. Phys. **81**, 4014.

Takahata, T., S. Araki and T. Shinjo, 1989, J. Magn. Magn. Mater. **82**, 287.

Takanashi, K., Y. Obi, Y. Mitani and H. Fujimori, 1992, J. Phys. Soc. Japan **61**, 1169.

Tanaka, A., Y. Shimizu, H. Kishi, K. Nagasaka and M. Oshiki, 1997, IEEE Trans. Magn. **33**, 3592.

Tomlinson, M.E., R.J. Pollard, D.G. Lord and P.J. Grundy, 1992, J. Magn. Magn. Mater. **11**, 79.

Tosin, G., L.F. Schelp, M. Carara, J.E. Schmidt, A.A. Gomes and M.N. Baibich, 1993, J. Magn. Magn. Mater. **121**, 399.

Tsoi, M., A.G.M. Jansen, J. Bass, W.C. Chiang, M. Seck, V. Tsoi and P. Wyder, 1998, Phys. Rev. Lett. **80**, 4281.

Tsoukatos, A., S. Gupta and Y. Huai, 1997, IEEE Trans. Magn. **33**, 3514.

Tsunashima, S., M. Jimbo, T. Kanda, S. Goto and S. Uchiyama, 1993, J. Magn. Magn. Mater. **121**, 429.

Tsunashima, S., M. Jimbo, Y. Imada and K. Komiyama, 1997, J. Magn. Magn. Mater. **165**, 111.

Tsutsumi, K., P. de Haan, M. Eisenberg, D. Monsma and J.C. Lodder, 1996a, J. Magn. Magn. Mater. **156**, 327.

Tsutsumi, K., P. de Haan, M. Eisenberg, D. Monsma and J.C. Lodder, 1996b, J. Magn. Magn. Mater. **156**, 328.

Ueda, Y., N. Hataya and H. Zaman, 1996a, J. Magn. Magn. Mater. **156**, 350.

Ueda, Y., S. Ikeda, S. Hama and A. Yamada, 1996b, J. Magn. Magn. Mater. **156**, 353.

Ustinov, V.V., and E.A. Kravtsov, 1995, J. Magn. Magn. Mater. **148**, 307.

Ustinov, V.V., E.A. Kravtsov, L.N. Romashev and M.A. Miliyaev, 1996a, J. Magn. Magn. Mater. **156**, 337.

Ustinov, V.V., N.G. Bebenin, L. Romashev, V.I. Minin, M.A. Milyaev, A.R. Del and A.V. Semerikov, 1996b, Phys. Rev. B **54**, 15958.

Ustinov, V.V., A.B. Rinkevich, L.N. Romashev and V.I. Minin, 1998, J. Magn. Magn. Mater. **177–181**, 1205.

Uwatoko, Y., G. Oomi, T. Sakai, K. Saito, K. Takanashi and H. Fujimori, 1995, J. Magn. Magn. Mater. **140–144**, 583.

Valet, T., and A. Fert, 1993, Phys. Rev. B **48**, 7099.

Valet, T., P. Galtier, J.C. Jacquet, C. Mény and P. Panissod, 1993, J. Magn. Magn. Mater. **121**, 402.

Van Alphen, E.A.M., and W.J.M. de Jonge, 1995, Phys. Rev. B **51**, 8182.

Vasko, V.A., V.A. Larkin, P.A. Kraus, K.R. Nikolaev, D.E. Grupp, C.A. Nordman and A.M. Goldman, 1997, Phys. Rev. Lett. **78**.

Vas'kovskij, V.O., and A.V. Svalov, 1996, J. Magn. Magn. Mater. **157–158**, 285.

Vas'kovskij, V.O., V.N. Lepalovskij, V.G. Muhchametov and J.M. Jarmoshenkco, 1995, J. Magn. Magn. Mater. **148**, 325.

Vavra, W., S.F. Cheng, A. Fink, J.J. Krebs and G.A. Prinz, 1995, Appl. Phys. Lett. **66**, 2579.

Vedyayev, A., B. Dieny and N. Ryzhanova, 1992, Europhys. Lett. **19**, 329.

Vedyayev, A., C. Cowache, N. Ryzhanova and B. Dieny, 1993, J. Phys. Cond. Matter **5**, 8289.

Vedyayev, A., B. Dieny, N. Ryzhanova, J.B. Genin and C. Cowache, 1994, Europhys. Lett. **25**, 465.

Vedyayev, A., M. Chshiev, N. Ryzhanova, B. Dieny, C. Cowache and F. Brouers, 1997a, J. Magn. Magn. Mater. **172**, 53.

Vedyayev, A., N. Ryzhanova, B. Dieny, P. Dauget, P. Gandit and J. Chaussy, 1997b, Phys. Rev. B **55**, 3728.

Velez, M., and I.K. Schuller, 1998, J. Magn. Magn. Mater. **184**, 275.

Vélu, E., C. Dupas, W. Nabhan, F. Trigui, J.P. Renard and D. Renard, 1992, J. Appl. Phys. **71**, 503.

Voegeli, B., A. Blondel, B. Doudin and J.Ph. Ansermet, 1995, J. Magn. Magn. Mater. **151**, 388.

Vouille, C., A. Fert, A. Barthélémy, S.Y. Hsu, R. Loloee and P.A. Schroeder, 1997, J. Appl. Phys. **81**, 4573.

Vouille, C., A. Fert, A. Barthélémy, S.Y. Hsu, R. Loloee and P.A. Schroeder, 1999, to appear in September 1st issue of Phys. Rev. B **60**.

Wang, D., J. Anderson and J.M. Daughton, 1997, IEEE Trans. Magn. **33**, 3520.

Watanabe, H., E. Hirota, A. Okada, K. Hamada, I. Ishida, H. Sakakima and M. Satomi, 1994, J. Phys. Soc. Japan **63**, 762.

Watson, M.L., W.D. Doyle and H. Fujiwara, 1993, J. Appl. Phys. **73**, 5518.

Wellock, K.P., B.J. Hickey, D. Greig, J. Walker, J. Xu and N. Wiser, 1994, J. Appl. Phys. **75**, 7055.

Wellock, K.P., B.J. Hickey, J. Xu, M.J. Walker and N. Wiser, 1995, J. Magn. Magn. Mater. **140–144**, 585.

Willekens, M.M.H., Th.G.S.M. Rijks, H.J.M. Swagten and W.J.M. de Jonge, 1995a, J. Appl. Phys. **78**, 7202.

Willekens, M.M.H., Th.G.S.M. Rijks, H.J.M. Swagten and W.J.M. de Jonge, 1995b, in: Magnetic Ultrathin Films, Multilayers and Surfaces, MRS Symp. Proc., Vol. 384, (MRS, Pittsburg, Pennsylvania) p. 391.

Xiao, J.Q., J.S. Jiang and C.L. Chien, 1992, Phys. Rev. Lett. **68**, 3749.

Yamamoto, H., T. Okuyama, H. Dohnomae and T. Shinjo, 1991, J. Magn. Magn. Mater. **99**, 243.

Yamamoto, H., Y. Motomura, T. Anno and T. Shinjo, 1993, J. Magn. Magn. Mater. **126**, 437.

Yan, M., S. Li, C. Yu, W. Lai, W. Ku and S. Ge, 1995, J. Magn. Magn. Mater. **140–144**, 539.

Yan, M.L., W.Y. Lai, L. Yin and S.H. Liou, 1997, J. Appl. Phys. **81**, 4782.

Yanagihara, H., K. Pettit, M.B. Salamon, E. Kita and S.S.P. Parkin, 1997, J. Appl. Phys. **81**, 5197.

Yang, Q., S.F. Lee, P. Holody, R. Loloee, P.A. Schroeder, W.P. Pratt Jr. and J. Bass, 1994a, Physica B **194–196**, 327.

Yang, Q., P. Holody, S.F. Lee, L.L. Henry, R. Loloee, P.A. Schroeder and J. Bass, 1994b, Phys. Rev. Lett. **72**, 3274.

Yang, Q., P. Holody, L.L. Henry, W.P. Pratt, P.A. Schroeder and J. Bass, 1995, Phys. Rev. B **51**, 3226.

Yasuna, K., M. Terauchi, A. Otsuki, K.N. Ishihara and P.H. Shingu, 1997, J. Appl. Phys. **82**, 2435.

Young, S., B. Dieny, B. Rodmacq, J. Mouchot and M.H. Vaudaine, 1996, J. Magn. Magn. Mater. **162**, 38.

Yu, C.T., K. Westerholt, K. Theis-Bröhl and H. Zabel, 1997, J. Appl. Phys. **82**, 5560.

Zahn, P., I. Mertig, M. Richter and H. Eschrig, 1995, Phys. Rev. Lett. **75**(16), 2996.

Zahn, P., J. Binder, I. Mertig, R. Zeller and P.H. Dederich, 1998, Phys. Rev. Lett. **80**, 4309.

Zeltser, A.M., and N. Smith, 1996, J. Appl. Phys. **79**, 9224.

Zeng, X.T., and H.K. Wong, 1996, J. Appl. Phys. **79**, 6279.

Zhang, S., and W.H. Butler, 1994, Phys. Rev. B **51**, 10085.

Zhang, S., and P.M. Levy, 1991a, J. Appl. Phys. **69**, 4786.

Zhang, S., and P.M. Levy, 1991b, Phys. Rev. B **45**, 8689.

Zhang, S., and P.M. Levy, 1991c, Phys. Rev. B **43**, 11048.

Zhang, S., and P.M. Levy, 1993a, Mater. Res. Soc. Symp. Proc. **313**, 53.

Zhang, S., and P.M. Levy, 1993b, Phys. Rev. B **47**, 6776.

Zhang, S., and P.M. Levy, 1993c, J. Appl. Phys. **73**, 5315.

Zhang, S., and P.M. Levy, 1996, Phys. Rev. Lett. **77**, 916.

Zhang, S., and P.M. Levy, 1998, Phys. Rev. B **57**, 5336.

Zhang, S., P.M. Levy and A. Fert, 1992, Phys. Rev. B **45**, 8689.

Zhang, H., R.W. Cochrane, Y. Huai, M. Mao, X. Bian and W.B. Muir, 1994, J. Appl. Phys. **75**, 6534.

Zoll, S., A. Dinia, J.P. Jay, C. Mény, G.Z. Pan, A. Michel, L. El Chahal, V. Pierron-Bohnes, P. Panissod and H.A.M. Van der Berg, 1998, Phys. Rev. B **57**, 4842.

chapter 2

NMR OF THIN MAGNETIC FILMS AND SUPERLATTICES

P.C. RIEDI, T. THOMSON and G.J. TOMKA

School of Physics and Astronomy
University of St. Andrews
Fife KY16 9SS
Scotland, U.K.

Handbook of Magnetic Materials, Vol. 12
Edited by K.H.J. Buschow
© 1999 Elsevier Science B.V. All rights reserved

CONTENTS

1. Introductory survey 100
   1.1. Introduction 100
   1.2. Overview 105
2. The magnetic field at a nucleus 105
   2.1. Introduction 105
   2.2. The effective magnetic field of Co 107
   2.3. Theory of HFF in bulk material 109
   2.4. HFF of disordered Co alloys 110
   2.5. HFF of thin films 113
3. Conventional nuclear magnetic resonance 114
   3.1. Introduction 114
   3.2. Motion of an isolated magnetic moment 115
   3.3. Nuclear magnetism at thermal equilibrium 116
   3.4. Longitudinal relaxation 117
   3.5. Linear and circular polarization of rf fields 117
   3.6. Free induction decay 118
   3.7. Spin echoes 119
   3.8. Electric field gradient (EFG) 120
   3.9. Magnitude of NMR signals 121
   3.10. The measurement of the distribution of effective fields at the nuclei 121
   3.11. Knight shift and nuclear relaxation 122
4. NMR of ferromagnetic materials 123
5. Magnetism and NMR of cobalt 126
   5.1. Introduction 126
   5.2. NMR of hcp Co 126
   5.3. NMR of fcc Co 129
   5.4. NMR relaxation of Co 130
6. Cobalt films 130
   6.1. Introduction 130
   6.2. Face centred cubic cobalt films 131
   6.3. Hexagonal close packed cobalt films 133
   6.4. Body centred cubic cobalt 134

7. NMR in Co/Cu superlattices 141
7.1. Basics of NMR in Co/Cu superlattices 141
7.2. Crystal phase and orientation in Co/Cu superlattices 143
7.3. NMR studies of strain in the Co layers of Co/Cu superlattices 153
7.4. Anisotropy measured by NMR in Co/Cu superlattices 156
7.5. Effect of deposition technique and substrate/buffer on Co/Cu multilayers 159
7.6. Effect of annealing Co/Cu superlattices 163
7.7. Temperature dependence of NMR in Co/Cu multilayers 166
7.8. Correlation of NMR in Co/Cu superlattices with other properties 166
8. NMR in Co–Cr based thin films 169
8.1. Introduction to Co–Cr thin films 169
8.2. Bulk alloys as NMR references 174
8.3. NMR in Co–Cr thin films 177
8.4. NMR in Co–Cr thin alloy films 177
8.5. NMR in Co/Cr multilayers 191
9. NMR investigations of Co based thin films 193
9.1. NMR studies of Co/Au multilayers 193
9.2. NMR studies of Co/Ag multilayer and alloy thin films 196
9.3. NMR investigations of Co/Pt and Co/Pd multilayers 199
9.4. NMR work on Co/Fe multilayers 208
9.5. ^{55}Mn and ^{59}Co NMR studies of Co/Mn multilayer and alloy thin films 210
9.6. Miscellaneous Co-based thin films 215
10. NMR studies in thin films utilizing nuclei other than ^{59}Co 223
10.1. ^{63}Cu and ^{65}Cu NMR in thin films 223
10.2. ^{51}V NMR studies of multilayers 230
10.3. NMR in other thin films and multilayers 232
10.4. NMR in metallic superconducting multilayers 246
10.5. NMR experiments on thin film Rare Earth elements 250
References 253

1. Introductory survey

1.1. Introduction

The study of the properties of thin magnetic films and multilayers has been one of the most active areas of research in magnetism in recent years. The potential technical importance of the giant magnetoresistance effect (GMR) discovered in antiferromagnetically coupled Fe/Cr systems produced by sputtering, Baibich et al. (1988), Binasch et al. (1989), has intensified the theoretical and experimental study of structures with reduced dimensionality, see Chapter 1 of this volume for a review. A key aspect of this work is the relationship between the structural and magnetic properties of the material. One early problem, for example, was that Co/Cu multilayers grown by molecular beam epitaxy (MBE) had a much smaller MR than those grown by sputtering. Since the interface of a MBE grown material is expected to be well defined relative to that of a sputtered sample it was thought that surface roughness was essential for GMR. A ^{59}Co nuclear magnetic resonance (NMR) study showed however that the MR *increased* from 4% to 40% as the interfacial quality of a series of MBE grown Co/Cu (1 1 1) multilayers improved, Thomson et al. (1994a, 1994b).

The ordered electronic magnetism of a ferromagnet induces a static effective (hyperfine) magnetic field (HFF) at a nucleus even in the absence of an external field. In the present review we aim to show how NMR using the HFF is able to provide detailed information on the structural and magnetic properties of thin films and multilayers. Since the great majority of the NMR work on thin films has used the ^{59}Co nucleus we summarize the results for cobalt:

1. Cobalt can exist in the face centred cubic (fcc), hexagonal close packed (hcp) or, in sufficiently thin films with appropriate under/seed layers, body centred (bcc) structures. The NMR spectra from the fcc and hcp phases are quite different, fig. 1.1, and the bcc spectra is thought to be a single line near 198 MHz. It is therefore straightforward to determine the crystal structure of a film by NMR while it is sometimes difficult to distinguish cubic from twinned hexagonal by X-rays.
2. The difference in the lattice constant between a cobalt layer and the substrate, or between adjacent layers of a different element, produces strain in the layer. The change in the NMR frequency of cobalt with pressure has been measured and therefore the strain in a layer can be evaluated from the NMR spectrum, figs 1.2 and 1.3.
3. The nature of an interface can be studied by NMR because the NMR frequency of ^{59}Co depends on the moments on the nearest neighbor (NN) atoms, more distant neighbors usually have only a small effect. The shift of the ^{59}Co frequency from the value in the pure metal due to one or more impurity atoms in the NN shell has been

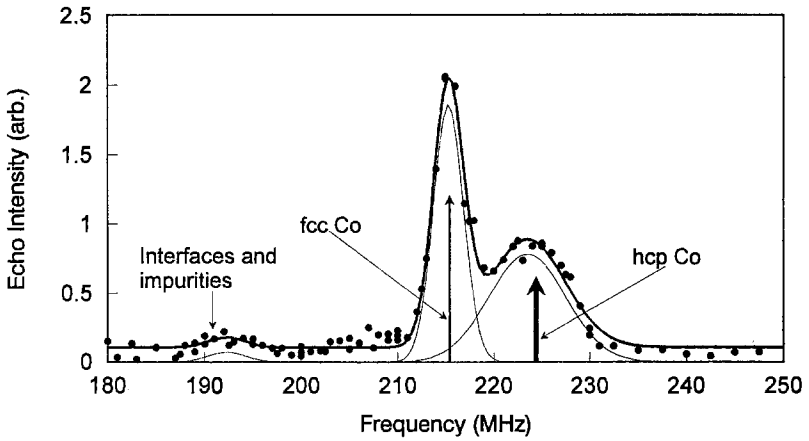


Fig. 1.1. ^{59}Co NMR spectrum for Cu/Co(102Å)/Cu continuous film at $T = 4.2$ K. Note the modeled contributions from the impurity, fcc and hcp terms. After Thomson et al. (1997).

found for many elements from experiments on alloys containing typically 1% of the impurity. At a perfect interface of a Co/Cu (1 1 1) superlattice, for example, three Co atoms in the NN shell would be replaced by Cu atoms and the ideal ^{59}Co spectrum would consist of two lines: one from the interface and one from the interior of the cobalt layer. As may be seen in fig. 1.2(c), the best MBE grown material does show a two line spectrum although the width of the lines is greater than might be expected from measurements on bulk material. A more typical result for MBE grown material is analyzed in fig. 1.3.

4. Multilayers of the highest quality are grown by MBE but sputtering and electrodeposition are more attractive techniques for applications because they are cheaper and quicker. The interface region is then less well defined than in the best MBE grown material but may contain areas of perfect alignment. The NMR spectrum for a sputtered Co/Cu (1 0 0) multilayer shown in fig. 1.4, for example, contains lines due to cobalt atoms surrounded by 0–4 copper atoms. A perfect (1 0 0) interface would have produced a two line spectrum from cobalt atoms surrounded by either 0 or 4 copper atoms.
5. A second NMR method for studying interfacial mixing in Co/X multilayers is to look for the X resonance due to the HFF induced by the cobalt magnetization. The NMR frequencies for many impurities in cobalt have been measured using dilute alloys of bulk material. The presence of, e.g., Mn in a cobalt layer can therefore be detected because the ^{55}Mn NMR frequency as a dilute impurity in cobalt is known to be 380 MHz which is well separated from the 217.4 MHz line of ^{59}Co, fig. 1.5.
6. The NMR signal from a ferromagnet is much stronger than would be predicted from conventional NMR theory. The enhancement factor (η) of the signal arises because of an interaction between the radio frequency (rf) field and the ordered electronic magnetization. Measurements of η across the NMR spectrum of a multilayer may be interpreted in terms of the *local* magnetic stiffness. It has been shown for example

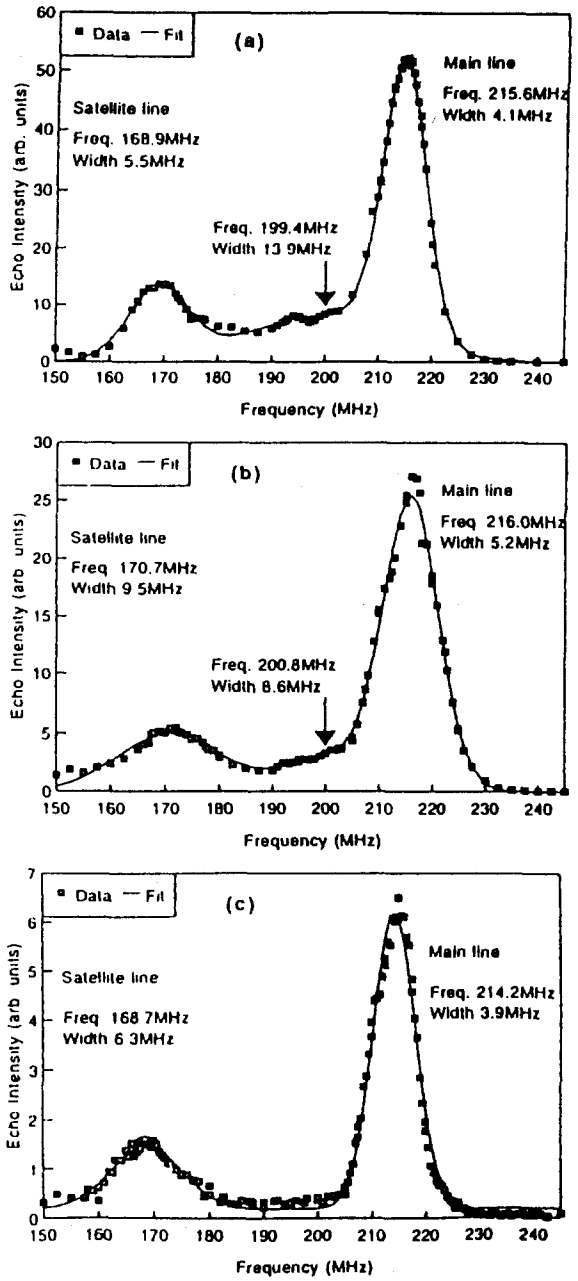


Fig. 1.2. ^{59}Co NMR spectra, corrected for ω^2 and frequency dependence of spin–spin relaxation time, for a series of Co/Cu (1 1 1) multilayers: (a) $\Delta R/R = 4\%$; (b) $\Delta R/R = 22\%$; (c) $\Delta R/R = 40\%$. Note the *increase* of $\Delta R/R$ as the contribution from defects in the interfaces (180–210 MHz) decreases. The unstrained fcc Co NMR frequency at 4.2 K is 217.4 MHz. After Thomson et al. (1994b).

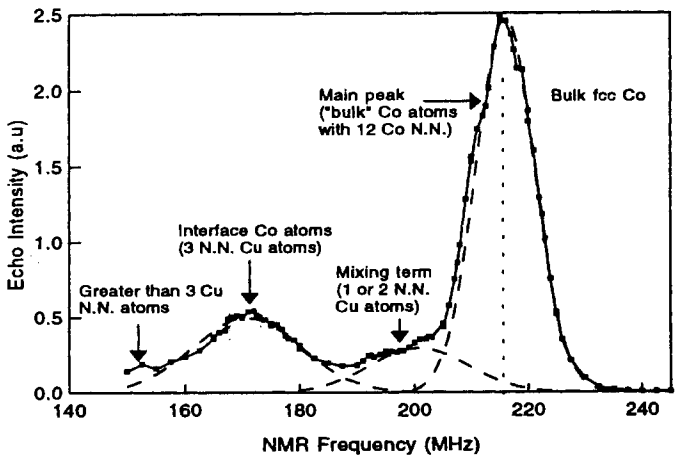


Fig. 1.3. Typical ^{59}Co NMR spectrum at 4.2 K for a good quality MBE grown Co/Cu (1 1 1) multilayer.

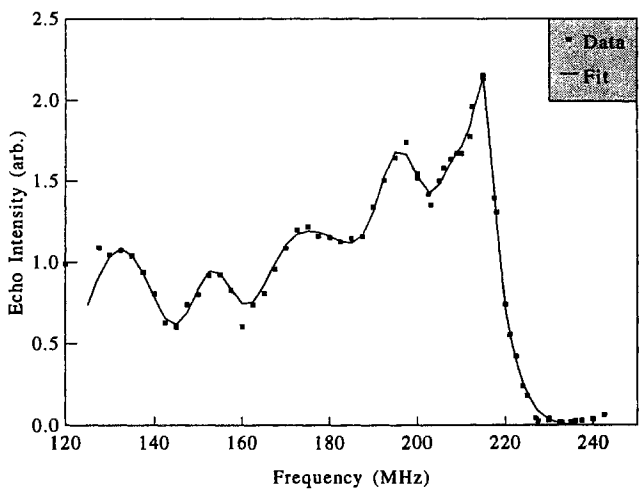


Fig. 1.4. ^{59}Co NMR spectrum for a sputtered Co/Cu (1 0 0) multilayer with [Cu(20.6Å)/Co(10.7Å)]$_{\times 12}$. The spectrum was fitted with Gaussian functions for the main grain boundary and satellite lines. After Thomson et al. (1996c).

that the coercive force at the Co/Cu (1 1 1) interface is typically some 0.026 T, and that this is reflected by an interface anisotropy of around 0.036 T while in the interior of the Co layer the anisotropy can be as large as 0.123 T, as detailed in section 7.4.

Finally, we note three further possible NMR experiments that have either not yet succeeded or have not been reported in any detail:

1. At a site of non-cubic symmetry there is an interaction between the nuclear quadrupole moment of ^{59}Co and the local electric field gradient (EFG) in the crystal. The

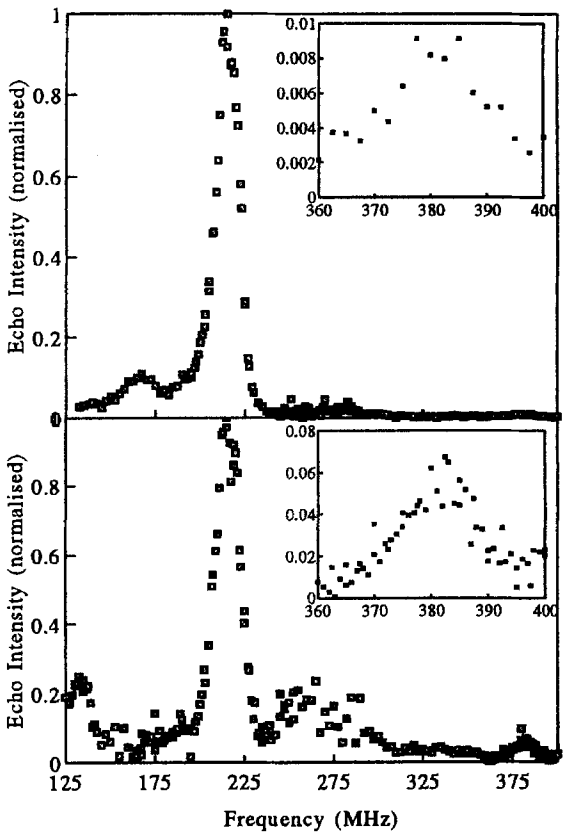


Fig. 1.5. ^{59}Co and ^{55}Mn NMR spectra at 4.2 K of rf sputtered multilayers: (a) [Co(30Å)/Mn(10Å)]$_{\times 10}$; (b) [Co(30Å)/Mn(30Å)]$_{\times 10}$. The ^{55}Mn NMR in the interior of the Co layer is enlarged in the inserts. After Thomson et al. (1996b).

effect is small, three orders of magnitude below the strength of the magnetic interaction, but easily observed in bulk hcp Co because it leads to a modulation of the spin echo decay, fig. 3.2. This effect has not been reported in thin films, presumably because the EFG is not sufficiently well defined due to defects or a distribution of strain in the layers. In principle the effect should also be observable for fcc Co in a thin film because the cubic symmetry is broken at the interface.

2. The NMR relaxation rate depends upon the fluctuations of the electronic magnetization. The fluctuation spectrum in the restricted geometry of a thin film must differ from that of the bulk material but there has been little experimental, and no theoretical, work reported so far.
3. A thin film may be patterned, e.g., by an electron beam, to produce an array of islands with typical lateral dimensions ~0.2 × 3 μm, Kirk et al. (1997). The NMR spectra and relaxation times of these arrays should exhibit new features.

1.2. Overview

In preparing this survey we have assumed that the reader has little knowledge of the NMR of ferromagnetic materials but has some familiarity with the preparation and properties of thin magnetic films. The theory of the HFF, with particular application to bulk and thin film cobalt is discussed in section 2. The elements of NMR are introduced in section 3 and the distinguishing features of the NMR of ferromagnets in section 4. Section 5 summarizes the NMR properties of ^{59}Co in bulk fcc and hcp cobalt. Section 6 concerns the properties of single layers of the three possible crystal structures of cobalt and the following sections reviews multilayers. A valuable source of information on the NMR of multilayers, concentrating on the work of the Strasbourg group, is to be in found reports of Panissod et al. (1996) and Panissod (1995, 1997).

General note

The majority of the NMR spectra discussed in this article were produced by sweeping the spectrometer frequency without applying an external magnetic field to the sample. The best value for the conversion factor between the frequency and field for resonance of ^{59}Co in conventional NMR is now considered to be 10.054 MHz T^{-1}, but in many papers the older value of 10.1 MHz T^{-1} has been used, see section 5. The HFF of ^{59}Co in cobalt is negative, i.e., anti-parallel to the direction of the magnetization, see section 2. The application of an external magnetic field therefore leads to a reduction of the NMR frequency.

Units and notation

In magnetism the standard SI units commonly used in many areas of physics have not yet been universally accepted, and in many areas can be cumbersome and in some cases are still not agreed. For these reasons, many papers and books reviewed in this article have been published using CGS magnetic units and terms. This is probably because, as stated by Parker (1990), the simplicity of using CGS units and terms often outweighs the fundamental worth of the SI system. Also many properties such as magnetization, M, magnetic induction (or flux density), B, and magnetic field intensity, H, are vector properties, and the demagnetizing factor, N_d, and permeability μ are tensor properties, however such notation is frequently omitted in the literature. We also note that there is some inconsistency in the literature in the use of B and H, for example, in discussing the magnetic anisotropy. In this review we have been as consistent as possible in our general discussion of the literature, though, to assist the reader, for specific references we have made appropriate use of terms and units as originally used by the authors.

2. The magnetic field at a nucleus

2.1. Introduction

The electronic magnetization of a ferromagnetic material induces a magnetic field at each nucleus. It is possible to perform NMR in the static component of this hyperfine field (HFF), B_{hf}, even in the absence of an external magnetic field. (The material will then normally be in a multidomain state. The consequences of this for NMR are discussed

in section 4.) Since B_{hf} arises from the spontaneous magnetization at temperature T, it appears reasonable to write an equation of the form

$$B_{hf} = A(T)\sigma(T), \tag{2.1}$$

where $\sigma(T)$ is the magnetization per unit mass and A is called the hyperfine coupling constant. However, in general A is not a constant but is found to be a function of temperature and pressure. (Equation (2.1) is often written in terms of the magnetization per unit volume, $M(T)$, but this is undesirable because it introduces an inherent volume dependence to A.) The investigation of thin film magnetization by NMR is limited to low temperature, because of the problem of the signal to noise ratio discussed in section 3.9. In the low temperature limit of spin wave theory A is found to be independent of temperature at constant volume (Edwards 1976; Riedi 1973, 1977, 1979), and B_{hf} is then proportional to the spontaneous magnetization.

The volume dependence of B_{hf} is important for the understanding of the NMR of multilayers, because interfacial strain will change the lattice constants from their values in bulk material. Under pressure M decreases for Fe, Co and Ni at low temperature, table 5.1, but the magnitude of B_{hf} increases for Co and Ni, table 5.2. Janak (1979) has shown how the contributions of the different electronic shells to the magnetization and HFF change with pressure.

In bulk material it is generally true that a reduction of the magnetization, by alloying for example, leads to a reduction of the magnitude of the average HFF, but in thin films the relationship between the two quantities is more complicated. On a free monolayer for example the magnitude of the magnetic moment per atom is greater than that of the bulk, but the magnitude of the HFF is decreased. A fuller discussion is given in section 2.5.

An example of the contributions to B_{hf} for Fe and Co given by a recent calculation is shown in table 2.1. The negative signs indicate that the direction of the field is anti-parallel

TABLE 2.1

Computed hyperfine fields (Tesla) for bcc Fe and fcc Co (see Guo and Ebert 1996).

Shell	bcc Fe	fcc Co
1s	−2.05	−1.84
2s	−52.18	−43.69
2p	0.17	−0.16
3s	29.10	26.09
3p	−0.07	0.07
Core sum	−25.02	−19.36
s	−7.28	−7.54
p	0.09	0.17
d	1.46	4.46
f	−0.03	−0.01
Valence sum	−5.77	2.92
Total	−30.79	−22.28
Experiment	−33.9	−21.6

to the magnetization. It will be seen that some of the individual electron shells produce fields greater than, or comparable to, the resultant value of B_{hf} and in consequence it is difficult to decide how accurately B_{hf} can be calculated. This point will be returned to below, but it is worth noting that the difference between the experimental and calculated value of the B_{hf} of Fe, for example, *increased* after the introduction of improved, fully relativistic, calculations.

The present review is largely devoted to an analysis of experimental work on thin films and will not attempt to survey the extensive literature on the calculation of the magnetic properties of metals. Instead, one calculation of the properties of pure metals and ideal multilayers and one on alloys will be discussed in some detail. Early computational work using the Local Spin Density Functional (LSDF) method is reviewed by Moruzzi et al. (1978) and more recent reviews may be found in Moruzzi and Marcus (1993) and Brooks and Johansson (1993).

In the next sections the contributions to B_{hf} in bulk Co are discussed in more detail. The relationship between the distribution of HFF and the local environment in a disordered alloy is considered in section 2.4 The special magnetic properties of surface atoms, obviously of great importance for the analysis of the NMR of multilayers, are reviewed in section 2.5.

2.2. *The effective magnetic field of Co*

The effective magnetic field at the nucleus will be written in the form

$$\boldsymbol{B}_{eff} = \boldsymbol{B}_{hf} + \boldsymbol{B}_{i},$$

where $\boldsymbol{B}_i$ is the macroscopic internal magnetic field in the sample. In a single domain ellipsoid

$$\boldsymbol{B}_i = \boldsymbol{B}_0 + \mu_0(1 - N)\boldsymbol{M},$$

where $\boldsymbol{B}_0$ is the applied field and N the demagnetizing coefficient. The value of N is 1/3 for a sphere and 1(0) for $\boldsymbol{M}$ perpendicular (parallel) to the surface of a thin film.

While the equations above are strictly correct, the classical Lorentz field, $\mu_0 M/3$, is sometimes considered to be a separate contribution to B_{eff}. The Lorentz field is ~0.6 T for Co, which is only some 3% of B_{hf}. The accuracy with which B_{hf} can be calculated for Co is less than 3% but the NMR measurements can sometimes be accurate to better than 0.02%.

The value of B_{hf} may be derived from a single operator, section 2.3, but it is customary to partition it into terms that can be related to the spin and orbital components of the magnetization. It is also useful to distinguish between the contributions to B_{hf} from the core (1s–3p) electrons and the valence electrons,

$$\boldsymbol{B}_{hf} = \boldsymbol{B}_c + \boldsymbol{B}_v.$$

The value of B_c for Co is almost entirely due to s electrons, table 2.1, but the valence term will be split to distinguish between s and non-s electrons,

$$\boldsymbol{B}_v = \boldsymbol{B}_s + \boldsymbol{B}_{ns}.$$

The non-s electron term comes from the orbital and dipole moments,

$$\boldsymbol{B}_{\mathrm{ns}} = \boldsymbol{B}_{\mathrm{orb}} + \boldsymbol{B}_{\mathrm{d}}.$$

In bulk Co B_{d} is small, but it becomes important in thin films, section 2.6.

The largest contribution to B_{hf} of Co comes from $B_{\mathrm{c}} \sim -20$ T, but both $B_{\mathrm{s}} \sim -10$ T, and the orbital term $\sim +10$ T, are important. The individual terms for B_{hf} defined above,

$$\boldsymbol{B}_{\mathrm{hf}} = \boldsymbol{B}_{\mathrm{c}} + \boldsymbol{B}_{\mathrm{s}} + \boldsymbol{B}_{\mathrm{orb}} + \boldsymbol{B}_{\mathrm{d}}, \tag{2.2}$$

will now be considered in more detail. A discussion of B_{d} will be left until section 2.5. The origin of B_{c} and B_{s} is the Fermi contact interaction between the nuclear spin and the spin of s electrons.

Fermi contact interaction

The Fermi contact interaction has the form $\boldsymbol{I} \cdot \boldsymbol{S}$ where I is the value of the nuclear spin and S an unpaired electron in a s state. The core 1s, 2s and 3s shells each contain two electrons of opposite spin, whose contact interaction would normally cancel, but the attractive exchange interaction between the 3d spin moment and the s electrons of parallel spin leads to a net density of anti-parallel s electrons at the nucleus. The Fermi contact interaction with the core s electrons makes the largest contribution to the effective field at the nucleus of Fe and Co, table 2.1, so B_{c} is negative, i.e., anti-parallel to the magnetization.

The magnitude of B_{c} is proportional to the electronic spin moment of the atom. Guo and Ebert (1996) calculate that for Co

$$\boldsymbol{B}_{\mathrm{c}} = -11.3\,\mu_{\mathrm{s}} \tag{2.3}$$

where B_{c} is in Tesla and μ_{s} in Bohr magneton. Rather larger coefficients of proportionality, e.g., -13 T/μ_{B}, have commonly been used by experimentalists, see Riedi et al. (1987). It should be noted that the decision to include the contribution of the 3s electron shell in B_{c} is somewhat arbitrary, since it overlaps with the 3d shell.

Orbital contribution

The orbital contribution to B_{hf} is by far the largest for the magnetic rare earth metals, apart from Gd, see McCausland and Mackenzie (1979). The orbital moment of Co is largely quenched, table 2.2, but the orbital moment makes a much larger contribution to B_{hf} than to the magnetization. The value of B_{orb} is proportional to the orbital moment. Guo and Ebert (1996) calculate that

$$B_{\mathrm{orb}} = +63\,\mu_{\mathrm{orb}}. \tag{2.4}$$

The orbital moment of hcp Co is anisotropic, section 5.2, so the value of B_{orb} depends on the direction of the magnetization in the crystal. In a multidomain sample of hcp Co a broad distribution of B_{hf} is observed, fig. 4.2, due to the rotation of the moments through the domain walls.

Transferred field

The polarization of the valence electrons contributes some −3 T to B_{hf} for pure Co and can also induce appreciable fields at the nuclei of "non-magnetic" atoms such as Cu, section 2.4.

2.3. *Theory of HFF in bulk material*

The theoretical calculations of HFF predict significant differences between the properties of the surface of a thin film and the bulk material. Before considering the behaviour of thin films we briefly review the present state of the theory of the HFF of bulk materials. An example of a recent state-of-the art calculation is that of Guo and Ebert (1996). This was a fully relativistic spin polarized density functional calculation. All of the terms in eq. (2.2) are found from the relativistic operator, and the individual terms identified by considering the perturbation method for making relativistic corrections to the non-relativistic theory of HFF.

The calculated contributions of the individual electron shells to the HFF of Fe and Co are shown in table 2.1 and of the spin and orbital moments of the three phases of Co in table 2.2. These values were all calculated using the experimental lattice constants. An alternative approach that has often been used is to make a completely first principles calculation. In this case the lattice constant is found by minimizing the energy of the system.

The values of the spin moment calculated by the spin density functional method are found to agree with the experimental values to within 2%, table 2.2. The calculated orbital moment is found to be only 50% of the experimental value and the value for B_{orb} for Co should be nearer 10 T than the 4.5 T given in table 2.1. After making this correction the agreement between theory and experiment is remarkably good for the HFF of fcc Co, but it can be seen that this is in a sense rather spurious, because the same correction increases the discrepancy for bcc Fe.

In summary, the modern spin density calculations give good agreement with the experimental values of the magnetization of the 3d metals, where the orbital moment makes only a small contribution to the total moment per atom, but the HFF is more sensitive to the necessary approximations made in the calculations. The individual contributions to the HFF are proportional to their respective moments at constant volume but the pressure dependence of the HFF is different from that of the magnetization. Janak (1979) showed that

TABLE 2.2

The values of the spin (m_s), orbital (m_o), and dipole (m_d), contributions to the total magnetic moment of cobalt (μ_B/atom). The calculated values of Guo and Ebert (1996) are shown in brackets. (See sections 5 and 6 for a more detailed discussion of the magnetic properties of cobalt.)

Crystal structure	m_s	m_o	m_d	m_{tot}
fcc	1.611 (1.631)	0.14 (0.074)	(0.0)	1.751 (1.705)
hcp ($M \| c$)	1.714 (1.596)	0.14 (0.077)	(−0.006)	1.728 (1.667)
hcp ($M \perp c$)	1.706 (1.596)	0.13 (0.072)	(0.004)	1.719 (1.672)
bcc	1.57 (1.743)	0.14 (0.080)	(0.0)	1.71 (1.823)

the magnitude of the core contribution to the HFF of Fe, Co and Ni, decreased under pressure, as expected since the moment per atom decreases under pressure, but that the valence contribution actually increases because the decrease in the size of the unit cell overcomes the decrease of the exchange polarization. This effect is sufficiently large in Co and Ni for the pressure derivative of the magnitude of the HFF to become positive, section 5.1.

2.4. HFF of disordered Co alloys

The introduction of an impurity atom into a ferromagnetic metal leads to a distribution of HFF at the host nuclei and a HFF at the nucleus of the impurity. In general the screening of the impurity by the electrons of the host will lead to an oscillatory RKKY-like variation of the HFF of the host about the value of the HFF of the pure metal. Stearns (1971), for example, attempted to fit the measured distributions of HFF of Fe alloys to a model of the HFF at the six nearest neighbor (NN) shells of the impurity. In Co alloys however it is rarely possible to identify clearly the effect of the impurity much beyond the NN shell. The shift in the Co HFF at the NN sites of an impurity is to lower frequencies, with the exception of Fe, and of the order of 10 MHz, table 2.3 and fig. 2.1. The Co linewidth in pure fcc Co powder is about 0.7 MHz so in a dilute (~1%) alloy the satellite line from

TABLE 2.3

The hyperfine fields (HFF) and NMR frequencies of dilute impurities in fcc cobalt. Where the sign of HFF has been measured it is indicated by a plus or minus sign. The impurity HFF are only given to 2 significant figures because they may depend on alloy concentration and preparation, see the references for more details. The shift of the cobalt HFF due to one impurity atom in the nearest neighbor shell is also shown. (The ^{59}Co frequency is reduced for all impurities except Fe.)

Element	Isotope	Impurity NMR in Co [1] T (MHz)	^{59}Co shift (MHz)
Al	^{27}Al	3.2 (36)	−22 [2]
Si	^{29}Si		−16 [2]
V	^{51}V	4.8 (54)	−40 [3]
Cr	^{53}Cr		−32 [4]
Mn	^{55}Mn	−36.14 (380.150)	−37 [5]
Fe	^{57}Fe	−33 (46)	+9 [4]
Co	^{59}Co	−21.69 (217.4)	0
Ni	^{61}Ni	19 (72)	−7.5 [6]
Cu	^{63}Cu, ^{65}Cu	16 (180.193)	−16 [4,7]
Ge	^{73}Ge		−16 [2]
Nb	^{93}Nb		−47 [2]
Ru	^{99}Ru, ^{101}Ru	41.5 (79.86)	−25 [4]

References:

[1] Rao (1979)
[2] Kobayashi et al. (1966)
[3] Kawakami et al. (1972)
[4] Mény et al. (1993a, 1993b)
[5] Yasuoka et al. (1971)
[6] Riedi and Scurlock (1967a, 1967b)
[7] Mény et al. (1992)

the Co NN of the impurity is well separated from the main line. The moments of the more distant neighbors of the impurity however usually only contribute to a broadening of the NMR spectrum.

The clearest satellite lines are observed for alloys such as $Co_{1-c}Ni_c$ where the impurity has little effect on the NN Co moments, fig. 2.1. In this case the effect of 2 or 3 impurities in the NN shell is simply additive and the Co HFF for n impurities may be estimated from the simple expression,

$$B_n \sim B_{Co} - 0.6n(\mu_i - \mu_{Co}) \tag{2.5}$$

where μ_i and μ_{Co} are the impurity and Co moments and the, negative, HFF are in Tesla. The relative intensities of the ^{59}Co satellite lines corresponding to n NN in a fcc $Co_{1-c}X_c$ random alloy are given by the coefficients of the binomial expansion

$$I(n) = \frac{N!c^n(1-c)^{(N-n)}}{n!(N-n)!}$$

with N equal to 12.

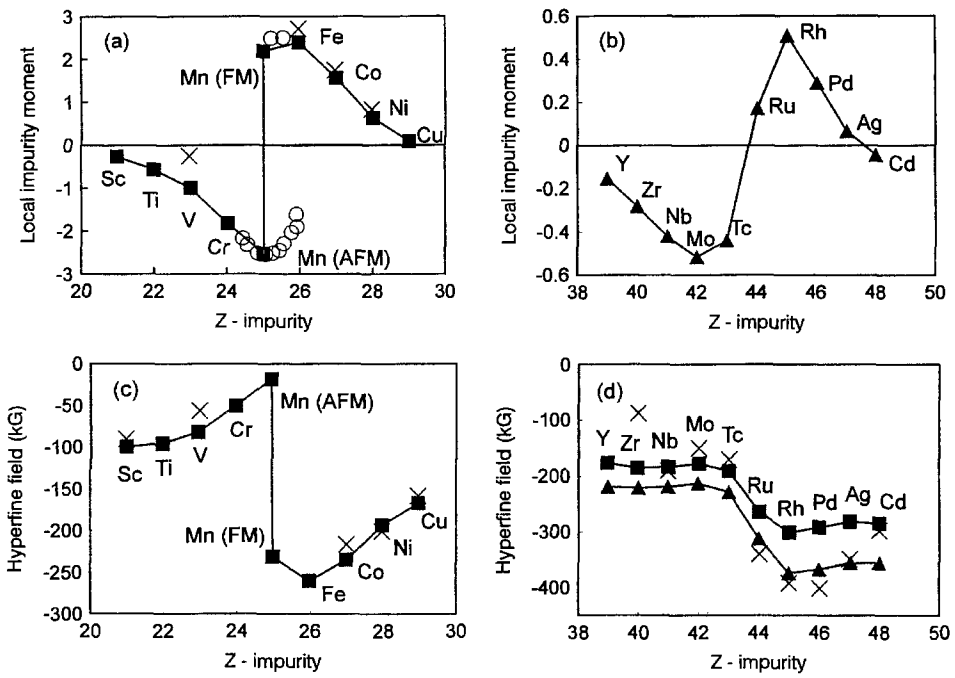


Fig. 2.1. The calculated moments and HFF for an isolated impurity in Co. After Stepanyak et al. (1994). The experimental values are shown by crosses. (a) The local moments for 3d impurities in Co using integer values of the atomic number (squares) and noninteger values of the atomic number (open circles). (b) The local moments for 4d impurities in Co. (c) The HFF for 3d impurities in Co. (d) The HFF for 4d impurities in Co.

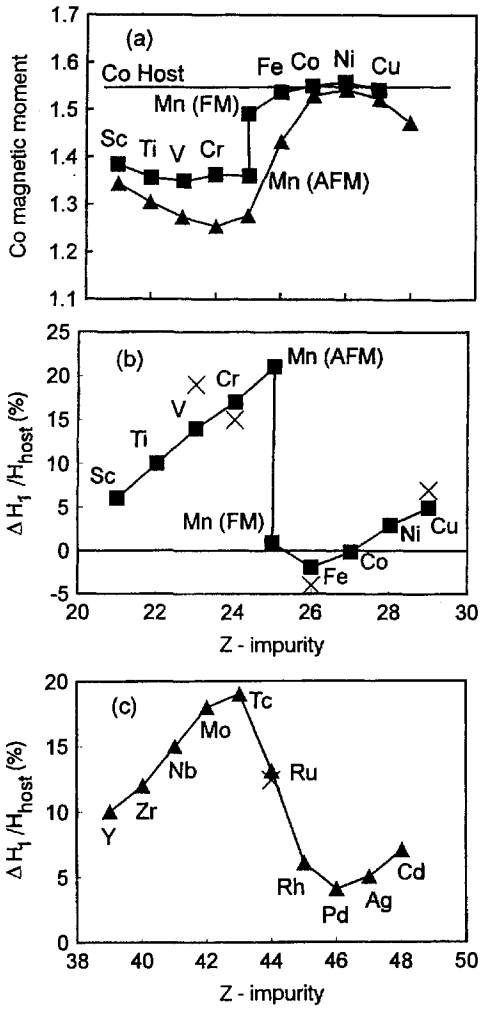


Fig. 2.2. The calculated moments and HFF for Co NN of single impurity atoms. After Stepanyak et al. (1994). The experimental values are shown by crosses. (a) The magnetic moment of Co atoms on the first shell around 3d and 4d impurities. (b) The normalized change of the HFF of Co atoms on the first shell around 3d impurities. (c) The normalized change of the HFF of Co atoms on the first shell around 4d impurities.

The relative strength of the satellite lines increases with the concentration c of the impurities in the NN shell but the line broadening due to the unresolved HFF shifts from the more distant neighbors eventually smears out the individual lines. In the most favorable cases, such as $Co_{1-c}Ni_c$ for $c < 0.1$, satellite lines are observed for $n = 1, 2$ and 3, Riedi and Scurlock (1967a, 1967b). The experimental values for $(B_1 - B_{Co})$ are given in table 2.3. While the environment at the interface of a Co multilayer is obviously not really comparable to that of a random alloy, the HFF shifts in multilayers are often found to be in good agreement with those shown in table 2.3.

The theory of the magnetic moment and HFF of Co has been extended to allow the calculation of the effect of an impurity on the host. The moment and HFF of the impurity and the NN Co atoms have been found using the local-density approximation and the Korringa–Kohn–Rostoker Green's function method (Stepanyuk et al. 1994). The calculated results are generally in good agreement with experiment, figs 2.1 and 2.2.

The outstanding problem, highlighted by the results shown in fig. 2.1, is the magnetic state of Mn as a dilute impurity in Co. Remarkably, the energy of ferromagnetic and antiferromagnetic Co–Mn coupling is found to be almost identical, although in both cases there is a large moment at the Mn site. The antiferromagnetic configuration was calculated to be the ground state. Neutron scattering experiments provide some evidence for both states, see Stepanyuk et al. (1994) for a review. The calculated HFF of Mn in Co is $-25(-2.5)$ T for the ferromagnetic (antiferromagnetic) configuration. Values of ~ -30 T have usually been measured, but $+10$ T has also been reported, table 2.3.

A second method to distinguish between the two possible states of Mn in Co is to look for the Co NN satellite line in a dilute Co–Mn alloy. In the state with ferromagnetic coupling the moments of Co and Mn are so similar that the NN satellite line is probably concealed within the intense Co line from more distant Co atoms, but the antiferromagnetic alignment should lead to a huge shift of the NN HFF. The simple empirical expression given in eq. (2.5) above leads to a decrease of the magnitude of the HFF at the NN Co site by some 2.6 T and the calculated value, fig. 2.1, is 4.8 T. However, there does not appear to have been any report of a NMR line this far below the main Co resonance. Some of the confusion over the state of Mn in Co probably arises from metallurgical problems and more neutron and NMR work is needed to clarify the position. The NMR results on Co/Mn multilayers are discussed in section 9.5.

2.5. *HFF of thin films*

The connection between the HFF and the magnetic moments of a ferromagnetic material has been seen in section 2.2 to be rather complicated, but in bulk material a reduction of the average magnetic moment, e.g., by alloying with a non-magnetic element, generally leads to a reduction of the mean HFF. Mössbauer HFF measurements on Fe alloys for example have been found to be in agreement with an equation of the form

$$B_{\mathrm{hf}} = a\mu_{\mathrm{Fe}} + b\mu,$$

where B_{hf} is the mean HFF, μ_{Fe} is the Fe moment, μ is the average moment per atom, and a and b are constants (Johnson et al. 1963). However, it has been shown both by theory and experiment that in a monolayer of Fe the magnetic moment is larger than in the bulk while the magnitude of the HFF is greatly reduced. In the extreme case of a free monolayer of Fe the moment has been calculated to have increased from the bulk value of $2.2\,\mu_{\mathrm{B}}$ to $3.18\,\mu_{\mathrm{B}}$, while the magnitude of the (negative) HFF decreased from 30 T to 10 T, Ohnishi et al. (1984). A review of the computational work on ultra-thin layers is given by Freeman and Wu (1991).

A free monolayer cannot of course be realized in practice, but the very sensitive conversion electron Mössbauer technique can be used to measure the HFF of a single atomic layer of Fe without removing the film from the UHV chamber. The single active layer may form

the surface of the film or be covered by other layers. A review of this work is given in Gradmann (1993). A monolayer of Fe on a W (1 0 0) surface, with a covering of Ag, for example was found to have a moment of 2.53 μ_B and a HFF of −11.9 T (Gradmann et al. 1989). The calculated values were 2.17 μ_B and −12.2 T (Hong et al. 1988). The large reduction in the magnitude of the surface HFF of Fe comes about because the valence s electron contribution B_s changes sign. The core HFF, B_c, does become more negative with the increased spin moment in the surface but this effect is too small to compensate for the change of B_s.

The poor signal to noise ratio of NMR, relative to that of conversion electron Mössbauer experiments, precludes the measurement of a monolayer of Co in a UHV system near room temperature but the connection between the magnetic moment and the HFF at the interfaces of a Co/X multilayer may be important. The increased moment found for the surface layer of an Fe film is an example of a general effect that is also observed in small particles, see, e.g., Gantefore and Eberhardt (1996). The atoms in the surface have more atomic-like wave functions, as a result of the reduced bonding to the other atoms of the material, and therefore their moments are closer to those given by Hund's rules. The Curie temperature of the surface is however lower than the bulk value.

The HFF of Co multilayers has been calculated by Guo and Ebert (1996). They find that B_c is proportional to the spin magnetic moment, eq. (2.3), and B_{orb} to the orbital moment, eq. (2.4). The magnetic dipole moment ($B_{ns} - B_{orb}$), which is small in bulk Co, can become important in multilayers. Guo and Ebert found that this contribution to the HFF is also proportional to the moment

$$B_d = -3.1\,\mu_d$$

where B_d is in T and μ_d in μ_B. There is however no apparent correlation between B_{hf} and the total Co moment in multilayers.

The difference between B_{hf} of the surface and the bulk of Co is calculated to be smaller than for Fe because B_s changes by some 10(20) T for Co(Fe). B_{hf} is calculated to be very anisotropic in some Co multilayers. The value of B_{hf} for a monolayer of Co on Pd for example is predicted to change from −8.45 T to −14.3 T as the magnetization moves from normal to the (1 1 1) plane to in the plane. As would be expected, the origin of this is large change is the anisotropy of the orbital and dipolar moments. The spin moment, and therefore the s electron contribution to the HFF, is isotropic.

The HFF for Co multilayers are calculated for perfectly plane interfaces between the layers and it is difficult to make allowances for the imperfections of a real surface. The calculated value for two atomic layers of Co and six layers of Cu for example is −15 T. In a Co/Cu (1 1 1) multilayer with 7 atomic layers of Co per multilayer repeat unit the calculated HFF at the interface is −18 T. This is in reasonable agreement with the value of −16 T predicted from dilute alloy experiments for Co atoms with 3 Cu NN, table 2.3.

3. Conventional nuclear magnetic resonance

3.1. Introduction

The object of NMR is to manipulate the equilibrium nuclear magnetization of the material, which in paramagnetic materials is many orders of magnitude smaller than the magnetization due to the electrons, by radio frequency (rf) fields and then to use the information

gained from the response of the system to understand the properties of the material. This information may be of static properties, e.g., the electron density and effective magnetic field sensed by the nucleus or of the spectrum of fluctuating magnetic fields in the material. A semi-classical treatment of NMR will prove sufficient for our purpose, since only the most straightforward techniques have been applied to magnetic thin films, but a full understanding of nuclear spin dynamics requires the density matrix of quantum mechanics. A good introduction to NMR is given by Slichter (1989). A review of some modern NMR techniques is given in Bagguley (1992). A powerful modern theoretical technique, the analytical tensor formalism, has recently been shown to be applicable to the NMR of normal and ferromagnetic materials (Shakhmuratova 1995). The significant differences between the NMR of ferromagnets and normal solid state NMR are brought out in section 4.

3.2. Motion of an isolated magnetic moment

In the semi-classical description of NMR, the nucleus is treated as a magnetic moment μ_n which precesses about a magnetic field B_0 that is conventionally taken to be in the z direction. Quantum mechanics shows that μ_n is related to the angular momentum of the nucleus I by the equation

$$\boldsymbol{\mu}_n = \gamma_n \boldsymbol{I}, \tag{3.1}$$

where the gyromagnetic ratio, γ_n, varies widely for different nuclei, table 3.1.

The torque on the magnetic moment in a uniform field B_0 is given by the rate of change of angular momentum

$$\frac{d\boldsymbol{I}}{dt} = \boldsymbol{\mu}_n \times \boldsymbol{B}_0,$$

$$\therefore \frac{d\boldsymbol{\mu}_n}{dt} = \boldsymbol{\mu}_n \times \gamma_n \boldsymbol{B}_0, \tag{3.2}$$

therefore, considering one end of μ_n to be fixed in space, the vector $\boldsymbol{\mu}_n$ generates a cone with axis along B_0.

The most convenient mathematical treatment of eq. (3.2) is to transform from the static laboratory frame (x, y, z) to a rotating reference frame (x', y', z') where z' is coincident with z. The field seen by the moment in the frame rotating with angular frequency ω' is,

$$\boldsymbol{B}_{rot} = \left(B_0 - \frac{\omega'}{\gamma_n}\right)\hat{z}'. \tag{3.3}$$

When

$$\omega' = \omega_0 = \gamma_n B_0,$$

the moment sees no effective field and is fixed along one direction in the rotating frame. Transforming to the laboratory frame the angular frequency of the precession of the moment about $\boldsymbol{B}_0$ is, therefore,

$$\boldsymbol{\omega}_0 = -\gamma_n \boldsymbol{B}_0,$$

TABLE 3.1

Nuclear spin, gyromagnetic ratio and natural abundance for selected nuclei. The relative strength of the NMR signal for given conditions may be estimated using eq. (3.20), but will also depend on the transverse relaxation time (T_2) and linewidth.

Nucleus	$2I$	$\gamma_n/2\pi$ (MHz/T)	Abundance %
^{1}H	1	42.57	99.98
^{51}V	7	11.19	100
^{55}Mn	5	10.55	100
^{59}Co	7	10.1 [1], 10.054 [2]	100
^{63}Cu, ^{65}Cu	3	11.29, 12.09	69.31
^{89}Y	1	2.095	100
^{159}Tb	3	10.1	15.14
^{165}Ho	7	8.77	100

[1] Old value, still often used.

[2] The best value for Co in a nonmagnetic host, Walstedt et al. (1967). See also section 5.2.1 for ferromagnetic host.

and the frequency for resonance is

$$\nu_0 = \left|\frac{\omega_0}{2\pi}\right| = \left|\frac{\gamma_n B_0}{2\pi}\right|. \tag{3.4}$$

Equation (3.4) contains the essence of NMR, the frequency for resonance is proportional to the field at the nucleus. However, it will be seen that in practice the effective field at the nucleus is not exactly equal to the external field B_0, although the difference in weakly magnetic materials is usually less than one percent.

3.3. Nuclear magnetism at thermal equilibrium

Nuclear magnetic moments are some thousand times smaller than the magnetic moment of the electron, they are of the order of the nuclear magneton

$$\mu_N = \frac{e\hbar}{2m_p} \simeq 5.05 \times 10^{-27}\,\mathrm{J\,T^{-1}},$$

where m_p is the mass of the proton. The quantization of angular momentum restricts I in eq. (3.1) to integer and half integer values. The energy of the nucleus in the field B_0 is given by

$$\varepsilon = -\gamma_n \hbar B_0 m$$

where m goes in integer steps from $-I$ to I.

The high temperature limit can always be taken in conventional NMR so, from elementary statistical mechanics, the nuclear magnetization is given by

$$M = \frac{n\gamma_n^2\hbar^2 I(I+1)}{3kT} B_0, \tag{3.5}$$

and the static susceptibility is defined as

$$\chi_0 = \frac{M}{H} = \frac{\mu_0 M}{B_0}. \tag{3.6}$$

The nuclear magnetization is so small, at 300 K in a field of 10 T the difference in population of the two levels for protons is only ~3 ppm, that it can usually only be detected against the background electronic magnetization by using NMR. Notice that M is along the external field B_0. In the x–y plane the random phases of the precessing nuclei average to zero. Nuclear magnetic resonance may be viewed as a technique for establishing and detecting a coherently precessing nuclear magnetization in the x–y plane.

3.4. Longitudinal relaxation

The expression (3.5) gives the equilibrium nuclear magnetization in a field B_0. It is clear however that if the sample was suddenly placed in the field B_0 the magnetization could not be established instantly, in fact it is commonly found to come to equilibrium as

$$M(t) = M(\infty)\left(1 - e^{-t/T_1}\right). \tag{3.7}$$

The longitudinal, or spin lattice, relaxation time, T_1, can vary from μs to hours, depending upon the material and the temperature, and has a strong influence on the design of a NMR experiment. Two other, transverse, relaxation times will be considered in section 3.6.

3.5. Linear and circular polarization of rf fields

The motion of a magnetic moment in a steady field B_0 was seen in section 3.2 to be a precession on the surface of a cone with axis parallel to B_0. The rf field produced by an alternating current in a solenoid is however linearly polarized along the axis of the solenoid. The linearly polarized field can be represented as two counter rotating fields of the same angular frequency but half the amplitude

$$2B_1 \cos(\omega_{RF} t) = B_1\left[e^{i\omega_{RF} t} + e^{-i\omega_{RF} t}\right]. \tag{3.8}$$

In NMR the rf field is set at right angles to the static field, i.e., in the x–y plane. On transforming to the rotating reference frame described in section 3.2 we see that, for

$$\omega_0 = \omega_{RF} = \omega',$$

one sense of rotation of the rf field is fixed in the x'–y' plane, conventionally along x', and the other rotates at $2\omega_0$. Only one sense of rotation can therefore interact strongly with the nuclear moments and the effective field in the rotating frame

$$\boldsymbol{B}_{\text{rot}} = \left[\left(B_0 - \frac{\omega'}{\gamma_n}\right)\hat{z}' + B_1\hat{x}'\right], \tag{3.9}$$

is simply $B_1\hat{x}'$ at exact resonance.

We shall see in the next section that in pulsed NMR the resonance at ω_0 may be excited when ω_{RF} is close to, but not necessarily equal to, ω_0. In this case the rotating reference frame is usually considered to rotate at ω_{RF}, leading to a small component of the field $(B_0 - \omega_{RF}/\gamma_n)$ along $\hat{z}'$.

3.6. *Free induction decay*

The application of the rf field given by eq. (3.8), with $\omega_{RF} = \omega_0$, to a magnetic system in thermal equilibrium in a static field B_0 in the z direction, will cause the moments to precess about the effective field in the rotating frame, which at exact resonance was seen in eq. (3.9) to be simply B_1 along $\boldsymbol{x}'$. After a time t_w the spins will have rotated through an angle

$$\theta = \gamma_n B_1 t_w. \tag{3.10}$$

If the pulse is turned off when

$$\gamma_n B_1 t_w = \frac{\pi}{2}, \tag{3.11}$$

a "$\pi/2$ pulse", the moments will lie along y' in the rotating reference frame, fig. 3.1. In the laboratory frame there is now a nuclear moment M in the x–y plane precessing at ω_0. The

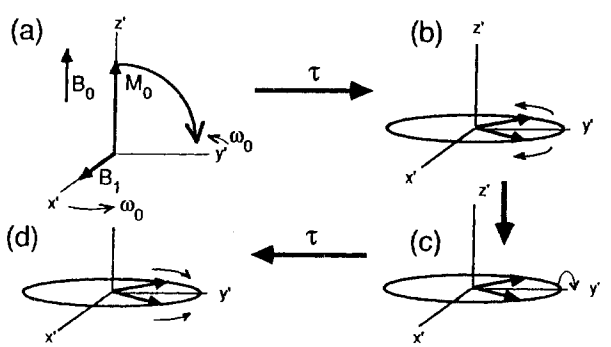


Fig. 3.1. (a) A $\pi/2$ pulse along x' at $t = 0$ takes M_Z to y' in the rotating frame. (b) Free induction decay. (c) A π pulse after time t. (d) An inhomogeneously broadened line produces a spin echo after a time $2t$.

changing magnetic flux produced by the rotating M will induce a voltage proportional to $\omega_0 M$ in a pick up coil.

In liquids a finite magnetization may exist for a time of order T_1 in the x–y plane, which may be seconds, but in solids this free induction decay (FID) is typically lost in the receiver noise after less than 100 μs and may be unobservable if the decay is so fast that the receiver has not recovered from the effects of the rf pulse. The simplest form of the transverse relaxation is

$$A(t) = A(0)\mathrm{e}^{-t/T_2}, \tag{3.12}$$

where T_2, the transverse relaxation time, is a measure of how fast the spins de-phase.

In the NMR literature the symbol T_2 is reserved for the irreversible decay of the nuclear magnetization in the transverse plane. When, as in ferromagnetic materials, the FID decays largely because of a static distribution of effective fields the transverse relaxation is written as T_2^* and, for $T_2^* < T_2 < T_1$, the nuclear moments are still in the x–y plane after the FID has decayed as

$$A(t) = A(0)\mathrm{e}^{-t/T_2^*}, \tag{3.13}$$

although their vector sum is zero.

3.7. Spin echoes

One of the most important discoveries in NMR was made by Hahn when he noticed that the macroscopic transverse nuclear magnetization could be recovered for nuclei in a distribution of static fields by applying a second rf pulse. Although an echo can be obtained for any second pulse that is not a multiple of 2π in eq. (3.10), the simplest picture is obtained after the sequence ($\pi/2$–t–π), fig. 3.1. At time $2t$ the nuclear moments that have not been subject to a T_2 relaxation process come back into phase and the magnitude, of the spin echo, is given by

$$A(2t) = A(0)\mathrm{e}^{-2t/T_2}. \tag{3.14}$$

The true transverse relaxation time can therefore be recovered by measuring $A(2t)$ as a function of time. The width of the echo is of order T_2^* since it is equivalent to two FID back to back.

The large rf pulse needed to produce a $\pi/2$ pulse with a sufficiently short t_w, section 3.10, saturates the receiver and the NMR signal cannot be observed for a "dead time" typically of order 3–10 μs. The great experimental advantage of the spin echo measurement over the FID occurs when $T_2^* \ll T_2$, as in strongly magnetic materials for example. It may then be impossible to observe the FID, because the signal is far below the receiver noise level after the dead time, but the spin echo can still be observed.

3.8. Electric field gradient (EFG)

A nucleus with spin 1/2 may be considered to be a spherical charge distribution and will therefore not be influenced by the EFG. Nuclei with spin greater than 1/2 may be treated as spheroidal charge distributions with quadrupole moment Q. The effect of the EFG on a nucleus of spin greater than 1/2 in a site of less than cubic symmetry is to tend to split the spectrum into $2I$ lines. In a single crystal, or in a ferromagnetic material in zero external magnetic field, the EFG leads to a splitting of the central magnetic transition which depends on the angle (θ) between the EFG and the magnetic field.

Only axial symmetry will be discussed in detail because of the algebraic complexity of the general case, see Carter et al. (1977). When the nuclear interaction with the magnetic field is much greater than that with the EFG the nuclear energy levels may be derived by first order perturbation theory,

$$E_m = \gamma_n B_0 m + \frac{h\nu_Q}{4}\left(3\cos^2\theta - 1\right)\left[m^2 - \frac{I(I+1)}{3}\right], \tag{3.15}$$

where

$$\nu_Q = \frac{3e^2qQ}{2hI(2I-1)}, \tag{3.16}$$

θ is the angle between B_0 and the axis of the EFG; NB eq. (3.16) is the most frequently used definition of ν_Q but e^2qQ/h is sometimes used.

The NMR spectra for a single crystal is therefore found to consist in principle of $2I$ lines at frequencies shifted from $\gamma_n B_0$ by

$$\nu_m^{(1)} = -\nu_Q\left(m - \frac{1}{2}\right)\frac{1}{2}\left(3\cos^2\theta - 1\right). \tag{3.17}$$

However, in solids with a broad distribution of magnetic fields at the nuclei, section 3.10, the splitting given by eq. (3.17) may be concealed within the envelope of the distribution. The presence of the EFG may then be detectable as a modulation of the spin echo decay, Abe et al. (1966). The full expression for the echo modulation given by Abe et al. is

$$m(2\tau) = \sum_{n=0}^{2I-1} c_n \cos(2n\nu_Q\tau + \delta_n), \tag{3.18}$$

where I is the nuclear spin, but in practice only the lower harmonics are observed. Fekete et al. (1978), for example, measured the NMR of a single crystal of hcp Co, section 5.2, and found that the echo decay of ^{59}Co, which has a spin of 7/2, could be described by eq. (3.18) with $n = 0, 1, 2$ and two exponential decay functions, fig. 3.2.

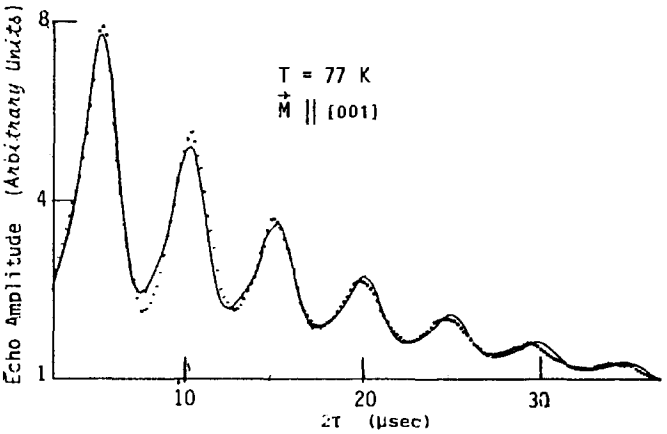


Fig. 3.2. Spin-echo decay modulations for hcp Co at 77 K. Points represent experimental values and the solid curve is calculated by the model, see Fekete et al. (1978).

3.9. Magnitude of NMR signals

Provided that the NMR linewidth is sufficiently narrow for all the nuclear spins to be rotated by a rf pulse of width t_w, the spin echo signal at time $2t$ from the centre of the first pulse will be given by an expression of the form

$$S(t) = \text{const}\,\omega_0 M f(t) \tag{3.19}$$

where the constant depends upon the circuit characteristics, ω_0 is the NMR frequency, M is the equilibrium nuclear magnetization, eq. (3.5), and $f(t)$ is a decay function, e.g., eq. (3.14).

From eq. (3.5)

$$S(t) = \text{const}\,\frac{\omega_0 n \gamma_n^2 I(I+1) B_0}{T} f(t). \tag{3.20}$$

Apart from the magnitude of $S(0)$, the important factor that determines if a NMR spin echo is detectable is the ratio of T_2 or T_2^* to the recovery time of the spectrometer. A NMR receiver in the 100 MHz frequency range is saturated, "dead", for typically, 3–10 μs after the rf pulse so the FID decay may be undetectable and the spin echo highly attenuated for materials with short relaxation times. It will be seen from eq. (3.20) that $S(0)$ is proportional to the reciprocal of the absolute temperature, and T_2 increases with decreasing temperature, so most NMR studies of the rather small number of nuclei in a thin film have been limited to the helium ($T \leqslant 4.2$ K) range.

3.10. The measurement of the distribution of effective fields at the nuclei

When the width, $\delta\omega$, of a NMR line is sufficiently small that the $\pi/2$ pulse condition, eq. (3.11), can be satisfied for $\delta\omega t_w \ll 1$, using the available rf power, then the line shape

is obtained by Fourier transforming the FID or the spin echo, see, e.g., Slichter (1989). The distribution of B_{eff} is frequently too wide for the inequality to be satisfied and then only a packet of spins near $\omega_{\text{RF}} \pm 1/t_{\text{w}}$ contributes to the FID or spin echo. A full analysis of the relationship between the spin echo and the distribution of B_{eff} is given by Walstedt (1992). The shape and position of the spin echo change as the width of the distribution of B_{eff} increases but it is still possible to reconstruct the NMR spectrum if the spectrometer is phase coherent, e.g., Lord and Riedi (1995).

The method employed in conventional NMR is to plot the rf phase insensitive quantity S as a function of the external field B_0, where S is defined by the equation

$$S = \left(S_{\varphi}^2 + S_{(\varphi+\pi/2)}^2\right)^{1/2}. \tag{3.21}$$

Here S_{φ} is the integral of the echo at the, unknown, phase φ. Alternatively, S may be plotted as a function of ω_{RF} for a given external field B_0. This is the most common case for ferromagnetic materials, section 4, where B_0 is often chosen to be zero. The ^{59}Co NMR of a Co/Cu superlattice shown in fig. 1.1 was measured in this manner. Note that when T_2 varies across the spectrum, and is less than or comparable to the dead time of the spectrometer, it is necessary to extrapolate the spin echo signals to zero pulse spacing using eq. (3.14) or some more complicated function if the echo decay is non-exponential.

In practice the magnitude of NMR signals ranges from mV for ^{1}H in water at room temperature to fractions of μV for materials with wide NMR lines or nuclei of low isotopic abundance with small γ_{n}. In the latter case extensive signal averaging is required to extract the signal from thermal noise and any spurious background signals in the receiver following the strong rf pulse.

3.11. Knight shift and nuclear relaxation

The magnetic field at the nucleus is never equal to the applied field B_0 because of the effect of the electronic magnetization set up by B_0. In simple metals such as Cu the field at the nucleus is given by an equation of the form

$$B_{\text{eff}} = B_0(1 + K), \tag{3.22}$$

where K, the Knight shift, is independent of temperature and $\sim 10^{-3}$. The origin of K is the Fermi contact interaction between the conduction electrons and the nuclear spin, section 2.2. In transition metals the 3d electrons are also important and K is a function of temperature, see Carter et al. (1977).

The relaxation times T_1 and T_2, provide information on the fluctuations of the magnetic fields in the material. In the rotating reference frame, fluctuations of the transverse fields along x' and y' will contribute to T_1, while fluctuations along y' or z' contribute to T_2. Therefore in the laboratory frame it is fluctuations at ω_0 that are important for T_1 but fluctuations at both ω_0 and zero frequency contribute to T_2.

In simple metals the contact interaction is the most important mechanism for T_1, leading, for free conduction electrons, to the relationship with the Knight shift

$$K^2 T_1 T = \frac{\mu_{\text{B}}^2}{\pi \hbar \gamma_{\text{n}}^2 k_{\text{B}}} = \zeta_0, \tag{3.23}$$

first derived by Korringa. The experimental value of K^2T_1T/ζ_0 is typically about 2 for metals such as Cu or Al, due to the effect of electron-electron interactions, see Carter et al. (1977).

4. NMR of ferromagnetic materials

Reviews of the NMR of ferromagnetic materials have been given by McCausland and Mackenzie (1979), Dormann (1991) and Figiel (1991). The distribution of B_{eff} of ferromagnetic materials is usually so wide that the NMR spectrum has to be constructed using the point by point integration of the spin echo as a function of frequency or external field described in section 3.10. While this is not unusual in the NMR of strongly paramagnetic materials there are a number of unique features to the NMR of ferromagnets.

NMR in zero external field

The existence of the HFF described in section 2 makes it possible to display the distribution of B_{hf} by sweeping the frequency of the spectrometer, rather than sweeping the external field as in conventional NMR.

Frequency range

Conventional NMR is typically carried out in a field of some 10 T, provided by a superconducting magnet. The NMR frequency for most isotopes is therefore below 150 MHz, table 3.1. The HFF of ferromagnets are often far larger than 10 T, e.g., that of ^{59}Co in fcc Co is -21.7 T and of ^{165}Ho in Ho is 737 T, corresponding to frequencies of $\sim$200 MHz and 6467 MHz, respectively. The frequencies for selected isotopes are given in table 2.3. Lord and Riedi (1995) describe a spin echo spectrometer designed for swept frequency operation up to 1000 MHz and McCausland and Mackenzie (1979) review spectrometers for the microwave region.

Enhancement effect

The first observation of the NMR of a ferromagnet, Co, showed that the signal was as strong as in electron spin resonance (Portis and Gossard 1960). The anomalously strong signal arises because the radio frequency field drives the ordered electronic moments of the ferromagnet as well as the nuclear moments and NMR is observed as a modulation of the motion of the electronic magnetization. In a spherical particle consisting of a single domain the magnetization and HFF will lie along the easy (z) direction, fig. 4.1. A linear rf field along x of amplitude $2B_1$ will tip the magnetization through a small angle $2B_1/B_A$ where B_A is the anisotropy field (frequently also denoted by H_k in the literature). Since B_{hf} is tied to the direction of the magnetization, a linear field of magnitude $2B_1(B_{\text{eff}}+B_A)/B_A$ in the x direction is induced at the nucleus. This field is normal to B_{hf} and will induce nucleus transitions so the field is said to be enhanced by the factor

$$\eta_d \sim B_{\text{eff}}/B_A \tag{4.1}$$

which for fcc Co is $\sim$100.

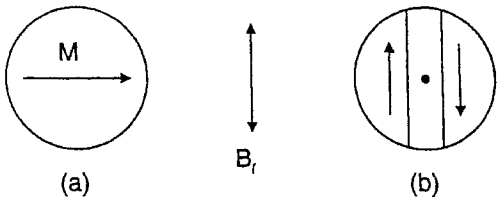


Fig. 4.1. Optimum geometry for (a) domain and (b) domain wall enhanced NMR.

If an external magnetic field B_0 is applied along the easy direction

$$\eta_d \sim B_{eff}/(B_0 + B_A). \tag{4.2}$$

Unless the sample is in the form of very small particles (~100 Å) it will normally divide into domains as considered below. The domain structure may be removed by a sufficiently large external field but from eq. (4.2) this reduces the enhancement considerably.

The ^{59}Co signals from fcc Co observed by Portis and Gossard were far stronger than would be expected from an enhancement of ~100 and it was shown that in a multidomain particle the nuclei in the domain walls could experience a greater enhancement of the rf field than those in domains. When a linear rf field is applied in the z direction to a sample containing a 180° wall in the z–y plane the wall may move in the x direction, leading to an enhancement that varies throughout the wall (McCausland and Mackenzie 1979)

$$\eta_w \sim \frac{VB_{eff}}{2\mu_0 MA}\chi_e\left(\frac{d\Psi}{dx}\right), \tag{4.3}$$

where $\Psi(x)$ is the angle of the local magnetization within the wall relative to the domain magnetization for a particle of volume V, average wall susceptibility χ_e and wall area A. In fcc Co the maximum value of η_w, at the centre of the wall, is typically ~10^4.

It was emphasized above that the wall only "may" move because wall motion is restricted by strain and defects, particularly in materials of high anisotropy, and in addition the wall may be thought of as a damped simple harmonic oscillator with its own natural resonant frequency (ν_w) so the motion will depend upon the ratio of ν_w to the NMR frequency. The most obvious consequence of eq. (4.3) is that in domain wall enhanced NMR there can be no unique rf field at the nuclei. The value of η_w will be a maximum at the wall centre and decreases as the wall blends into the domain. It appears that in many multidomain materials the signals come from nuclei at the wall centre and wall edges rather than from the bulk of the domain, see, e.g., Bailey et al. (1973).

A more serious problem for domain wall enhanced NMR arises when the magnetization is strongly anisotropic, since the anisotropy of the HFF may then lead to a different NMR frequency and a different linewidth for wall centre and wall edge or domain signals. As will be seen in fig. 4.2, although there is only one type of lattice site in hcp Co, the NMR spectrum of a single crystal is a function of the rf power for pulses of fixed length because the domain wall centre and edge signals have different frequencies and enhancements.

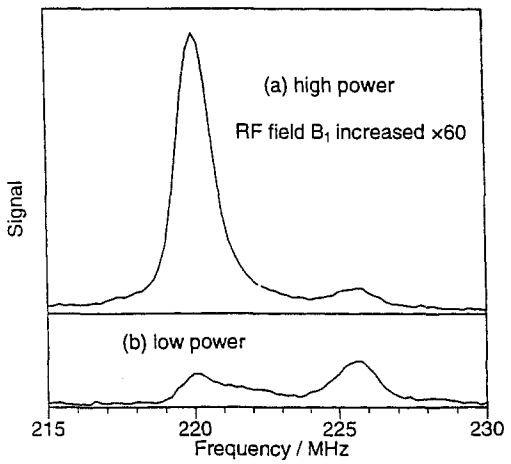


Fig. 4.2. Power dependence of ^{59}Co NMR of a multi-domain hcp Co single crystal.

Local enhancement effect and magnetic stiffness

In a good Co/Cu multilayer the Co NMR signal from the interface is well separated from that of the interior of the Co layer, e.g., fig. 1.2. It is therefore possible to measure a local enhancement factor through the Co layer. Provided domain wall motion is not important the enhancement factor may be related to the local anisotropy field and hence to the coercive force by eq. (4.2). Thomson et al. (1994a, 1995) ensured that their samples were in the single domain state by applying fields of up to 0.4 T in the plane of the film. They found that the value of the anisotropy field at the interface (340–360 Oe) was close to that of the coercive force (260 Oe) of the films while the interior of the films had an anisotropy field some 2–4 times larger, see section 7.4. Panissod et al. (1997) measured the relative stiffness of different regions of Co multilayers by studying the full NMR spectrum as a function of the magnitude of the rf field.

NMR relaxation by domain wall fluctuations

The values of T_1 and T_2 found in zero external field NMR are shorter than in a single domain material and the relaxation is usually highly non-exponential, fig. 4.3, so the quoted values of T_1 and T_2 are a matter of definition.

Effect of an external magnetic field

The NMR signal from nuclei in a domain wall does not change frequency when an external field is applied in the easy axis direction but decreases in magnitude as the field is increased. Once the domain structure has been removed the value of $\mathrm{d}\nu/\mathrm{d}B_0$ approaches the value of $\gamma/2\pi$ for the nucleus.

Demagnetizing field

The nuclei in a saturated ellipsoid with magnetization M experience a demagnetizing field $-\mu_0 NM$, where N is the demagnetizing factor. Nuclei in a domain wall are shielded

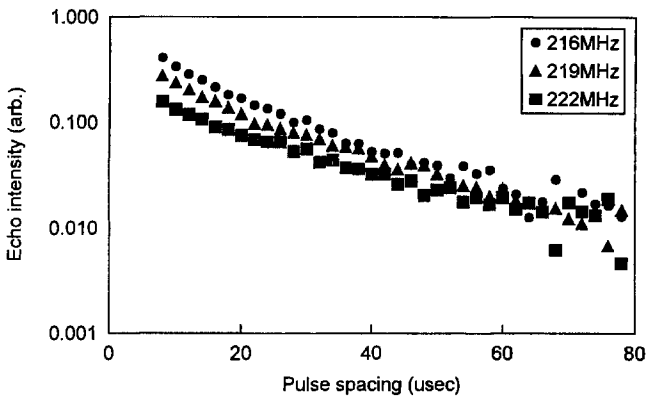


Fig. 4.3. Variation of the ^{59}Co spin-echo decay time as a function of frequency showing that the relaxation time is both not constant over the frequency range investigated and not a simple exponential function. After Thomson et al. (1994a, 1994b).

from this field and therefore have a different NMR frequency from the value extrapolated from high field measurements, see section 5.3.1.

5. Magnetism and NMR of cobalt

5.1. Introduction

The equilibrium form of cobalt at low temperature is hexagonal close packed but the face centred cubic phase is stable in fine particles. Cobalt sponge for example has a typical dimension of 25 μm and is largely fcc. It is possible to pass from the fcc to hcp structures by introducing defect planes and this material has an NMR frequency between that of fcc and hcp cobalt. Particles of cobalt sponge contain domain walls, but below about 200 Å cobalt particles are single domain and have a different NMR frequency, section 5.3.

The magnetic and NMR properties of fcc and hcp cobalt are summarized in tables 5.1 and 5.2. Due to the high Curie point of cobalt the magnetization and HFF are essentially independent of temperature in the helium temperature range. They are both however a function of pressure or strain, an effect which is particularly important in thin films and multilayers. The pressure coefficients of magnetization and HFF derived from measurements made under hydrostatic pressure are shown in tables 5.1 and 5.2 but it should be remembered that the strain between two multilayers is highly directional.

The NMR properties of hcp and fcc cobalt at low temperature in both the multidomain and single domain state are discussed in sections 5.2 and 5.3. The bcc form of cobalt is only found in thin films and is discussed in section 6.4.

5.2. NMR of hcp Co

5.2.1. Uniform magnetization

The most detailed NMR study of a single crystal of hcp Co was carried out by Fekete et al. (1976, 1978). All the measurements were carried out in fields of more than 2.5 T to

TABLE 5.1

Crystallographic and magnetic properties of cobalt, see Wijn (1986) and Riedi et al. (1987).

	T (K)	hcp	fcc
Lattice constant (Å)	293	$a = 2.5070$ $c = 4.0698$	$a = 3.5445$
	0	$a = 2.501$ $c = 4.058$	
Transition hcp → fcc	722		
$\mu_0 M$ (T)	0	[0 0 0 1] 1.6376 [1 0 1 0] 1.6295	1.661
Magnetic moment/atom (μ_B)	0	[0 0 0 1] 1.728 [1 0 1 0] 1.719	1.751
$(\partial \ln \mu/\partial p)_T$ (Mbar)$^{-1}$	room temperature	−0.22	
$(\partial \ln V/\partial p)_T$ (Mbar)$^{-1}$	room temperature	−0.53	
Spectroscopic factor (g)		2.19	2.06–2.10
Magnetomechanical factor (g')		1.838	

TABLE 5.2

Low temperature NMR properties of multidomain cobalt in zero external field, see Wijn (1986) and Riedi et al. (1987). The gyromagnetic ratio, γ_n, is taken to be such that $\gamma_n/2\pi = 10.054$ MHz/T (Walstedt et al. 1967), but in many papers the original value of 10.1 MHz/T has been used. See also the comment after eq. (5.1).

	fcc cobalt	hcp cobalt
Frequency at 0 K (MHz)	217.4	228 (wall centre) 220 (wall edge)
Hyperfine field at 0 K (T)	−21.62	−22.7 (wall centre) −21.9 (wall edge)
$(\mathrm{d} \ln \nu/\mathrm{d}p)$ (Mbar)$^{-1}$	0.488, 0.601[a]	0.615[a]
Approximate transverse relaxation time T_2 (μs)	50	40
Approximate transverse relaxation time T_1 (μs)	200–20 000	

[a]Room temperature

ensure that the material was in a single domain state. A 5 mm sphere was polished until the fractional deviation from a perfectly spherical shape was estimated to be ±0.002 with a surface roughness of ~1 μm. The measured NMR linewidth of 0.1 T was consistent with these estimates.

The Knight shift of hcp Co was measured by Fekete et al. (1976) using this polished single crystal sphere. It was found to be necessary to apply fields of more than 2.5 T, some four times the demagnetizing field, to remove all trace of the effect of domain structure.

The NMR frequency was then a linear function of the field up to the maximum field of 7 T with

$$\gamma_{\text{eff}}/2\pi = 10.249 \pm 0.007 \text{ MHz/T}. \tag{5.1}$$

The difference between this value and the best estimate of $\gamma/2\pi$ for ^{59}Co in dilute insulating compounds, 10.054 MHz/T, table 5.2, was related to the ferromagnetic band structure of Co. Equation (5.1) should be used for the conversion between HFF and NMR frequency of ferromagnetic cobalt but this result is not well known and either of the values in table 5.2 has commonly been used. Some of the apparent discrepancies between different values of the HFF in the literature undoubtedly arise from the choice of γ but it is not always clear which value has been employed.

The effective field at 4.2 K, extrapolated to zero external field, was found to be given by

$$B_{\text{hf}} = -22.60 + 0.573 \frac{3\cos^2\theta - 1}{2}, \tag{5.2}$$

where B_{hf} is in Tesla, θ is the angle between the magnetization and the c axis and the value of $\mu_{\text{eff}}/2\pi$ given in eq. (5.1) was used to convert from frequency to field. The equivalent result in frequency units is

$$\nu = 231.63 - 5.87 \frac{3\cos^2\theta - 1}{2}, \tag{5.3}$$

where ν (MHz) is always taken to be positive. It should be noted that eqs (5.2) and (5.3) are the extrapolation to zero field from the single domain state of a sphere, they are not correct for a multidomain particle, see eq. (5.5). The anisotropy of B_{hf} arises from the contributions of the orbital and spin dipolar fields as described in section 2.

The EFG at the Co nucleus is too small to produce satellite lines of the central NMR line but its effect is observable as a modulation of the spin echo decay, section 3.8. The echo amplitude was found, fig. 3.2, to be in good agreement with the theory, eq. (3.18). At 4.2 K the quadrupole splitting, defined in eq. (3.16), was given by

$$\nu_{\text{Q}} = 0.0244 + 0.1691 \frac{3\cos^2\theta - 1}{2}, \tag{5.4}$$

where ν_{Q} is in MHz and θ is the angle between the magnetization and the c axis. A value of 5.5 ± 0.2 μs had earlier been found for the period of the echo oscillation in zero external field, Riedi and Scurlock (1967a, 1967b), corresponding to a frequency of 0.182 ± 0.008 MHz in eq. (5.4), showing that these signals came from domain wall edges, see sections 4.2 and 5.2.2.

5.2.2. Multidomain hcp Co

The NMR of hcp Co in zero external field has been observed in single crystals and thin polycrystalline plates. At the centre of a domain wall the Co moments are normal to the easy c axis and rotate towards the c direction at the wall edge. The majority of the Co

moments in the domains are parallel to the c axis. The anisotropy of the HFF, eq. (5.2), leads to a broad distribution of HFF in multidomain hcp Co, fig. 4.2.

The demagnetizing field in a multidomain particle is close to zero while in a saturated Co sphere it is equal to $-\mu_0 M/3 = -0.546$ T. Since the HFF is negative, eq. (5.2), the NMR frequency in a multidomain sample is *lower* than in a single domain and eq. (5.3) becomes

$$\nu = 226.0 - 5.87 \frac{3\cos^2\theta - 1}{2}. \tag{5.5}$$

The largest enhancement of the rf field is at the centre of the wall, section 4, so the most prominent feature in the distribution at low power is at the high frequency end of the spectrum, in agreement with eq. (5.5) with θ equal to 90°. As the rf power is increased, the feature near 220 MHz grows in intensity, fig. 4.2. This value is close to that given by eq. (5.5) with θ equal to 0, but Bailey et al. (1973) showed that the line is due to nuclei at the wall edge, rather than from the domain. The distinction can be made because the most effective direction for the rf field is normal to the static effective field. As explained in section 4, wall enhanced NMR is therefore favored when the rf field is parallel to the easy c axis while signals from the domain require the field normal to c.

The EFG of hexagonal Co has been measured in zero external field by both spin echo (Riedi and Scurlock 1967a, 1967b) and continuous wave methods (Kawakami et al. 1972). In section 5.2.1 it was seen that the best value reported for ν_Q with the magnetization parallel to the c axis, measured on a single crystal sphere, was 193.5 ± 0.7 kHz. The values found in the multidomain state were 182 ± 8 kHz and 207 ± 5 kHz, by spin echo and continuous wave NMR, respectively. It is therefore possible to obtain a reliable measure of the EFG in bulk hexagonal cobalt without applying an external magnetic field. However, there have not been any reports of the measurement of the EFG of a cobalt film or multilayer, possibly because a unique EFG does not exist due to the effect of lattice strains.

5.3. NMR of fcc Co

5.3.1. Single domain particles

The NMR of single domain fcc Co particles was first studied by Gossard et al. (1965) and Yasuoka and Lewis (1969). The particles were formed on the surface of γ alumina. Their average size, and the width of the distribution of sizes, depended upon the growth conditions. Estimates of the particle size from X-ray diffraction line widths were about a factor of two smaller than from electron microscopy. The latter were considered to be more reliable and will be used here. Particles of diameter greater than about 200 Å were found to be multidomain and those of diameter less than 50 Å were super-paramagnetic at room temperature.

The most detailed measurements were made on a sample of average particle size 140 Å (Yasuoka and Lewis 1969). The NMR technique used did not provide an accurate value for the linewidth, ~2 MHz, but the relative position of the line centre as a function of temperature could be estimated more accurately. The NMR frequency in the low temperature limit was 222.2 MHz, i.e., some 4.8 MHz above that of multidomain fcc Co. This is rather

smaller than the frequency shift of 5.5 MHz calculated in the previous section for an isolated spherical single domain particle and was attributed to the effect of particle–particle interactions.

Thomson et al. (1997) studied Co nanoclusters embedded in a 2450 Å thick SiO_2 matrix. A broad NMR spectrum was observed with peaks near 222 and 243 MHz. The diameter of the particles was estimated from transmission electron microscopy measurements to be about 30 Å. The 222 MHz line confirmed that the particles were single domain, as expected from the earlier work described above, but the origin of the 243 MHz line was not clear. It was tentatively attributed to surface atoms with an enhanced magnetic moment but, as was discussed in section 2.6, the HFF of surface atoms does not necessarily scale with the magnetic moment.

5.3.2. Multi-domain fcc Co

The NMR of fcc Co has mostly been studied in chemically reduced Co sponge. The particle size is ~25 μm. A small amount of the hcp phase and intermediate fault structures is usually present. The spin echo decay is non-exponential, with the fastest relaxation at the centre of the line. The full linewidth at half-height (FWHM), after correcting for the variation in T_2, is ~0.7 MHz (0.7 T). The fcc NMR line is a simple shape, unlike the hcp Co spectrum shown in fig. 4.2, because the Co orbital moment is isotropic in the fcc phase.

5.4. NMR relaxation of Co

The intrinsic relaxation times for a ferromagnetic material cannot be measured in a sample containing mobile domain walls because the fluctuating fields associated with the wall vibrations provide the strongest relaxation mechanism. However, the application of an external field, greater than the demagnetizing field, to a powder containing particles of a variety of shapes will lead to a distribution of B_{eff} that may also change the relaxation times. The internal field in a single crystal sphere is uniform but the rf field is both attenuated and phase shifted in a metal due to the skin effect. For these reasons it may be expected that relaxation will be studied in films in the future although the weak signals due to the small number of atoms in a film will always present technical difficulties.

Estimates of T_1 and T_2 for Co are given in table 5.2. The values for multidomain material are not well defined, because the relaxation is non-exponential, fig. 4.3. Relaxation times can provide information on the magnetic structure of a thin film because when they are found to be appreciably longer than those shown in the table it indicates that there are unlikely to be mobile domain walls present.

6. Cobalt films

6.1. Introduction

The main interest in the NMR study of thin films has been in the properties of multilayers, with particular regard to the interfacial region. In this section we consider experiments where the emphasis was on the properties of a single layer of cobalt before turning to multilayers in section 7. Depending on the substrate and the deposition conditions it is possible to obtain cobalt films, up to some critical thickness, in all three crystal phases: fcc,

hcp and bcc. As was remarked in the Introductory Survey and section 5, one of the strengths of ^{59}Co NMR is the clear distinction between the fcc and hcp spectra that can be seen in bulk samples and therefore used to analyze the structure of thin films and multilayers. The position with regard to bcc cobalt is less clear because this phase is only obtained as a thin film which probably always contains some defects or contamination from adjacent layers. The greater part of this section is therefore devoted to a survey of the properties of bcc cobalt, the fcc and hcp phases of thin layers are discussed in more detail in section 7.

6.2. Face centred cubic cobalt films

The critical thickness above which the fcc phase of cobalt begins to transform to the stable low temperature hcp phase is a strong function of the material, crystal orientation and temperature of the substrate. A typical value for the critical thickness for cobalt on Cu (1 1 1) is about 60 Å (Thomson et al. 1995), fig. 6.1. It has been claimed that 1000 Å thick fcc cobalt films can be stabilized by epitaxial growth on Cu (1 1 0) (Harp et al. 1993), but unfortunately these films have not been studied by NMR. It was found that these thick fcc cobalt films transformed to the hcp phase after annealing to 470 K.

The extreme sensitivity of the balance between the growth of fcc and hcp cobalt was demonstrated by de Gronckel et al. (1994). Cobalt films of 1000 Å thickness were grown by

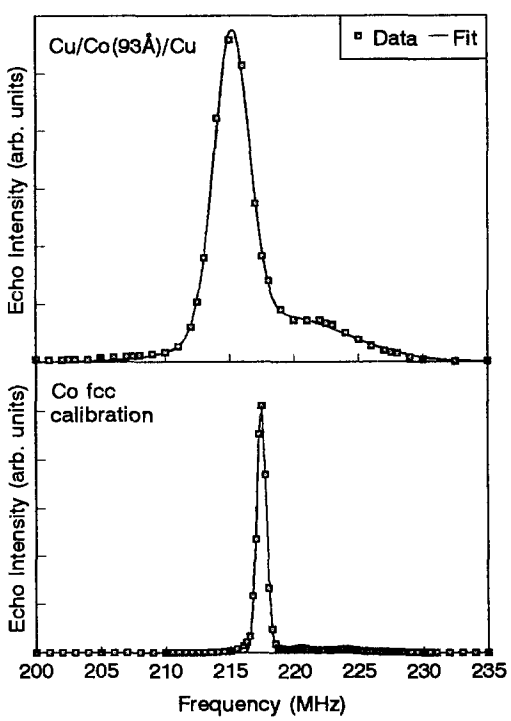


Fig. 6.1. ^{59}Co NMR spectrum for Cu(34Å)/Co(93Å) (1 1 1) trilayer film at 4.2 K in zero applied field. After Thomson et al. (1995).

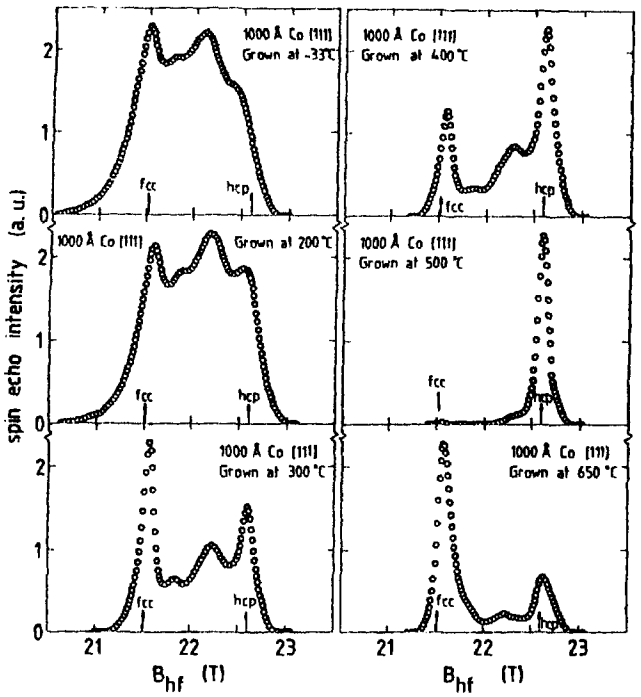


Fig. 6.2. NMR spectra of 1000-Å Co films grown on mica showing the variation in structure as a function of the growth temperature. The spectra were recorded at a frequency of 190 MHz, with the magnetic field applied parallel to the film plane and at a temperature of 1.4 K. After de Gronckel et al. (1994).

MBE on substrates of mica, oxidized silicon, and glass at temperatures between −33°C and 800°C. The films were found to be polycrystalline for substrate temperatures below 200°C. Above 200°C the X-ray diffraction measurements showed that the (1 1 1) fcc or (0 0 2) hcp orientation was dominant. The NMR spectra were analyzed for contributions from regions with either fcc, hcp or intermediate (stacking fault) structure, figs 6.2 and 6.3. The remarkable feature of these spectra is that the fcc and stacking fault structures are favored by deposition at low temperatures where hcp is the stable form for bulk material. As the mica substrate temperature increases above 200°C the number of stacking faults decreases but the pure hcp phase only forms when the substrate is near 500°C. The influence of the substrate on film growth was demonstrated by growing 1000 Å films at 500°C on mica and oxidized silicon at the same time. The film on mica was almost pure hcp, fig. 6.2, but that on oxidized silicon was a nearly equal mixture of fcc, hcp and stacking faults.

The ^{59}Co NMR spectrum of fcc cobalt in multidomain particles at 4.2 K consists of a single line with, typically, a peak value at 217.4 MHz and a full width at half maximum (FWHM) of 0.7 MHz. The outstanding feature of fcc Co films is that the FWHM is found to be about 10 MHz and the peak position is displaced due to lattice strain. While the greatly increased FWHM could be partly due to a distribution of strain within the cobalt layer, the fact that the linewidth is so similar in many samples suggests that it is due to the pseudo-

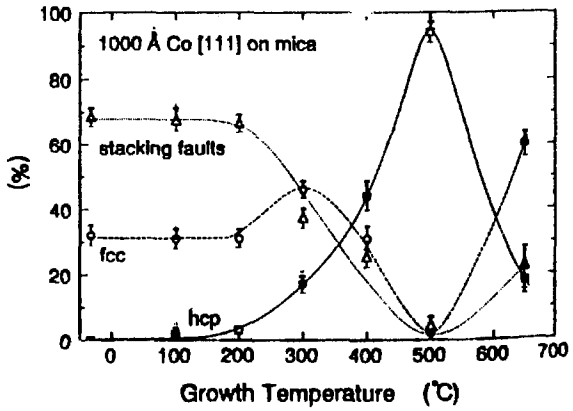


Fig. 6.3. The percentage of the fcc phase (circles), hcp phase (squares), and stacking faults (triangles) in 1000-Å-thick Co films grown on mica substrates as a function of the growth temperature. The results are derived from the NMR spectra in fig. 6.2. The lines are guides to the eye. After de Gronckel et al. (1994).

two dimensional structure of the films. One consequence of the increased FWHM is that it is difficult to resolve small ^{59}Co frequency shifts and line broadening due to impurity neighbors beyond the nearest neighbor shell.

A second difference between thin films and bulk material is that the oscillatory spin echo decay due to the small electric field gradient (EFG) at the cobalt nucleus in hcp cobalt has never been observed in thin films. This effect should in principle also be observable in the fcc phase of a thin film because the effect of lattice strain at an interface must break the cubic symmetry.

6.3. Hexagonal close packed cobalt films

The discussion of the growth of cobalt films in section 6.2 has emphasized how the growth conditions and substrate determine the structure of the film. Cobalt films on copper normally grow at first with the fcc structure but on a gold (1 1 1) substrate an hcp structure has been observed with the *c* axis normal to the film plane. Le Dang et al. (1986a) studied the NMR of an 80 Å thick film at 1.8 K in fields of up to 1.2 T applied along the *c* axis. In zero field the HFF distribution, fig. 6.4, has a broad maximum near 228 MHz. It was seen in section 5.2 that the HFF of hcp cobalt is anisotropic. The value of 220 MHz is associated with spins along the *c* axis and 228 MHz with spins normal to the *c* axis. It was concluded that, as expected, in zero external field the magnetization for an 80 Å film lies in the plane.

The NMR spectrum was then measured as a function of the magnetic field along the *c* axis and analyzed to find the angle that the magnetization made with the normal to the plane of the film. The necessary values of the anisotropy and demagnetizing fields of the film were found from ferromagnetic resonance (FMR) experiments (Chappert et al. 1986). A rather surprising feature of the FMR measurements on the 80 Å cobalt film was that the anisotropy field of the film at 10 K (0.386 T) was only some 55% of its value at room

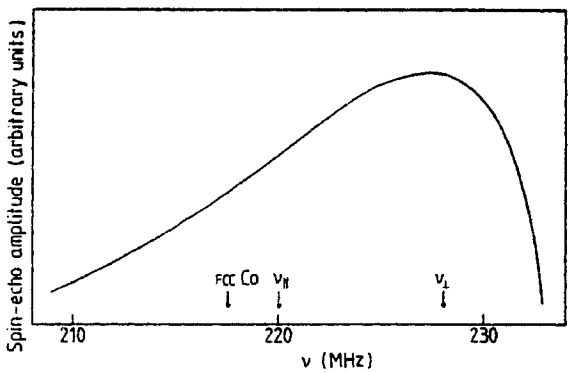


Fig. 6.4. ^{59}Co spin-echo spectrum at 1.8 K in zero external field for a Au/Co(80Å)/Au film with the magnetization in the plane. The arrows indicate the nuclear resonance frequencies of bulk hcp cobalt in domains ($\nu_{\parallel}$) and at the centre of 180° Bloch walls ($\nu_{\perp}$) and that of fcc cobalt. After Le Dang et al. (1986a).

temperature while that of bulk cobalt (1.41 T) is 135% of the room temperature value. The discrepancy was attributed to internal stresses due to the differential thermal expansion between cobalt and gold.

6.4. Body centred cubic cobalt

6.4.1. Theory

First principles LSPD calculations of the energy of Co at 0 K, as a function of the atomic spacing in a cubic lattice, show that a minimum energy exists for a ferromagnetic bcc phase, see, e.g., Prinz (1991) for a review of the early work. Bcc Co is, however, at best metastable. The absolute minimum of the energy for cubic Co occurs for the fcc phase. Liu and Singh (1993) have calculated that bulk bcc Co is unstable with respect to a tetragonal distortion into the fcc phase. The calculated energy of a constant volume of body centred tetragonal (bct) Co is shown in fig. 6.5. The fcc phase lies in a deep energy minimum and the bcc phase at a local maximum. Bulk bcc Co can therefore transform continuously to the fcc structure.

In practice bcc Co is stabilized by depositing Co onto a suitable substrate but then tends to transform to hcp, rather than fcc, Co. The path from bcc to hcp Co has not been worked out in detail, but Liu and Singh (1993) point out that one possibility is a compressive tetragonal strain along the bct [1 0 0] direction coupled with a shear of the (1 0 0) bct planes.

The layer by layer stability of bcc Co on a substrate has not been investigated theoretically. The thickest film reported, 357 Å Prinz (1985), appears to have been composed of nanocrystals separated by grain boundaries. Liu and Singh (1993) showed that any diffusion of As from the GaAs substrate into the Co would lower the magnetization appreciably ($-3.8\ \mu_B$/As atom) but could not increase the stability of the bcc phase. More recent experiments, discussed in the next section, suggest that perhaps only some five atomic layers (10 Å) can be grown with a free Co surface before the hcp phase begins to form.

Calculations of the magnetic moment per atom of Co suggest that both the spin and the orbital moment is largest in the bcc phase, see table 2.2. Earlier calculations are reviewed

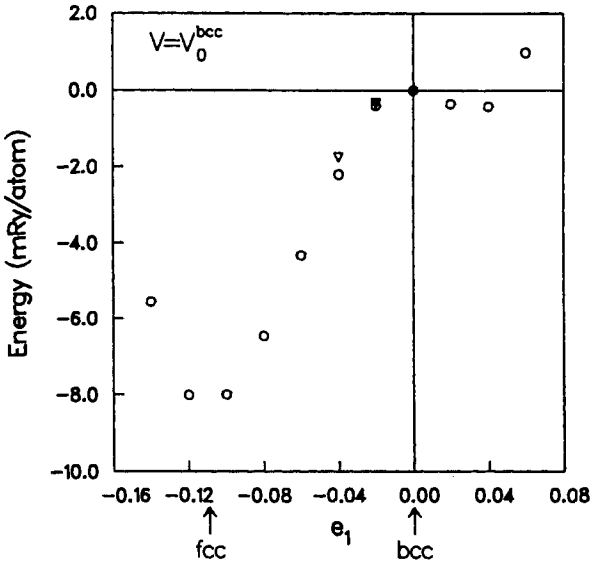


Fig. 6.5. Total energy vs. tetragonal strain for bcc Co. The volume is fixed at the calculated equilibrium value for bcc Co, and the energies are measured with respect to the total energy of bcc Co. The circles are calculated energies for pure Co, while the triangles are calculated energies for Co_7As supercells. After Liu and Singh (1993).

by Prinz (1991). The orbital moment given in table 2.2 is estimated to be perhaps 50% too small but the spin moment should be reliable to about 5%. It is not a trivial matter to measure the magnetization of a thin film, and neutron scattering experiments show that the moment can vary through the film (Bland et al. 1991a, 1991b), but some measurements on bcc Co give a value of 1.7 μ_B/atom in agreement with the calculations (Dekoster et al. 1993c).

The theory of the hyperfine field at the ^{59}Co nucleus was discussed in section 2. A recent calculation (Guo and Ebert 1996) led to values of $-22.28(-17.3)$ T for the HFF of fcc(bcc) Co. The magnitude of the field for fcc Co is greater than the experimental value of -21.6 T because the calculation under-estimates the (positive) contribution of the orbital moment. The first measurement of the HFF of bcc Co (Riedi et al. 1987), using a 357 Å thick film, gave a value of -16.6 T, which was attributed to the low magnetic moment of this thick film, but the more recent measurements described in section 6.4.3, seem to confirm that the value of the HFF of the best bcc Co is -19.7 T.

6.4.2. Growth and magnetization of bcc Co films

The presence of small oriented grains of bcc Co in sputtered Co/Cr was reported by Walmsley et al. (1983). A new interest in this phase began after Prinz (1985) demonstrated MBE growth of bcc Co on a GaAs substrate. (A review of the early work is given in Prinz 1991.) Prinz noted that while $Fe_{1-x}Co_x$ alloys are only stable in the bcc phase up to $x = 0.75$, the extrapolation to $x = 1$ predicted a lattice constant of 2.819 Å for bcc Co. This is only 0.2% less than that of the lattice constant of GaAs divided by two. A (1 1 0) GaAs

substrate was used to stabilize a 357 Å thick film of bcc Co that had a lattice constant of 2.827 Å and a magnetization of 1.53 μ_B/Co atom. The lattice constant of the grains of bcc Co produced by Walmsley et al. (1983) was 2.77 Å, showing the effect of stress transmitted by the matrix.

The 357 Å film grown by Prinz is the thickest reported for bcc Co. The bcc structure of this film was confirmed by conversion electron X-ray-absorption fine structure experiments (Idzerda et al. 1989), but the low intensity of the signal suggested that the material was nanocrystalline. The NMR experiments discussed below support this conclusion.

Bcc Co films up to 100 Å thick grown by MBE on (0 0 1) GaAs have been reported by Subramanian et al. (1994) and Bland et al. (1991a, 1991b). The latter group measured the magnetization profile of the film by polarized neutron reflection. The best fit to the measurements lead to a moment of 1.0 μ_B at the GaAs interface, 1.7 μ_B in the centre of the film and an average moment of 1.4 μ_B/Co atom. The low average moment, close to that of the 357 Å thick film discussed above, suggests that this film contained a large number of defects. Attempts to improve the quality of bcc Co grown on (0 0 1) GaAs were unsuccessful (Gu et al. 1995). They concluded that in this case the stable phase is hcp Co with the (1 2 1 0) plane parallel to the (0 0 1) plane of GaAs.

Kim et al. (1995) grew 15–20 atomic layers of strained bcc Co on a (0 1 0) TiAl substrate by MBE. The unit mesh in the plane of the film was found to be a rhombus with sides of 2.855 Å and angles between the sides of 89.068° and 90.932°. The 0.9% tensile strain in the plane was accompanied by a decrease of the interlayer spacing by 0.86%. This result is interesting because it demonstrates the possibility of studying the range of stability of bcc Co by growing films on a non-cubic metal substrate.

Prinz (1985) had been careful to find a substrate that nearly matched the anticipated lattice constant of bcc Co, 2.82 Å, but it is now known that bcc Co can be grown on films of bcc Fe; despite the fact that the lattice constant for bulk Fe is 2.86 Å. Li and Tonner (1989) grew bcc Fe films on a fcc Ag (0 0 1) substrate and then 3 atomic layers of bcc Co on top of the Fe. (When Co was deposited directly on to the Ag a complex structure, consistent with body centred tetragonal Co, was observed.)

Houdy et al. (1991) and Boher et al. (1992) described the growth of sputtered Fe/Co multilayers on Si (1 1 1) wafers. The X-ray diffraction pattern for $t < 20$ Å was consistent with bcc Co with lattice constant 2.83 Å. The magnetization measurements were consistent with a model involving an enhanced magnetization at the Co/Fe interface and a moment of 1.58 μ_B/Co atom in the interior of the Co layer.

The most extensive study of the MBE growth of Co on Fe films has been made by Dekoster et al. (1993a, 1993b, 1993c). A summary of their results is given in table 6.1. The optimum temperature of the MgO (0 0 1) substrate for the growth of bcc Co was found to be 175°C. Films of similar quality were also grown on a GaAs (1 1 0) substrate held at this temperature. The maximum thickness of bcc Co that could be grown on an Fe film was found to be 10 Å for a free Co surface, after which the hcp phase began to form. Surprisingly, however, up to 21 Å of bcc Co could be stabilized by growing at least 24 Å of bcc Fe between the Co layers. The average bcc Co moment, deduced from magnetization measurements was found to be 1.71 μ_B, considerably greater than that of the earlier films grown on GaAs.

6.4.3. NMR of bcc Co

A summary of the NMR experiments on bcc Co is given in table 6.1. The early NMR measurements, on films 100–357 Å thick on GaAs, found broad distributions of effective fields with a maximum near 170 MHz (Riedi et al. 1987; Bland et al. 1991a, 1991b). While this was a much lower frequency than that of fcc Co it was consistent with the lower magnetic moment of the bcc films. The long transverse relaxation time (T_2) of the 357 Å film, 180 μs compared to 25 μs for fcc Co films, showed that there were no mobile domain walls in the material. This could arise as a result of the film consisting of nanocrystallites separated by grain boundaries as suggested by the X-ray measurements of Idzerda et al. (1989).

The rf sputtered films of bcc Co on Fe, Houdy et al. (1991) and Boher et al. (1992) also showed broad distributions of HFF, fig. 6.6. A comparison of the NMR and X-ray data for different thicknesses of film lead to the conclusion that the bcc Co line occurred at a frequency of 198 MHz. The NMR spectrum for 8 Å layers of Co is due to interfacial effects but from 13 to 18 Å the line attributed to bcc Co is partially resolved. The very long T_2, 400 μs, quoted for these sputtered films suggests that there are no mobile domain walls present, just as in the 357 Å film on GaAs discussed above.

The low NMR frequency found for bcc Co on GaAs might be attributable to diffusion of As into the Co, but this cannot be the case for Fe/Co because an Fe atom in the nearest

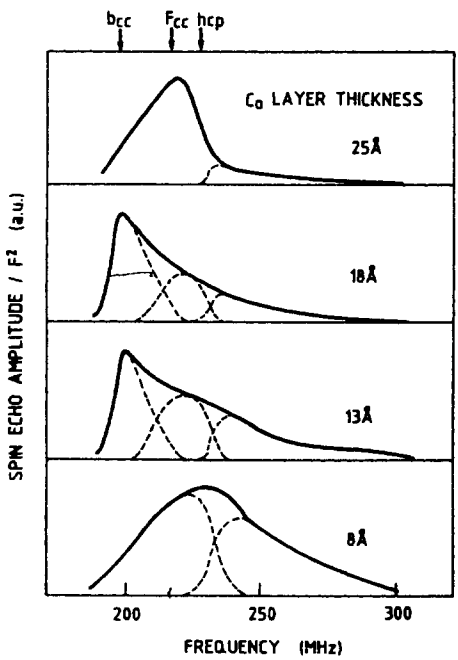


Fig. 6.6. Cobalt spin-echo spectra at $T = 4$ K of different CoFe multilayers with variable Co layer thickness (indicated in the figure). Fe layer thicknesses are fixed at 9 or 28 Å but the shape of the NMR spectra has been found to be independent of this parameter. The bulk hcp and fcc Co NMR frequencies are reported in the figure together with the assumed bcc Co NMR frequency. After Boher et al. (1992).

TABLE 6.1
Growth, magnetization and NMR properties of bcc Co films.

Growth	Substrate	Temperature (°C)	Thickness Å	Magnetic moment (μ_B)	NMR (linewidth) (MHz)	T_2 (μs)	Comments
MBE [1]	(1 1 0) GaAs		357 Co	1.5[a]	167 (75) [2]	180	Nanocrystals [3]
MBE [4]	(0 0 1) GaAs		100 Co	1.4[b]	170 (10)	76	Nanocrystals [3]
Sputter [5]	(1 1 1) Si		d_{Fe}/8–20 Co/d_{Fe} d_{Cr}/8–20 Co/d_{Cr}	1.6[a]	198 (20)	400	Overlapping spectra
MBE [6,7]	(1 1 0) GaAs		$d_{Fe}/d_{Co}/d_{Fe}$	1.71[a] [8]	198 (10)		Clear bcc Co line for $d_{Co} = 6$–20 Å
MBE [7]	(0 0 1) Mg	20–250 (175 optimum)			198 (9)		Visible $d_{Co} < 20$ Å See text for details

[a] From magnetization measurements.
[b] Neutron measurements. Moment varies through film.

References:

[1] Prinz (1985)
[2] Riedi et al. (1987)
[3] Idzerda et al. (1989)
[4] Bland et al. (1991a, 1991b)
[5] Houdy et al. (1991), Boher et al. (1992)
[6] Dekoster et al. (1993a)
[7] Dekoster et al. (1993b)

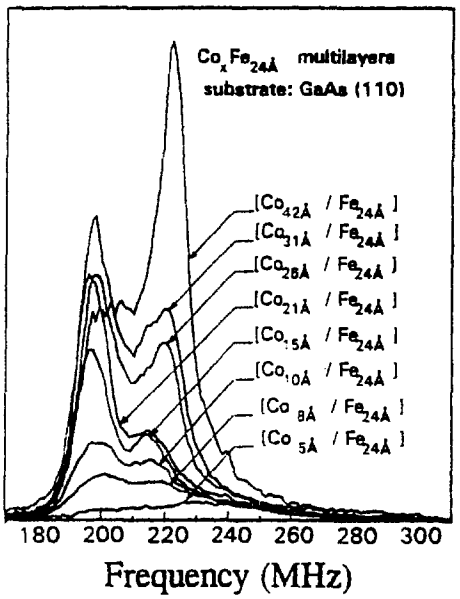


Fig. 6.7. ^{59}Co NMR spectra at 1.6 K in $Co_xFe_{25\ Å}$ multilayers grown on GaAs (1 1 0), the integral intensity of each spectrum is set proportional to the Co layer thickness. After Panissod et al. (1996).

neighbor shell of a Co atom *increases* the Co NMR frequency by some 9 MHz, table 2.3. The effect of Fe on the Co NMR spectrum can clearly be seen in fig. 6.6. The signals extending to 300 MHz are due to the formation of an Fe–Co alloy at the interface between the Fe and Co layers.

While the analysis of the NMR spectra of the sputtered Co films shown in fig. 6.6 might be thought to be open to question, the 198 MHz value for bcc Co has now been confirmed by experiments on Fe/Co multilayers grown by MBE (Dekoster et al. 1993a, 1993b, 1993c) as is also discussed in section 9.4. A series of $[t_{Co}/t_{Fe}]_{\times 25}$ superlattices was studied on (1 1 0) GaAs and (1 0 0) MgO substrates, with 5 Å $< t_{Co} <$ 42 Å and $t_{Fe} = 24$ Å. The ^{59}Co NMR as a function of t_{Co} is shown in fig. 6.7 for the (1 1 0) GaAs substrate. The 10 Å thick Co layer is 5 atomic layers thick. The broad distribution near 212 MHz comes from the Co/Fe interface and the strong narrow line at 198 MHz from the interior of the layer. Up to a Co thickness of 21 Å the intensity of the 198 MHz line grows relative to that of the interface line and there is no evidence of the hcp Co signal at above 220 MHz. Similar results were obtained for ($t_{Co} = 21$ Å)/($t_{Fe} = 24$ Å) on GaAs and MgO substrates. As the Co thickness increased above 21 Å the hcp Co signal begins to appear, but it will be seen in fig. 6.7 that the bcc Co line is still present for $t_{Co} = 42$ Å. This stabilizing effect of an *overlayer* of Fe on the bcc Co phase is remarkable in view of the 10 Å limit for a free Co surface.

The distribution of ^{59}Co HFF of Co/Fe multilayers has been analyzed (Jay et al. 1996; Panissod et al. 1996) in terms of NMR lines from four environments: (1) bcc Co (198 MHz); (2) bcc Co at an interface with Fe (214 MHz), and broader distributions due

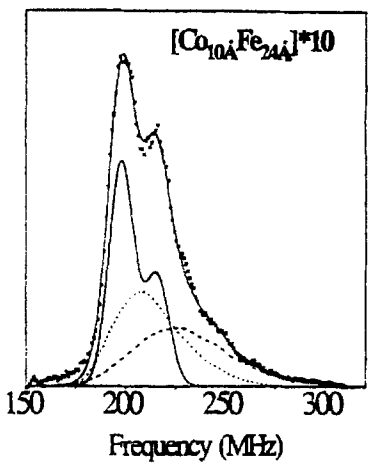


Fig. 6.8. Experimental and model spectra in a Co/Fe bcc sample superlattice grown on GaAs (1 1 0) showing contributions to the calculated spectra. Solid lines: bulk bcc Co and its sharp interface with Fe; dotted: interface between bulk Co and CoFe alloy; dashed: CoFe alloy. After Panissod et al. (1996).

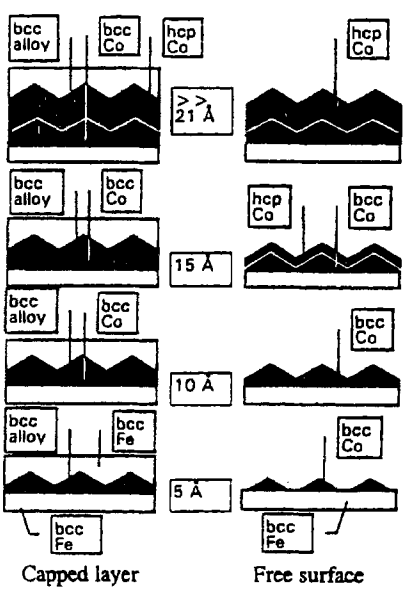


Fig. 6.9. Cross section image of Co/Fe superlattices as seen by NMR and RHEED (after Panissod et al. 1996).

to; (3) bcc Co at an interface with a bcc Fe–Co alloy; and (4) the Fe–Co alloy, fig. 6.8. In order to account for the relative intensities of the four lines as a function of the Co thickness it was necessary to assume a model in which the bcc Co grows as islands with a pyramidal shape, fig. 6.9. A full discussion of the model, which accounted for both NMR

and RHEED data, is given by Panissod et al. (1996). The main conclusion was that a thickness of 10–11 Å of bcc Co seems to be the stability limit for the Co–Fe interface, whether the Fe is below the Co or on both sides. The growth of 21 Å of bcc Co in the presence of an overlayer is due to an inter-mixing with a rough hcp Co surface and an alloyed Co–Fe layer. A final check on the consistency of the model was made by measuring the ^{59}Co spectra of bcc Co–Fe alloy films prepared by codeposition (Wojcik et al. 1997).

7. NMR in Co/Cu superlattices

7.1. Basics of NMR in Co/Cu superlattices

In zero applied field and at a fixed temperature (usually between 1.5 and 4.2 K) the analysis of NMR spectra in superlattices proceeds by a number of stages. The first part of any analysis is to identify the major lines in the spectrum. In the case of Co the lines associated with the two well known phases (fcc/hcp) are well established (see sections 5.2 and 5.3). The effect of spacer layer atoms on the effective magnetic field at the nucleus can be determined by studying dilute alloys of the same material (see section 2.4). This yields the change in effective magnetic field per substitution of the spacer layer atom, and hence the expected frequency of the ideal (abrupt) interface line can be calculated. In the case of Cu in Co a frequency shift of approximately −16 MHz per substituted Cu atom is obtained. Integrating the area under both the main and interface line allows an estimate of the amount of ideal interface to be made. Strain within a superlattice can also be investigated using NMR as the effective magnetic field is extremely sensitive to inter-atomic spacing. Strain has the effect of producing a small change in the measured NMR frequency and is particularly helpful where epitaxial registry leads to a distortion of the lattice due to a lattice constant mismatch. At room temperature Co has a lattice constant $a_0 = 3.544$ Å, and Cu has a lattice constant $a_0 = 3.615$ Å and hence a mismatch of ~2% exists in Co/Cu superlattices. The effect of strain is calibrated from pressure measurements and the results can be expressed as either a change in volume/lattice parameter or an effective pressure. Additional information can be obtained by varying the temperature or applying a magnetic field to the superlattice and this is discussed as the points arise.

The published work on NMR studies of Co/Cu superlattices is shown in table 7.1. The table shows that the two most important deposition techniques are molecular beam epitaxy (MBE) and sputtering. Initially we shall be concerned with explaining the results from superlattices produced by MBE as the better epitaxial registry leads to a film closer to the ideal. Co/Cu superlattices have been produced with three orientations (1 0 0), (1 1 0) and (1 1 1) however most attention has been devoted to the (1 1 1) orientation. Figure 7.1 shows spectra from both the first work on MBE grown Co/Cu (1 1 1) and some more recent high resolution results.

Figure 7.1 conveniently shows most of the features of NMR in superlattices. The first observation is that the main line is significantly different between the two sets of spectra. The main line in fig. 7.1(a)–(d) is clearly the envelope resulting from two or more individual lines. The NMR line produced by Co in the fcc phase is centred at 217.4 MHz ($T = 4.2$ K) while the anisotropy of the hcp phase leads to two lines at 220 and 228 MHz and is usually observed as a broad line centred at ~222 MHz. Fitting the envelope can therefore give an

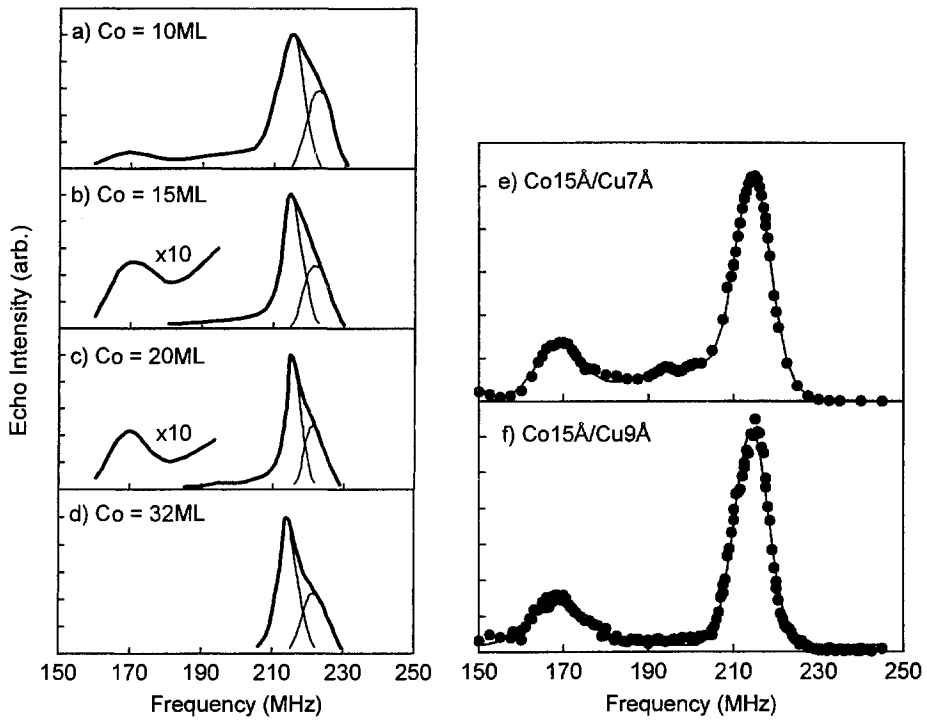


Fig. 7.1. ^{59}Co NMR spectra of Co/Cu (1 1 1) superlattices: (a)–(d) as a function of Co layer thickness in monolayers (ML) together the fits to simple Gaussian functions (after Le Dang et al. 1990); (e)–(f) for different substrate/buffer layers: (e) – GaAs/Ge/Co/Cu and (f) – sapphire/Nb/Cu, where again the data were fitted to simple Gaussian functions. After Thomson et al. (1994b).

estimate of the amount of fcc and hcp Co in the bulk environment where Co is surrounded by 12 Co nearest neighbors. This can also be thought of as fcc Co with hcp-like stacking faults.

Another, smaller line occurs at ~168 MHz, fig. 7.1(f) this corresponds to the atomic environment where three nearest neighbor Co atoms have been replaced by Cu. In the (1 1 1) orientation this is the ideal (abrupt) interface. As each Co layer has two interfaces the ratio of the intensity of the main to the interface line should scale with the thickness of the Co layer and this is observed in fig. 7.1(a)–(c). Comparing the integrated area of the main and interface line gives information on the percentage of interface where no mixing of the layers has occurred. Intensity outside these two lines is indicative of mixing, here Co is surrounded by 10 Co + 2 Cu and/or 11 Co + 1 Cu. This deviation from the ideal can clearly be seen in fig. 7.1(a)–(e) while the spectrum in fig. 7.1(f) has a significantly greater amount of ideal interface.

Having considered the positions of the lines and their integrated areas, we will now consider what information can be extracted from the NMR spectrum. As previously mentioned a change in strain is reflected in the NMR frequency. Unstrained fcc Co in the bulk environ-

ment (12 NN Co) has a frequency of 217.4 MHz at 4.2 K, as the Cu lattice is 2% larger than the fcc Co lattice an extensive strain in the plane of the superlattice and a commensurate reduction in fcc Co NMR frequency is expected. Assuming that the Co lattice expands to dimensions of the Cu lattice would imply a NMR frequency 204.9 MHz. The main fcc Co line has never been observed at such low frequencies. The lattice constant must therefore be some average of the Co and Cu values. Lattice distortion so that fcc becomes slightly fct is also possible, as indeed is some combination of these explanations.

In the case of the interface line the situation is less clear. There is general agreement that substitution of a near neighbor Co atom by Cu produces a frequency shift of -16 MHz $\pm$ 1 MHz (Mény et al. 1993b), however, in some work on dilute alloys a figure of -18 MHz (Le Dang et al. 1990) per Cu substitution has been suggested. Hence as the frequency shift associated with strain is small, it is not possible to be unambiguous in assigning particular frequencies for the interface line to the effects of strain. It should be pointed out that both a distortion of the lattice from fcc to fct and a small reduction in magnetic moment per atom due to weakened exchange interactions might be expected in the interfacial region.

Finally it is worth noting that the width of the lines can also give a valuable clue as to the overall quality of the superlattice. The width of the line is determined by the distribution of effective magnetic field at the nucleus and can therefore give a qualitative indication of the density of defects, inclusions, grain boundaries, etc.

7.2. Crystal phase and orientation in Co/Cu superlattices

7.2.1. Crystal phase of Co in Co/Cu multilayers

In section 7.1 it was shown that the sensitivity of NMR to the local atomic environment provided an excellent method of determining the crystal structure of Co in thin film superlattices. In this section the work on crystal phases is explained in more detail for Co containing superlattices grown with various orientations of the principle crystallographic axes.

At temperatures below $T = 673$ K Co exists in a stable hcp phase, but a finely divided powder of Co is fcc at low temperatures provided that the grain size does not exceed a few microns. It is also possible to stabilize fcc Co in a thin film or superlattice provided that the layer thickness is not too great.

Figure 7.2 shows a series of NMR spectra for Co/Cu superlattices with increasing Co layer thickness (Le Dang et al. 1991), together with the spectrum from a thick Co film. A cross-over from fcc to hcp is clearly visible as the Co layer thickness increases, fitting the data to Gaussian functions gives an estimate of the thickness at which the film ceases to be mainly fcc of 65 Å for Co/Cu in the (1 1 1) orientation. A similar result was obtained by Thomson et al. (1995), on high quality MBE grown Cu/Co/Cu (1 1 1) trilayers with better defined atomic environments where a transition from fcc to hcp at ~60 Å was observed. A slightly lower value ~50 Å is indicated by the measurements of Mény et al. (1992) on sputtered superlattices, however as the transition from fcc to hcp is dominated by stacking faults the values obtained are in remarkably good agreement. This seem entirely consistent as less good epitaxial registry is to be expected with sputtered films. Both of these papers also note that increasing the thickness of the Cu spacer layers assists propagation of the fcc lattice though the subsequent Co layer.

TABLE 7.1

Published work on NMR studies of Co/Cu superlattices.

Reference	Growth technique	Substrate/buffer	Structure	Orientation	Comments (important result)
Le Dang et al. (1990)	MBE	GaAs	Co(20–65Å)/Cu(23Å) total thickness 1500 Å	(1 1 1)	Atomically abrupt interfaces for (1 1 1) orientation identified by NMR satellite line structure. Co layers have fcc stacking symmetry and an epitaxially induced in-plane lattice expansion.
de Gronckel et al. (1991a)	MBE	Si	(i) $[Co(40Å)/Cu(21Å)]_{\times 20}$ (ii) $[Co(12–40Å)/Cu(21Å)]_{\times 20}$	—	Co/Cu, Co/Ir, Co/Au and Co/Pd multilayers reported. A linear dependence of in-plane strain on inverse Co thickness was observed for Co/Cu. Interfacial roughness of about one atomic layer was deduced.
Le Dang et al. (1991)	MBE	GaAs	Co(5–100Å)/Cu(23Å) total thickness 1500 Å	(1 1 1)	Co in fcc phase observed for Co layers up to 65 Å following which it becomes hcp. HFF is isotropic for fcc Co and anisotropic for hcp with the anisotropic part having the same order of magnitude and sign as the bulk. Interfacial region extends over 2 or 3 atomic layers.
de Gronckel et al. (1991b)	MBE	Si/Cu(200Å)	(i) $[Co(12Å)/Cu(42Å)]_{\times 40}$ (ii) Co(6–50Å)/Cu(21Å) total thickness 2000 Å (iii) Co(12–40Å)/Cu(42Å) total thickness 2000 Å	(1 1 1)	Nanostructure and local strain investigated in fcc (1 1 1) multilayers. Uniform in-plane strain is inversely proportional to Co layer thickness. Interface consists of one layer of mixed Co and Cu atoms.

TABLE 7.1
(Continued)

Reference	Growth technique	Substrate/buffer	Structure	Orientation	Comments (important result)
Suzuki et al. (1992)	MBE	(i) MgO(1 0 0)/Ag(2000Å)/Cu(200Å) (ii) Si(1 1 1)/Ag(2000Å)/Cu(200Å)	(i) (a) Co(4Å)/Cu(4Å) (b) Co(8Å)/Cu(8Å) (c) Co(16Å)/Cu(16Å) total thickness 2000 Å (ii) (a) Co(4Å)/Cu(4Å) (b) Co(8Å)/Cu(8Å) (c) Co(16Å)/Cu(16Å) total thickness 2000 Å	(i) (1 0 0) (ii) (1 1 1)	Differences between (1 0 0) and (1 1 1) investigated. All samples are essentially single crystals but (1 1 1) oriented multilayers have many stacking faults. (1 0 0) oriented samples have rougher interfaces than (1 1 1) multilayers.
Mény et al. (1992)	Sputtered	(i) Si/Fe (ii) Si/Fe (iii) Si/Cu (iv) Si/Cu (v) Si/Cu	(i) $[Co(15Å)/Cu(15Å)]_{\times 30}$ (ii) $[Co(15Å)/Cu(20Å)]_{\times 30}$ (iii) $[Co(60Å)/Cu(20Å)]_{\times 30}$ (iv) $[Co(60Å)/Cu(60Å)]_{\times 30}$ (v) $[Co(60Å)/Cu(90Å)]_{\times 30}$	(1 1 1)	Multilayer phase depends on layer thickness. Thicker Cu layers give more fcc phase, thicker Co tends to hcp. Intermixing occurs over 3 atomic layers for thin Co layers.
Giron et al. (1992)	Diode rf sputtered	Si(1 0 0)/Cu(300Å)	$[Co(12.6Å)/Cu(20.9Å)]_{\times 30}$	(1 0 0)	NMR as a function of angle of applied field shows large anisotropic HFF where Co atoms have 1 Cu NN.
Renard et al. (1992)	MBE	Glass/Au(1 1 1)(250Å)	(i) $[Co(3Å)/Cu(3Å)]_{\times 80}$ (ii) $[Co(3Å)/Cu(5Å)]_{\times 60}$ (iii) $[Co(5Å)/Cu(3Å)]_{\times 60}$ (iv) $[Co(5Å)/Cu(5Å)]_{\times 50}$ (v) $[Co(10Å)/Cu(10Å)]_{\times 25}$	(1 1 1)	Large MR observed for multilayers in fcc phase with near atomically flat interfaces. These atomically flat interfaces probably needed for good AF coupling.
Lord et al. (1993)	MBE	(i) GaAs/Ge(500Å)/Co(15Å)/Au(10Å) (ii) GaAs/Ge(500Å)/Co(15Å)/Cu(200Å)	(i) (a) $[Co(15Å)/Cu(7Å)]_{\times 20}$ (b) $[Co(15Å)/Cu(18Å)]_{\times 20}$ (ii) (b) $[Co(15Å)/Cu(7Å)]_{\times 20}$ (b) $[Co(15Å)/Cu(18Å)]_{\times 20}$	(1 1 1)	Large MR observed for multilayers in fcc phase with near atomically flat interfaces. Average strain greater for multilayer with Au buffer.

TABLE 7.1
(Continued)

Reference	Growth technique	Substrate/buffer	Structure	Orientation	Comments (important result)
Saito et al. (1993a)	Ion beam sputtered	MgO(1 1 0)	$[Co(10Å)/Cu(10Å)]_{\times 100}$	(1 1 0)	Sputter bias voltage dependence of alloying at interface. Uniform 50/50 interface alloy gives small MR whereas a non-uniform interfacial alloy leads to large MR.
Inomata et al. (1993)	Ion beam sputtered	MgO(1 1 0)	(i) $[Co(10Å)/Cu(8–38Å)]_{\times 100}$ (ii) $[Co_xFe_{1-x}(10Å)/Cu(10Å)]_{\times 16}$ $x = 0.75–1$ (iii) $CoFe(10Å)/Cu(10Å)]_{\times 16}$ (iv) $Ni_{0.80}Fe_{0.20}(15Å)/Cu(6–38Å)]_{\times 16}$	(1 1 0)	Interfacial quality and MR found to be sensitive to sputtered bias voltage for Co/Cu, CoFe/Cu and Ni/Fe/Cu multilayers. Inclusion of about 10 at% Fe in Co layer of Co/Cu increases MR. MgO(1 1 0) gives uniaxial anisotropy leading to low Ms and high MR sensitivity.
Le Dang et al. (1993a)	dc magnetron sputtered	(i) Si(1 0 0)/Cu(50Å) (ii) Si(1 0 0)/Fe(50Å)	(i) (a) $[Co(10Å)/Cu(9Å)]_{\times 40}$ (b) $[Co(10Å)/Cu(9Å)]_{\times 20}$ (c) $[Co(20Å)/Cu(9Å)]_{\times 40}$ (d) $[Co(30Å)/Cu(9Å)]_{\times 20}$ (ii) (a) $[Co(10Å)/Cu(9Å)]_{\times 40}$ (b) $[Co(10Å)/Cu(9Å)]_{\times 20}$ (c) $[Co(20Å)/Cu(9Å)]_{\times 40}$ (d) $[Co(30Å)/Cu(9Å)]_{\times 20}$	(1 1 1)	Effect of buffer layer (Cu or Fe) on interfacial quality and MR studied. Thin Co layers on Fe buffers lead to greatest MR, these multilayers also have the most fcc-like character.

TABLE 7.1
(Continued)

Reference	Growth technique	Substrate/buffer	Structure	Orientation	Comments (important result)
Panissod et al. (1993)	(i) UHV evaporation (ii) dc magnetron sputtered (iii) rf diode sputtered	(i) Si/Cu (ii) Si/Fe (iii) Si/Ta	(i) Co/Cu(20–90Å) (ii) Cu/Co(x)/Cu/NiFe x = 10–100 Å (iii) Cu(10Å)/Co(x)/Cu(22Å)/NiFe(50Å)/FeMn(80Å)/Ta(50Å) x = 20, 30, 40, 50, 60, 75 Å	Mostly (1 1 1)	Effect of different deposition methods, buffer layers and Co/Cu layer thicknesses on interface and bulk Co. Thicker Co layers favor hcp phase. Fe buffer layers give more, step-like, ideal interfaces only with some deposition methods.
Mény et al. (1993b)	dc magnetron sputtered	Si/Ta(50Å)	Cu(10Å)/Co(x)/Cu(22Å)/NiFe(50Å)/FeMn(80Å)/Ta(50Å) x = 20, 30, 40, 50, 60, 75 Å	(1 1 1)	Spin valve; interfacial quality as a function of Co layer thickness. hcp stacking faults in a basically fcc structure, significant number of bulk defects together with non-ideal interfaces.
Suzuki et al. (1993)	Magnetron sputtered	Si/Fe(0–150Å)/Cu(20Å)	[Co(10Å)/Cu(20Å)]$_{\times 16}$	(1 1 1)	Structure and MR as a function of Fe buffer thickness. Critical change at Fe = 30 Å. Below this clusters form at the interfaces while above Co atoms are distributed randomly.
Saito et al. (1993b)	Ion beam sputtered	MgO(1 1 0)	[Co(10Å)/Cu(10Å)]$_{\times 100}$	(1 1 0)	Interfacial quality and MR studied as a function of sputter bias voltage. Uniform 50/50 alloy at the interfaces gives small MR whereas a non-uniform interfacial alloy leads to large MR.

TABLE 7.1
(Continued)

Reference	Growth technique	Substrate/buffer	Structure	Orientation	Comments (important result)
Clarke et al. (1994)	rf diode sputtered	Si/Cu(1 0 0)(300Å)	$[Co(8–60Å)/Cu(8–60Å)]_{\times 30}$	(1 0 0)	fcc (1 0 0) oriented layers grown using appropriate substrate and buffer. Anisotropic HFF in applied magnetic field confirmed local (1 0 0) texture.
Suzuki et al. (1994)	MBE	GaAs(1 1 0)/Ge/ Co(1 1 0)(15Å)/ Au(1 1 1)(20Å)	$[Co(15Å)/Cu(8–20Å)]_{\times 30}$	(1 1 1)	Atomically abrupt interfaces over significant areas. fcc phase with a low density of stacking faults. Other techniques suggest a paramagnetic layer at the interfaces.
Suzuki et al. (1994)	Magnetron sputtered	Si/Fe(50Å)	$[Co(10Å)/Cu(22Å)]_{\times 16}$	(1 1 0)	Interfaces deliberately mixing by cosputtering Co and Cu. X-rays not sensitive to mixed layers of less than 3 Å NMR is very sensitive. Co and Cu atoms randomly mixed at interface.
van Alphen et al. (1994a)	MBE	Si	(i) Co(12–35Å)/Cu(42Å) total thickness 2000 Å (ii) Co(6–40Å)/Cu(21Å) total thickness 2000 Å	(1 1 1)	Comparison of strain in Co/Ni, Co/Ag and Co/Cu multilayers. Critical thickness for the transition from coherent to incoherent strain in Co layer is between 21 and 42 Å.
Thomson et al. (1994a)	MBE	(i) GaAs/Ge(500Å)/ Co(15 Å)/Cu(200 Å) (ii) GaAs/Ge(500Å)/ Co(15Å)/Au(10Å)	(i) $[Co(15Å)/Cu(7Å)]_{\times 20}$ (ii) $[Co(15Å)/Cu(7Å)]_{\times 20}$	(1 1 1)	Magnetic anisotropy field measured independently in the bulk and at the interfaces using the NMR enhancement factor. Anisotropy field at the interfaces was close to coercivity while in the interior of the layers it increased with increasing MR.

TABLE 7.1
(Continued)

Reference	Growth technique	Substrate/buffer	Structure	Orientation	Comments (important result)
Thomson et al. (1994b)	MBE	(i) GaAs/Ge(500Å)/ Co(15Å)/Cu(200Å) (ii) GaAs/Ge(500Å)/ Co(15Å)/Au(10Å) (iii) Sapphire/Nb(30Å)/Cu(20Å)	(i) $[Co(15Å)/Cu(7Å)]_{\times 20}$ (ii) $[Co(15Å)/Cu(7Å)]_{\times 20}$ (iii) $[Co(15Å)/Cu(9Å)]_{\times 20}$	(1 1 1)	Increases in MR correlated with more ideal, atomically abrupt interfaces. Greater single crystal like character from lattice matched interfaces generates increased coherent strain.
Thomson et al. (1995)	MBE	Sapphire/Nb	(i) Cu(15Å)/Co(25Å)/Cu(15Å) (ii) Cu(34Å)/Co(93Å)/Cu(34Å) (iii) Cu(15Å)/Co(102Å)/Cu(15Å) (iv) Cu(23Å)/Co(178Å)/Cu(23Å)	(1 1 1)	fcc to hcp transition measured as a function of Co layer thickness for (1 1 1) oriented multilayers. Below Co = 60 Å, fcc phase dominates while above this thickness Co principally grows in the hcp phase. Cu underlayer thickness also important with thicker Cu favoring the fcc phase.
Schreiber et al. (1995)	MBE	Sapphire/Nb	(i) $[Co(31Å)/Cu(20Å)]_{\times 10}$ (ii) $[Co(47Å)/Cu(26Å)]_{\times 10}$	(1 1 1)	Thicker Co layers result in a transformation from fcc to hcp through an increased number of stacking faults.
Saito et al. (1995a)	rf sputtered	Si	$[Co(7.9Å)/Cu(9.4Å)]_{\times 30}$	(1 1 1)	Effect of annealing on structure and its correlation to MR investigated. Annealing at 200°C leads to modification of the atomic structure, not visible to X-rays, that cause changes in MR.

TABLE 7.1
(Continued)

Reference	Growth technique	Substrate/buffer	Structure	Orientation	Comments (important result)
Saito et al. (1995b)	Ion beam sputtered	MgO(1 1 0)	$[Co(10Å)/Cu(10.5Å)]_{\times 100}$	(1 1 0)	Temperature dependence of HFF measured at low temperature for fcc Co/Cu multilayers. A greater temperature dependence at the interfaces than in the interior of the layers was observed.
Kubo and Kioke (1989)	Ion beam sputtered	MgO(1 1 0)	(i) $[Co(10Å)/Cu(10Å)]_{\times 100}$ (ii) $[NiFe(20Å)/Cu(50Å)/Co(10Å)/Cu(50Å)]_{\times 10}$	(1 1 0)	Correlation between interfacial quality and MR measured as a function of multilayer composition, bias voltage and annealing. Both interlayer exchange coupling and interfacial magnetization depend on atomic structure at the interface. A useful review/summary paper.
Thomson et al. (1996a)	MBE	Sapphire/Nb(60Å)/Cu(30Å)	$[Co(11.5Å)/Cu(7Å)]_{\times 20}$	(1 1 1)	Effect of annealing at a range of temperatures up to 320°C on structure and its correlation to MR investigated. Slight deterioration of interfacial quality by annealing led to a reduction in MR, strain in the interior of multilayer was also relaxed.
Thomson et al. (1996c)	Sputtered	Sapphire(1 1 2 0)	(i) $[Co(44Å)/Cu(18Å)]_{\times 6}$ (ii) $[Co(10.7Å)/Cu(20.6Å)]_{\times 12}$	(i) (1 1 1) (ii) (1 0 0)	MBE like flat interfaces from careful control of sputtering conditions. (1 1 1) and (1 0 0) geometry's show the expected difference in nearest neighbor configuration.

TABLE 7.1
(Continued)

Reference	Growth technique	Substrate/buffer	Structure	Orientation	Comments (important result)
van Alphen et al. (1996)	Electrodeposition	(i) Si(1 0 0)/Cu(200Å)	(i) (a) $[Co(7.5Å)/Cu(40Å)]_{\times 51}$ (b) $[Co(10Å)/Cu(40Å)]_{\times 50}$ (c) $[Co(12.5Å)/Cu(40Å)]_{\times 51}$ (d) $[Co(16.5Å)/Cu(40Å)]_{\times 63}$	(i) (1 0 0)	Electrodeposited multilayers measured. Multilayers deposited on Au similar to those on Cu buffer. Interfacial roughness of about 3 Å is independent of Co layer thickness.
		(ii) Si(1 0 0)/Au(500Å)	(ii) details not given	(ii) (1 1 1)	Non-randomly distributed Cu impurities found in Co layers. Electrodeposition leveling agents have large effect on NMR spectrum.
Valet et al. (1993)	rf diode sputtered	Si(1 0 0)/Fe(50Å)	NiFe(50Å)/Cu(50Å)/Co(x)/Cu(50Å) x = 10, 30, 50, 70, 100 Å total thickness 2000 Å	(1 1 1) weak	Examine the effect of replacing alternate Co layers with NiFe. Results similar to Co/Cu but possibly with greater interfacial mixing
Nakamura et al. (1993)	UHV	Mylar/Cr(50Å)	[NiFe(15Å)/Cu(35Å)/ Co(15Å)/Cu(35Å)]$_{\times 20}$	(1 1 1)	Examine the effect of replacing alternate Co layers with NiFe. Results similar to Co/Cu but spectrum more reminiscent of CoCu alloy, indicating more interfacial mixing.
Goto et al. (1993a)	Ion beam sputtered	Si(1 0 0)/Fe(50Å)	(i) Co(10Å)/Cu(100Å) (ii) Co(10Å)/Cu(200Å) (iii) Co(10Å)/Cu(500Å)		^{63}Cu NMR studies of spin polarization oscillation. Line broadening inconsistent with AFM coupling contributions from other effects Kondo, electric field gradient probably important. Also see related work in section 10.1 where NMR from Cu nuclei is discussed more fully.

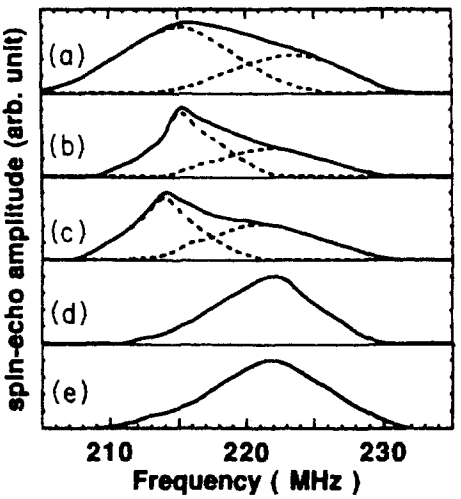


Fig. 7.2. ^{59}Co NMR spectra in zero field for a Co/Cu (1 1 1) superlattice with Co layer thicknesses of (a) 20 Å, (b) 40 Å, (c) 65 Å, (d) 100 Å. (e) Spectrum for a single Co layer of 1000 Å. The dashed lines represent spectral intensity due to atoms in the fcc and hcp phases. After Le Dang et al. (1991).

7.2.2. *Orientation of Co in Co/Cu multilayers*

Examination of table 7.1 shows that most of the Co/Cu superlattices studied by NMR have been oriented with the (1 1 1) plane parallel to the film surface, i.e., the [1 1 1] direction is normal to the plane of the film. As explained in section 7.1, for this orientation the ideal (abrupt) interface requires that 3 nearest neighbor Co atoms are substituted by Cu. In the case of the (1 0 0) orientation the ideal interface environment has Co surrounded by 8 nearest neighbor Co and 4 nearest neighbor Cu, while for the (1 1 0) orientation this becomes 7 nearest neighbor Co and 5 nearest neighbor Cu.

Figure 7.3 shows data after Suzuki et al. (1992) from two similar MBE grown Co(4Å)/Cu(4Å) superlattices, one grown on Si (1 1 1) with a (1 1 1) orientation and the other grown on MgO (1 0 0) oriented in the (1 0 0) direction. Similar data has also been collected on high quality sputtered superlattices (Thomson et al. 1996c). Examining the spectra for the (1 1 1) oriented superlattice in fig. 7.3(a) shows the expected behavior, a narrow line associated with bulk fcc Co at ~217 MHz and a second line at ~168 MHz indicative of the ideal planar environment with 9 Co and 3 Cu nearest neighbors. The spectrum for the (1 0 0) orientation fig. 7.3(b) is slightly more complicated. Here the atomic environment with 1, 2, and 3 Co nearest neighbor substituted by Cu are all approximately equal, the ideal interface line where Co is surrounded by 8 Co and 4 Cu has a greater intensity. Given that the layers of Co are only 4 Å thick this result is to be expected and shows that a significant part of the superlattice has ideal planar interfaces and is (1 0 0) oriented. The actual frequency of this ideal planar interface line ~115 MHz (Suzuki et al. 1992) or 132 MHz (Thomson et al. 1996c) is somewhat lower than might be anticipated from a reduction of 16 MHz per substituted atom, i.e., ~150 MHz, however, this is not unexpected as substituting 4 Co atoms with Cu inevitably reduces the exchange interaction and so will reduce the effective magnetic field at the nucleus and hence the NMR frequency.

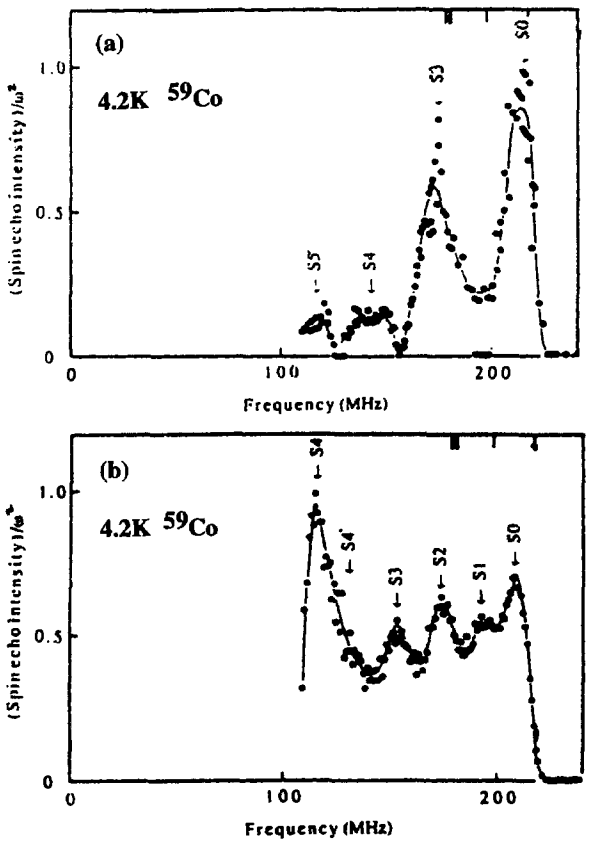


Fig. 7.3. Co(4Å)/Cu(4Å) superlattices at 4.2 K (a) oriented (1 1 1), (b) oriented (1 0 0). The lines are assigned letters S_0, S_1 etc. to indicate the atomic environment. S_0 is the bulk line, S_1 is the first satellite due to 11 Co and 1 Cu NN and so on. After Suzuki et al. (1992).

Work on (1 1 0) oriented superlattices has to date been restricted to sputtered materials and has concentrated on the effects of sputtering bias voltage, deliberate interfacial mixing, annealing and measuring temperature. The position of the ideal planar interface line has not been firmly established as measurements on either MBE or high quality sputtered superlattices are required. Taking the arguments given for the (1 0 0) orientation, a frequency of ~100 MHz might be expected for the ideal planar interface line with 7 Co and 5 Cu nearest neighbors.

7.3. NMR studies of strain in the Co layers of Co/Cu superlattices

The lattice constants for fcc Co and fcc Cu are sufficiently closely matched to allow epitaxial registry to occur, as discussed above, at room temperature the Co lattice parameter $a_0 = 3.544$ Å and the Cu lattice parameter of $a_0 = 3.615$ Å resulting in a lattice mismatch of ~2%. However epitaxial registry must modify either the Co or Cu lattice, or both. The

effective magnetic field is highly sensitive to interatomic spacing as the spin densities of both the 3d and valence electrons at the nucleus are modified. The combined effect of the spin density modifications produces a reduction in the effective magnetic field as the fcc Co lattice is expanded from its equilibrium dimensions. As the fcc Cu lattice is larger than its Co counterpart epitaxial registry would be expected to lead to an extensive in-plane strain and a commensurate reduction in the centre frequency of the NMR lines.

The size of the interfacial strain has been estimated by combining measurements of the bulk modulus B_T and the change Δ of ^{59}Co NMR frequency ν under hydrostatic pressure P at temperature T

$$\frac{\Delta V}{V} = \frac{3\Delta a}{a} = -\alpha \frac{\Delta \nu}{\nu},$$

where

$$\alpha = \left[B_T \left(\frac{\partial \ln \nu}{\partial P} \right)_T \right]^{-1}$$

is of the order unity and V is the volume. The value of B_T for hcp Co at room temperature and the room temperature value of $(\partial \ln \nu / \partial P)_T$ for fcc Co, tables 5.1 and 5.2, have mostly been used in the literature, leading to a value of α of 1.16. NMR experiments on thin films are, however, carried out at temperatures near 0 K, and using the value for $(\partial \ln \nu / \partial P)_T$ at 4.2 K, from table 5.2, leads to a value of 0.97 for α. Since the correct value of B_T is not known, and interfacial strain is in any case non-hydrostatic, the difference between these two estimates of α is not significant.

Results from a typical series of high quality MBE grown Co/Cu (1 1 1) superlattices are shown in table 7.2, after Thomson et al. (1994b). The table also shows the magnetoresistance expressed as a percentage, given by the maximum value of the ratio of the decrease in resistance ΔR on the application of a field to the value of the resistance R in the applied field.

TABLE 7.2

The frequency of the main line for a series of [Co(15Å)/Cu(7 or 9Å)]$_{\times 20}$ superlattices grown on different substrate/buffer layers with different magnetoresistances. The shift in NMR main line is expressed solely in terms of pure volume lattice expansion and equivalent hydrostatic pressure. (The situation must be more complicated since it would be expected that the expansion of the Co lattice in the plane would be accompanied by a contraction normal to the plane.) The final entry shows the effect of expanding the Co lattice spacing to match that of the Cu lattice. After Thomson et al. (1994b).

Substrate/buffer	$\Delta R/R$ (%)	Main line freq. (MHz)	Equivalent pressure (kbar)	Equivalent lattice expansion $\Delta V/V$ (%)
GaAs/Ge/Co/Cu	4	215.6	−16	0.9
GaAs/Ge/Co/Au	22	216.0	−12	0.7
Sapphire/Nb/Cu	40	214.2	−29	1.5
Co → Cu	—	204.9	−113	5.9

The results are shown both as an equivalent hydrostatic pressure and as a uniform expansion of the lattice in three dimensions. Table 7.2 clearly shows that the measured frequency shift is much less than would be expected if the Co lattice were expanded to the dimensions of the Cu lattice. It also seems apparent that the result cannot be accounted for by a simple average of a strained Co lattice and a compressed Cu lattice.

A number of explanations have been proposed for the observed frequency shift due to strain. The initial interpretation by Le Dang et al. (1990) proposed that a strain gradient exists within the bulk of the Co layers so that layer adjacent to the interfaces were effectively expanded to the Cu lattice whilst layers in the interior were partially relaxed. This hypothesis also provided an explanation for the X-ray work which suggested that the lattice expansion was greater than 1%.

The initial work on strain in Co/Cu superlattices was followed up by a more comprehensive study de Gronckel et al. (1991a, 1991b). Here the thicknesses of both the Co and Cu layers were varied in a systematic way. The NMR signals from the bulk and originating from Co sites with 11 Co nearest neighbors (i.e., with a single Cu nearest neighbor) lines were then plotted, as shown in fig. 7.4.

Figure 7.4(a) shows that for atoms in the bulk environment ΔB_{eff} depends on both t_{Co} and t_{Cu} and that for a given t_{Cu} the strain is inversely proportional to t_{Co} for $t_{\text{Co}} > 6$ Å. Comparing the bulk and 11 Co, 1 Cu environments, fig. 7.4(b) shows that the relative change in B_{eff} is similar for both these atomic environments. This suggests similar atomic dimensions throughout the superlattice and hence coherent strain. Later work by the same

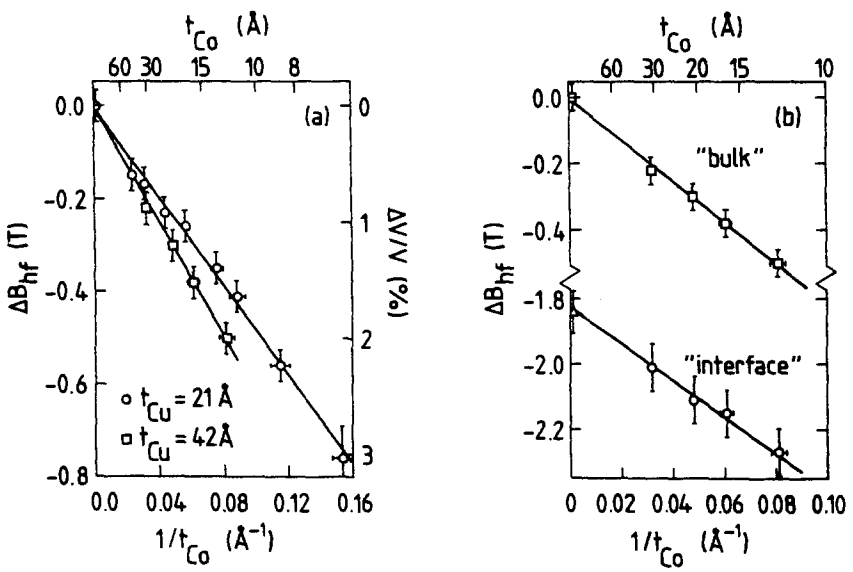


Fig. 7.4. (a) Change in effective magnetic field $\Delta B_{\text{eff}} = \Delta B_{\text{hf}}$, determined from NMR spectra measured in field, as a function of the reciprocal Co thickness $1/t_{\text{Co}}$ for Co/Cu (1 1 1) superlattices with copper layer thickness of $t_{\text{Cu}} = 21$ and 42 Å. (b) $B_{\text{eff}} = \Delta B_{\text{hf}}$ as a function of t_{Co} for bulk and 11 Co, 1 Cu atomic environments with $t_{\text{Cu}} = 42$ Å. The reference sample used was a 1000 Å single layer of Co. After de Gronckel et al. (1991a, 1991b).

authors (van Alphen et al. 1994a) comparing results from Co/Ni, Co/Ag and Co/Cu superlattices concluded that in general Co/Cu superlattices were in a transition region between coherent and incoherent strain as neither mechanism could fully explain all the observations.

Finally it is worth mentioning that strain effects have also been observed in sputtered Co/Cu (1 1 0) superlattices (Saito et al. 1993a). In this work a large uniaxial magnetic anisotropy was explained in terms of lattice expansion.

7.4. Anisotropy measured by NMR in Co/Cu superlattices

In this section we shall discuss anisotropy in Co/Cu superlattices. This discussion will concentrate on two aspects of measurement in these systems. The first is a review of work on the effects of changing the orientation of applied fields or of the crystallographic directions upon the NMR resonance frequencies, and the second is a discussion of a method of deducing the local anisotropy field via changes in domain enhancement on the application of an external field.

7.4.1. Anisotropic hyperfine fields at ^{59}Co nuclei

Bulk Co with the hcp structure has resonant frequencies at 220 MHz and 228 MHz when the magnetic moment are parallel and perpendicular to the c axis, respectively (Kawakami et al. 1972). This anisotropy in the hyperfine field originates principally from the anisotropy of the orbital magnetic moment, as described in section 2.2. This anisotropic hyperfine field does not occur in fcc Co due to its higher symmetry. The anisotropy in the hyperfine field of hcp Co is small and the effect on the NMR signal depends on a number of factors. In particular on the relative orientation of the c-axis of the hcp Co, the rf excitation field, the magnetic moment (the hyperfine field being antiparallel to the magnetization) and any external magnetic field together with associated demagnetizing factors. See sections 2.3 and 5 for further details.

Several studies of the anisotropy of the hyperfine field in Co/Cu superlattices have been made (Le Dang et al. 1991; Giron et al. 1992, 1993) by applying static magnetic fields and observing the effect on the NMR spectra. The simplest case is when the c-axis is perpendicular to the plane of the film. If the applied magnetic field and rf excitation are orthogonal to each other and both in the plane of the film (which is a standard configuration used for measuring thin films) then increasing the magnetic field leads to a practically equal shift in resonance frequency as for Co $\gamma = 1.0054$ MHz/kOe and the hyperfine field is isotropic within the plane of the film. As the hyperfine field in hcp Co is only slightly anisotropic its angular variation can be described by

$$H_{\mathrm{n}}(\theta) = H_{\mathrm{iso}} + H_{\mathrm{ani}} \frac{3\cos^2\theta - 1}{2},$$

where H_{iso} and H_{ani} are the isotropic and anisotropic components respectively, and θ is the angle between the magnetization and the applied field. Anisotropic behaviour can be observed if the c-axis is tilted with respect to the film normal or the applied field is perpendicular to the plane of the film.

One of the first NMR studies of Co/Cu (1 1 1) multilayers (Le Dang et al. 1991) found that the hcp component of the multilayer gave a similar value for H_{ani} to that found in the bulk. This is evidence that the hcp-like regions of Co/Cu multilayers are indeed similar to bulk hcp Co.

7.4.2. Magnetic anisotropy studies using NMR enhancement effect

NMR is observable in ferromagnetic materials due to the enhancement effect discussed in section 4. In a domain wall or in a domain within a low anisotropy material the enhancement factor is of the order of $\eta \approx 10^3$. Thus the response of the nuclei to an applied resonant rf field is largely determined by the electronic enhancement factor η. In a spin echo experiment the magnitude of the received echo is also proportional to η. In the absence of domain walls the strength of the NMR signal for a particular environment can be related to the domain enhancement factor η_d, arising from the magnetic susceptibility of moments in the domain rather than in the domain walls, where $\eta_d \gg 1$ by

$$\text{signal} \propto \eta_d \propto \frac{B_{eff}}{B_{app} + B_{ani}}, \tag{7.1}$$

where B_{eff} is the effective field at the nucleus, B_{app} is the applied field, B_{ani} is the anisotropy field experienced by the nuclei under consideration.

Thus by measuring the area under a particular NMR line as a function of field, after applying a sufficiently large field to ensure that all the domain walls have been swept out, the magnetic anisotropy field can be determined for that particular environment (Thomson et al. 1994a).

Figure 7.5 shows the field dependence of the integrated echo intensity under both the bulk NMR line (with 12 Co NN) and the ideal planar interface line (with 9 Co NN and 3 Cu NN). Results from two multilayer films are shown, one with $\Delta R/R = 4\%$ (fig. 7.5(a) and (b)) and one with $\Delta R/R = 22\%$ (fig. 7.5(c) and (d)). The parameters obtained from fitting eq. (7.1) are summarized in table 7.3.

Table 7.3 shows that the interfacial anisotropy field determined from NMR measurements is, within error, the same for both samples and is similar to the coercivity. The anisotropy field measured for atoms in a bulk environment is larger than that measured at the interfaces, and shows significant differences between the two samples. This then implies that magnetization reversal is nucleated at the interfaces. The ratio of bulk to interface anisotropy was found to be approximately double for the sample exhibiting a stronger GMR effect.

Experiments of this type, although time consuming to perform, do provide a unique method of probing the anisotropy field, as the measurement is confined to a particular type of atomic environment. In passing, it should be noted that with the correct geometry of sample orientation and excitation coil, information can also be on the domain structure. This is implied in fig. 7.5, as a pronounced dip in the NMR signal is observed at the coercive field.

A method of investigating the relative local enhancement factor is to make a three dimensional plot of the spin echo intensity versus frequency and rf power (Oliviera and Guimaraes 1997; Panissod et al. 1997). The magnitude of the spin echo signal is a function of the product of the local enhancement and the peak rf magnetic field, see sections 3.7

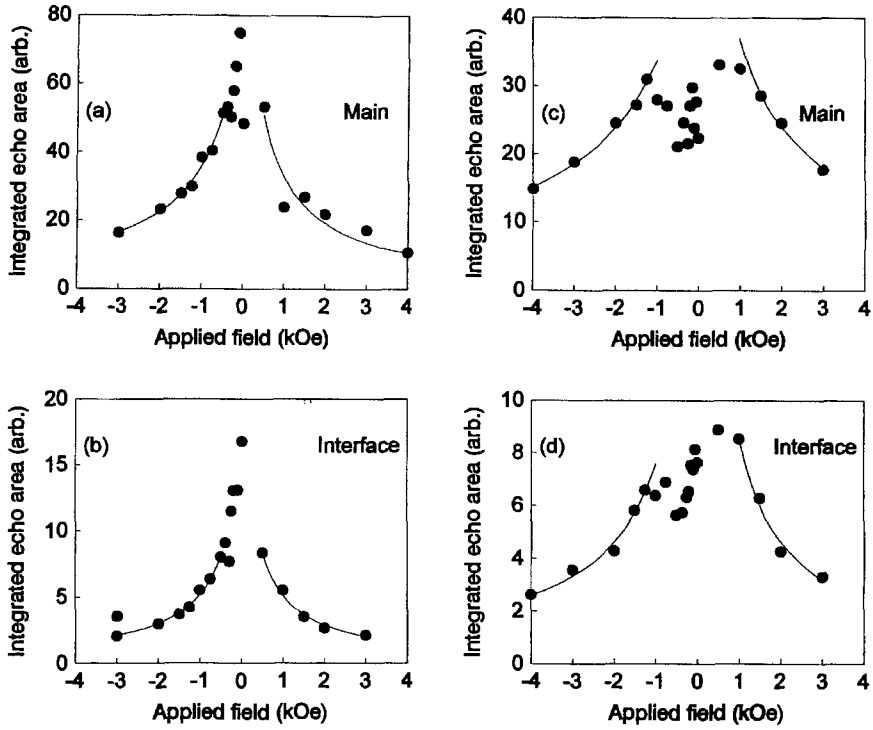


Fig. 7.5. Example of NMR used to measure anisotropy fields both in the interior of a Co layer and independently at the Co layer interface. After Thomson et al. (1994a).

TABLE 7.3

Anisotropy fields determined from field dependence of NMR, and coercivity as measured on a vibrating sample magnetometer. NMR was measured at 4.2 K and coercivity, H_c at 8 K. Uncertainty in NMR measurements ~100 Oe. After Thomson et al. (1994a).

Substrate/buffer	$\Delta R/R$	Anisotropy field (Oe)		Coercive field (Oe)
		Bulk	Interface	
GaAs/Ge/Co/Cu	4%	550	340	260
GaAs/Ge/Co/Au	22%	1230	360	260

and 4. Therefore, a peak at a given frequency at low rf power indicates a large enhancement effect. The advantage of this method is that it can be performed in zero external field and is therefore simpler and quicker than the method of Thomson et al. (1994a), but the disadvantage is that domain and wall enhancement is not distinguished.

7.5. Effect of deposition technique and substrate/buffer on Co/Cu multilayers

As can be seen from table 7.1, a large number of substrate/buffer combinations have been used as a basis for growing Co/Cu multilayers. The choice of which combination to use depends on the desired texture of the multilayer and to a lesser extent on the deposition technique. However, for a given technique and substrate/buffer, the NMR results are consistent in that the nearer the interface approaches the ideal planar (abrupt) configuration then the greater the GMR. The correlation of NMR with magnetotransport is discussed more fully in section 7.7. Here we concentrate on how the choice of substrate/buffer leads to different interfacial quality, and the effect that this has on the NMR spectrum.

7.5.1. Effect of substrate/buffer and sputter/MBE on Co/Cu interfacial quality

The NMR spectrum from a multilayer containing only ideal planar interfaces would show a bulk line (fcc, hcp or some mix of the two) and a single interface line depending on the orientation, e.g., (1 1 1), (1 1 0) or (1 0 0). Figure 7.1(e) and (f) in section 7.1 clearly showed the effect of substrate and buffer on the interfacial region for two similar MBE grown multilayers (Thomson et al. 1994b). Figure 7.1(e) is the NMR spectrum for a Co/Cu (1 1 1) multilayer grown on GaAs/Ge(500Å)/Co(15Å)/Cu(200Å) while fig. 7.1(f) shows the spectrum from a similar MBE multilayer grown on sapphire/Nb(60Å)/Cu(30Å). The spectrum for the latter sample clearly has less spectral intensity outside the bulk and ideal interface lines and therefore significantly less mixing at the interface. The most comprehensive single piece of work comparing the effects of substrate/buffer and growth techniques was completed by Panissod and Mény (1993). Figure 7.6 gives an overview of how different deposition techniques and substrates/buffers affect the interfacial structure.

Figure 7.6(a) is an example of a nearly perfect interfacial spectrum and was observed on a sample consisting of a single layer of Co(20Å) (1 1 1) grown on a single crystal of Cu and capped with Fe, thus ensuring only one Co/Cu interface. More usually, particularly with sputtered multilayers, samples exhibit a number of satellite lines which are more or less resolved. In particular, spectra can be modeled by assuming lines at ~200 MHz and ~183 MHz corresponding to an atomic environment in which Co NN have been replaced by 1 and 2 Cu NN, respectively.

The spectrum in fig. 7.6(b) is from a UHV-evaporated multilayer. The first three satellite lines are of similar height after the effect of the width of the bulk line is allowed for. Modeling work by de Gronckel et al. (1991b) and Mény et al. (1992) on this spectrum suggest that this sample still has sharp atomic interfaces, but that they contain a large number of single atomic height defects.

Figure 7.6(c) was produced by diode sputtering and exhibits a NMR spectrum similar to a CoCu alloy with a strong first satellite (arising from the Co nuclei with 11 Co and 1 Cu NN) a smaller second satellite and an extended tail. This spectrum is characteristic of a multilayer with extensive interfacial mixing. Figure 7.6(d) is an intermediate case with both an observable third satellite line and the alloy-like features described for fig. 7.6(c). This sample therefore has islands of ideal planar interface separated by more mixed regions.

More detailed studies of the effect that the buffer layer has on the interface structure have been undertaken by growing identical multilayers on Si substrates with either Cu or Fe buffer layers (Le Dang et al. 1993a; Panissod and Mény 1995). The structure dependence of the thickness of Fe buffer layers has also been studied (Suzuki et al. 1993).

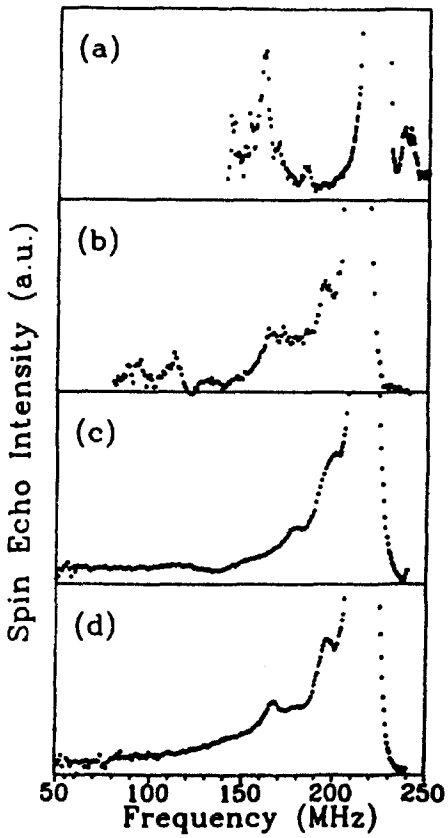


Fig. 7.6. Examples of interface NMR spectra as a function of buffer layer and deposition technique (all samples grown on Si substrates). (a) Single crystal Cu buffer, UHV evaporation, (1 1 1) texture; (b) Cu buffer, UHV evaporation, (1 1 1) texture; (c) Fe buffer, rf diode sputtered, no well defined growth direction; (d) Ta buffer, dc magnetron, (1 1 1) texture. After Panissod and Mény (1993).

Figure 7.7 shows two sputtered multilayers with different buffer layers, fig. 7.7(a) is grown on a Fe buffer and fig. 7.7(b) on a Cu buffer. The sample grown on Fe exhibits an interfacial spectrum with some ideal planar interface. In contrast, the sample grown on Cu shows an extended structureless spectrum characteristic of a disordered, mixed interface. Studies of the Fe layer thickness dependence of the structure suggested the existence of a critical Fe buffer layer thickness for sputtered multilayers (Suzuki et al. 1993). However, the nature of the structural transition appears unclear as NMR and X-ray data essentially gave different results.

The above description gives some indication of how NMR can assist film growers in their quest for materials with specific characteristics. The results highlighted should be taken as a guide to general trends rather than specific instruction, for example, Fe rather than Cu buffer layers do not always give multilayers with higher quality interfaces if other deposition parameters are changed.

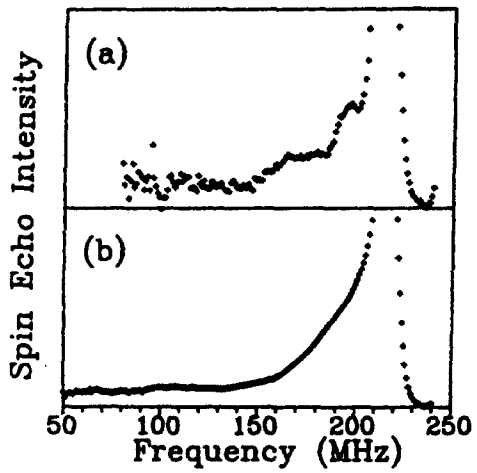


Fig. 7.7. ^{59}Co spectra of dc magnetron sputtered Co/Cu multilayers with (a) Fe and (b) Cu buffer layers grown on Si substrates (after Panissod and Mény 1993).

7.5.2. Effect of replacing alternate Co layers in Co/Cu multilayers with permalloy (NiFe)

Two publications (Valet et al. 1993 and Nakamura et al. 1993) have reported ^{59}Co NMR results on films where every alternate Co layer has been substituted with permalloy (NiFe) to give a repeating structure of Cu/Co/Cu/NiFe. The motivation behind this work was to reduce the value of the external field needed for GMR. NMR results show that the Co/Cu interfaces are similar to multilayers without the addition of the permalloy layers. Details of any smaller, second order effects such as small changes in interfacial mixing proved difficult to analyze unambiguously, as Co/Cu control samples made by the same method would have to be produced alongside the samples containing NiFe.

7.5.3. NMR studies of electrodeposited Co/Cu multilayers

Electrodeposition is potentially an extremely attractive technique to produce magnetic multilayers, as it is both fast and economical. Initially the multilayers produced by electrodeposition were essentially alloys with no discernible interface structure on a local atomic scale. However, some NMR work by van Alphen et al. (1996) has shown that this technique has now improved and local interfacial environments similar to sputtered multilayers can now be obtained, fig. 7.8.

Similar results were obtained for multilayers grown on Au buffer layers with the (1 1 1) texture (as determined from X-ray measurements), although one would anticipate that the two different textures would produce different spectra for ideal planar interfaces. Clearly these materials are still fairly disordered, however progress in their deposition has been made and on the evidence of fig. 7.8 it may well be possible to use NMR in the future to obtain detailed information on the local atomic environment.

7.5.4. Effect of bias voltage on sputtered Co/Cu multilayers

Sputtering is the most technologically useful of the deposition techniques. Studies of interfacial quality as a function of sputtering parameters is therefore of considerable inter-

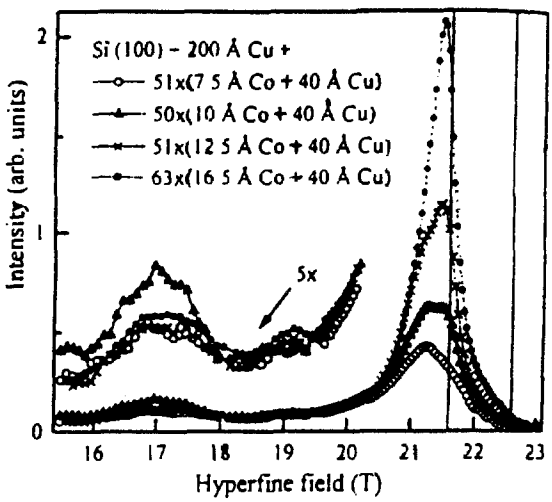


Fig. 7.8. NMR spectra at $T = 1.6$ K of electrodeposited Co(x)/Cu(40Å) grown on a Si/Cu substrate/buffer with (1 0 0) texture. The low frequency side of the spectrum is magnified 5 times to show the interface structure. After van Alphen et al. (1996).

est as Co/Cu multilayers are potential magnetic sensors. Several NMR investigations have been undertaken (Saito et al. 1993a, 1993b, and Inomata et al. 1993) to examine the interfacial structure as a function of sputtering bias voltage V_B. Figure 7.9 shows the change in NMR spectra for a series of [Co(10Å)/Cu(10Å)]$_{\times 100}$ multilayers oriented in the (1 1 0) direction as the bias voltage is increased from 400 to 1400 V.

All the spectra show a wide distribution of intensity indicative of substantial interfacial mixing. However, within these wide distributions there are significant differences between the spectra. The bulk lines are close to the fcc Co values, as no shoulders are observed on the high frequency side of this line, the amount of hcp Co must be very small. Co/Cu multilayers oriented in the (1 1 0) direction have an ideal planar interface consisting of Co surrounded by 7 Co + 5 Cu NN. None of the spectra show a pronounced line that could be associated with this environment and therefore an alloy-like interfacial region must have formed. The spectra can be modeled using

$$P(X_i) = X_i + \alpha_i(1 - X_i),$$

where P is the probability of a Co atom at a particular NN Co site, X_i is the average fraction of Co atoms in the ith layer and α_i is the atomic short range order parameter in the ith layer. This model indicates that alloying occurs mostly within one atomic plane of the interface for $V_B = 400$–600 V and within two atomic planes for $V_B = 1000$–1400 V. The sample grown at $V_B = 600$ V most closely approximates an ideal planar configuration. This sample also exhibits the largest MR which is consist with the work shown in fig. 7.1(e) and (f) on high quality MBE grown multilayers.

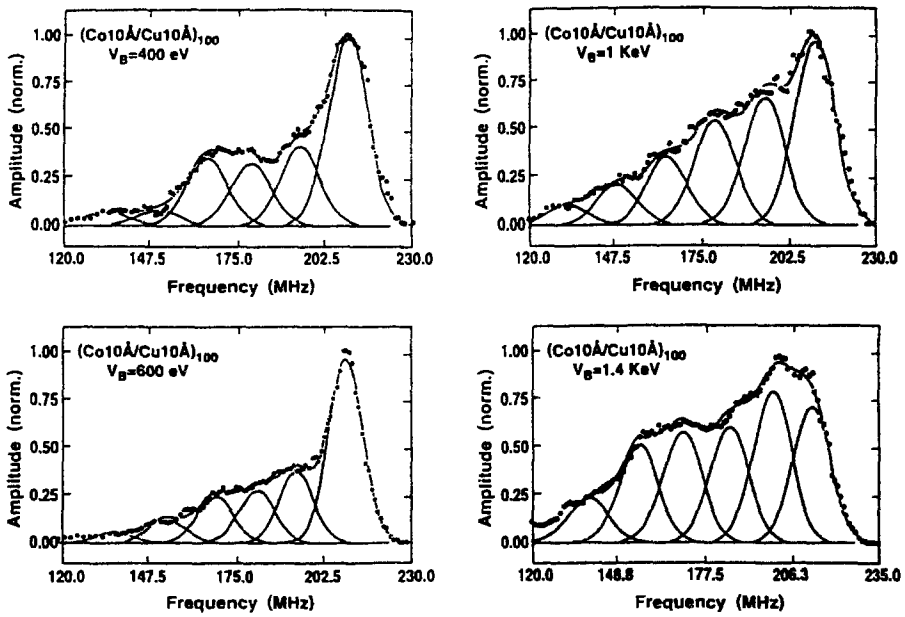


Fig. 7.9. ^{59}Co NMR spectra of $[Co(10Å)/Cu(10Å)]_{\times 100}$ multilayer in zero applied field at $T = 4.2$ K as a function of V_B. The main line is due to fcc Co, the low frequency satellites are due to the increasing substitution of Co with Cu, i.e., (11 Co + 1 Cu NN, 10 Co + 2 Cu NN.). All spectra were corrected for ω^2. After Saito et al. (1993b).

7.6. *Effect of annealing Co/Cu superlattices*

Thermal annealing is perhaps the oldest and most important technique used to control material parameters. Annealing Co/Cu multilayers at moderate temperatures (200–300 °C) leads to considerable modification of their magnetic and magnetotransport properties. This presumably occurs due to some changes in the structure of the multilayer.

The sensitivity of NMR to the nearest neighbor environment enables structural changes on a length scale of a few angstroms to be investigated. The most systematic NMR study of annealing effects to date has been completed by Thomson et al. (1996a) on MBE grown multilayers, work on sputtered multilayers has also been undertaken (Saito et al. 1995a). The study of MBE grown multilayers by Thomson et al. (1996a) involved measuring five identical samples, listed in table 7.4, of $[Co(11.5Å)/Cu(7Å)]_{\times 20}$ grown on sapphire/Nb/Cu with a Au cap.

Previous X-ray measurements by Laidler and Hickey (1996) on the same samples, showed no discernible changes in the multilayer structure as a result of annealing. However, it was observed that the Au capping layer formed an alloy with the final Cu layer, and this resulted in a change of scale in the absolute value of the resistivity, as seen in table 7.4. Notice too, that the MR decreases as a result of annealing.

The ^{59}Co NMR spectra for the unannealed and the most heavily annealed (320°C for 45 min) MBE grown Co/Cu (1 1 1) samples are shown in fig. 7.10. The spectra exhibit the

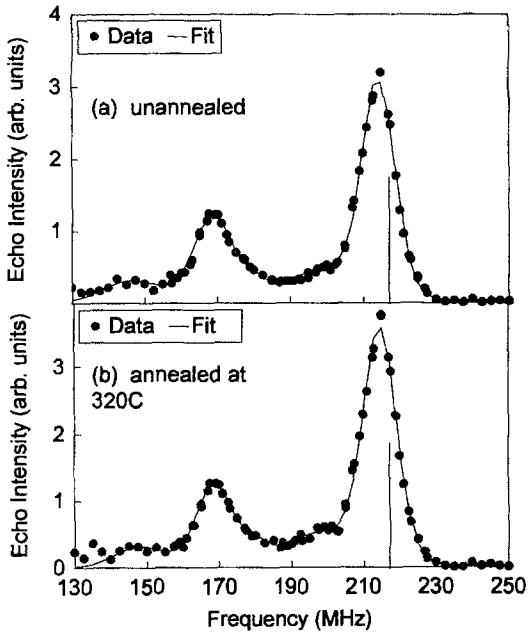


Fig. 7.10. ^{59}Co spin echo spectra for Co/Cu (1 1 1) multilayer films with structure sapphire/Nb(60Å)/Cu(30Å)/[Co(11.5Å)/Cu(7Å)]$_{\times 20}$/Au(38Å): (a) unannealed, (b) annealed at 320°C for 45 mins. All data taken at 4.2 K and corrected for ω^2 and variations in the spin–spin relaxation time T_2. The vertical bars mark the position of the centre of the NMR line from unstrained fcc Co powder. After Thomson et al. (1996a).

TABLE 7.4

Magnetoresistance measurements at $T = 4.2$ K for a series of annealed MBE grown [Co(11.5Å)/Cu(7Å)]$_{\times 20}$/Au(38Å) multilayer films. ρ_S is the saturation resistivity at 4 Tesla and $\Delta\rho$ the change in resistivity between zero applied field and saturation. MR is $\Delta\rho/\rho_S$ expressed as %. After Thomson et al. (1996a).

Annealing conditions	ρ_S (Ω cm)	$\Delta\rho$ (Ω cm)	MR (%)
Unannealed	8.2	3.0	36.6
200°C for 45 mins	9.0	3.4	37.8
260°C for 45 mins	12.0	4.4	36.7
290°C for 45 mins	14.4	4.7	32.6
320°C for 45 mins	18.6	5.8	31.1

two expected lines, one from the bulk environment (~215 MHz) and one from the ideal planar interface (~168 MHz) with relatively weak spectral intensity outside these two lines. This shows that a substantial fraction of ideal planar interface is present. The spectra show a small reduction in frequency due to the extensive in-plane strain caused by the lattice mismatch between Co and Cu (section 7.3). It is apparent that no gross changes have occurred

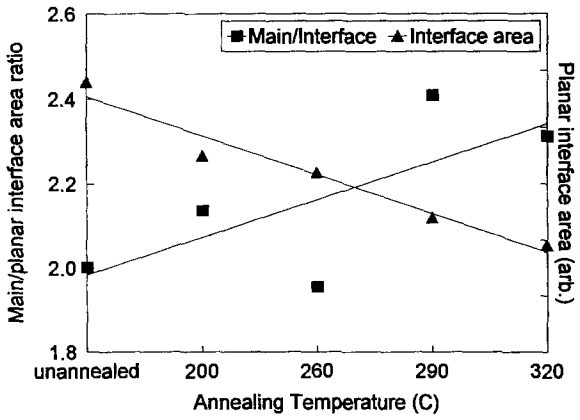


Fig. 7.11. Ratio of main to planar interface line intensity, and the normalized interface line area as a function of annealing temperature. The trend in the ratio is clear and shows a decrease in the number of atoms in the ideal atomic environment relative to the bulk. This interpretation is confirmed by the decrease in the area under the interface line. After Thomson et al. (1996a).

as a result of annealing. This is somewhat surprising and demonstrates that Co/Cu (1 1 1) multilayers, prepared with a careful choice of substrate and buffer layer structure, are resistant to change up to temperatures in excess of 300°C. However, closer examination reveals some smaller effects. One method of determining changes in the interfacial structure is to take the ratio of the area under the main line to that of the area under the ideal planar interface line. As the area under a line is directly proportional to the number of atoms in the particular environment, it is also possible to compare the areas of the ideal interface lines directly, provided that relative sample volumes can be determined accurately.

Figure 7.11 shows both the main/planar interface line ratio, and the integrated area under the planar interface line as a function of annealing temperature. The ratio of the main/planar interface line increases with annealing temperature. This could be due to either an increase in the relative number of atoms in the bulk environment or a decrease in the number of atoms in the planar interface environment. Examination of the areas of the interface lines shows that the later is true. The area under the main line does not change systematically and remains approximately constant. Hence these measurements were able to identify that a small deterioration of interfacial quality had occurred as a result of annealing.

Changes in the position of the main and planar interface lines, reflecting changes in the strain state, are shown in fig. 7.12. The planar interface line remains constant whereas the main line shows a trend towards higher frequencies at higher annealing temperatures reflecting changes in strain, in the interior of the Co layers. The results in fig. 7.12 show a clear trend, in that all the samples show less strain following annealing. This is consistent with the finding that the amount of planar interface reduces with annealing, as less planar interface implies less epitaxial registry and so less strain in the interior of the Co layers. A similar strain relaxation, following annealing, has been observed in sputtered Co/Ag multilayers van Alphen et al. (1995) where the effects were substantially larger.

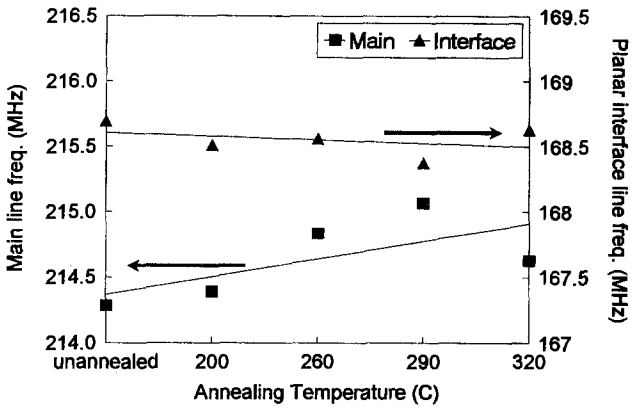


Fig. 7.12. Centre frequency of the main and planar interface NMR lines change as a function of annealing temperature. The interface line frequency remains constant whereas the main line frequency increases. It is worth pointing out that this increase in frequency is independent of the details of the model used to fit the spectra. The uncertainty in the fit of the centre frequency is 50 kHz. After Thomson et al. (1996a).

The NMR work on annealed Co/Cu multilayers was thus able to identify small structural changes in local order where, due to their relative insensitivity to short range order, X-rays had been unable to determine modifications to the multilayer structure.

7.7. Temperature dependence of NMR in Co/Cu multilayers

A limited amount of work has been done on the temperature dependence of the NMR spectra by Saito et al. (1995b). Here sputtered multilayers consisting of [Co(10Å)/Cu(10.5Å)]$_{100}$ oriented in the (1 1 0) direction were prepared and measured between 1.5 and 30 K. The spectra exhibited a broad low frequency tail characteristic of a mixed interfacial region, similar to fig. 7.9. All the satellite lines showed a marked temperature dependence with a large reduction in hyperfine field of 240 G/K, fig. 7.13, whereas the bulk line showed a much more modest reduction in frequency.

This substantial reduction was cited as evidence that the thermal excitation of interfacial magnons is different from that of bulk magnons. However, given the limited nature of this study it is clear that considerable additional work is needed on the temperature dependence of NMR before any firm conclusions can be drawn.

7.8. Correlation of NMR in Co/Cu superlattices with other properties

In this section on Co/Cu multilayers we have concentrated on the structural information that NMR can give, and in particular, how sensitive measurements can be conducted, to provide information about buried interfaces, crystal structure and the state of strain. Such information is difficult to determine using other techniques and this gives NMR considerable utility in probing these materials. Where appropriate, correlation with magnetization and magnetotransport measurements has been mentioned, together with complementary structural techniques such as X-ray diffraction. This has then been related to growth or post growth treatments of the sample, as illustrated in fig. 7.14.

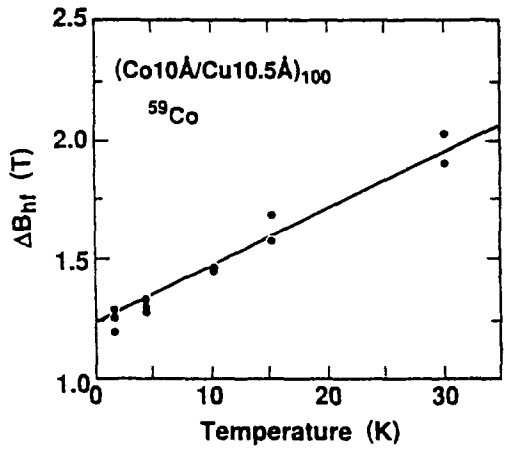


Fig. 7.13. Temperature dependence of the spacing of hyperfine field satellite lines for a sputtered [Co(10Å)/Cu(10.5Å)]$_{\times 100}$ multilayer. After Saito et al. (1995b).

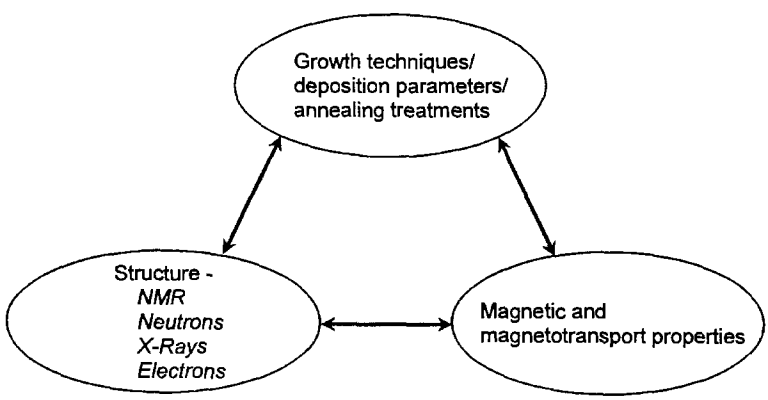


Fig. 7.14. Central role of structure in understanding magnetic properties.

However the object of studying these materials is to examine the intimate link that exists between the magnetic/magnetotransport properties and the multilayer structure. In this final section we shall briefly summarize the work on Co/Cu systems by discussing the magnetic and magnetotransport properties in multilayers where NMR measurements have been undertaken.

The most important correlation made by NMR has been between magnetoresistance and the structure of the interface, as can be seen in table 7.5. Here the key feature is how changes in the interface on an atomic scale, lead to changes in the spin dependent scattering and hence magnetoresistance. MBE grown samples provide the best systems to study, as the structural quality of these materials allows easier analysis of the data and hence an unambiguous correlation between magnetoresistance and structure. In sputtered multilayers

TABLE 7.5
NMR results explicitly correlated with magnetization and magnetotransport measurements.

Publication	Multilayer	Technique	Comments
Thomson et al. (1994b)	MBE (1 1 1) $[Co(15Å)/Cu(7–9Å)]_{\times 20}$	MR	Increasing ideal planar interface and epitaxial registry leads to increased MR
Renard et al. (1992)	MBE (1 1 1) $[Co(6–20Å)/Cu(6.3–21Å)]_{\times 12–42}$	MR	Large AF coupling and MR dependent on low interfacial roughness (mixing)
Suzuki et al. (1993)	Sputtered (1 1 1)/(1 1 0) $[Co(10Å)/Cu(20Å)]_{\times 16}$	MR	Reduced interfacial mixing correlated with increase in MR
Le Dang et al. (1993a)	Sputtered (1 1 1) $[Co(10–30Å)/Cu(9Å)]_{\times 20–40}$	MR, Magnetization	Decrease in MR correlated with an increase in stacking faults (fcc→hcp) and grain boundaries
Saito et al. (1995a)	Sputtered (1 1 1) $[Co(7.9Å)/Cu(9.4Å)]_{\times 30}$	MR, Magnetization	Correlation between changing interface structure and MR/magnetization
Saito et al. (1993a, 1993b, 1995c) and Inomata et al. (1993)	Sputtered (1 1 0) $[Co(10Å)/Cu(10Å)]_{\times 100}$ $[Ni_8Fe_2(20Å)/Cu(50Å)/Co(10Å)/Cu(50Å)]_{\times 10}$	MR, Magnetization	Maximum in MR correlated with maximum in M_s, minimum in M_r/M_s and less interfacial mixing

this correlation is sometimes considerably more difficult to identify due to the fitting and modeling work necessary to obtain even qualitative results.

In MBE grown multilayers there is now a considerable body of evidence that shows that the nearer that the interfaces approach the ideal planar configuration, then the greater the MR. The quality of the interface may be obtained from the NMR spectrum by comparing the NMR intensity in the bulk and ideal interface lines, and also by examining the spectral intensity outside these regions. The interfacial quality can also sometimes be judged by considering the state of strain in the interior of the Co layers (bulk environment). The lattice mismatch between Co and Cu, discussed in sections 7.1 and 7.3, ensures that multilayers with good epitaxial registry over large lateral dimensions >100 Å are subject to an extensive in-plane strain in the case of the Co atoms, and presumably a compressive strain in the case of the Cu atoms. This effect is seen, for example, when MBE multilayers are annealed causing both the strain to relax and a correlated reduction in MR.

In sputtered Co/Cu multilayers the largest body of published work, summarized by Saito et al. (1995c), and the final entry in table 7.5, considers the effect of sputtering bias volt-

age on magnetic properties, magnetoresistance and interfacial quality. Unlike the MBE grown multilayers work on sputtered multilayers usually relies very heavily on the fitting and modeling procedures adopted and so cannot be expected to provide the same quality of data. However general trends can still be obtained and if the multilayers are grown with sufficient care then good quality results can be obtained, as in the work of Thomson et al. (1996c).

8. NMR in Co–Cr based thin films

8.1. Introduction to Co–Cr thin films

The Co–Cr thin film system has been extensively studied due to its technological importance as a magnetic recording media, for a recent review see Lodder 1998. The initial interest (Iwasaki and Takemura 1975) stemmed from the fact that with the correct preparation conditions and substrate/buffer layers Co–Cr in its thin film form exhibits perpendicular magnetic anisotropy and is therefore a potential perpendicular magnetic recording media. However as yet perpendicular magnetic recording has not made an impact as a significant recording technology. More recently interest has focused on the use of Co–Cr based alloy thin films for conventional longitudinal magnetic recording which are, at the time of writing, the material of choice for computer hard disk media. Given this significance to the magnetic recording industry an extensive literature exists on Co–Cr based thin films (for a good general overview see Mee and Daniel 1996). However, as in the previous section it is our intention to concentrate on the NMR work carried out on this material rather than provide an extensive review of the whole subject. NMR studies have been completed on Co–Cr based thin films with both perpendicular and in-plane anisotropy as shown in table 8.1. The key feature of Co–Cr as an alloy thin film is the compositional separation (CS) that occurs, unusually for 3d metal alloys, in this material. This compositional separation into Co-rich and Cr-rich regions increases both the saturation magnetization and coercivity of the material, and crucially changes the microstructure from continuous alloy into quasi-particulate. Magnetic materials in the form of small magnetic regions, typically a few tens of nanometers, relatively isolated from each other are required, as small stable domains and smooth transition regions are essential for high density magnetic recording.

NMR is an extremely valuable tool with which to probe compositional separation as it is sensitive only to the Co-rich regions. The reason for this is that the overall composition of a Co–Cr alloy thin film is of the order of $Co_{80}Cr_{20}$ and that for a Cr content of Cr $>$ 25 at% a Co–Cr alloy ceases to be ferromagnetic. Hence Cr-rich regions are not probed by NMR while Co-rich regions have NMR spectra resembling dilute Co–Cr alloys. Hence calibrating with homogeneous alloys allows quantitative data to be obtained on the Cr content of the Co-rich regions, as discussed in section 8.2.2.

A number of studies using NMR to determine compositional separation in alloy thin films as a function of deposition parameters have been undertaken. Studies have also been completed on film thickness, the effect of additive elements and the result of using different under/buffer layers. The work on Co–Cr based alloy films is detailed in section 8.4. Finally unlike Co/Cu discussed in the previous section, relatively few investigations of Co/Cr multilayers have been completed and this work is summarized in section 8.5.

TABLE 8.1

NMR work on Co–Cr thin films together with a brief comment on the most important result contained in each publication. Note: CS = composition separation, T_s = substrate temperature during deposition.

Reference	Growth technique	Substrate/buffer	Composition	Thickness (Å)	Comments (important result)
Stearns et al. (1988)			$[Co(21–54Å)/Cr(21–54Å)]_{\times 70–25}$	N/A	Co/Cr multilayers studied. Abstract only.
Yoshida et al. (1990)	Evaporation	Polyimide/Ge	$Co_{75.9}Cr_{24.1}$	3600	Good calibration samples, complicated spectra on alloy thin films shows CS.
Houdy et al. (1991)	rf sputtered	Si(1 1 1)	$[Co(7–37Å)/Cr(7–37Å)]_{\times 120–22}$	N/A	Change in crystal structure investigated as a function of Co layer thickness in Co/Cr multilayers. Initial bcc phase changes to fcc/hcp at Co = 15 Å. Intermixing over at least 7 Å in Co layers. Possible antiferromagnetic coupling between Co layers.
Takei and Maeda (1991)	rf sputtered	Polyimide	$Co_{78}Cr_{22}$	6000	CS as a function of substrate temperature in the range T_s = 30–400°C. Cr content of Co rich region is estimated to be 5–7%.
Maeda and Takei (1991)	dc magnetron sputtered	Polyimide/Cr	$Co_{86}Cr_{12}Ta_2$	500	CS studied as a function of substrate temperature (25–250°C) during deposition. Increased temperature gives greater CS with Co rich region of $Co_{0.97}Cr_{0.03}$ and leads to more particulate-like films.

TABLE 8.1
(Continued)

Reference	Growth technique	Substrate/buffer	Composition	Thickness (Å)	Comments (important result)
Henry et al. (1993)	UHV evaporation	Mica/Ru(160Å)	$[Co(8–32Å)/Cr(8Å)]_{\times 10}$	N/A	Intermixing of Co/Cr over 11 Å, 1.8 Co monolayers are magnetically dead at interface, Co has fcc/hcp structure rather than bcc. The Cr layers consist of distorted bcc (1 1 0) crystallites.
Lodder et al. (1993a)	Single source evaporation and co-evaporation	Si	$Co_{81.4–72.4}Cr_{18.6–27.6}$	1860–7530	CS studied as a function evaporation method for films deposited at room temperature and 400°C. Co-evaporated films show most CS even at low deposition temperatures.
Maeda (1993)					Short review of CS and NMR in CoCr alloy thin films with useful reference list.
Lesnik et al. (1985c)	rf sputtered	Si/Cu	$Co_{78}Cr_{22}$	30 000	CS in CoCr alloy thin films deposited at elevated substrate temperatures. Co rich regions approximately $Co_{0.95}Cr_{0.05}$. CS present within grains.
Takei et al. (1994a)	rf sputtered	Polyimide	$Co_{78}Cr_{22}$	5000	Magnetic anisotropy field derived from enhancement factors as a function of substrate temperature during deposition. Two magnetic components observed for films deposited at 400°C.

TABLE 8.1
(Continued)

Reference	Growth technique	Substrate/buffer	Composition	Thickness (Å)	Comments (important result)
Rogers et al. (1994b)	rf sputtered	Polyester (PET) Polyimide/Ge	$Co_{79}Cr_{21}$	4000	Effect of Ge underlayer and substrate temperature on CS investigated. At high temperature CS occurs in both substrate/buffer combinations with Co rich regions of $Co_{0.95}Cr_{0.05}$. CS is important both within grains and Cr-rich grain boundaries.
Takei et al. (1994b)	rf sputtered	Polyimide	$Co_{78}Cr_{22}$	4000	Study the effect of sputter bias voltage on compositional separation (CS), M_s, H_c, H_k and X-ray rocking curves. Slight positive bias increases CS.
Maeda et al. (1994a, 1994b)	dc sputtered	PET Polyimide	$Co_{86}Cr_{12}Ta_2$ $Co_{78}Cr_{13}Pt_9$ $Co_{62.5}Cr_{7.5}Ni_{30}$	3600 400 500	Effect of Ge underlayer and substrate temperature on CS investigated. At high temperature CS occurs in both substrate/buffer combinations with Co rich regions of $Co_{0.95}Cr_{0.05}$. CS is important both within grains and Cr-rich grain boundaries. Possible magnetic induced phase separation.

TABLE 8.1
(Continued)

Reference	Growth technique	Substrate/buffer	Composition	Thickness (Å)	Comments (important result)
Rogers et al. (1994c)	rf sputtered	Cr underlayer	$Co_{82.8}Cr_{14.6}Ta_{2.6}$	400	CS studied as a function of Cr underlayer texture and substrate temperature. Different texture in Cr underlayers did not change the extent or pattern of CS. Reduced intergranular exchange coupling was thought to have a microstructure origin related to grain boundaries. CS increased with increasing substrate temperature. A novel idea for Ta induced in-grain CS was proposed.
Rogers et al. (1994a)	rf sputtered	Polyimide and glass	$Co_{78}Cr_{22}$ $Co_{86}Cr_{12}Ta_2$	100–200 000	Differences in CS between Co–Cr and Co–Cr–Ta as a function of film thickness. Thinner films lead to greater CS with Ta promoting a finer pattern of Co rich regions.
Hirono et al. (1995)	Electron-cyclotron-resonance (ECR) Plasma sputtered rf sputtered	Glass NaCl Polyimide	$Co_{78}Cr_{22}$	1000	ECR sputtering gives better defined CS and finer grains than conventional rf sputtering with closely packed Co enriched regions separated by less than 50 Å.
Rogers et al. (1995b)	rf sputtered				Good review article on NMR work undertaken in Co–Cr based alloy thin films and the dependence of CS on deposition parameters and alloy composition.

8.2. Bulk alloys as NMR references

The ability of Cr to supply electrons to the 3d band means that unlike Cu, described in the previous section, which effectively acts as a hole in the Co nearest neighbor shell, the substituted Cr atom acts as an "enhanced" hole. This leads to a reduction in the magnetic moment and hence the NMR frequency associated with the concentration of Cr within a region, i.e., the dipole term in the total hyperfine field, as well as a specific effect for the nearest neighbor substitution of Co with Cr.

8.2.1. Calibration of the substitution of Cr into the Co nearest neighbor shell

The effects of substituting Cr into Co are studied using calibration samples of finely divided, homogeneous powdered alloys, see section 2.4. Figure 8.1 shows the NMR spectra obtained for a set of calibration samples containing between 0–21.6 at% Cr, details of the preparation method are contained in the report of Yoshida et al. (1990). Above Cr = 25 at%, the homogeneous alloys are no longer ferromagnetic and hence zero field NMR cannot be performed.

Figure 8.1(a) shows the spectrum for pure Co. The main line is centred at 225 MHz showing that this sample is in the hcp phase. Two frequencies are associated with Co in the hcp phase, 220 MHz and 228 MHz, corresponding to the magnetization vector directed along the c-axis and in the basal plane respectively. In practice the two NMR lines lead to a single broader resonance line centred at an intermediate frequency, as show in fig. 8.1(a). A closer examination of this spectrum reveals a small additional feature at 217 MHz corresponding to Co in the fcc phase.

Figure 8.1(b) and (c) show Co–Cr in the dilute alloy limit, here at most one Co nearest neighbor has been replaced by Cr. The addition of a small amount of Cr slightly broadens the main peak (M) and produces a broad, weak satellite line (S_1) at the lower frequency of ~180 MHz. Increasing the Cr concentration to Cr = 5.6 at%, fig. 8.1(d) results in the appearance of a second satellite line (S_2) at about 130 MHz. Further increases in the amount of Cr, fig. 8.1(e) Cr = 13.3 at%, the intensity of the satellite lines becomes stronger than that of the main line. At a Cr concentration of Cr = 21.6 at%, fig. 8.1(f), the spectral intensity associated with the M, S_1 and S_2 lines were converted into one very broad line with a centre frequency of approximately 80 MHz.

The results displayed in fig. 8.1 can be analyzed in terms of a random alloy using the binomial theorem. In the dilute alloy limit, the hyperfine field acting on a Co nucleus is essentially proportional to the local magnetic moment of the parent Co atom and that of its nearest neighbors, and may be analyzed using an expression like that of eq. (2.5). Calculations based on the binomial theorem and using the measured reduction in saturation magnetization by Yoshida et al. (1990), predict that one Co NN atom substituted by Cr should produce an NMR frequency of 177.4 MHz, which is close to that of the first satellite S_1 in fig. 8.1, but see also table 2.3 for a slightly different value (Mény et al. 1993a, 1993b).

The case of the second satellite line, S_2 in fig. 8.1, presents an additional level of theoretical complexity, since in the hcp structure two impurity atoms can arrange themselves in nine different configurations. In the case of Cu impurities these configurations are effectively identical, since the Cu atom does not, to a first approximation, affect the magnetic moment of the remaining Co atoms. In contrast, as mentioned earlier, Cr does affect the

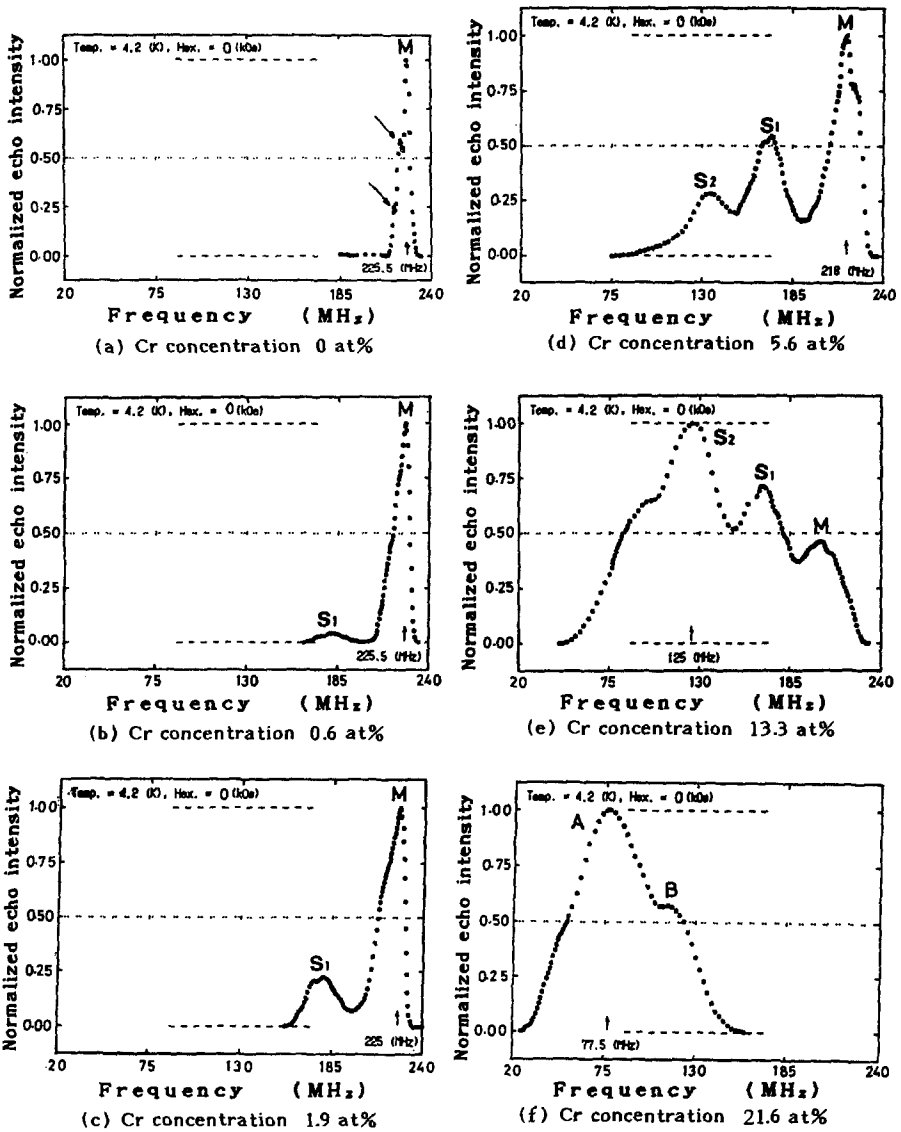


Fig. 8.1. Zero field ^{59}Co NMR spin-echo spectra at $T \simeq 4.2$ K of homogeneous Co–Cr alloy calibration samples made by vacuum evaporation and annealed at 1000°C for 2 hours (after Yoshida et al. 1990).

magnetic moment of the neighboring Co atoms and so the configuration becomes important. The calculations of Yoshida et al. (1990) show that there is a spread of frequencies between 113–142 MHz corresponding to these nine impurity configurations. Taking a weighted average of these results gives a theoretical value for S_2 of 132 MHz which is close to the observed value of 134 MHz. Given the spread of frequencies calculated for this environment, it would be expected that the S_2 line is broader than S_1. A further very

broad line has also been observed by Takei and Maeda (1991) in the region of 100 MHz. This line can be tentatively identified as corresponding to an atomic environment in which three of the NN Co atoms have been replaced by Cr. However at this concentration of Cr the magnetic moment on the Co atoms is severely reduced and a larger number of different impurity configurations is possible. This leads to a broad, poorly defined NMR line.

Finally, fig. 8.1(f) shows the NMR spectrum for an alloy with Cr = 21.6 at%. This is close to the ferromagnetic limit and the effect of the reduced magnetic moment on the spectrum is obvious. Here only a very broad featureless peak centred at 80 MHz is observed. Quantitative data on composition can be obtained from this moment reduction and this is discussed in the following section.

8.2.2. Modification of NMR line positions by Cr concentration

At the beginning of this section it was noted that the average Cr concentration within a region had the effect of reducing the magnetic moment of the Co atoms in the region and consequently the hyperfine field. This reduction in hyperfine field (and hence NMR frequency) allows an estimate of the average Cr concentration to be made in the Co-rich regions of Co–Cr alloy thin films where compositional separation has occurred. A number of studies of the frequency of the "bulk" Co line (i.e., the line arising from Co nuclei with 12 NN Co atoms) as a function of Cr concentration have been undertaken (Yoshida et al. 1990; Takei and Maeda 1991; Mény et al. 1993a, 1993b), the results of which are summarized in fig. 8.2.

Using the data of fig. 8.2 the reduction in the bulk NMR line frequency is estimated to be 2 MHz/at% Cr over the range Cr = 0–15 at%. Errors in this analysis are of the order of ±1 at%. Hence NMR is able to provide a quantitative insight into the composition of the Co-rich regions of compositionally separated Co–Cr alloy films.

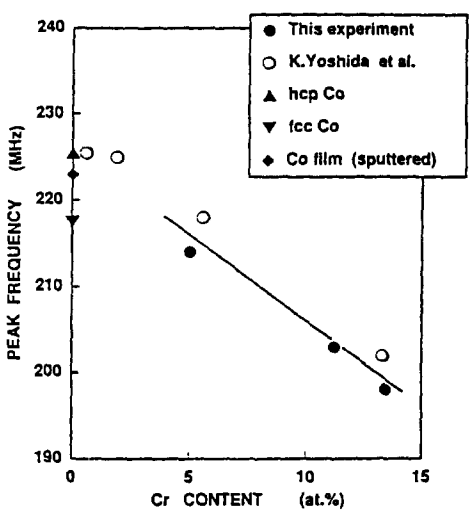


Fig. 8.2. Centre frequencies of main resonance lines (M) for homogeneous Co–Cr powdered alloy samples as a function of Cr concentration. The line is a guide to the eye only. After Takei and Maeda (1991).

A similar analysis using the first two satellite lines S_1 (11 Co and 1 Cr) and S_2 (10 Co and 2 Cr) has also been undertaken. However the width of these lines contributed significantly to the uncertainty in the results, and in practice only the main line can be use to calculate the Cr concentration accurately and reproducibly. In the remainder of section 8 we shall discuss results in terms of the compositions deduced from the measurement of homogeneous powdered alloys, as outlined above.

8.3. NMR in Co–Cr thin films

In contrast to the work on Co/Cu described in the previous section where the majority of NMR studies were conducted on multilayer materials, NMR investigations of Co–Cr have centred on sputtered alloy films. Table 8.1 details the NMR work on Co–Cr thin films together with a brief comment on the most important result contained in each publication.

Table 8.1 clearly shows that the most valuable information obtained from NMR studies relates to the compositional separation that occurs in Co–Cr thin alloy films. Inspection of the spectrum from a Co–Cr film immediately indicates whether or not compositional separation (CS) has occurred, while using the calibration techniques outlined in the previous section allows quantitative analysis of CS to be undertaken. The single most important factor determining CS is the substrate temperature (T_S), however other factors can also be important. All these aspects of Co–Cr alloy thin films are described in the following section (8.4), while Co/Cr multilayers are discussed in section 8.5.

8.4. NMR in Co–Cr thin alloy films

8.4.1. NMR of Co–Cr alloy films as a function of substrate temperature

The importance of substrate temperature (T_S) in generating compositional separation is well established in Co–Cr based thin alloy film. NMR measurements are able to both detect CS and provide quantitative data on the Cr content of the Co-rich regions, as discussed in the previous section (8.2.2) on calibration. Figure 8.3 (after Takei and Maeda 1991) gives a clear example of the emergence of a highly Co-enriched component in an sputtered alloy film of average composition $Co_{78}Cr_{22}$ as the substrate temperature is increased from 30°C to 400°C.

A similar dependence of CS on substrate temperature has been observed in all Co–Cr based thin alloy films as has been demonstrated for example by Maeda and Takei (1991), Takei and Maeda (1991), Lodder et al. (1993a), Maeda et al. (1994a), Rogers et al. (1994b). The analysed data from fig. 8.3 is displayed in table 8.2 using the calibration data described earlier. Table 8.2 shows the substrate temperature, main line centre frequency and estimated Cr content in the Co-rich regions.

It is noteworthy that a highly Co-enriched component is observed even in films where the substrate temperature is as low as $T_S = 100$°C, and where the volume fraction of the Co-rich regions is rather small. This indicates that the highly Co-enriched component starts to form during the initial stages of compositional separation. The implication is that CS occurs by a nucleation and growth mechanism rather than, for example, by a spinodal type decomposition. However the identification of the CS mechanism is not simple because the precipitation that occurs during film growth is different from that which occurs during the preparation of bulk alloys used for calibration.

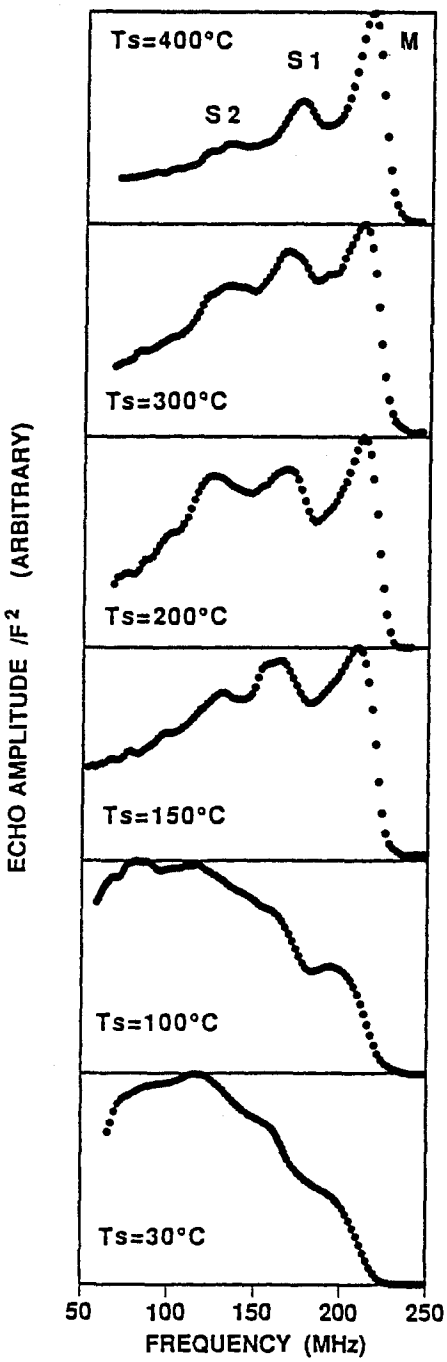


Fig. 8.3. ^{59}Co spin-echo NMR spectra at $T = 4.2$ K of $Co_{78}Cr_{22}$ rf sputtered alloy films as a function of substrate temperature (after Takei and Maeda 1991).

TABLE 8.2
Main NMR line frequency giving Cr content for Co-rich regions vs. substrate temperature for spectra in fig. 8.3.

Substrate temperature T_S (°C)	Centre frequency of main line (MHz)	Cr content of Co-rich regions (at%)
150	210	7–9
200	212	6–8
300	212	6–8
400	215	5–7

The effects of substrate temperature will also be discussed in some of the following sections, where studies have, for example, been undertaken on Co–Cr based films with either Ta, Pt or Ni additives. However the essential ideas described here remain valid, that (i) substrate temperature plays a crucial role in CS and (ii) that NMR provides an extremely useful tool with which to probe CS.

8.4.2. Effect of sputtering bias voltage on Co–Cr alloy thin films

In the preceding section, the importance of substrate temperature in producing CS was emphasized, suggesting that a thermally-activated, diffusion-limited process is responsible for CS during film growth. The role of energetic ion bombardment in modifying the structure of a growing film is widely accepted. In this section the effect of modifying the energetic ion bombardment by changing the sputtering bias voltage (V_B) is explored.

Three representative NMR spectra, for different bias voltages, from a series $Co_{78}Cr_{22}$ thin alloy films are shown in fig. 8.4(a).

These films were grown at $T_S = 200$°C by rf magnetron sputtering with the bias voltage ranging from -100 to $+75$ V (Takei et al. 1994b; Rogers et al. 1995b). Magnetization data for the same series of films are shown in fig. 8.4(b). The effect of sputtering bias voltage on CS and the NMR spectra is clearly seen. A negative V_B encourages homogeneity, producing a NMR spectrum, for the film grown at $V_B = -50$ V, reminiscent of the bulk homogeneous alloy whilst a positive bias voltage of $V_B = +50$ V enhances CS. The frequency of the main line of the $V_B = +50$ V spectrum is approximately 215 MHz corresponding to a Cr content of Cr $= 5 \pm 1$ at%. Studies of the microstructure using transmission electron microscopy (TEM) together with a selective chemical etching technique show that changes in the NMR spectra are correlated with a significant modification of the microstructure (Takei et al. 1994b). A regular strip pattern, the so-called chrysanthemum pattern (CP) is observed in the films sputtered with a positive bias voltage, whereas only wide ill-defined boundaries between Co-rich and Cr-rich regions are observed for the negative bias voltage films. The orientation of the c-axis of the hcp Co is also affected by the bias voltage. A negative V_B promotes c-axis orientation perpendicular to the plane, thus producing films suitable of perpendicular recording. The saturation magnetization of these films is reduced. This reduction is consistent with a lower CS.

The results presented above suggest that Ar^+ ion bombardment causes initial random mixing, followed by the rapid quenching of the surface atoms. The problem then becomes

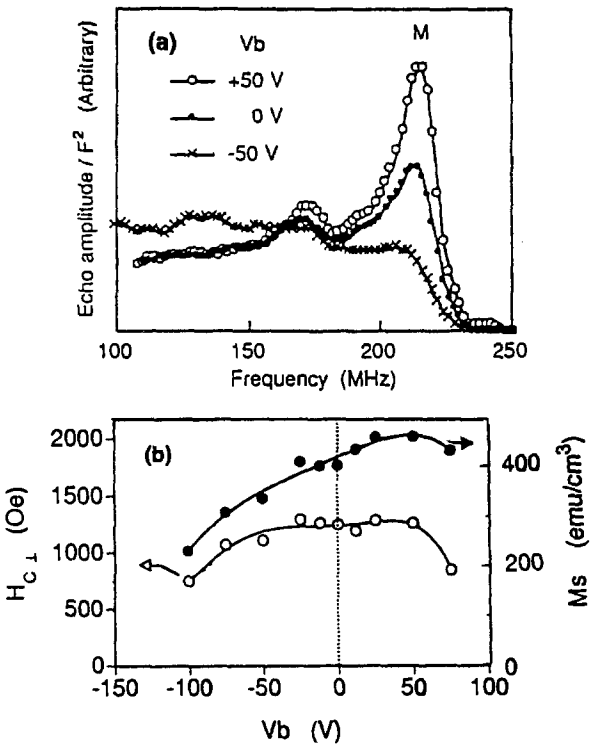


Fig. 8.4. Effect of varying the sputter bias voltage on the (a) the NMR spectra and (b) the magnetic properties (M_s and H_c) of 4000 Å $Co_{78}Cr_{22}$ films deposited at $T_s = 200°C$. After Rogers et al. (1995b) and Takei et al. (1994b), respectively.

one of reconciling the apparently contradictory observations that increasing the substrate temperature leads to increased CS whilst increasing the ion bombardment of a growing film (increased negative V_B) leads to the opposite effect. Although both growth modes seem to enhance surface diffusion of the adatoms, the kinetic process of ion bombardment is qualitatively different to that of thermal diffusion. The difference lies in the fact that the highly excited atoms near an ion impact site are able to travel significant distances, of the order of tens of nm, within a very short time scale (typically psec) thus producing on average a randomizing effect. Thermal diffusion, by contrast, promotes migration between neighboring lattice sites on times scales of seconds. Also it should be noted that since compositional separation is considered to appear at thermal equilibrium, the short life time of the adatom excitation may also be important in that there is insufficient time for CS to occur. Note that the bias voltage has a strong influence on the microstructure. This, together with compositional separation, indicates that CS is essentially a surface process that occurs during deposition.

Though Rogers et al. (1995b) and Takei et al. (1994b) do provide a detailed information on the effect of sputtering bias voltage on Co–Cr alloy thin films there remains considerable

scope for additional work in this highly relevant area of atomic surface mobility and the interesting compositional and microstructural effects that it can produce.

8.4.3. NMR of evaporated and ECR plasma sputtered Co–Cr based thin films

The technological importance of sputtering as a thin film deposition technique has ensured that most of the NMR work on Co–Cr based materials has been carried out on either dc or rf sputtered films. However a few studies have been undertaken on evaporated films (Yoshida et al. 1990; Lodder et al. 1993a), and recently, a report of NMR work on electron-cyclotron-resonance (ECR) plasma sputtered films was published (Hirono et al. 1995). The results from films produced by these methods are the subject of this section.

Different deposition techniques give different microstructures leading to modified compositional separation which result in differences in the NMR spectra. One of the first papers on Co–Cr thin alloy films was a study of films produced by evaporation (Yoshida et al. 1990). These early NMR results on evaporated films confirmed the existence of compositional separation, and associated electron microscopy work suggested that differences existed between evaporated and sputtered films. A more comprehensive study of evaporated films was undertaken by Lodder et al. (1993a) on obliquely evaporated Co–Cr films from both a single alloy source and using co-evaporation from two elemental sources. The oblique angle of evaporation allows process induced compositional separation to occur, enhancing the inhomogeneity between the Co-rich and Cr-rich regions of the film. The angle α_i between the film normal and the evaporation flux was chosen to be $\alpha_i = 27.5°$ for the results displayed in figs 8.5 and 8.6.

Figure 8.5 shows the NMR spectra obtained for three different single source evaporated Co–Cr alloy films where the average Cr content ranged from Cr = 13.2 at% to Cr = 26.6 at%. Spectra from four co-evaporated films are shown in fig. 8.6. Using the analysis techniques described in section 8.2.2 the NMR results together with magnetization data allow the Cr content of the Co-rich regions and their volume ratios to be estimated. This data is summarized in table 8.3. This work shows that single source evaporated Co–Cr films behave in a similar way to sputtered films, and that compositional separation is promoted by elevated substrate temperatures. In addition co-evaporated films exhibit a process-induced CS where the degree of separation produced at room temperature is similar to that of a single source film grown at high temperature.

The second deposition method we discuss in this section is the recently developed technique of electron-cyclotron-resonance plasma sputtering (Ono et al. 1984; Matsuoka and Ono 1989). This technique has the advantage of low sputtering gas pressure together with low energy/high current density leading to enhanced surface diffusion, the Ar pressure during deposition is typically 6×10^{-4} Torr. ECR sputtered films have the advantage over conventionally sputtered materials, in that high saturation magnetization and coercivity can be obtained simultaneously with small grain size. This is demonstrated in fig. 8.7 which shows the changes in the magnetic properties and the mean grain size measured at the surface by AFM as a function of deposition temperature.

The NMR result for a $Co_{78}Cr_{22}$ film grown at the optimum substrate temperature of 200°C is shown in fig. 8.8 and shows that a high degree of compositional separation has occurred, as comparison with the bulk alloy shows. The well defined line at 214 MHz is indicative of a highly Co-rich region of composition $Co_{94}Cr_6$. This NMR result confirms

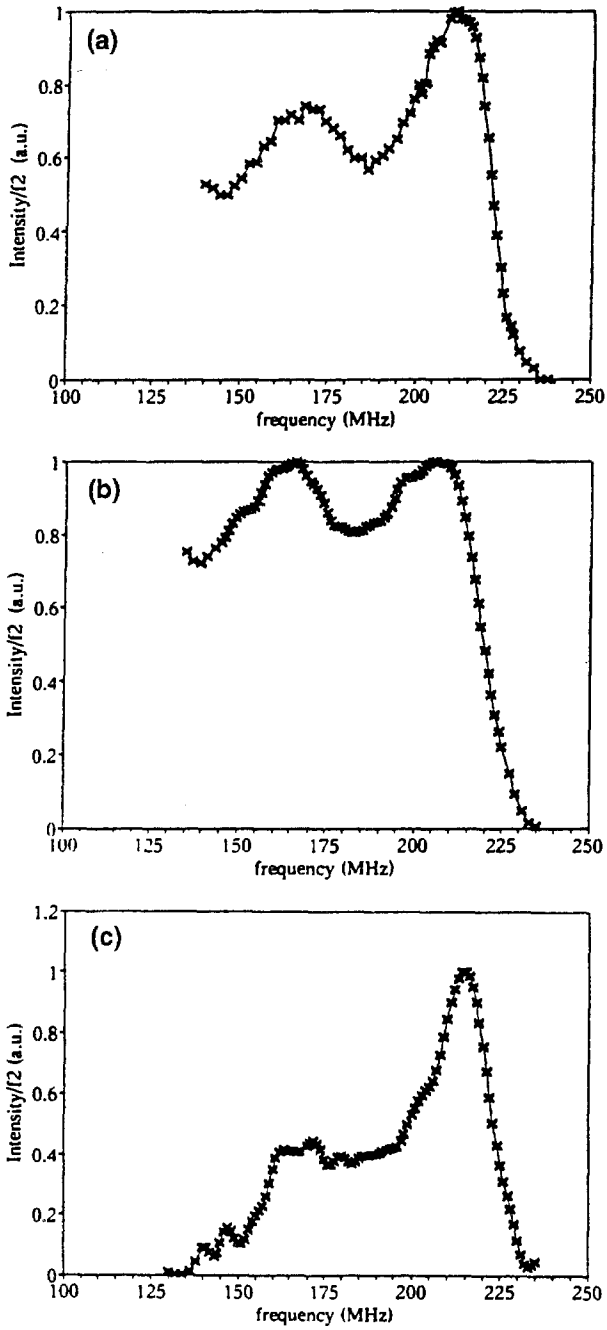


Fig. 8.5. ^{59}Co NMR spectra at $T = 4.2$ K of single source evaporated Co–Cr samples grown at RT and 400°C, for the thicknesses shown and having various average compositions: (a) RT, 1860 Å and Cr = 13.2 at%; (b) RT, 2270 Å and Cr = 18.6 at%; (c) 400°C, 2070 Å and Cr = 26.6 at%. After Lodder et al. (1993a).

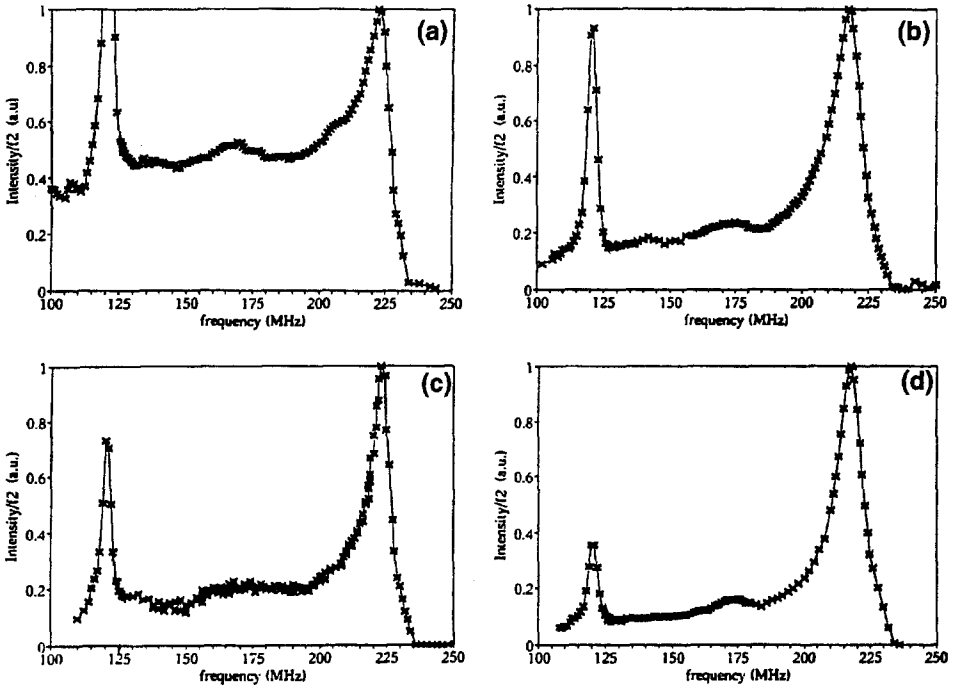


Fig. 8.6. ^{59}Co NMR spectra at $T = 4.2$ K of co-evaporated Co–Cr samples: (a) RT, 3560 Å and Cr = 24.7 at%; (b) 400°C, 3990 Å and Cr = 27.6 at%; (c) RT, 6480 Å and Cr = 21.5 at%; (d) 400°C, 7530 Å and Cr = 27.3 at%. The peak around 120 MHz results from a material component of the sample holder. After Lodder et al. (1993a).

TABLE 8.3

Summary of NMR and magnetization data for evaporated thin alloy films (Lodder et al. 1993a).

Sample	Figure (Ref.)	Film thickness (Å)	at% Cr (Xrf)	NMR local at% Cr		Calculated volume ratio	
				C_f	C_l	V_f	V_l
Co-evaporated RT	Fig. 8.6(a)	3560	24.7	3.0	36.9	0.36	0.64
	Fig. 8.6(c)	6480	21.5	2.5	33.6	0.39	0.61
Co-evaporated 400°C	Fig. 8.6(b)	3990	27.6	5.9	42.1	0.40	0.60
	Fig. 8.6(d)	7530	27.3	5.3	43.2	0.42	0.58
One source RT	Fig. 8.5(a)	1860	13.2	9.1	30.7	0.81	0.19
	Fig. 8.5(b)	2270	18.6	11.6	39.6	0.75	0.25
One source 400°C	Fig. 8.5(c)	2070	26.6	7.4	42.3	0.45	0.55

Notes:

C_f: concentration of Co-rich component without any Cr atoms among the nearest neighbors of Co;

C_l: concentration of less ferromagnetic components;

V_f: volume ratio of Co-rich component without any Cr atoms among the nearest neighbors of Co;

V_l: volume ratio of less ferromagnetic components;

RT: room temperature;

Xrf: X-ray fluorescence measurement.

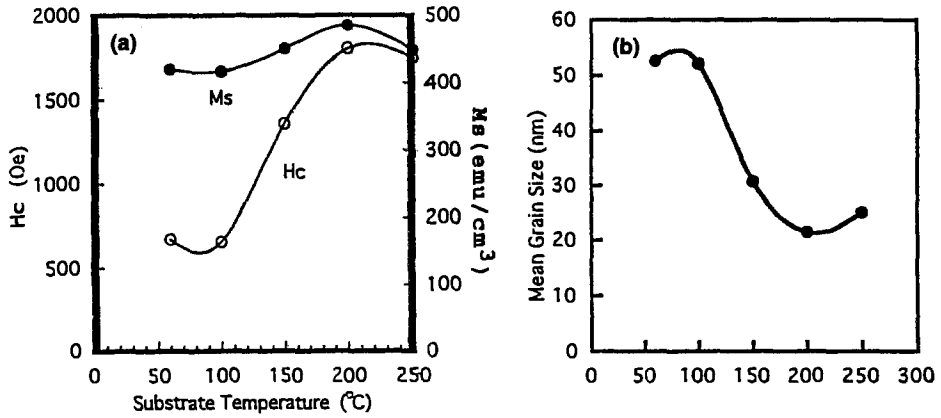


Fig. 8.7. Effect of substrate temperature for a 1000 Å thick $Co_{78}Cr_{22}$ film on (a) saturation magnetization and coercivity and (b) mean grain size as measured by AFM. After Hirono et al. (1995).

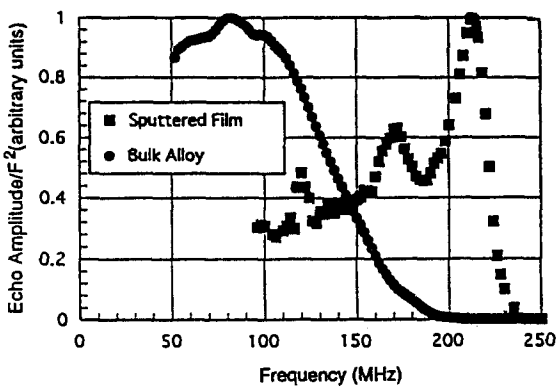


Fig. 8.8. ^{59}Co NMR spectrum for a $Co_{78}Cr_{22}$ 1000 Å film grown at 200°C together with a reference sample of the same composition. After Hirono et al. (1995).

that ECR plasma sputtered Co–Cr films exhibit a compositionally separated microstructure. This with the finer grain structure shown in fig. 8.7(b) potentially offers a more homogeneous distribution of finer Co-enriched regions leading to enhanced recording performance.

8.4.4. Studies of the effect of underlayers on Co–Cr based thin films

The importance of under or buffer layers to the recording performance of Co–Cr based thin films is well established as demonstrated for example by Fisher et al. (1986), Khan et al. (1991) and Christner et al. (1990). In particular the role of Cr underlayers appears to be a critical factor in determining recording noise (O'Grady 1990; Beardsley 1991; Shen et al. 1992). NMR studies of the effect of underlayers have been completed on Co–Cr–Ta films with Cr underlayers (Rogers et al. 1994a) and on $Co_{79}Cr_{21}$ films with Ge

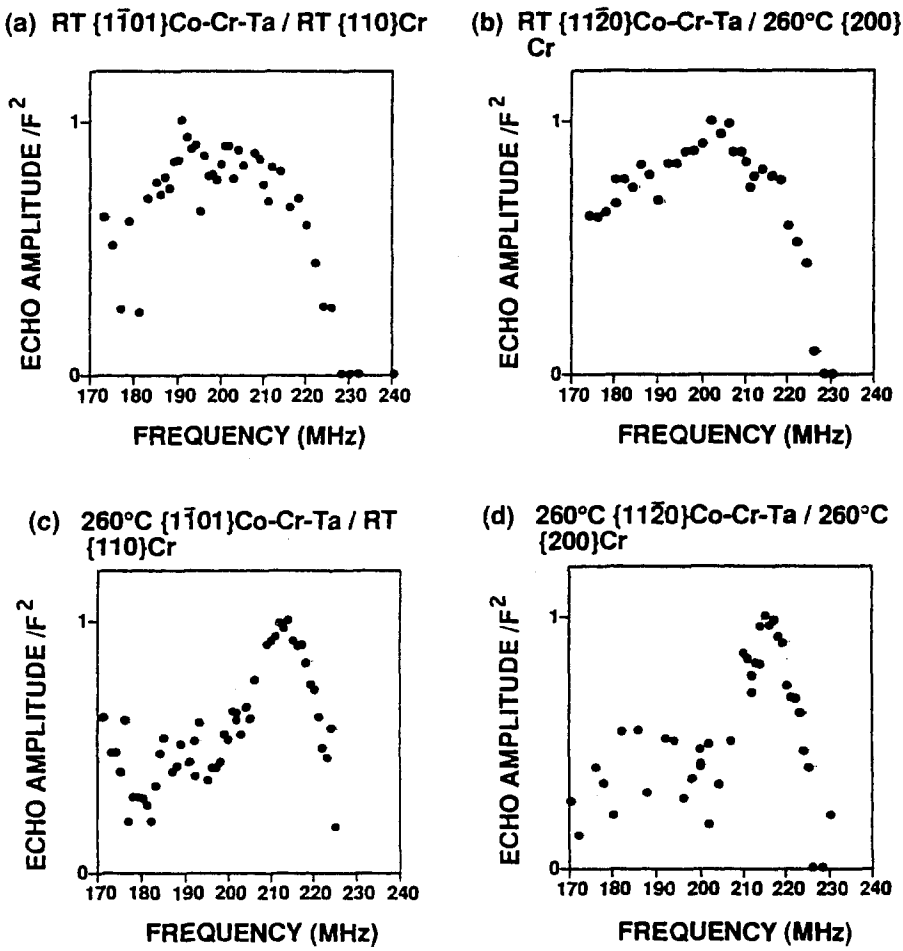


Fig. 8.9. ^{59}Co NMR spectra for the $Co_{82.8}Cr_{14.6}Ta_{2.6}$(400Å)/Cr(600Å) films listed in table 8.4. After Rogers et al. (1994a).

underlayers (Rogers et al. 1994b). Here we concentrate on the role of the crystallographic texture of the underlayer. It has been suggested (Rogers et al. 1994a) that one effect of the Cr underlayer is the promotion of a crystallographic texture in which the magnetic easy axis lies, essentially, in the plane of the film, Cr underlayers are also likely to increase the Cr-enrichment at the grain boundaries. Difference in recording performance have been noted (O'Grady 1990; Beardsley 1991; Shen et al. 1992) for {1 1 0}Cr/{1 $\bar{1}$ 0 1}Co–Cr–Ta and {2 0 0}Cr/{1 1 $\bar{2}$ 0}Co–Cr–Ta texture with the former exhibiting improved media noise characteristics. A series of four $Co_{82.8}Cr_{14.6}Ta_{2.6}$/Cr films with different textures were investigated using NMR (Rogers et al. 1994a). The details of which, together with some of their magnetic properties, are given in table 8.4. Spectra for these films are shown in fig. 8.9.

TABLE 8.4
Substrate temperature, texture and magnetic properties for a series of $Co_{82.8}Cr_{14.6}Ta_{2.6}$(400Å)/Cr(600Å) films (after Rogers et al. 1994a).

Sample	T_s (°C) Co–Cr–Ta/Cr	Texture Co–Cr–Ta/Cr	ΔM (peak)	H_c (Oe) in-plane
A	RT/RT	$\{1\bar{1}01\}/\{110\}$	+0.58	788
B	RT/260	$\{11\bar{2}0\}/\{200\}$	+0.68	796
C	260/RT	$\{1\bar{1}01\}/\{110\}$	+0.07	1662
D	260/260	$\{11\bar{2}0\}/\{200\}$	+0.17	1752

Figure 8.9 clearly shows that the films deposited at higher temperatures have significantly greater compositional separation as shown by the relatively sharp main lines centred at approximately 215 MHz, fig. 8.9(c) and (d). This centre frequency indicates that the Co-rich regions have a composition of $\sim Co_{94}Cr_6$. The films deposited at room temperature fig. 8.9(a) and (b) show some CS with the NMR frequency centred at approximately 200 MHz giving a composition of $Co_{88}Cr_{12}$. The NMR measurements were unable to discriminate between the different textures indicating that the composition of the Co-rich regions is not sensitive to the texture. However it is perfectly possible to speculate that the distribution of Co-rich regions does change and hence lead to changes in recording performance.

Results obtained for Co–Cr thin films deposited on Ge (Rogers et al. 1994b) underlayers mirror the results for Cr underlayers. Here, again, substrate temperature was found to be the determining factor leading to compositional separation, with the NMR spectra showing no significant differences for films deposited on substrates with and without Ge underlayers.

8.4.5. NMR and thickness dependence of compositional separation in Co–Cr based thin films

A number of the NMR studies of Co–Cr based thin films have used films of different thicknesses, however only one paper to date (Rogers et al. 1994a) has systematically investigated the effect of film thickness on compositional separation using NMR. In this study (Rogers et al. 1994a) both $Co_{78}Cr_{22}$ and $Co_{86}Cr_{12}Ta_2$ films were investigated, the NMR results from which are shown in fig. 8.10. Both sets of films were deposited at $T_s = 200$°C by rf sputtering. The spectra for compositional homogeneous bulk samples are included for comparison.

Figure 8.10 shows that all the films exhibit a strong main line centred above 200 MHz. This clearly demonstrates that a Co-rich component exists an all the films and that compositional separation occurs throughout film growth. However as the film thickness increases it can be seen that the main line shifts to lower frequencies whilst the relative height of the satellite peak ($\sim$175 MHz) increases. The shift in the main line indicates that the Co content of the Co-rich regions is decreasing. The relative increase in the satellite line strength shows that the proportion of the film which is homogeneous increases (Maeda and Takei 1991; Takei and Maeda 1991). Both Co–Cr and Co–Cr–Ta films have a main line frequency of

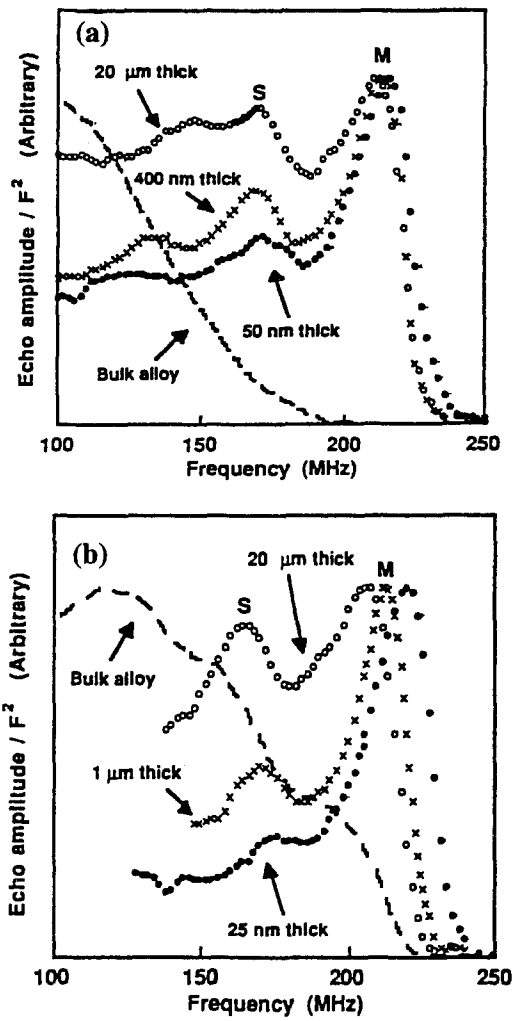


Fig. 8.10. ^{59}Co spin-echo NMR spectra as a function of film thickness for (a) $Co_{78}Cr_{22}$ film deposited at T_s = 200°C and (b) $Co_{86}Cr_{12}Ta_2$ film deposited at T_s = 200°C.

$\geqslant$218 MHz for film thicknesses of less than 500 Å. This corresponds to a Co-rich region Co $\geqslant$ 96 at%, and demonstrates that substantial CS occurs in the initial growth stage. For a film thickness of 20 μm the main line frequencies are around 212 MHz for the Co–Cr film and 205 MHz for the Co–Cr–Ta film. This corresponds to a Co-rich component of Co = 93 at% and Co = 90 at%, respectively. Since the average Co content is Co = 78 at% for the Co–Cr film considerable CS is still present. However for the Co–Cr–Ta film, the average Co content is Co = 86 at% and so only weak CS is present in this film.

NMR as a function of film thickness together with TEM work and magnetization data (Rogers et al. 1994a, 1994b, 1994c) has demonstrated that thinner films have a higher

density of smaller Co-enriched regions. Magnetization measurements show a decrease in M_S with increasing film thickness for both Co–Cr and Co–Cr–Ta films as a result of the reduction in proportion of the film that is compositionally separated.

8.4.6. NMR studies of the effect of additives in Co–Cr based thin films

The intense interest in Co–Cr based thin films arises from their use as recording media in disk drives, as mentioned in section 8.1. The production processes of longitudinal recording media may utilize Co–Cr alloyed with a small quantity of one or more additional elements such as Ta, Pt or Ni to improve the media's recording performance. In the preceding sections, mention has been of these ternary/quaternary alloys where appropriate. In this section, we review a more systematic account of the differences between three types of ternary alloy thin films Co–Cr–X where X is Ta, Pt or Ni. This work was performed by Maeda et al. (1994a, 1994b). The films investigated were (i) $Co_{86}Cr_{12}Ta_2$, (ii) $Co_{78}Cr_{13}Pt_9$ and (iii) $Co_{62.5}Cr_{7.5}Ni_{30}$ all the films were 500 Å thick and grown by in-line dc magnetron sputtering at $T_s = 25°C$ or 150°C on Cr underlayers. Figure 8.11 shows the NMR spectra obtained from these three samples together with reference bulk alloys of the sample composition.

In all the Co–Cr–X alloy films the NMR signal above 200 MHz becomes stronger as the substrate temperature increases from 25°C to 150°C, indicating the promotion of compositional separation. Comparison of the films with the reference alloys shows the Co–Cr–Ta film exhibits the greatest differences and therefore the largest CS. The Co–Cr–Pt film also shows considerable CS, however the Co–Cr–Ni system is significantly less compositionally separated and this may explain why both Co–Cr–Ta and Co–Cr–Pt films show good recording characteristics. As a cross-reference it should be noted that in section 8.4.4 on the effect of Cr underlayers in promoting CS is discussed for both Co–Cr and Co–Cr–Ta films.

8.4.7. NMR studies of magnetic anisotropy in Co–Cr thin films

In section 4 it was noted that NMR signals are more easily observable in ferromagnetic materials due to the enhancement effect of the electronic magnetization. Thus from eq. (4.2), in single domain systems the magnetic field at the nuclei due to the rf pulse can be written as

$$B_1 = B_{\text{eff}} B_{\text{rf}} / (B_0 + B_A), \tag{8.1}$$

where B_1 – total rf field at the nucleus perpendicular to the easy axis, B_{eff} – the effective magnetic field at the nucleus (hyperfine field), along the easy axis, B_{rf} – the applied rf field perpendicular to the easy axis, B_0 – any applied dc field along the easy axis, B_A – the anisotropy field along the easy axis.

If B_A is single valued then the maximum NMR signal is obtained for a particular value of B_{rf}. If however, B_A has a distribution of values then examining the NMR signal as a function of B_{rf} gives information on this distribution. Note that, as discussed in section 4, the presence of domain walls result in an additional enhancement of the signal and must be taken into account in the determination of anisotropy fields or in comparative studies of the effects of anisotropy fields on the NMR spectra.

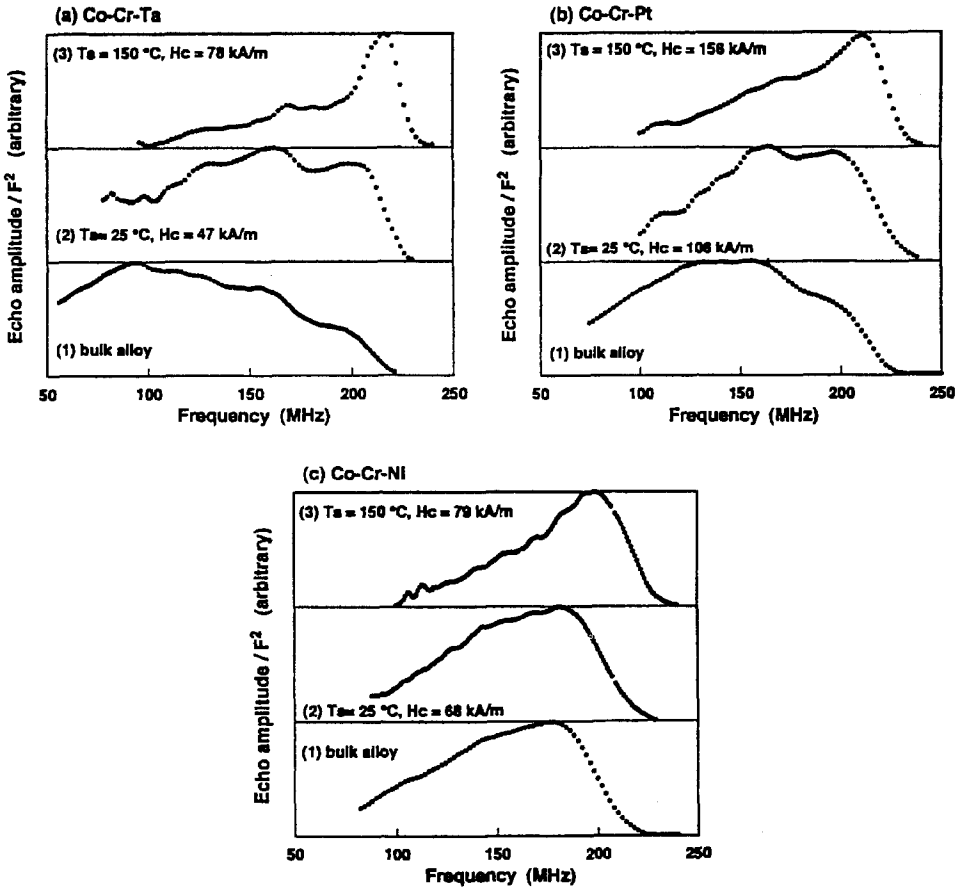


Fig. 8.11. ^{59}Co NMR spectra for films deposited at $T_s = 25$ and 150°C together with a reference alloy spectrum for (a) $Co_{86}Cr_{12}Ta_2$, (b) $Co_{78}Cr_{13}Pt_9$, (c) $Co_{62.5}Cr_{7.5}Ni_{30}$. After Maeda et al. (1994a).

Magnetic anisotropy has been studied using NMR in a series of $Co_{78}Cr_{22}$ films, 5000 Å thick, grown at substrate temperatures between 40–400°C (Takei et al. 1994a). The magnetic properties of this series of films are listed in table 8.5 together with the dispersion in the hcp Co c-axis orientation ($\Delta\theta_{50}$) obtained from X-ray diffraction measurements.

Figure 8.12 shows the variation of echo intensity at 214 MHz as a function of rf pulse amplitude B_{rf} for the films listed in table 8.5. A single peak is observed for the film grown at $T_s = 40$°C labeled (x) in fig. 8.12. As T_s increases this peak broadens towards higher B_1 giving a shoulder to peak (x) labeled (x′). This shoulder suggests the development of another magnetic component with a higher anisotropy field. However it should be noted that only Co nuclei which have resonant frequencies of 214 MHz are able to contribute to this spectral intensity. The (x′) peak appears to be largest for the film grown at $T_s = 300$°C and this corresponds to the highest value of $H_{k\perp}$ in table 8.5. It is suggested (Takei et al. 1994a)

TABLE 8.5
Properties of 5000 Å thick $Co_{78}Cr_{22}$ films deposited at various substrate temperatures (after Takei et al. 1994a).

Sample number	T_s (°C)	$\Delta\theta_{50}$ (°)	M_s (emu/cm^3)	$H_{c\perp}$ (Oe)	$H_{c\parallel}$ (Oe)	$H_{k\perp}$ (Oe)
1	40	3.3	364	233	139	4580
2	100	4.0	386	566	291	5020
3	150	4.9	417	873	312	5890
4	200	4.9	486	1240	380	6300
5	300	8.9	478	1830	538	6390
6	400	>10	400	1440	933	4980

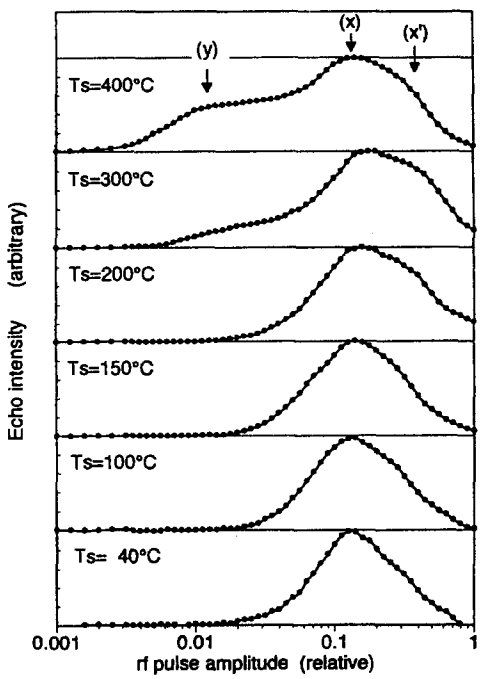


Fig. 8.12. Variation of ^{59}Co spin echo intensity as a function of rf pulse amplitude (B_{rf}) for a series of films grown with T_s = 40–400°C at a frequency of 214 MHz (after Takei et al. 1994a).

that this high B_A component may be attributed to magnetically isolated regions which develop as the extent of the compositional inhomogeneity increases, assuming that the decreased demagnetization factor contributes to the increased B_A. An additional peak starts to develop at position (y) for $T_s \geqslant 300$°C. Peak (y) represents a magnetic component with low H_A, approximately 1/10 of that of the remainder of the sample, however its volume fraction is quite small.

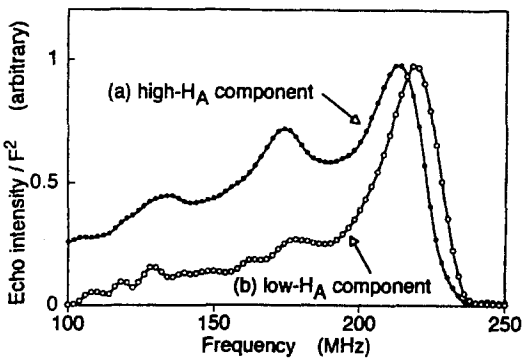


Fig. 8.13. ^{59}Co spin echo spectra for a $Co_{78}Cr_{22}$ film deposited at $T_s = 400°C$ measured at the rf magnetic field amplitude indicated by (x) and (y) in fig. 8.12. After Takei et al. (1994a).

If the magnetic anisotropy has two distinct values as with the film grown at $T_s = 400°C$, then it is possible to take NMR spectra for each anisotropy field. Such spectra are shown in fig. 8.13, (a) for the high B_A component and (b) for the low B_A components for the respective pulse amplitude conditions (x) and (y) in fig. 8.12.

Figure 8.13 shows that the satellite line intensities for the low B_A spectrum (b) are reduced compared with the high B_A spectrum (a). Figure 8.13 also shows that the low B_A main line position (219 MHz) is at a higher frequency than the corresponding high B_A line (213 MHz), indicating that the low B_A regions are more Co-rich. Using the calibration techniques described in section 8.2.2 the low B_A regions are estimated to have Cr = 2 at% while the higher B_A regions have Cr = 5 at%. Thus NMR is able to give useful information on inhomogeneities within the Co-rich, compositionally separated regions which cannot be obtained by other techniques such as FMR.

8.5. NMR in Co/Cr multilayers

In the introductory section it was noted that the majority of NMR work on thin film Co–Cr had been done on alloy films. However a small literature exists on Co/Cr multilayers (Stearns et al. 1988; Houdy et al. 1991; Henry et al. 1993) and this is the subject of this section. The most comprehensive NMR study of these systems completed prior to 1998 is the work of Henry et al. (1993), where structural characterization using RHEED and magnetization measurements were combined with NMR. A series of multilayer films where the Cr thickness was fixed at 8 Å and with Co thickness of 8, 16, 24 and 32 Å were prepared by UHV evaporation onto mica substrates with a Ru buffer layer (Henry et al. 1993). Ten multilayer repeat units were deposited together with a 40 Å Cr protection layer. The NMR spectra obtained from the films with the three thickest Co layers 16, 24 and 32 Å are shown in fig. 8.14. (The multilayer with Co(8Å)/Cr(8Å) produced no measurable NMR signal.)

The frequency of the main line (220 MHz) shows that the Co is essentially in the hcp phase with some fcc stacking faults throughout the Co layer. This is demonstrated by the

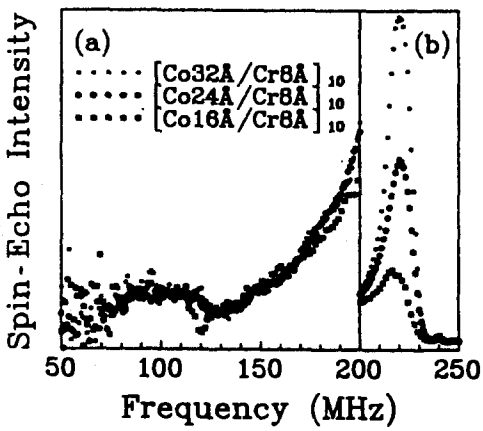


Fig. 8.14. ^{59}Co NMR spectra of [Cr(8Å)/Co(t_{Co})]$_{\times 10}$ multilayers with t_{Co} = 16, 24 and 32 Å. The low frequency side of the spectra (a) are magnified 4 times while the high frequency side (b) shows the increase of the main line intensity with increasing Co layer thickness. After Henry et al. (1993).

fact that the main line frequency does not depend on the Co layer thickness and so the reduction in frequency from the expected 228 MHz (for magnetization in the [0 0 0 1] plane) cannot be attributed to strain, as strain would be expected to change as a function of Co layer thickness.

The extended tail below the main line originates from Co atoms in the interfacial regions, where at least one Co nearest neighbour atom has been substituted by Cr. The low frequency side of the spectrum of the films with Co layers of 24 and 32 Å essentially superimpose. This shows that these two multilayers have the same interfacial structure. The interface spectrum for the 16 Å Co layer film is slightly different. Here, the Co thickness dependence of the main intensity allows an estimate to be made of the amount of interfacial mixing in the Co layers. However, as the NMR measurement averages over all the interfaces it is not possible to obtain reliable information on any asymmetries that might be present between the way in which Co grows on Cr and Cr grows on Co. The data in fig. 8.14 suggest that interfacial mixing extends over approximately 11 Å or 5 monolayers. This relatively large (c.f. Co/Cu) value is consistent with both the fact that no signal could be observed in the Co(8Å) multilayer and that the Co(16Å) multilayer shows a different interface structure compared with the two thicker Co layer samples.

In an attempt to extract more detailed information on the concentration profile of the interfacial region a number of interface models were developed (Henry et al. 1993). The result of this work suggested that the Cr content of the first mixed layer was relatively low Cr = 3–7 at% and then increased rapidly in the second and third mixed layers, saturating at Cr = 50–80 at%. Figure 8.15 shows the results of the model of the Cr concentration in the mixed interfacial region. This model indicates that approximately 1.8 Co monolayers at the interface are magnetically dead. Magnetization measurements are consistent with the proposition that the interfacial region consists of about 5 monolayers of which approximately 1.4 are magnetically dead. This is in good agreement with the estimate obtained from NMR measurements.

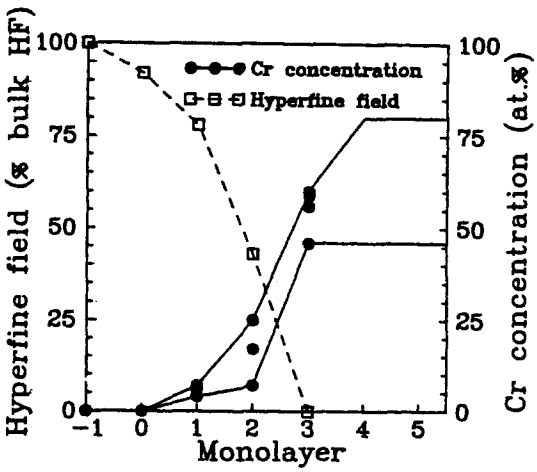


Fig. 8.15. Cr concentration and average hyperfine field (to first order, magnetization) profile in the interface. The monolayer at zero corresponds to a full plane of Co atoms which is in contact with the interface. The two continuous lines show the minimum and maximum monolayer concentration value, consistent with the interface model. After Henry et al. (1993).

The earlier work of Houdy et al. (1991), which was based mainly on X-ray diffraction, had suggested that some of the Co was in the bcc phase. However there is no real evidence of a NMR line at the 198 MHz associated with bcc Co. An unambiguous identification of bcc Co is difficult in Co–Cr spectra which, because of the large dependence of the resonant frequency of ^{59}Co nuclei on Cr concentration (−2 MHz/at% Cr), often extend from 240 MHz to below 100 MHz.

9. NMR investigations of Co based thin films

In the previous two chapters we have discussed the contribution made by NMR to the understanding of Co–Cu and Co–Cr thin films. The technological importance of these materials has ensured that both these systems have been studied in considerable depth. However a significant amount of work on other Co based thin films has also been undertaken, although perhaps not as exhaustively as Co–Cu and Co–Cr. In this section we review the work carried out on these other Co based thin films.

9.1. NMR studies of Co/Au multilayers

Although the Co/Au system was among the first of the artificial layered materials produced relatively few NMR studies have been published (Le Dang et al. 1986a; Cesari et al. 1989; de Gronckel et al. 1991a; Beauvillain et al. 1996). This is in part explained by the comparatively unexciting magnetic properties of this system. However it remains a relatively straightforward multilayer to produce and is often used to check the deposition characteristics of sputtered or MBE growth chambers. The NMR work completed on Co/Au thin films is detailed in table 9.1.

TABLE 9.1
NMR studies of Co/Au thin film trilayers and multilayers.

Reference	Growth technique	Substrate/buffer	Composition	Orientation	Comments (important result)
Le Dang et al. (1986a)	UHV evaporation	Au(260Å)	Au/Co(80Å)/Au	*c*-axis perpendicular to plane	Crystal phase and the anisotropy of the Co hyperfine field studied in Co/Au multilayers. Polycrystalline Co layers found to have hcp structure with the anisotropy in the hyperfine field similar to that of bulk hcp Co.
Cesari et al. (1989)	UHV evaporation	Glass	Au/Co(3–80Å)/Au	*c*-axis essentially perpendicular to plane	Changes in phase of Co examined as a function of Co layer thickness for Au/Co/Au trilayers. NMR not observed of Co < 20 Å, low frequency tail observed for Co < 40 Å. Co principally in hcp phase with *c*-axis fluctuating about the film normal.
de Gronckel et al. (1991a)	HV evaporation	Oxidized Si	$[Co(40Å)/Au(24Å)]_{\times 20}$		Co/Au multilayers compared with Co/Ir and Co/Cu. Co in fcc phase but the NMR line is rather broad compared with Co/Cu.
Beauvillain et al. (1996)	UHV evaporation	Silica	Au(250Å)/Co(70Å)/Au(100Å)	(1 1 1)	The effects of substrate induced strain in Co/Au multilayers evaluated. Removing the multilayer from its substrate resulted in a decreased anisotropy field as measured by a shift in the NMR spectrum.

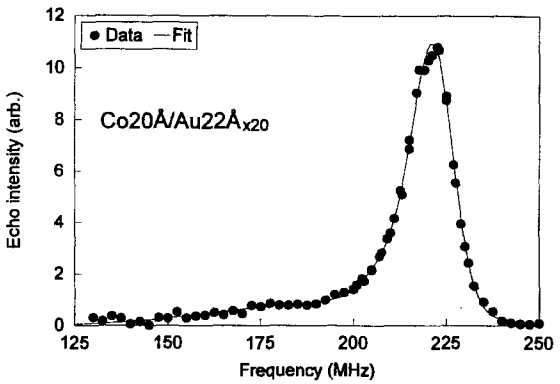


Fig. 9.1. ^{59}Co NMR spectrum of [Co(20Å)/Au(22Å)]$_{x20}$ multilayer grown by MBE on a GaAs/Ge/Co substrate/buffer (Thomson et al. unpublished).

The lattice mismatch between Au (fcc a_0 = 4.08 Å) and Co (fcc a_0 = 3.54 Å) ensures that the well defined epitaxial registry, which leads to strong signals from a specific interface environment in Co/Cu, is absent in Co/Au. However Au provides a good platform on which to grow thin Co layers as it produces a well oriented surface (parallel to (1 1 1)) and is atomically flat over large (~1000 Å) lateral dimensions. Both Au/Co/Au trilayers (Le Dang et al. 1986a; Cesari et al. 1989; Beauvillain et al. 1996) and multilayers [Co/Au]$_x$ have been studied by NMR. A typical result is shown in fig. 9.1.

Figure 9.1 shows that Co is essentially in the hcp phase as the frequency of the main line is centred at 222 MHz. This together with the width of the line and its asymmetry are characteristic of the results from both trilayers and multilayers. The greater spectral intensity in the low frequency side of the spectrum indicates that some fcc stacking faults are present. A study of Co layer thickness in Au/Co/Au trilayers (Cesari et al. 1989) revealed that the frequency of the main line increased towards 228 MHz as the Co layer thickness was increased. A small reduction in the width of the line was also observed. These results show that a reduction in fcc stacking faults occurs as the Co thickness increases and the Co becomes pure hcp. This result is in agreement with work done on Co/Cu (1 1 1), where increasing the thickness of the Co layers also led to a more hcp like structure.

Work has also been done to determine the contribution that strain makes to the magnetic anisotropy in Au/Co/Au trilayers (Beauvillain et al. 1996). Two similar Co films were grown on a Au capped silica substrate, one film was deposited at room temperature whilst the other was deposited at 130°C. Spectra for both films are shown in fig. 9.2(a). Sample A, grown at room temperature, clearly shows both the fcc (217.4 MHz) and hcp (220–228 MHz) phases while sample B grown at 130°C shows much greater hcp character. These results are in line with those in fig. 9.1 which demonstrate that Co in the Co/Au system is essentially hcp in character.

Removal of the films from the silica substrate has a significant effect on the NMR spectra fig. 9.2(b). The trilayers were removed from the substrate by coating the film with nitro-cellulose varnish, which adheres well to the top Au surface, and then peeling the film off the silica substrate. The nitro-cellulose varnish contracts at low temperature leading to the

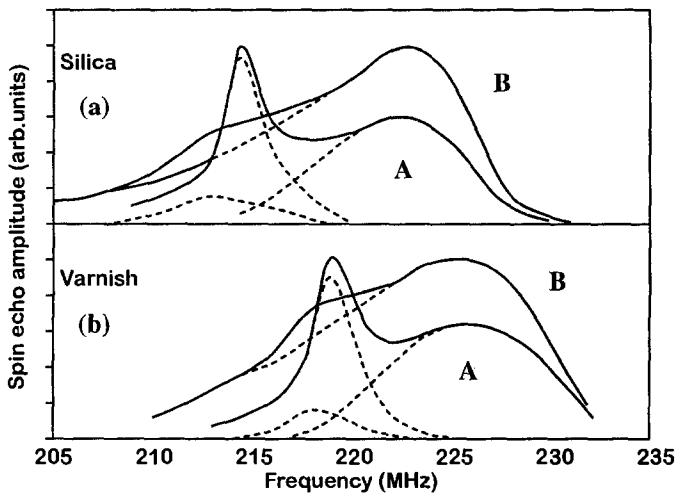


Fig. 9.2. ^{59}Co spin echo spectra for Au(250Å)/Co(70Å)/Au(100Å) trilayers at $T = 2$ K (a) as deposited on to the silica substrate at RT (A) and 130°C (B), and (b) the same films following removal from the substrate using nitro-cellulose varnish. After Beauvillain et al. (1996).

positive shift in frequency of 3 MHz observed in fig. 9.2. Expressed in terms of volume, a shift of 3 MHz suggests $\delta V/V = -1.2\%$. This leads to a negative magnetoelastic contribution to the magnetic anisotropy, dramatically reducing the total anisotropy field. Hence the NMR results give a direct explanation of the magnetic properties of the trilayer.

9.2. NMR studies of Co/Ag multilayer and alloy thin films

NMR investigation have been undertaken on both Co–Ag alloy thin films (Lodder et al. 1993b) and Co/Ag multilayers (van Alphen et al. 1994b, 1995). Although there has been a significant amount of interest in this system due to the giant magnetoresistance (MR) exhibited by both alloy and multilayer films only a limited number of NMR studies have been conducted and published as shown in table 9.2.

The results quoted (Lodder et al. 1993b) for granular alloys suggest compositional separation similar to that which occurs in Co–Cr (see section 8.4) is also present in these alloy films. Co/Ag multilayers have received more attention and two related studies on the effect of Co layer thickness (van Alphen et al. 1994b) and post-deposition annealing (van Alphen et al. 1995) have been completed. A series of films, each containing 100 bilayers, where the Ag layer thickness was kept constant at 20 Å were deposited on to Si (1 0 0) by magnetron sputtering. The Co layer thickness was varied between Co = 4 Å and Co = 100 Å. NMR results for the films with Co layers between 4 and 15 Å are shown in fig. 9.3. The intensity is normalized to the nominal Co thickness.

It is clear that Co exists in the bulk environment even for layers of only nominally 4 Å thick, i.e., 2 monolayers. Hence Co cannot grow in a layer-by-layer mode, but rather as three-dimensional islands. The relative intensities of the bulk and interface lines are shown in fig. 9.4 together with their ratio. Increasing the thickness of

TABLE 9.2
NMR studies of Co/Ag multilayer and alloy thin films.

Reference	Growth technique	Substrate/buffer	Composition	Orientation	Comments (important result)
Lodder et al. (1993b)	H.V. co-evaporation	Si(1 0 0)	$Co_{85-35}Ag_{15-65}$	(1 1 1)	NMR results quoted but not shown. Compositional separation similar to that observed in Co–Cr alloy thin films was reported.
van Alphen et al. (1994b)	Magnetron sputtering	Si(1 0 0)	$[Co(4–100Å)/Ag(20Å)]_{\times 100}$	(1 1 1)	Co/Ag multilayers studied as a function of Co layer thickness. Co found to be in a mixed fcc, hcp and stacking fault phase. For Co < 10 Å a 3D island (~50 Å diam.) growth mode is observed. The ideal (1 1 1) interface line is measured at 174 MHz.
van Alphen et al. (1995)	Magnetron sputtering	Si(1 0 0)	Co(8Å)/Ag(20Å) Co(15Å)/Ag(20Å)	(1 1 1)	Strain relaxation, phase separation and interfacial roughness investigated in Co/Ag multilayers as a function of thermal annealing. Annealing produces a strain relaxation resulting in the growth of Co clusters and a change in interfacial roughness due to a loss of coherence at flatter interfaces. Co cluster growth initially results in an increased magnetoresistance.

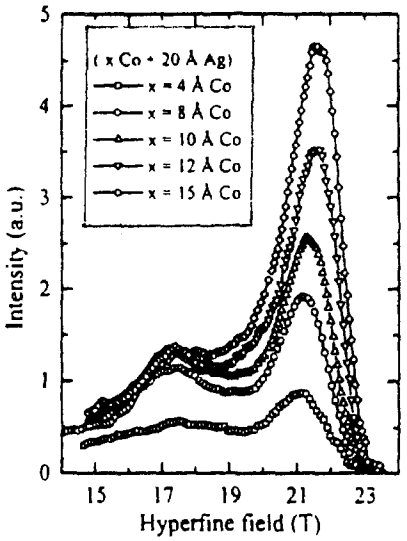


Fig. 9.3. ^{59}Co NMR spectra for $[Co(x)/Ag(20Å)]_{\times 100}$ multilayers where 4 Å < x < 15 Å measured at 1.5 K. The integral of the spectra are normalized to the nominal Co thickness and the spectra are corrected for enhancement. After van Alphen et al. (1994b).

the Co layers to 10 Å results in a similar relative increase in both the bulk and interface NMR signal implying that either the number of three dimensional islands increases or that the islands grow larger. Increasing the Co layer thickness further only increases the bulk spectral intensity demonstrating that Co then grows as a continuous layer. This implies that the first few Co layers are essentially clusters up to 5 monolayers thick. Fitting a simple model of the ratio of interface to bulk spectral intensity allows the lateral dimensions of the islands to be estimated at about 50 Å.

Work on annealed Co/Ag multilayers (van Alphen et al. 1995) demonstrates that annealing promotes smoother interfaces, strain relaxation and phase separation. Figure 9.5 shows the effect of annealing Co/Ag multilayers with Co thicknesses 8 Å and 15 Å made by magnetron sputtering.

Contributions from nuclei in both the bulk (~21 Tesla) and interfacial (<20 Tesla) environments are clearly seen. The line at 17.5 T is assigned to Co atoms at a locally flat (1 1 1) interface. The main and interface lines are much broader than similar lines found in Co/Ni and Co/Cu multilayers where Co is mainly in the fcc phase and this is interpreted as a mixture of fcc and hcp Co together with stacking faults.

The important feature is that a similar shift in the main line to higher frequencies is observed for both multilayers. This is caused by strain relaxation which is attributed to a growth of the Co clusters described earlier as well as a loss of coherence between Co and Ag atoms at flatter (more perfect) interfaces. Magnetoresistance measurements as a function of annealing temperature show a somewhat different behaviour. The Co = 8 Å sample has a well defined maximum in MR at 350°C whereas the Co = 15 Å sample does

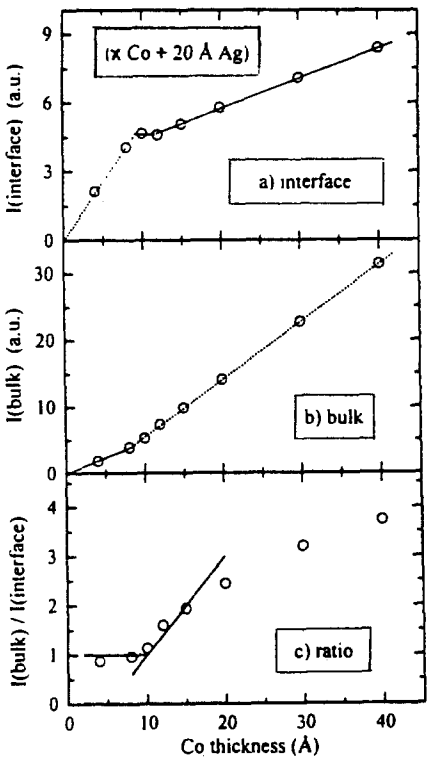


Fig. 9.4. NMR spectral intensity as a function of Co layer thickness for multilayers with the structure $[Co(x)/Ag(20Å)]_{100}$ for (a) the interface (corresponding to the integrated signal for hyperfine fields 15–19.5 T); (b) the bulk (19.5–23 T); and (c) the ratio between the bulk and interface. The dotted lines are only as a guide to the eye. After van Alphen et al. (1994b).

not. Given that the strain relaxation is similar in both samples it is clear that in these multilayers strain is not an important factor for MR. The suggested mechanism (van Alphen et al. 1995) for the observed change in MR is a change in the cluster size and separation. This occurs as a result of the different as deposited structures, i.e., granular for Co = 8 Å and continuous for Co = 15 Å, as previously mentioned.

9.3. NMR investigations of Co/Pt and Co/Pd multilayers

We consider these two multilayer systems together as they have strong similarities. Both have fcc crystal lattices with similar lattice constants ~3.90 Å which are about 9% greater than for fcc Co (3.54 Å). Pt and Pd readily alloy with Co and both are easily polarized, so that magnetic moments of a substantial fraction of a Bohr magneton can be induced. These factors lead to considerable complication in interpreting NMR data and this may account for the relatively few NMR studies that have been completed, despite the considerable interest in these materials as potential recording media. The NMR studies completed are detailed in table 9.3.

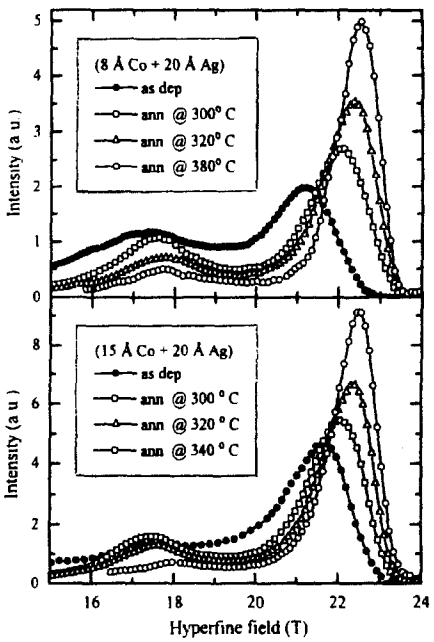


Fig. 9.5. ^{59}Co NMR spectra of (a) $[Co(8Å)/Ag(20Å)]_{\times 100}$ and (b) $[Co(15Å)/Ag(20Å)]_{\times 100}$ as a function of annealing temperature. All the spectra are normalized to the Co thickness.

9.3.1. NMR studies of Co/Pd multilayers

The study of de Gronckel et al. (1989) on Co/Pd [1 0 0] multilayers grown by UHV e-beam evaporation examined the NMR spectrum as a function of both Co and Pd layer thicknesses as shown in fig. 9.6.

Interpretation of these spectra is complicated by the fact that the hyperfine field distribution was determined by varying the applied field at fixed rf frequency. However clear differences exist between the multilayers where Co $\geqslant$ 20 Å and those with much thinner individual Co layers. The multilayers with thick Co layers have essentially the same spectral profile as a single layer Co film, fig. 9.6(a) and (b). This shows that the contribution from Co in the bulk environment dominates as expected. Reducing the layer thickness to Co = 20 Å (fig. 9.6(c)) and Co = 8 Å (fig. 9.6(d)) leads to a considerable shift in spectral intensity to lower frequencies. Examining the Co = 20 Å spectrum in detail shows two broad lines centred at 203 and 213 MHz, while the Co = 8 Å multilayer has a single broad line centred at 200 MHz. Similar results (de Gronckel et al. 1989) were obtained for Co/Pd multilayers oriented in the [1 1 1] direction demonstrating that to a first approximation the frequency shift is isotropic. The data on Co/Pd multilayers was interpreted in terms of an expansion of the Co lattice by the larger Pd lattice. However the role of interfacial mixing was not discussed and given the miscibility of the elements it seems unlikely that such mixing can be ignored.

A more recent NMR study (Lesnik and Gontarz 1995) of sputtered Co/Pd multilayers concluded that significant interfacial mixing occurred, as for thin Co $\leqslant$ 10 Å layers no

TABLE 9.3
NMR investigations of Co/Pt and Co/Pd multilayers.

Reference	Growth technique	Substrate/buffer	Composition	Orientation	Comments (important result)
Co/Pd multilayers					
de Gronckel et al. (1989)	UHV e-beam evaporation	Glass or NaCl/Ti(100Å)/Pd(100Å)	Co(8–200Å)/Pd(13.5–90Å)	(1 1 1)	Co/Pd multilayers studied by FMR and NMR. FMR showed that anisotropy changed to perpendicular to plane below Co = 8 Å, anisotropy also observed to increase for Pd < 20 Å. NMR demonstrated polycrystalline fcc Co, with shift to lower frequencies for decreasing Co thickness which was assigned to Co lattice expansion by Pd.
Lesnik and Gontarz (1995)	Magnetron sputtering	Glass	Co(4.4–13.7Å)/Pd(3.9–19.9Å)	(1 1 1)-weak	NMR not observed in most Co/Pd multilayers studied. Two resonance lines described, possibly due to interfacial mixing.
Co/Pt multilayers					
Le Dang et al. (1992)	UHV evaporation	Glass	(i) $[Co(26Å)/Pt(32Å)]_{\times 6}$ (ii) $[Co(14Å)/Pt(20Å)]_{\times 15}$ (iii) $[Co(10Å)/Pt(20Å)]_{\times 16}$		Co/Pt multilayers studied as a function of Co layer thickness together with calibration work using dilute powdered alloys. Increased 210 MHz line observed for samples with thin Co layers and ascribed to the formation of a 4 Å thick, Co_3Pt alloy at the interfaces.

TABLE 9.3
(Continued)

Reference	Growth technique	Substrate/buffer	Composition	Orientation	Comments (important result)
Le Dang et al. (1993b)	MBE	GaAs(0 0 1)/Ag(1 1 0)(200Å)	$[Co(43Å)/Pt(17.5Å)]_{\times 15}$	(1 1 0)	Strain and lattice distortion investigated in (1 1 0) Co/Pt multilayers. A large tensile strain exerted by Pt on the Co layers leads to orthorhombic distortion and three orthogonal magnetic anisotropy axes of which the in-plane anisotropy is particular strong (8 kOe). This is reflected in three hyperfine field values associated with these axes.
Le Dang et al. (1994)	MBE	(i) Sapphire(0 0 0 1)/Pt(1 1 1)(30Å) (ii) GaAs(1 1 1)/Ag(1 1 1)(200Å)	(i) $[Co(35Å)/Pt(18Å)]_{\times 15}$ (ii) $[Co(52Å)/Pt(18Å)]_{\times 15}$	(1 1 1)	NMR in Co/Pt multilayers studied as a function applied field. Substantial changes in spectrum with applied field indicates the presence of antiferromagnetic coupling for Co(52Å)/Pt(18Å). Co mainly in the hcp phase with 30% in the fcc phase.

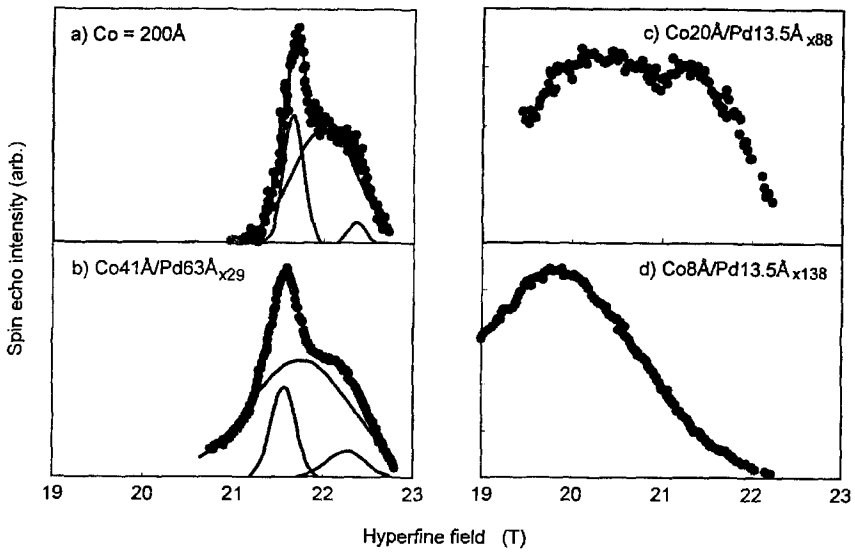


Fig. 9.6. Hyperfine field distribution of Co/Pd multilayers with [1 0 0] texture with layer thicknesses as shown. The NMR measurements were carried out at fixed frequency (185 MHz) and at a temperature of 1.4 K. The data in (a) and (b) are fitted to a superposition of simple Gaussian functions which are also shown. After de Gronckel et al. (1989).

NMR signal was observed. In films with thicker Co layers two NMR peaks separated by 20 MHz were observed an described in terms of the replacement of Co NN with Pd.

9.3.2. NMR studies of Co/Pt multilayers

Co/Pt multilayers have been studied by Le Dang (Le Dang et al. 1992, 1993b, 1994) in a series of papers. Calibration work in random CoPt alloys (Le Dang et al. 1994) showed that the frequency shift following the substitution of one NN Co by Pt was only ~8 MHz, fig. 9.7. This is much less than the frequency shift found for substituting Co by Cu. In a Co_3Pt alloy (well outside the dilute impurity limit) a broad resonance centred near 208 MHz is observed. This reflects the small differences in frequency between the various discrete lines leading them to merge into one broad line.

The relatively small change in hyperfine field due to substituting Pt is almost certainly due to induced polarization on the Pt impurity atoms. Using data from the Co_3Pt alloy the resonant frequency of a 50 : 50 CoPt alloy was calculated to be 182 MHz.

Spectra for three UHV evaporated Co/Pt multilayers with different layer thicknesses are shown in fig. 9.8. The multilayer with Co = 26 Å has a centre frequency of ~224 MHz, characteristic of Co in the hcp phase. Decreasing the Co layer thickness leads to a large reduction in the spectral intensity at ~224 MHz. Comparing the spectral intensity for all the spectra in fig. 9.8 with that from the calibration alloys leads to a consistent picture whereby the first 4 Å of a Co layer is alloyed with Pt. This value is consistent with data from a Faraday rotation experiment (Krishnan 1991) where the interface layer was estimated to be 3 Å.

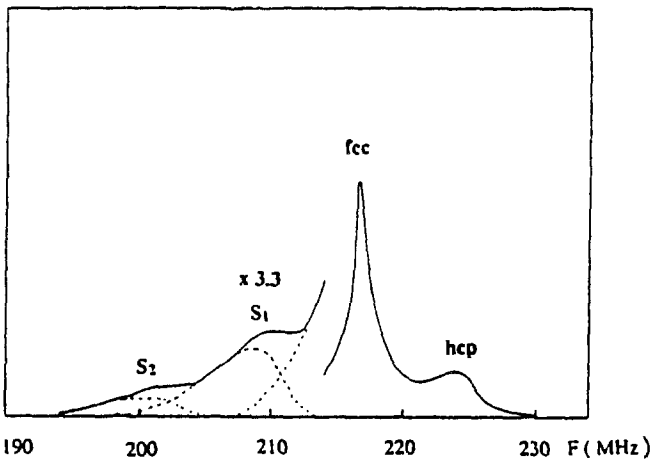


Fig. 9.7. ^{59}Co spin echo spectrum for a $Co_{98}Pt_2$ random alloy at $T = 77$ K. The main line is due to fcc Co with some higher frequency contribution from hcp Co. S_1 and S_2 are the satellite lines arising from environments with, respectively, one or two Pt nearest neighbors.

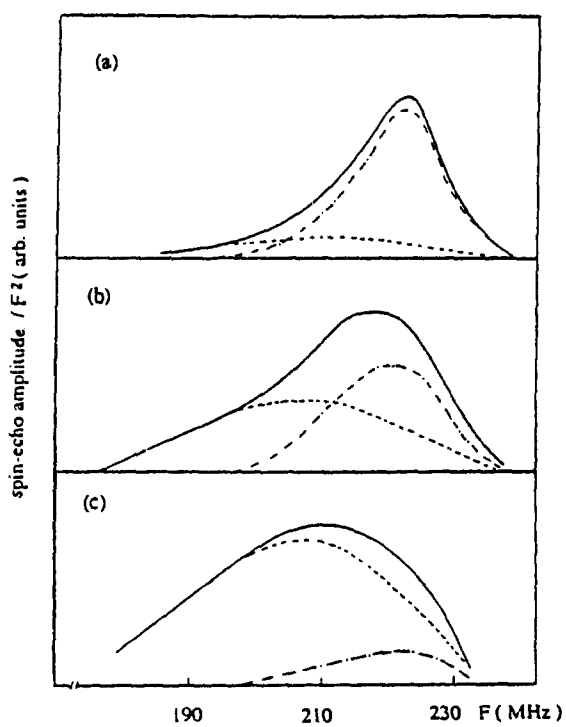


Fig. 9.8. ^{59}Co spectra of Co/Pt multilayers taken at $T = 2$ K: (a) $[Co(26Å)/Pt(32Å)]_{\times 6}$; (b) $[Co(14Å)/Pt(20Å)]_{\times 15}$; and (c) $[Co(10Å)/Pt(20Å)]_{\times 16}$. The contributions from hcp Co and Co_3Pt alloy are indicated on the graphs.

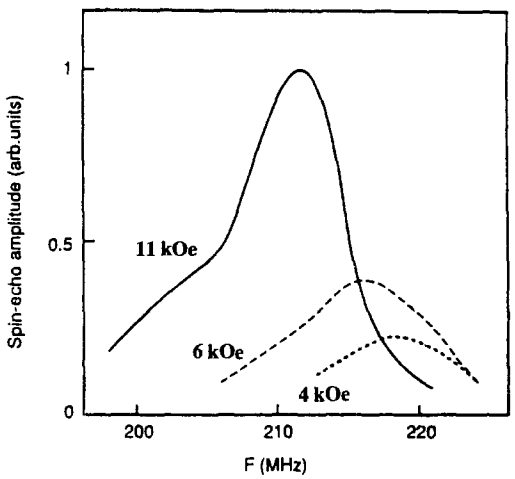


Fig. 9.9. ^{59}Co NMR line intensity as a function of dc field applied along the in-plane hard axis. All measurements carried out at $T = 2$ K. After Le Dang et al. (1993b).

This initial work was followed up by studies on the orthorhombic distortion of the Co lattice by Pt in (1 1 0) oriented Co/Pt multilayers (Le Dang et al. 1993b), and an investigation of antiferromagnetic coupling (Le Dang et al. 1994) in Co/Pt. Lattice distortion in MBE grown Co/Pt (1 1 0) multilayers was investigated by measuring NMR in $[Co(43Å)/Pt(17.5Å)]_{\times 15}$ as a function of angle of applied field. The film was deposited onto a GaAs (0 0 1) substrate with a Ag (1 1 0) 200 Å buffer layer. This produced a film with orthogonal, in-plane, easy and hard axes. Initially the rf field B_1 was oriented along the in-plane hard direction while the dc field was applied along the in-plane easy direction. NMR spectra were recorded for applied field between 0 and 8 kOe. The broad line centred at ~220 MHz in zero applied field shifted uniformly to lower frequencies at the expected rate of −1 MHz/kOe. Interchanging the rf and dc field axes produced significant changes in the NMR spectra. In zero applied field the NMR signal was too small to be observable, however increasing the dc applied field increased the NMR signal as shown in fig. 9.9.

The lack of signal in zero applied field indicates that no enhancement (see section 4) from within domains is occurring as the rf field is either parallel or antiparallel to the magnetization and therefore cannot exert a torque on the nuclear magnetic moments. This, of course, assumes that domain wall enhancement usually the dominant mechanism is not important. Using the assumption of domain only enhancement and the fact that the enhancement factor η is inversely proportional to the anisotropy field (eq. (4.1)) it is possible to use measurements of NMR signal intensity vs. applied field to investigate anisotropy. Figure 9.10 shows NMR intensity as a function of the two orientation of applied field, described above, together with a fit to the anisotropy field model described by (Le Dang et al. 1993b). Clear differences between the field dependence of the two orientations is immediately apparent. Fitting to the anisotropy field model gives an in-plane anisotropy field of 8 kOe showing that the two in-plane axes are not equivalent. The third axis (normal to the plane) is different to the two in-plane axes as shown in fig. 9.11.

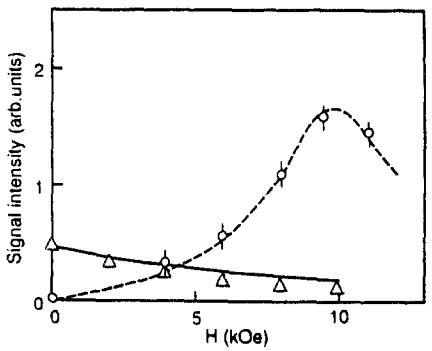


Fig. 9.10. ^{59}Co spin echo intensity as a function of dc applied field (a) parallel to the easy axis (triangles) and (b) parallel to the hard axis (circles). The lines are the fits to the anisotropy field model described in Le Dang et al. (1993b) giving an anisotropy field of 8 kOe.

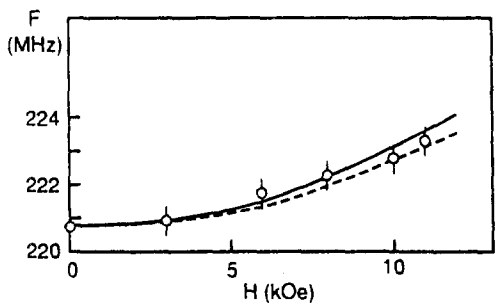


Fig. 9.11. ^{59}Co NMR frequency as a function of applied field perpendicular to the plane.

Fitting to the same anisotropy field model and allowing for demagnetizing effects, the anisotropy between the in-plane easy axis and the axis perpendicular to the plane is found to be smaller than between in-plane easy and hard axes. Hence three orthogonal, inequivalent magnetic anisotropy axes exist in these Co/Pt (1 1 0) multilayers.

Antiferromagnetic coupling in Co/Pt multilayers has also been investigated using NMR by Le Dang et al. (1994). Here the evolution of the NMR spectrum was studied as a function of applied field. Figure 9.12 shows how the form of the spin echo spectrum changes as a result of increasing applied field for a MBE grown [Co(52Å)/Pt(18Å)]$_{\times 15}$ multilayer.

The broad peak observed in the zero field spectrum is characteristic of hcp Co. As the applied field increases a continuous change in line shape is observed rather than just the expected shift to lower frequencies expected from the gyromagnetic ratio of ^{59}Co sites. The spectrum in an applied field B_0 of 4 kOe shows the presence of a new, sharp line in the low frequency side of the spectrum. Rotating the sample demonstrated that this line was not connected with any in-plane anisotropy, and so this change in line shape was ascribed to antiferromagnetic coupling. This interpretation is supported by considering how the enhancement factor η might change in an antiferromagnet when an external field is ap-

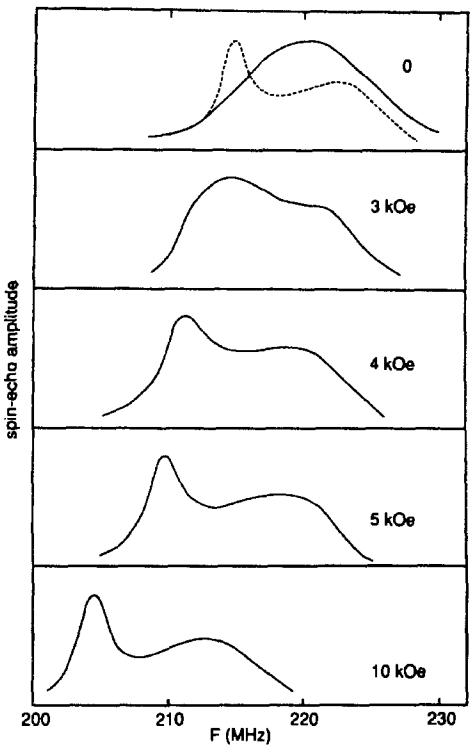


Fig. 9.12. ^{59}Co spin echo spectra for GaAs/Ag(200Å)/[Co(52Å)/Pt(18Å)]$_{\times 15}$ multilayers as a function of applied field parallel to the plane at 2 K. The dashed line at zero applied field is the spectrum for a (1 1 1) oriented Au/Co(70Å)/Au trilayer exhibiting a sharp fcc and broad hcp line. After Le Dang et al. (1994).

plied. If antiferromagnetic regions are only loosely coupled with other regions then η will vary locally within the sample. Hence at zero applied field only regions with high enhancement can be observed. This signal drops rapidly as the applied field becomes stronger than the anisotropy field B_A. If the applied field is greater than the antiferromagnetic flip field then all magnetization vectors will be in-plane perpendicular to the applied field. It is then possible to show (Le Dang et al. 1994) that

$$\eta = \frac{B_{\text{eff}}}{B_0},$$

which is just the result obtained for a ferromagnetic film with $B_0 \gg B_A$. Hence in a saturating field the spin echo spectrum gives the true distribution of hyperfine field. Once this saturating field is applied, no further changes in the form of the spectrum occur and so a reliable estimate of the fcc fraction in the film can be made. The fcc fraction for the sample shown in fig. 9.12 is 30%. The consequences of both interfacial mixing and the polarization of Pt in the presence of an applied field were not discussed by (Le Dang et al. 1994). Hence it is a little unclear as to whether or not these effects might also contribute

to some of the observed features in fig. 9.12. However, this is one of the few examples where NMR has successfully been used to observed antiferromagnetically coupled multilayers.

9.4. NMR work on Co/Fe multilayers

A brief account of the NMR work on Co/Fe multilayers is given here for completeness, but see also section 6.4.3 where the stabilization of bcc Co films by bcc Fe underlayers *and* overlayers is discussed. Table 9.4 details the NMR work published on Co/Fe multilayers.

Initial NMR studies (Boher et al. 1992) of rf sputtered Co/Fe multilayers showed the presence of a low frequency line centred at 198 MHz for multilayers where the Co thicknesses was less than Co = 20 Å. The NMR spectra were found not to depend on the Fe layer thickness. A number of different X-ray techniques indicated that only a bcc structure present and so the low frequency NMR line at 198 MHz was assigned to Co in the bcc phase.

This initial work was followed up in subsequent publications by Dekoster (Dekoster et al. 1993a, 1993b) who undertook NMR studies of high quality MBE grown Co/Fe multilayers. Figure 9.13 shows their results for a series of MBE grown films where the Fe layer thickness is held constant at Fe = 24 Å while the Co layer thickness varies from 10 to 42 Å.

The evolution of the NMR spectrum with Co layer thickness is clear. Thin Co = 10 Å layers result in a dominant line at 198 MHz while the spectrum for Co = 42 Å shows that the hcp Co line at 220 MHz is more prominent. In addition to the 198 MHz line the Co = 10 Å multilayer also has a second line centred at 212 MHz. This second line is probably due to the bcc Co/Fe interface as the larger magnetic moment on Fe leads to a greater hyperfine field at the interface compared to bcc Co. This contrasts with the situation in, for example, Co/Cu where Cu contributes close to zero magnetic moment.

Comparison of NMR and in-situ RHEED data taken during deposition showed an interesting difference between the thickness at which the bcc Co reverted to hcp. During film growth the critical thickness for bcc Co was found to be less than 10 Å after which hcp Co began to form. The NMR data taken post-deposition indicated that the critical bcc $\Rightarrow$ hcp transition thickness was 20 Å. The discrepancy between these data demonstrates that depositing a Fe layer onto a thin Co layer forces the Co back into the bcc phase for Co layer thicknesses in the range 10 Å < Co < 20 Å. Further study (Dekoster et al. 1993b) of MBE Co/Fe multilayers grown on MgO substrates, as a function of substrate temperature T_S during deposition, explored the thermodynamic limits for the formation of bcc Co. T_S was varied between 20°C and 250°C and the optimum temperature was determined to be 175°C. This temperature gives sufficient mobility to the freshly deposited Co atoms whilst ensuring that Co–Fe interdiffusion did not dominate. This result was confirmed by the successful growth of Co/Fe multilayers on GaAs substrates at T_S = 175°C which produced high quality films. These studies also showed that the formation of bcc Co required a minimum Fe layer thickness. Below Fe = 24 Å the NMR results showed that some hcp Co was formed even when the Co layer thickness was less than 20 Å and hence Fe layers of at least 24 Å are required to ensure that the bcc structure is maintained throughout the multilayer stack.

TABLE 9.4
^{59}Co NMR work on Co/Fe multilayers.

Reference	Growth technique	Substrate/buffer	Composition	Orientation	Comments (important result)
Boher et al. (1992)	rf sputtered	Si(1 1 1)	Co(8–100Å)/Fe(8–100Å) (total thickness kept constant at ~2000 Å)	(1 1 0)	Crystal phase of Co investigated in bcc Co/Fe multilayers as a function of layer thicknesses. NMR line at 198 MHz due to bcc Co. bcc Co stabilized for Co layer thickness less than Co = 20 Å.
Dekoster et al. (1993a)	MBE	GaAs(1 $\bar{1}$ 0)	[Co(5–42Å)/Fe(24Å)]$_{\times 25}$	(1 1 0)	bcc Co formation in Co/Fe multilayers studied. NMR line of bcc Co confirmed at 198 MHz. Co/Fe interface line at 212 MHz. Recrystallization of bcc Co for layers 10 Å < Co < 20 Å by subsequent deposition of Fe.
Dekoster et al. (1993b)	MBE	(i) GaAs(1 $\bar{1}$ 0) (ii) MgO(0 0 1)	(i) [Co(5–42Å)/Fe(16–42Å)]$_{\times 25}$ (ii) [Co(21Å)/Fe(24Å)]$_{\times 10}$	(1 1 0)	Growth temperature dependence of bcc Co studied. The optimum substrate temperature for the formation of bcc Co in Co/Fe multilayers found to be T = 175°C. Fe layer thickness dependence of bcc Co also investigated, Fe layers of at least Fe = 24 Å needed for good bcc Co.

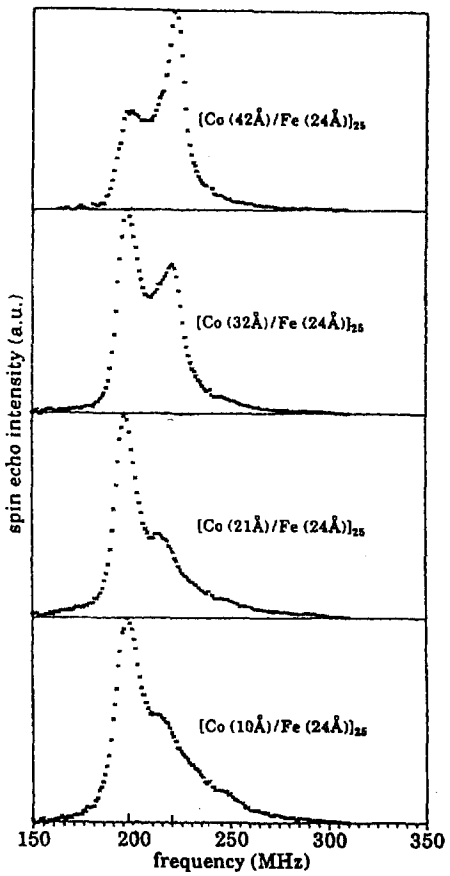


Fig. 9.13. ^{59}Co NMR spectra at 1.6 K in a series of [Co(x)/Fe(24Å)]$_{25}$ multilayers grown on a GaAs ($1\bar{1}0$) substrate. After Dekoster et al. (1993a).

9.5. *^{55}Mn and ^{59}Co NMR studies of Co/Mn multilayer and alloy thin films*

The complex structural and magnetic behaviour of Mn make Co/Mn potentially one of the most interesting multilayer systems to study. However both the difficulty of producing high quality multilayer films and the reluctance of many MBE growers to contaminate their deposition chambers with Mn has to date restricted work on this system. The two early publications on Co/Mn multilayers produced by Le Dang and co-workers (Sakakima et al. 1986; Le Dang et al. 1986b) together with subsequent work are listed in table 9.5.

The initial work was principally concerned with analyzing the NMR results in terms of Co layer thickness. Figure 9.14 shows a series of NMR spectra where Co layer thickness, Mn layer thickness and number of bilayers all vary. Expressing the data in terms of Co signal per Co layer showed that the multilayers behave as if approximately 8 Å of the Co layers did not contribute to the NMR signal and were thus considered magnetically dead. Figure 9.14 shows that for Co $\leqslant$ 25 Å a very broad spectrum is observed with an

TABLE 9.5

^{55}Mn and ^{59}Co NMR work on Co/Mn multilayers and alloy thin films.

Reference	Growth technique	Substrate/buffer	Composition	Orientation	Comments (important result)
Sakakima et al. (1986)	UHV evaporation	Si or glass	Co(7–70Å)/Mn(7–70Å)		Preliminary ^{59}Co and ^{55}Mn NMR results reported on Co/Mn multilayers. Broad spectrum (170–430 MHz) for Co $\leqslant$ 25 Å, and a much sharper (200–250 MHz) for Co $\geqslant$ 36 Å.
Le Dang et al. (1986b)	UHV evaporation	Glass	Co(10–71Å)/Mn(10–73Å)		Co/Mn multilayers studied as a function of layer thicknesses. Co layers not continuous for Co $\leqslant$ 25 Å leading to 420 MHz line. fcc phase considered unlikely as no strong low frequency (<217 MHz) lines. Unidirectional anisotropy found from asymmetry of spectra in an applied field.
Rogers et al. (1995a)	rf magnetron sputtered	Polyimide	$Co_{0.75}Mn_{0.25}$(350Å)		CoMn fcc alloy thin films studied to examine possible compositional separation as found in CoCr (section 8). Homogeneous composition found for films deposited onto a substrate at room temperature and compositional separation found for films deposited at where the substrate temperature was $T_s = 300°C$.
Thomson et al. (1996b)	Sputtered	(i) Glass (ii) MgO (iii) MgO(0 0 1) (iv) MgO(0 0 1)	(i) $Co_{0.98}Mn_{0.02}$ (ii) $Co_{0.98}Mn_{0.02}$ (iii) [Co(30Å)/Mn(10Å)]$_{\times 10}$ (iv) [Co(30Å)/Mn(30Å)]$_{\times 10}$	 (iii) (0 0 1) (iv) (0 0 1)	Co/Mn multilayer and alloy films studied. Coexistence of Co in fcc and hcp phase. Possible fct for multilayer samples. NMR from Mn aligned both parallel and antiparallel to Co measured. Greater interfacial mixing found for Co = 30 Å which is consistent with work suggesting that the stability limit for epitaxial growth of Mn on Co is ~20 Å.

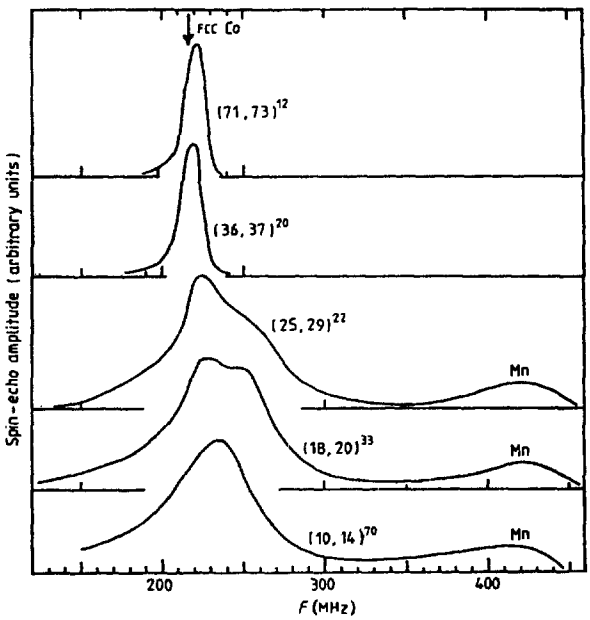


Fig. 9.14. Co and Mn spin-echo spectra in multilayered $(t_{Co}–t_{Mn})^n$ films. The arrow indicates the resonance frequency of fcc Co. After Le Dang et al. (1986b).

additional peak at a frequency greater than 400 MHz, whereas for Co $\geqslant$ 36 Å the spectrum is characterized by a much sharper line centred near 222 MHz and no peak above 400 MHz. These spectra were explained by assuming that for Co $\leqslant$ 25 Å the film was not continuous. It was also noted that the lack of a strong low frequency tail (<217 MHz) meant that it was unlikely that the multilayers with Co < 25 Å had a fcc structure. The line observed at 420 MHz was ascribed to Mn surrounded by 12 nearest neighbor Co atoms. However both previous and subsequent studies show that Mn in this atomic environment has a resonant frequency of 378 MHz and so the origin of this line is not entirely clear.

Exchange coupling between Co and Mn layers was investigated by measuring the NMR spectrum as a function of the magnitude of magnetic field applied parallel to the plane of the film. The coercivity was identified by a sharp drop in the NMR signal. The asymmetric nature of this characteristic drop showed that these multilayers possessed a unidirectional anisotropy.

CoMn alloy thin films were studied by Rogers (Rogers et al. 1995a) for indications of compositional separation effects similar to those found in CoCr alloy films as described in section 8.4.5. Their work on 350 Å thick, $Co_{0.75}Mn_{0.25}$ alloy films showed that just as in CoCr films increasing the substrate temperature produced significant structural and magnetic changes. Comparison with bulk CoMn alloys demonstrated that films deposited with substrate temperature T_s held close to room temperature produced films with similar saturation magnetization and NMR spectrum to that of the bulk alloy. Alloy films deposited at T_s = 300°C showed a three fold increase in saturation magnetization with

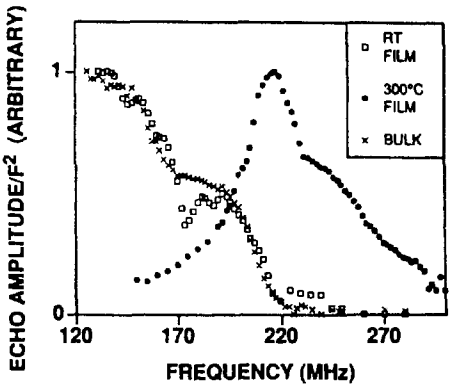


Fig. 9.15. The spin-echo NMR frequency spectra for a compositionally homogeneous $Co_{75}Mn_{25}$ bulk alloy and $Co_{75}Mn_{25}$ thin films deposited both at RT and 300°C. After Rogers et al. (1995a, 1995b).

$M_s = 114$ emu/g (c.f. RT $M_s = 35$ emu/g). These films also had a substantially modified NMR spectrum as shown in fig. 9.15.

The peak at 218 MHz indicates regions of almost pure Co and shows that as is the case with CoCr, substrate temperature play a key role in determining the magnetic and structural properties of CoMn alloy films.

Results from investigations of dilute CoMn powdered alloys, alloy thin films and Co/Mn multilayers are detailed by Thomson et al. (1996b). This work clearly shows the complex nature of the CoMn system. This complexity arises in part due to the small energy difference between the parallel alignment (ferromagnetically (FM) coupled) of Mn with Co and the antiparallel (antiferromagnetically (AFM) coupled) configuration (Stepanyuk et al. 1994). This effectively introduces an additional level of complexity into the analysis of NMR results as each structural configuration has two possible spin orientations and of course it should also be remembered that NMR is observed from both Co and Mn nuclei.

The zero field NMR spectra for sputtered, dilute alloy thin films are shown in fig. 9.16(a) and (b) while the spectra obtained from multilayers are given in fig. 9.16(c) and (d). The main features of the alloy film spectra, fig. 9.16(a) and (b), were analyzed as follows. The main peak, 210–230 MHz shows Co in both the fcc and hcp phases, although clearly the ratio of these phases is influenced by the substrate and growth conditions. A number of satellite lines are observed between 197 MHz and 212 MHz and these are due to grain boundary effects and/or Co atoms with 11 Co and 1 Mn nearest neighbors (NN) with Mn aligned parallel to the Co. The ^{55}Mn resonant line at 377.5 MHz is due to a single Mn impurity FM coupled to 12 Co NN. A line between 170–180 MHz was found in all the spectra and is probably due to Co with 11 Co and 1 Mn NN where the Mn is aligned antiparallel to the Co.

NMR results from the multilayers, fig. 9.16(c), (d), show spectra similar to those found for the dilute alloy films but with some additional features. The most interesting of these are the spectral intensity between 240–300 MHz, the appearance of a well defined line at 131 MHz for the multilayer with thick Mn (Mn = 30 Å) layers and a significantly stronger

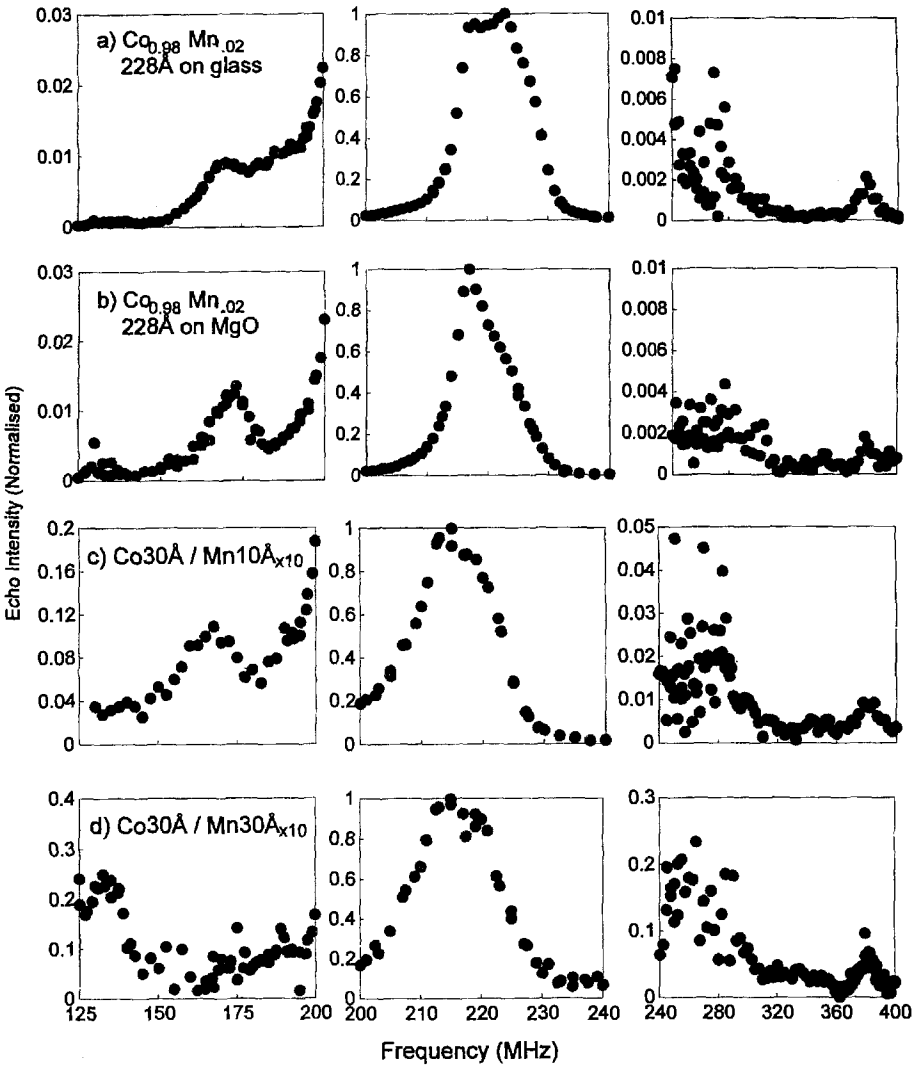


Fig. 9.16. ^{59}Co and ^{55}Mn 4.2 K NMR spectra of: $Co_{0.98}Mn_{0.02}$, 228 Å thick, sputtered alloy films. The films were sputtered simultaneously on (a) a glass substrate and (b) a MgO substrate. Co/Mn multilayers (c) [Co(30Å)/Mn(10Å)]$_{\times 10}$ and (d) [Co(30Å)/Mn(30Å)]$_{\times 10}$. After Thomson et al. (1996b).

resonance at 377.5 MHz. The feature between 240–300 MHz remains unexplained but is observed in other CoMn systems and so does not appear to be an artifact of the particular samples measured here. The line at 131 MHz is thought to be due to Co with 10 Co and 2 Mn NN with the Mn aligned antiparallel. The greater intensity at 377.5 MHz indicates that more interfacial mixing has occurred and is consistent with the idea that the stability limit for epitaxial growth of Mn on Co is ~20 Å.

As can be seen from the data and analyzes presented here, the rich structural and magnetic diversity of the CoMn system makes this a particularly attractive area for future study. However the problem of producing high quality Co/Mn multilayers has yet to be completely solved.

9.6. Miscellaneous Co-based thin films

In this final section on NMR studies of Co-based metallic thin films we survey the work completed on a range of materials where to date only one or two papers have been published. Table 9.6 details all the work covered in this section while the following subsections provide an overview of the results.

9.6.1. NMR studies of Co/Ni multilayers and alloy thin films

Co/Ni multilayers have been studied by de Gronckel (de Gronckel et al. 1992) while NMR measurements on CoNi alloys have been reported by Takei and Maeda (Takei and Maeda 1992). We consider first the work on Co/Ni multilayers. Here NMR investigations were undertaken on multilayers where the Co thickness ranged between 10 Å and 42 Å while the Ni layers were held constant at Ni = 42 Å. In marked contrast to Co/Pd, Co/Ir and Co/Au multilayers (de Gronckel et al. 1989, 1991a) effectively no hcp Co was observed, a result confirmed by X-ray diffraction. The X-ray diffraction also showed that the multilayers had a (1 1 1) texture. Spectra as a function of number of Co layer thickness are shown in fig. 9.17.

Two features of these spectra are readily apparent; firstly the linear increase in the main peak intensity as a function of Co layer thickness and secondly, the spectral intensity on the low frequency side of the main peak which indicates the presence of more than one satellite line. The inset in fig. 9.17 shows the ratio between the most prominent satellite line (~20.1 T = 202 MHz) and the main line. This indicates that the relative increase of the main line varies as $n_{Co} - 4$, where n_{Co} is the number of Co atomic planes, and shows that the interface consists of at least two mixed layers.

Strain effects were investigated by examining the change in hyperfine field of the main line, fig. 9.18, as a function of Co layer thickness. Comparative data for Co/Cu multilayers is also given. The linear relationship between change in hyperfine field of the main line, ΔB_{hf}, and Co layer thickness strongly indicates that these multilayers have uniform strain across the entire Co layer for thicknesses between Co = 10–42 Å. Lattice mismatch between Co and Ni is approximately 0.6% (Ni is smaller) while between Co and Cu it is 2% (Cu is larger). The change in hyperfine field $\Delta B_{hf}/B_{hf}$ is proportional to change in volume $\Delta V/V$. Comparing Co/Cu and Co/Ni multilayers produces excellent agreement between the ratio of the strain and the ratio of the lattice mismatch confirming that lattice mismatch is indeed the source of the change in hyperfine field as Co layer thickness is increased.

We next consider the case of CoNi alloy thin films. The importance of compositional inhomogeneities in determining magnetic properties (e.g., high coercivity) and magnetic recording performance has provided the motivation for many of the NMR studies described in this article, e.g., CoCr, CoRu and CoNiP. CoNi alloy films have also been studied (Takei and Maeda 1992) with the objective of determining whether or not compositional separation occurs in this system. Alloy films of $Co_{0.33}Ni_{0.67}$ and $Co_{0.65}Ni_{0.35}$ and thickness 4000 Å were prepared by rf sputtering with substrate temperature held at T_s = 40°C and

TABLE 9.6

Overview of NMR work on Co-based thin films where only a limited literature exists.

Reference	Growth technique	Substrate/buffer	Composition	Orientation	Comments (important result)
Co/Ni, de Gronckel et al. (1992)	MBE	Si/Au(300Å)	$[Co(10–41Å)/Ni(42Å)]_{\times 50}$	(1 1 1)	Interfacial mixing and local strain studied in fcc Co/Ni multilayers. Interfacial mixing occurs over at least two atomic layers. Uniform strain in Co layers for 10 Å < Co < 42 Å.
CoNi, Takei and Maeda (1992)	rf sputtered	not given	(i) $Co_{0.33}Ni_{0.67}$(4000Å) (ii) $Co_{0.65}Ni_{0.35}$(4000Å)		Compositional distribution was studied as a function of substrate temperature in CoNi alloy thin films. Spectra similar to those expected for random alloys were found for all substrate temperatures indicating that no compositional separation had occurred demonstrating the importance of Cr in the compositional separation of CoNiCr.
CoNiP, Homma et al. (1992)	Electroless deposition from chemical bath	Polyimide	(i) $Co_{0.31}Ni_{0.62}P_{0.07}$ (ii) $Co_{0.39}Ni_{0.55}P_{0.06}$ (iii) $Co_{0.47}Ni_{0.47}P_{0.06}$ (all 1500 Å thick)		Compositional inhomogeneities studied in electroless deposited CoNiP alloy films. Compositional inhomogeneities confirmed with Co rich regions in the hcp phase linked to the existence of high perpendicular coercivity. Annealing studies showed an increase in both Co rich regions and perpendicular anisotropy.

TABLE 9.6
(Continued)

Reference	Growth technique	Substrate/buffer	Composition	Orientation	Comments (important result)
Co/Ru, Dinia et al. (1992)	MBE	Mica			Co/Ru multilayers in hcp phase studied. Perpendicular anisotropy found for layers where Co < 15 Å. Suggestion that there is some extensive interfacial mixing over >2 ML.
CoRu, Maeda et al. (1993)	rf magnetron sputtered	Polyimide	$Co_{0.70}Ru_{0.30}$	*c*-axis perpendicular to plane	Compositional inhomogeneities in hcp CoRu alloy thin films investigated. Compositional separation found for substrate temperatures $T_s = 400°C$ in $Co_{0.70}Ru_{0.30}$ alloy film. This is unlikely to be an intermetallic phase so magnetically induced separation may be able to account for CS in thin alloy films.
Co/Ir, de Gronckel et al. (1991a)	HV evaporation	Si	$[Co(40Å)/Ir(24Å)]_{\times 27}$		Co/Ir, Co/Au, Co/Cu and Co/Pd multilayers compared. In Co/Ir the Co is mostly in the fcc phase. Some interfacial mixing as demonstrated by a low hyperfine field tail.
Co/Sb, Takanashi et al. (1984b)	UHV evaporation	Mylar/Sb(40Å)	(i) $[Co(4Å)/Sb(20Å)]_{\times 99}$ (ii) $[Co(8Å)/Sb(20Å)]_{\times 99}$ (iii) $[Co(15Å)/Sb(20Å)]_{\times 99}$ (iv) $[Co(30Å)/Sb(20Å)]_{\times 99}$		Interfaces of Co/Sb multilayers investigated. Interfacial mixing occurs over several atomic layers. Possible formation of $CoSb_2$ and/or $CoSb_3$ at the interfaces deduced from electric quadrupole broadening.

TABLE 9.6
(Continued)

Reference	Growth technique	Substrate/buffer	Composition	Orientation	Comments (important result)
Co/Sn, Jedryka et al. (1989)	UHV evaporation	Kapton	(i) $[Co(48Å)/Sn(146Å)]_{\times 55}$ (ii) $[Co(32Å)/Sn(98Å)]_{\times 75}$ (iii) $[Co(25Å)/Sn(108Å)]_{\times 75}$ (iv) $[Co(17Å)/Sn(36Å)]_{\times 162}$ (v) $[Co(16Å)/Sn(49Å)]_{\times 162}$ (vi) $[Co(13Å)/Sn(54Å)]_{\times 162}$		Co/Sn multilayers with different layer thicknesses studied. rf power dependence of spectrum used to monitor progress of phase transformation at interfaces from crystalline to amorphous phase. Critical contribution from interfaces found during the first few hours of rapid diffusion.
Co/Zr, Smardz et al. (1995)	dc magnetron sputtered	Glass	Co(5–80Å)/Zr(5–70Å) (total thickness 500 Å)		Co/Zr multilayers with different layer thicknesses studied. Co in hcp phase for Co $<$ 50 Å, and in a mixed hcp/fcc phase for Co $>$ 50 Å. Sharp transition from polycrystalline to nanocrystalline for Co $=$ 26 Å shown by a drastic broadening of spectrum and shortening of T_2.
Co/Si, Kotov et al. (1995)	Evaporation	Si(1 0 0)	$[Co(200Å)/Si(800Å)]_{\times 10}$		Co/Si multilayers studied as a function of annealing temperature. Initial single wide line centred at 215 MHz progressively become two lines at 211 MHz and 217 MHz on annealing up to 650°C. Appearance of the two lines is correlated with the $\alpha \rightarrow \beta$ phase transformation of Co at 470°C and hence the high frequency line is associated with hcp Co while the low frequency line is ascribed to fcc Co.

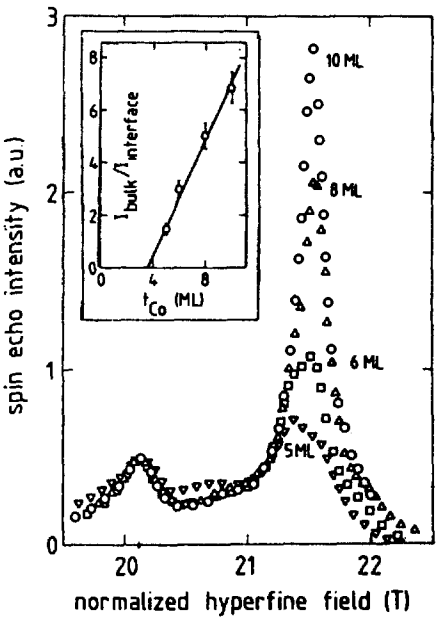


Fig. 9.17. In field spectra (corrected for enhancement) of [1 1 1] fcc Co_3Ni_{42} multilayers, showing the systematic increase in intensity ratio between the main line and the most intense satellite with increasing Co thickness t_{Co} (in monolayers). The spectra have been normalized in intensity and in HFF to the most intense satellite. The inset shows the bulk/interface intensity ratio as a function of Co thickness. The data in the inset are corrected for differences in spin–spin relaxation times. After de Gronckel et al. (1992).

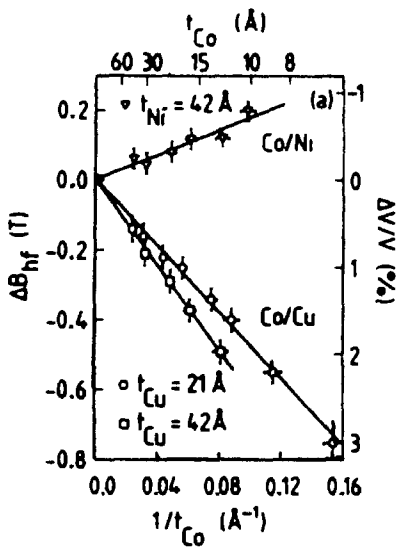


Fig. 9.18. Hyperfine field derived from in-field spectra vs. inverse Co thickness $1/t_{Co}$ for [1 1 1] Co/Ni and Co/Cu multilayers. The lines are least squares fits to the data. After de Gronckel et al. (1992).

T_s = 200°C. The NMR results show that no compositional separation occurs in these films and that the data is comparable to both measured random bulk alloys and to spectra simulated assuming a random distribution of atoms.

9.6.2. NMR of CoNiP alloy films

CoNiP alloy films with potential as a recording medium were studied by NMR. The study had similar objectives to the work described in section 8 on CoCr, and to other work on CoMn and CoRu, namely the investigation of compositional inhomogeneities and their effect on magnetic properties and magnetic recording performance. Alloy films with composition $Co_{0.31}Ni_{0.62}P_{0.07}$, $Co_{0.39}Ni_{0.55}P_{0.06}$ and $Co_{0.47}Ni_{0.47}P_{0.06}$ all 1500 Å thick were produced by an electroless deposition technique. The NMR of these films was measured and compared to a $Co_{0.35}Ni_{0.65}$ bulk alloy. The results show a broadening of the spectrum to a width of ~80 MHz compared with the $Co_{0.35}Ni_{0.65}$ bulk alloy which had a centre frequency of 160 MHz and a width of ~40 MHz. The film with greatest perpendicular coercivity had more spectral intensity centred at 185 MHz. The general broadening of the thin film spectra was associated with a compositionally inhomogeneous state with the greater spectral intensity around 185 MHz in the high coercivity film indicating a greater inhomogeneity. It was estimated that the 185 MHz frequency corresponded to the local atomic environment of a $Co_{0.40}Ni_{0.60}$ alloy. Annealing samples of $Co_{0.47}Ni_{0.47}P_{0.06}$ at 350°C resulted in greater spectral intensity in the 185 MHz and a doubling of the perpendicular coercivity to 2800 Oe. Annealing at 500°C produced spectra close to that expected for the bulk fcc alloy indicating that the previous meta-stable hcp phase had been lost. Thus NMR was able to confirm the existence of compositional inhomogeneities and provide evidence of a link between inhomogeneity, structure (hcp/fcc) and coercivity measured perpendicular to the plane of the film.

9.6.3. NMR studies of Co/Ru multilayers and alloy films

Only a limited amount of ^{59}Co NMR work has been completed on CoRu thin films. NMR results on Co/Ru multilayers quoted by Dinia (Dinia et al. 1992) but not presented, suggest that Co/Ru interfaces extend over a number of atomic layers in MBE grown multilayers. A more detailed study of compositional separation in CoRu alloy thin films was undertaken by Maeda (Maeda et al. 1993). Here alloy films prepared by rf sputtering with a composition of approximately $Co_{0.70}Ru_{0.30}$ were compared to a reference bulk alloy of the same composition and a more dilute $Co_{0.87}Ru_{0.13}$ alloy thin film. The composition $Co_{0.70}Ru_{0.30}$ was chosen so that the alloy had a Curie temperature close to room temperature making changes in composition separation easier to identify. Figure 9.19 shows the NMR spectra for two alloy films deposited at T_s = 100°C and T_s = 400°C together with the reference samples.

The film deposited at T_s = 100°C is similar to the bulk alloy whereas the film deposited at T_s = 400°C as a somewhat different spectrum. The T_s = 400°C film exhibits two new peaks at 210 MHz (M) and 175 MHz (S) compared to the reference spectra. Analyzing this data in terms of assigning the 210 MHz line to an atomic environment where Co is surrounded by 12 Co NN and the 175 MHz line to the 11 Co and 1 Ru environment gives a Co rich region of the film where the Ru content is reduced to approximately Ru = 10 at%. The implication of this work is that as Co and Ru do not form intermetallic phases then

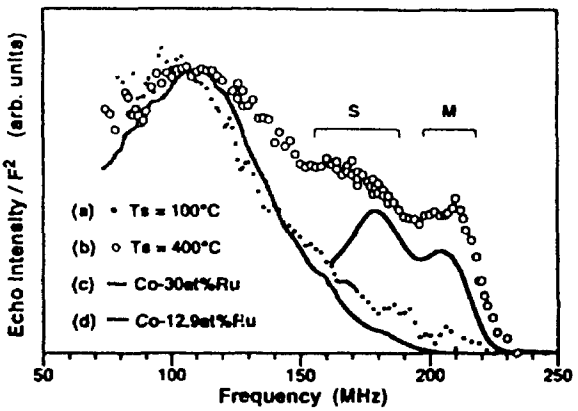


Fig. 9.19. NMR spectra for (a) $T_S = 100°C$ film, (b) $T_S = 400°C$ film, (c) Co–30 at% Ru bulk alloy film and (d) Co–12.9 at% Ru film. After Maeda et al. (1993).

this phase separation is magnetically induced. This might then imply that magnetically induced separation occurs in technologically important alloys such as CoCr thin films. Thus magnetically induced separation rather than some precursor to an intermetallic phase could also be important in producing the fine compositional separation essential for high density magnetic recording.

9.6.4. NMR of Co/Ir multilayers

Although there is no published work exclusively devoted to Co/Ir, de Gronckel (de Gronckel et al. 1991a) included NMR results from $[Co(40Å)/Ir(24Å)]_{\times 27}$ as part of a larger study of NMR in multilayers. ^{59}Co NMR spectra were measured at a fixed frequency of 195 MHz with the swept field applied either parallel or perpendicular to the plane of the film. The major difference between the spectra with the field applied parallel and perpendicular is a shift to lower applied swept fields as a result the demagnetizing field. The enhanced low field tail in the spectrum indicates the presence of Co atoms with a slightly lower hyperfine field than bulk fcc Co. This is probably due to some interdiffusion at the interfaces. The hyperfine field of the main line demonstrates that Co is mostly in the fcc phase but with some hcp character which could be due to stacking faults.

9.6.5. NMR work on Co/Sb multilayers

One of the earliest NMR studies on multilayers was undertaken on Co/Sb (Takanashi et al. 1984b). A series of four films with nominal Co layer thicknesses of Co = 4, 8, 15, 30 Å were prepared under UHV conditions with the Sb layer thickness held constant at Sb = 20 Å. Zero field NMR was observed for both the Co = 15 Å and Co = 30 Å multilayer films but not for the films with thinner Co layers. This suggests that interfacial mixing occurs over several layers. Swept field measurements at a fixed frequency of 45 MHz gave spectra consistent with electric quadrupole broadening with a Knight shift approximately ten times greater (~1.5 kOe) than that observed in pure hcp Co indicating the formation of a $CoSb_2$ or $CoSb_3$ two dimensional compound at the interfaces.

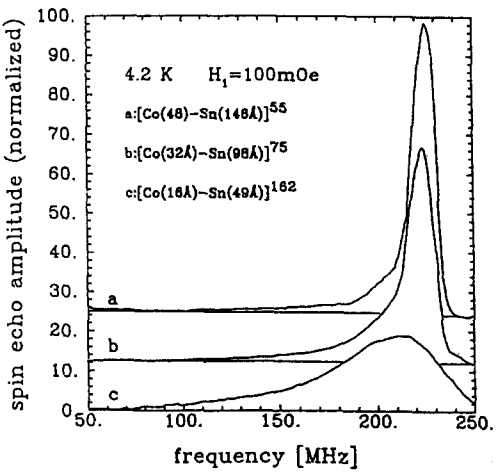


Fig. 9.20. ^{59}Co NMR spectra in 3 sets of Co/Sn multilayers with overall Co concentration of 45% and periodicity of ratio 1 : 2 : 3. After Jedryka et al. (1989).

9.6.6. NMR of Co/Sn multilayers

Co/Sn multilayers have been studied using ^{59}Co NMR by Jedryka (Jedryka et al. 1989). The purpose of their work was to investigate the formation of amorphous CoSn as Co diffuses into the Sn layers. Samples with a range of Co and Sn layer thicknesses such that the total bilayer repeat distance was 65 Å, 130 Å or 195 Å and the ratio of Co to Sn layers was either 4, 3, 2 or 1 were prepared by UHV evaporation on to Kapton with the substrate temperature held at T_S = 77 K. The multilayers were then measured by zero field ^{59}Co NMR as a function of room temperature annealing time. Spectra from the as deposited multilayers, fig. 9.20, show a clear bulk environment Co resonance in the films with thick Co layers as well as a low frequency tail associated with the Co/Sn interface. Modeling this data indicated that at each interface the mixing region extended about 5 Å into the Co layer.

Measurements to determine the optimum rf power required to produce the maximum spin echo amplitude as a function of room temperature annealing time were also undertaken. These measurements are able to distinguish between amorphous and crystalline regions as the distribution of NMR enhancement factors is very different in the magnetically soft amorphous phase compared to the bulk crystal. The results from this study showed that three distinct regions exist: (a) an initial small decrease in signal amplitude that occurred during the first 15 minutes followed by (b) a more rapid drop within the first few hours and finally (c) a very slow decline over several weeks. These results were explained in terms of initial nucleation of amorphous regions followed by growth of the regions and finally a slow increase as all the Co near the interface is converted from the crystalline state. At this point it becomes increasingly difficult for Co in the interior of the layer to migrate to the Sn layer.

9.6.7. NMR investigation of Co/Zr multilayers

^{59}Co NMR work on Co/Zr multilayers is detailed by Smardz et al. (1995). The multilayers were produced by dc magnetron sputtering onto glass substrates. X-ray measurements

indicate that a 5 Å alloy layer is formed at the interfaces. NMR measurements on multilayers with thick, Co > 100 Å, layers showed Co in both the fcc and hcp phases. Reducing the Co layer thickness to Co < 50 Å resulted in only the hcp phase being detected, in contrast to Co/Cu multilayers where thin Co layers favor the fcc phase. A further decrease in Co layer thickness produces substantial broadening of the NMR spectrum for Co = 26 Å with both increased low frequency spectral intensity and an increased high frequency component. A reduction in the transverse relaxation time from ~140 μs to 10 μs is also observed. These data are indicative of the mixing of Co and Zr which leads to soft magnetic properties due to a reduction in the Co grain size from polycrystalline to nanocrystalline. The NMR is also correlated to changes in the domain structure as observed by Kerr microscopy.

9.6.8. NMR study of Co/Si metallic/semiconductor multilayers

Although we have concentrated on metallic multilayers in this section we conclude with a brief mention of a ^{59}Co NMR study undertaken on Co/Si multilayers as metallic/semiconductor hybrid systems are likely to be of some importance in the future. NMR measurements were reported on Co/Si by Kotov (Kotov et al. 1995) on evaporated Co(200Å)/Si(800Å) multilayers as a function of annealing temperature. The initial hyperfine field distribution centred at 215 MHz and ~10 MHz wide was shown to condense into two distinct lines at 211 MHz and 217 MHz as annealing temperature is increased from 200°C to 650°C. These lines were ascribed to the fcc (211 MHz) and hcp (217 MHz) phases of Co. However the large shift in frequencies from those expected for fcc (217.4 MHz) and hcp (220–228 MHz) Co was not well explained and further work on this system is clearly needed.

10. NMR studies in thin films utilizing nuclei other than ^{59}Co

We complete this review of NMR work on thin metallic films by considering studies involving resonances of nuclei other than ^{59}Co. The 100% natural abundance and high sensitivity of ^{59}Co makes this element particularly suitable for many thin film NMR experiments where the amount of material is strictly limited. However a number of studies have been successfully undertaken with other nuclei most notably ^{55}Mn, ^{63}Cu and ^{65}Cu, ^{51}V and recently rare earth elements such as Ho and Tb.

In organizing this section we have first included a section on Cu resonances followed by V. The third section is included to detail the limited number of publications that do not fit naturally into any other part of this work. We conclude the article by considering rare earth films and multilayers.

10.1. ^{63}Cu and ^{65}Cu NMR in thin films

This subsection describes some of the work published on NMR studies of ^{63}Cu and ^{65}Cu in thin films and multilayers. NMR investigations of Cu nuclei are also mentioned in other subsections of this section. We have tried to subdivide the sections in a way that we hope the user will find most convenient so, for example, Cu resonances from superconducting Cu/Nb multilayers are included in subsection 10.4.1 rather than in this section. NMR studies which includes resonances from Cu and other nuclei are detailed in section 10.3.

10.1.1. NMR studies of Fe/Cu multilayer films

Cu resonances have been studied in Fe/Cu multilayers as a method of determining spin polarization oscillations in the non-magnetic Cu spacer layer. NMR can directly probe the spin polarization of conduction electrons through measurements of the Knight shift. Similar studies of spin polarization in CuCo and CuFe bulk alloys using spin echo NMR have been reported by Lang et al. (1972) and by Boyce and Slichter (1974). Essentially the "extra" Knight shift produced by polarization of the conduction electrons leads to a series of satellite peaks around the main peak The shift in frequency of these satellite peaks is determined by the strength of the interaction (field) responsible for polarizing the electrons.

A series of papers listed in table 10.1, from the group in Nanjing, China, have explored these Cu resonances. Their work may be summarized by considering the paper of Jin et al. (1994a) which contains most of the important results. Their experiments were conducted on a Brücker MSL-300 spectrometer using a pulsed echo/Fourier transform method. The applied magnetic field of 7 Tesla was oriented parallel to the film plane. The Multilayer films studied consisted of $[Fe(60Å)/Cu(25Å)]_{\times 50}$ and were prepared by rf sputtering on to glass substrates. A 4000 Å Cu film was used as a reference sample. X-ray analysis of the films demonstrated that the films were polycrystalline with a (1 1 1) texture.

Figure 10.1 shows ^{63}Cu spin echo NMR spectra for both the reference and multilayer films together with the ^{65}Cu resonance for the multilayer film. All the spectra measured had a strong signal at a frequency of 79.74320 MHz corresponding to a ^{63}Cu resonance from various sample holder components. The differences between the ^{63}Cu spectrum from the single thick Cu film fig. 10.1(a) and the ^{63}Cu fig. 10.1(b) and ^{65}Cu fig. 10.1(c) NMR spectra obtained from the $[Fe(60Å)/Cu(25Å)]_{\times 50}$ multilayer are immediately apparent. The fact that the satellite structure appears in both the ^{63}Cu and ^{65}Cu multilayer spectra but not in the ^{63}Cu spectrum for the single Cu layer reference film is considered good evidence of polarization of the conduction electrons. Similar satellite structures have been observed in films sputtered on to both glass and kapton substrates and in $[Fe(22Å)/Cu(17Å)]_{\times 50}$ multilayers (Xu et al. 1994).

The polarization (exchange) fields can be determined from the frequency shifts on the satellite lines shown in fig. 10.1 and these are given in table 10.2. The difference in the exchange fields for the ^{63}Cu and ^{65}Cu isotopes is less than 5% as can be seen from table 10.2. Making the simplest assumption which is that the regions producing the oscillations are equally spaced normal to the planes of the film gives an average oscillation period of 4–5 Å within the Cu layer. However this value is significantly less than either the theoretical prediction of 9 Å (Bruno and Chappert 1992), or other experimental data which gives the oscillation period as 12 Å (Petroff et al. 1991). Although modeling work based on a spatially damped pseudo one dimensional oscillatory RKKY interaction in which the nuclei are discontinuously located and hence see discrete values of spin polarization could reproduce the spectra in fig. 10.1 (Zhai et al. 1995b). However to our knowledge similar resonances have yet to be observed by other groups. This clearly remains an intriguing area for further research as NMR potentially offers a very powerful technique for studying electron polarization in non-magnetic spacer layers.

10.1.2. NMR studies of Ni/Cu multilayers

NMR from Cu nuclei in Ni/Cu multilayers has been studied by Goto et al. and reported in a progression of papers (Goto et al. 1993a, 1993b, 1993c). The substantial results are

TABLE 10.1

Summary of ^{63}Cu and ^{65}Cu NMR work completed on Fe/Cu multilayers.

Reference	Growth technique	Substrate/buffer	Structure	Orientation	Comments (important result)
Jin et al. (1993)	rf sputtered	Glass and kapton	$[Fe(60Å)/Cu(25Å)]_{\times 50}$	(1 1 1)	Use Cu NMR to study spin polarization and coupling in Fe/Cu multilayers. Spin polarization in Cu layer observed as satellite lines in Knight shift spectrum. Average period of spin oscillation in Cu layer estimated to be 4–5 Å.
Jin et al. (1994a)	rf sputtered	Glass and kapton	$[Fe(60Å)/Cu(25Å)]_{\times 50}$	(1 1 1)	Spin polarization in Cu layer of Fe/Cu multilayers observed as satellite lines in Knight shift spectrum.
Xu et al. (1994)	rf sputtered	Glass	(i) $[Fe(22Å)/Cu(17Å)]_{\times 50}$ (ii) $[Fe(60Å)/Cu(12Å)]_{\times 50}$ (iii) $[Fe(60Å)/Cu(8Å)]_{\times 50}$	(1 1 1) slight	Spin polarization of conduction electrons investigated in Fe/Cu multilayers. Evidence of spin polarization related to interlayer coupling and penetration of exchange field into non-magnetic layer.
Zhai et al. (1995b)	rf sputtered	Kapton	(i) $[Fe(60Å)/Cu(25Å)]_{\times 50}$ (ii) $[Fe(22Å)/Cu(17Å)]_{\times 50}$	(1 1 1)	Spin polarization studied in Fe/Cu and Fe/Ag multilayers. Knight shift satellite structure due to spin polarization of Cu layer conduction electrons fitted to RKKY theory. Magneto-optic data reported for Pd, Ag and Al spacer layers
Zhai et al. (1995a)	rf sputtered	Glass and kapton	$[Fe(60Å)/Cu(25Å)]_{\times 50}$	(1 1 1)	Spin polarization in conduction electrons in Cu layer of Fe/Cu multilayers observed as satellite lines in Knight shift spectrum.

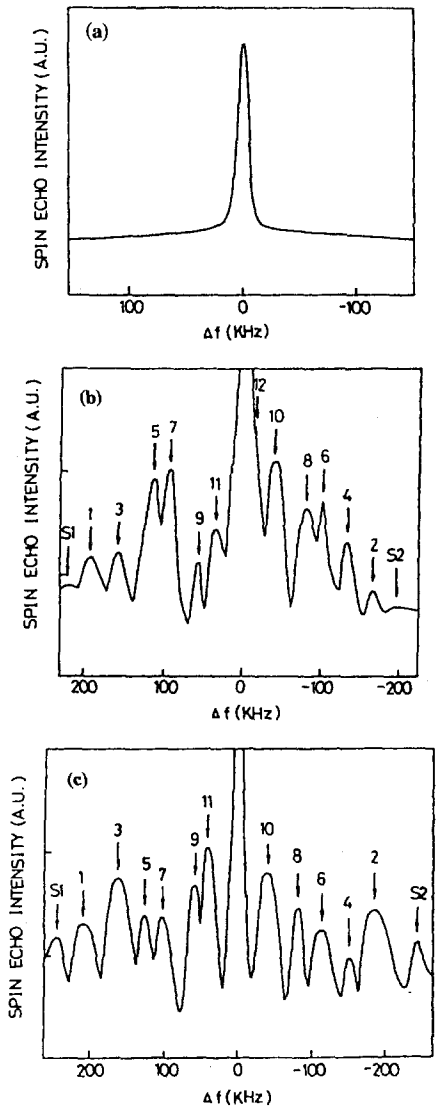


Fig. 10.1. Spin-echo spectrum in 7 T (a) of ^{63}Cu nuclei in a single 400 nm Cu film, (b) of ^{63}Cu nuclei in a [Fe(60Å)/Cu(25Å)]$_{50}$ multilayer deposited on a glass substrate, (c) of ^{65}Cu nuclei in the same sample as in (b). After Jin et al. (1994a).

contained in the report of Goto et al. (1993c) and we concentrate our review on this work. The aim of the investigations was similar to that described in the previous section 10.1.1 on Fe/Cu multilayers, namely to study spin polarization in the nonmagnetic Cu layers of these magnetic/nonmagnetic multilayer systems. The spin polarization oscillation is sampled at the resonating nuclei through the hyperfine interaction between the nuclear mag-

TABLE 10.2

The exchange fields in kOe determined from ^{63}Cu satellite lines (first row) and ^{65}Cu satellite lines (second row) corresponding to the peaks labeled in figs 10.1(b) and 10.1(c), respectively. After Xu et al. (1994).

Hs1	Hs2	H1	H2	H3	H4	H5	H6	H7	H8	H9	H10	H11	H12
—	—	72	−62	58	−50	43	−38	36	−30	21	−15	14	−5
82	−78	70	−61	56	−51	43	−38	35	−29	20	−15	14	—

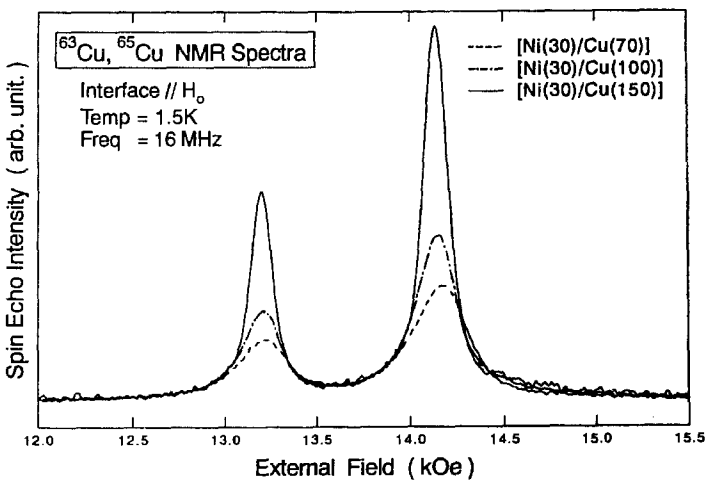


Fig. 10.2. The Cu NMR spectra of the [Ni(30Å)/Cu(x)] superlattices, where x = 70, 100 and 150 Å at 1.5 K and 16 MHz. The external field was applied parallel to sample surfaces. The two peaks correspond to ^{65}Cu (at around 13.2 kOe) and ^{63}Cu (at around 14.2 kOe). Spectra have been normalized to match the tails of the resonance lines. After Goto et al. (1993c).

netic moments and the conduction electrons. Multilayers with relatively thick Cu layers were prepared on Mylar substrates with a Cr = 30 Å buffer layer by UHV electron beam deposition. The multilayer structure was [Ni(30Å)/Cu(x)]$_{\times n}$ where x = 70, 100 or 150 Å with corresponding n = 29, 20 or 10. All samples had a fcc (1 1 1) texture and are detailed in table 10.3 together with a summary of the results obtained. ^{63}Cu and ^{65}Cu NMR spectra for all three multilayers are shown in fig. 10.2.

The swept field spectra were taken at fixed frequency of 16 MHz and at T = 1.5 K. The external magnetic field was sufficient to align the magnetic moments of the Ni layers parallel to the field direction. The problem is then how to relate these NMR spectra to the spin polarization of the conduction electrons. Unlike the Fe/Cu spectra shown in the previous section (10.1.1) there is no discernible satellite structure, making it impossible to estimate the spin polarization oscillation period. It is worth emphasizing that this is the result that might be anticipated and that the appearance of such a well defined satellite structure in Fe/Cu is somewhat unexpected. The asymptotic form of the spin polarization

TABLE 10.3
Summary of ^{63}Cu and ^{65}Cu NMR work completed on Fe/Cu multilayers.

Reference	Growth technique	Substrate/buffer	Structure	Orientation	Comments (important result)
Goto et al. (1993b)	UHV electron beam evaporation	Mylar/Cr = 30 Å	(i) $[Ni(30Å)/Cu(70Å)]_{\times 29}$ (ii) $[Ni(30Å)/Cu(100Å)]_{\times 20}$ (iii) $[Ni(30Å)/Cu(150Å)]_{\times 10}$	(1 1 1)	Spatial spin polarization oscillation in Cu spacer layer of Ni/Cu multilayers investigated. Anisotropic line widths found as a function of applied field angle, a phenomenon which is not observed in bulk alloys and is related to electronic structure of the Cu layers.
Goto et al. (1993c)	UHV electron beam evaporation	Mylar/Cr = 30 Å	(i) $[Ni(30Å)/Cu(70Å)]_{\times 29}$ (ii) $[Ni(30Å)/Cu(100Å)]_{\times 20}$ (iii) $[Ni(30Å)/Cu(150Å)]_{\times 10}$	(1 1 1)	Spatially varying spin polarization oscillation in Cu layers of Ni/Cu multilayers studied. Damping exponent of oscillation found to be -1 which reflects to topology of the Cu Fermi surface. Anisotropy in line widths as a function of applied field due to the initial oscillation conditions determined by the interface.
Goto et al. (1993a)					Brief mention of Ni/Cu multilayers in title, no substantive work. Paper concentrates on spin polarization in Co/Cu multilayers.

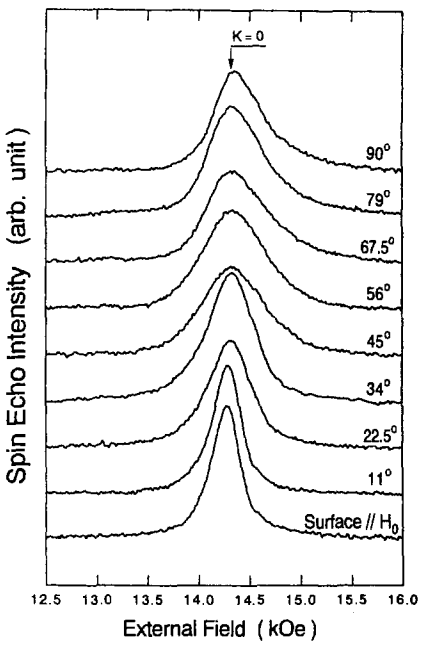


Fig. 10.3. Angular dependence of the ^{63}Cu contribution in the Cu spectra for [Ni(30Å)/Cu(70Å)] superlattice. The angle is defined as that between the external field direction and the sample surfaces. After Goto et al. (1993c).

function at a distance x from the interface can be assumed to be

$$U_z(x) = Ax^{\alpha} \cos(2\pi x/p + \phi),$$

where A – amplitude of polarization, α – damping exponent, p – oscillation period, ϕ – phase shift.

The damping exponent can be found from the line width as to a first approximation the full width at half maximum (FWHM) intensity corresponds to the amplitude, where x equals one quarter of the Cu layer thickness. Hence α can be estimated by fitting the observed FWHM with the function $\mathrm{FWHM}(t_{\mathrm{Cu}}) = A(t_{\mathrm{Cu}}/4)^{\alpha}$. This gives a value of -1.10 ± 0.12 which is close to the theoretically expected value of $\alpha = -1$. The significance of this value for the damping exponent is that for a pseudo one dimensional free electron system a value of $\alpha = -2$ is expected. Theoretical analysis by Bruno and Chappert (1992) demonstrates that a value of $\alpha = -1$ could be expected for a system where a vector connecting two stationary points on the Cu Fermi surface is perfectly nested.

Measurements of the NMR spectrum as a function of the angle of applied field are also reported by Goto et al. (1993c). The angle θ of the applied field is defined as the angle between the film surface and the field. The spectral dependence on angle is shown in fig. 10.3 for the ^{63}Cu resonance from the [Ni(30Å)/Cu(70Å)]$_{\times 29}$ multilayer. A clear anisotropy in the spin echo line width is seen as a function of angle.

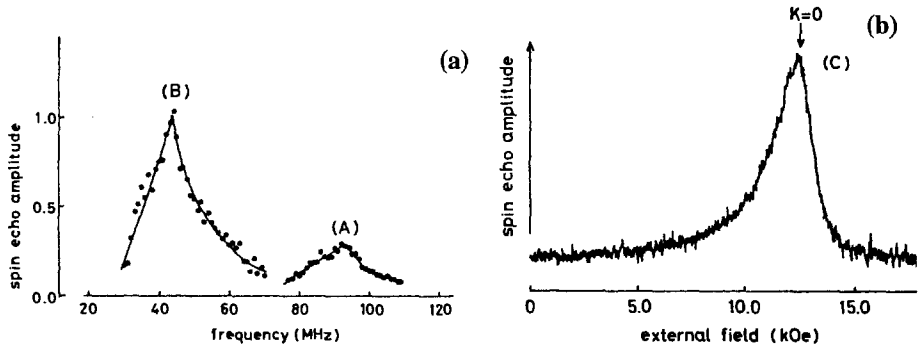


Fig. 10.4. NMR spectra of ^{51}V in Fe–V multilayered film (a) swept frequency in zero field at 1.3 K, (b) swept field at 14.0 MHz, 4.2 K. After Takanashi et al. (1982).

Similar behaviour has also been observed in other systems, e.g., Fe/V (Takanashi et al. 1984a) and appear to be a universal characteristic of magnetic/nonmagnetic multilayers. It is thought that the changes in the NMR spectrum are due to changes in the form of spin polarization as the results shown in fig. 10.4 are not expected from conventional RKKY theory. Analyzing the results in more detail shows that the damping constant α is independent of angle and indicates that the likely cause of the anisotropy in the line widths is due to a change in the initial conditions at the interface. However work of this type is really only just beginning and remains a fruitful area for further investigation.

10.2. ^{51}V NMR studies of multilayers

The fact that V is not a ferromagnetic element means that the hyperfine field in which the nuclei precess must be due to either an applied external field or polarization due to the close proximity to a ferromagnetic element such as Fe. This has restricted the number of ^{51}V NMR experiments, however work has been published on two multilayer systems Fe/V and Ag/V. Although ^{51}V NMR has not been extensively studied it happens that some of the earliest papers on NMR in multilayer films reported work on Fe/V. The papers are listed in table 10.4.

The work published on superconducting V/Ag multilayers (Imai et al. 1987) employed similar techniques to those described in section 10.4.1 on superconducting Nb/Cu multilayers. The superconducting nature of V in V/Ag multilayers was probed by measuring the ^{51}V spin-lattice relaxation time (T_1) in order to obtain the superconducting energy gap. The results obtained indicate that the order parameter in the V layers increases as temperature decreases irrespective of the existence of the proximity effect. Hence once T_c is determined by the influence of the Ag layers through the proximity effect, neither the proximity effect or the dimensional crossover changes the superconducting energy gap.

10.2.1. ^{51}V NMR studies of Fe/V multilayers

Early NMR work on thin film multilayers was reported by Takanashi et al. (1982, 1984a) for the Fe/V system. These papers showed swept frequency spectra taken in zero applied field and swept field spectra taken at constant frequency for Fe(100Å)/[V(30Å)/

TABLE 10.4

Published ^{51}V NMR studies of metallic multilayers.

Reference	Growth technique	Substrate/buffer	Structure	Orientation	Comments (important result)
Takanashi et al. (1982)	UHV evaporation	Mylar/Fe(100Å)	$[V(30Å)/Fe(15Å)]_{\times 59}$ with V(30Å)/Fe(100Å) cap		^{51}V NMR observed in Fe/V multilayers from V situated near the interface.
Takanashi et al. (1984a)	UHV evaporation	Mylar/Fe(100Å)	$[V(30Å)/Fe(15Å)]_{\times 59}$ with V(30Å)/Fe(100Å) cap		^{51}V NMR used to study interfaces in Fe/V multilayers. Interfacial mixing extends over 3 atomic layers. NMR also observed from V atoms situated in the interior of the V layer. Some anisotropy found in the hyperfine field measured for interior atoms suggesting that Fe modifies the electronic states at some distance from the interfaces.
Takanashi et al. (1986a)	UHV evaporation	Mylar/Fe(100Å)	$[V(30Å)/Fe(15Å)]_{\times 59}$ with V(30Å)/Fe(100Å) cap		^{51}V NMR in Fe/V multilayers shows interfacial mixing extends over 3 atomic layers. Fe and V concentrations estimated in the intermixed layers and suggest the formation of a new type of alloy. Results for Fe/Mn and Co/Sb multilayers are also given.
Imai et al. (1987)	not given	not given	(i) $[V(60Å)/Ag(30Å)]_{\times 29}$ (ii) $[V(200Å)/Ag(400Å)]_{\times 10}$		^{51}V spin-lattice relaxation time (T_1) measured in superconducting V/Ag multilayers to establish how the superconducting energy gap (order parameter) varies with temperature. Order parameter found to increase as temperature decreases to maximum value of $2\Delta(0) = 3.5\, k_B T$.

$Fe(15Å)]_{\times 59}/V(30Å)/Fe(100Å)$ multilayer films deposited onto Mylar substrates under UHV (10^{-9} Torr) conditions. Figure 10.4 shows both swept frequency and swept field spectra (Takanashi et al. 1982, 1984a).

The relative intensity of the feature labeled (A) in fig. 10.4(a) appears to be in doubt as the later paper (Takanashi et al. 1984a) showed a slightly different spectrum. The essential features of the two spectra in fig. 10.4 are the peaks marked as (A) 77–110 MHz ($-98 < H_n < -69$ kOe), (B) 30–60 MHz ($-68 < H_n < -27$ kOe) and (C) with a width at half intensity of 2.7 kOe centred around a peak at −26.7 kOe. These lines were interpreted in the following way: the authors first dismissed any spectral contribution from ^{57}Fe nuclei which would normally produce a broad zero field line centred around 46 MHz at $T = 4.2$ K, as the sensitivity of Fe is significantly less than that of V and ^{57}Fe is only 2.2% natural abundant. Qualitatively the peaks observed at ~40 MHz (B) and ~90 MHz (A) are due to ferromagnetically ordered V sites in the Fe/V interfacial region with magnetic moments induced by the proximity of Fe. The peak (C) in the swept field spectrum fig. 10.4(b) is due to nearly nonmagnetic sites in the interior of the V layers. A more quantitative analysis showed that models which assumed a flat (ideal) interface failed to reproduce the observed frequency spectrum. However the correct hyperfine field distribution could be simulated by assuming that some interfacial mixing had occurred. The simulation showed that the experimental data could be reproduced when interfacial mixing occurred over three atomic layers and gave the average concentration of the three layers as $Fe_{0.95}V_{0.05}$, $Fe_{0.50}V_{0.50}$ and $Fe_{0.05}V_{0.95}$. However, as the authors note, this data should not be taken as a universal guide as both the concentration gradient and the extent of interfacial alloying are sensitive to the deposition condition employed.

The peak (C) in the swept field spectrum fig. 10.4(b) is due to ^{51}V in a nearly nonferromagnetic environment, i.e., in the interior of the V layers. Measurement of this resonance as a function of the angle of applied field showed that the hyperfine field was anisotropic, with the peak of the resonance shifted to higher fields when the external field was applied perpendicular to the plane of the film. As the shift in peak position was found to be independent of the magnitude of the resonance field in the range 8–40 kOe it was concluded that change in peak position must be due to some anisotropy in the hyperfine field. Measurements of the Korringa relaxation rate ($1/T_1T$) showed a value of about half of that expected for V metal and demonstrated that the electronic states of V at some distance from the interface are modified by the intimate contact with Fe at the interface.

10.3. NMR in other thin films and multilayers

In this subsection we collect together all the NMR work on thin films and multilayers that does not fall readily into any other category. As such, works on a number of different nuclei are described the most important of which is ^{57}Fe. The individual title heading have been chosen to indicate the systems described.

10.3.1. ^{57}Fe and ^{61}Ni NMR studies of NiFe (permalloy) based thin films

NMR work on thin permalloy ($Ni_{0.80}Fe_{0.20}$) films has been reported by Lesnick et al. (Lesnik and Kharitonskii 1985a; Lesnik et al. 1985c; Lesnik and Golub 1993). Their investigations were aimed at examining diffusion effects at the grain boundaries of permalloy films. A considerable number of Russian papers (in Russian) exists on NMR in

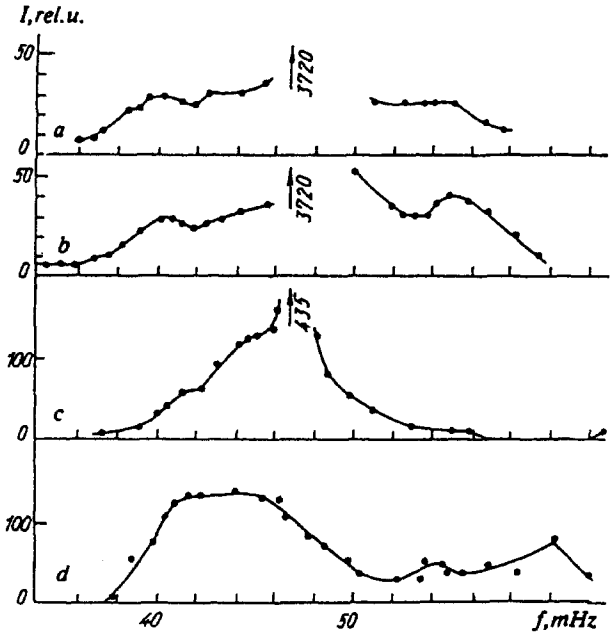


Fig. 10.5. NMR spectra at 1.5 K of trilayer (Fe–Ni)–(^{57}Fe)–(Fe–Ni) film: (a) untreated; after annealing for 1 h at (b) 473 K, (c) 623 K, (d) 773 K. After Lesnik et al. (1985c).

permalloy based films and the interested reader is recommended to consult the report of Pokatilov et al. (1990) and the references contained within. In this article we shall restrict ourselves to reviewing the results published in literature that is more readily accessible as listed in table 10.5.

Diffusion studies were undertaken on trilayer structures where a central layer of enriched ^{57}Fe was allowed to diffuse into permalloy layers on either side. The trilayer structures consisted of $Ni_{0.80}Fe_{0.20}/^{57}Fe/Ni_{0.80}Fe_{0.20}$ with grain sizes of the order of 150–200 Å which were carefully annealed at various temperatures. After each annealing process the NMR spectrum was recorded. In this way the progress of any diffusion process could be monitored. This procedure potentially has uses in other thin film systems where diffusion effects at grain boundaries are important.

Figure 10.5 shows a series of NMR spectra measured at $T = 1.5$ K for $Ni_{0.80}Fe_{0.20}/^{57}Fe/Ni_{0.80}Fe_{0.20}$ trilayer films as a function of anneal temperature. The films were deposited on to mica substrates at room temperature and consisted of two 1500 Å layers of non-magnetostrictive $Ni_{0.80}Fe_{0.20}$ permalloy separated by a 500 Å, 92% enriched ^{57}Fe layer. The trilayers were then annealed for 1 hour at temperatures between 373 and 773 K. Experiments as a function of annealing time showed that little changes occurred in the hyperfine field distribution as the annealing time was increased. The initial (unannealed) spectrum fig. 10.5(a) for a trilayer showed a narrow well defined line at 46.6 MHz from the ^{57}Fe layer against a background of weak signals at 40.5 MHz, 43.5 MHz and 54.5 MHz. In bulk permalloy ^{61}Ni resonance lines are normally observed at 48 and 54.5 MHz and this

TABLE 10.5

NMR work on permalloy ($Ni_{0.80}Fe_{0.20}$) based thin films.

Reference	Growth technique	Substrate/buffer	Structure	Orientation	Comments (important result)
Lesnik and Kharitonskii (1985a)	not given – deposited at 10^{-7} Pa	not given	$Ni_{0.80}Fe_{0.20}$(1200–1500Å)/ ^{57}Fe(500Å)/$Ni_{0.80}Fe_{0.20}$(1200–1500Å)		^{57}Fe and ^{61}Ni nuclei in permalloy thin films used to investigated changes in hyperfine field distribution due to diffusion caused by annealing. Grain boundary diffusion studied by the migration of an enriched ^{57}Fe layer.
Lesnik et al. (1985c)	not given – deposited at 1.3×10^{-5} Pa	Mica	$Ni_{0.80}Fe_{0.20}$(1500Å)/^{57}Fe(500Å)/ $Ni_{0.80}Fe_{0.20}$(1500Å)		^{57}Fe and ^{61}Ni NMR used to measure changes in hyperfine field distribution due to diffusion caused by annealing permalloy thin films. Results compared with plastic deformation experiments.
Pokatilov et al. (1990) (in Russian)			(i) $Co_{0.78}Ni_{0.22}$ (ii) $Co_{0.58}Fe_{0.31}Ni_{0.11}$ (iii) $Co_{0.58}Fe_{0.11}Ni_{0.31}$		Title of paper "NMR study of thin Co based ferromagnetic films". Starting point to investigate Russian literature concerning NMR studies of thin films.
Lesnik and Golub (1993)	Evaporation	Mica	$Ni_{0.80}/Fe_{0.20}$(300Å)/Co(70–300Å)		^{59}Co NMR enhancement factor and relaxation rate reported as a function of Co layer thickness at room temperature. Results show that induced anisotropy field decreases with Co layer thickness.

accounts for the spectral intensity above the ^{57}Fe line in these films. ^{57}Fe resonances at 40.5 and 43.5 MHz are associated with $Ni_{0.80}Fe_{0.20}$ and $Ni_{0.65}Fe_{0.35}$, respectively. Spectral intensity below 38 MHz is due to ^{57}Fe located at grain boundaries. Figure 10.5(b)–(d) show the evolution of the diffusion process as the anneal temperature is increased. At $T = 473$ K some minor changes occur in the hyperfine field distribution particularly at the low frequency end of the spectrum which could indicate diffusion of ^{57}Fe towards the grain boundaries. As the temperature is increased to $T = 623$ K more radial changes occur and the ^{57}Fe line at 46.6 MHz is substantially reduced, demonstrating that large scale diffusion has occurred. The reduction of the 46.6 MHz line is accompanied by a shift in the line at 40.5 MHz to 41.5 MHz. A further increase in the annealing temperature to $T = 773$ K, fig. 10.5(d), effectively washes out the structure of the spectrum and replaces it with a broad peak centred at 44–45 MHz. A new line also appears at 60.5 MHz due to the ^{61}Ni resonance from $Ni_{0.65}Fe_{0.35}$. This shows that diffusion of the ^{57}Fe layer is complete given that the equivalent homogeneous composition for the trilayer structure is $Ni_{0.63}Fe_{0.37}$. These results demonstrate that NMR can be used to monitor diffusion processes through their early stages where grain boundaries offer the most energetically favorable route for mixing to proceed.

10.3.2. ^{55}Mn and ^{57}Fe NMR of Fe/Mn multilayers

Takanashi et al. have studied a range of Fe/Mn multilayer films and detail their results in the report of Takanashi et al. (1986b). They also a mention the same NMR work in a slightly different context (Takanashi et al. 1986a) as listed in table 10.6.

A total of four multilayer films were deposited in UHV onto cold (approximately −50°C) Mylar substrates (Takanashi et al. 1986b) as listed in table 10.6. X-ray and electron diffraction measurements showed that bcc structures were formed in all of the Fe layers while the α-Mn structure is only found in the multilayers with the greatest Mn thickness, i.e., Mn = 50 Å (samples A and B).

The ^{55}Mn signal is due to resonances from two different sources; The first are those associated with antiferromagnetic sites in the interior of the α-Mn layers, while the second are associated with ferromagnetic sites near the interfaces. Figure 10.6 shows the NMR spectra for samples B, C and D where the Mn layer thickness is progressively reduced. Figure 10.7 is the spectrum for sample A – $[Fe(15Å)/Mn(50Å)]_{\times 80}$ – which has the thinner Fe layers. The α-Mn structure is known to have four crystallographically inequivalent sites I, II, III and IV (Yamada 1970), however NMR could not be observed from the nuclei of atoms at sites II, III and IV as a result of lack of sensitivity and/or the existence of significant spectral intensity due to Mn atoms close to the interface.

Hence the only distinguishable signals from ^{55}Mn at antiferromagnetic sites are due to resonances from nuclei in atoms situated at site I with a frequency close to 200 MHz. This resonance line is observed for both multilayers with Mn = 50 Å, fig. 10.6(a) and fig. 10.7. The scale of fig. 10.6(a) for the $[Fe(50Å)/Mn(50Å)]_{\times 80}$ multilayer somewhat obscures the line however fig. 10.7 for the $[Fe(15Å)/Mn(50Å)]_{\times 80}$ multilayer clearly shows the 200 MHz line.

In contrast to the signal from ^{55}Mn at antiferromagnetic sites, resonance from nuclei at ferromagnetic sites was observed over a wide range of frequencies for all the Fe/Mn multilayers as can be seen from both figs 10.6 and 10.7. The spectrum of the sample with

TABLE 10.6
NMR work on Fe/Mn multilayers.

Reference	Growth technique	Substrate/buffer	Structure	Orientation	Comments (important result)
Takanashi et al. (1986b)	UHV evaporation	Mylar	A = $[Fe(15Å)/Mn(50Å)]_{\times 80}$ B = $[Fe(50Å)/Mn(50Å)]_{\times 80}$ C = $[Fe(50Å)/Mn(15Å)]_{\times 80}$ D = $[Fe(50Å)/Mn(8Å)]_{\times 80}$		NMR observed from antiferromagnetic and ferromagnetic sites. Interfacial mixing region extends over ~15 Å, similar to Co/Mn.
Takanashi et al. (1986a)	UHV evaporation	Mylar	(i) $[Fe(50Å)/Mn(50Å)]_{\times 80}$ (ii) $[Fe(50Å)/Mn(15Å)]_{\times 80}$ (iii) $[Fe(50Å)/Mn(8Å)]_{\times 80}$		Alloy formation at the interfaces of Fe/Mn, Fe/V and Co/Sb multilayers compared. Results for Fe/Mn show interfacial mixing/alloying over many more atomic layers than Fe/V.

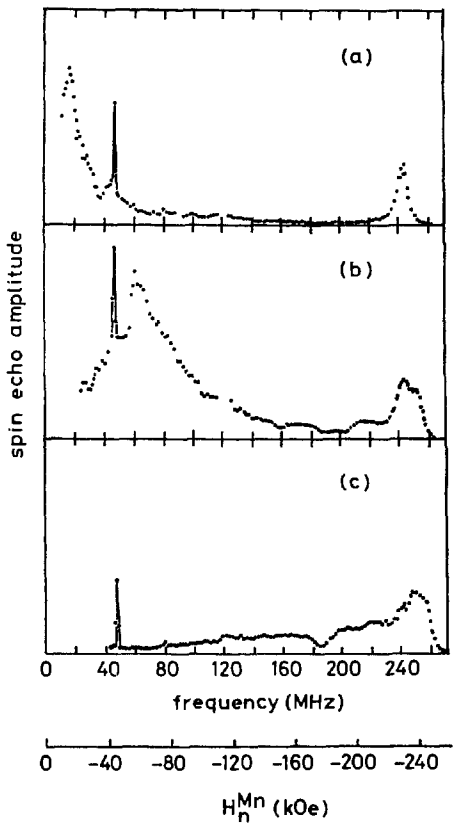


Fig. 10.6. The ^{55}Mn spin echo frequency spectra at zero external field and 1.3 K, which are associated with the ferromagnetic sites in (a) Fe(50Å)/Mn(50Å), (b) Fe(50Å)/Mn(15Å) and (c) Fe(50Å)/Mn(8Å). Intensities are normalized to the peak near 242 MHz. The sharp peak around 47 MHz is associated with ^{57}Fe in the Fe layer. After Takanashi et al. (1986a, 1986b).

thin Fe layers, [Fe(15Å)/Mn(50Å)]$_{\times 80}$, shown in fig. 10.7, demonstrates quite different behaviour to that of the other multilayers. Here the spin echo amplitude is about two orders of magnitude smaller and the line at 242 MHz normally associated with dilute Mn in bcc Fe is not observed. The NMR spectra in fig. 10.6, where all the multilayers have Fe = 50 Å, show sharp lines centred around 47 MHz due to ^{57}Fe in the Fe layers. This was confirmed by measurements of the transverse relaxation time (T_2) which showed that T_2 at the 47 MHz peak was significantly longer than at other frequencies. The peak around 242 MHz corresponds to the resonant frequency expected from ^{55}Mn in dilute FeMn alloys and indicates the presence of Mn in the interior of the Fe layers. The general trend as Mn layer thickness is reduced is a shift in the weigh of the spectral intensity to higher frequencies. In particular the spectral intensity at frequencies less than 150 MHz effectively disappears when the Mn layer is reduced to 8 Å (with the exception of the 47 MHz line due to ^{57}Fe in the Fe layer). Modeling work based on the assumption that interfacial mixing

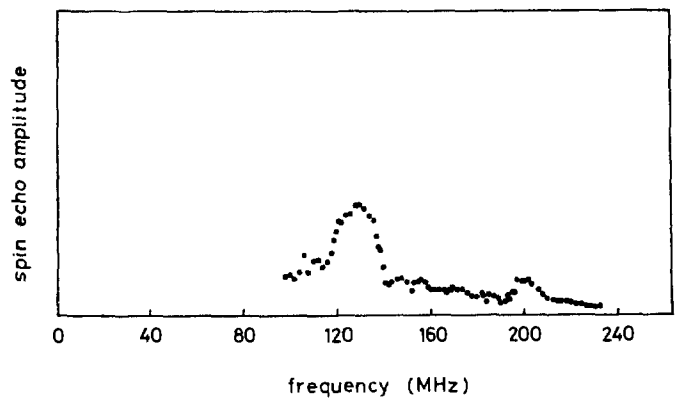


Fig. 10.7. The ^{55}Mn spin echo frequency spectrum at zero external field and 1.3 K, which are associated with the ferromagnetic sites in Fe(15Å)/Mn(50Å). After Takanashi et al. (1986a, 1986b).

occurs only when Fe is deposited on Mn showed that alloying occurred over a number of atomic layers and suggested that layers with Mn concentration significantly larger than the thermodynamic stability limit of $Fe_{0.95}Mn_{0.05}$ could be formed. The interfacial region was estimated to extend over at least 15 Å. This is supported qualitatively by the extensive changes that occurs to the NMR spectrum as the Mn layer thickness is reduced from 15 Å to 8 Å. These results are similar to those found for Co/Mn multilayers where again the interfacial mixing region has been shown to extend over approximately 15 Å.

10.3.3. ^{55}Mn and ^{63}Cu NMR studies of Heusler alloy (Cu_2MnAl) films

Heusler alloy films (Cu_2MnAl) have been studied by Le Dang et al. (1988b) using zero field NMR. Although only one work has been published on NMR investigations of Heusler alloy films, table 10.7, we mention it here as it illustrates the utility of NMR in determining ordered crystalline states. The work shows that the nuclei of non-ferromagnetic elements, e.g., Cu and Mn exhibit NMR when combined in a ferromagnetic alloy, cf. the previous work described in this section where an applied magnetic field is required to produce Cu resonances.

Figure 10.8 shows the zero field NMR spectra for a series of thick (~1 μm) Cu_2MnAl films, produced by sputtering, as a function of the substrate temperature during deposition (T_s).

The resonant frequencies corresponding to ^{55}Mn, ^{63}Cu and ^{65}Cu are 227 MHz, 241 MHz and 259 MHz, respectively, and are similar to the bulk Heusler alloy. The broad featureless NMR spectrum for T_s = 60°C clearly demonstrates that this film is not in an ordered state. As substrate temperature is increased an evolution in the NMR spectrum is seen until at 170°C clear resonance lines are observed. This shows that a much more ordered crystalline structure has formed which is in agreement with magnetization measurements. However line broadening indicates that some atomic disorder is still present. Increasing T_s further leads to degradation of the signal until the spin echo becomes unobservable above T_s = 210°C. The signal then reappears at approximately $T_s \sim$ 300°C. This reappearance

TABLE 10.7
NMR work on Heusler (Cu_2MnAl) alloy thin films.

Reference	Growth technique	Substrate/buffer	Structure	Orientation	Comments (important result)
Le Dang et al. (1988b)	Sputtered	not given	Cu_2MnAl ($\sim$1 μm)		^{55}Mn and ^{63}Cu NMR studies of Heusler alloy films as a function of deposition temperature (T_s) and annealing. At low T_s Cu_2MnAl is disordered while at higher T_s a well defined spectrum is observed with maximum amplitude at 167°C, in agreement with magnetization measurements.

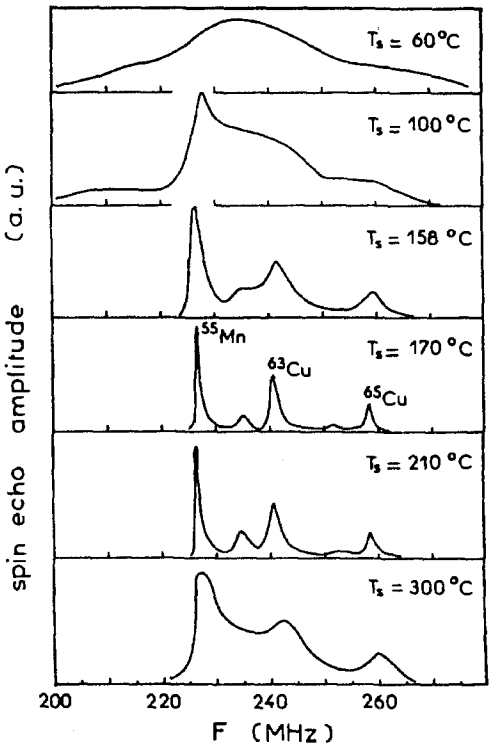


Fig. 10.8. ^{55}Mn, ^{63}Cu and ^{65}Cu spin echo spectra at 4.2 K in sputtered Cu_2MnAl Heusler alloy films deposited at substrate temperature T_S. The lines between the main peaks are due to deviation from exact stoichiometry. After Le Dang et al. (1988b).

was analyzed in terms of the formation of different crystal structures (phases) at different substrate temperatures. The optimum temperature for formation of Cu_2MnAl is around $T_S = 167°C$. At higher temperatures around $T_S = 250°C$ the formation of other phases of CuMnAl are strongly favored. However as T_S is increased beyond 250°C no one phase is particularly favored and this leads to the reappearance of Cu_2MnAl giving rise to the high T_S NMR signal.

10.3.4. NMR investigations of MnSb based multilayers

Mn/Sb based multilayers have been investigated by Le Dang et al. (1989) who studied Mn/Sb with thin Mn layers and by Takanashi et al. (1992) who considered PtMnSb/CuMnSb multilayers based on the C_{1b}-type Heusler alloys, as listed in table 10.8.

Although both of these works involved Mn/Sb based multilayers the purpose of the two investigations was quite different. The work of Le Dang et al. (1989) concentrated on studying anisotropy effects in the hyperfine field, while Takanashi et al. (1992) worked on interdiffusion at the interfaces in PtMnSb/CuMnSb multilayers.

We consider first interdiffusion in PtMnSb/CuMnSb multilayers. The multilayer films were prepared by rf sputtering on to glass substrates keeping the thickness of the CuMnSb

TABLE 10.8
Mn/Sb based multilayer films.

Reference	Growth technique	Substrate/buffer	Structure	Orientation	Comments (important result)
Takanashi et al. (1992)	rf sputtered	Glass	(i) PtMnSb(100Å)/CuMnSb(100Å) (ii) PtMnSb(500Å)/CuMnSb(100Å) (number of layers not given)		Resonances from ^{195}Pt, ^{55}Mn, ^{121}Sb and ^{123}Sb measured. MnSb precipitates in the PtMnSb layers leaving these layers deficient in Pt and promoting Pt diffusion into the CuMnAl layers.
Le Dang et al. (1989)	UHV electron beam evaporation	(i) Kapton/Sb(600Å) (ii) Kapton/Sb(700Å)	(i) $[Sb(120Å)/Mn(12Å)]_{\times 27}$ (ii) $[Sb(50Å)/Mn(2Å)]_{\times 90}$		^{55}Mn and ^{121}Sb NMR measured. Mn/Sb layers grow with c-axis perpendicular to plane. Hyperfine field tensor deduced. Mn clusters in Mn = 2 Å multilayer.

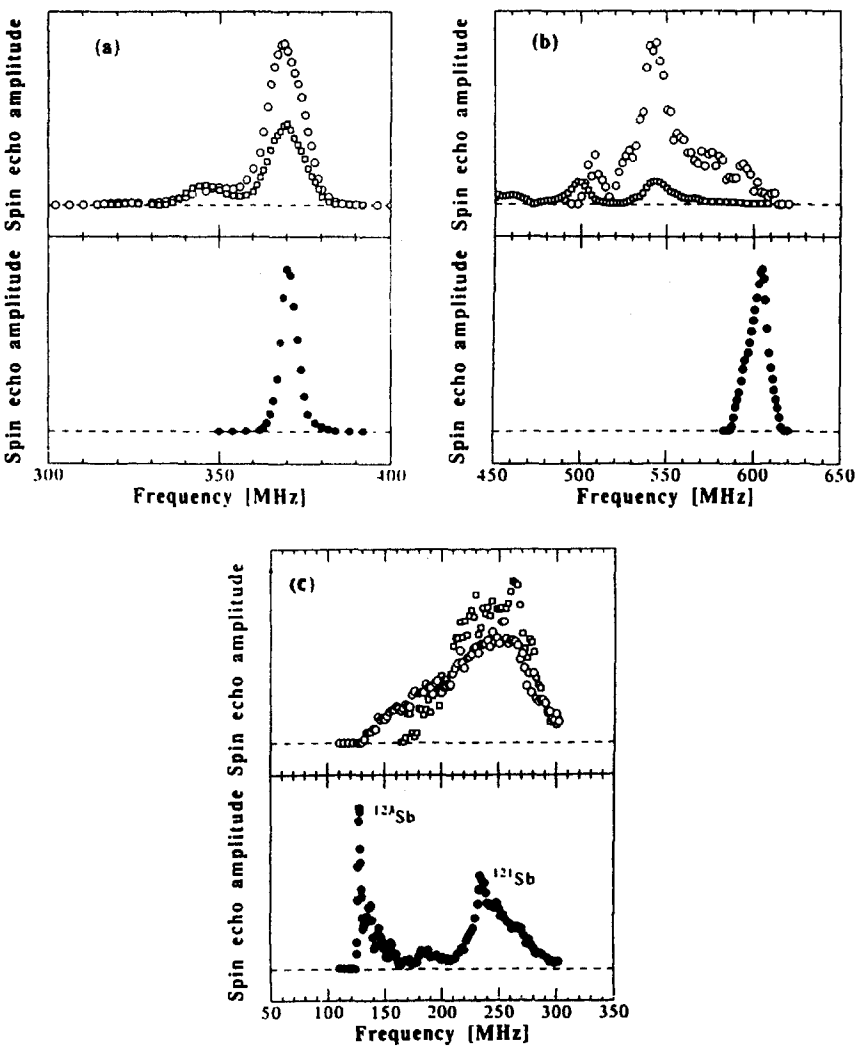


Fig. 10.9. Spin echo spectra at 4.2 K: (a) ^{55}Mn in PtMnSb(t)/CuMnSb(100Å) multilayer films with t = 500 Å (open squares), t = 100 Å (open circles) and a single layer film of PtMnSb (dots); (b) ^{195}Pt in PtMnSb(t)/CuMnSb(100Å) multilayer films with t = 500 Å (open squares), t = 100 Å (open circles) and a single layer film of PtMnSb (dots); (c) NMR spectra in PtMnSb(t)/CuMnSb(100Å) multilayer films with t = 100 Å (open squares), t = 10 Å (open circles) and a single layer film of PtMnSb (dots). After Takanashi et al. (1992).

layers constant at 100 Å and varying the PtMnSb thickness between 100 Å and 1000 Å. Resonance signals could be observed from ^{195}Pt, ^{55}Mn, ^{121}Sb and ^{123}Sb nuclei as shown in fig. 10.9 for various thicknesses of PtMnSb layers. Comparative data for single layer alloy films are also shown.

The line positions in the ^{55}Mn spectra, fig. 10.9(a), of PtMnSb/CuMnSb are similar to those of the single layer alloy film. The ^{195}Pt spectra, fig. 10.9(b), show that the multilayer

line positions are shifted to lower frequency with respect to the reference single layer alloy film. Hence the hyperfine field at the Pt sites appears to be more sensitive to interfacial mixing than at Mn sites. This is at least reasonable as the hyperfine field at the Pt nuclei depends mainly on conduction electron polarization whereas the hyperfine field at Mn nuclei is, in principal, due to core electron polarization of the Mn parent atom. Nevertheless it is surprising that even in the interior of reasonably thick (500 Å) PtMnSb layers the influence of interfacial mixing is able to perturb the local electronic structure over several hundred angstroms. This is much greater than the size of the interfacial mixing region which from magnetization measurements is estimated to be ~25 Å. Figure 10.9(c) shows spectra in the frequency range expected for ^{121}Sb and ^{123}Sb as obtained for the reference single layer alloy film. The spectra from the multilayer films were not considered to be due to Sb as the two characteristic resonances from ^{121}Sb and ^{123}Sb were not observed as distinct lines. However the spectra are in the same frequency range as ferromagnetic MnSb with the NiAs type structure. Hence these resonances were considered to be due to Mn atoms in a MnSb precipitate with the implication that the PtMnSb layers are deficient in Pt due to Pt diffusing into the CuMnSb layers. It was also noted that the intensities of both the ^{55}Mn and ^{195}Pt spectra decreased with decreasing PtMnSb but that the ^{55}Mn spectral intensity due to MnSb increased. This is a curious result and remains unexplained at present.

In the introduction to this section it was mentioned that the work Le Dang et al. (1989) concentrated on studying a rather different aspect of Mn/Sb based multilayers, namely the anisotropy of the hyperfine field. The multilayers used in this study were grown at room temperature on Kapton substrates by electron beam evaporation in UHV. Two samples were produced $[Sb(120Å)/Mn(12Å)]_{\times 27}$ and $[Sb(50Å)/Mn(2Å)]_{\times 90}$ on Sb buffer layers of 600 Å and 700 Å, respectively. The samples were subsequently annealed at 150°C to improve crystallinity. In this review we concentrate on the NMR results from the ^{55}Mn nucleus as ^{121}Sb qualitatively gives the same results.

Figure 10.10 shows zero applied field ^{55}Mn spectra for the two samples together with a spectrum for a bulk powder alloy as a reference. The ^{55}Mn spectrum for the as deposited films produce a broad featureless spectrum shown by the dotted lines. Annealing the multilayers resulted in the spectra shown as solid lines. X-ray diffraction measurements showed that the sample with Mn = 2 Å had unsurprisingly formed MnSb clusters and that these clusters had their c-axes perpendicular to the plane of the film. It was supposed that for the Mn = 2 Å sample the shift in frequency shown in fig. 10.10(c) arose partially from a demagnetizing field associated with the clusters.

The Mn quadruple coupling for the multilayer deduced from transverse relaxation (T_2) measurements was close to that of the bulk powder sample. Measuring the sample with an applied magnetic field of 12 kOe in the plane of the film showed the sign of the hyperfine field was negative as the principal contribution to the HFF is due to core electron polarization. Similar measurements for ^{121}Sb indicated a positive hyperfine field due mainly to conduction electron polarization. Torque magnetometry measurements (Okita and Makino 1968) on MnSb single crystals showed that the first order uniaxial anisotropy constant, K_1, is negative and about an order of magnitude greater than the positive second order term K_2.

The hyperfine field tensor was determined by measuring NMR with a field applied perpendicular to the plane of the film. As the magnetization is rotated towards the c-axis the

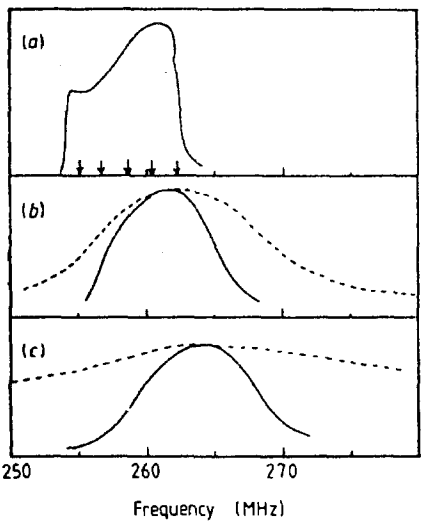


Fig. 10.10. ^{55}Mn spin echo spectra at 4 K for MnSb films. The solid lines show the spectra after annealing at 150 °C. The dashed lines show the normalized results before annealing. The arrows show expected positions of quadrupole lines. (a) Powder sample; (b) Mn layer thickness of 12 Å; (c) Mn layer thickness of 2 Å. After Le Dang et al. (1989).

quadrupole splitting varies approximately as $3\cos^2\theta - 1$ where θ is the angle between the effective resonance field and the magnetization. This can be monitored in an NMR experiment by measuring the line width of the peak as shown in fig. 10.11 for the Mn = 2 Å clustered sample.

Modeling this data leads to the theoretical curves also shown in fig. 10.11 and demonstrates that for the Mn = 2 Å sample the principal contribution to the anisotropy field comes from the first uniaxial anisotropy constant K_1. The shift in levels between the theoretical and experimental curves is due to the dominant contribution from the isotropic core polarization term which is of course included in the experimental results. K_2 only has an appreciable effect when θ is small as shown by the similarity of the two curves (A and B in fig. 10.11) where the second order anisotropy field is assumed to be $H_{A2} = 1$ kOe (curve A) and $H_{A2} = 3$ kOe (curve B) here $H_A = 2K_2/M_s$. Using these values for anisotropy fields it is possible to calculate the shift in resonant frequency as a function of applied field and this is shown as the dotted line in fig. 10.12.

The anisotropic part of the effective hyperfine field is then given by the difference between the calculated curve and the experimental data. In the case of the multilayer with Mn = 12 Å the values for the perpendicular and parallel hyperfine field at ^{55}Mn were found to be 249 kOe and 264 kOe, respectively, leading to an estimation of the dipole field, from measurements of nuclear quadrupole coupling, of 17.7 kOe for Mn. This anisotropy probably originates from 3d spin and charge asymmetries. Similar results for Sb led to an estimate of 36 kOe, in qualitative agreement with the observed values of −13 kOe and 21 kOe for Mn and Sb, respectively.

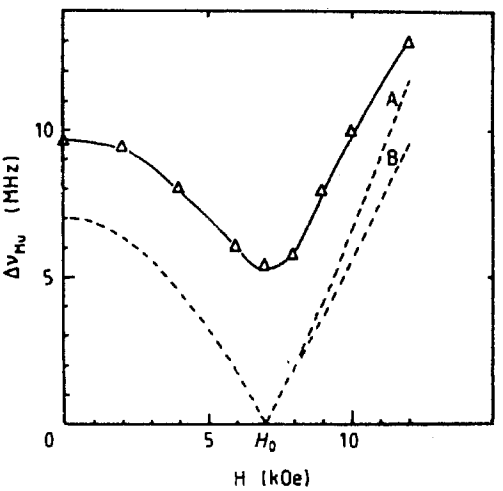


Fig. 10.11. Variation in the Mn linewidth at half maximum as a function of DC magnetic field applied perpendicular to film plane with manganese layer thickness of 2 Å (cluster sample). The theoretical variation in the total quadrupole splitting is shown by the dashed lines. $H_{A2} = 1$ kOe (curve A) and $H_{A2} = 3$ kOe (curve B). After Le Dang et al. (1989).

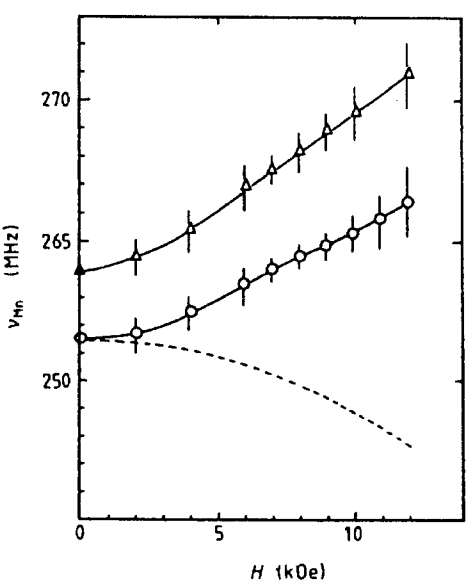


Fig. 10.12. Variation in the ^{55}Mn resonance frequency as a function of DC magnetic field applied perpendicular to film plane with manganese layer. The theoretical frequency shift due to DC and demagnetizing fields is shown by the dashed line. Data for a manganese layer thickness of 2 Å (open triangles). Data for a manganese layer thickness of 12 Å (open circles). After Le Dang et al. (1989).

10.4. NMR in metallic superconducting multilayers

Although a number of papers have been published on NMR studies of superconducting multilayers many of these contain detailed analysis of NMR and other data within the framework of BCS theory. It is not our intention to cover the theory of superconductivity in detail as it falls beyond the scope of the current article, rather we hope to give a flavor of the NMR experiments that can be performed together with a brief outline of the results obtained.

10.4.1. ^{63}Cu and ^{93}Nb NMR in superconducting Cu/Nb multilayers

Cu/Nb multilayers are not conventional ferromagnetic thin film multilayers, however we include a brief summary of the NMR work on this system both for completeness and to demonstrate how the technique of NMR can give information on superconducting thin films through the study of the nuclear spin lattice magnetization relaxation time T_1.

The interest in Cu/Nb multilayers arises from the interlayer interactions where the superconducting electron pair state in the Nb layers has a quasi macroscopic coherence length which leads to a strong proximity effect across the Nb/Cu interface and hence superconductivity within the Cu layers. NMR is particularly useful in the study of these multilayers as it is element specific and hence can selectively measure one type of layer in the multilayer. The work published to date on Cu/Nb multilayers is detailed in table 10.9.

Although five papers are detailed in table 10.9 the essence of the NMR work in superconducting multilayers can be gained by considering the early papers of Aoki et al. (1987a, 1987b). They studied multilayers consisting of [Cu(400Å)/Nb(245Å)]$_{\times 50}$ which were prepared by rf sputtering on to glass substrates. The ac susceptibility measurements showed a single superconducting transition at $T_c = 4.6 \pm 0.3$ K which is the expected value for bulk Nb. NMR measurements were undertaken using a conventional phase coherent pulsed spectrometer. The ^{63}Cu and ^{65}Cu spectrum taken at 4.1 MHz and $T = 4.2$ K is shown in fig. 10.13.

The two lines, free from the influence of Nb absorption, from ^{63}Cu and ^{65}Cu are clearly visible in fig. 10.13. The longitudinal relaxation time T_1 for the ^{63}Cu line was measured by the NMR field cycling method allowing T_1 determination in zero external field. At temperatures $T < T_c$ the decay in nuclear magnetization was well fitted by a single exponential function, indicating a simple homogeneous process. Data from these single exponential fits of T_1^{-1} are plotted as a function of temperature in fig. 10.14.

Initially, as the temperature is lowered past T_c, the relaxation rate T_1^{-1} is observed to increase, this is then followed by a rapid decrease and finally at temperatures below 0.8 K the relaxation rate becomes almost proportional to T. This temperature behaviour of the relaxation rate is commonly observed in superconductors. Analysis of the data on Cu/Nb multilayers leads to the conclusion that the superconducting energy gap is 2.4 $k_B T_c$ in the Cu layers. The effect of applying an external magnetic field of 3.6 kOe is also shown in fig. 10.14. In this case T_1 follows the Korringa relation $T_1 T = 1.3$ s K which is close to the value obtained in normal Cu metal. These results demonstrate that the Cu layer in these multilayers exhibits a real superconducting character and that an external field 3.6 kOe was sufficient to return the Cu layer to its normal conducting state.

Finally we note the ^{93}Nb NMR has also been observed in Cu/Nb multilayers by Kohori et al. (1994). They observed a two component peak for ^{93}Nb measured at 41.132 MHz

TABLE 10.9

^{63}Cu and ^{93}Nb NMR work on Cu/Nb superconducting multilayers.

Reference	Growth technique	Substrate/buffer	Structure	Orientation	Comments (important result)
Aoki et al. (1987a)	rf sputtered	Glass	$[Cu(400Å)/Nb(245Å)]_{\times 50}$		Nuclear spin lattice relaxation time (T_1) measured for the ^{63}Cu resonance as a function of temperature. Superconducting energy gap deduced and field dependence of proximity effect superconductivity measured.
Aoki et al. (1987b)	rf sputtered	Glass	$[Cu(400Å)/Nb(245Å)]_{\times 50}$		Nuclear spin lattice relaxation time (T_1) measured for the ^{63}Cu resonance as a function of temperature. Superconducting energy gap deduced and field dependence of proximity effect superconductivity measured.
Zheng et al. (1989)	rf sputtered	(i) Ag (foil) (ii) Glass (iii) Glass	(i) Cu (200Å)/Nb(200Å) (ii) Cu (400Å)/Nb(200Å) (iii) Cu (600Å)/Nb(200Å) (30–50 repeat units exact details not available)		T_1 measured for the ^{63}Cu resonance as a function of temperature. Below the superconducting T_c, T_1^{-1} at first increases and then decreases rapidly becoming proportional to T at ~0.8 K.
Zheng et al. (1991)	rf sputtered	(i) Ag (foil) (ii) Glass (iii) Glass	(i) Cu(200Å)/Nb(200Å) (ii) Cu(400Å)/Nb(200Å) (iii) Cu(600Å)/Nb(200Å) (30–50 repeat units exact details not available)		T_1 measured for the ^{63}Cu resonance as a function of temperature. BCS like behaviour just below T_c replaced by Korringa like relaxation at $T \sim 0.8$ K. Superconducting proximity effect in Cu layers have anisotropic energy gap. ^{93}Nb NMR also measured.

TABLE 10.9
(Continued)

Reference	Growth technique	Substrate/buffer	Structure	Orientation	Comments (important result)
Kohori et al. (1994)	UHV evaporation	Ag (foil)	(i) Cu(200Å)/Nb(200Å) (ii) Cu(400Å)/Nb(200Å)		^{63}Cu and ^{93}Nb NMR measured. Temperature dependence of T_1 investigated. Large electric field gradient found at ^{93}Nb sites due to bcc Nb lattice distortion.

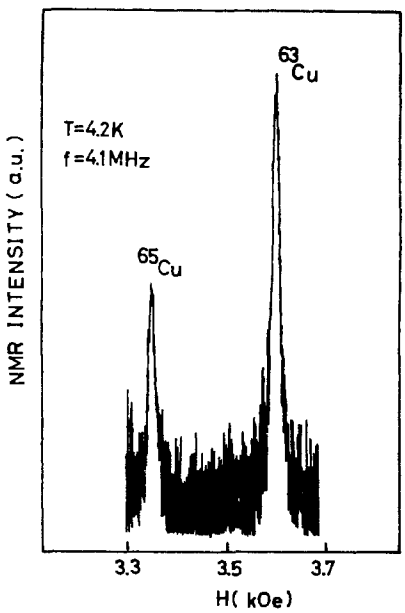


Fig. 10.13. Observed NMR spectrum of the Cu/Nb sample. After Aoki et al. (1987b).

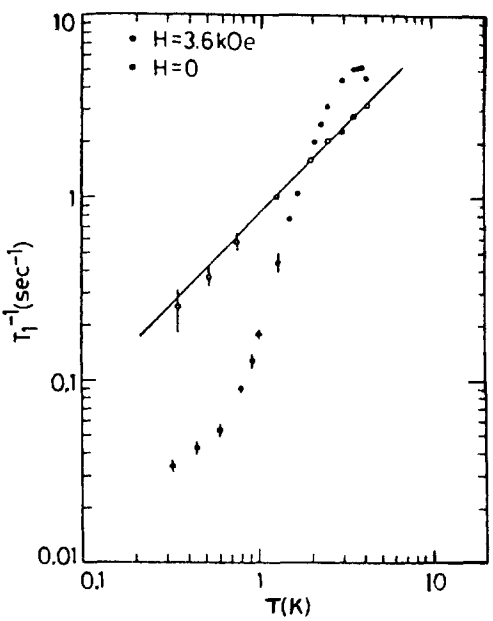


Fig. 10.14. The NMR relaxation rate T_1^{-1} of the Cu layer at temperature T with (open circles) and without (dots) an external field. After Aoki et al. (1987b).

with $H_{app} = 8.5$ kOe, a narrow line superimposed on a much broader feature. The broad feature was associated with an electric quadrupole field induced by the distortion of the Nb bcc lattice.

10.5. NMR experiments on thin film Rare Earth elements

NMR studies of Rare Earth (RE) elements in thin film form is very much in its infancy. This is due in part to the difficulty of preparing good quality thin films, but mostly as a result of the lack of availability of NMR spectrometers with an appropriate frequency range. The NMR studies considered to date in this article have mostly involved nuclei from the 3d (1st series) transition metals with resonant frequencies of less than 1000 MHz, e.g., bulk Co ~220 MHz. This contrasts with resonant frequencies for some rare earth elements such as Ho and Tb which are several GHz and hence require a custom built spectrometer optimized for thin film work. The recent advent of UHV MBE deposition systems dedicated to producing rare earth thin films, means that high quality films including multilayers are now becoming available for study by NMR.

At the time of compiling this article we have found only one reference to NMR work on thin rare earth films using ^{165}Ho and two using ^{159}Tb, table 10.10. However work presented at recent conferences, and as yet not in the literature, shows that other rare earth thin films are being actively investigated with those containing Tb of particular interest.

The rare earth alloy thin film studied by Graham et al. (1993) consisted of a trilayer structure of Y/$Ho_{0.05}Dy_{0.95}$/Y with a relatively thick (3000 Å) HoDy alloy layer where Ho is close to the dilute alloy limit. The film was grown by MBE on a sapphire substrate with a Nb buffer. NMR measurements were made in a resonant cavity capable of being tuned between 3000 and 7000 MHz. Figure 10.15(a) shows a ^{165}Ho spectrum from the dilute HoDy alloy film taken at $T = 4.2$ K with an 8 Tesla applied field.

The seven line quadrupole split spectrum is characteristic of ^{165}Ho as it has nuclear angular momentum of $I = 7/2$. The lines in this spectrum are significantly sharper than those observed in bulk alloys by Mackenzie et al. (1974) and indicate a high degree of crystallinity. Figure 10.15(b) reveals an additional satellite line only just observable in fig. 10.15(a). This same fine structure is associated with each of the seven quadrupole lines and is well fitted by two Gaussian functions of relative weight 1 and 0.67. This is close to the expected relative probabilities for a given Ho atom to have zero or one Ho nearest neighbor in a $Ho_{0.05}Dy_{0.95}$ random alloy. The greater width of the satellite line is probably due to the fact that not all of the 12 possible nearest neighbor sites are equivalent in an applied magnetic field. The 4.4 MHz shift in the relative position of the satellite lines indicates that the presence of a Ho atom in the probe Ho nearest neighbor shell increases the transferred hyperfine field by 0.5 T.

In applied fields of less than 3 T the ^{165}Ho NMR spectrum changes significantly. The transverse relaxation time (T_2) becomes much shorter allowing only the outer quadrupole satellite lines to be measured accurately. This is due to their smaller transition matrix elements. The exact form of the outer quadrupole spectrum depends on whether or not the sample is cooled in zero field. Figure 10.16 shows the highest frequency quadrupole line both before and after the application of a 8 T magnetic field.

The zero field cooled spectrum consists of two components with frequencies of 6738 MHz and 6752 MHz. Application and subsequent removal of a field of 8 T enhances

TABLE 10.10
Rare Earth thin films studied by NMR.

Reference	Growth technique	Substrate/buffer	Structure	Orientation	Comments (important result)
Li et al. (1996)	MBE	Sapphire/Nb	$Y/Tb_{1-x}Y_x/Y$ $x = 0.10, 0.05$ (Alloy = 3000 Å)	c-axis perpendicular to plane	Fine structure on ^{159}Tb lines due to 0–3 Y nearest neighbors Y not a simple magnetic dilutant.
Li et al. (1996)	MBE	Sapphire/Nb	$Y_{300}/(Tb_{40}/Y_{20})_{25}/Y_{70}$	c-axis perpendicular to plane	Thermally activated interdiffusion. Diffusion length varies from layer to layer.
Graham et al. (1993)	MBE	Sapphire/Nb	$Y/Ho_{0.05}Dy_{0.95}/Y$ (HoDy alloy = 3000 Å)	c-axis perpendicular to plane	Field dependence of hyperfine field splitting of dilute Ho in a Dy thin film matrix studied. ^{165}Ho spectral lines observed to be sharper than in bulk. Quadrupole splitting is clearly observed with a systematic satellite structure on each of the 7 lines which could be due to the coexist of ferromagnetic and helimagnetic phases.

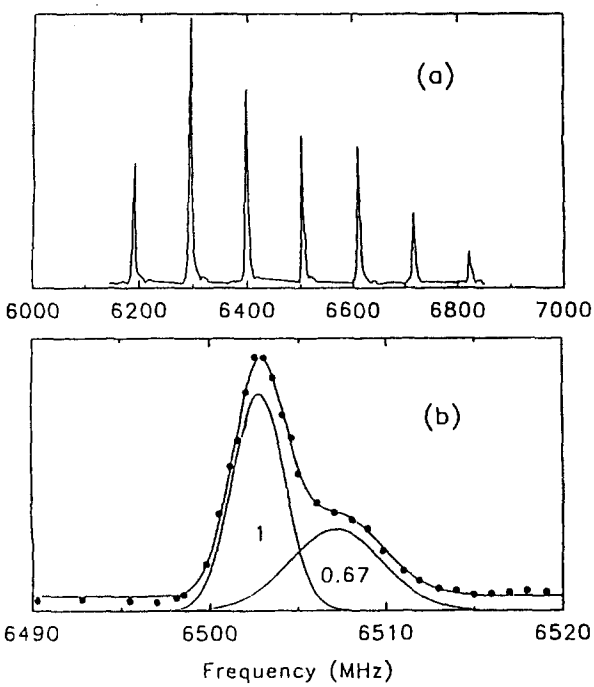


Fig. 10.15. (a) NMR spectrum characteristic of ^{165}Ho measured at 8 T and 1.4 K for a Y/$Ho_{0.05}Dy_{0.95}$/Y trilayer. (b) Expanded view of central line revealing an additional satellite. The relative areas of the Gaussian components are shown beneath the curves. After Graham et al. (1993).

the 6738 MHz line while reducing the intensity of the 6752 MHz line. The authors explained this effect by considering the possibly that two magnetic phases coexist, namely a ferromagnetic phase and a helimagnetic phase. In Dy/Y films where Dy is made sufficiently thin (<3000 Å) it is possible to completely suppress the ferromagnetic phase, however at low temperatures an applied field of 1 T is sufficient to restore ferromagnetic order which remains even when the applied field is removed. Films with thicker (>3000 Å) Dy layers show a behaviour similar to that of the bulk material with T_c reduced by 5 K. The Y/$Ho_{0.05}Dy_{0.95}$/Y film considered here is an intermediate case and as a working model it was suggested that the low frequency line (6738 MHz) was due to nuclei in the interior of the film where the relaxation conditions allow more bulk-like properties and hence bulk-like ferromagnetic order. The 6752 MHz line is then due to nuclei whose parent atoms are in more constrained, helimagnetically order regions, presumably close to the interfaces.

The ^{159}Tb NMR of bulk and thin film samples of Tb–Y alloys containing 5% and 10% Y was investigated by Li et al. (1996), table 10.10. The usual Tb spectrum was obtained, consisting of a central line near 3000 MHz and quadrupole split lines some 600 MHz above and below the central frequency. Fine structure on the lines from the thin film samples was characterized as due to Tb with 0–3 Y nearest neighbors. The magnitude of the splitting was less than half that expected for an impurity atom with zero moment indicating that Y is not a simple dilutant.

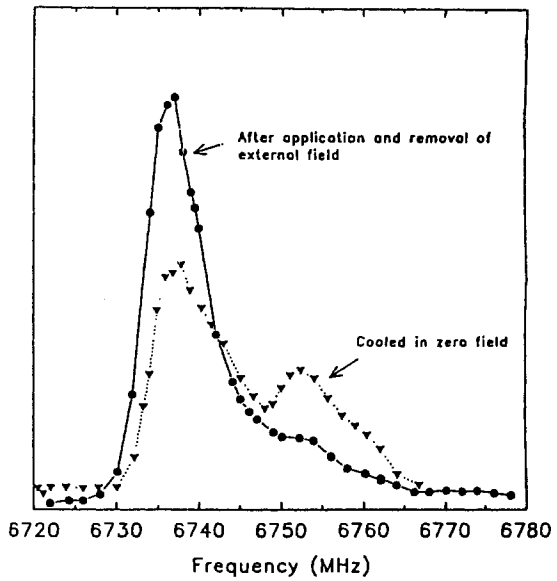


Fig. 10.16. Profile of the highest frequency quadrupole satellite line for a Y/$Ho_{0.05}Dy_{0.95}$/Y trilayer measured before (triangles) and after (circles) the application of an external 8 T field. After Graham et al. (1993).

Interdiffusion in the Tb/Y system was studied in a superlattice by Li et al. (1997), table 10.10. The ^{159}Tb spectrum was analyzed using a model in which the Y diffusion into a Tb layer was thermally activated and varied from layer to layer.

In conclusion we hope that this article will have at least given some flavor of just how valuable the contribution of microscopic, hyperfine techniques are to the understanding of thin film systems and shown that it is able to provide useful information for both fundamental and more applied research.

Acknowledgements

The authors would like to acknowledge the following for their kindness in supplying reprints and comments on their work: W.J.M. de Jonge, N.A. Lesnik, Y. Maeda, and P. Panissod. The financial support of the UK Engineering and Physical Sciences Research Council for NMR work at St. Andrews is gratefully acknowledged.

References

Abe, H., H. Yasuoka and A. Hirai, 1966, J. Phys. Soc. Japan **21**, 77.

Aoki, R., G.Q. Zheng, Y. Kohori, Y. Oda, K. Asayama, S. Wada and Y. Obi, 1987a, Jpn. J. Appl. Phys. **26**, 1455.

Aoki, R., Y. Kohori, G.Q. Zheng, Y. Oda, K. Asayama and S. Wada, 1987b, J. Phys. Soc. Japan **56**, 4495.

Bagguley, D.M.S. (ed.), 1992, Pulsed Magnetic Resonance (Oxford Univ. Press, Oxford).

Baibich, M.N., J.M. Broto, A. Fert, F. Nguyen Van

Dau, F. Petroff, P. Etienne, G. Creuzet, A. Friederich and J. Chazelas, 1988, Phys. Rev. Lett. **61**, 2472.

Bailey, S.G., D.C. Creagh and G.V.H. Wilson, 1973, Phys. Lett. A **44**, 229.

Beardsley, I.A., and J.G. Zhu, 1991, IEEE Trans. Magn. **27**, 5037.

Beauvillain, P., C. Chappert, K. Le Dang, R. Megy, S.O. Mahfoud and P. Veillet, 1996, J. Magn. Magn. Mater. **154**, 160.

Berzhanskii, V.N., and S.N. Polulyakh, 1989, Fizika Tverdogo Tela **31**, 256.

Binasch, G., P. Grünberg, F. Saurenbach and W. Zinn, 1989, Phys. Rev. B **39**, 4828.

Bland, J.A.C., R.D. Bateson, P.C. Riedi, R.G. Graham, H.J. Lauter, J. Penfold and C. Shackleton, 1991a, J. Appl. Phys. **69**, 4989.

Bland, J.A.C., J. Penfold and C. Shackleton, 1991b, J. Magn. Magn. Mater. **126**, 364.

Bogdanova, K., V.A. Golenischevkutuzov, M.I. Kurkin and E.A. Turo, 1995, J. Magn. Magn. Mater. **144**, 731.

Boher, P., F. Giron, Ph. Houdy, F. Beaudelet, A. Fontaine, J.M. Ladouceur, E. Dartyge, P. Beauvillain, C. Chappert, P. Veillet and K. Le Dang, 1992, J. Appl. Phys. **71**, 1798.

Boyce, J.B., and C.P. Slichter, 1974, Phys. Rev. Lett. **32**, 61.

Brooks, M.S.S., and B. Johansson, 1993, in: Ferromagnetic Materials, Vol. 7, ed. K.H.J. Buschow (North-Holland, Amsterdam) p. 139.

Bruno, P., and C. Chappert, 1992, Phys. Rev. B **46**, 261.

Campos, A., J. Englich, H. Lütgemeier, M. Marysko, P. Novak and W. Zinn, 1992, J. Magn. Magn. Mater. **104**, 431.

Campos, A., H. Lütgemeier and P. Novak, 1993, J. Magn. Magn. Mater. **125**, 279.

Carter, G.C., L.H. Bennet and D.J. Kahan, 1977, Metallic Shifts in NMR (Pergamon Press, Oxford).

Cesari, C., J.P. Faure, G. Nihoul, K. Le Dang, P. Veillet and D. Renard, 1989, J. Magn. Magn. Mater. **78**, 296.

Chappert, C., K. Le Dang, P. Beauvillain, H. Hurdequint and D. Renard, 1986, Phys. Rev. B **34**, 3192.

Chappert, C., P. Beauvillain, P. Bruno, J.P. Chauyineau, M. Galtier, K. Le Dang, C. Marliere, R. Megy, D. Renard, J.P. Renard, J. Seiden, F. Trigui, P. Veillet and E. Velu, 1991, J. Magn. Magn. Mater. **93**, 319.

Chow, G.M., L.K. Kurihara, K.M. Kemner, P.E. Schoen, W.T. Elam, A. Ervin, S. Keller, Y.D. Zhang, J. Budnick and T. Ambrose, 1995, J. Mater. Res. **10**, 1546.

Christner, J.A., R. Ranjan, R.L. Peterson and J.I. Lee, 1990, J. Appl. Phys. **63**, 3260.

Clarke, R., D. Barlett, F. Tsui, B.X. Chen and C. Uher, 1994, J. Appl. Phys. **75**, 6174.

de Gronckel, H.A.M., C.H.W. Swuste, K. Kopinga and W.J.M. de Jonge, 1989, Appl. Phys. A **49**, 467.

de Gronckel, H.A.M., J.A.M. Bienert, F.J.A. den Broeder and W.J.M. de Jonge, 1991a, J. Magn. Magn. Mater. **93**, 457.

de Gronckel, H.A.M., K. Kopinga, W.J.M. de Jonge, P. Panissod, J.P. Schille and F.J.A. den Broeder, 1991b, Phys. Rev. B **44**, 9100.

de Gronckel, H.A.M., B.M. Mertens, P.J.H. Bloemen, K. Kopinga and W.J.M. de Jonge, 1992, J. Magn. Magn. Mater. **104**, 1809.

de Gronckel, H.A.M., P.J.H. Bloemen, E.A.M. van Alphen and W.J.M. de Jonge, 1994, Phys. Rev. B **49**, 11327.

Dekoster, J., E. Jedryka, C. Mény and G. Langouche, 1993a, Europhys. Lett. **22**, 433.

Dekoster, J., E. Jedryka, C. Mény and G. Langouche, 1993b, J. Magn. Magn. Mater. **121**, 69.

Dekoster, J., E. Jedryka, C. Mény and G. Langouche, 1993c, J. Magn. Magn. Mater. **126**, 12.

de Vries, J.J., P.J.H. Bloemen, M.T. Johnson, J.A. de Stegge, A. Reinders and W.J.M. de Jonge, 1994, J. Magn. Magn. Mater. **129**, 1129.

Dinia, A., K. Ounadjela, A. Arbaoui, G. Suran, D. Müller and P. Panissod, 1992, J. Magn. Magn. Mater. **104**, 1871.

Dormann, E., 1991, in: Handbook on the Physics and Chemistry of Rare Earths, Vol. 14, eds K.A. Gschneidner Jr. and L. Eyring (North-Holland, Amsterdam) p. 63.

Droste, R., G. Stern and J.C. Walker, 1986, J. Magn. Magn. Mater. **54–57**, 763.

Dumelow, T., and P.C. Riedi, 1987, Hyp. Interact. **35**, 1061.

Ebert, H., and M. Battocletti, 1996, Solid State Commun. **98**, 785.

Edwards, D.M., 1976, J. Phys. F **6**, L289.

Fekete, D., A. Grayeveskey, D. Shaltiel, U. Goebel, E. Dormann and N. Kaplan, 1976, Phys. Rev. Lett. **36**, 1566.

Fekete, D., H. Boasson, A. Grayevski, V. Zevin and N. Kaplan, 1978, Phys. Rev. B **17**, 347.

Fert, A., P. Grünberg, A. Barthelemy, F. Petroff and W. Zinn, 1995, J. Magn. Magn. Mater. **140–144**, 1.

Figiel, H., 1991, Magn. Res. Rev. **16**, 101.

Fisher, R.D., J.C. Allen and J.L. Pressesky, 1986, IEEE Trans. Magn. **22**, 352.

Freeman., A.J., and R.-q. Wu, 1991, J. Magn. Magn. Mater. **100**, 497.

Gantefore, G., and W. Eberhardt, 1996, Phys. Rev. Lett. **76**, 4975.

Giron, F., P. Boher, K. Le Dang and P. Veillet, 1992, J. Phys. Cond. Matter **31**, L425.

Giron, F., P. Boher, P. Houdy, P. Beauvillain, K. Le Dang and P. Veillet, 1993, J. Magn. Magn. Mater. **121**, 24.

Gleason, K.K., 1995, Trac-Trends Anal. Chem. **14**, 104.

Gossard, A.C., and A.M. Portis, 1959, Phys. Rev. Lett. **3**, 164.

Gossard, A.C., A.M. Portis, M. Rubinstein and R.H. Lindquist, 1965, Phys. Rev. **138**, A1415.

Goto, A., H. Yasuoka, A. Hayashi and Y. Ueda, 1992, J. Phys. Soc. Japan **61**, 1178.

Goto, A., H. Yasuoka, K. Takanashi, K. Saito and H. Fujimori, 1993a, J. Magn. Magn. Mater. **126**, 358.

Goto, A., H. Yasuoka, H. Yamamoto and T. Shinjo, 1993b, J. Magn. Magn. Mater. **124**, 285.

Goto, A., H. Yasuoka, H. Yamamoto and T. Shinjo, 1993c, J. Phys. Soc. Japan **62**, 2129.

Gradmann, U., 1993, in: Ferromagnetic Materials, Vol. 7, ed. K.H.J. Buschow (North-Holland, Amsterdam) p. 1.

Gradmann, U., M. Przybylski, H.J. Elmers and G. Liu, 1989, Appl. Phys. A **49**, 563.

Graham, R.G., J.W. Ross, D.S. Bunbury, M.A.H. McCausland, R.C.C. Ward and M.R. Wells, 1993, J. Phys. Cond. Matter **5**(1), L647.

Gu, E., M. Gester, R.J. Hicken, C. Daboo, M. Tselepi, S.J. Gray, J.A.C. Bland, L.M. Brown, T. Thomson and P.C. Riedi, 1995, Phys. Rev. B **52**, 14704.

Guo, G.Y., and H. Ebert, 1996, Phys. Rev. B **53**, 2492.

Hamada, N., K. Terakura, K. Takanashi and H. Yasuoka, 1985, J. Phys. F **15**, 835.

Harp, G.R., R.F.C. Farrow, D. Weller, T.A. Rabedeau and R.F. Marks, 1993, Phys. Rev. B **48**, 17538.

Henry, Y., C. Mény, A. Dinia and P. Panissod, 1993, Phys. Rev. B **47**, 15037.

Hirono, S., M. Igarashi, Y. Koshimoto and Y. Maeda, 1995, IEEE Trans. Magn. **31**, 2812.

Homma, T., H. Asai, T. Osaka, K. Takei and Y. Maeda, 1992, Chem. Lett. **9**, 1783.

Hong, S.C., A.J. Freeman and C.L. Fu, 1988, Phys. Rev. B **38**, 12156.

Hono, K., Y. Maeda, J.L. Li and T. Sakurai, 1993, IEEE Trans. Magn. **29**, 3745.

Houdy, P., P. Boher, F. Giron, F. Pierre, C. Chappert, P. Beauvillain, K. Le Dang, P. Veillet and E. Velu, 1991, J. Appl. Phys. **69**, 5667.

Idzerda, Y.U., W.T. Elam, B.T. Jonker and G.A. Prinz, 1989, Phys. Rev. Lett. **62**, 2480.

Imai, T., M. Takigawa, H. Yasuoka, T. Mizutani, N. Hosoito and T. Shinjo, 1987, Jpn. J. Appl. Phys. **26**, 1457.

Inomata, K., Y. Saito and S. Hashimoto, 1993, J. Magn. Magn. Mater. **121**, 350.

Iwasaki, S., and K. Takemura, 1975, IEEE Trans. Magn. **11**, 1173.

Janak, J.F., 1979, Phys. Rev. B **20**, 2206.

Jay, J., E. Jedryka, M. Wojcik, J. Dekoster, G. Langouche and P. Panissod, 1996, Z. Phys. B **101**, 329.

Jedryka, E., P. Panissod, P. Guilmin and G. Marchal, 1989, Hyp. Interact. **51**, 1103.

Jeffrey, F.R., P.D. Murphy and B.C. Gerstein, 1981, Phys. Rev. B **23**, 2099.

Jin, Q.Y., Y.B. Xu, H.R. Zhai, C. Hu, M. Lu, Y. Zhai, G.L. Dunifer, H.M. Naik and M. Ahmad, 1993, J. Magn. Magn. Mater. **126**, 285.

Jin, Q.Y., Y.B. Xu, H.R. Zhai, C. Hu, M. Lu, Q.S. Bie, Y. Zhai, G.L. Dunifer, R. Naik and M. Ahmad, 1994a, Phys. Rev. Lett. **72**, 768.

Jin, Q.Y., Y.B. Xu, Y. Zhai, M. Lu, Q.S. Bie, S.L. Jiang and H.R. Zhai, 1994b, Chin. Phys. Lett. **11**, 53.

Johnson, C.E., M.S. Ridout and T.E. Cranshaw, 1963, Proc. Phys. Soc. **81**, 1079.

Kawakami, M., T. Hihara, Y. Koi and T. Wakiyama, 1972, J. Phys. Soc. Japan **33**, 1591.

Khan, M.R., S.Y. Lee, S.L. Duan, J.L. Pressesky, N. Heiman, D.E. Speliotis and M.R. Scheinfein, 1991, J. Appl. Phys. **69**, 4745.

Kim, S.K., F. Jona and P.M. Marcus, 1995, Phys. Rev. B **51**, 5412.

Kirk, K.J., J.N. Chapman and C.D.W. Wilkinson, 1997, Appl. Phys. Lett. **71**, 539.

Kobayashi, S., K. Asayama and J. Itoh, 1966, J. Phys. Soc. Japan **21**, 65.

Kohori, Y., T. Kohara, Y. Oda, M. Nishikawa, E. Kita and A. Tasaki, 1994, Physica B **194**, 2383.

Kotov, V.V., S.P. Likhtorovich, A.I. Matvienko, M.M. Nishchenko and A.N. Pogorily, 1995, J. Magn. Magn. Mater. **148**, 83.

Krishnan, R., 1991, Solid State Commun. **77**, 499.

Krishnan, R., K. Le Dang and P. Veillet, 1985, Phys. Lett. A **110**, 170.

Kubo, H., and I. Koike, 1989, Hyp. Interact. **51**, 1069.

Kumeda, M., Y. Tsujimura, Y. Yonezawa, A. Morimoto and T. Shimizu, 1985, Solid State Commun. **55**, 409.

Kuo, Y.C., S.T. Jiang and Z.S. Gao, 1993, J. Magn. Magn. Mater. **118**, 200.

Laidler, H., and B.J. Hickey, 1996, J. Appl. Phys. **79**, 6250.

Lang, D.V., J.B. Boyce, C. Lo and C.P. Slichter, 1972, Phys. Rev. Lett. **29**, 776.

Le Dang, K., and M. Naoe, 1988, J. Appl. Phys. **63**, 4119.

Le Dang, K., P. Veillet, C. Chappert, P. Beauvillain and D. Renard, 1986a, J. Phys F: Metal Phys. **16**, L109.

Le Dang, K., P. Veillet, H. Sakakima and R. Krishnan, 1986b, J. Phys. F: Metal Phys. **16**, 93.

Le Dang, K., P. Veillet, K. Ounadjela and G. Suran, 1987, J. Phys. C: Cond. Mater. **20**, L195.

Le Dang, K., P. Veillet, H. Sakakima and R. Krishnan, 1988a, J. Physique **49**, 1713.

Le Dang, K., P. Veillet, R. Krishnan, A. Morisako, M. Matsumoto and M. Naoe, 1988b, J. Appl. Phys. **63**, 4119.

Le Dang, K., P. Veillet, P. Beauvillain, N. Nakayama and T. Shinjo, 1989, J. Phys. Cond. Matter **1**, 6153.

Le Dang, K., P. Veillet, H. Hui, F.J. Lamelas, C.H. Lee and R. Clarke, 1990, Phys. Rev. B **41**, 12902.

Le Dang, K., P. Veillet, P. Beauvillain, C. Chappert, H. He, F.J. Lamelas, C.H. Lee and R. Clarke, 1991, Phys. Rev. B **43**, 13228.

Le Dang, K., P. Veillet, R. Krishnan and H. Lassri, 1992, Appl. Phys. Lett. **61**, 994.

Le Dang, K., P. Veillet, E. Velu, S.S.P. Parkin and C. Chappert, 1993a, Appl. Phys. Lett. **63**, 108.

Le Dang, K., P. Veillet, C. Chappert, R.F.C. Farrow, R.F. Marks and D. Weller, 1993b, Phys. Rev. B **48**, 14023.

Le Dang, K., P. Veillet, C. Chappert, R.F.C. Farrow, R.F. Marks, D. Weller and A. Cebollada, 1994, Phys. Rev. B **50**, 200.

Lesnik, N.A., and S.Y. Kharitonskii, 1985a, Phys. Metals **5**, 701.

Lesnik, N.A., and S.Y. Kharitonskii, 1985b, Phys. Metals **6**, 627.

Lesnik, N.A., V.N. Pushkar, L.M. Sandler and S.Y. Kharitonskii, 1985c, Phys. Metals **5**, 960.

Lesnik, N.A., and S.Y. Kharitonskii, 1986, Industrial Laboratory–USSR **52**, 624.

Lesnik, N.A., and V.O. Golub, 1993, Int. J. Mod. Phys. B **7**, 511.

Lesnik, N.A., and R. Gontarz, 1995, J. Magn. Magn. Mater. **144**, 607.

Lesnik, N.A., Y.V. Kudryavtsev, R. Gontazh, V.V. Kotov, D.J. Podyalovsky and B.P. Voznyuk, 1991, Ukrainskii Fizicheskii Zhurnal **36**, 1434.

Li, D., Y.W. Chung, S.T. Yang, M.S. Wong, F. Adibi and W.D. Sproul, 1994, J. Vac. Sci. Technol. **12**, 1470.

Li, H., and B.P. Tonner, 1989, Phys. Rev. **40**, 10241.

Li, Y., J.W. Ross, M.A.H. McCausland, D.St.P. Bunbury, M.R. Wells and R.C.C. Ward, 1996, J. Phys.: Cond. Matter **8**, 11291.

Li, Y., J.W. Ross, M.A.H. McCausland, D.St.P. Bunbury, M.R. Wells and R.C.C. Ward, 1997, J. Phys.: Cond. Matter **8**, 6301.

Liu, A.Y., and D.J. Singh, 1993, Phys. Rev. B **47**, 8515.

Lodder, J.C., 1998, Handbook of Magnetic Materials, Vol. 11, ed. K.H.J. Buschow (North-Holland, Amsterdam) p. 291.

Lodder, J.C., H. Vankranenburg, K. Takei and Y. Maeda, 1993a, J. Magn. Magn. Mater. **18**, 248.

Lodder, J.C., P. Dehaa and H. Vankranenburg, 1993b, J. Magn. Magn. Mater. **128**, 219.

Lord, J.S., and P.C. Riedi, 1995, Meas. Sci. Technol. **6**, 149.

Lord, J.S., H. Kubo, P.C. Riedi and M. J. Walker, 1993, J. Appl. Phys **73**, 6381.

Mackenzie, I.S., M.A.H. McCauseland and A.R. Wagg, 1974, J. Phys. F: Metal Phys. **4**, 315.

Maeda, Y., 1993, Adv. Mater. **5**, 210.

Maeda, Y., and K Takei, 1991, IEEE Trans. Magn. **27**, 4721.

Maeda, Y., K. Takei and D.J. Rogers, 1993, Jpn. J. Appl. Phys. **32**, 4540.

Maeda, Y., K. Takei and D.J. Rogers, 1994a, J. Magn. Magn. Mater. **134**, 315.

Maeda, Y., K. Takei and D.J. Rogers, 1994b, J. Magn. Magn. Mater. **137**, 233.

Matsuoka, M., and K. Ono, 1989, Jpn. J. Appl. Phys. **28**, 503.

McCausland, M.A.H., and I.S. Mackenzie, 1979, Adv. Phys. **28**, 305.

Mee, C.D., and E.D. Daniel, 1996, Magnetic Recording Technology, 2nd edn (McGraw-Hill).

Mény, C., P. Panissod and R. Loloee, 1992, Phys. Rev. B **45**, 12269.

Mény, C., P. Panissod, P. Humbert, J.P. Nozieres, V.S. Speriosu, B.A. Gurney and R. Zehringer, 1993a, J. Magn. Magn. Mater. **121**, 406.

Mény, C., E. Jedryka and P. Panissod, 1993b, J. Phys. C: Cond. Matter **5**, 1547.

Moruzzi, V.L., J.F. Janak and A.R. Williams, 1978, Calculated Electronic Properties of Metals (Pergamon Press, New York).

Moruzzi, V.L., and P.M. Marcus, 1993, in: Ferromagnetic Materials, Vol. 7, ed. K.H.J. Buschow (North-Holland, Amsterdam) p. 97.

Nakamura, H., T. Suzuki, M. Shiga, H. Yamamoto and T. Shinjo, 1993, J. Magn. Magn. Mater. **126**, 364.

Nurgaliev, T.K., M.A. Shamsutdinov and V.V. Plavskii, 1988, Fizika Tverdogo Tela **30**, 2869.

O'Grady, K., 1990, IEEE Trans. Magn. **26**, 1570.

Ohnishi, S., M. Weinart and A.J. Freeman, 1984, Phys. Rev. B **30**, 36.

Okita, T., and Y. Makino, 1968, J. Phys. Soc. Japan **25**, 120.

Oliviera, I.S., and A.P. Guimaraes, 1997, J. Magn. Magn. Mater. **170**, 277.

Ono, T., C. Takahashi and S. Matsuo, 1984, Jpn. J. Appl. Phys. **23**, L534.

Panissod, P., 1995, Hyp. Interact. **95**, 12.

Panissod, P., 1997, in: Frontiers in Magnetism of Reduced Dimensional Systems, NATO ASI Series (Kluwer, Dordrecht).

Panissod, P., and C. Mény, 1993, J. Magn. Magn. Mater. **126**, 16.

Panissod, P., J.P. Jay, C. Mény, M. Wojcik and E. Jedryka, 1996, Hyp. Interact. **97–98**, 75.

Panissod, P., C. Mény, M. Wojcik and E. Jedryka, 1997, Mater. Res. Soc. **475**, 157.

Parker, R.J., 1990, in: Advance in Permanent Magnetism (Wiley, New York).

Pauthenet, R., 1982, J. Appl. Phys. **53**, 8187.

Petroff, F., A. Barthelemy, D.H. Mosca, D.K. Lottis, A. Fert, P.A. Schroeder, W.P. Pratt and R. Loloee, 1991, Phys. Rev. B **44**, 5355.

Pokatilov, V.S., S.V. Kapelnitskii and V.N. Karazeyev, 1990, Fizika Tverdogo Tela **32**, 1982

Portis, A.M., and A.C. Gossard, 1960, J. Appl. Phys. **31**, 205S.

Prinz, G.A., 1985, Phys. Rev. Lett. **54**, 1051.

Prinz, G.A., 1991, J. Magn. Magn. Mater. **100**, 469.

Rao, G.N., 1979, Hyp. Interact. 7, 141.

Reich, S., and A.J. Vega, 1985, J. Appl. Phys. **58**, 2759.

Renard, J.P., P. Beauvillain, C. Dupas, K. Le Dang, P. Veillet, E. Velu, C. Marliere and D. Renard, 1992, J. Magn. Magn. Mater. **115**, 147.

Rhyne, J.J., and R.W. Erwin, 1995, in: Ferromagnetic Materials, Vol. 8, ed. K.H.J. Buschow (North-Holland, Amsterdam) p. 1.

Riedi, P.C., 1973, Phys. Rev. B **8**, 5243.

Riedi, P.C., 1977, Phys. Rev. B **15**, 43.

Riedi, P.C., 1979, Phys. Rev. B **20**, 2203.

Riedi P.C., 1989, Hyp. Interact. **49**, 335

Riedi, P.C., and R.G. Scurlock, 1967a, Phys. Lett. A **24**, 42.

Riedi, P.C., and R.G. Scurlock, 1967b, Proc. Phys. Soc. **92**, 117.

Riedi, P.C., T. Dumelow, M. Rubinstein, G.A. Prinz and S.B. Qadri, 1987, Phys. Rev. **36**, 4595.

Rogers, D.J., Y. Maeda and K. Takei, 1994a, IEEE Trans. Magn. **30**, 3972.

Rogers, D.J., Y. Maeda, K. Takei, J.N. Chapman, J.P.C. Bernards and C.P.G. Schrauwen, 1994b, J. Magn. Magn. Mater. **130**, 433.

Rogers, D.J., Y. Maeda, K. Takei, Y. Shen and D.E. Laughlin, 1994c, J. Magn. Magn. Mater. **135**, 82.

Rogers, D.J., Y. Maeda and K. Takei, 1995a, J. Appl. Phys. **78**, 5842.

Rogers, D.J., Y. Maeda and K. Takei, 1995b, Scripta Metall. Mater. **33**, 1553.

Saito, Y., K. Inomata, A. Goto and H. Yasuoka, 1993a, J. Phys. Soc. Japan **62**, 1450.

Saito, Y., K. Inomata, A. Goto and H. Yasuoka, 1993b, J. Magn. Magn. Mater. **126**, 466.

Saito, Y., K. Inomata, M. Nawate, S. Honda, A. Goto and H. Yasuoka, 1995a, Jpn. J. Appl. Phys. **34**, 3088.

Saito, Y., K. Inomata, A. Goto, H. Yasuoka, S. Uji, T. Terashima and H. Aoki, 1995b, Phys. Rev. B **51**, 3930.

Saito, Y., K. Inomata, K. Yusu, A. Goto and H. Yasuoka, 1995c, Phys. Rev. B **52**, 6500.

Sakakima, H., R. Krishnan, M. Tessier, K. Le Dang and P. Veillet, 1986, J. Magn. Magn. Mater. **54–57**, 785.

Schreiber, F., H.A.M. de Gronckel, I.A. Garifullin, P. Bodeker, K. Brohl and J. Pelzl, 1995, J. Magn. Magn. Mater. **148**, 152.

Shakhmuratova, L.N., 1995, Phys. Rev. A **51**, 4733.

Shen, Y., D.E. Laughlin and D.N. Lambeth, 1992, IEEE Trans. Magn. **28**, 3261.

Singh, D.J., 1992, Phys. Rev. B **45**, 2258.

Siqueira, M., J. Nyeki, C.P. Lusher, B.P. Cowan and J. Saunders, 1994, Phys. Rev. B **50**, 13069.

Slichter, C.P., 1989, Principles of Magnetic Resonance, 3rd edn (Springer-Verlag, Berlin).

Smardz, L., K. Le Dang, H. Niedoba and K. Chrzumnicka, 1995, J. Magn. Magn. Mater. **144**, 569.

Stearns, M.B., 1971, Phys. Rev. B **4**, 4081.

Stearns, M.B., Y.D. Zhang and J.I. Budnick, 1988, J. Appl. Phys. **63**, 3222.

Stepanyuk, V.S., R. Zeller, P.H. Dederichs and I. Mertig, 1994, Phys. Rev. B **49**, 5157.

Subramanian, S., R. Sooryakumar, G.A. Prinz, B.T. Jonker and Y.U. Idzerda, 1994, Phys. Rev. B **49**, 17319.

Suzuki, Y., T. Katayama and H. Yasuoka, 1992, J. Magn. Magn. Mater. **104**, 1843.

Suzuki, M., Y. Taga, A. Goto and H. Yasuoka, 1993, J. Magn. Magn. Mater. **126**, 495.

Suzuki, M., Y. Taga, A. Goto and H. Yasuoka, 1994, Phys. Rev. B **50**, 18580.

Swinnen, B., J. Dekoster, G. Langouche and M. Rots, 1995, Phys. Rev. B **52**, 5962.

Takanashi, K., H. Yasuoka, K. Kawaguchi, N. Hosoito and T. Shinjo, 1982, J. Phys. Soc. Japan **51**, 3743.

Takanashi, K., H. Yasuoka, K. Kawaguchi, N. Hosoito and T. Shinjo, 1984a, J. Phys. Soc. Japan **53**, 4315.

Takanashi, K., H. Yasuoka, K. Takahashi, N. Hosoito, T. Shinjo and T. Takada, 1984b, J. Phys. Soc. Japan **53**, 2445.

Takanashi, K., H. Yasuoka and T. Shinjo, 1986a, J. Magn. Magn. Mater. **54–57**, 783.

Takanashi, K., H. Yasuoka, N. Nakayama, T. Katamoto and T. Shinjo, 1986b, J. Phys. Soc. Japan **55**, 2357.

Takanashi, K., M. Watanabe, H. Fujimori and H. Yasuoka, 1992, J. Magn. Magn. Mater. **104**, 1751.

Takahashi, M., H. Shoji, Y. Hozumi, T. Wakiyama, Y. Takeda and Y. Itakura, 1994, IEEE Trans. Magn. **30**, 4449.

Takei, K., and Y. Maeda, 1991, Jpn. J. Appl. Phys. **30**, 1125.

Takei, K., and Y. Maeda, 1992, Jpn. J. Appl. Phys. **31**, 2734.

Takei, K., D.J. Rogers and Y. Maeda, 1994a, Jpn. J. Appl. Phys. **33**, 1027.

Takei, K., D.J. Rogers and Y. Maeda, 1994b, Jpn. J. Appl. Phys. **33**, 5739.

Thompson, M.E., D.A. Burwell, C.F. Lee, L.K. Myers and K.G. Valentine, 1995, Adv. Chem. Ser. **245**, 231.

Thomson, T., H. Kubo, J.S. Lord, P.C. Riedi and M.J. Walker, 1994a, J. Appl. Phys. **76**, 6504.

Thomson, T., P.C. Riedi and D. Greig, 1994b, Phys. Rev. B **50**, 10319.

Thomson, T., P.C. Riedi, K. Brohl and P. Bodeker, 1995, J. Magn. Magn. Mater. **148**, 34.

Thomson, T., P.C. Riedi and B.J. Hickey, 1996a, J. Appl. Phys. **79**, 5119.

Thomson, T., P.C. Riedi, Q. Wang and H. Zabel, 1996b, J. Appl. Phys. **79**, 6300.

Thomson, T., P.C. Riedi, C. Morawe and H. Zabel, 1996c, J. Magn. Magn. Mater. **156**, 89.

Thomson, T., P.C. Riedi, S. Sankar and A.E. Berkowitz, 1997, J. Appl. Phys. **81**, 5549.

Tsuru, K., N. Uryu, K. Le Dang and P. Veillet, 1986, J. Magn. Magn. Mater. **54–57**, 1199.

Urbaniakkucharczyk, A., and L. Wojtczak, 1985, Acta Phys. Polonica A **68**, 271.

Valet, T., P. Galtier, J.C. Jacquet, C. Mény and P. Panissod, 1993, J. Magn. Magn. Mater. **121**, 402.

van Alphen, E.A.M., H.A.M. de Gronckel, P.J.H. Bloemen, A.S. van Steenberg and W.J.M. de Jonge, 1993, J. Magn. Magn. Mater. **121**, 77.

van Alphen, E.A.M., S.G.E. te Velthuis, H.A.M. de Gronckel, K. Kopinga and W.J.M. de Jonge, 1994a, Phys. Rev. B **49**, 17336.

van Alphen, E.A.M, P.A.A. van de Heijden and W.J.M. de Jonge, 1994b, J. Appl. Phys. **76**, 6607.

van Alphen, E.A.M, P.A.A. van de Heijden and W.J.M de Jonge, 1995, J. Magn. Magn. Mater. **144**, 609.

van Alphen, E.A.M., A.H.J. Colaris, S.K.J. Lenczowski, H.A.M. de Gronckel, C. Schönenberger and W.J.M. de Jonge, 1996, J. Magn. Magn. Mater. **156**, 29.

Voznyuk, B.P., N.A. Lesnik, Y.A. Podyelets and V.N. Pushkar, 1990a, Hyp. Interact. **59**, 361.

Voznyuk, B.P., R. Gontaj, J. Dubovic, Y.W. Kudryavtsev and N.A. Lesnik, 1990b, Fizika Tverdogo Tela **32**, 694.

Walker, J.C., R. Droste, G. Stern and J. Tyson, 1984, J. Appl. Phys. **55**, 2500.

Walmsley, R., J. Thompson, D. Friedman, R.M. White and T.H. Geballe, 1983, IEEE Trans. Magn. **19**, 1992.

Walstedt, R.E., 1992, in: Pulsed Magnetic Resonance, ed. D.M.S. Bagguley (Oxford Univ. Press, Oxford) p. 242.

Walstedt, R.E., J.H. Wernik and V. Jaccarino, 1967, Phys. Rev. **162**, 301.

Weller, D., Y. Wu, J. Stohr, M.G. Samant, B.D. Hermsmeier and C. Chappert, 1996, Phys. Rev. B **49**, 12888.

Wijn, H.P.J., 1986, Vol. 19, ed. Landolt-Bornstein (Springer-Verlag, Berlin).

Wojcik, M., J.P. Jay, P. Panissod, E. Jedryka, J. Dekoster and G. Langouche, 1997, Z. Phys. B **103**, 512.

Xu, Y.B., M. Lu, Q.Y. Jin, C. Hu, Y.Z. Miao, Y. Zhai, Q.S. Bie, H.R. Zhai, G.L. Dunifer, R. Naik and M. Ahmad, 1994, J. Appl. Phys. **75**, 6190.

Yamada, T., 1970, J. Phys. Soc. Japan **28**, 596.

Yasuoka, H., and A. Goto, 1995, Mater. Sci. Eng. B **31**, 177.

Yasuoka, H., and R.T. Lewis, 1969, Phys. Rev. **183**, 559.

Yasuoka, H., S. Hosinouchi, Y. Nakamura, M. Matsui and K. Adachi, 1971, Phys. Status Solidi B **46**, K81.

Yoshida, K., H. Kakibayashi and H. Yasuoka, 1990, J. Appl. Phys. **68**, 705.

Yoshida, K., T. Takayama and H. Yasuoka, 1991, J. Appl. Phys. **69**, 5184.

Zhai, H.R., M. Lu, Y.B. Xu, Q.Y. Jin, Q.S. Bie, H. Wang, Y. Zhai, X.B. Zhu, Y.Z. Miao and B.X. Gu, 1995a, J. Magn. Magn. Mater. **144**, 533.

Zhai, Y, X.B. Zhu, C. Hu, J.G. Zhu and H.R. Zhai, 1995b, Chin. Phys. Lett. **12**, 237.

Zheng, G., Y. Kohori, Y. Oda, K. Asayama, R. Aoki, Y. Obi and H. Fujimori, 1989, J. Phys. Soc. Japan **58**, 39.

Zheng, G.Q., Y. Kitaoka, Y. Oda, K. Asayama, Y. Obi, H. Fujimori and R. Aoki, 1991, J. Phys. Soc. Japan **60**, 599.

chapter 3

FORMATION OF 3D-MOMENTS AND SPIN FLUCTUATIONS IN SOME RARE-EARTH–COBALT COMPOUNDS

NGUYEN HUU DUC and P.E. BROMMER

Cryogenic Laboratory, Faculty of Physics
National University of Hanoi
334 Nguyen Trai, Thanh xuan, Hanoi
Vietnam

Van der Waals–Zeeman Instituut
Universiteit van Amsterdam
Valckenierstraat 65, 1018 XE Amsterdam
The Netherlands

Handbook of Magnetic Materials, Vol. 12
Edited by K.H.J. Buschow
© 1999 Elsevier Science B.V. All rights reserved

CONTENTS

1. Introduction 263
2. Theory of itinerant-electron metamagnetism (IEMM) 267
   2.1. Stable magnetic state in the independent-electron approximation 267
   2.2. Effects of spin fluctuations 275
3. Laves phase compounds with non-magnetic rare-earths 281
   3.1. ACo_2 compounds with A = Y, Lu, Sc, and Hf 281
   3.2. $A(Co,M)_2$ compounds with M = Al, Ga, Sn 291
   3.3. $(Y,Lu)(Co,M)_2$ compounds with invariable crystal cell parameter 311
   3.4. Invariable d-electron concentration $Y(Co_xAl_yCu_z)_2$ compounds 313
   3.5. $Y(Co_{1-x}M_x)_2$ compounds with M = Fe, Ni, Cu 314
4. Magnetic lanthanide-Co_2 compounds 315
   4.1. RCo_2 and $(R,Y)Co_2$ compounds 315
   4.2. Magnetic phase transitions in $R(Co_{1-x}M_x)_2$ compounds 344
   4.3. Other $R(Co,M)_2$ compounds (M = Mn, Ni, and Rh) 357
5. 4f- and 3d-magnetism instability in $TmCo_2$-based compounds 358
6. Field-induced magnetic phase transitions in $R(Co,Al)_2$ Laves phase compounds 363
   6.1. Field-induced non-collinear magnetic structures in the Al-stabilized RCo_2 compounds 363
   6.2. Field-induced magnetic phase transitions in a ferrimagnet with one unstable magnetic sublattice. . 365
   6.3. Field-induced magnetic structures of three coupled sublattices 366
   6.4. Exchange interactions in RCo_2 369
   6.5. Concluding remarks on RCo_2 compounds 370
7. Other itinerant-electron metamagnetic systems 373
   7.1. RCo_3-based compounds 373
   7.2. The RCo_5 compounds 382
   7.3. The $Ce_2Co_7B_3$ compounds 383
   7.4. The $Co(S_{1-x}Se_x)_2$ compounds 386
   7.5. Final remarks 388

References 389

Abbreviations

AF	antiferromagnetic
DOS	density of states
CEF	crystalline electric field
F	ferromagnetic
f.u.	formula unit
FOT	first-order transition
IEMM	itinerant electron metamagnetism
LMTO	linear muffin tin orbital
MMT	metamagnetic transition
NMR	nuclear magnetic resonance
P	paramagnetic
R	lanthanide
HR	heavy lanthanide
LR	light lanthanide
SF	strongly ferromagnetic
SOT	second-order transition
T	transition metal
WF	weakly ferromagnetic
WRS	Wohlfarth–Rhodes–Shimizu

List of symbols

a	lattice parameter
a_n	coefficients in the Landau expansion of the free energy of the d-subsystem
A	coefficient of the spin-fluctuation resistivity ($\rho_{sf} = AT^2$)
A_n	coefficients in the Landau expansion of the free energy of the d-subsystem, taking into account effects of spin fluctuations
A_{ij}	spin–spin coupling parameter
A_{RR}	spin–spin coupling parameter between R spins
A_{RT}	spin–spin coupling parameter between R and T spins
A_{TT}	spin–spin coupling parameter between T spins
b_n	coefficients in the Landau expansion of the free energy of the 4f-subsystem
$\boldsymbol{B}$	magnetic induction vector ($\mu_0 \boldsymbol{H}$); B idem (scalar) ($\mu_0 H$)
B_c	critical magnetic induction for the metamagnetic transition

B_{t1}, B_{t2}	idem (lower and upper) for the collinear-noncollinear phase transitions
$\boldsymbol{B}^{R}_{mol}$	effective molecular field acting on R moment in R–T compounds
$\boldsymbol{B}^{T}_{mol}$	effective molecular field acting on T moment in R–T compounds
C	heat capacity; also: magnetovolume parameter
C	Curie–Weiss constant; also specified for rare earth R as C_R
c_n	coefficients in the Landau expansion of the free energy of the system containing both 4f-spin and itinerant electrons
D	exchange stiffness constant
F	free energy
g_J	Landé factor
I	effective interaction energy between the d electrons
J_R	the total angular momentum for the 4f ions
J_R	quantum number of the total angular momentum, also short J
k_B	Boltzmann constant
m_i	magnetic moment of one ion
m_R	magnetic moment of one R ion
m_T	magnetic moment of one T ion
$\boldsymbol{M}_i$	sublattice magnetization vector (also as molar moment)
M_i	sublattice magnetization (scalar) (also as molar moment)
M_f	magnetization of the R sublattice (also as molar moment)
M_d	magnetization of the d-subsystem (also as molar moment)
M_s	spontaneous magnetization (also as molar moment)
$N(\varepsilon_F)$	density of states at the Fermi level
N_R	number of R atoms per mole
N_T	number of T atoms per mole
n_{ij}	molecular-field coefficient
n_{RR}	intrasublattice molecular-field coefficient
n_{RT}	intersublattice molecular-field coefficient
n_{TT}	intrasublattice molecular-field coefficient
p	pressure
p_{eff}	effective paramagnetic d-moment
R	resistance
S	entropy
S	Stoner enhancement factor
S	thermopower
S_R	spin (operator) of the 4f ion
S_T	spin (operator) of the 3d ion
T	temperature
T_C	Curie temperature
T_F	Fermi temperature
T_{max}	temperature at which the paramagnetic susceptibility shows a maximum
T^*	temperature above which the magnetic susceptibility obeys the Curie–Weiss law
T_{sf}	spin fluctuation temperature

T_3	temperature at which the a_3-coefficient in the Landau expression of the free energy of the d-subsystem changes sign
W	bandwidth
χ_d	paramagnetic susceptibility of the d-subsystem
$\Delta\varepsilon$	exchange splitting
$\Delta R/R(0)$	magnetoresistance (relative)
$\Delta\rho$	excess resistivity representing the influence of the magnetic lanthanide atoms interacting with the itinerant Co-matrix.
ε	conduction-electron energy
ε_F	Fermi level
γ	electronic specific-heat constant
κ	compressibility
λ	molecular-field coefficient representing electron–electron interactions
λ_{ep}	electron–phonon contribution to mass enhancement
λ_{sp}	spin-fluctuation contribution to mass enhancement
$\lambda_\parallel$	longitudinal magnetostriction
$\lambda_\perp$	transverse magnetostriction
μ_B	Bohr magneton
ν_n	derivatives of density of states divided by the density of state at the Fermi level, i.e., $N^{(n)}(\varepsilon_F)/N(\varepsilon_F)$
Θ_p	paramagnetic Curie temperature
ρ	electrical resistivity
ρ_0	residual resistivity
ρ_c	resistivity due to the cyclotron motion of the conduction electrons
ρ_{ep}	resistivity due to phonon scattering
ρ_{sf}	resistivity due to spin-fluctuation scattering
ρ_{spd}	resistivity due to spin-disorder scattering
ω	volume magnetostriction
ω_s	spontaneous magnetostriction
$\xi(T)^2$	mean square of the fluctuating magnetic moment

1. Introduction

Among the intermetallic rare-earth compounds with 3d transition-metals, those which exhibit a magnetic instability of the 3d-subsystem are of particular interest. In combination with large magnetovolume effects, these compounds exhibit a number of characteristic properties which make them suitable for checking various physical theories. In this chapter, we focus attention on the Co-based Laves phase compounds (RCo_2; as usual, Y and Sc are considered as R-elements, too). In contrast to the isostructural RNi_2 and RFe_2 compounds, in which the d-electron subsystem is either non-magnetic, i.e., paramagnetic (RNi_2), or bears a stable magnetic moment (RFe_2), in the RCo_2 compounds the hybridized itinerant 3d–5d electron subsystem (3d–4d in case of YCo_2) shows to some extent an intermediate behavior. The RCo_2 compounds with the non-magnetic R-ions Y and Lu are exchange enhanced Pauli paramagnets and undergo a metamagnetic transition (MMT), i.e., a field-induced magnetic phase transition from the paramagnetic to the ferromagnetic state under

an external magnetic field exceeding a certain critical value. This critical field (or induction) was found to be 69 T and 74 T for YCo_2 and $LuCo_2$, respectively (Goto et al. 1989, 1990). In the RCo_2 compounds with magnetic R ions, in the ordered state the molecular field may exceed the critical field necessary to induce the metamagnetic transition in the d-electron subsystem. The concurring magnetic-phase transitions at T_C are of first order (FOT) in RCo_2 with R = Er, Ho and Dy, and of second order (SOT) in the others (Duc et al. 1992a).

Itinerant-electron metamagnetism (IEMM) of the d-electron subsystem is supposed to have its origin in peculiar band structures near the Fermi level (ε_F) and can be accounted for quantitatively by calculations of the density of states (DOS) $N(\varepsilon)$ (Yamada et al. 1984; Yamada and Shimizu 1985; Cyrot and Lavagna 1979). It is well known, however, that in many cases the collective excitations in the highly correlated d-electron subsystem play a very great role for the systems with a strong energy dependence of $N(\varepsilon)$ near ε_F. It is widely recognized that spin fluctuations can significantly influence the finite temperature properties of an itinerant magnet (Moriya 1979, 1991; Gratz et al. 1995a, 1995b; Duc et al. 1991; Burzo et al. 1994). Quenching of spin fluctuations in (external and internal) magnetic fields has been observed in low-temperature specific-heat measurements (Ikeda et al. 1991) as well as in magnetoresistance measurements (Duc 1994; Duc et al. 1995a; Duc and Oanh 1997). The RCo_2 Laves phase compounds, thus, have been a typical example to investigate not only IEMM but also the effects of spin fluctuations. IEMM and spin fluctuations are interesting not only in themselves, but, in addition, by studying these phenomena it is possible to understand more deeply some aspects of the theory of itinerant-electron metamagnetism and open up the possibilities incorporated in this theory for describing different unusual effects observed in experiments.

The Laves phase compounds consist of two kinds of atoms, A and B, with formula AB_2. The A atom is a relatively left-hand transition element in the Periodic Table, e.g., Sc, Y, lanthanides or actinides, whereas the B atom is a relatively right-hand 3d-transition element, e.g., Fe, Co and Ni, etc. There are three typical crystal structures in the Laves phase, so-called C15-, C14-, and C36-type structures. In the C15-type structure, the A atoms make up the diamond structure. In the spaces of the diamond lattice of the A atoms, tetrahedra of four B atoms are inserted (see fig. 1(a)). Looking at this cubic structure along the [1 1 1] direction, one can sketch a hexagonal-like structure (see fig. 1(b)). The C14- and C36-type structures are presented in figs 1(c) and (d), respectively. These cubic and hexagonal structures are closely related as they result from different stackings of the same atomic layers. The possibility to form a Laves phase compound is mainly governed by the relative size of the constituting atom. As shown in fig. 2, the Laves phase compounds do occur only in case the ratio between the atomic radii of the A and B atoms is near the ideal "rigid sphere" value, $R_A/R_B = \sqrt{3/2}$ (Yamada and Aoki 1993).

The crystal structure and the magnetic state of the B-sublattice at low temperature are listed in tables 1–3 for various AB_2 Laves phase compounds, where A are the 3d, 4d and 5d transition metals, lanthanides and actinides, and B are Mn, Fe, Co, and Ni. These compounds have been extensively studied in the past decades. The simple structure makes these compounds suited for a complete analysis of magnetic interactions as a function of the A element and of the B partner. For the general properties of the compounds under consideration we refer the reader to the reviews written by Sechovskí and Havela (1988), Franse and Radwanski (1993) and Yamada and Aoki (1993).

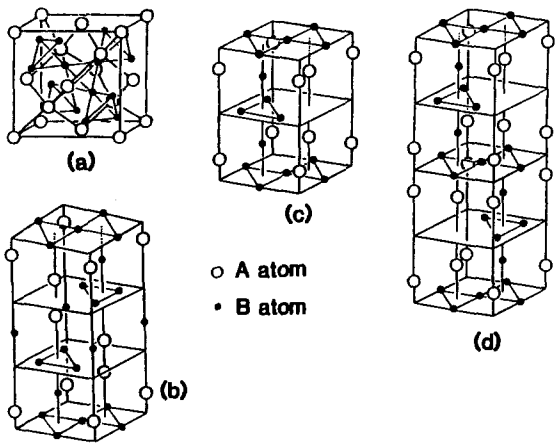


Fig. 1. Three typical Laves phase structures: (a) and (b) – cubic C15-type, (c) – C14-type and (d) – C36-type. Large open and small closed circles denote the positions of the A and B atoms, respectively.

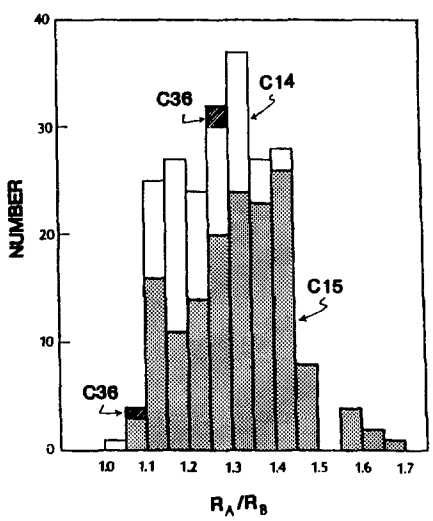


Fig. 2. Number of C15-, C14-, and C36-type structures against the ratio between the atomic radii of the A and B atoms R_A/R_B.

The chapter is organized as follows. At the beginning of section 2 the basic concepts of the first part of the theory of itinerant-electron magnetism – in the independent-electron approximation – are described. Then, magnetic properties of the systems consisting of both itinerant electrons and localized spins are formulated on the basis of the s–d model. The effects of spin fluctuations on the magnetic behavior, heat capacity, and magnetoresistance are also briefly introduced. Section 3 deals with metamagnetism, magnetovolume effects, and spin fluctuations in the nearly ferromagnetic compounds $Y(Lu)Co_2$, $Y(Lu)(Co,M)_2$

TABLE 1

Crystal structure and magnetic state for the AB_2 compounds (A = 3d, 4d, and 5d transition metals and B = Mn, Fe, Co and Ni). Antiferromagnetic, ferromagnetic and paramagnetic states are denoted by AF, F, and P, respectively.

	A						
B	Sc	Y	Ti	Zr	Hf	Nb	Ta
Mn	C14 P	C15 AF	C14 P	C14 P	C14	C14 P	C14 P
Fe	C14 F	C15 F	C14 AF	C15 F	C15 F	C14 AF	C14 AF
Co	C15 P	C15 P	C15 P	C15 P	C15 P	C15 P	C15 P
Ni	C15 P	C15 P					

TABLE 2

Crystal structure and the 3d-sublattice magnetic state for the lanthanide–T_2 compounds (T = Mn, Fe, Co and Ni) at low temperatures. Antiferromagnetic, ferromagnetic, canted, helix and paramagnetic states are denoted by AF, F, C, H, and P, respectively. S means superconducting ($CeCo_2$).

	R													
T	La	Ce	Pr	Nd	Sm	Eu	Gd	Tb	Dy	Ho	Er	Tm	Yb	Lu
Mn			C14 C15 AF	C14 AF	C14 C15 AF		C15 C	C15 H	C15 C	C14 C15 P	C14 P	C14 P		C14 P
Fe	C15 F	C15 F	C15 F	C15 F	C15 F	C15 F	C15 F	C15 F	C15 F	C15 F	C15 F	C15 F	C15 F	C15 F
Co		C15 S	C15 F	C15 F	C15 F	C15 F	C15 F	C15 F	C15 F	C15 F	C15 F	C15 F	C15 F	C15 P
Ni	C15 P	C15 P	C15 P	C15 P	C15 P	C15 P	C15 P	C15 P	C15 P	C15 P	C15 P	C15 P	C15 P	C15 P

(M = Fe, Ni, Al, Si, Ga, ...) and $(Y_{1-x}R_x)Co_2$ ($x < 0.15$). The 4f–3d exchange interaction and its effect on the induced Co-metamagnetic behavior is presented in section 4 for the magnetic rare-earth–Co_2 compounds. In this section, the role of the magnetic R-atom as well as the influence of the 3d electrons affecting the character of the magnetic phase transitions and spin fluctuation scattering are discussed. High-field magnetization in RCo_2 with one unstable magnetic sublattice and in those with two stable magnetic sublattices is discussed in section 5. In section 6, we try to proceed towards a better understanding of magnetism in RCo_2 compounds in a systematic consideration of the variations of physical parameters when going from heavy to light lanthanide compounds. This is substantiated by

TABLE 3

Crystal structure and the 3d-sublattice magnetic state for the actinide–T_2 compounds (T = Mn, Fe, Co and Ni) at low temperatures. Antiferromagnetic, ferromagnetic and paramagnetic states are denoted by AF, F, and P, respectively.

	A		
T	U	Np	Pu
Mn	C15 P	C15 F	C15 P
Fe	C15 F	C15 F	C15 F
Co	C15 P	C15 AF	C15 P
Ni	C14 F	C15 F	C15 P

some studies on artificial "invariable lattice parameter" and "invariable 3d-electron concentration" compounds. Finally, in section 7, we briefly discuss some other compounds with a magnetic instability (RCo_3, RCo_5, $Ce_2Co_7B_3$, $Co(Se,S)_2$), and present an outlook on further developments.

We wish to emphasize that this chapter is primarily intended as a survey of experimental data for the RCo_2 compounds and related ones. The theory is summarized for the benefit of the reader and it is therefore not complete.

2. Theory of itinerant-electron metamagnetism (IEMM)

2.1. Stable magnetic state in the independent-electron approximation

2.1.1. Itinerant-electron system

The itinerant-electron model of magnetism in metals is based on a simple assumption that the magnetic electrons are independent and obey Fermi–Dirac statistics. In addition, essential electron–electron exchange interactions are included by the use of the molecular-field hypothesis. With these assumptions, it is possible to write down the total free energy F per mole of an itinerant ferromagnet as the sum of the (kinetic) energy of itinerant electrons and the interaction energy, both as a function of the magnetic moment M. The magnetic behavior then can be determined by considering the stability condition, $\partial^2 F/\partial M^2 > 0$ which leads to the so-called Stoner criterion for ferromagnetism:

$$\bar{I} = IN(\varepsilon_F) > 1, \tag{1}$$

where I is the effective interaction energy between the electrons related to the coefficient of the molecular field λ by the relation $I = 2\mu_B^2\lambda$. $N(\varepsilon_F)$ is the density of states at the Fermi level in the paramagnetic ground state ($M = 0$).

At 0 K, the eventually resulting equilibrium magnetic states can be characterized as (i) paramagnetic (if $IN(\varepsilon_F) < 1$), (ii) weakly itinerant ferromagnetic (if $IN(\varepsilon_F) > 1$ but neither $N^{\pm}(\varepsilon_F) = 0$) and (iii) strongly itinerant ferromagnetic (if $IN(\varepsilon_F) > 1$ and either $N^{+}(\varepsilon_F) = 0$ or $N^{-}(\varepsilon_F) = 0$ (or very small)). $N^{+}(\varepsilon_F)$ is the density of states at the Fermi level in the magnetic state for the up-spin band. Analogously, $N^{-}(\varepsilon_F)$ for the down-spin band.

The behavior of an itinerant paramagnet in an applied magnetic field depends not only on the value of $N(\varepsilon)$ at the Fermi level, but also on its form near the Fermi level. Wohlfarth and Rhodes (1962) have pointed out that a MMT may occur if there exists a maximum in the paramagnetic susceptibility. Shimizu (1982) has obtained a more precise condition for the appearance of the MMT. The Wohlfarth–Rhodes–Shimizu (WRS) theory is briefly reviewed as follows.

In the case where the resulting splitting of the subbands is much smaller than their bandwidth, the band-splitting $\Delta\varepsilon$ and therefore the magnetization are small parameters. The free energy $F(M)$ can be expanded in powers of M as

$$F(M) = \frac{1}{2}a_1(T)M^2 + \frac{1}{4}a_3(T)M^4 + \frac{1}{6}a_5(T)M^6 - M \cdot B, \tag{2}$$

where the Landau expansion coefficients a_1, a_3, and a_5 are determined by the properties of the $N(\varepsilon)$ curve near $\varepsilon = \varepsilon_F$ and can be represented as a series in even powers of temperature (Wohlfarth and Rhodes 1962; Edwards and Wohlfarth 1968; De Châtel and De Boer 1970; Shimizu 1981; Brommer and Franse 1990). Elaborate expressions for these coefficients are given in these references. We restrict ourselves here to indicate the main contributions in the coefficients $a_1(T)$ and $a_3(T)$ only:

$$a_1(T) = \left(\chi_0^{-1}(T) - \lambda\right) = \frac{1}{2\mu_B^2 N(\varepsilon_F)}\left(1 - \bar{I} + \alpha T^2 + \cdots\right), \tag{3}$$

where $\chi_0^{-1}(T)$ is the inverse Pauli susceptibility and

$$\alpha = \left(\pi^2 k_B^2/6\right)\left(\nu_1^2 - \nu_2\right), \tag{4}$$

$$a_3(T) = \frac{1}{2\mu_B^2 N(\varepsilon_F)}\gamma, \tag{5}$$

with

$$\gamma = \frac{1}{24\mu_B^2 N(\varepsilon_F)^2}\left(3\nu_1^2 - \nu_2\right), \tag{6}$$

where

$$\nu_n = \frac{N^{(n)}(\varepsilon_F)}{N(\varepsilon_F)}. \tag{7}$$

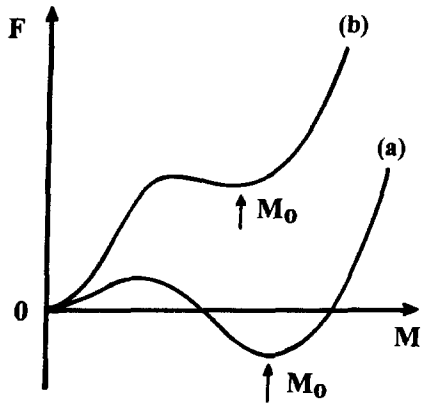


Fig. 3. Magnetic part of the free energy as a function of magnetization: (a) and (b) show the curves corresponding to $a_1a_5/a_3^2 < 3/16$ and $1/4 > a_1a_5/a_3^2 > 3/16$. After Yamada (1993).

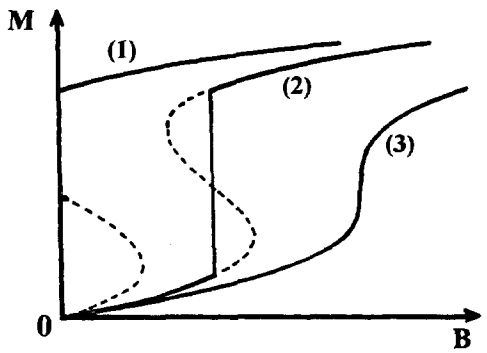


Fig. 4. Schematic curves of $M(B)$ for the ferromagnetic (1), metamagnetic (2) and paramagnetic (3) states.

We see that the coefficient $a_3(T)$ does have a negative sign in case $\nu_2 > 3\nu_1^2$, i.e., in case the curvature of the DOS near ε_F is sufficiently large and positive. In fact, in the case of $a_1 > 0$, $a_3 < 0$, $a_5 > 0$, and $a_1a_5/a_3^2 < 1/4$, it can be seen from eq. (2) that the free energy $F(M)$ has two minima: one at $M = 0$ and another one at a finite value of M $(=M_0)$ (see fig. 3). When $a_1a_5/a_3^2 < 3/16$, $F(M_0)$ is negative as shown by curve (a). Then, the ferromagnetic state at $M = M_0$ is most stable. When $1/4 > a_1a_5/a_3^2 > 3/16$, $F(M_0)$ is positive as shown by curve (b) and the state at $M = M_0$ is metastable. However, this metastable state can be stabilized by an external magnetic field and a MMT from the paramagnetic to the ferromagnetic state occurs at a critical field B_c. In fact, such a transition does occur in a much larger range of the ratio a_1a_5/a_3^2 (see fig. 4). In the case of $a_1 > 0$, $a_3 < 0$, $a_5 > 0$ and $a_1a_5/a_3^2 > 9/20$, $M(B)$ increases monotonically with increasing B (curve 3). On the other hand, when $9/20 > a_1a_5/a_3^2 > 3/16$, the magnetization curve $M(B)$ is S-shaped (curve 2), corresponding to a metamagnetic first-order transition with

hysteresis. Consequently, the condition for the appearance of the MMT is given as

$$a_1 > 0, \quad a_3 < 0, \quad a_5 > 0, \quad \text{and} \quad 9/20 > a_1 a_5 / a_3^2 > 3/16. \tag{8}$$

When $a_1 a_5 / a_3^2 < 3/16$, the system becomes ferromagnetic even at $B = 0$, as shown by curve (1) in fig. 4.

As stated before, the negative a_3 value is a necessary condition for a MMT to occur. In this case, we see from eq. (3) that, at low temperatures, the coefficient $a_1(T)$ will decrease with increasing temperature, because $\alpha \sim \nu_1^2 - \nu_2 < 0$ (since $a_3 \sim 3\nu_1^2 - \nu_2 < 0$). Eventually, at higher temperatures, higher order terms will cause an increase again, so, in fact we expect a minimum in $a_1(T)$. Hence, the initial susceptibility $\chi(T, B = 0) = a_1(T)^{-1}$ will show the maximum as a function of temperature. The experimental observation of the susceptibility maximum, thus was taken as an indication of the possible occurrence of a MMT in the itinerant paramagnet (Wohlfarth and Rhodes 1962; Yamada 1991, 1993).

The equation of state can be determined from the equilibrium condition:

$$B = a_1(T)M + a_3(T)M^3 + a_5(T)M^5. \tag{9}$$

According to eq. (9), the field dependence of the magnetization and that of the differential susceptibility of an itinerant paramagnet, respectively, can be represented in the form

$$\begin{aligned} M(T, B) &= \frac{1}{a_1(T)} B - \frac{a_3(T)}{a_1(T)^4} B^3 + \cdots \\ &= \chi(T, 0)B - a_3(T)\chi(T, 0)^4 B^3 + \cdots, \end{aligned} \tag{10}$$

$$\chi(T, B) = \chi(T, 0)\left[1 - 3a_3(T)\chi(T, 0)^3 B^2\right] + \cdots. \tag{11}$$

The character of these field dependencies is also determined by the sign of the $a_3(T)$ coefficient. One can see from eq. (11) that the susceptibility increases with an increasing field, in case $a_3(T)$ is negative. As already mentioned above, this corresponds to the condition of the susceptibility maximum as a function of temperature.

Thus far the MMT has been described for an itinerant-electron paramagnet ($a_1 > 0$). It should be noted that in the model under consideration, the FOT induced by an applied magnetic field can also arise when the zero-field state is magnetically ordered, i.e., $a_1 < 0$. These are the field-induced transitions from a weakly ferromagnetic into a strongly ferromagnetic state. Shimizu (1982) has described such a transition by including the term $(1/8)a_7 M^8$ into the expression of the free energy (2). Then, if $a_3 > 0$, $a_5 < 0$ and $a_7 > 0$ for some suitable ratio of the magnitude of these coefficients, this transition will be a FOT. The behavior of magnetization of such a weakly ferromagnetic system is shown schematically in fig. 5.

Although in the theory for itinerant-electron magnetism volume effects have always been considered to be of prime importance, in the model discussed thus far these effects were either ignored or treated only rather implicitly. For the 3d-transition metals and their compounds, however, large magnetovolume effects have been calculated and observed. In

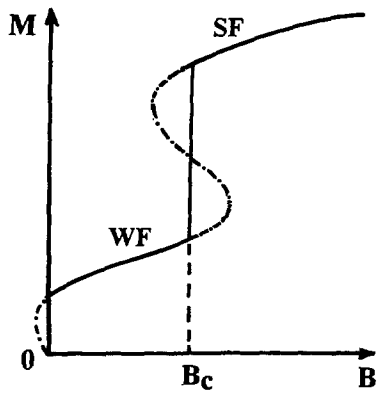


Fig. 5. Schematic magnetization curve for a weakly ferromagnetic (WF) system undergoing a MMT into the strongly ferromagnetic (SF) state in an external magnetic field.

fact, also for the RCo_2 compounds, large volume increases ($\Delta V/V \sim 0.5\%$) are systematically observed to occur at the transition towards ferromagnetism (Givord and Shah 1972; Wada et al. 1988), indicating that the contribution from the elastic-energy term may be important. This has been confirmed by band structure calculation on YCo_2 (Schwartz and Mohn 1984), showing that YCo_2 is a Pauli paramagnet at the equilibrium volume but a ferromagnet at a slightly larger volume. Subsequently, Hathaway and Cullen (1991) have incorporated the effect of volume variations to discuss the magnetic properties of the RCo_2 compounds. Duc et al. (1992b) have treated a simple model, in which the interplay between the magnetic energy and the elastic energy is taken into account explicitly: $F_{tot} = F_{elec} + F_{elas}$ (where F_{elec} and F_{elas} are the electronic and elastic energies, respectively). Moreover, the chosen density of states curve $N(\varepsilon)$ [$=(10/(\pi W^2))\sqrt{W^2 - \varepsilon^2}$, where $2W$ is the bandwidth] exhibits a negative curvature everywhere (i.e., $\nu_2 < 0$). Hence, a MMT cannot be connected with a negative sign of $a_3(T)$ as discussed in the preceding section, where implicitly the free energy expansion was performed at constant volume. In the present model, however, both F_{elec} and F_{elas} depend on the volume. F_{elas} is the usual lattice contribution ($\sim\Omega^2$, where Ω is the normalized volume). The band energy contribution to F_{elec} is directly proportional to the bandwidth W. If the d-electrons are treated in the tight-binding approximation, the variation of the bandwidth with volume is given by $W = W_0 \exp(-q\Omega)$, where q is of the order of 1 to 5/3 for 3d electrons (Slater and Koster (1954)). As a consequence, the parameter $a_1(\Omega, T)$ will change the sign at the critical volume Ω_c, i.e., the Stoner criterion becomes satisfied. Under these conditions, for the chosen parameters at a band filling of about 9.6 3d electrons per atom, the competition between the elastic energy which increases with volume and the electronic energy which decreases when the volume increases will give a typical variation of the total energy $F_{tot}(\Omega, M(\Omega))$ with two minima characteristic of the stable and metastable magnetic states. In the presence of an applied (and/or exchange) field a MMT, associated with a large volume discontinuity, then occurs for a critical field. Equivalently, however, an expansion of the function $F_{tot}(\Omega(M), M)$ in powers of M^2 would lead to a description in very much the same way

as given in the preceding section. Anyway, in this model, the expansion is not necessary, because everything can be calculated exactly. Note that similar models for non-magnetic transitions have been proposed for other systems where strong volume effects are observed, in particular, in cerium heavy-fermion compounds (Lavagna et al. 1983; Ohkawa 1989).

2.1.2. Localized moments interacting with itinerant electrons

2.1.2.1. The Inoue–Shimizu model (Inoue and Shimizu 1982). The magnetic properties of a system consisting of localized magnetic moments interacting with itinerant electrons have been discussed in terms of the so-called s–d model (e.g., Takahashi and Shimizu 1965, 1966). On the basis of such a model, Bloch and Lemaire (1970), Bloch et al. (1975) and Cyrot and Lavagna (1979) have explained the magnetic properties of the RCo_2 compounds. In these models, the localized 4f-moments are considered as exerting an effective field on the itinerant d-electron subsystem. The free energy has thus been expanded in powers of M_d only (see also Jarlborg and Freeman 1981; Levitin and Markosyan 1988). Inoue and Shimizu (1982), however, have presented a version of the s–d model, in which the free energy is expanded in the proper thermodynamic variable (with respect to the applied external field), i.e., the total magnetization of both the d-electrons M_d and the localized spins M_f. In this case, the free energy can be considered as the sum of two separate contributions depending on the magnetization of the itinerant subsystem and that of the 4f moment, respectively, together with one coupling term proportional to the product of these magnetizations. The expression of the free energy is therefore written as:

$$F = F_d + F_f - n_{RCo} M_d M_f, \tag{12}$$

where F_d is the free energy of the itinerant d-electron subsystem already described in eq. (2):

$$F_d = \frac{1}{2} a_1 M_d^2 + \frac{1}{4} a_3 M_d^4 + \frac{1}{6} a_5 M_d^6 - B M_d, \tag{13}$$

and F_f is the free energy of the localized spin system, which is given as (Shimizu 1981; Inoue and Shimizu 1982)

$$F_f = \frac{1}{2} b_1 M_f^2 + \frac{1}{4} b_3 M_f^4 + \cdots - B M_f \tag{14}$$

with

$$b_1(T) = \frac{3 k_B T}{N_R J(J+1)(g\mu_B)^2} - n_{RR}, \tag{15}$$

$$b_3(T) = \frac{9}{20} \frac{k_B T[(2J+1)^2 + 1]}{N_R^3 J^3 (J+1)^3 (g\mu_B)^4}. \tag{16}$$

Here, n_{RR} and n_{RCo} are the molecular-field coefficients representing the interactions between the 4f moments and the R–Co intersublattice interactions, respectively.

In order to obtain an expression in a power series of M ($= M_d + M_f$), one minimizes F with respect to M_f or M_d on condition that M is constant, obtaining

$$F = \frac{1}{2} c_1 M^2 + \frac{1}{4} c_3 M^4 + \cdots, \tag{17}$$

where

$$c_1 = \frac{a_1(T) b_1(T) - n_{RCo}^2}{Q}, \tag{18}$$

$$c_3(T) = \frac{1}{Q^4}\{b_3(T)[a_1(T) + n_{RCo}]^4 + a_3(T)[b_1(T) + n_{RCo}]^4\} \tag{19}$$

with

$$Q = a_1(T) + b_1(T) + 2n_{RCo}.$$

The Curie temperature T_c is determined from $c_1(T_c) = \chi(T_c)^{-1} = 0$, which gives

$$T_C = C_R(n_{RR} + n_{RCo}^2 \chi_{Co}). \tag{20}$$

In fact, this is the condition for a second order transition (SOT) to occur. A first order transition (FOT) will occur if the condition $c_3(T_C) < 0$ is satisfied. In practice, however, the FOT Curie temperature T_C^1 does not differ very much from the SOT Curie temperature derived from eq. (20).

Making use of this equation, one can write $c_3(T_C)$ as

$$c_3(T_C) = \frac{b_3(T_C) + a_3(T)[\chi_d(T_C) n_{RCo}]^4}{\{1 + [\chi_d(T_C) n_{RCo}]\}^4}. \tag{21}$$

In the free-energy expansion for the system of localized moments, eq. (14), the coefficients b_n are positive and a FOT will not occur. For an itinerant electron system, the $a_3(T)$-term can be negative (see preceding section), and a FOT is possible. Presently, in the s–d model, where the localized spins and the itinerant electrons coexist, $c_3(T_C)$ in eqs (19) or (21) shows both possibilities of being negative or positive depending on the relative contributions of the negative value of $a_3(T_C)$ and the positive value of $b_3(T_C)$. Thus, both a FOT and a SOT can occur in the s–d model, even at low temperatures. As discussed in section 4, this model has been successfully applied to explain the type of the magnetic phase transitions not only in RCo_2 compounds but also in a number of more complicated compounds such as $(R_xY_{1-x})Co_2$, $R(Co,Cu)_2$ and $R(Co,Al)_2$, etc. (see Duc et al. 1992a). For compounds such as $Tb_xHo_{1-x}Co_2$ (Duc et al. 1989), however, the exchange field acting on a Tb moment differs from that acting on a Ho moment. Consequently, the total R magnetization cannot be used as a proper (internal) thermodynamic variable. In this case, the free energy should be considered as the sum of three coupled contributions and the Inoue–Shimizu model cannot be applied straightforwardly. A generalization of the Inoue–Shimizu model for an arbitrary number of interacting contributions has been made by Brommer (1989) (see also Duc et al. 1993a).

2.1.2.2. A generalization of the Inoue–Shimizu model (Brommer 1989). The first attempt to generalize the Inoue–Shimizu model was to describe a system with a mixture of different kinds of R atoms, such as $(R_i, R_j)Co_2$ compounds. Such an attempt was carried out by Brommer (1989). In this version, however, the R–R interaction within the R sublattice was ignored and the R–Co coupling parameter A_{RCo} was assumed to be constant for all R elements. It is now generally accepted that the interaction between R moments is by no means small (Lee and Pourarian 1976; Duc et al. 1993a, 1993b, 1995a). The basic interactions between R spins and (itinerant) Co spins appear to increase when going from the heavy to the light lanthanide compounds. The same behavior is true for the R–R interactions. Taking into account all these factors, an elaborate version of the generalized Inoue–Shimizu model was presented by Duc et al. (1993a). The approach is given below.

The free energy of a system of coupled magnetic subsystems is written as

$$F = \sum F_j(M_j) - \sum n_{ij} M_i M_j, \tag{22}$$

$$F_j = \frac{1}{2} a_{1j} M_j^2 + \frac{1}{4} a_{3j} M_j^4 + \frac{1}{6} a_{5j} M_j^6, \tag{23}$$

where

$$a_{1j} = \chi_j^{-1} - n_{jj}.$$

Here, χ_j^{-1} is the inverse magnetic susceptibility of the non-interacting moment in the subsystem j, n_{jj} and n_{ij} are the intra-subsystem and inter-subsystem molecular-field coefficients, respectively.

Writing the expression of the free energy in terms of the (total) molar magnetization in the form of eq. (17), Brommer (1989) has derived expressions for the Landau coefficients c_n. In the case where the interaction between the R moments is neglected, the coefficient c_3 is given by

$$c_3 = \frac{1}{q^4}\left[a_3 + \sum_j x_j b_{3j}\left(\frac{n_{dj}}{b_{1j}}\right)^4\right], \tag{24}$$

where x_j is the R_j concentration; $\sum x_j = 1$, and

$$q = 1 + \sum_j x_j \frac{n_{dj}}{b_{1j}}. \tag{25}$$

The generalized expressions and their simplifications can be also used in the case where one of the rare-earth ions is non-magnetic. For $R_xY_{1-x}Co_2$, for instance, the magnetic lanthanide R would be represented by, say, R_1 and the non-magnetic one, Y, by R_2. If we eliminate the explicit concentration dependence of q (eq. (25)), i.e., of the denominator in eq. (24), by the substitution $xn_{d1}/b_1 = a_d/n_{d1}$ (at the critical temperature using the analog of eq. (18)), the resulting expression for $c_3(T_C)$ is identical to that given by Inoue–Shimizu (1982), see eq. (21).

2.2. *Effects of spin fluctuations*

2.2.1. *Spin fluctuations*

The band theory as discussed above can only be considered as a first step in the theory of itinerant-electron magnetism, since it is based on the concept of independent electrons. The next step is to describe (collective) thermal excitations and the finite temperature properties of the interacting itinerant-electron system. We discuss here the so-called spin-fluctuations by recalling first the short-range order of a ferromagnetic spin system just above the Curie temperature. The spin–spin correlation time, τ, and the correlation length both increase until they become infinite at $T = T_C$. In other words, the range of spin order becomes larger and larger in space and stays longer and longer in time as the magnetic instability is approached. A nearly magnetic (itinerant-electron) system behaves much in the same way when the temperature is lowered. However, the range of spin order at low temperatures remains finite and, in fact, is now measured by the Stoner enhancement factor S. The (collective) excitations of great correlation length and a finite "life-time" give rise to fluctuations in space and time of the magnetization of the system and, hence, are named spin fluctuations (Schrieffer 1968; Moriya 1985).

In general, the effects of spin fluctuations on the physical properties of the system depend on the temperature through a "scaling" ratio (T/T_{sf}). Here, the "spin fluctuation temperature" T_{sf} is given by $T_{sf} = T_F/S$, where T_F is the Fermi temperature and S is the Stoner enhancement factor $(1 - IN(\varepsilon_F))^{-1}$. At low temperatures $(T < T_{sf})$ the spin fluctuations are dominating. Below, a brief description of the effects of spin fluctuations on the magnetic behavior, specific heat, and magnetoresistance will be given in order to be able to explain qualitatively the experimental results presented in the next section.

2.2.2. *Magnetic behavior*

In order to incorporate the effect of spin fluctuations, the free energy is considered to be a functional of the local spin density $\boldsymbol{m}(\boldsymbol{r})$ (Shimizu 1981; Yamada 1991, 1993). The magnetic free energy F is written as

$$F = \frac{1}{V}\int \mathrm{d}\boldsymbol{r}\, f(\boldsymbol{r}), \tag{26}$$

where V is the volume.

$$f(\boldsymbol{r}) = \frac{1}{2}a_1|m(\boldsymbol{r})|^2 + \frac{1}{4}a_3|m(\boldsymbol{r})|^4 + \frac{1}{6}a_5|m(\boldsymbol{r})|^6 + \cdots + \frac{1}{2}D|\nabla \cdot m(\boldsymbol{r})|^2 + \cdots - \boldsymbol{m}(\boldsymbol{r})\boldsymbol{B}, \tag{27}$$

where $\boldsymbol{m}(\boldsymbol{r})$ is the magnetization density. The Landau coefficients a_i were already given as a function of T in eqs (3) and (5). D is the exchange stiffness constant.

Introducing the thermal average of the square of the fluctuating magnetic moment, $\xi(T)^2$, from eqs (26) and (27) one obtains the equation of state in the magnetic system with bulk magnetization M in an external field B at temperature T as

$$B = A_1(T)M + A_3(T)M^3 + A_5(T)M^5 + \cdots, \tag{28}$$

i.e., in this approximation the spin fluctuation correction reduces to the renormalization of the expansion coefficients in the equation of state (28):

$$A_1(T) = a_1 + \frac{5}{3} a_3 \xi(T)^2 + \frac{35}{9} a_5 \xi(T)^4, \tag{29}$$

$$A_3(T) = a_3 + \frac{14}{3} a_5 \xi(T)^2, \tag{30}$$

$$A_5(T) = a_5, \tag{31}$$

and

$$\xi(T)^2 = 2k_B T \sum \chi_q, \tag{32}$$

where χ_q is the wave number dependent susceptibility.

Paramagnetic susceptibility. $\chi(T, B)$ at $B = 0$ is equal to $1/A_1(T)$, where $A_1(T)$ is given by eq. (29). It is easy to see that the terms due to spin fluctuations modify the variation of the magnetic susceptibility. In the case of $a_1 > 0, a_3 < 0$ and $a_5 > 0$, at low temperatures $\chi(T)$ is mainly governed by the first term in eq. (29) and shows a T^2-dependence. $\xi^2(T)$ increases rapidly with increasing temperature and reaches an upper limit determined by the charge neutrality condition, at a certain temperature T^*. At $T > T^*$ the system behaves as a local moment system, and the Curie–Weiss type of the magnetic susceptibility may be essential at high temperatures.

The temperature T_{max}, where $\chi(T)^{-1}$ reaches a minimum, is given by $\partial A_1(T)/\partial T$. Since $\partial A_1(T)/\partial T$ is now governed by $\xi^2(T)$, the temperature dependence of a_1 can be ignored, and the susceptibility attains a maximum at the temperature where $\partial A_1(T)/\partial \xi^2(T) = 0$ (Yamada 1991, 1993).

Hence,

$$\xi(T_{max})^2 = -\frac{3}{14} \frac{a_3}{a_5} \tag{33}$$

and

$$\chi(T_{max}) = \left[a_1 - \frac{5}{28} \frac{a_3^2}{a_5} \right]^{-1}. \tag{34}$$

For $a_1 a_5 / a_3^2 < 5/28$, $\chi(T_{max})$ would become negative. Then, the condition for the appearance of a maximum in $\chi(T)$ is

$$a_1 > 0, \quad a_3 < 0, \quad a_5 > 0, \quad \text{and} \quad a_1 a_5 / a_3^2 > 5/28. \tag{35}$$

In addition, it is noted from this approach that T_{max} given by eq. (33) is also the temperature at which $A_3(T) = 0$. This means that $A_3(T)$ changes sign from negative to positive

at T_{max}. However, as shown in section 3.2, in the analysis of experimental data the temperature T_3 at which $a_3(T)$ changes sign was taken to be far from T_{max}. Of course, the "intrinsic" temperature dependence of the coefficients $a_j(T)$, caused by the band profile, may not be negligible in some cases. In fact, the concurrence of this "intrinsic" (and calculated) temperature dependence together with the temperature dependence caused by the contribution of the spin fluctuations plays an important role in the work of Yamada and Shimizu (1990).

Metamagnetic transition. The differential susceptibility $\chi(T, B)$ $(= dM/dB)$ can be obtained from the equation of state (28), which results also from eq. (11) by replacing a_1, a_3, and a_5 by $A_1(T)$, $A_3(T)$, and $A_5(T)$. So the conditions for the appearance of the MMT are those given in eq. (8).

The MMT disappears at T_0 when $A_1(T)A_5(T)/A_3(T)^2 = 9/20$. Using eqs (29)–(31), this condition leads to

$$\xi(T_0)^2 = \frac{|a_3|}{a_5}\left[\frac{3}{14} - \sqrt{\frac{45}{266}}\sqrt{\frac{a_1a_5}{a_3^2} - \frac{5}{28}}\right]^{-1}, \tag{36}$$

which is positive when $a_1a_5/a_3 < 9/20$. As seen from eqs (33) and (36), $\xi(T_0)^2$ is smaller than $\xi(T_{max})^2$. T_0 is then always lower than T_{max}, as $\xi(T)^2$ is a monotonically increasing function of T (see eq. (32)).

The system becomes ferromagnetic at $B = 0$ when $A_1(T)A_5(T)/A_3(T)^2 < 3/16$. Similarly, the critical temperature T_1, at which the ferromagnetic state becomes unstable and the first-order transition occurs, is given as

$$\xi(T_1)^2 = \frac{|a_3|}{a_5}\left[\frac{3}{14} - \sqrt{\frac{36}{7}}\left(\frac{a_1a_5}{a_3^2} - \frac{5}{28}\right)\right]^{-1}. \tag{37}$$

Clearly, T_1 is found to be lower than T_0 $(T_1 < T_0 < T_{max})$.

Under the condition (35) for the appearance of a susceptibility maximum χ_{max} at T_{max}, the characteristics of IEMM, which is corrected by the effects of spin fluctuations, are summarized as follows:

(i) For $5/28 < a_1a_5/a_3^2 < 3/16$, the ferromagnetic state becomes stable below T_1, the MMT occurs at $T_1 < T < T_0$.
(ii) For $3/16 < a_1a_5/a_3^2 < 9/20$, the system is paramagnetic at $B = 0$ and the MMT occurs at $0 < T < T_0$.
(iii) For $9/20 < a_1a_5/a_3^2$, the susceptibility shows a maximum at T_{max}, but a MMT does not occur.

When taking into account the effects of spin fluctuations, an expression for the temperature dependence of the critical field B_c of metamagnetism cannot be obtained analytically. However, near the limit $a_1a_5/a_3^2 = 3/16$, where $B_c = 0$ at $T = 0$, one can get $B_c(T)$ of the lowest order as

$$B_c(T) = \frac{1}{2}\sqrt{\frac{|a_3|}{3a_5}}\left[a_1 - \frac{3}{16}\frac{a_3^2}{a_5}\right] + O(T^2). \tag{38}$$

As $O(T^2) > 0$, $B_c(T)$ is expected to increase with increasing T as T^2.

Finally, from eqs (33), (34) and (38), $B_c(0)$ is given as

$$B_c(0) = \sqrt{\frac{7}{18}} \frac{\xi(T_{max})^2}{\chi(T_{max})} \left[\frac{20}{21} - \frac{1}{20} \frac{\chi(T_{max})}{\chi(0)}\right]. \tag{39}$$

Since $\xi(T_{max})^2$ is proportional to T_{max}, when T_{max} is low, a linear relation between the values of $B_c(0)$ and T_{max} can be obtained (Yamada 1993). In the Fermi liquid model (Misawa 1988, 1995), a logarithmic form of the free energy with respect to temperature and magnetization can explain the relation between the susceptibility maximum and the critical field.

2.2.3. Heat capacity

The interaction of electrons with spin fluctuations contributes to their self-energy and gives rise to an effective mass and therefore to the enhancement of the linear term of the electronic heat capacity. In addition, a contribution of the form $T^3 \ln(T/T_{sf})$ to the electronic heat capacity is also predicted. For the exchange enhanced paramagnets and weak ferromagnets, the full expression for the heat capacity at temperatures below T_{sf} is given as (see Ikeda et al. 1991)

$$C = \gamma_0 T \left[\frac{m^*}{m} + \alpha_0 \left(\frac{T}{T_{sf}}\right)^2 \ln\left(\frac{T}{T_{sf}}\right)\right] + \beta T^3, \tag{40}$$

where $m^*/m = 1 + \lambda_{ep} + \lambda_{sp}$ is the zero temperature many-body mass enhancement, which includes electron–phonon (λ_{ep}) and spin fluctuation (λ_{sp}) contributions. γ_0 is an electronic specific-heat constant determined from the DOS, $\alpha_0 = (6\pi^6/5)(S-1)^2/S$ and β is the coefficient of lattice heat capacity. S is the Stoner enhancement factor.

In an applied magnetic field, the electronic specific heat constant (first term of eq. (40)) is reduced due to the reduction of the paramagnon enhancement factor λ_{sp}. It has been pointed out that the field dependence of the electronic specific heat constant at 0 K is given as (Béal-Monod et al. 1968)

$$\frac{\Delta\gamma}{\gamma(0)} = 0.1 \frac{S}{\ln S} b^2, \tag{41}$$

where $\Delta\gamma = \gamma(0) - \gamma(B)$ and $b = \mu_B B/(k_B T_{sf})$.

The interplay of the field dependence of the above three terms in eq. (40) causes the change of the heat capacity to be complex. On the other hand, these three quantities do not vary in the same manner, i.e., the applied magnetic field may have no effect on one or both of the others. These variations have led to a classification of the magnetic field dependence of the heat capacity into six types as discussed by Ikeda et al. (1991). For the discussion in this chapter, we mention here two types only (see figs 6(a) and (b)).

- *Type 1 behavior*: There is no $T^3 \ln T$ dependence of the heat capacity but λ_{sp} is usually quite large (≈ 2). With an increasing magnetic field γ decreases, while β is a constant. This is the case for $LuCo_2$ and $ScCo_2$.

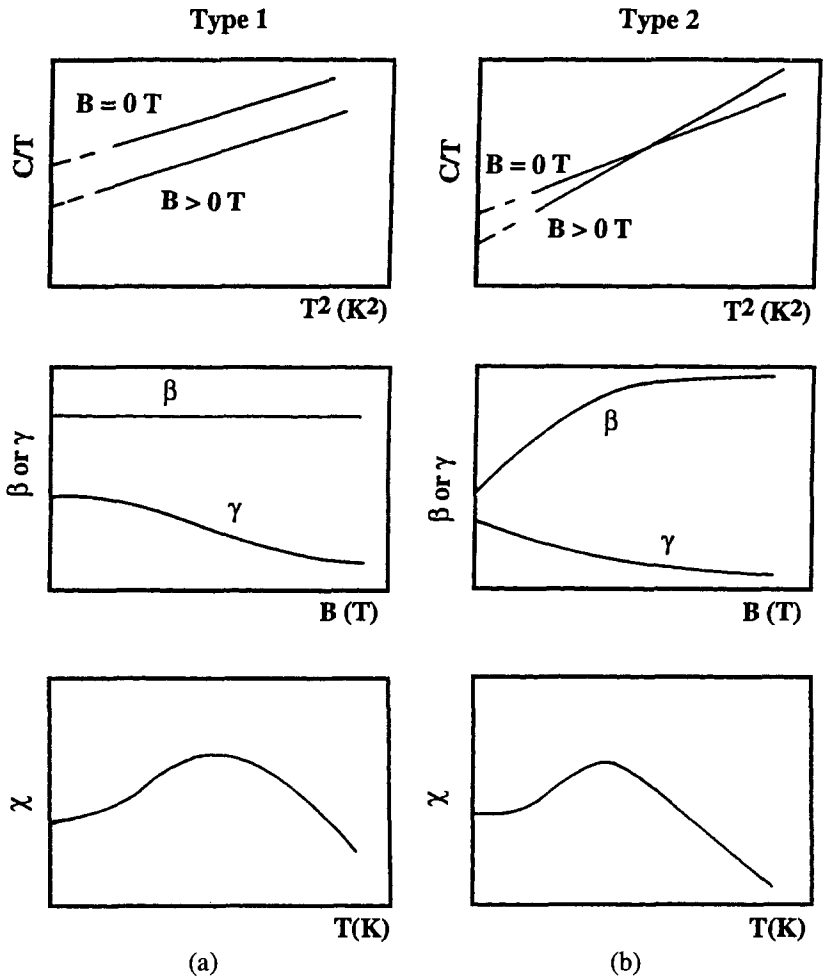


Fig. 6. Schematic representation of the low-temperature heat capacity as a function of magnetic field and the magnetic susceptibility of type-1 (a) and type-2 (b) spin fluctuators.

- *Type 2 behavior*: There is no $T^3 \ln T$ dependence of the heat capacity, but γ is strongly suppressed and β is enhanced in an applied magnetic field. This behavior was observed in YCo_2 (see section 3.1 below).

The corresponding magnetic susceptibility of these materials is also included in the figure (fig. 6).

2.2.4. Magnetoresistance

The transport properties of the itinerant-electron system depend, on the one hand, on the details of the band structure in the neighbourhood of the Fermi level, in the paramagnetic state as well as in the ferromagnetic state. On the other hand, these properties are influenced

by the scattering mechanism. The scattering by spin fluctuations has been extensively discussed in the literature. In order to show the effects of spin fluctuations on the transport properties, a correct separation of different scattering contributions, based on the validity of Mathiessen's rule, is necessary. For highly exchange-enhanced paramagnetic materials, the total electrical resistivity $\rho(B, T)$ can be written as

$$\rho(B, T) = \rho_0(B) + \rho_{ep} + A(B)T^2. \tag{42}$$

The first term in eq. (42) is the residual resistivity. It includes a spin fluctuation contribution through the relation $\rho_0 = (m^*/ne^2)\tau_0$, where m^*, n, and e are the effective mass, the concentration, and the charge of the carrier, respectively, and where τ_0 is the relaxation time of scattering due to impurities, lattice defects and other imperfections. ρ_0 is expected to decrease with an increasing magnetic field, since the spin fluctuation contribution to $m^*(B) \sim \rho_{sp}$ does (see section 2.2.3). The second term is the contribution due to the phonon scattering, and the third term, AT^2, is due to both the interband electron–electron scattering (Appel 1963) and spin fluctuations (Mills and Lederer 1966).

Theoretical calculations concerning the influence of spin fluctuations on the transport properties mainly deal with the low-temperature limit. Coqblin et al. (1978) and later Moriya (1985) have extended the calculations to higher temperatures. It was found that, at low temperatures, the spin fluctuation scattering is strongly temperature-dependent with a tendency to saturate at elevated temperatures. This cross-over occurs at T_{sf}. Within the long-wavelength approximation, the contributions of spin fluctuations to the magnetoresistance are summarized as follows (Ueda 1976; Coqblin et al. 1978; Moriya 1985):

- At low temperatures $T < T_{sf}$: the magnetoresistance is negative and proportional to the square of the applied magnetic fields. The prefactor A of the T^2 term in the resistivity is proportional to T_{sf}^{-2} and becomes smaller with increasing magnetic fields. This is due to the quenching of the spin fluctuation scattering.
- At elevated temperatures: spin fluctuation scattering saturates somewhat above T_{sf}. According to Coqblin et al. (1978), the resistivity of the systems with high values of S can go through a maximum above T_{sf} followed by a negative slope towards the high temperature region.

The effects of a cyclotron orbital Lorentz force acting on the conduction electrons have been observed in many metals and semimetals. Taking into account this effect, the total magnetoresistance of itinerant-electron magnets is written as

$$\Delta\rho(B, T) = \Delta\rho_c(B, T) + \Delta\rho_{sf}(B, T), \tag{43}$$

where $\Delta\rho_c$ is the positive contribution due to the cyclotron motion of the conduction electrons, and $\Delta\rho_{sf}$ is the negative contribution due to the spin fluctuations. At low temperature $\Delta\rho_c(B, T)$ is proportional to B^2. A positive magnetoresistance $\Delta\rho(B, T)$ is possible at low temperatures if $\Delta\rho_c(B, T) > |\Delta\rho_{sf}(B, T)|$. The field effects of $\Delta\rho_c(B, T)$ weaken with increasing temperature, so the sign of $\Delta\rho(B, T)$ may change from positive to negative. Actually, as observed in many alloys, the magnetoresistance $\Delta\rho(B, T)$ is positive only in the low temperature range.

In the strongly enhanced itinerant compounds considered in this chapter, spin fluctuation scattering is certainly expected to play an important role. Nevertheless, one should keep in mind that, especially in case a (meta)magnetic transition does occur, the shifts of bands in the magnetized state are far from negligible, and may have a profound effect on the transport properties. Moreover, by alloying some details of the band structure may change with appreciable effects on the transport properties. This point is elaborated in the discussion of the experimental data in the following sections.

3. Laves phase compounds with non-magnetic rare-earths

3.1. ACo_2 compounds with A = Y, Lu, Sc, and Hf

The electronic structure of R–T intermetallics (R: rare-earth; T: transition metal) can be described as the association of a relatively narrow T 3d band with a wider (and higher in energy) R 5d (or Y 4d) band. These two bands are close to each other. Hence, the 3d–5d (or 3d–4d) hybridization is important. The Fermi level often lies in the region where this hybridization occurs. Thus, in general, alloying of the 3d elements with rare-earth metals, first, leads to a decrease of the DOS at the Fermi level and, then, weakens the 3d magnetism. This effect is illustrated for yttrium compounds as shown in fig. 7 in a plot of the magnetic moment per 3d ion as a function of Y-concentration. The system reaches a critical concentration range at YCo_2, where the alloy is close to the conditions required for the onset of magnetism (Stoner criterion). The Y(Lu)Co_2 compounds, thus, do not order magnetically, but exhibit strongly enhanced paramagnetism. The susceptibility of YCo_2 and $LuCo_2$ compounds increases with increasing temperature, passing at 250 K and 370 K, respectively, a flat maximum (Lemaire 1966; Ikeda et al. 1984). The $ScCo_2$ compound shows a very similar behavior, indicating that it is an inherent property of the Co sublattice.

The magnetic behavior of ACo_2 (A = Y, Lu and Sc) has been described by Burzo et al. (1994) on the basis of susceptibility measured up to 1100 K. In addition to an exchange enhanced paramagnetism with a susceptibility maximum at T_{max} as mentioned above, the Curie–Weiss behavior of the magnetic susceptibility at $T > T^*$ ($> T_{max}$) was pointed out (see figs 8–10). In this high-temperature range, the values of the effective cobalt moments p_{eff}(Co) are 3.7 and 3.86 μ_B/at. for YCo_2 and $LuCo_2$, respectively. Note that effective Co^{+2} moments up to 4.6 μ_B/at. were experimentally determined for the Co metal (Vonsovski 1971). Following the theory of spin fluctuations, it is possible that in ACo_2 compounds the local spin fluctuations $\xi(T)^2$ become saturated at $T > T^*$ and the charge neutrality condition determines the effective moments, in a way characteristic of Co^{2+} ions (Moriya 1979). The data obtained from the magnetic measurements on YCo_2 and $LuCo_2$ are listed in table 4. Magnetic data for $ScCo_2$ and $HfCo_2$ are also included. The effective Co moments and the paramagnetic Curie temperature Θ_p seem to show a regular trend as a function of the lattice constant. As discussed below, the same trend is seen in the electronic specific heat of YCo_2, $LuCo_2$, and $ScCo_2$. The temperature T_{max} results from a competition between the susceptibility increase at low temperatures due to spin fluctuations and the susceptibility decrease in the classical regime at high temperatures. However, its behavior is irregular.

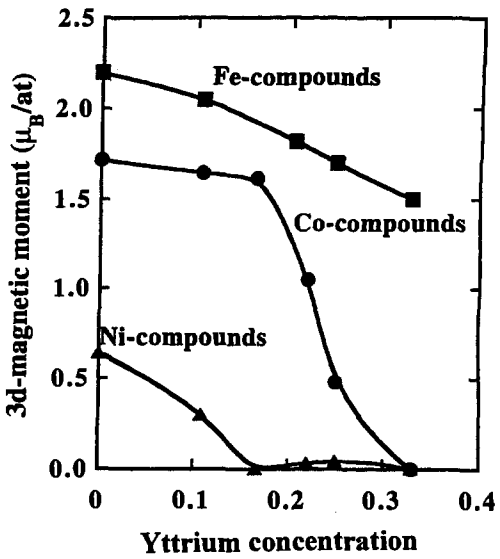


Fig. 7. 3d-magnetic moment as a function of yttrium concentration in Y–Ni, Y–Co and Y–Fe intermetallics.

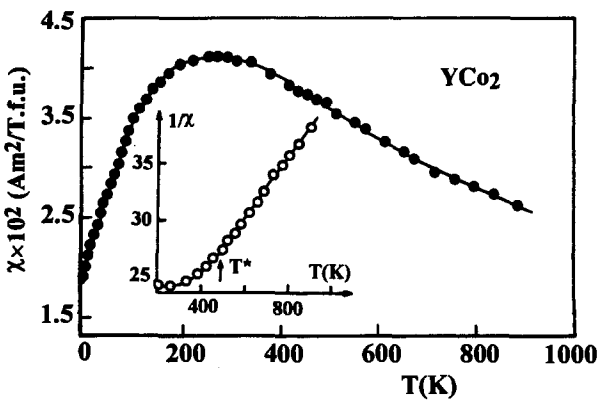


Fig. 8. Temperature dependence of the magnetic susceptibility of YCo_2. In the inset, the high-temperature behavior of the reciprocal susceptibility is shown. After Burzo et al. (1994).

TABLE 4

Lattice constant (a) and magnetic characteristics (see text) of ACo_2 compounds.

Compound	a (Å)	T_{max} (K)	p_{eff}(Co)	Θ_p (K)
YCo_2	7.215	260	3.7	380
$LuCo_2$	7.121	370	3.86	410
$ZrCo_2$	6.957	90	—	—
$ScCo_2$	6.927	550	3.92	625
$HfCo_2$	6.919	90	4.1	—

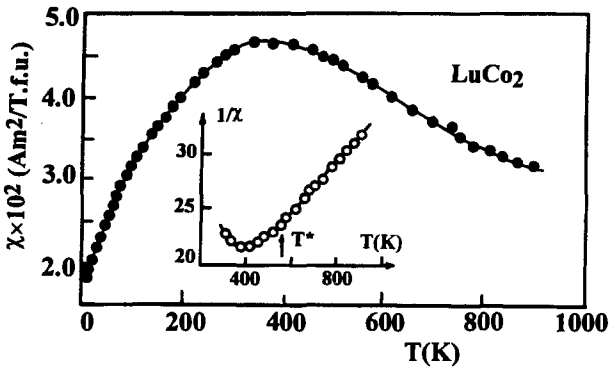


Fig. 9. Temperature dependence of the magnetic susceptibility of $LuCo_2$. In the inset, the high-temperature behavior of the reciprocal susceptibility is shown. After Burzo et al. (1994).

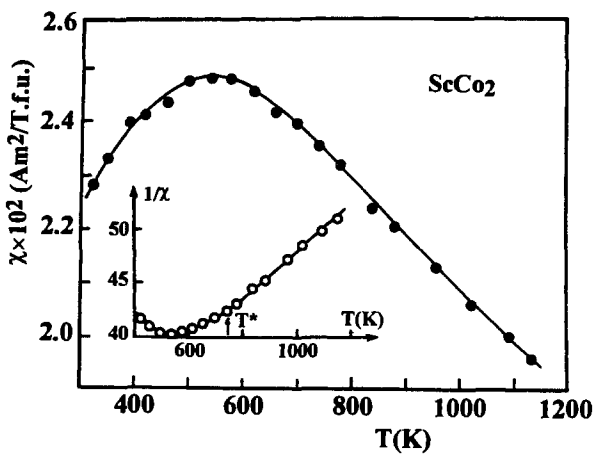


Fig. 10. Temperature dependence of the magnetic susceptibility of $ScCo_2$. In the inset, the high-temperature behavior of the reciprocal susceptibility is shown. After Burzo et al. (1994).

A detailed analysis shows that the magnetic susceptibility of YCo_2 and $LuCo_2$ is linearly dependent on T^2 for $T < 15$ K (see fig. 11). This is in agreement with Béal-Monod (1982), who shows that the paramagnon results – for a general band structure – lead to a temperature dependence of the susceptibility of the form:

$$\chi(T) = S\chi(0)\left[1 + \frac{\pi^6}{6}\left(\frac{2\nu_2}{\nu_0} - 1.2\frac{\nu_1^2}{\nu_0^2}\right)S^2T^2\right]. \tag{44}$$

Theoretical studies were also devoted to the analysis of the magnetic behavior of these systems. Yamada et al. (1984) calculated the electronic structure of d-electrons in ACo_2 compounds by using the self-consistent tight binding approximation. Starting from the

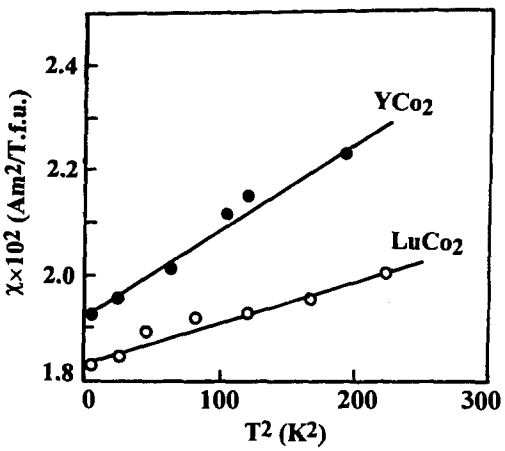


Fig. 11. Thermal variation of the susceptibility for YCo_2 and $LuCo_2$ at $T \leqslant 15$ K as a function of T^2. After Burzo et al. (1994).

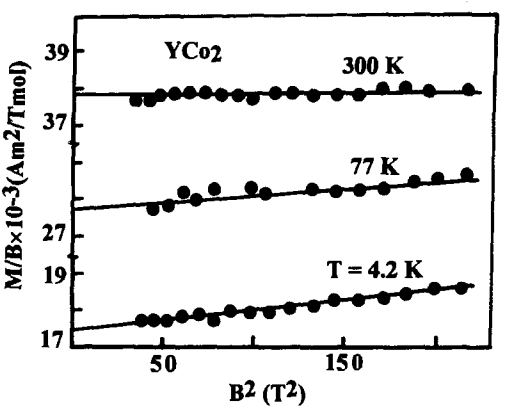


Fig. 12. Plots of M/B vs. B^2 at 4.2 K, 77 K and 300 K for YCo_2. After Bloch et al. (1975).

calculated DOS and taking into account the effects of spin fluctuations, the authors show that the observed magnetic susceptibility may be explained by a sharp peak of the DOS around the Fermi level. The different magnetic behavior of ACo_2 (A = Y, Lu, Sc and Hf) is mainly attributed to the difference between atomic potentials of A and Co and, then, to the different degree of mixing of the d bands. This result is consistent with the above argument and points to an important volume effect on the 3d–5d(4d) hybridization.

As regards the metamagnetic behavior of a paramagnet showing a susceptibility maximum, Bloch et al. (1975) have measured the magnetization of a polycrystalline YCo_2 sample. The results are shown in fig. 12 in a plot of $M(T)/B$ vs. B^2. At 4.2 K and 77 K, the slopes of these curves indicate an increase of the susceptibility with increasing magnetic fields, corresponding to a negative value of the coefficient a_3 in eqs (10) or (11). At

300 K, however, a_3 is positive. By fitting eq. (18) to the 4.2 K curve in fig. 12, the authors found $a_3(0) \approx a_3$ (4.2 K) ≈ -50 T(mol/A m^2)^3. The increase of susceptibility at 4.2 K by about 20% between 0 and 35 T has also been observed by Schinkel (1978). Bloch et al. (1975) have also analyzed the temperature dependence of the susceptibility of YCo_2 in terms of eqs (3), (4) and (11). They found that ν_2 in eq. (4) was positive and obtained the thermal variation of $a_3(T)$ as

$$a_3(T) = a_3(0)\left[1 - \left(\frac{T}{T_3}\right)^2\right], \tag{45}$$

where $a_3(0) = -6.92$ T(mol/A m^2)^3 and $T_3 = 250$ K.

This value of $a_3(T)$ is smaller than that deduced from the field dependence of susceptibility by a factor of 7. However, it supports the idea of a change of the sign of a_3 at about 200 K and the possibility of a MMT which may occur at a magnetic field higher than that which exists in most laboratories. Realistic band structure calculations yield a value of around 80 T for the critical magnetic field of the MMT in YCo_2 (Cyrot and Lavagna 1979; Yamada and Shimizu 1985). A great effort to study metamagnetism in the Laves phase compounds has been made out using the molecular field due to the magnetic rare-earths (see section 4). The MMT was directly studied in YCo_2 and $LuCo_2$ thanks to the availability of magnetic fields up to 100 T (Goto et al. 1989, 1990, 1991). As shown in fig. 13, the MMT was directly observed in YCo_2 and $LuCo_2$ at 69 T and 74 T, respectively. In $ScCo_2$, however, no MMT can be observed in fields up to 120 T. Band calculations for $ScCo_2$ with a cubic Laves structure have been carried out as a function of the lattice constant (Terao and Yamada 1997). The critical field of the metamagnetic transition is obtained as 135 T and about 740 T at the observed and theoretical lattice constants, respectively.

The MMT of YCo_2 is very sharp at low temperatures, but it broadens rapidly with increasing temperature. The MMT is smeared out and is not observed above $T \approx 100$ K (see fig. 14). This temperature corresponds to the tricritical point above which the MMT becomes a second order phase transition. In addition, the critical field B_c increases quadratically with temperature (see fig. 15). This positive shift of $B_c(T)$ has been derived from the theory of spin fluctuations (Yamada 1993).

The effects of spin fluctuations, as introduced in the preceding section (2), must be taken into account for the ACo_2 systems having a large Stoner enhancement factor S. However, experimentally, the effects of spin fluctuations (or paramagnons) were first evidenced by specific-heat measurements. The results of specific-heat measurements under high magnetic fields are presented in figs 16–18 for $LuCo_2$, $ScCo_2$, and YCo_2, respectively (Ikeda et al. 1980, 1984, 1991; Gschneidner Jr. and Dhar 1984; Gschneidner et al. 1985). As can be seen, for $LuCo_2$ and $ScCo_2$ all the C/T vs. T^2 curves are linear and parallel. They decrease with increasing magnetic fields for $B > 2.5$ T. There is, however, no evidence for a contribution of a $T^3 \ln T$ term in the heat capacity. As already mentioned in section 2, this is type 1 behavior of spin fluctuations. For YCo_2, the spin fluctuations are of type 2 behavior: the C/T vs. T^2 straight lines for various fields tend to cross one another with a decreasing intercept and increasing slopes with increasing magnetic fields (Ikeda et al. (1984)). The value of the electronic specific-heat constant γ is listed in table 5 for YCo_2, $LuCo_2$ and $ScCo_2$. γ equals 36.2, 23.3, and 18.4 mJ mol^{-1} K^{-2}, respectively. This

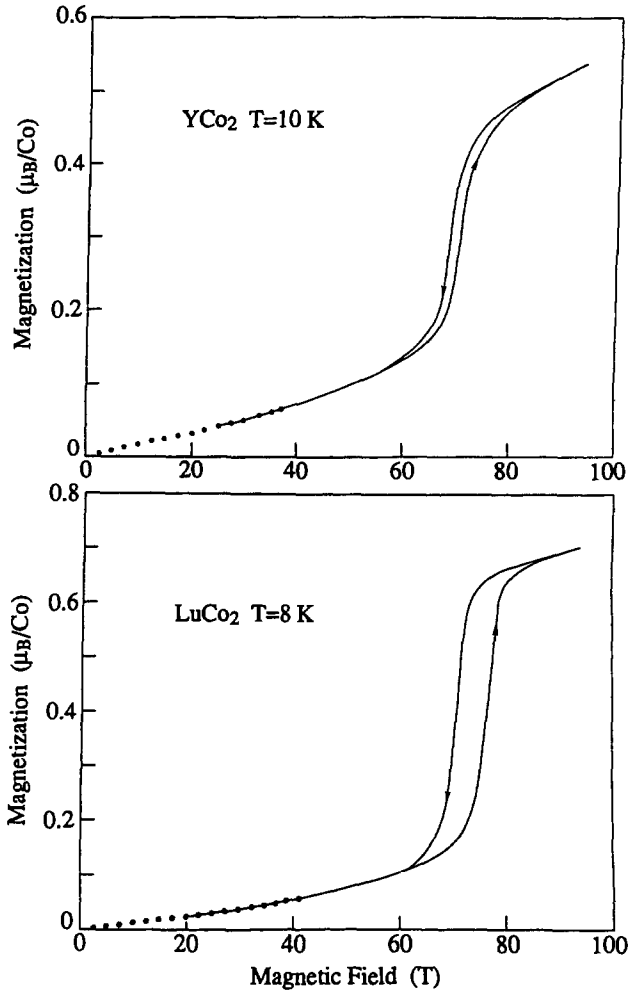


Fig. 13. High-field magnetization data for YCo_2 and $LuCo_2$. After Goto et al. (1991).

is much higher than the value observed for YFe_2 and YNi_2, where the 3d sublattice is either magnetic (YFe_2) or non-magnetic (YNi_2). γ values obtained from DOS-calculations would decrease from YFe_2 to YNi_2 through YCo_2. Practically, a good agreement between experimental and theoretical results was obtained for YFe_2 and YNi_2: $\gamma = 7.6$ or 6.5 and 5.2 or 4.7 mJ mol^{-1} K^{-2}, respectively. This is not the case for YCo_2, where the theoretical value is smaller than the experimental one. In this case, the enhancement of γ was attributed to the effect of paramagnons.

The percentage shift of the electronic specific-heat constant $\Delta\gamma/\gamma(0)$ caused by an applied magnetic field is presented in fig. 19. Fitting the model of Béal-Monod et al. (1968), i.e., eq. (41), it turned out that $S = 15.5$ and $T_{sf} = 17$ K for $ScCo_2$, $S = 22.5$ and

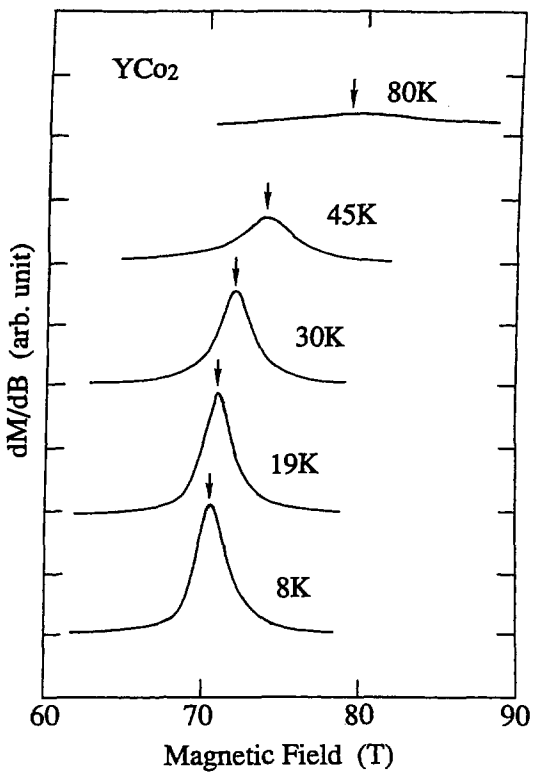


Fig. 14. Plots of dM/dB vs. B at different temperatures for YCo_2. The arrows indicate the magnetic field at which dM/dB shows a maximum. After Goto et al. (1994a).

$T_{sf} = 29$ K for YCo_2 and $S = 16.7$ and $T_{sf} = 15$ K for $LuCo_2$ (Ikeda et al. (1991)). Using a uniform enhancement model, Hertel et al. (1980) have calculated the shift of the electronic specific heat with $S = 10$, $\lambda_{sp} = 0.37$. In this case, the experimental results can be well described by $T_{sf} = (23 \pm 2)$ K for $ScCo_2$, $T_{sf} = (40 \pm 5)$ K for YCo_2 and $T_{sf} = (18 \pm 2)$ K for $LuCo_2$.

The electrical resistivity of the non-magnetic Laves phases ACo_2 compounds has been studied intensively (Gratz and Zuckermann 1982; Burkov et al. 1988; Duc et al. 1991; Fournier and Gratz 1993; Gratz et al. 1995a). The temperature variation of the electrical resistivity of YCo_2, $LuCo_2$, and $ScCo_2$ in the range from 4.2 to 1000 K is presented in fig. 20(a) (Gratz et al. 1995a, 1995b). For comparison, the $\rho(T)$ curves of YAl_2 and $LuNi_2$ are included. Assuming validity of the Mathiessen rule (eq. (42)), the contributions of spin fluctuation scattering in these compounds were determined by subtracting the $\rho(T)$ curve of YAl_2 or $LuNi_2$ from those of YCo_2, $LuCo_2$, and $ScCo_2$. The obtained results are shown in fig. 20(b). As can be seen, the spin fluctuation scattering $\rho_{sf}(T)$ is characterized by a steep increase at low temperatures followed by a maximum at 220 K (YCo_2), 250 K ($LuCo_2$), and 330 K ($ScCo_2$). At high temperatures, $\rho_{sf}(T)$ decreases nearly linearly with

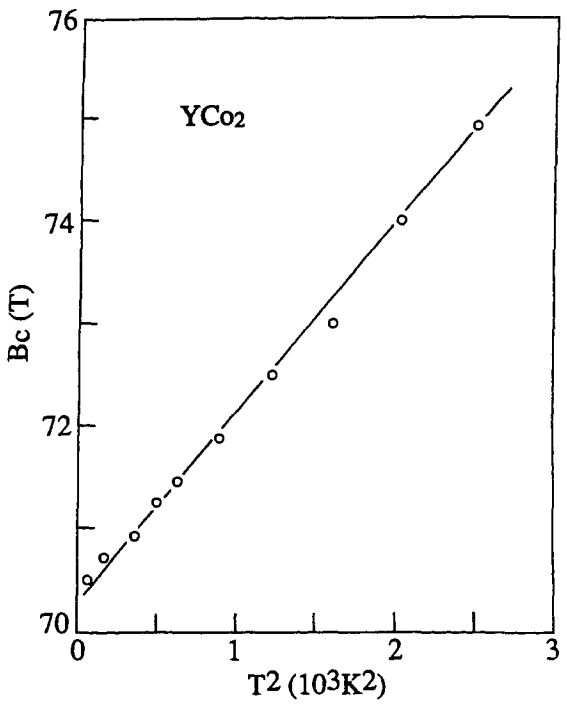


Fig. 15. Plot of the critical field B_c as a function of T^2 for YCo_2. After Goto et al. (1994a).

TABLE 5
Electronic properties of the ACo_2 compounds.

Compound	γ (mJ mol^{-1} K^{-2})	A (nΩ cm K^{-2})	T_{sf} (K)	T_{sf}^* (K)
YCo_2	36.2 [1], 34.2 [2]	16 [3,4]	45 [3,4]	29 [5], 40 [6]
$LuCo_2$	26.6 [7]	12 [3,4]	55 [3,4]	15 [5], 18 [6]
$ZrCo_2$	23.3 [8]	—	—	—
$ScCo_2$	18.4 [7]	4.3 [3,4]	90 [3,4]	17 [5], 23 [6]

References:

[1] Muraoka et al. (1977a)
[2] Bloch and Lemaire (1970)
[3] Fournier and Gratz (1993)
[4] Gratz et al. (1995a, 1995b)
[5] Ikeda et al. (1991)
[6] Hertel et al. (1980)
[7] Ikeda et al. (1984)
[8] Muraoka et al (1979)

increasing temperature. A detailed analysis shows that the spin fluctuation part of the resistivity depends quadratically on T at low temperatures (i.e., $\rho_{sf} = AT^2$ as predicted by the theory of spin fluctuations (see eq. (42); this result is presented in fig. 21). Here A equals 16, 12, and 4.3 nΩ cm^2 K^{-2} for YCo_2, $LuCo_2$, and $ScCo_2$, respectively. It is interesting to note that the corresponding A/γ ratios (where γ is the electronic specific heat constant) fit

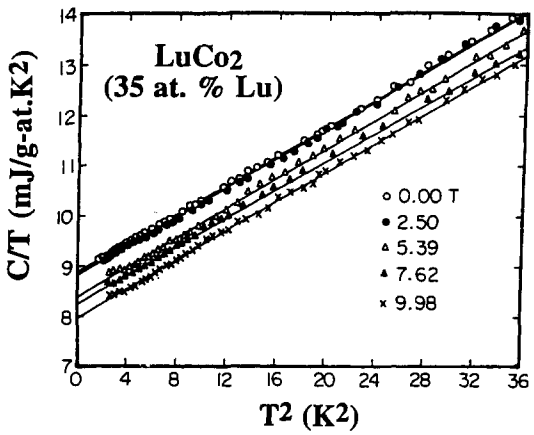


Fig. 16. Low-temperature heat capacity of $LuCo_2$ (35 at.% Lu) in applied magnetic fields. After Ikeda et al. (1984).

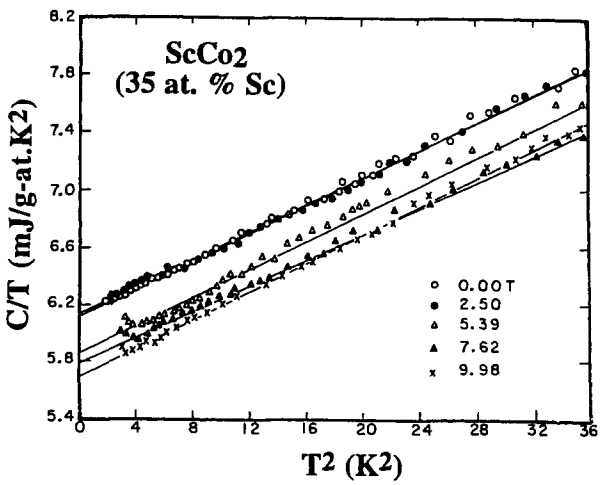


Fig. 17. Low-temperature heat capacity of $ScCo_2$ (35 at.% Sc) in applied magnetic fields. After Ikeda et al. (1984).

well into the region for spin fluctuation compounds in the so-called Kadowaki–Woods plot (Kadowaki and Woods 1986), see fig. 22 (Gratz et al. 1995a). These findings suggest that the spin fluctuation scattering of the conduction electrons is dominating the $\rho(T)$ behavior. The value of A decreases under high pressure (see fig. 23).

Although there is no theoretical justification, the value of the spin fluctuation temperature T_{sf} was usually estimated from the position of the maximum in the $d\rho/dT$ curves (Fournier and Gratz 1993). It yields T_{sf} values of 45, 50, and 55 K for YCo_2, $LuCo_2$, and $ScCo_2$, respectively. About the same values have been deduced from the coefficient A (i.e.,

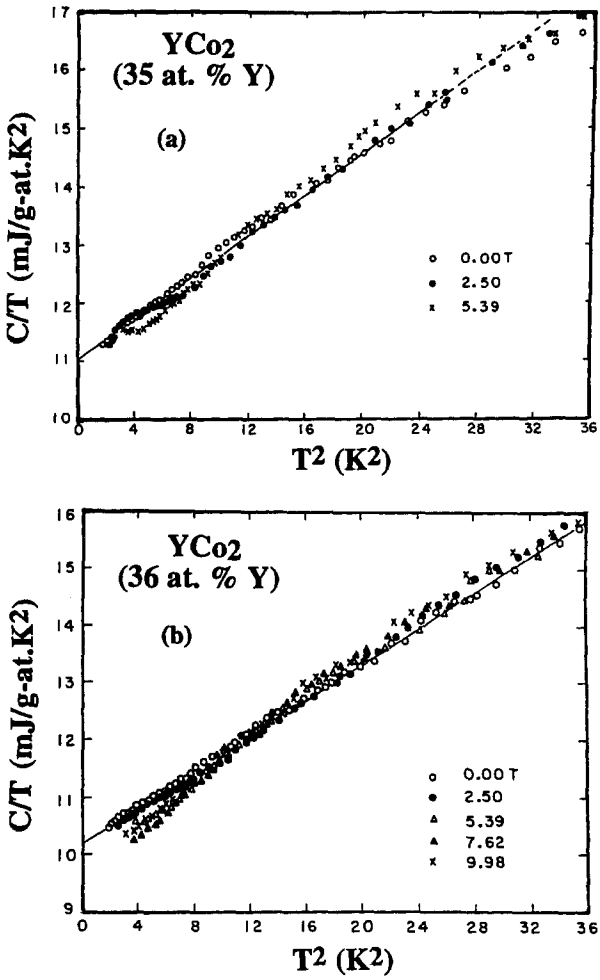


Fig. 18. Low-temperature heat capacity of YCo_2 (35 at.% Y (a) and 36 at.% Y (b)) in applied magnetic fields. After Ikeda et al. (1984).

$T_{sf} \sim A^{-2}$). However, as mentioned above, they are in contrast to those estimated from specific-heat data.

The transverse magnetoresistance of YCo_2 as a function of the magnetic field at 4.2 K is shown in fig. 24 (Gratz (1992)). In contrast to what the spin fluctuation theory predicts (see section 2.2.4), here the positive sign of $\Delta\rho/\rho$ is observed. We will discuss in section 3.2 that this is due to the contribution caused by the cyclotron motion of the conduction electrons. The decrease of $\Delta\rho/\rho$ ($B = 10$ T) with increasing temperature (see the inset of fig. 24), on the one hand, reflects the decrease of $\Delta\rho_c$. On the other hand, in the competition with $\Delta\rho_c$, $\Delta\rho_{sf}$ may be dominant at high temperatures. At very high fields spin fluctuations are suppressed (Burkov et al. 1998).

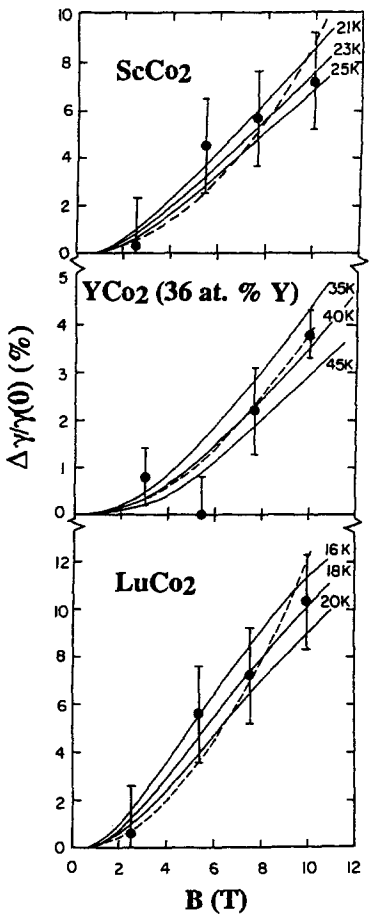


Fig. 19. The percentage shift of the electronic specific-heat constant of $ScCo_2$, YCo_2, and $LuCo_2$ caused by an applied magnetic field. The points are the experimental data while the solid and dashed lines are the theoretical results based on the models of Hertel et al. (1980) and Béal-Monod et al. (1968), respectively. The values listed by the solid curves are the chosen T_{sf} values. After Ikeda et al. (1991).

3.2. $A(Co,M)_2$ compounds with M = Al, Ga, Sn

For attempts to lower the critical magnetic field of the MMT in ACo_2, the discovery by Yoshimura and Nakamura (1985) of the onset of ferromagnetism in the dilute system $Y(Co_{1-x}Al_x)_2$ is an important starting point. Al-substitution in this system expands the lattice at the rate $da/dx = 5.44 \times 10^{-3}$ Å/(%Al) and enhances the magnetic susceptibility (Aleksandryan et al. 1985; Yoshimura and Nakamura 1985). Finally, the appearance of spontaneous magnetic order in $Y(Co_{1-x}Al_x)_2$ takes place at $x \sim 0.12$. The maximum values of the spontaneous magnetization and the critical temperature are $0.14\,\mu_B$/Co at. and 26 K, respectively, at $x \approx 0.16$ (Armitage et al. 1990; Duc et al. 1992c). The weak ferromagnetism in these compounds was associated with the volume effect. However, it was

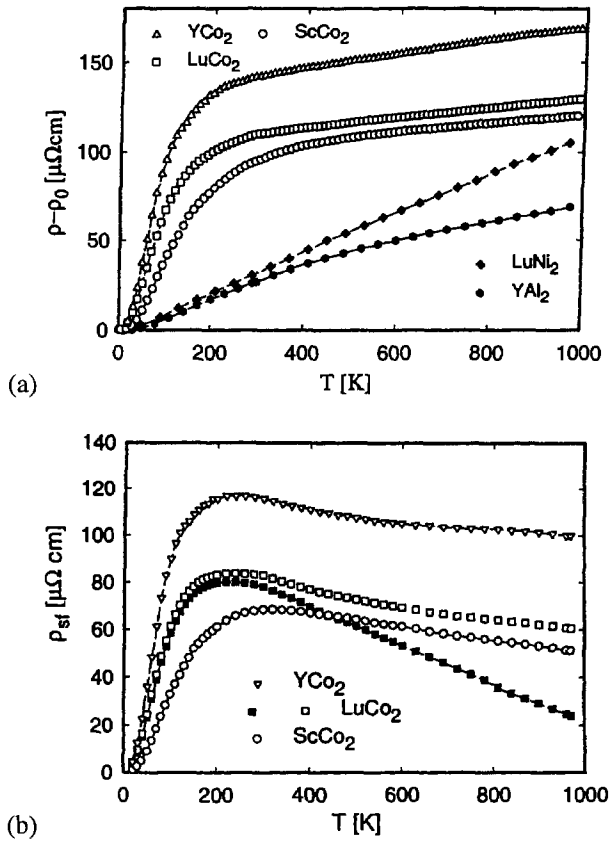


Fig. 20. (a): Temperature dependence of $[\rho - \rho_0]$ for the spin-fluctuation compounds YCo_2, $LuCo_2$, and $ScCo_2$. For comparison the resistivity of the isostructural non-spin fluctuation compounds YAl_2 and $LuNi_2$ is shown. After Gratz et al. (1995a). (b): Temperature dependence of the excess resistivity for the spin-fluctuation compounds YCo_2, $LuCo_2$, and $ScCo_2$. After Gratz et al. (1995a).

(∇): $[\rho - \rho_0]_{YCo_2} - [\rho - \rho_0]_{YAl_2}$; ($\square$): $[\rho - \rho_0]_{LuCo_2} - [\rho - \rho_0]_{YAl_2}$;
($\bigcirc$): $[\rho - \rho_0]_{ScCo_2} - [\rho - \rho_0]_{YAl_2}$; ($\blacksquare$): $[\rho - \rho_0]_{LuCo_2} - [\rho - \rho_0]_{YNi_2}$.

conjectured that a partial substitution of Al, with an unfilled 3d band (the electronic configuration of $3d^0$), for Co would decrease the density of d-electrons and shift the Fermi level toward lower energies with a higher density of states. This leads the Stoner criterion to be fulfilled. Metamagnetism in these compounds was first studied in magnetic fields up to 42 T by Aleksandryan et al. (1985) and Sakakibara et al. (1986, 1987). These studies also showed that the critical field B_c decreased with increasing Al-content. For YCo_2, B_c was roughly estimated to be 66 T. A similar but less sharp MMT was found in $Lu(Co_{1-x}Al_x)_2$ (Sakakibara et al. 1987, 1988; Gabelko et al. 1987; Endo et al. 1988) and $Sc(Co_{1-x}Al_x)_2$ (Ishiyama et al. 1987).

A complete study of IEMM in the nearly ferromagnetic $Y(Co_{1-x}Al_x)_2$ compounds was performed by Sakakibara et al. (1989, 1990a) in magnetic fields up to 100 T. The temper-

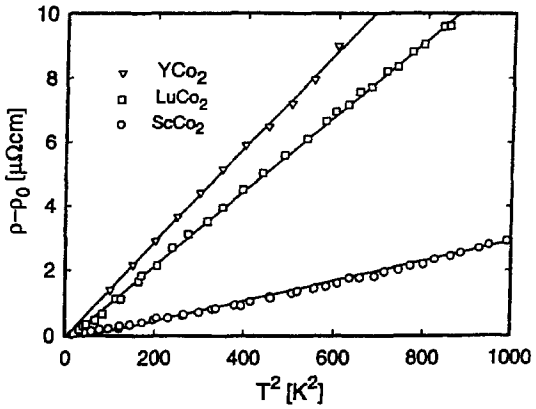


Fig. 21. $[\rho - \rho_0]$ vs. T^2 for the spin-fluctuation compounds YCo_2, $LuCo_2$, and $ScCo_2$. After Gratz et al. (1995a).

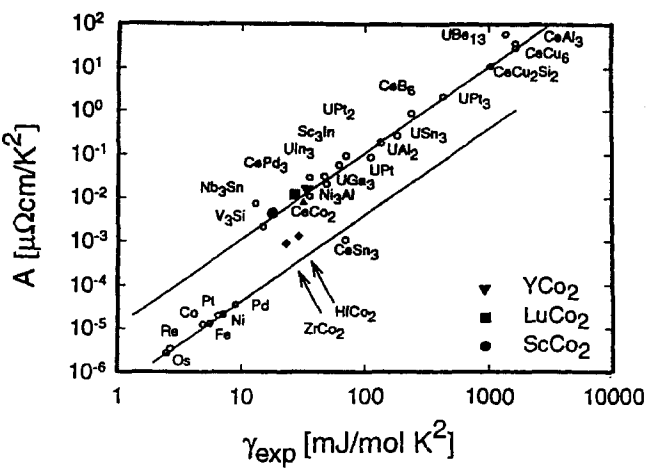


Fig. 22. Position of the three spin fluctuators within the Kadowaki–Woods plot. After Gratz et al. (1995a).

ature dependence of the magnetic susceptibility and the field dependence of the magnetic moment are presented in figs 25 and 26, respectively. For all compounds under consideration, both the temperature T_{max} of the susceptibility maximum and the critical field B_c decrease with increasing Al-concentration, see fig. 27. These results reveal a simple correlation between B_c and T_{max} (fig. 28), that is B_c/T_{max} = constant. This may suggest that T_{max} and B_c are of the same band-structure origin. Indeed, this relation was derived from the theory of spin fluctuations (Yamada 1991, 1993; see section 2.2). The above correlation between susceptibility maximum and metamagnetism was also evidenced in $Lu(Co_{1-x}Al_x)_2$ (Endo et al. 1988; Sakakibara et al. 1990b) and in the nearly ferromagnetic alloys $TiBe_2$ and Ni_3Ga (Acker et al. 1981; Schinkel et al. 1973), albeit with a different value of the B_c/T_{max} ratio. As already reported for YCo_2, B_c shows a quadratic temper-

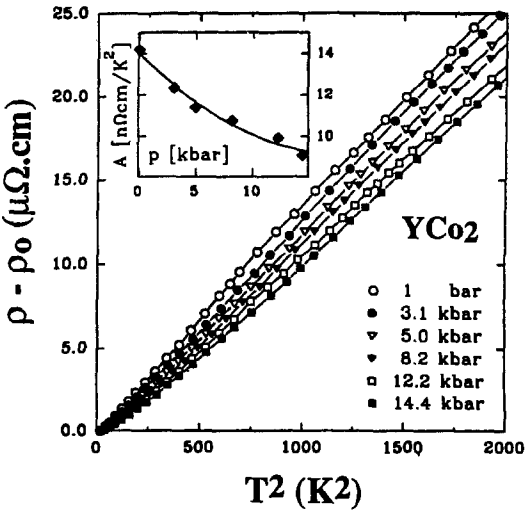


Fig. 23. $[\rho - \rho_0]$ vs. T^2 for the spin fluctuation compounds YCo_2 under pressure. The inset shows the plot of A vs. p. After Fournier and Gratz (1993).

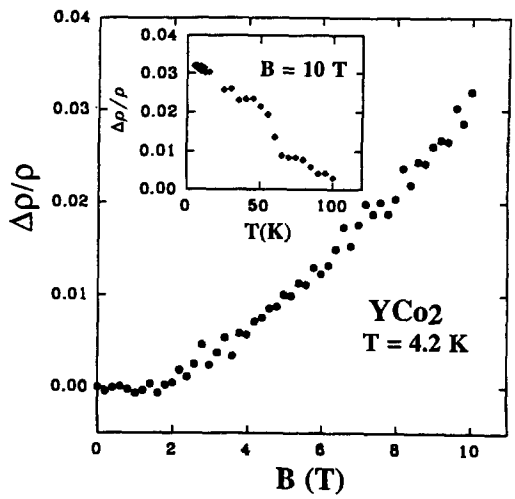


Fig. 24. Magnetoresistance of YCo_2. The inset shows $\Delta\rho(B = 10\ \mathrm{T})/\rho$ vs. T. After Fournier and Gratz (1993).

ature increase, while the MMT is smeared out and, above $T \approx 100$ K, is even no longer observed. Moreover, B_c is increased under pressure. In addition, Yamada (1993) predicted that the MMT disappeared at a critical pressure p_c and p_c decreased with increasing temperature.

A nonlinear Arrott plot is a characteristic for all nearly ferromagnetic and weakly ferromagnetic $Y(Co_{1-x}Al_x)_2$ compounds (see fig. 29). This behavior exists up to $T \approx 80$ K. At

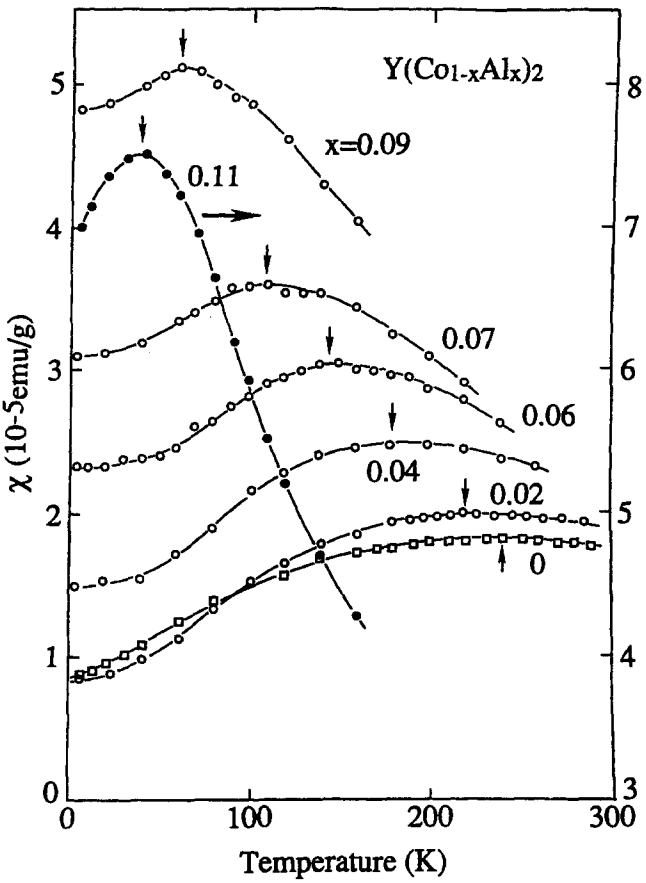


Fig. 25. Temperature dependence of the magnetic susceptibility for $Y(Co_{1-x}Al_x)_2$. The down and up arrows indicate the temperature at which susceptibility shows a maximum. After Sakakibara et al. (1989, 1990a, 1990b).

higher temperatures, the Arrott plots become linear. In the case of a nonlinear Arrott plot, the description of magnetization curves needs higher power terms in the equation of states

$$B/M = A_1 + A_3M^2 + A_5M^4 + A_7M^6 + \cdots. \tag{46}$$

For the nearly ferromagnetic compounds, the MMT from the paramagnetic to the ferromagnetic state is described with $A_1 > 0$, $A_3 < 0$ and $A_5 > 0$ ($A_7 = 0$). For the weakly ferromagnetic compounds, the phase transition is from the weakly ferromagnetic to the strongly ferromagnetic state. In this case $A_1 < 0$, $A_3 > 0$, $A_5 > 0$ and $A_7 > 0$. We list the values of the Landau coefficients for $Y(Co_{1-x}Al_x)_2$ in table 6 (Duc, unpublished). Note that the ratio of A_1A_5/A_3^2 ranges from 0.33 to 0.43, i.e., consistent with the so-called "Yamada range" (Yamada 1993) for the MMT $3/16 < A_1A_5/A_3^2 < 9/20$. In this presentation, the critical magnetic field is determined by the inflection point in the Arrott plot.

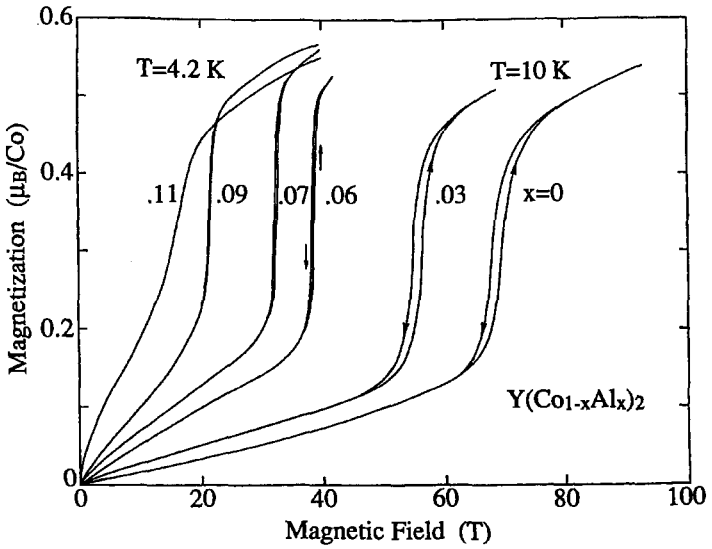


Fig. 26. Magnetic moment as a function of B for $Y(Co_{1-x}Al_x)_2$. After Sakakibara et al. (1989).

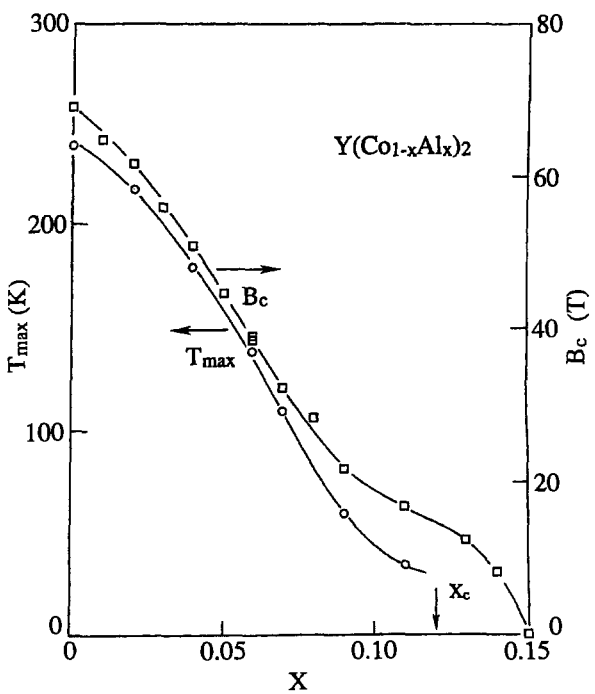


Fig. 27. Al-concentration dependence of B_c and T_{max} for $Y(Co_{1-x}Al_x)_2$. After Goto et al. (1994a).

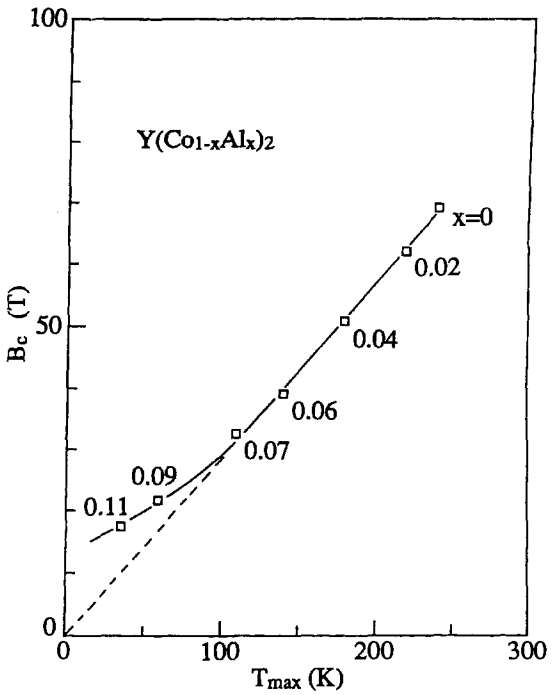


Fig. 28. Plot of B_c vs. T_{max} for $Y(Co_{1-x}Al_x)_2$. After Sakakibara et al. (1989, 1990a).

TABLE 6

The Landau coefficients A_1 (in T(mol/A m^2)), A_3 (in T(mol/A m^2)^3), A_5 (in T(mol/A m^2)^5) and A_7 (in T(mol/A m^2)^7) for $Y(Co_{1-x}Al_x)_2$, derived from the analysis of the magnetization data of Sakakibara et al. (1989). The critical field of the MMT, B_c (in T) is also included.

$Y(Co_{1-x}Al_x)_2$	A_1	A_3	A_5	A_7	B_c
$x = 0.0$	48.3	−2.84	0.055	—	68
0.03	39.4	−2.46	0.051	—	54
0.06	22.8	−1.22	0.02	—	39
0.07	15.6	−0.66	0.01	—	33
0.09	10.3	−0.47	0.009	—	22
0.11	3.76	0.21	−0.016	0.038	18
0.145	−1.76	3.25	−0.625	0.066	12
0.20	−0.05	6.5	−2.820	0.042	7

The volume change in the paramagnetic $Y(Co_{1-x}Al_x)_2$ compounds at the metamagnetic transition was reported by Wada et al. (1988). The longitudinal magnetostriction curves are presented in fig. 30. A large magnetostriction jump has been found around the MMT for $x = 0.095$. With increasing x, the magnetostriction rapidly decreases. The transverse

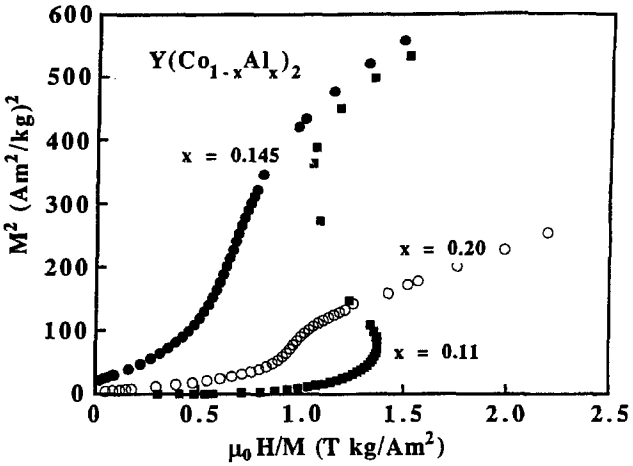


Fig. 29. Arrott plots at 4.2 K for $Y(Co_{1-x}Al_x)_2$. After Duc et al. (1993a).

TABLE 7

The mean values of the constants $\bar{a}$ (in $(10^6\ T)^{-1}$) and $\bar{b}$ (in $(10^6\ T)^{-2}$) for the forced magnetostriction (see text), the spontaneous magnetostriction ω_s (in 10^{-5}), and the magnetovolume coupling constant κC (in $10^{-3}\ \mu_B^{-2}$) for $Y(Co_{1-x}Al_x)_2$. Data are taken from Wada et al. (1988) for the compounds with $x = 0.095$, 0.105, 0.12 and from Duc et al. (1993c) for the remaining compounds.

$Y(Co_{1-x}Al_x)_2$	$\bar{a}$	$\bar{b}$	ω_s	κC	
				(a)	(b)
$x = 0.095$	—	—	—	—	14.0
0.105	—	—	—	—	4
0.120	—	—	—	—	2
0.145	16.2	80	5.80	9.06	9.70
0.160	11	45	8.0	8.86	8.34
0.175	11	7	7.15	9.45	8.94
0.185	10.2	−12	6.90	12.5	11

(a) From thermal expansion
(b) From forced magnetostriction

magnetostriction shows a quantitative agreement with the longitudinal one, indicating an isotropic expansion. This behavior of volume magnetostriction is attributed to the induced Co-moments. For this purpose, the relation $\omega = (3\Delta l/l) = \kappa C M_{Co}^2$ has been used. However, a large scattering in the value of κC was found (see table 7). A similar behavior was also observed for $Lu(Co,Al)_2$ compounds (Iijma et al. 1989). For the weakly ferromagnetic $Y(Co_{1-x}Al_x)_2$ compounds, the forced magnetostriction at 4.2 K also shows a behavior similar to that of the volume magnetostriction. It presents a nonlinear field dependence and can be described by simple expression $\lambda_i = a_i B + b_i B^2$ with $\lambda_i = \lambda_\perp$ or

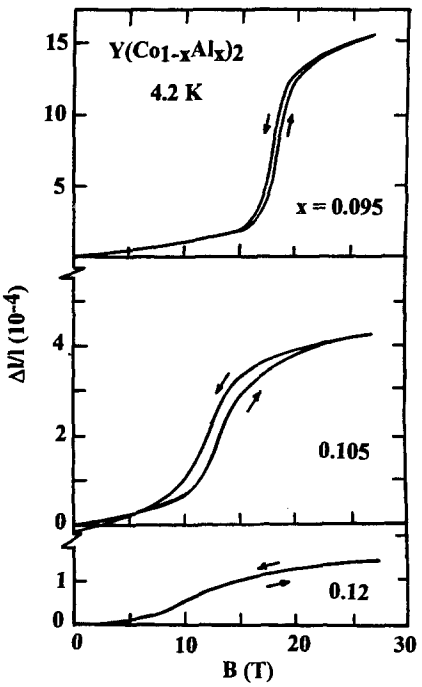


Fig. 30. $\Delta l/l$ vs. B for $Y(Co_{1-x}Al_x)_2$. After Wada et al. (1988).

$\lambda_\parallel$; $a_i = a_\perp \approx a_\parallel$ and $b_i = b_\perp \approx b_\parallel$ (Armitage et al. 1990). In addition, Duc et al. (1993c) showed that the magnetostriction data reflected a more complex dependence not only on the field strength but also on the orientation of the applied magnetic field (see fig. 31). Nevertheless, the volume magnetostriction $\bar{\lambda} = (\lambda_\parallel + 2\lambda_\perp)$ obeys the above mentioned law $\bar{\lambda} = \bar{a}B + \bar{b}B^2$. The obtained values for the coefficients $\bar{a}$ and $\bar{b}$ are listed in table 7. A slight decrease of $\bar{a}$ with increasing x is observed, whereas $\bar{b}$ is strongly decreased and changes the sign at $x = 0.185$, suggesting a change in the 3d magnetic character with increasing Al concentration. The nonlinear behavior of the volume magnetostriction is attributed to the strong magnetic-field dependence of the induced Co moments. In this case, the magnetostriction satisfies the usual relation $\omega = \kappa C(M_B^2 - M_0^2)$ (see fig. 32). The obtained values of κC are listed in table 7. The temperature dependence of the spontaneous volume magnetostriction ω_s below the ordering temperature is shown in fig. 33 (Duc et al. 1993c). At 0 K, the Co magnetic moments reach their maximum value with $\omega_s = \kappa C M_0^2$. The present data indicate an almost similar value for κC in all the investigated compounds (see also table 7). These values of κC well agree with those deduced from the forced magnetostriction measurements.

The decrease of B_c with increasing Al content and the volume anomaly due to the formation of 3d magnetism in $Y(Co_{1-x}Al_x)_2$ can be described in terms of the model proposed by Duc et al. (1992b), see section 2.1. In this context, the magnetic behavior of the $Y(Co_{1-x}Al_x)_2$ compounds is summarized in fig. 34. This effect of volume on the IEMM

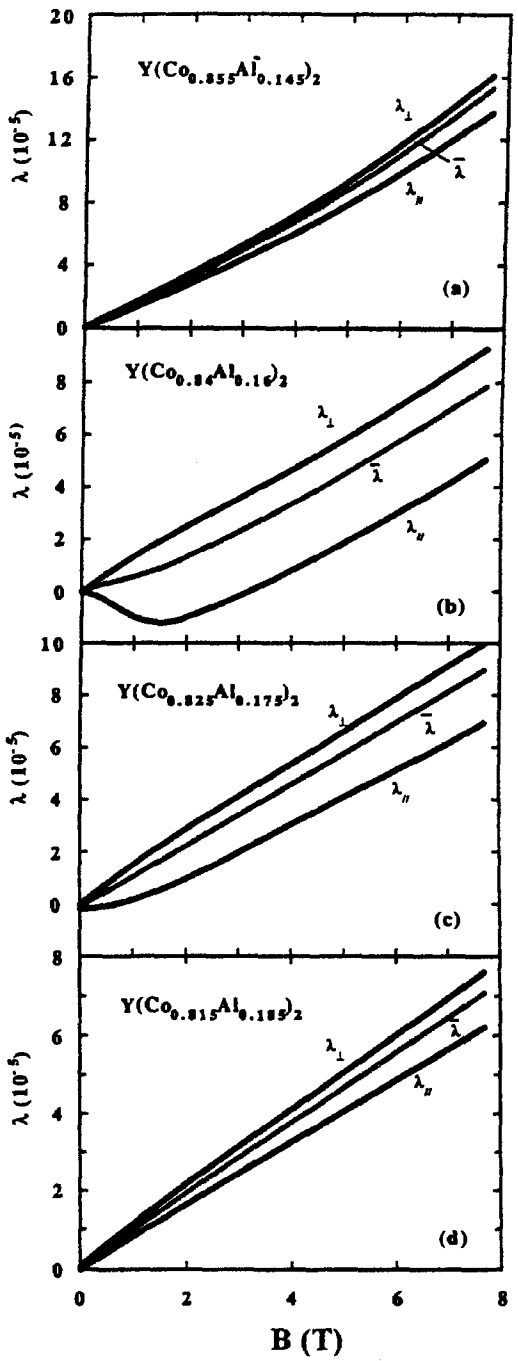


Fig. 31. Linear magnetostriction at 4.2 K for a number of the ferromagnetic $Y(Co_{1-x}Al_x)_2$ compounds. After Duc et al. (1993c).

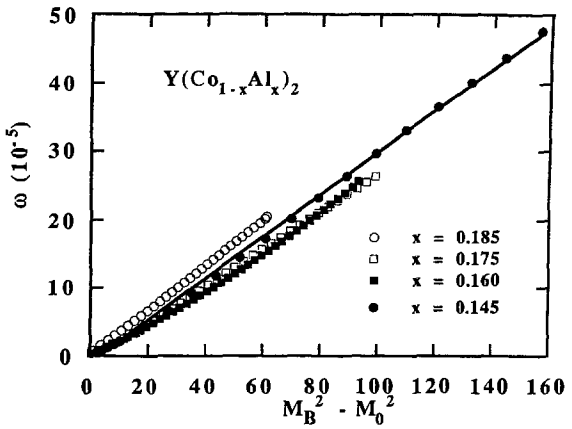


Fig. 32. The forced magnetostriction ω vs. $(M_B^2 - M_0^2)$ for a number of the ferromagnetic $Y(Co_{1-x}Al_x)_2$ compounds. After Duc et al. (1993c).

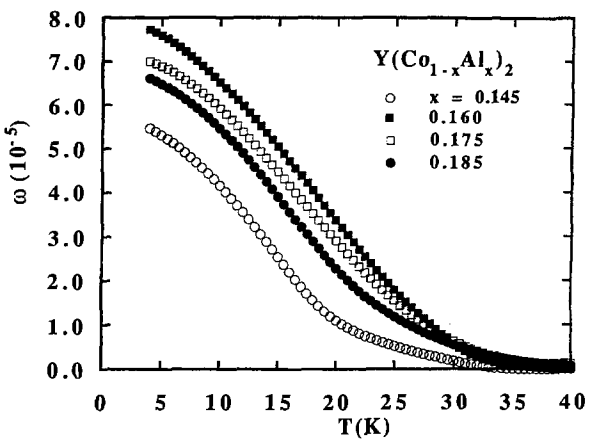


Fig. 33. Spontaneous volume magnetostriction $\omega = \omega_S$ as a function of temperature for a number of the ferromagnetic $Y(Co_{1-x}Al_x)_2$ compounds. After Duc et al. (1993c).

is strongly supported by the study of the $Lu(Co_{1-x}Sn_x)_2$ compounds (Murata et al. 1993, 1994a): at a partial substitution of Sn for Co, initially the lattice parameter increases and the critical field B_c decreases for $x < 0.04$. For $x > 0.06$, the lattice parameter almost saturates, and B_c remains constant at about 40 T. As can be seen in fig. 35, a linear relationship between B_c and the lattice parameter a exists in this system.

Pressure effects on the metamagnetic behavior were reported for $Lu(Co_{0.88}Ga_{0.12})_2$ by Goto et al. (1994a). The pressure dependence of the magnetization process for this compound at 4.2 K is presented in fig. 36. This compound is a ferromagnet at 0 kbar. With increasing pressure the MMT appears and the critical field increases linearly. Figure 37

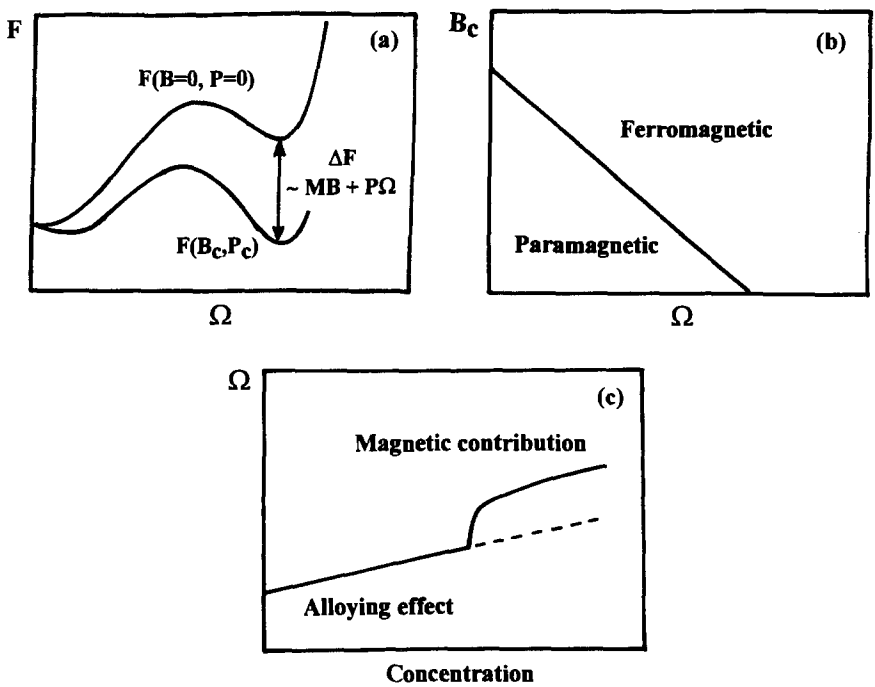


Fig. 34. Schematic diagrams of (a) total energy, (b) critical magnetic field, and (c) volume anomaly for IEMM, predicted from Duc et al. (1992b).

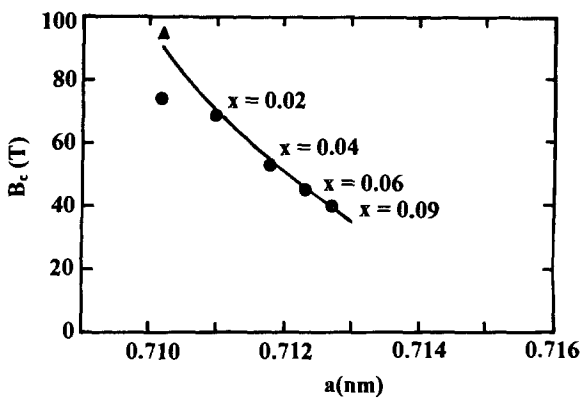


Fig. 35. Plot of B_c as a function of the lattice parameter for $Lu(Co_{1-x}Sn_x)_2$: (•) – experimental and (△) – theoretical. After Murata et al. (1994a).

shows the temperature dependence of susceptibility at different pressures. The application of pressure decreases the magnetic susceptibility and increases T_{max}. The increase of B_c and decrease of $\chi(0)$ under pressure can be understood in terms of the volume dependence

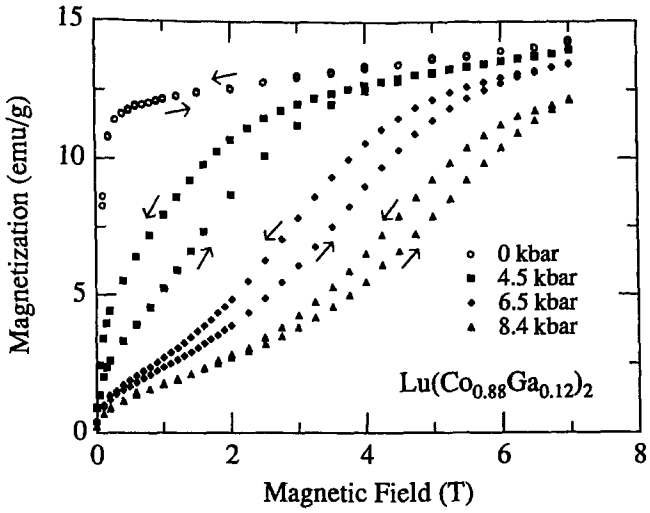


Fig. 36. Pressure effect on the magnetization process of $Lu(Co_{0.88}Ga_{0.12})_2$. After Goto et al. (1994a).

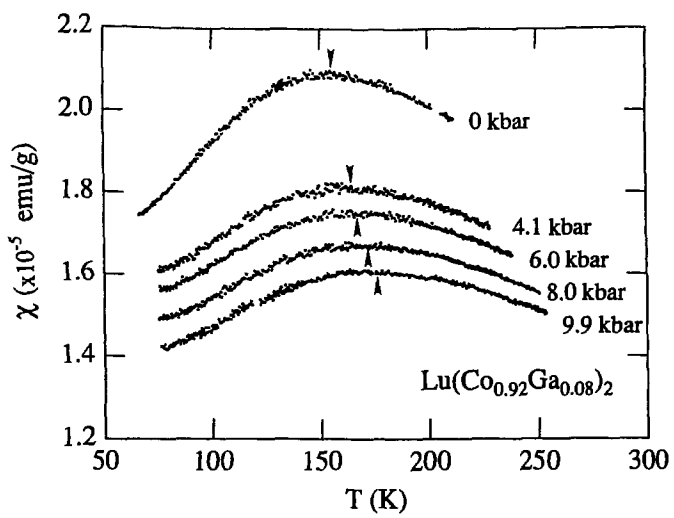


Fig. 37. Pressure effect on the susceptibility of $Lu(Co_{0.88}Ga_{0.12})_2$. The down and up arrows indicate the temperature at which the susceptibility shows a maximum. After Goto et al. (1994a).

of the bandwidth. However, the shift of T_{max} towards higher temperature reflects the effect of spin fluctuations. According to Yamada's theory (Yamada 1993), T_{max}^2 is proportional to the inverse of $\chi(0)$.

Weak itinerant ferromagnetism is extremely sensitive to pressure. As an illustration, typical magnetization curves and Arrott plots under different pressures are given in

TABLE 8

The critical pressure p_c at which T_c extrapolates linearly to zero, pressure dependence of the spontaneous magnetization and the T_c value for $Y(Co_{1-x}Al_x)_2$.

$Y(Co_{1-x}Al_x)_2$	p_c (kbar)		dM_0/dp	dT_c/dp	$d\ln M_0/d\ln V$	$d\ln T_c/d\ln V$
	(a)	(b)	(10^{-3} μ_B/kbar)	(K/kbar)		
$x = 0.145$	5.6	5.6	−11.6	−3.2	154	190
0.160	7.7	9.5	−10.2	−3.4	114	138
0.175	—	8.9	—	—	—	—
0.185	6.1	8.2	−10.5	−3.1	149	174
0.20	6.4	—	−3.3	−1.6	117	166

(a) Derived from dT_c/dp

(b) From the magnetization data

figs 38(a), (b) for $Y(Co_{0.85}Al_{0.15})_2$. As listed in table 8, all the weakly ferromagnetic $Y(Co_{1-x}Al_x)_2$ compounds show a large value of $d\ln T_c/d\ln V$ ($\geqslant 138$) and $d\ln M_0/d\ln V$ ($\geqslant 114$). As regards the volume effects on the 3d-magnetism in the $Y(Co_{1-x}Al_x)_2$ compounds, Al-substitution for Co is considered to cause a negative chemical pressure Δp (kbar) $= -226x$ (Armitage et al. 1990). Considering the pressure effect on the onset of ferromagnetism in this system, one expected that the critical pressure p_c at which 3d magnetic order is destroyed increases continuously with increasing x. Experimentally, however, p_c shows a tendency to increase only for $x \leqslant 0.16$. For $x > 0.16$, p_c slightly decreases with increasing x (see table 8). In fact, the change in the chemical pressure between $x = 0.145$ and $x = 0.16$ is roughly equal to the change in p_c (Duc et al. 1993a, 1993b, 1993c). A similar result was previously indicated for the relation between x and p_c in the concentration range between the onset and the optimum values of x for ferromagnetism, i.e., $0.12 \geqslant x \geqslant 0.155$ (Armitage et al. 1990). For concentrations larger than the optimum x value, the effects of the volume expansion and the 3d–p hybridization on the weakening of the Co–Co interactions which leads to the decrease of T_c, may explain the unexpected variation of $p_c(x)$ shown in table 8.

The appearance of itinerant metamagnetism in the system $Lu(Co_{1-x}Al_x)_2$ is in many ways reminiscent of the features observed in $Y(Co_{1-x}Al_x)_2$ compounds. One can see from fig. 39, which shows the magnetic phase diagram for the $Lu(Co_{1-x}Al_x)_2$ compounds, that in the concentration range $0 \leqslant x \leqslant 0.07$ the compounds are paramagnetic and exhibit a MMT. For compositions with $0.078 \leqslant x \leqslant 0.9$, a weakly ferromagnetic order arises here. A transition from a weakly ferromagnetic to a strongly ferromagnetic state occurs in applied magnetic fields at low temperature. The phase transition from the ferromagnetic state to the paramagnetic state, however, is diffuse, and it is difficult to accurately determine the ordering temperature. For the compositions with $0.095 \leqslant x \leqslant 0.208$ the compounds are strongly ferromagnetic. The FOT from the paramagnetic state to the ferromagnetic state was evidenced by a jump in the lattice parameter at about 150 K (Gabelko et al. 1987). The variation in magnetization and resistivity, however, is gradual (Duc, unpublished).

The large differences in magnetic behavior between $Y(Co_{1-x}Al_x)_2$ and $Lu(Co_{1-x}Al_x)_2$ systems are well explained in the study of Dubenko et al. (1994a, 1994b) on the $(Y_{1-t}Lu_t)(Co_{0.88}Al_{0.12})_2$ compounds. The concentration dependence of the spontaneous

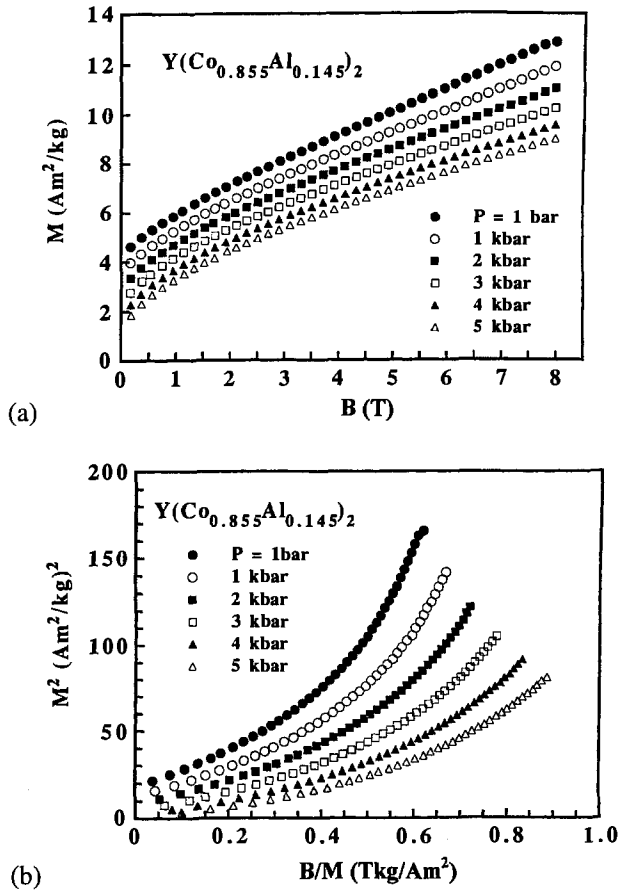


Fig. 38. Magnetization (a) and Arrott plots (b) under pressure for $Y(Co_{0.855}Al_{0.145})_2$.

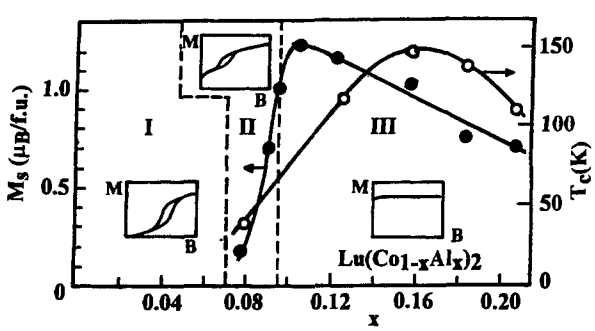


Fig. 39. Magnetic-phase diagram of $Lu(Co_{1-x}Al_x)_2$. The insets show a schematic form of $M(B)$ in the paramagnetic (I), weakly ferromagnetic (II) and strongly ferromagnetic (III) phases. After Levitin and Markosyan (1988).

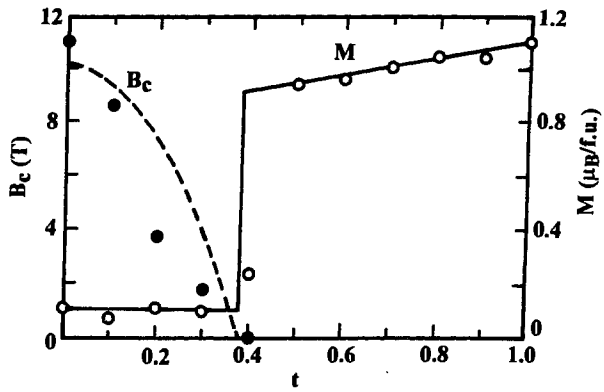


Fig. 40. Concentration dependence of M, the observed magnetic moment (open circles), and that of B_c, the critical field of the MMT (closed circles), for $(Y_{1-t}Lu_t)(Co_{0.88}Al_{0.12})_2$. After Dubenko et al. (1994a).

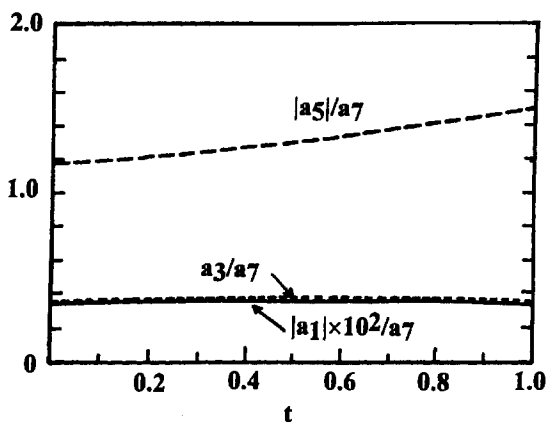


Fig. 41. Concentration dependencies of the scaled Landau coefficients A_1/A_7, A_3/A_7, A_5/A_7 for $(Y_{1-t}Lu_t)(Co_{0.88}Al_{0.12})_2$. After Dubenko et al. (1994a) (for historical reasons, in this figure, A_1 is written as a_1, and so on).

moment in this system at 4.2 K is shown in fig. 40. At $t > t_c$ (= 0.38) a strongly ferromagnetic state appears; the spontaneous moment is rather large and increases with increasing t. On the other hand, at $t < t_c$ the weakly ferromagnetic state with a magnetic moment of about 0.1 μ_B per formula unit appears and is independent of t. In this concentration range, there exists a MMT from a weakly ferromagnetic to a strongly ferromagnetic state. By making use of the phenomenological Landau expansion of the energy up to the eighth power of the magnetization (see section 2.1 and eq. (46)), it is explicitly shown that small changes in the Landau coefficients lead to the transition from a weakly to a strongly ferromagnetic state. The concentration dependencies of the coefficients A_1/A_7, A_3/A_7 and A_5/A_7, and the calculated energy are illustrated in figs 41 and 42, respectively.

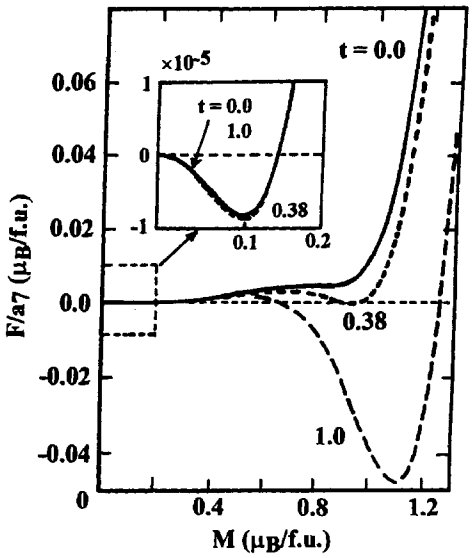


Fig. 42. Scaled free energy $F(M)/A_7$ as a function of the magnetic moment M, calculated for $t = 0.0$, 0.38, and 1.0 for $(Y_{1-t}Lu_t)(Co_{0.88}Al_{0.12})_2$. The inset shows the enlarged curves of $F(M)/A_7$ at small M. After Dubenko et al. (1994a) (see also caption to fig. 41).

In order to investigate the origin of the magnetic behavior in the $Y(Co_{1-x}Al_x)_2$ and $Lu(Co_{1-x}Al_x)_2$ systems, low-temperature specific-heat measurements have also been carried out (Pillmayr et al. 1990; Wada et al. 1990). The concentration dependence of the electronic specific heat constant γ is shown in fig. 43 for both $Y(Co_{1-x}Al_x)_2$ and $Lu(Co_{1-x}Al_x)_2$. The γ value of $Y(Co_{1-x}Al_x)_2$ shows a broad maximum in the weakly ferromagnetic region, while that of $Lu(Co_{1-x}Al_x)_2$ sharply decreases around $x = 0.09$. These results reveal that spin fluctuations play a dominant role in the nearly ferromagnetic state as well as in the weakly ferromagnetic state. In contradistinction, spin fluctuations are quenched in the strongly ferromagnetic state. The trend of the growing extent of spin fluctuations is thought to be due to the lattice expansion. However, as discussed below, peculiarities in the band-structure may also contribute to this enhancement of γ.

Quenching of spin fluctuations at the MMT observed directly from specific heat measurements was reported for $Lu(Co_{1-x}Ga_x)_2$ by Murata et al. (1993) (see fig. 44). For the $Y(Co_{1-x}Al_x)_2$ system, however, the significant decrease of the electronic specific heat due to the MMT has been derived from thermodynamical considerations. For this purpose, one first discusses the above mentioned quadratic temperature increase of $B_c(T)$. From the Clausius–Clapeyron equation

$$\Delta S = -\Delta M \frac{\partial B_c}{\partial T} = -2\alpha \Delta M T \tag{47}$$

it can be inferred that the entropy difference ΔS across the transition is negative and roughly linear in T, since the magnetization jump ΔM is always positive and is expected to

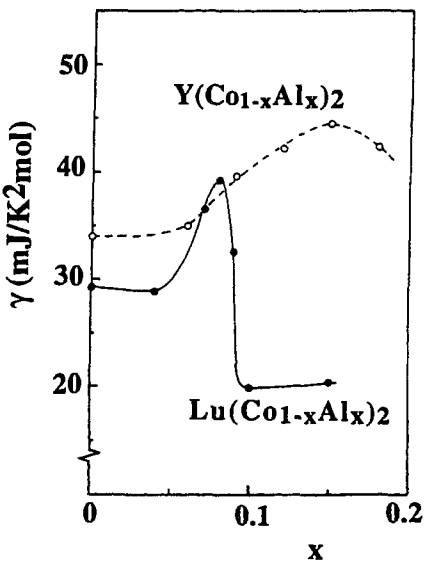


Fig. 43. Plot of γ vs. x in the $Lu(Co_{1-x}Al_x)_2$ and $Y(Co_{1-x}Al_x)_2$ compounds. After Pillmayr et al. (1990).

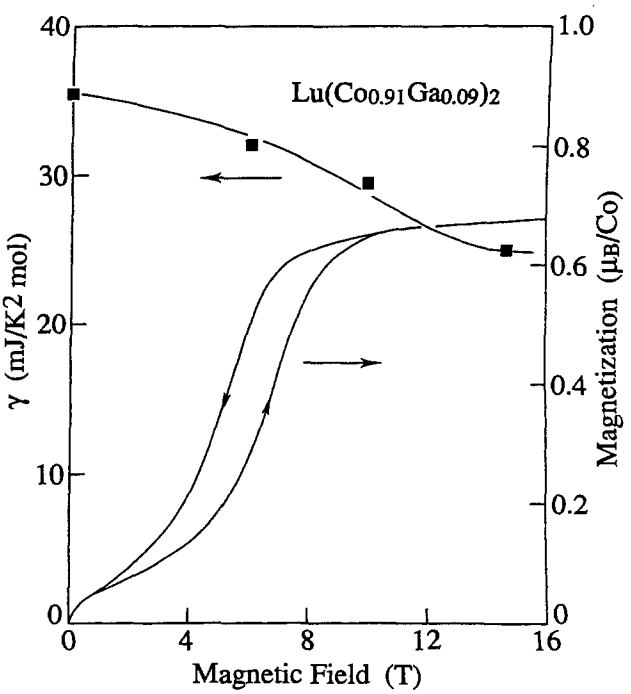


Fig. 44. Field dependence of the magnetization and that of the electronic specific heat constant for $Lu(Co_{0.91}Ga_{0.09})_2$. After Murata et al. (1993).

TABLE 9

Electronic specific heat change $\Delta\gamma$ at the MMT for a number of $Y(Co_{1-x}Al_x)_2$ and $Y(Co_{1-x}Ga_x)_2$ compounds.

Compounds	B_c (T)	$\Delta\gamma$ (mJ/mol K^2)	
		(a)	(b)
$Y(Co_{0.89}Al_{0.11})_2$	17	—	9.0 [1]
$Y(Co_{0.90}Al_{0.10})_2$	23	—	8.0 [1]
$Lu(Co_{0.91}Ga_{0.09})_2$	5	10.5* [2]	13.1 [1]
$Lu(Co_{0.88}Ga_{0.12})_2$	0.2	16.9* [2]	—

(a) Data derived from specific-heat measurement
(b) Data derived from thermodynamic analysis
(*) Data determined at $B = 10$ T

References:
[1] Sakakibara et al. (1992)
[2] Murata et al. (1993)

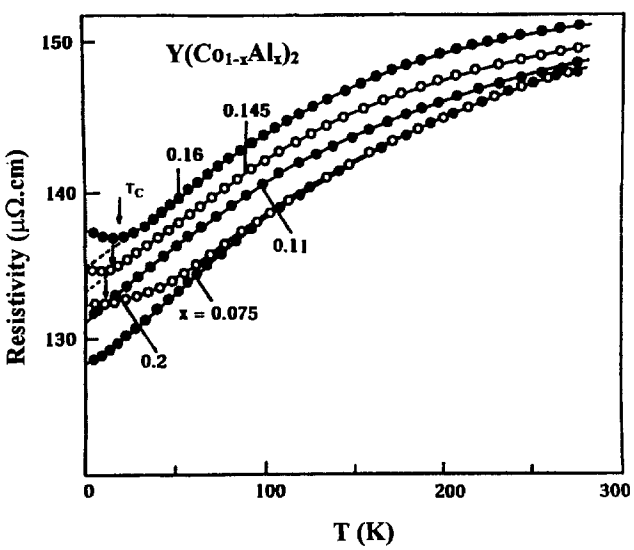


Fig. 45. Temperature dependence of the electrical resistivity for $Y(Co_{1-x}Al_x)_2$. After Duc et al. (1995a).

vary only slowly as a function of T. In metallic systems, low temperature entropy mainly comes from the electronic contribution: $S(T) \sim \gamma T + O(T^3)$. The T-linear dependence of ΔS is, thus, naturally understood by an abrupt change in γ at the MMT. Data of the change of the electronic specific heat $\Delta\gamma$ at the MMT are collected and listed in table 9 for several compounds. See also Mitamura et al. (1995b) and Goto and Sakakibara (1993).

Electrical resistivity and magnetoresistance data for the $Y(Co_{1-x}Al_x)_2$ system reported by Duc (1994) and Duc et al. (1995a) are presented in figs 45 and 46, respectively. For all

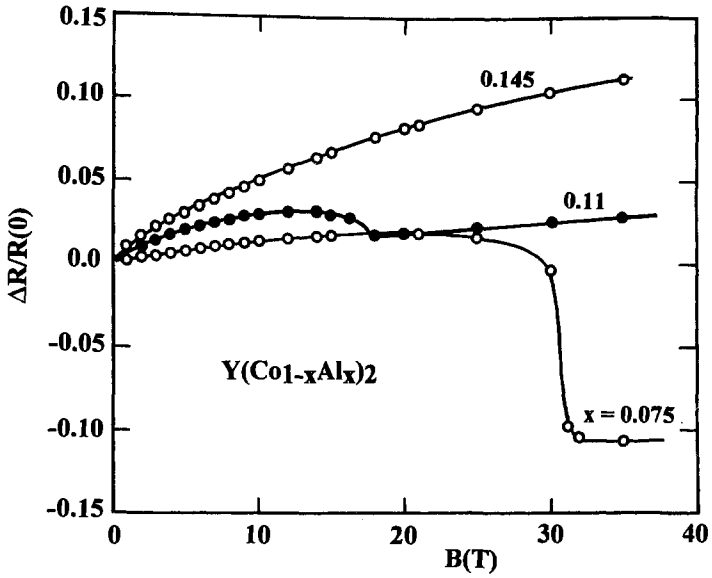


Fig. 46. Magnetoresistance as a function of the magnetic field for $Y(Co_{1-x}Al_x)_2$. After Duc et al. (1995a).

samples, the resistivity tends to saturation above 100 K. The $x = 0.075$ compound appears to exhibit a somewhat stronger temperature dependence than the other compounds. For the compounds with $x \geqslant 0.145$, for which weak ferromagnetism occurs, an upturn of the resistivity is observed at low temperature. The residual resistivity values (ρ_0) increase with increasing x and reach a maximum value at $x = 0.16$. This variation of ρ_0 is rather similar to that of the electronic heat capacity (Wada et al. 1990 and Pillmayr et al. 1990) and the 3d-magnetic moment (Duc et al. 1993c). Since the effective mass m^* is proportional to the mass-enhancement factor due to spin fluctuations (see section 2.2.4), the enhancement of ρ_0 as well as γ in the paramagnetic $Y(Co_{1-x}Al_x)_2$ compounds was previously considered as an indication of the growing extent of spin fluctuations due to the volume expansion. Nevertheless, the maximum of ρ_0 is found for the ferromagnetic compounds. This phenomenon may also be related to the peculiarities in the DOS into which the carriers can be scattered. The decrease of ρ_0 indicates that the peculiarities are "averaged out" at the compounds with high Al-concentration. This is consistent with the band calculations by Aoki and Yamada et al. (1992), in the sense that the sharp peak in the DOS of Co is appreciably destroyed when Co is replaced by Al to form the $Y(Co_{1-x}Al_x)_2$ compounds. Moreover, 3d-magnetism also plays an important role in the resistivity behavior of these compounds. For the weakly ferromagnetic compounds, a linear relationship between $\Delta R/R(0)$ and M^2 is found in fields up to 38 T. This relation is also valid for the extra magnetic contribution in the ordered state: $\Delta\rho_m(T)/\rho_0 \sim M_s(T)^2$, where M_s is the spontaneous magnetization (see fig. 47).

For the nearly ferromagnetic $Y(Co_{1-x}Al_x)_2$ compounds, a discontinuous reduction of $\Delta R/R(0)$ is observed at the metamagnetic transition. This discontinuity becomes less pronounced with increasing Al-content. This observation is consistent with the decrease of the

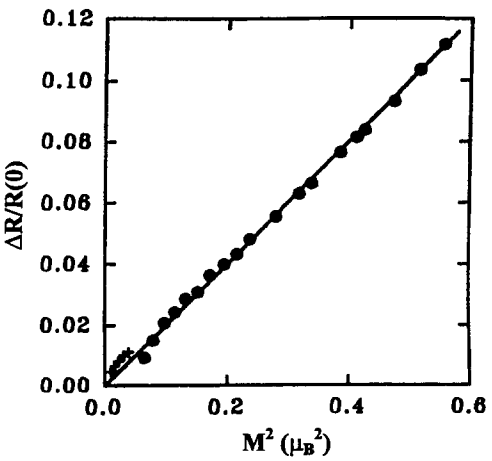


Fig. 47. Plot of $\Delta R/R(0)$ vs. M^2 for $Y(Co_{1-x}Al_x)_2$. (•) in high fields at 4.2 K; (+) spontaneous magnetization. After Duc et al. (1995a).

thermal variation of the resistivity noted above. The effect may be described by stating that the resistivity in the "low spin state" (or "spin fluctuation state") is higher than that in the "high spin state" (or "strongly ferromagnetic state"). In so far as this difference is ascribed to a suppression of spin fluctuations, the magnitude of the drop in resistivity at the MMT can be regarded as a measure for the amplitude of the spin fluctuations. Obviously, the drop ascribed to the spin fluctuations is much larger than the increase expected on the basis of the contribution proportional to M^2 discussed above.

3.3. (Y,Lu)(Co,M)$_2$ compounds with invariable crystal cell parameter

The evolution of magnetic properties of ACo_2 is related to the increase of DOS at the Fermi level $N(\varepsilon_F)$. Nevertheless, for $A(Co_{1-x}Al_x)_2$ systems this evolution has been interpreted in quite different ways. Some authors (Yoshimura and Nakamura 1985; Sakakibara et al. 1986, 1987; Endo et al. 1988) supposed that the increase of $N(\varepsilon_F)$ as aluminum substitutes cobalt is caused by the narrowing of the d-band due to the increase of the crystal cell parameter (the metallic radius of Al, $r_{Al} = 1.432$ Å is considerably larger than that of Co, $r_{Co} = 1.252$ Å). Aleksandryan et al. (1985), however, considered that the main reason for the change in the magnetic properties of $Y(Co_{1-x}Al_x)_2$ is due to the decrease of the 3d-electron concentration when Co ($3d^7$-configuration) is replaced by Al ($3d^0$-configuration). To separate these two parameters, high-pressure experiments are important. Indeed, as mentioned above, the effect of pressure has been evidenced for several weakly ferromagnetic compounds. In order to acquire a more complete understanding of the nature and features of the evolution of the magnetic properties of $A(Co_{1-x}Al_x)_2$, there is another route to isolate the various factors affecting the band structure. Gabelko et al. (1987) have synthesized a series of $(Y_{1-t}Lu_t)(Co_{1-x}Al_x)_2$ compounds, in which the lattice parameter $a(x)$ was maintained constant. Here, since the lattice parameter a of YCo_2 (= 7.221 Å) is substantially greater than that of $LuCo_2$ (= 7.121 Å), by choosing a suitable Lu concentration t the condition $a((Y_{1-t}Lu_t)(Co_{1-x}Al_x)_2) = \text{const} = a(YCo_2)$

could be satisfied in rather a broad concentration range up to $x = 0.22$. Magnetic investigations have shown that the variation of the critical field of MMT with changing x is very close to that of the systems $Y(Co_{1-x}Al_x)_2$ and $Lu(Co_{1-x}Al_x)_2$: $dB_c/dx \sim 6$ T/(%Al). In these systems, ferromagnetic ordering arises at approximately the same Al concentration $x_c \sim 0.1$. This comparison of compounds with an invariable crystal cell parameter $(Y_{1-t}Lu_t)(Co_{1-x}Al_x)_2$ and compounds with a varying lattice parameter (increasing with increasing x) shows that the change in the unit cell volume may not be the dominant factor affecting the magnetic properties of ACo_2 compounds, but that the concentration of the 3d electrons plays the most important role. In this study, however, different effects of the hybridization between the 3d and 4d states in $Y(Co_{1-x}Al_x)_2$ and that between the 3d and 5d states in $Lu(Co_{1-x}Al_x)_2$ are not yet investigated. The distinction between the characteristics of the 4d electrons of Y and those of the 5d electrons of Lu, as mentioned above in section 3.2, causes quite different magnetic behaviors of these systems. In addition, as will be seen below, one should also consider the effects of hybridization between the 5d(4d) and the p states.

There is also another possibility to investigate a system with a constant lattice parameter. That is a series of $R(Co_{1-x}Si_x)_2$ compounds. Since the atomic radius of Si is smaller than that of the Co atoms, the lattice constant is expected to be reduced in these systems. However, it was found that within experimental error the change in the lattice parameter is so small that it cannot be detected in the $R(Co_{1-x}Si_x)_2$ systems with R = Gd, Tb, Dy, Er, Y, and Sc (Michels et al. 1990; Duc 1996; and Cuong et al. 1998b). For the $Lu(Co_{1-x}Si_x)_2$ compounds, a linear decrease of the lattice constant with a rate of $da/dx = -4 \times 10^{-4}$ Å/(%Si) was shown (Murata et al. 1994b). This, however, is negligible compared to that of 5.5×10^{-3} Å/(%Al) in the $Y(Co,Al)_2$. Thus, one can consider these systems as systems of an invariable crystal unit cell. The magnetic investigations show that replacing Co by Si in the $A(Co_{1-x}Si_x)_2$ compounds leads to susceptibility enhancement and to reduction of the critical field of MMT, but does not trigger the itinerant ferromagnetic state as that observed in $A(Co,Al)_2$ (Murata et al. 1994b; Michels et al. 1990). We will present in the next section (Duc 1996; Duc and Oanh 1997) that for the compounds with magnetic rare-earths, the variation of the 3d-magnetic moment in $R(Co_{1-x}Si_x)_2$ is still rather similar to that in the $R(Co_{1-x}Al_x)_2$ compounds. In a more detailed analysis, this finding was related to the d–p hybridization, which shows various effects on the magnetic behavior and 4f–3d exchange interactions in the rare-earth intermetallics (Duc and Givord 1995; Duc 1997). Indeed, band calculations performed for $Y(Co_{1-x}Al_x)_2$ and $Y(Co_{1-x}Si_x)_2$ (Aoki and Yamada 1992) have shown that the DOS for YCo_2 is characterized by two sharp peaks below the Fermi level ε_F. By partially substituting Al for Co, the fragile peak at higher energy is reduced, whereas in the Co 3d band, ε_F shifts towards lower energy. As a result, the d(Co)-DOS happens to be relatively increased and a ferromagnetic state is formed in the $Y(Co,Al)_2$ system. In the case of substitution of Si for Co, the peak of d(Co)-DOS at higher energy is already destroyed at $x = 0.25$, whereas a broad peak at ε_F is established in the local p(Si)-DOS. Additionally, it was found that the height of the p(Si)-DOS is larger than that of the p(Al) ones and that most of the occupied p(Si) states appear in the lower energy region. This difference in the degree of the d–p hybridization is due to the extra p(Si) electron (compared to Al) and is the reason for the differences in the magnetic ordering phenomena observed in these two systems. Under the

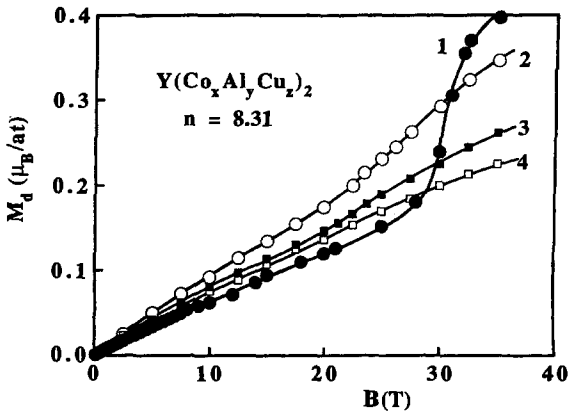


Fig. 48. High-field magnetization of $Y(Co_xAl_yCu_z)_2$. See the text and table 10 for the alloy compositions of samples No. 1–4. After Duc and Tai (1993).

condition of invariable volume, the hybridization between the d(Co) and p(Al and/or Si) states has been shown to play an important role in the 3d magnetism of the $R(Co_{1-x}Al_x)_2$ and $R(Co_{1-x}Si_x)_2$ systems. The NMR study of the magnetically ordered state of the weak itinerant ferromagnet $Y(Co,Al)_2$ (Yoshimura and Nakamura 1990) has also suggested that the stability of ferromagnetism in this system may be related to the hybridization between the 3d wave function of Co and the s- or p-like wave function.

3.4. Invariable d-electron concentration $Y(Co_xAl_yCu_z)_2$ compounds

The MMT of the invariable d-electron concentration $Y(Co_xAl_yCu_z)_2$ compounds was studied by Duc and Tai (1993). In YCo_2 the average number of d-electrons (including 3d(Co) and 4d(Y)) is considered to be 9 (Voiron 1973; Bloch et al. 1975). The 3d configurations at Al and Cu are $3d^0$ and $3d^{10}$, respectively. Then, the Al and Cu concentrations were chosen so that the total number of d-electrons remains constant in all the considered alloys. The lattice parameters and estimated number of d-electrons of these samples are presented in table 10. The high-field magnetization data are shown in fig. 48. For the $Y(Co_{0.925}Al_{0.075})_2$ compound (sample No. 1), a clear MMT takes place at $B_c = 30.3$ T. By substituting Al and Cu for Co, the low-field susceptibility is initially enhanced in sample No. 2, then it slightly decreases in samples No. 3 and No. 4. Moreover, it can also be found from this investigation that the alloying has strongly affected the MMT: with an increasing Cu(Al) concentration B_c slightly decreases whereas the magnetization jump at the transition falls fast and the MMT almost disappears in sample No. 4. As already mentioned, the effect of d-electron concentration can be isolated in this study. Thus, this decrease of B_c can be attributed to the volume effects caused by the lattice expansion. However, the smearing and disappearance of MMT in this system can also be related to the effect of Cu alloying. According to the approach to IEMM proposed by Duc et al. (1992b), the elastic properties may also play an important role. Since Cu is very stiff, the Cu alloying effect can cause an increase in the elastic constant and thus hamper the expansion to such an extent that

TABLE 10

The concentration of Co (x), Al (y), and Cu (z), the estimated d-electron number (n_d), the lattice parameter (a) and the critical magnetic field (B_c) for the $Y(Co_xAl_yCu_z)_2$ system.

No	x	y	z	n_d	a (Å)	B_c (T)
1	0.925	0.075	0.00	8.35	7.2660	30.3
2	0.890	0.080	0.03	8.31	7.2715	26.0
3	0.825	0.085	0.09	8.32	7.2800	22.5
4	0.800	0.088	0.112	8.35	7.2835	21.5

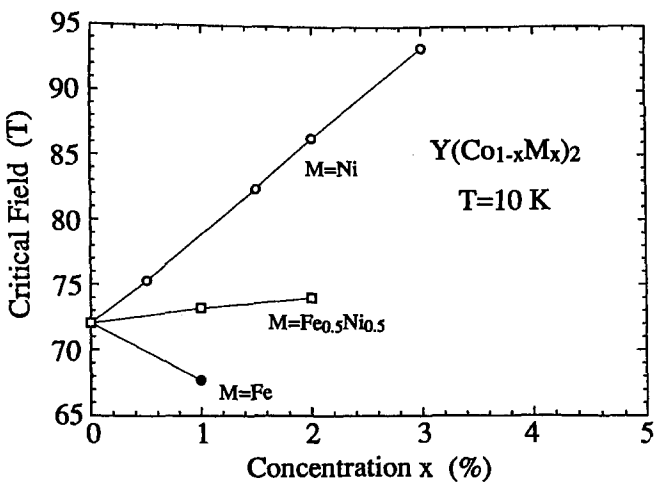


Fig. 49. Concentration dependence of B_c for the substituted compounds of $Y(Co_{1-x}M_x)_2$, M = Fe, Ni, and $Fe_{0.5}Ni_{0.5}$. After Goto et al. (1994a).

the system will stay in the paramagnetic state and the MMT disappears. Also, additional 3d(Co)–3d(Cu) mixing will modify the d-band structure. This factor, however, was not yet taken into account.

3.5. *$Y(Co_{1-x}M_x)_2$ compounds with M = Fe, Ni, Cu*

The existence of MMT in other magnetically enhanced systems was studied by Yoshimura et al. (1987). In the investigated magnetic fields up to 43 T, the MMT has been observed in the $Y(Co_{1-x}Fe_x)_2$ system in the concentration range $0.04 \leqslant x \leqslant 0.09$ near the onset of ferromagnetism. Other exchange-enhanced paramagnets $Y(Co_{1-x}Cu_x)_2$ and $(Y_{1-x}La_x)Co_2$ do not exhibit any MMT.

In order to get further information about the change of B_c by the shift of the Fermi level, the effects of Ni and Fe substitutions on the metamagnetic behavior of the YCo_2 Laves phase intermetallic compound were studied in pulsed magnetic fields up to 110 T by Goto et al. (1994b) and Mitamura et al. (1995a). The concentration dependence of

the metamagnetic critical field B_c for the substituted $Y(Co_{1-x}(Fe,Ni)_x)_2$ compounds is presented in fig. 49. A linear increase of B_c is observed for introduction of Ni ($dB_c/dx \sim 7$ T/(%Ni)), whereas the Fe doping is found to lower B_c (with a rate about 4.5 T/(%Fe)). This difference cannot be ascribed to a volume effect, since the lattice constant of YFe_2 is even larger than that of YCo_2. Moreover, the experimental results shown in fig. 49 seem to contradict the simple rigid band picture, in which symmetric changes are expected at least for low Ni and Fe contents. Indeed, an appreciable increase of 2 T is observed for $x = 2\%$ in the compound with simultaneous doping by equal amounts of Ni and Fe (see also fig. 49). This fact, however, can be entirely accounted for by the d electron number: Fe substitution shifts ε_F to the lower energy side, while the Ni substitution shifts it to the higher energy side. Consequently, the condition for the IEMM is satisfied at low and high magnetic fields for $Y(Co,Fe)_2$ and $Y(Co,Ni)_2$, respectively.

The results of Sakakibara et al. (1994) also suggest the existence of a critical Ni concentration near $x = 0.03$ above which the FOT disappears in the $Y(Co_{1-x}Ni_x)_2$ system. This is not simply explained by the randomness or disorder of the Co sublattice introduced by the substitution, because rather a sharp MMT (with $\Delta B \sim 2$ T) is still observed in the $Y(Co_{1-x}Al_x)_2$ system at the Al concentration of 10%. Further experimental and theoretical studies would be needed to clarify this point.

4. Magnetic lanthanide-Co_2 compounds

4.1. RCo_2 and $(R,Y)Co_2$ compounds

4.1.1. Ferrimagnetic spin ordering in RCo_2

In the intermetallic compounds based on magnetic lanthanides and transition metals, it is found as a rule (Campbell 1972; Buschow 1980; Franse and Radwanski 1993) that 4f–3d spin–spin coupling is antiferromagnetic, leading to the parallel alignment of 3d (Fe, Co, Ni) and 4f moments in the light lanthanide compounds and to the antiparallel alignment in the heavy lanthanide compounds. This universal picture can be understood by considering the role of hybridization between 5d and 3d states (Brooks and Johansson 1993; Duc 1997). The mechanism of the appearance of 3d-magnetism and 4f–3d coupling in RCo_2 is presented as follows.

For most lanthanide compounds, the 5d electrons on the R atoms are polarized by the exchange field from localized 4f moments. This polarization of 5d electrons would be in the same direction as that of the localized 4f moment. This is in accordance with the experimental observation that the 5d electrons do contribute a moment of $0.6\,\mu_B$ to the total value of $7.6\,\mu_B$/at. measured for Gd metal (Roeland et al. 1975) or of $0.1\,\mu_B$ in $GdNi_2$ (Farrell and Wallace 1966) and $GdAl_2$ (Swift and Wallace 1968). If the exchange field created by the (local) 4f moments is applied to the 5d electrons, the (parallel) up-spin 5d-band shifts towards the lower energy side and the down-spin 5d-band to the higher energy side, then, because of the difference in the relative position of the sub-bands, the hybridization of 5d and 3d states with up-spin becomes stronger than that of the states with down-spin (fig. 50). In case the Fermi level lies near the top of the 3d band, the (effective) number of 3d electrons with up-spin will be smaller than that with down-spin (a "white" area in the subbands represents the amount of 3d-character in the wave functions). Thus, a

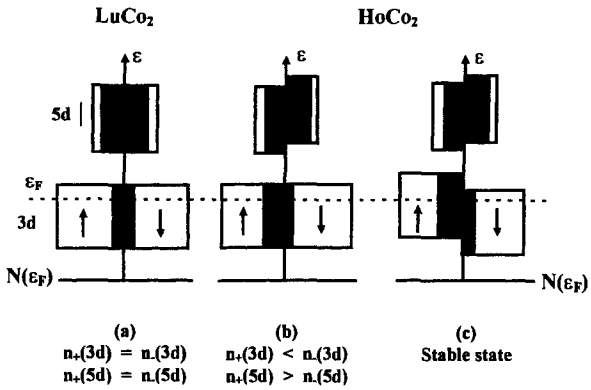


Fig. 50. Schematic DOS structure illustrating the formation of 3d magnetism in the magnetic lanthanide–Co_2 compounds.

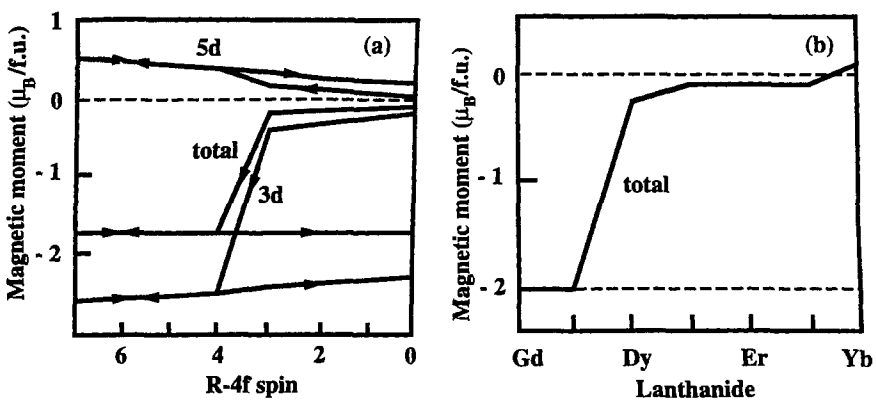


Fig. 51. (a) Calculated partial Co-3d, Gd-5d and total conduction electron moments of $GdCo_2$ as a function of the 4f-spin moment. The arrows denote the direction in which the 4f spin is changed. (b) Calculated total conduction electron moments of RCo_2, where R = Gd through Yb. After Nordström et al. (1992).

negative Co moment is induced. Furthermore, by the molecular field of the developed Co moment itself, the 3d bands with spin-up and down-spin will shift in the direction opposite to that of the corresponding 5d sub-band. The negative 3d moment is, thus, enhanced and stabilized in RCo_2 compounds. The influence of the 4f spin upon the magnetism of the transition metal in RCo_2 has been calculated by Nordström et al. (1992) using the self-consistent LMTO approximation. The resulting computed d-electron moment is shown in fig. 51(a) for $GdCo_2$ in which the 4f-spin moment on Gd was changed from zero to seven and then back again to zero. For increasing the 4f spin moment on Gd from zero to three (corresponding to Lu–Er) the moment induced on Co is small but at R = Ho the d-electron moment jumps to 1.75 μ_B/f.u. Both R-5d and Co-3d moments increase as the 4f spin increases, but they are always antiparallel. The effect of the 3d–5d hybridization on

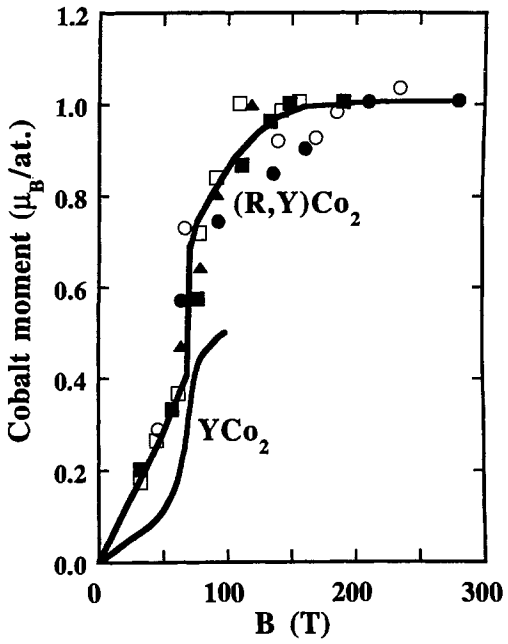


Fig. 52. Co-magnetic moment in $R_xY_{1-x}Co_2$. R = Gd (●), Tb (○), Dy (■), Ho (□) and Er (△). After Duc et al. (1992a).

the ferrimagnetic coupling between 3d and 5d spins (and then between 3d and 4f spins) is, thus, well demonstrated for this series of compounds. For the real system, i.e., with real lattice parameters, the results of calculations show a transition at R = Tb, see fig. 51(b).

4.1.2. Effect of a molecular field on the induced Co metamagnetic behavior

In a mean-field approach, the cobalt moment is assumed to be induced by the molecular field exerted by the localized 4f-moments. The 4f-spin dependence mentioned above, thus, is described as a molecular-field dependence of the Co-subsystem moment. Gignoux et al. (1975, 1977a, 1977b), Steiner et al. (1978), Levitin et al. (1982), and Duc et al. (1988a, 1992a) have measured the induced moments of Co in RCo_2 and $(R,Y)Co_2$ compounds. By changing the Y concentration, they can change the molecular field acting on the Co-subsystem. A complete collection of data of spontaneous Co magnetic moments was reported by Duc et al. (1992a), see fig. 52. The authors found that a metamagnetic transition of the Co-subsystem in $R_xY_{1-x}Co_2$ occurred at a molecular field which is lower than that in $ErCo_2$. The critical R-concentration x_c for the onset of 3d magnetism is equal to 0.75, 0.65, 0.55, 0.4, and 0.33 for RCo_2 with R = Er, Ho, Dy, Tb, and Gd, respectively. The value of x_c, however, can also be determined from the measurements of the specific heat and resistivity (see section 4.1.5). Under the assumption that in the RCo_2 (R = heavy lanthanide) compounds, the MMT occurs at the same (molecular) field, i.e., B_c is equal to 70 T as observed for $Y(Lu)Co_2$, it turns out that the value of the exchange coupling

parameter A_{RCo} is about 11.5×10^{-23} J. This is in support of Bloch and Lemaire's values (Bloch and Lemaire 1970), but is rather small compared with that deduced from high-field magnetization experiments (Ballou et al. 1993a, 1993b). We will return to this problem later (in section 6.2).

It is worthwhile to note that, in comparison, both the low-field susceptibility (i.e., below the critical field) and the magnitude of m_{Co} (about $0.55\,\mu_B$/Co at $B = 100$ T) in YCo_2 is rather smaller than that in RCo_2 compounds (0.8–$1.0\,\mu_B$/Co). In terms of the 3d–5d hybridization, this difference is related to the detailed way in which the 3d state hybridizes with the 5d states in the external and internal fields. In the calculations reported by Yamada and Shimizu (1985) for YCo_2 the magnetic field of 150 T applied in the same direction on Y and Co atoms yields the values of $0.454\,\mu_B$/at. Co and $0.1\,\mu_B$/at. Y for Co and Y atoms, respectively. Then, in order to estimate the magnetic moments in RCo_2, the magnetic field B^{Y}_{mol} at the Y-site was applied in the direction opposite to that of B^{Co}_{mol} at the Co-site. For $HoCo_2$ the local exchange field acting on the 5d electrons is taken to be -2400 T. Hence, in the calculations based on YCo_2, that value was assigned to B^{Y}_{mol} (Yamada and Shimizu 1985). On the other hand, the exchange field on Co from the localized 4f moments of Ho is $B^{Co}_{mol} = 156$ T (Gignoux and Givord 1979). The resulting values for m_{Co} and m_Y are 0.61 and $-0.236\,\mu_B$/at., respectively. In $HoCo_2$, the observed m_{Co} is about $0.8\,\mu_B$/Co (Gratz and Zuckermann 1982; Gratz et al. 1986). Subtracting the orbital contribution (of $0.14\,\mu_B$/Co), the spin part of the observed m_{Co} becomes $0.66\,\mu_B$. The agreement between the calculated and observed values of m_{Co} is satisfactory. Similarly, experimental observations of the enhancement of Co-susceptibilities (Gignoux and Givord 1979; Duc et al. 1993a) and magnetoresistance (Duc 1994) in the magnetic lanthanide–Co_2 compounds (in comparison to that in YCo_2), which had suggested earlier a slight variation in the d-band structure, can be discussed now in terms of a different degree of 3d–5d mixing caused by the different effects of the external and internal magnetic fields.

4.1.3. Anomalous magnetization process in the $R_xY_{1-x}Co_2$ compounds

In almost all RCo_2, the molecular field at the Co-sites, B^{Co}_{mol}, is larger than the metamagnetic transition field B_c and the Co magnetic moment is stabilized. The study of pseudobinary systems, where the heavy lanthanide (HR) is diluted by a non-magnetic element is an useful method to observe the collapse of the Co moment. For these HR–Co_2 ferrimagnets, the direction of B^{Co}_{mol} is antiparallel to that of the HR-moment and, hence, to that of the applied magnetic field B. This means that the effective field acting upon the Co-subsystem, B^{Co}_{eff} ($= B^{Co}_{mol} - B$) decreases with an increasing applied field. When B is large enough to satisfy $B^{Co}_{eff} < B_c$ the Co moment abruptly collapses, which corresponds to an inverse MMT. In principle, this case of the inverse MMT must occur in the HR-Co_2 compounds. However, it is difficult to observe this kind of MMT since the magnetic field required for the collapse of the Co moment is too large for usual magnetic facilities. A MMT was directly observed in $ErCo_2$ at $B = 52$ T, but is rather broad (fig. 53). The origins for this broadening of the transition will be discussed below. The collapse of the Co moment was observed at a lower field for the systems (Gd,Y)Co_2 (Yamaguchi et al. 1992), (Er,Y)Co_2 (Levitin et al. 1984a) and (Er,Lu)Co_2 (Wada et al. 1994; Bartashevich et al. 1997). The magnetization data are illustrated in fig. 54(a) for $Er_xLu_{1-x}Co_2$. In the region $0.8 \leqslant x \leqslant 0.65$, the magnetization increases anomalously with an increasing field suggesting the existence of

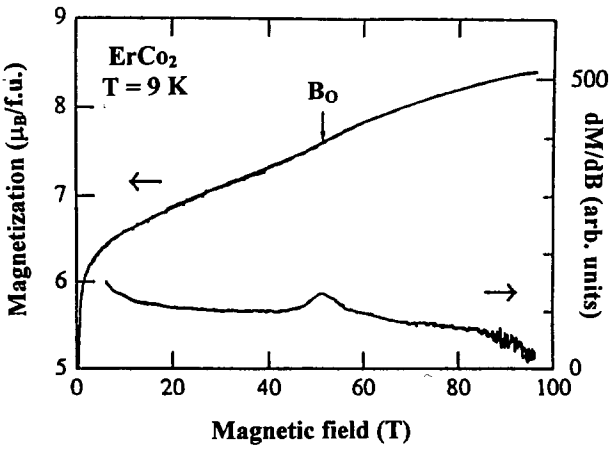


Fig. 53. High-field magnetization of $ErCo_2$. The down-arrow indicates a metamagnetic transition point. The dM/dB curve is also shown. After Bartashevich et al. (1997).

a MMT from the magnetic to the paramagnetic state. The volume magnetostriction curves $\omega(B)$ shown in fig. 54(b) exhibit anomalous shrinkage at the same fields, where the magnetization anomaly occurred. A great and negative volume change ω is consistent with the Co moment collapse model. No remarkable MMT is observed at $x = 0.65$. However, the volume magnetostriction is negative and relatively large. According to the NMR spectrum of this compound, part of the Co atoms remains in the magnetic state, and produces negative volume magnetostriction when their moments collapse. The concentration dependence of the metamagnetic transition field for the pseudobinary $Er_xLu_{1-x}Co_2$ compounds is shown in fig. 55. The values for the Lu-concentrations $(1 - x) = 0$, 0.2 and 1.0 lie on a straight line. In the concentration range $(1 - x) > 0.2$, however, the fields become smaller than expected according to this line. This is also attributed to the appearance of paramagnetic Co atoms, even in zero field. Ballou et al. (1992) have also reported an induced MMT for $Y_{1-t}Gd_t(Co_{0.915}Al_{0.085})_2$. As can be seen in fig. 56, the original $Y(Co_{0.915}Al_{0.085})_2$ compound shows a MMT at $B_c = 22.5$ T. The effect of substituting the Gd atom is simply to lower the applied magnetic field necessary to observe the MMT. At low fields, a collinear ferrimagnetic phase happens to be formed, with stable Gd and Co magnetic sublattices (fig. 56 for $t = 0.04$ and 0.1).

For the light lanthanide LR–Co_2 compounds, $\boldsymbol{B}^{Co}_{mol}$ is parallel to the LR-moment (and parallel to the external field $\boldsymbol{B}$). The applied field will strengthen the effective field acting on the Co-subsystem and easily bring pseudobinary compounds $LR_xY_{1-x}Co_2$ with $B^{Co}_{mol} < B_c$ to the MMT. We present in figs 57(a) and (b) the high-field magnetostriction data for the $Nd_xY_{1-x}Co_2$ compounds (Duc et al. 1992c, 1995a, 1995b). In the compounds with $x \approx 0.2$ to 0.32, the volume magnetostriction ω shows a positive contribution, and nonlinearly increases with an increasing magnetic field. The MMT, moreover, can be clearly seen in the $d\omega/dB$ vs. B curves. In view of the induced character of the Co moment, the relation $\omega = \kappa C M^2_{Co}$ has been considered, and appears to work satisfactory. It

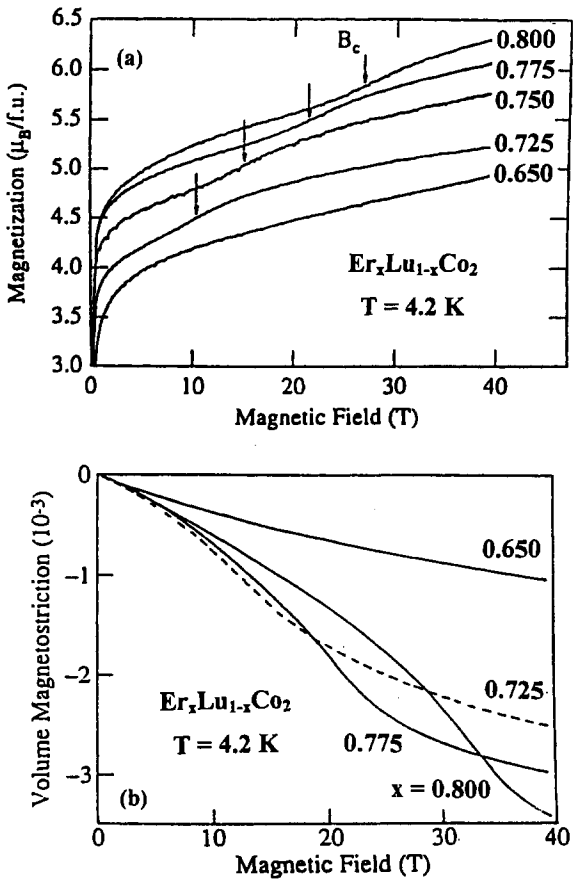


Fig. 54. Magnetization (a) and magnetostriction (b) curves at 4.2 K for $Er_xLu_{1-x}Co_2$ compounds. After Bartashevich et al. (1997).

was also found that κC was slightly increased in the $Nd_xY_{1-x}Co_2$ compounds that were close to the critical concentration for the onset of Co magnetism. As will be presented below in section 4.1.4, this may be related to an anomaly of the elastic properties at the MMT (Klimker and Rosen 1976). This may also be the reason why the MMT is more clearly detected by the magnetostriction measurements but is not so clear in the magnetization measurements. Nevertheless, it is clear that the MMT in this kind of compound is rather broad. Wada et al. (1994) have claimed that there are two origins for the broadening of the transition. One is a local environment effect and the other is a strong magnetocrystalline anisotropy. The former effect on the Co moment has been studied in detail on $Dy_xLu_{1-x}Co_2$ (Yoshimura et al. 1984a, 1984b) and does not appear in pure $ErCo_2$. The molecular field on each Co atom is determined by the number of nearest-neighbor magnetic R-atoms. Therefore, the statistical distribution of this number makes the MMT broad. The latter origin is more intrinsic. Due to the anisotropy field, some R-moment cannot ro-

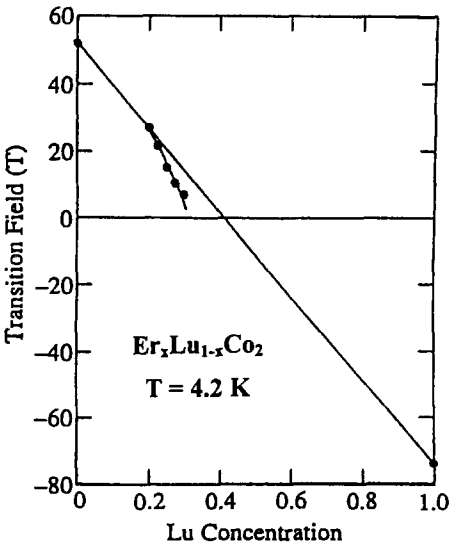


Fig. 55. B_c as a function of the Lu-concentration $(1 - x)$ for $Er_xLu_{1-x}Co_2$.

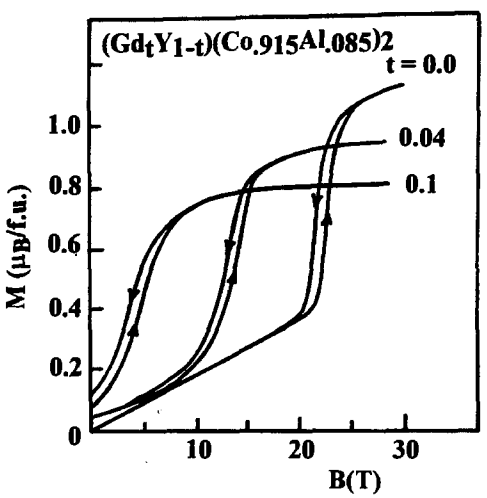


Fig. 56. Metamagnetic transitions in $Y_{1-t}Gd_t(Co_{0.915}Al_{0.085})_2$. After Ballou et al. (1992).

tate to the applied-field direction resulting in a distribution of the metamagnetic transition fields, too.

The multiple field-induced magnetic phase transitions in a ferrimagnet with one unstable magnetic sublattice will be discussed in section 5.

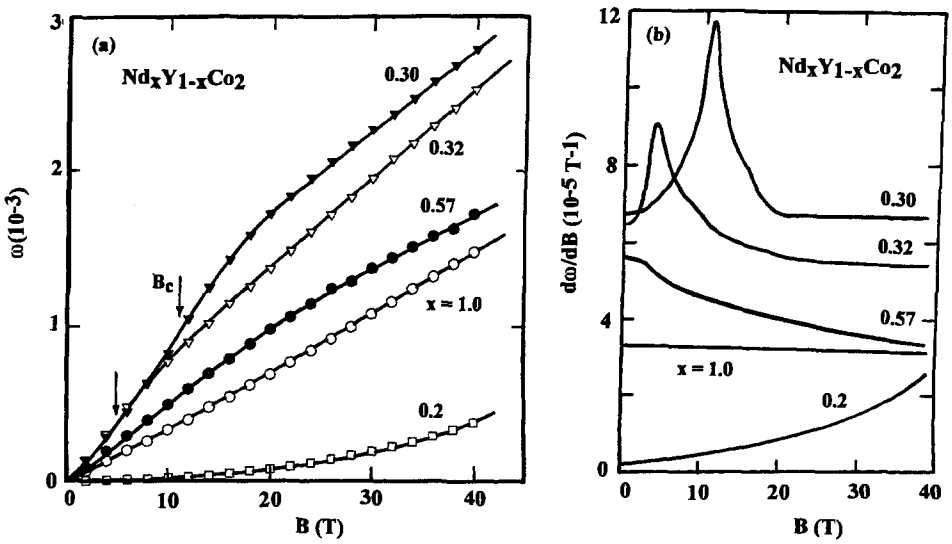


Fig. 57. Plots of ω (a) and $d\omega/dB$ (b) as a function of B at 4.2 K for the $Nd_xY_{1-x}Co_2$ compounds. After Duc et al. (1994).

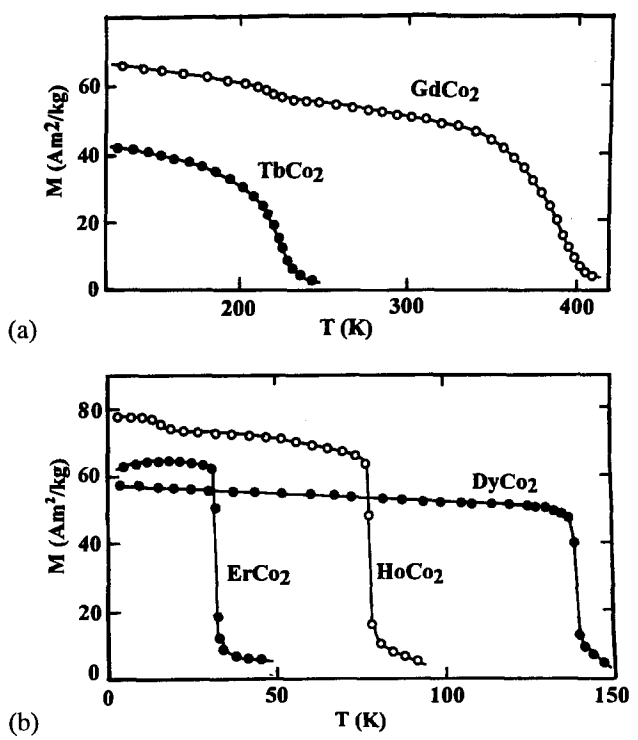


Fig. 58. Temperature dependence of the magnetization in RCo_2 compounds.

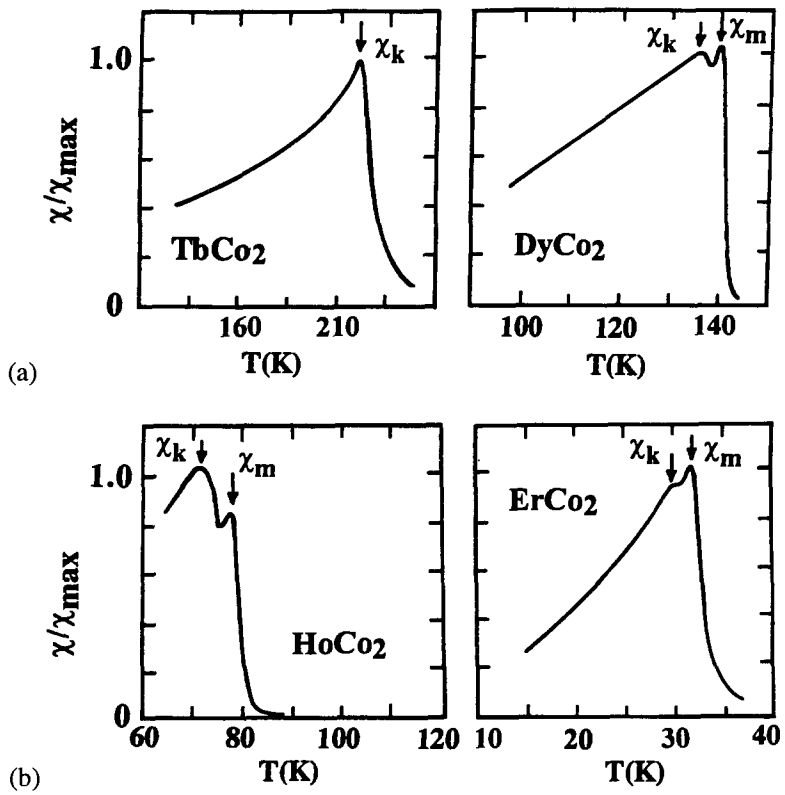


Fig. 59. A.c. susceptibility in the vicinity of T_c for RCo_2 compounds.

4.1.4. Magnetic phase transitions

The transitions from the paramagnetic state to a magnetically ordered one in RCo_2 have attracted much attention for more than 25 years. The transition at T_c found for the compounds with Dy (at 140 K), Ho (75 K), Er (32 K) appears to be of first order. It is characterized by a sharp change of the magnetization (Lemaire 1966; Duc et al. 1988a, 1988c; fig. 58), by a double peak of the a.c. susceptibility χ_{ac} in the vicinity of T_c (Duc et al. 1989; Duc 1996; see fig. 59), by a change in resistivity (Gratz et al. 1981; see fig. 60), by a large and sudden change of the volume (Minataka et al. 1976; see fig. 61), by a large peak of the specific heat (Voiron 1973; see fig. 62), and by a sharp anomaly of the elastic parameter (Klimker and Rosen 1976; see fig. 63(a), (b)). The transition in the compounds with high T_c, i.e., in $GdCo_2$ (400 K) and $TbCo_2$ (230 K), however, is of second order. This leads to a smooth change of the above mentioned physical parameters (see also figs 58–63). The T_c-value of 200 K was regarded as the border temperature below which the transition is of first order (Bloch et al. 1975). This argument was given in a discussion of the metamagnetic behavior of the 3d subsystem (Cyrot and Lavagna 1979), in particular, based on the connection of the change in the sign of the a_3-coefficient (Bloch et al. 1975; see also sections 2.1 and 3.1). Indeed, a change from SOT to FOT was

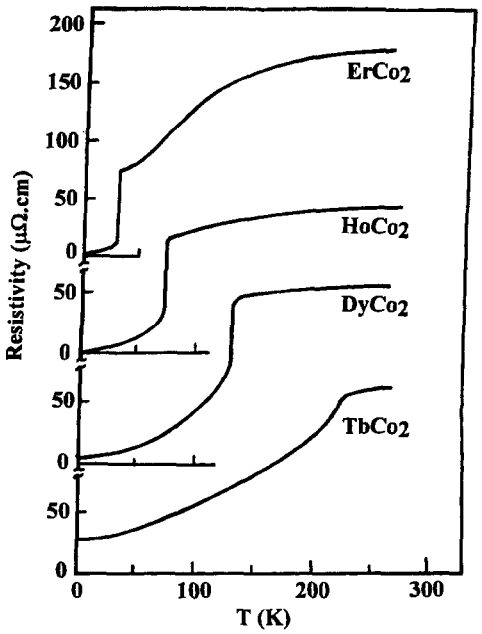


Fig. 60. Temperature dependence of the resistivity in RCo_2 compounds. After Gratz et al. (1981).

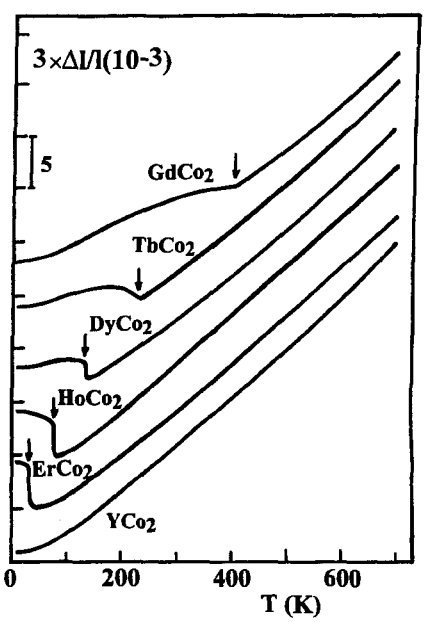


Fig. 61. Temperature dependence of $\Delta l/l$ in RCo_2 compounds. After Minataka et al. (1976).

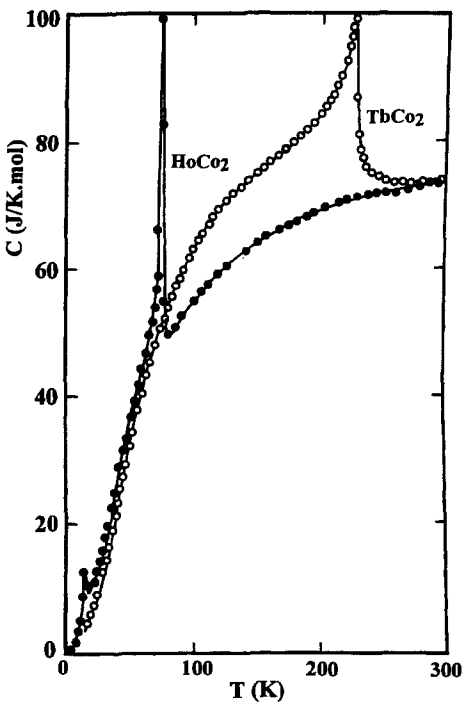


Fig. 62. Specific heat of the $TbCo_2$ and $HoCo_2$ compounds. After Voiron (1973).

observed in $Tb_xY_{1-x}Co_2$ (Franse et al. 1983; Levitin et al. 1984b), $Tb_xHo_{1-x}Co_2$ (Duc et al. 1989) (see figs 64(a), (b)) at about $x = 0.7$ ($T_c = 176$ K and 185 K, respectively). Such a change was not found in $(Gd_xY_{1-x})Co_2$ (Muraoka et al. 1977a). Moreover, the FOT in $DyCo_2$, $HoCo_2$, and $ErCo_2$ changes to SOT in $(Dy_xY_{1-x})Co_2$ (Duc et al. 1985; Yoshimura et al. 1984a, 1984b; see fig. 65) $Ho_xY_{1-x}Co_2$ (Steiner et al. 1978; see fig. 66) and $Er_xY_{1-x}Co_2$ (Duc et al. 1988c; see fig. 67) at $x \approx 0.4$, 0.5, and 0.7, respectively. See also Hauser et al. (1997a, 1997b). Franse et al. (1983) and Duc et al. (1989) have pointed out that the FOT in (Tb,Y)Co_2 observed at $x = 0.5$ and 0.3 is clearly evidenced by the magnetization measurements, but less clearly in the resistivity and thermal expansion. Berthier et al. (1986) have also reported that the FOT cannot be detected by the specific heat measurements for this system. This may be attributed to inhomogeneities rather than taken as an indication that the FOT-SOT borderline is approached.

Inoue and Shimizu (1982) estimated the value of $c_3(T_c)$ on the basis of eq. (21) for RCo_2 with $T_3 = 250$ K (see also eq. (45) or eq. (48) below) and $\chi_d(T_c)$ independent of T, and then were able to explain the type of the phase transition. Using eq. (21) and taking into account the temperature dependence of $\chi_d(T_c)$, Duc et al. (1988a, 1988b, 1989, 1991) explained the observed behavior in RCo_2 and (R,Y)Co_2. The calculated $c_3(T_c)$ results are illustrated in tables 11 and 12 for $Tb_xY_{1-x}Co_2$ and $Tb_xHo_{1-x}Co_2$, respectively. Clearly, the sign of $c_3(T_c)$ is in accordance with the type of transition. It was necessary here to adopt a lower T_3 value (178 K). A reduced value (150 K) was also adopted

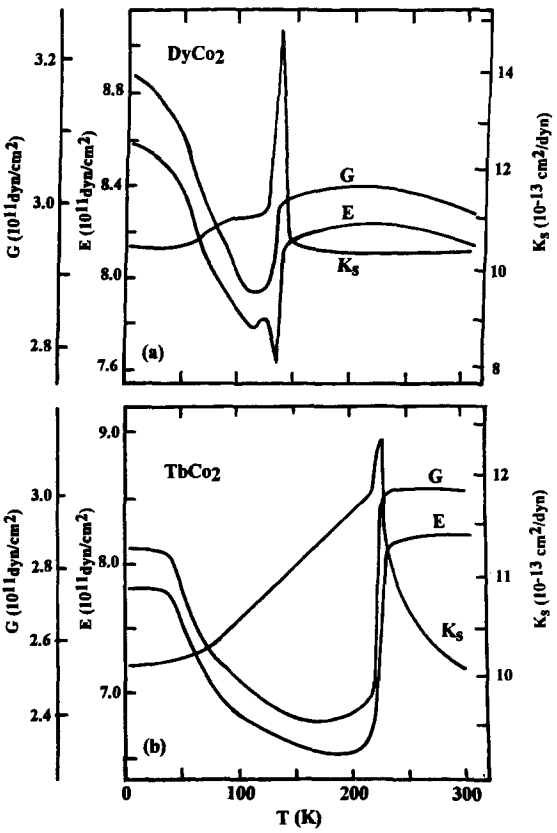


Fig. 63. Temperature dependence of Young's modulus (E), that of the shear modulus (G) and that of the adiabatic compressibility (K_s) for $DyCo_2$ (a) and $TbCo_2$ (b) compounds. After Klimker and Rosen (1976).

TABLE 11

The $c_3(T_c)$ values for the $Tb_xY_{1-x}Co_2$ compounds calculated with $a_3(0) = -6.8$ T(mol/A m^2)^3 and $T_3 = 178$ K.

x	T_c K	$100a_3(T_c)$ T(mol/A m^2)^3	$100c_3(T_c)$ T(mol/A m^2)^3
0.2	38	−649	−3.02
0.3	67	−584	−6.26
0.4	98	−474	−8.35
0.5	128	−328	−7.35
0.6	154	−171	−3.84
0.7	176	−15	−0.23
0.8	197	153	2.87
0.9	217	303	4.66
1.0	227	426	5.11

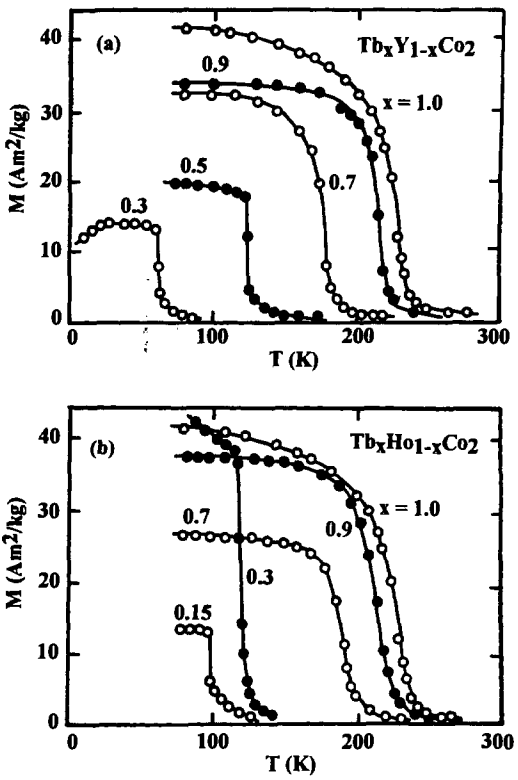


Fig. 64. Temperature dependence of the magnetization in (Tb,Y)Co_2 (a) and (Tb,Ho)Co_2 (b) compounds. After Duc et al. (1989).

TABLE 12

The $c_3(T_c)$ values for the $Tb_xHo_{1-x}Co_2$ compounds calculated with $a_3(0) = -6.8$ T(mol/A m^2)^3 and $T_3 = 178$ K.

x	T_c K	$100a_3(T_c)$ T(mol/A m^2)^3	$100c_3(T_c)$ T(mol/A m^2)^3
0.0	75	−559	−0.14
0.1	85	−525	−0.21
0.15	94	−490	−0.29
0.3	129	−323	−0.67
0.7	185	55	0.37
0.9	210	226	2.48
1.0	227	426	5.11

by Inoue and Shimizu (1988). A magnetic-phase diagram, i.e., the boundary between FOT and SOT in all (R,Y)Co_2 compounds, has been calculated with $T_3 = 178$ K and $a_3(0) = -15$ T(mol/A m^2) (see fig. 68). Moreover, the calculated values depend on the

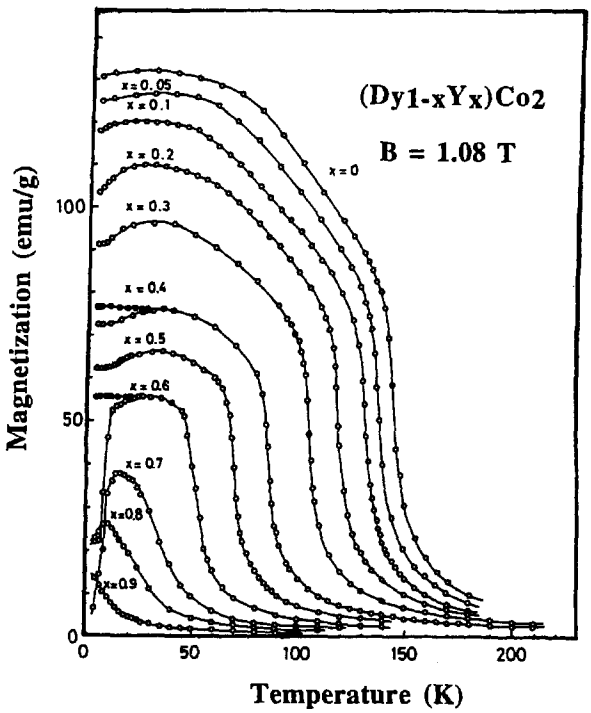


Fig. 65. Temperature dependence of the magnetization in (Dy,Y)Co_2 compounds. After Yoshimura et al. (1984b).

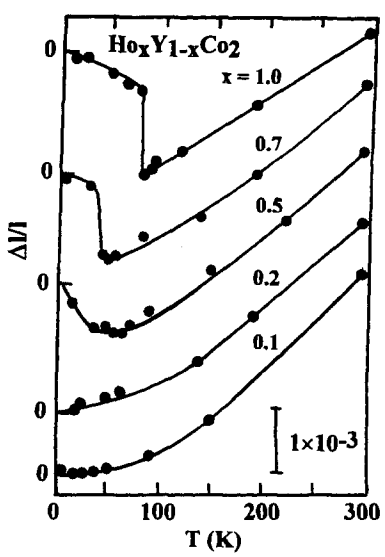


Fig. 66. Temperature dependence of $\Delta l/l$ in (Ho,Y)Co_2 compounds. After Steiner et al. (1978).

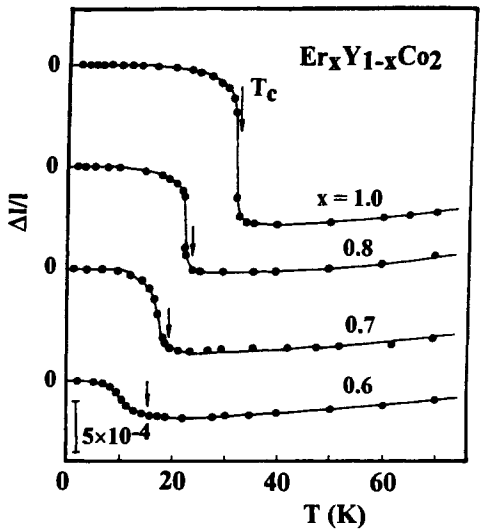


Fig. 67. Temperature dependence of $\Delta l/l$ in (Er,Y)Co_2 compounds. After Duc et al. (1988a).

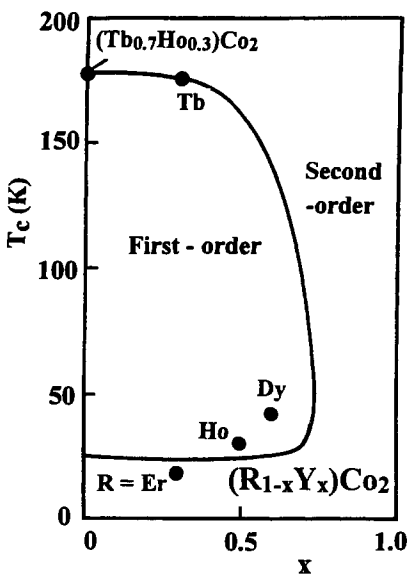


Fig. 68. Boundary between FOT and SOT for $R_xY_{1-x}Co_2$ compounds. Experimental values indicated for R = Tb, Dy, Ho, and Er. At $x = 0$: boundary value for (Tb,Ho)Co_2. After Duc et al. (1992a).

other parameters. One might wish, for instance, to find a more realistic value for, e.g., the b_1-coefficient by taking into account the crystalline electric field effects (CEF) or the R–R interactions. The magnetic behavior of lanthanide moments may be influenced by the

level splitting in the crystalline electric field, even to the extent that the CEF-effects are the cause of the occurrence of the SOT at relatively low temperatures. The CEF effect, which is larger in LR-Co_2 compounds than in HR-Co_2, may play an important role in the SOT of $NdCo_2$ and $PrCo_2$ (Bloch et al. 1975; Inoue and Shimizu 1988). Also, volume effects may be important. It has been suggested that going from HR- to LR-compounds the Co-subsystem is magnetically enhanced, with an optimum at the lattice parameter $a = 7.272$ Å (Duc et al. 1992a; see also section 4.2). In the presentation by Cyrot and Lavagna (1979), the increase of the 3d-magnetic susceptibility is also the cause of the disappearance of metamagnetic behavior. From this discussion, the study of the magnetic properties in the compounds in which both LR and HR atoms were present, appears to be very interesting. Duc et al. (1993a) have reported the investigation of magnetic transitions in (Nd,Dy)Co_2 and (Pr,Dy)Co_2. The substitution of Dy for Nd or Pr lowers the ordering temperature. The magnetic phase transition, however, changes from FOT to SOT at a Dy concentration x between 20% and 40% for both series of compounds as indicated by magnetization and resistivity measurements.

The influence of volume changes was taken into account by Duc et al. (1993a) by introducing a volume dependence of the a_3-coefficient in eq. (45), reproduced here in the form:

$$a_3(T) = a_3(0) + |a_3(0)|\left(\frac{T}{T_3}\right)^2. \tag{48}$$

A gradual change from "light" to "heavy" lanthanides brings along a corresponding lowering of the lattice parameter. Nevertheless, for simplicity, T_3 was taken to be equal to 178 K for all compounds (lattice parameters), having in mind that the T_3 contribution in eq. (48) is small, anyway, in the compounds with low Curie temperature. Only $a_3(0)$ was taken to be volume dependent, and, in fact, was assumed to vary from -15 T(mol/A m^2)^3 for $ErCo_2$ up to $+3.1$ T(mol/A m^2)^3 for $PrCo_2$, in a linear dependence on the lattice parameter, chosen in such a way that $a_3(0)$ changes the sign at a lattice parameter $a = 7.275$ Å (i.e., between $GdCo_2$ with $a = 7.256$ Å and $NdCo_2$ with $a = 7.300$ Å). According to the three-sublattice model, i.e., the generalization of the Inoue–Shimizu model (Brommer 1989; Duc et al. 1993a; see also section 2.1.2), the coefficient c_3 (at the temperature of the second order transition) was calculated. The results are presented in tables 13 and 14 for the (Nd,Dy)Co_2 and (Pr,Dy)Co_2 systems, respectively. Both R–Co and R–R interactions were taken into account. (Their strengths will be presented in the next section.) The model shows a change in the sign of $c_3(T_c)$ at concentrations that are in good agreement with the experimentally observed change of the type of magnetic transition from first to second order in the compounds under consideration. Since there are many adjustable parameters in the model, one undoubtedly can find various sets of parameters for which such a change of sign occurs. This approach proves the possibility to describe the change of the type of magnetic phase transition in rather a "complex" (HR,LR)Co_2 system in the generalized Inoue–Shimizu model.

The influence of external pressure is not only to reduce T_c (see fig. 69), but also to change the magnetic transition (if it is of first order) into a second order one. The critical pressure of this change is about 30 kbar (Voiron and Bloch 1971). The boundary between the FOT

TABLE 13

The $c_3(T_c)$ values for the $Dy_xNd_{1-x}Co_2$ compounds calculated with the lattice parameter dependence of $a_3(0)$ (see text) and $T_3 = 178$ K.

x	T_c K	$a_3(T_c)$ T(mol/A m^2)^3	$100c_3(T_c)$ T(mol/A m^2)^3
0.0	95	3.98	2.7
0.2	100	0.39	66.08
0.4	105	−1.63	−17.30
0.5	110	−2.41	−3.48
0.6	115	−3.09	−1.29
0.8	125	−4.11	−0.36
1.0	140	−4.16	−0.20

TABLE 14

The $c_3(T_c)$ values for the $Dy_xPr_{1-x}Co_2$ compounds calculated with the lattice parameter dependence of $a_3(0)$ (see text) and $T_3 = 178$ K.

x	T_c K	$a_3(T_c)$ T(mol/A m^2)^3	$100c_3(T_c)$ T(mol/A m^2)^3
0.0	56	3.41	1.71
0.2	69	0.35	12290.6
0.4	78	−2.02	−0.13
0.6	95	−3.79	−0.28
0.8	115	−4.72	−0.22
1.0	140	−4.16	−0.20

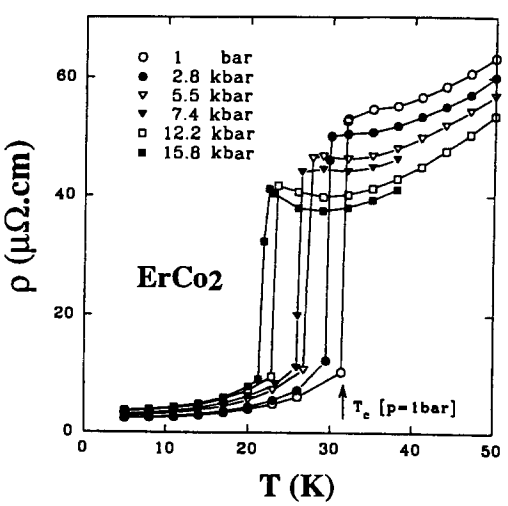


Fig. 69. Temperature dependence of the resistivity of $ErCo_2$ under pressure.

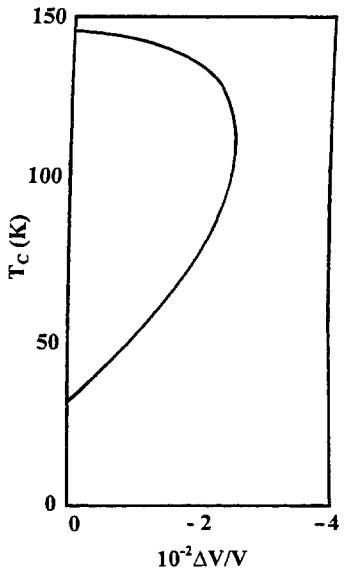


Fig. 70. Boundary between FOT and SOT with respect to the change in volume for the $R_xY_{1-x}Co_2$ compounds. After Inoue and Shimizu (1988).

and SOT in RCo_2 with respect to the change in the volume was studied in a similar way to that used for (R,Y)Co_2 compounds (Inoue and Shimizu 1988) by assuming that only $\chi_d(T)$ depends on the volume. Taking the value of $d \ln \chi_d(T)/d \ln V = 14$ reported by Voiron (1973), the boundary between FOT and SOT with respect to the change in volume was calculated. The results are presented in fig. 70. Physically, this may be related to the effect of volume on the magnetic behavior of the Co-subsystem: an increase of external pressure reduces the Co-susceptibility and increases the critical field of MMT and even destroys the metamagnetic behavior. Then the condition of FOT in the RCo_2 compounds is more difficult to fulfill under higher pressure and the transition becomes a SOT with a relative low value of dT_c/dp (Voiron 1973). See also Hauser et al. (1998) and Markosyan et al. (1998).

4.1.5. Magnetic and electronic properties of (R,Y)Co_2 in the vicinity of T_c

In section 4.1.3, the magnetic phase transitions have been presented for (R,Y)Co_2. The application of the theoretical model to explain this experimental observation has been done in section 4.1.4. In this sub-section, the physical properties of the system at the transition are discussed. At the FOT, not only the magnetization of itinerant electrons disappears but also the 4f-spins are suddenly disordered. Experimentally, these two aspects are visible in the change of the spontaneous volume magnetostriction (taken as an indication of the Co moment) and of the magnetic entropy (as an indication of the 4f moment) at T_c. Metamagnetism observed just above T_c (Lemaire 1966; Givord and Shah 1972; Steiner et al. 1978; Duc and Oanh 1997) strongly confirmed this picture of two distinct contributions (of lanthanide and Co moments). Magnetization isotherms are presented in figs 71(a), (b), (c) for polycrystalline $ErCo_2$, $HoCo_2$, and $DyCo_2$ samples. Metamagnetism is characterized by

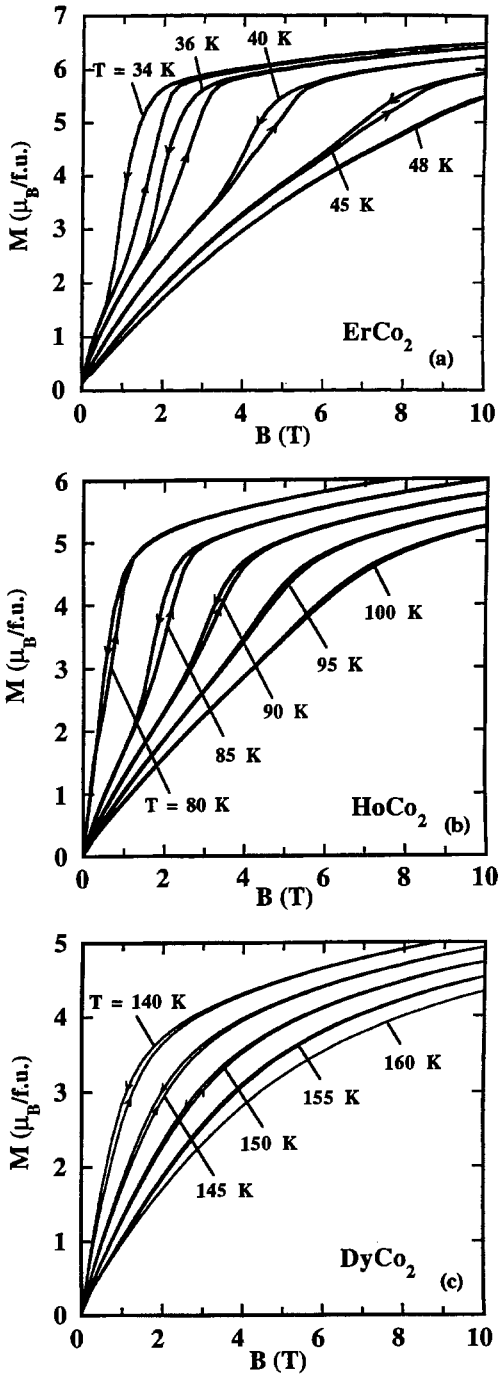


Fig. 71. Magnetization isotherms at $T > T_c$ for RCo_2: R = Er (a), Ho (b), and Dy (c).

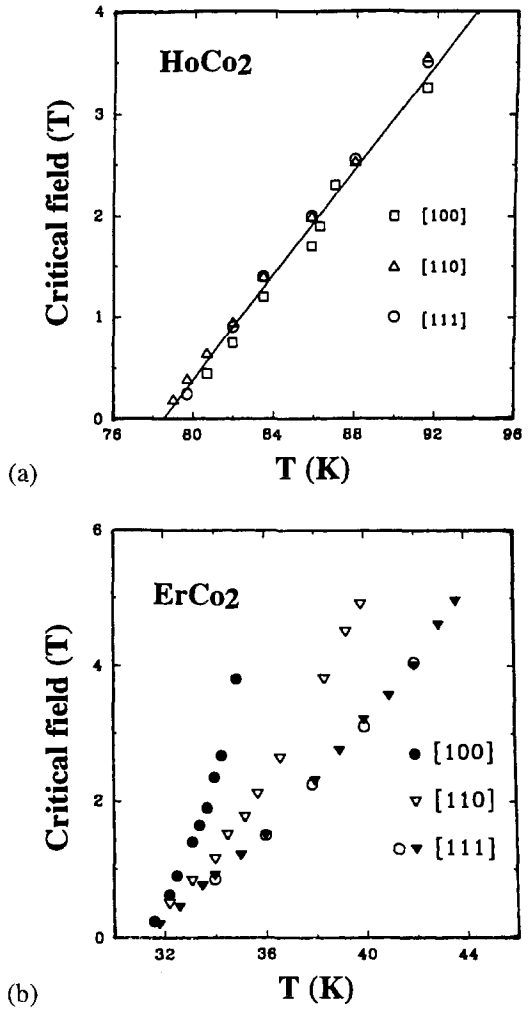


Fig. 72. Temperature dependence of B_c above T_c for $HoCo_2$ (a) and $ErCo_2$ (b); after Baranov and Kozlov (1992) and Aleksandryan et al. (1988), respectively.

(i) the large hysteresis of magnetization and (ii) the increase of the critical field (B_c) and the decrease of the magnetization jump at the MMT with increasing temperature. In addition, the MMT exists only in a small range of temperature, with $\Delta T \approx 20$ K above the FOT. In this temperature range an almost linear relationship between B_c and T was found. This behavior of B_c was also derived from the magnetoresistance, see below. No anisotropy of B_c has been found for $HoCo_2$ (Baranov and Kozlov 1992), in contrast to $ErCo_2$ (see fig. 72(a), (b)). The disappearance of the MMT is characterized by the disappearance of not only the magnetization jump but also of the hysteresis. For $DyCo_2$ the MMT is only weakly evident in the hysteresis of the magnetization curves above T_c. The Arrott plots

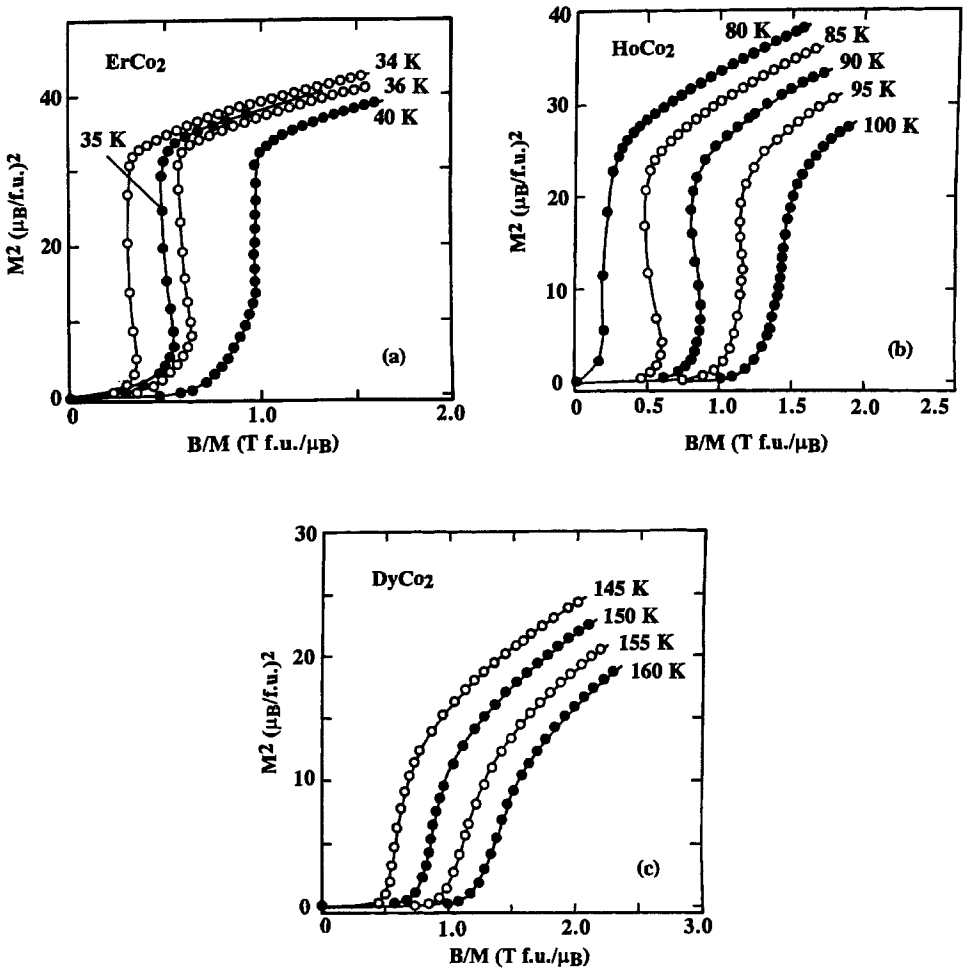


Fig. 73. Arrott plots at $T > T_c$ for RCo_2: R = Er (a), Ho (b) and Dy (c).

of the investigated compounds are presented in figs 73(a), (b), (c). They show an S-shape with two linear parts characteristic of the paramagnetic and ferromagnetic states in low and high magnetic fields, respectively.

The MMT above T_c has also been studied by means of magnetostriction measurements (Del Moral and Melville 1975; Duc et al. 1988a). As an illustration, magnetostriction isotherms are given for $DyCo_2$ and $HoCo_2$ in figs 74 and 75. As can be seen from these figures, $\lambda_{\parallel}$ is negative and $\lambda_{\perp}$ is positive at $T < T_c$, leading, correspondingly, to a very small volume magnetostriction ($\lambda = \lambda_{\parallel} + 2\lambda_{\perp} \approx 0$). Approaching T_c, the $\lambda_{\parallel}$ curves change their slope and become positive at $T > T_c$, whereas, in contrast, $\lambda_{\perp}$ still remains positive. As a result, it leads to a great change in volume. These features indicate that cobalt moments are induced by the applied magnetic field above T_c. The maximum value of this

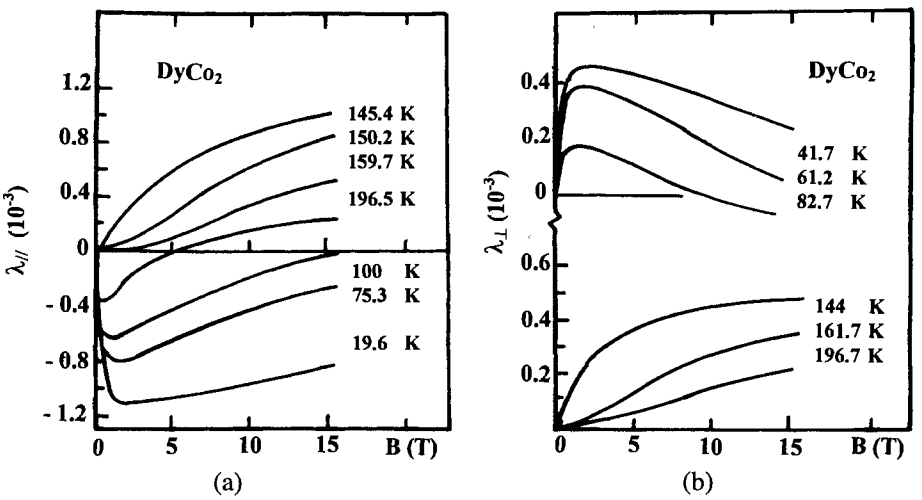


Fig. 74. Magnetostriction isotherms for $DyCo_2$. After Del Moral and Melville (1975).

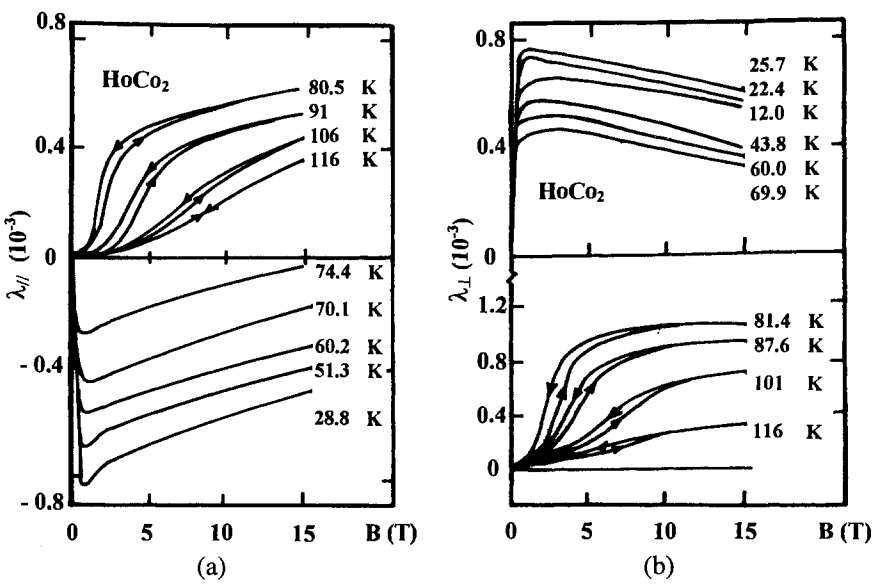


Fig. 75. Magnetostriction isotherms for $HoCo_2$. After Del Moral and Melville (1975).

field-induced volume magnetostriction is about 2×10^{-3}, of the same order as that of the spontaneous magnetostriction of RCo_2 compounds (of about $(4–6) \times 10^{-3}$), and, thus, corresponding to a Co moment of about $0.5\,\mu_B$/at. This is in agreement with the volume jump observed from the thermal expansion measurements and supports the above argument about the contribution of the itinerant electrons to the magnetization change at the MMT.

In this temperature range, for $DyCo_2$ the MMT is less abrupt in the magnetostriction data, in accordance with the observed magnetization data discussed above.

Lattice distortions, in some cases accompanied by spin reorientation, have been observed in RE Co_2 compounds with RE = Ho, Nd (Gratz 1983), RE = Pr, Nd, Sm (Gratz et al. 1994), RE = mixtures of Tb, Dy, Er (Aleksandryan et al. 1984a). From such observations Aleksandryan et al. (1987) conclude that the R–R interaction mostly influences λ_{111}, whereas Co-metamagnetism mostly influences λ_{100}.

A sharp drop in the resistivity at T_c is due to the suppression of spin-disorder scattering of the localized 4f moment (Gratz et al. 1981) and to the quenching of spin fluctuations (Gratz et al. 1987; Duc et al. 1991). The MMT above T_c in RCo_2 is also indicated in the magnetoresistance (see figs 76(a), (b), (c) for R = Er, Ho and Dy). In this case, as well as for the $Y(Co,Al)_2$ system (see fig. 46), the magnetoresistance data can be used to discuss directly the quenching of spin fluctuation scattering (Duc and Oanh 1997; Duc et al. 1997; see also section 4.2.2). The presence of spin fluctuations above T_c was also evidenced by the analysis of the resistivity measurements (Duc et al. 1991; Gratz et al. 1995a, 1995b). In order to discuss the influence of the magnetic lanthanide atoms, interacting with the itinerant Co matrix, the difference between the (total) resistivity of $(R,Y)Co_2$ and that of YCo_2 was considered. A similar analysis was performed by Gratz et al. (1995a, 1995b). As an illustration, the resulting curves $\Delta\rho(T)$ $[= \rho((R,Y)Co_2) - \rho(YCo_2)]$ are shown in figs 77–79 for the RCo_2, $(Dy,Y)Co_2$, and $(Tb,Y)Co_2$ compounds, respectively. We clearly see that for all the $(R,Y)Co_2$ compounds under consideration, these curves are characterized by a sharp drop at T_c. Above T_c the excess resistivity $\Delta\rho$ decreases with increasing temperature up to 250 K. Moreover, in a complete collection of $\Delta\rho(T_c)$ for all RCo_2 (R = Er, Ho, Dy, Tb, Nd and Pr), $\Delta\rho(T_c)$ shows a maximum at $T_c = 46$ K, the Curie temperature of $PrCo_2$ (see fig. 80). This behavior of $\Delta\rho(T)$ is, perhaps, of a more fundamental origin related to the properties of the itinerant electrons. The temperature where $\Delta\rho(T_c)$ reaches a maximum is comparable with the spin fluctuation temperature T_{sf} of the $Y(Lu)Co_2$ compounds (and/or the temperature where $d\rho/dT$ has a maximum, see section 3).

It is interesting to come back to the so-called "double-peak" in the a.c. susceptibility mentioned in section 4.1.3, see fig. 59. This double peak (denoted by χ_k and χ_m) was considered as a characteristic of the FOT (Duc et al. 1988b; Duc 1996; Duc and Oanh 1997), whereas in the samples showing the SOT only the single-peak λ-type anomaly is found (cf. χ_{ac} of $TbCo_2$). χ_k becomes weaker, broader and shifts to low temperatures in the presence of an applied magnetic field and at replacing R by Y (see, e.g., Franse et al. 1983). Thus, it is thought to be related to the magnetic anisotropy and the magnetization process in the ordinary ferromagnetic materials (the Hopkinson effect). The second narrow χ_m peak occurs at a temperature equal to the Curie temperature determined from magnetization, thermal expansion, and resistivity measurements. In an applied d.c. magnetic field, χ_m shifts to a higher temperature (see, e.g., Ho et al. 1981). It is an indication of the critical peak resulting from the para-process in these compounds. According to the Landau theory, the critical peak χ_m can be discussed on the basis of the expression for the differential susceptibility

$$\chi(T, B) = 1/(c_1 + 3c_3M^2). \tag{49}$$

For the SOT, this susceptibility shows a maximum at T_c, where $c_1(T_c) = 0$ (and M also vanishes). In practice, however, this maximum will merge with the (tail of the) Hopkinson

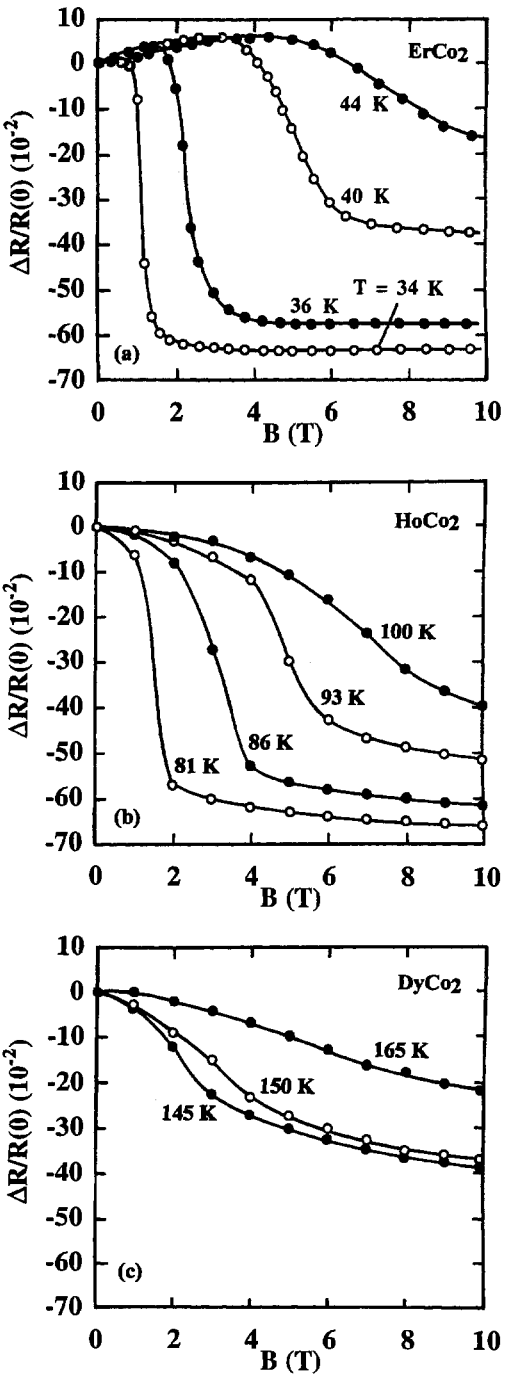


Fig. 76. Magnetoresistance at $T > T_c$ for RCo_2: R = Er (a), Ho (b), and Dy (c).

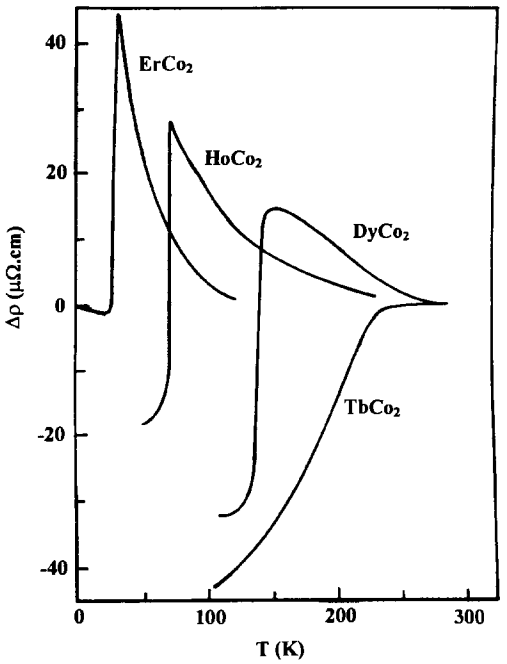


Fig. 77. Excess resistivity $\Delta\rho = \rho(RCo_2) - \rho(YCo_2)$ as a function of temperature (R = Er, Ho, Dy and Tb). After Duc et al. (1991).

effect, so that in low applied magnetic fields only the Hopkinson peak is observed. For the FOT, the contribution of the negative term proportional to c_3 in eq. (49) will enhance the susceptibility maximum of the para-process and then both the Hopkinson and the "critical" peak are observed. Notice, however, that Hauser et al. (1997a) discuss the two separate transitions observed in (Er,Y)Co_2 in terms of a decoupling of the two magnetic subsystems.

4.1.6. Electronic properties of (R,Y)Co_2 at low temperatures

The determination of the electronic specific-heat constant in the RCo_2 compounds is not unambiguous. Berthier et al. (1986) reported a γ-value between 10 and 20 mJ mol^{-1} K^{-2} for $TbCo_2$ and Tb-rich $Tb_xY_{1-x}Co_2$ compounds. In the case of $ErCo_2$, the estimated value of γ depends on the temperature range in which the extrapolation of the C/T vs. T^2 curve has been performed (Duc et al. 1988a). For $Ho_xY_{1-x}Co_2$, the specific heat was analyzed in detail (Hilscher et al. 1988). A variation of γ with changing R-concentration has been reported. A spin-wave contribution of the form $\beta T^{3/2}\exp(-T_0/T)$ was not found. A contribution of the $DT^3 \ln T$ terms was established for the compounds with low x-values. Anyway, rather a high value of γ (in comparison to that of YCo_2) has been deduced for RCo_2. Upon replacing R by Y, γ initially increases, reaches a maximum value and finally decreases drastically (for R = Er, Ho, Dy, see fig. 81(a)). The maximal γ value occurs at the concentration x_c for the onset of magnetism (see also section 4.1.2). This maximal γ value is 69, 90, 160, and 200 mJ mol^{-1} K^{-2} for (Tb,Y)Co_2, (Dy,Y)Co_2, (Ho,Y)Co_2, and

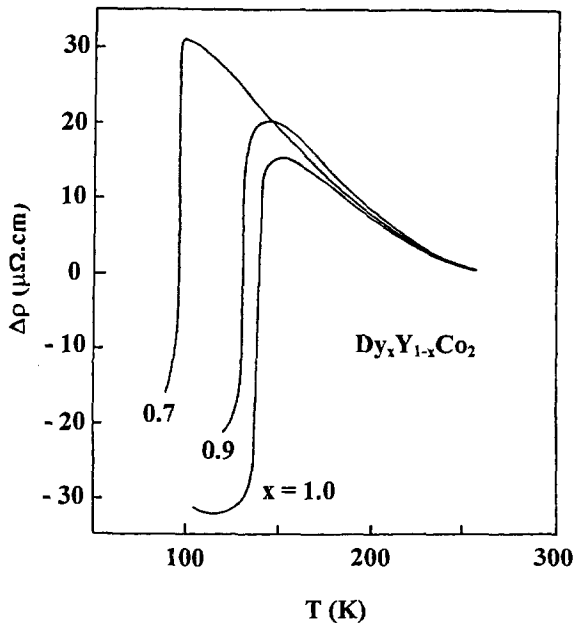


Fig. 78. Excess resistivity $\Delta\rho = \rho((Dy,Y)Co_2) - \rho(YCo_2)$ as a function of temperature. After Duc et al. (1991).

$(Er,Y)Co_2$, respectively (Kuentzler and Tari 1986; Pillmayr et al. 1987, 1988; Hilscher et al. 1988). Additionally, Hilscher et al. (1988) supposed that, similarly to the variation of the Curie temperature, the reciprocal maximal γ-value as well as $1/x_c$ vary linearly with the De Gennes factor (fig. 82). In these compounds, as can be seen from fig. 81(a), (b), the magnetic entropy and the Debye temperature show a similar behavior.

In terms of quenching of spin fluctuations in external fields as observed in the enhanced paramagnetic 3d system, one may expect that on replacing Y by R, the growing molecular field reduces the spin fluctuations, since this molecular field would induce an itinerant Co moment. However, the opposite was observed: the contribution of spin fluctuations increases up to x_c where actually the itinerant Co-magnetism is started to be induced. By analogy with the effects of the magnetic field on the specific heat of YCo_2, these results appear to be a paradox. Considering the random freezing of the 4f moments, however, Hilscher et al. (1988) have suggested that the local R molecular fields cancel each other and, therefore, are of minor importance for quenching of spin fluctuations up to x_c. With regard to the molecular field, the $(R,Y)Co_2$ compounds offer the possibility to vary the internal field as a function of lanthanide type and concentration and/or as a function of temperature (Duc 1994). The residual resistivity (ρ_0) values for $R_xY_{1-x}Co_2$ compounds with R = Er, Ho, and Dy are presented in fig. 83(a). By relating the concentration to the molecular field $B_{mol}^{Co}(\sim x(g_R - 1)J_R)$ arising from the lanthanide moments, the variation of ρ_0 for different cases can be presented in an identical plot, as shown in fig. 83(b). It nicely reproduces the observed picture for $\Delta R(B)/R(0)$ reported for the $Y(Co,Al)_2$ compounds in the external field: the positive magnetoresistance contribution is rather large at a low

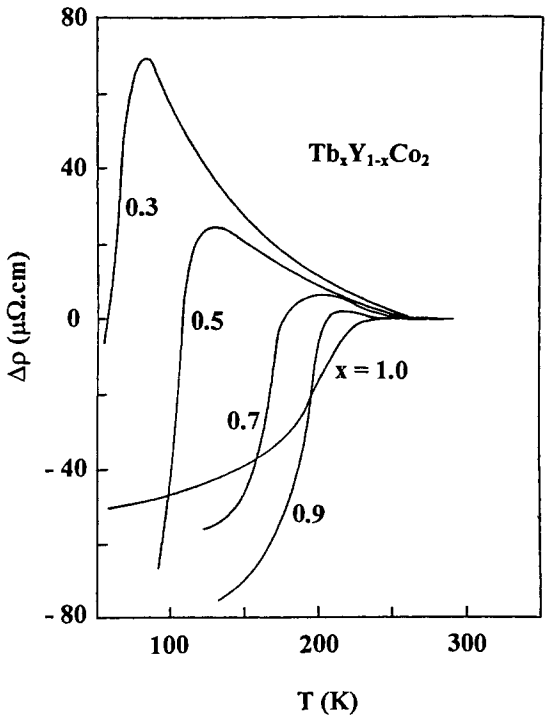


Fig. 79. Excess resistivity $\Delta\rho = \rho((Tb,Y)Co_2) - \rho(YCo_2)$ as a function of temperature. After Duc et al. (1991).

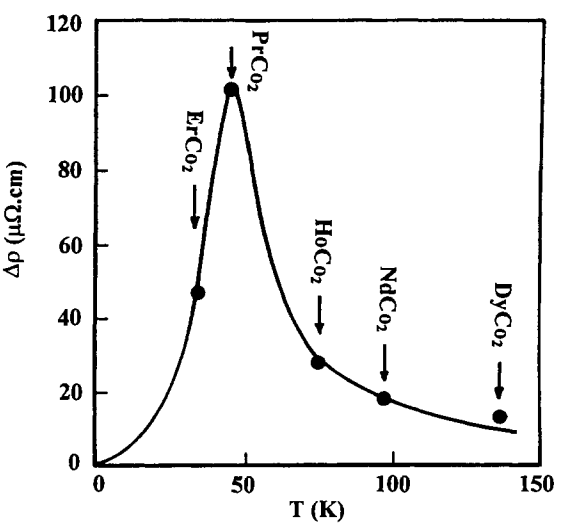


Fig. 80. Excess resistivity $\Delta\rho(T_c)$ as a function of temperature for RCo_2. After Duc and Hien (1994).

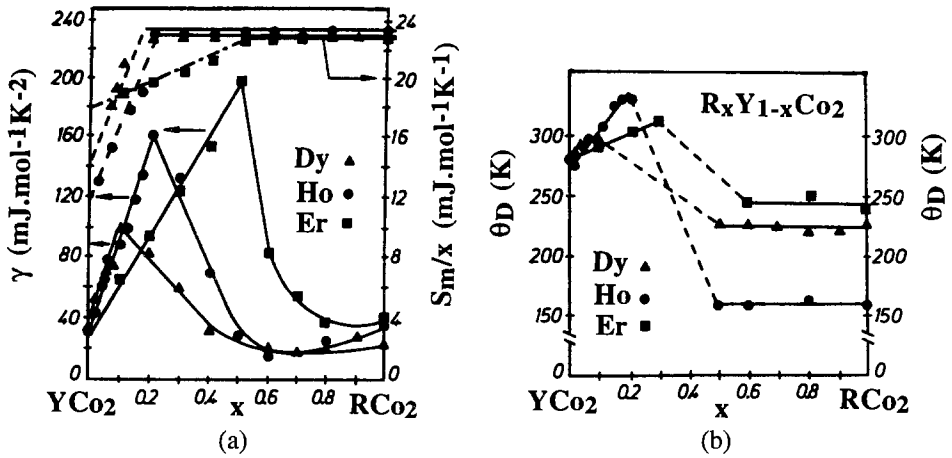


Fig. 81. (a) Electronic specific-heat constant (γ), magnetic entropy and (b) Debye temperature as a function of x in $R_xY_{1-x}Co_2$ for R = Er, Ho, and Dy. After Pillmayr et al. (1988).

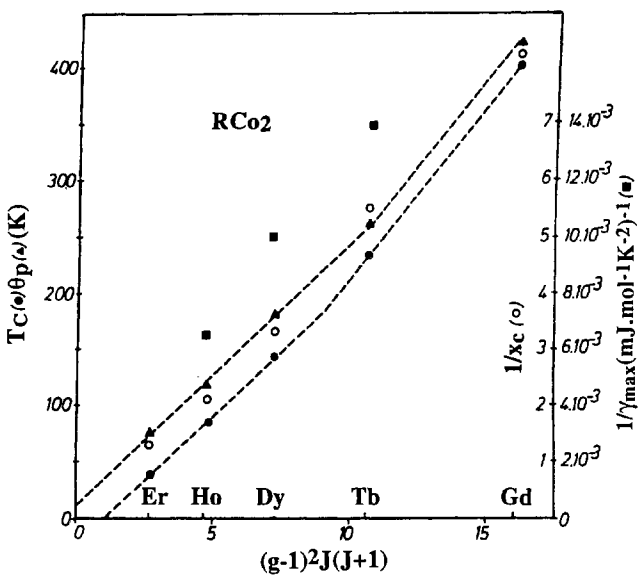


Fig. 82. Ferromagnetic (T_c) and paramagnetic (θ_p) Curie temperatures, reciprocal maximal γ value ($1/\gamma$) and the reciprocal critical concentration ($1/x_c$) as a function of the De Gennes factor for $R_xY_{1-x}Co_2$. After Hilscher et al. (1988).

molecular field, although the complete quenching still occurs at the field (of about 70 T), corresponding to the appearance of a Co magnetic moment in these compounds. This result would suggest that the molecular field at low concentration is still caused by magnetically ordered 4f-moments, thus, in contradiction to the picture presented above, where a random

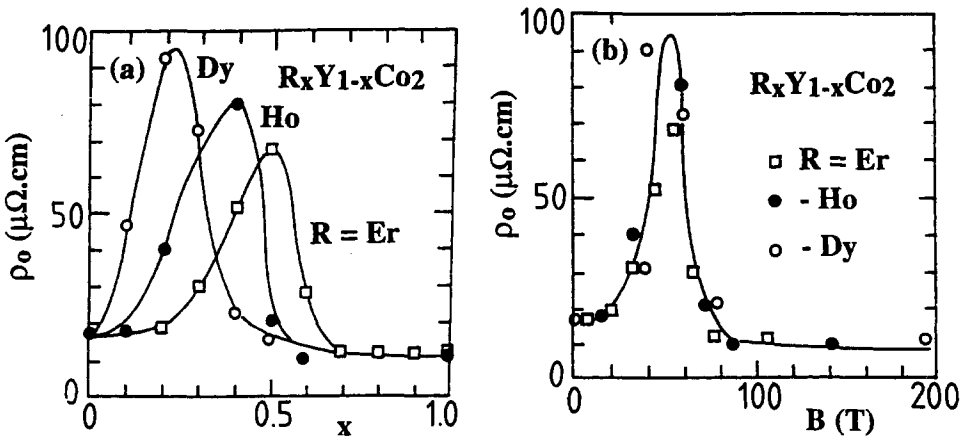


Fig. 83. The residual resistivity ρ_0 as a function of x (a), and as a function of the molecular field (b) in $R_xY_{1-x}Co_2$.

orientation was assumed. Nevertheless, without further detailed calculation the question remains open.

Finally, specific heat and thermal expansion are related by the so-called Grüneisen parameters. The molar specific heat C and the thermal expansion α, respectively, are expressed by the following equations (see, e.g., Duc et al. 1988a).

$$C = C_e + C_{ph} + C_m, \tag{50a}$$

$$C_e = \gamma T, \tag{50b}$$

$$C_{ph} = 27R\left(\frac{\theta_D}{T}\right)^{-3} \int_0^{\theta_D/T} \frac{x^4 e^x}{(e^x - 1)^2}\, dx, \tag{50c}$$

$$\alpha = \alpha_e + \alpha_{ph} + \alpha_m, \tag{51a}$$

$$\alpha_e = a_e T, \tag{51b}$$

$$\alpha_{ph} = b^*\left(\frac{\theta_D}{T}\right)^{-3} \int_0^{\theta_D/T} \frac{x^4 e^x}{(e^x - 1)^2}\, dx. \tag{51c}$$

One can define an electronic (Γ_e), a phonon (Γ_{ph}), and a magnetic (Γ_m) Grüneisen parameter as

$$\Gamma_i = \frac{3V\alpha_i}{\kappa C_i} \tag{52}$$

with i = e (electronic), ph (phonon) and m (magnetic). V is the molar volume and κ is the compressibility.

The electronic Grüneisen parameter can be written as

$$\Gamma_e = \frac{3Va_e}{\kappa\gamma}. \tag{53}$$

Taking for Γ_e the value of 2 and for κ the value of 9.4×10^{-12} m^3 J^{-1} (Voiron 1973), Duc et al. (1988a) have derived the value of 8.3×10^{-9} K^{-2} for a_e in $ErCo_2$. In particular, in this context, an increase of γ caused by the enhancement of spin fluctuations is also accompanied by the enhancement of the electronic thermal expansion coefficient a_e.

For the phonon Grüneisen parameter, we write

$$\Gamma_{ph} = \frac{3Vb^*}{27\kappa R}. \tag{54}$$

The numerical value for Γ_{ph} of $ErCo_2$ turns out to be 1.35. This value is not so sensitive to the R concentration in the (Er,Y)Co_2 system. The values for $\kappa\Gamma_{ph}$ in this series (between 12.6 and 14.5×10^{-12} m^2 N^{-1}) are rather close to the value 11.9×10^{-12} m^2 N^{-1} reported for the (Gd,Y)Cu_2 compounds (Luong et al. 1985).

Γ_m is calculated by eq. (52) from α_m and c_m (Duc et al. 1988a). For $ErCo_2$, Γ_m is equal to -15 for temperatures below 30 K. Note that Γ_m is negative and an order of magnitude larger than Γ_e and Γ_{ph}. Such high negative values are related to the enhancement of the itinerant-electron system. From the expression for T_c given earlier (eq. (20)) one may infer that T_c is (almost) proportional to the susceptibility of the itinerant-electron system. Consequently, Γ_m can be expected to be given roughly by

$$\Gamma_m = \kappa^{-1} \frac{\mathrm{d} \ln T_c}{\mathrm{d}p}. \tag{55}$$

We calculate with the Γ_m value of -15 a value for $\mathrm{d} \ln T_c/\mathrm{d}p$ of -1.4×10^{-2} kbar^{-1} for $ErCo_2$. A direct observation of this pressure dependence in high-pressure magnetization studies resulted in a value of -1.2×10^{-2} kbar^{-1} (Voiron 1973), in close agreement with the calculated result and demonstrating that the magnetic interactions between Er moments proceed via polarization of the itinerant d-electrons.

4.2. Magnetic phase transitions in $R(Co_{1-x}M_x)_2$ compounds

4.2.1. $R(Co_{1-x}Al_x)_2$ compounds

The effect of replacing Co by Al in $R(Co_{1-x}Al_x)_2$ is, first of all, the giant increase of the Curie temperature. This increase is rather strong for R = Tm, Er, Ho, and Dy (with a maximum at $x \sim 0.13$) (Gignoux et al. 1978; Aleksandryan et al. 1984b; Duc et al. 1992a, 1992b), but only slight for Tb and Gd (maxima at $x = 0.09$ and 0.03, respectively) (see fig. 84(a), (b)). Inoue and Shimizu (1988) have calculated T_c for $R(Co,Al)_2$ by using the same value of the R–R and R–Co exchange interactions as those in RCo_2 and the temperature dependence of the susceptibility for the corresponding $Y(Co_{1-x}Al_x)_2$ compound. The calculated results describe well the variation of T_c for the compounds with R = Gd,

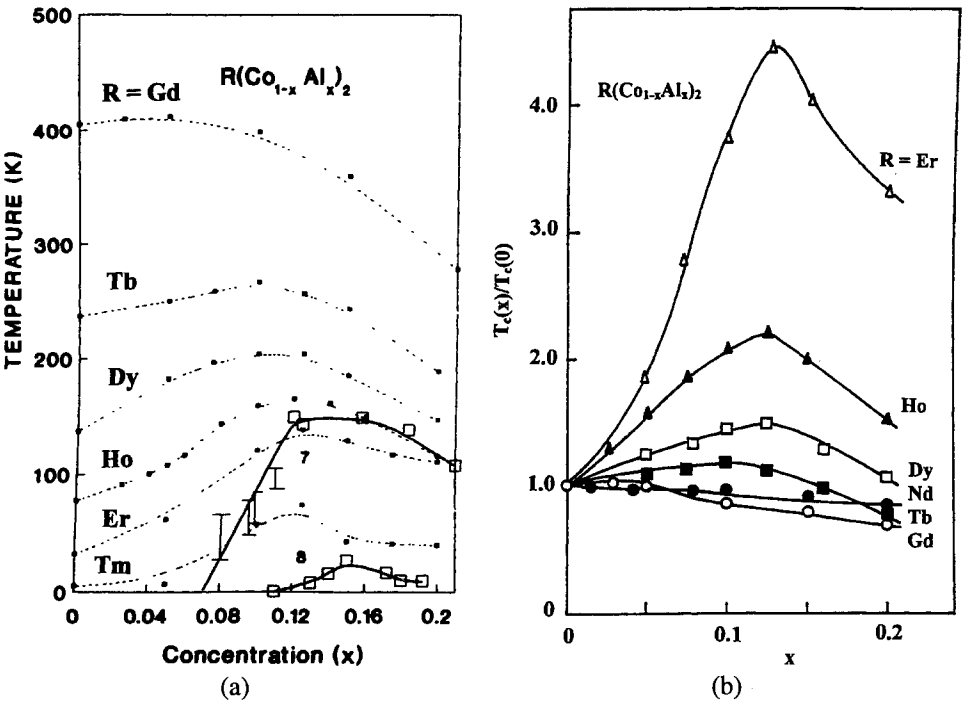


Fig. 84. (a) Curie temperature $T_c(x)$ and (b) the ratio $T_c(x)/T_c(0)$ as a function of x in $R(Co_{1-x}Al_x)_2$.

Tb, and Dy, but show a large scattering for R = Ho, Er, and Tm. Duc et al. (1992a), however, plotted the ratio T_c/T_c^{max} as a function of lattice parameter (see fig. 85). This figure suggests strongly a major influence of the volume and the existence of a "critical" lattice parameter $a_c = 7.27$ Å, above which T_c decreases with the lattice expansion. Notice that at roughly the same lattice parameter, $Y(Co,Al)_2$ becomes ferromagnetic.

Magnetic phase transitions of the $R(Co,Al)_2$ compounds were studied by means of magnetization, thermal expansion and resistivity. The thermal expansion data are illustrated in figs 86 and 87 for $R(Co,Al)_2$ with R = Dy and Ho, respectively. In $Dy(Co_{1-x}Al_x)_2$, $Ho(Co_{1-x}Al_x)_2$, and $Er(Co_{1-x}Al_x)_2$, a change from FOT to SOT occurs at $x = 0.025$, 0.075, and 0.075, respectively. In a first approximation, one expects a FOT in case $T_c < T_3 < T_{max}$ and a SOT, otherwise, see section 3.1. Experimentally, one finds that T_{max} decreases with increasing Al content both in $Lu(Co,Al)_2$ and $Y(Co,Al)_2$. Moreover, the critical field for the MMT decreases at the same time (see section 3.2). Taking this behavior as an indication that the influence of the peculiarities of the band structure is scaled towards lower temperatures, Duc et al. (1992d) expect $T_3(x)$ to decrease with increasing Al content x, too. Moreover, Yamada and Shimizu (1991), and Yamada (1991, 1993) have shown that, in a simple model based on a dominant role of spin fluctuations, the temperatures T_{max} and T_3 are closely related or even equal, see section 2.2.2. Guided by this conclusion, $T_3(x)$ was determined by scaling with $T_{max}(x)$, taking the T_{max} values observed in $Y(Co_{1-x}Al_x)_2$ and $Lu(Co_{1-x}Al_x)_2$, respectively. The c_3 values were calculated

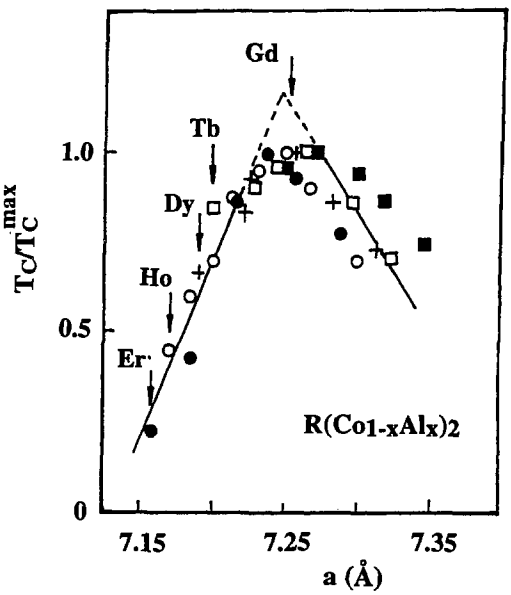


Fig. 85. $T_c(x)/T_c^{max}$ as a function of the lattice parameter in $R(Co_{1-x}Al_x)_2$. After Duc et al. (1992a).

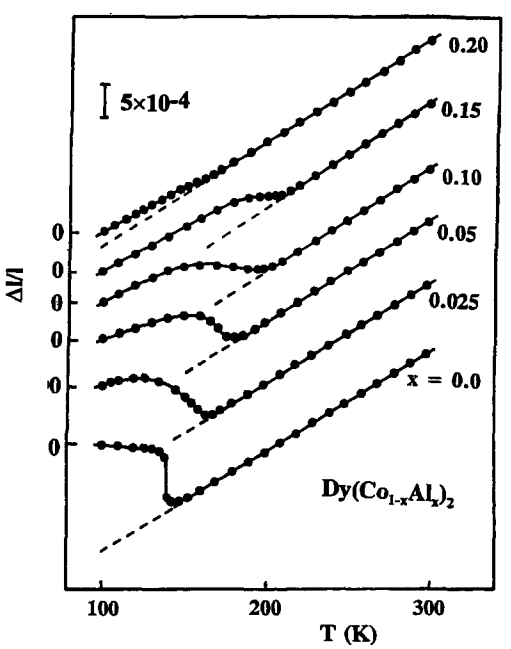


Fig. 86. Temperature dependence of $\Delta l/l$ in $Dy(Co,Al)_2$ compounds. After Duc et al. (1992d).

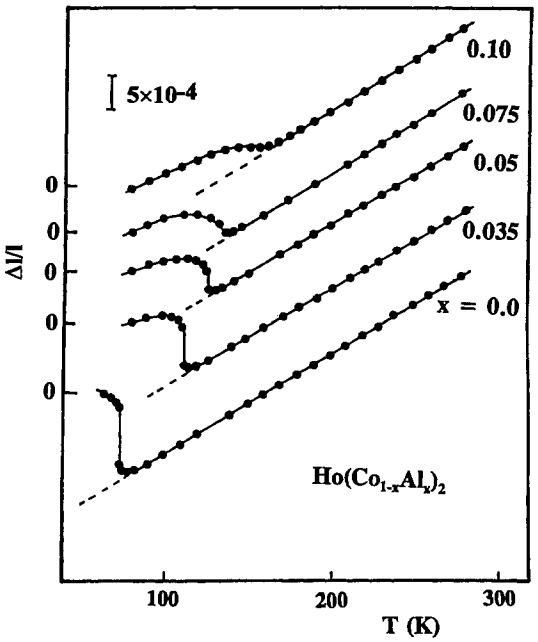


Fig. 87. Temperature dependence of $\Delta l/l$ in $Ho(Co,Al)_2$ compounds. After Duc et al. (1992d).

TABLE 15

T_3 (in K), the temperature at which $a_3(T)$ changes sign for $Lu(Co_{1-x}Al_x)_2$ (Lu) and for $Y(Co_{1-x}Al_x)_2$ (Y), the observed transition temperature T_c and $c_3(T_c)$ (in $T(mol/A\,m^2)^3$), calculated on the basis of the T_3 values for $Y(Co,Al)_2$.

x	T_3 (K)		$Dy(Co_{1-x}Al_x)_2$		$Ho(Co_{1-x}Al_x)_2$		$Er(Co_{1-x}Al_x)_2$	
	Lu	Y	T_c	$c_3(T_c)$	T_c	$c_3(T_c)$	T_c	$c_3(T_c)$
0.0	178	178	140	−12.0	75	−0.36	32.6	−0.018
0.025	160	145	162	45.8	90	−16.6		
0.050	145	125	180	575.3	120	−31.2	60	−56
0.065							70	−886
0.075	125	78	190	4406	140	35600	90	1570
0.1	100	35	200	72450	160	97710	120	532286

adopting the T_3-values taken from the $Y(Co_{1-x}Al_x)_2$ system. The T_3 values and results of calculations are listed in table 15. The transition temperature increases with increasing Al content, whereas T_3 decreases. For both $Dy(Co,Al)_2$ and $Ho(Co,Al)_2$ the sign of $c_3(T_c)$, or the cross-over of $T_3(x)$ and $T_c(x)$ agrees with the observed change of the type of transition, for either set of T_3 values. For the $Er(Co,Al)_2$ compounds, the change in sign of c_3, as calculated, agrees satisfactorily with the experimental observation of the change in type of the transition. If the c_3 parameters are calculated on the basis of the T_3 values

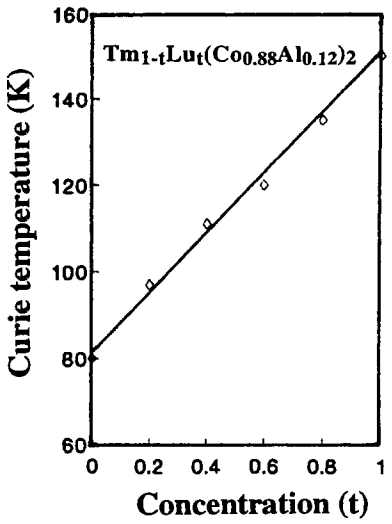


Fig. 88. Lu-concentration dependence of T_c in $Tm_{1-t}Lu_t(Co_{0.88}Al_{0.12})_2$.

for $Lu(Co,Al)_2$, however, no agreement is found. This suggests that the magnetic properties of the 3d subsystem in $Er(Co,Al)_2$ can be approximated better by those of $Y(Co,Al)_2$ than by those of $Lu(Co,Al)_2$. This may also be related to the so-called "lutetium paradox" (Dubenko et al. 1992a, 1992b). The Curie temperature of $R(Co,Al)_2$, where R is a magnetic lanthanide, is expected to be higher than that of the ferromagnetic $Y(Co,Al)_2$ and $Lu(Co,Al)_2$ compounds. For $Lu(Co_{1-x}Al_x)_2$ with $x \geqslant 0.12$, however, T_c was found to be almost the same as that of $Ho(Co,Al)_2$ and to be higher than that of $Er(Co,Al)_2$ and that of $Tm(Co,Al)_2$ and $Y(Co,Al)_2$ (fig. 84(a)). In addition, the Curie temperature *increases* linearly with the Lu concentration (t) in the $Tm_{1-t}Lu_t(Co_{0.88}Al_{0.12})_2$ system, fig. 88. The difference between energies of the 3d subsystem in $Y(Co_{0.88}Al_{0.12})_2$ and $Lu(Co_{0.88}Al_{0.12})_2$ has been discussed by Dubenko et al. (1994a) (see also section 3.2). These authors also calculate the total energy of the 3d subsystem for different $R(Co_{0.88}Al_{0.12})_2$ compounds. The results are presented in fig. 89. It is important to note here that the minimum energy calculated for $Tm(Co_{0.88}Al_{0.12})_2$ is higher than that for $Lu(Co_{0.88}Al_{0.12})_2$. The result, thus, is qualitatively consistent with experiments. In this way, not only the anomalous behavior of T_c observed for $R(Co,Al)_2$ can be understood but one can also infer that the electronic structure of d-electrons in $R(Co_{0.88}Al_{0.12})_2$ is almost the same as that in $Y(Co_{0.88}Al_{0.12})_2$ and is different from that in $Lu(Co_{0.88}Al_{0.12})_2$.

The influence of Al-atoms on the spin fluctuation scattering in $R(Co,Al)_2$ compounds was investigated by Duc et al. (1992e). The typical temperature dependence of resistivity is presented in figs 90 and 91 for $Ho(Co,Al)_2$ and $Nd(Co,Al)_2$ compounds, respectively. In accordance with the thermal expansion data (fig. 87), in $Ho(Co_{1-x}Al_x)_2$ with $x < 0.075$, the FOT at T_c shows up in a discontinuous change in the resistivity. The size of the step at T_c, however, is rapidly diminished with increasing Al content and vanishes for the compounds with $x = 0.1$. For $x = 0.2$ the resistivity below T_c increases with decreasing temperature

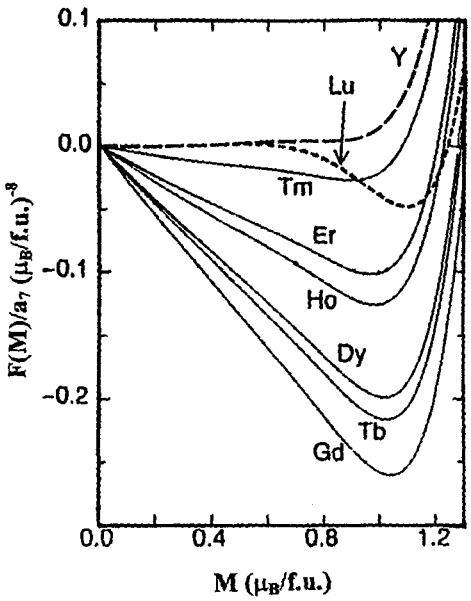


Fig. 89. The calculated (total) energy of the 3d sublattice in the different $R(Co_{0.88}Al_{0.12})_2$ compounds. After Dubenko et al. (1994a).

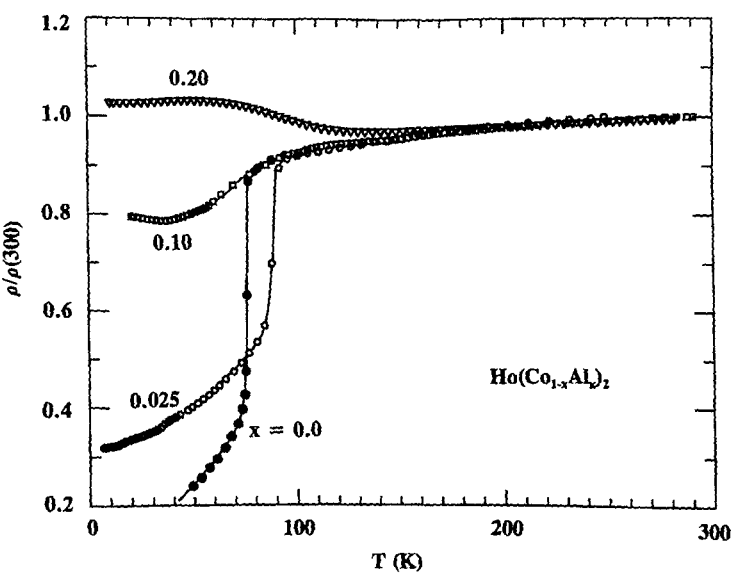


Fig. 90. Temperature dependence of the electrical resistivity of $Ho(Co,Al)_2$.

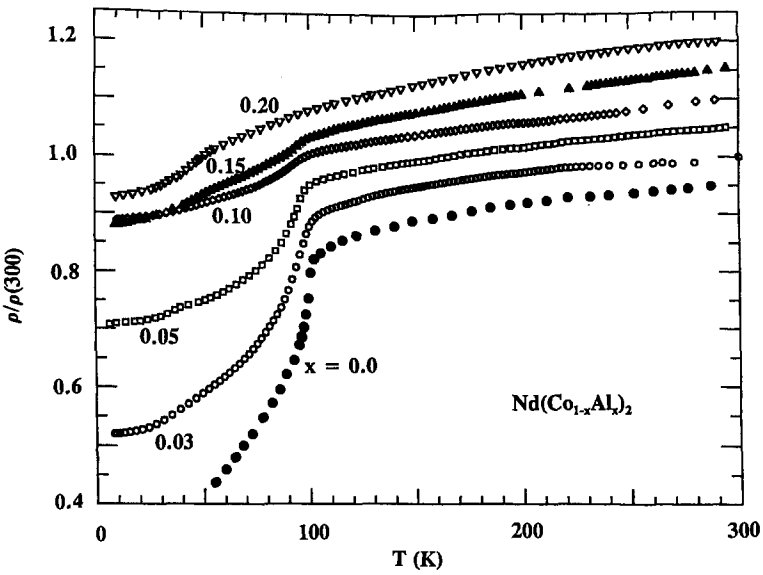


Fig. 91. Temperature dependence of the electrical resistivity of $Nd(Co,Al)_2$.

in the magnetic ordering phase. Analogous behavior was observed in the $Dy(Co,Al)_2$ compounds. For the $Nd(Co_{1-x}Al_x)_2$ compounds, the resistivity behavior connected with the magnetic ordering displays distinct differences with respect to the previous two systems: with increasing Al content the resistivity anomaly around T_c becomes less pronounced and for the compounds with $x = 0.2$ the resistivity continuously passes through the transition and no upturn is observed below T_c.

In search for some systematization, the resistivity was measured for a number of different $R(Co_{0.8}Al_{0.2})_2$ compounds, with R = Nd, Gd, Tb, Dy, Ho, Er, and Lu. The results are presented in fig. 92 in the normalized form of a $\rho/\rho(T_c)$ versus T/T_c plot. All the compounds are ferro- (or ferri-) magnetic materials with T_c ranging from 100 K to 310 K. The behavior of $\rho(T)$ strongly depends on the kind of lanthanide. For the compounds with R = Lu, Er, Ho, and Dy, an almost monotonic increase of resistivity is observed below T_c, whereas the resistivity in $Gd(Co_{0.8}Al_{0.2})_2$ and $Nd(Co_{0.8}Al_{0.2})_2$ decreases with decreasing temperature. In the ordered magnetic state a relative comparison for the resistivity of the $R(Co_{0.8}Al_{0.2})_2$ compounds was made by comparing $\rho(0)$ with $\rho(T_c)$, or by looking at $[\rho(0) - \rho(T_c)]/\rho(T_c)$, as illustrated by the inset of fig. 92. Note that, starting from Lu, the resistivity enhancement increases and reaches a maximum in the $Dy(Co_{0.8}Al_{0.2})_2$ compound, then starts to decrease in the $Tb(Co_{0.8}Al_{0.2})_2$ compound. Finally, the resistivity is totally suppressed in $Gd(Co_{0.8}Al_{0.2})_2$ and $Nd(Co_{0.8}Al_{0.2})_2$. A similar variation was observed for the d-magnetic moment in these compounds (see fig. 110 below). M_d is equal to 0.37 μ_B/at. in $Lu(Co_{0.8}Al_{0.2})_2$. For the compounds with the heavy lanthanides R = Er, Ho, Dy, and Tb, M_d is almost constant (about 0.8 μ_B/at.),whereas M_d starts decreasing at R = Gd and the light lanthanides. This may present a clue for the origin of the resistivity enhancement in the $R(Co,Al)_2$ compounds (see also Duc et al. 1995a). In the explanation of

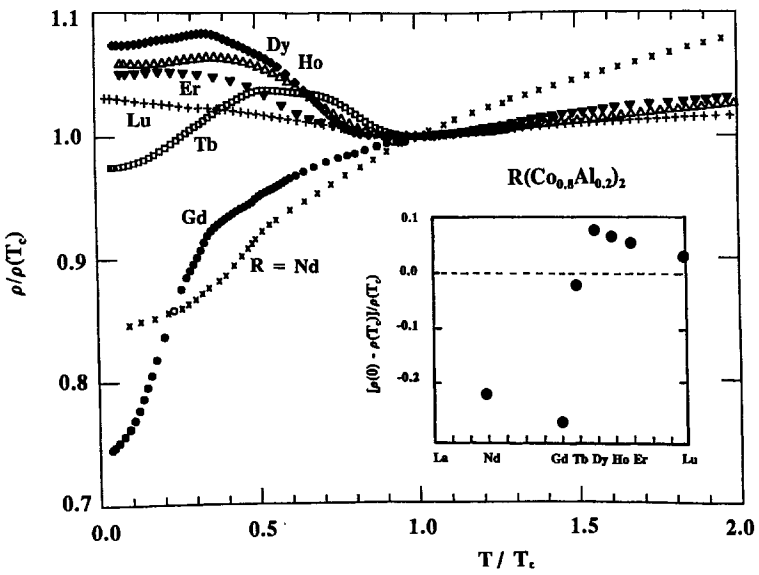


Fig. 92. Plot of $\rho/\rho(T_c)$ vs. T/T_c for $R(Co_{0.8}Al_{0.2})_2$. The inset shows the plot of $[\rho(0) - \rho(T_c)]/\rho(T_c)$ as a function of lanthanide element in $R(Co_{0.8}Al_{0.2})_2$. After Duc et al. (1992d).

Dubenko et al. (1994a, 1994b) for the "Lu paradox", only the difference of the d magnetism between (R,Y)Co_2 and Lu(Co,Al)$_2$ was shown. The present result reflects even a gradual distinction of the d-band magnetism in RCo_2 when going from heavy to light lanthanides.

4.2.2. $R(Co_{1-x}Si_x)_2$ compounds

The magnetic behavior of the (Y,Lu)(Co,Si)$_2$ compounds has been discussed in section 3.3. The present section deals with R(Co,Si)$_2$ compounds in which R is a magnetic rare earth. The magnetic and electrical properties of the R(Co,Si)$_2$ compounds (R = Gd, Tb, Dy, Ho, Er) with invariable lattice parameters have been investigated by Duc (1996) and Cuong et al. (1997, 1998a, 1998b). Under the condition of a fixed volume, somewhat similar effects as those in R(Co,Al)$_2$ on the enhancement of the ordering temperature, the variation of the d-magnetic moment and enhancement of resistivity below T_c (see figs 93–96) are still observed in the R(Co,Si)$_2$ compounds (with R = Er, Ho). As an illustration, we remark that the change from FOT to SOT was also observed in the compounds $R(Co_{1-x}Si_x)_2$ with R = Dy, Ho, and Er at x = 0.05, 0.075, and 0.1, respectively, see, for example, figs 95 and 96. In terms of the Inoue–Shimizu model, the character of these phase transitions can be explained in the same way as discussed for R(Co,Al)$_2$, in the consideration of the fact that the temperatures T_{max} and T_3 decrease as the Si-content increases in the Y(Lu)(Co,Si)$_2$ compounds (Duc 1996). For these R(Co,Si)$_2$ compounds, again, the decrease of $T_{max}(x)$ and the increase of $T_c(x)$ may be the reason for the change from FOT to SOT. The calculated results of $c_3(T_c)$ are listed in table 16 for the compounds with R = Er, Ho, and Dy (Duc and Oanh 1997).

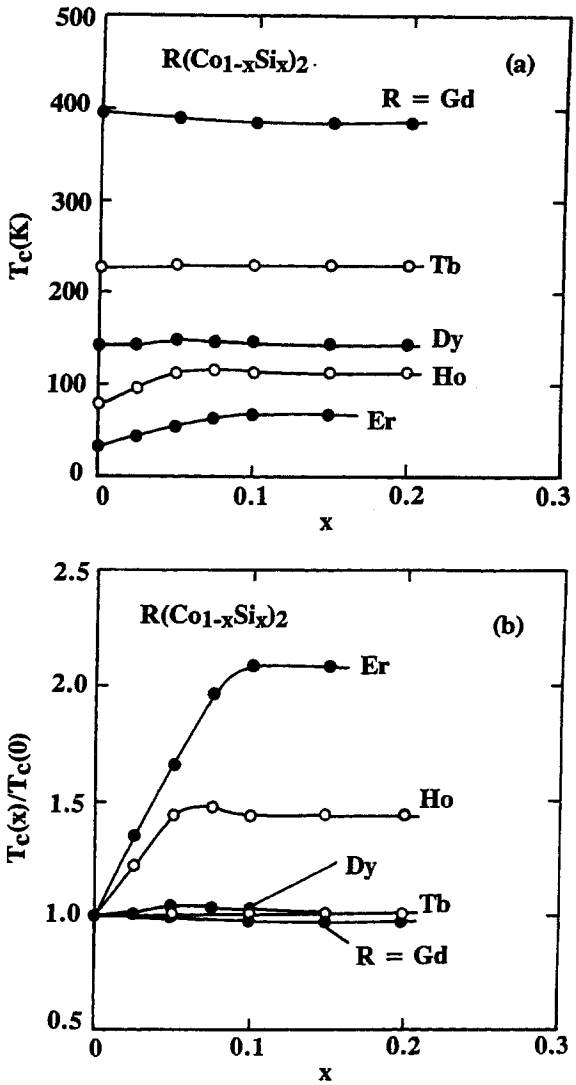


Fig. 93. T_c (a) and $T_c(x)/T_c(0)$ (b) as a function of x in $R(Co_{1-x}Si_x)_2$. After Duc and Oanh (1997).

The MMT above T_c was studied by means of magnetization and magnetoresistance measurements for $Er(Co,Si)_2$ and $Ho(Co,Si)_2$ (Duc et al. 1996). The magnetoresistance isotherms are illustrated in figs 97(a)–(c) for $Er(Co_{1-x}Si_x)_2$ (Cuong et al. 1998b). It is interesting to note that above the FOT, the magnetoresistance slightly increases with an increasing magnetic field below B_c, and then sharply drops at the MMT, whereas for the compounds with the SOT, the magnetoresistance is positive everywhere. Around T_c, in the RCo_2 compounds, the resistivity is governed by spin-disorder scattering on the (fluc-

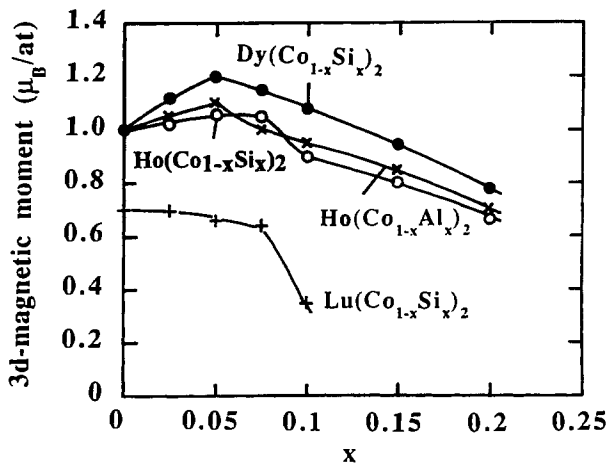


Fig. 94. Variation of the 3d-magnetic moment in $R(Co_{1-x}Si_x)_2$. After Duc and Oanh (1997).

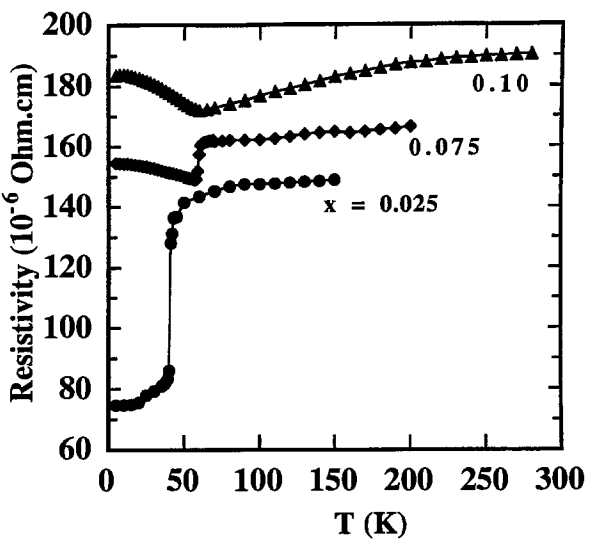


Fig. 95. Temperature dependence of the electrical resistivity in $Er(Co_{1-x}Si_x)_2$. After Cuong et al. (1998b).

tuating) lanthanide and cobalt magnetic moments (Duc et al. 1991). The suppression of resistivity is thought to be due to the ordering process of the 4f-moments and quenching of spin fluctuations at the Co-sites, see section 4.1.5. In these measurements, a positive contribution is clearly observed at low magnetic fields. This positive contribution might be connected to another mechanism, which becomes increasingly important with increasing Si content. A positive contribution to the magnetoresistance is ascribed to the cyclotron motion of the conduction electrons. We note that, for the $Y(Co,Al)_2$ system, where only

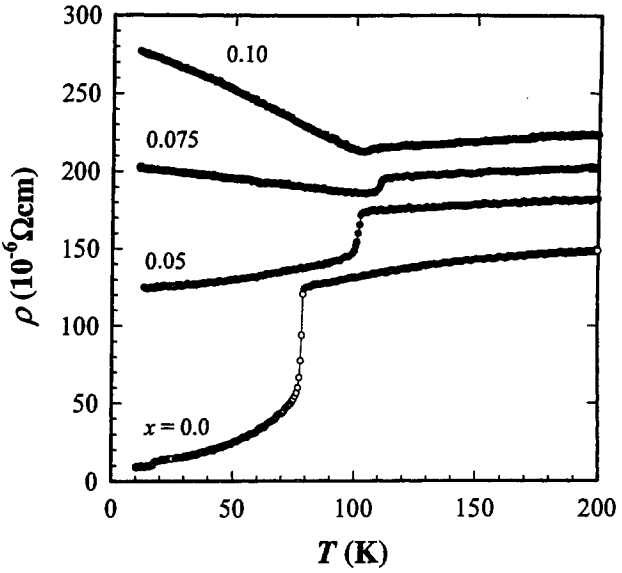


Fig. 96. Temperature dependence of the electrical resistivity in $Ho(Co_{1-x}Si_x)_2$. After Cuong et al. (1998a, 1998b).

TABLE 16

T_3, the temperature at which $a_3(T)$ changes sign for $Y(Co_{1-x}Si_x)_2$ (Y). T_c, the observed transition temperature, and $c_3(T_c)$ (in 10^{-2} T(mol/A m^2)^3), calculated on the basis of the T_3 values for $Y(Co,Si)_2$. After Duc and Oanh (1997).

x	T_3 (K)	$Dy(Co_{1-x}Si_x)_2$		$Ho(Co_{1-x}Si_x)_2$		$Er(Co_{1-x}Si_x)_2$	
	Y	T_c (K)	$c_3(T_c)$	T_c (K)	$c_3(T_c)$	T_c (K)	$c_3(T_c)$
0.0	178	142	−0.850	78	−0.089	32.6	−0.039
0.025	145	142	−0.086	95	−0.41	44	−0.085
0.050	100	148	6.8	112	−0.64	54	−0.41
0.075	80	146	25.2	115	13.9	64	−0.57
0.100	80	146	46.5	112	15.6	68	−1.48

the 3d magnetism is present, the positive contribution in eq. (43) was found to be consistent with a quadratic dependence on the magnetization as expected for a pure volume effect on the band magnetism (Duc et al. 1995a). Denoting this relationship as $\Delta R/R(0) = \alpha M^2$, it comes out that $\alpha = 0.2\ (\mu_B/Co)^{-2}$. For the $Er(Co_{0.9}Si_{0.1})_2$ compounds the magnetoresistance simply increases with increasing fields (see fig. 97(c)). In addition, the relationship between $\Delta R/R(0)$ and M^2 mentioned above is also valid, however, with a α-value of $2 \times 10^{-3}\ (\mu_B/Co)^{-2}$, i.e., two orders of magnitude smaller than that found for the $Y(Co,Al)_2$ compounds. This weak magnetoresistance effect in $Er(Co_{0.9}Si_{0.1})_2$ might be

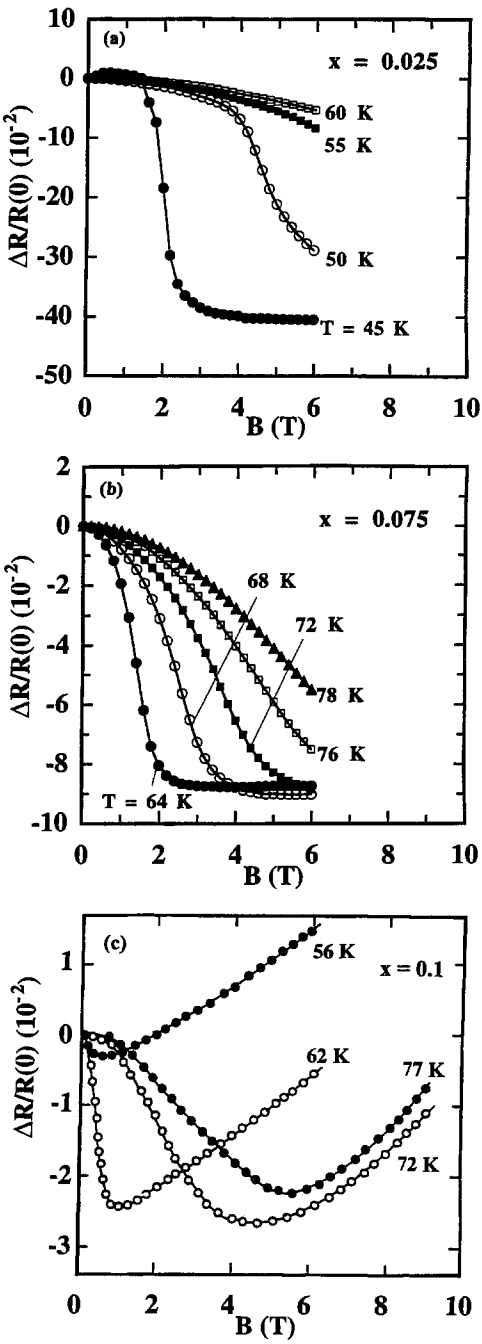


Fig. 97. Magnetoresistance isotherms at $T > T_c$ for $Er(Co_{1-x}Si_x)_2$: (a) $x = 0.025$, (b) $x = 0.075$, and (c) $x = 0.1$. After Duc (1996, 1997).

due to the compensation between the positive contribution, due to the mentioned volume effects and the negative one resulting from the 4f spin-disorder resistivity. In this way, instead of eq. (43), we can express the magnetoresistance as

$$\Delta R(B, T) = \Delta R_{\mathrm{v}}(B, T) + \Delta R_{\mathrm{spd}}(B, T) + \Delta R_{\mathrm{sf}}(B, T), \tag{56}$$

where the first term is a positive contribution caused by the formation of 3d magnetic moments. The second and third terms are the negative contributions from 4f spins and spin fluctuations.

For the compounds under consideration, the 4f and 3d magnetic moments are almost independent of the Si substitution. Thus, their contributions to the magnetoresistance may be assumed to be of the same order of magnitude in the whole range of Si concentrations. Furthermore, in connection with the above discussion of the compensation between $\Delta R_{\mathrm{v}}(B, T)$ and $\Delta R_{\mathrm{spd}}(B, T)$, one may conclude that the suppression of magnetoresistance is mainly the result of quenching of spin fluctuation scattering. Then, the suppression of magnetoresistance at the MMT can be considered as being caused by this quenching too. The magnetoresistance at the MMT, thus, can be considered as an useful tool to measure the effects of spin fluctuations in the investigated compounds.

4.2.3. $R(Co_{1-x}Cu_x)_2$ compounds

The average 3d magnetic moment, the susceptibility, and the specific heat of the $R(Co_{1-x}Cu_x)_2$ and $Y(Co_{1-x}Cu_x)_2$ compounds (Duc et al. 1988a, 1988c; Hien et al. 1986) confirm the picture that has been developed for the density of states curve of YT_2 compounds with T = Fe, Co, Ni (Cyrot and Lavagna 1979). The additional d electrons supplied on replacing Co partly by Cu bring the Fermi level to a flat part in the DOS curve. As a consequence, the spin fluctuation type of phenomena in the resistivity curve just above T_c is already lost on substituting 5% Cu for Co, whereas the temperature dependence of resistivity above T_c becomes less pronounced in all compounds in which part of Co has been substituted by Cu. Another consequence of the band filling on substituting Co for Cu is the change of the magnetic phase transition from FOT to SOT in the $R(Co_{1-x}Cu_x)_2$ compounds with R = Dy, Ho, and Er. This change can be understood in the Inoue–Shimizu model by taking into account the decrease of the 3d susceptibility with increasing Cu-content.

The values of the Curie temperature for the $R(Co_{1-x}Cu_x)_2$ compounds (R = Gd, Tb, Dy, Ho) are presented in fig. 98(a) in a plot of $T_c(x)/T_c(0)$ against x. As can be seen, the dependence of T_c on the Cu concentration is quite different in these $R(Co,Cu)_2$ compounds. For the $Gd(Co_{1-x}Cu_x)_2$ compounds, T_c gradually decreases with the increasing x-value, whereas for the $R(Co_{1-x}Cu_x)_2$ compounds with R = Dy, Ho, and Er such a decrease of T_c only occurs for $x < 0.1$. At $x > 0.1$, T_c increases with increasing Cu-concentration. In order to better understand the variation of T_c in these compounds, the plot of T_c as a function of $(g-1)^2 J(J+1)$ is presented in fig. 98(b) for $x = 0$, 0.1, 0.2, and 0.3. The experimental data reveal that the slope of T_c vs. $(g-1)^2 J(J+1)$ decreases with roughly 30% at replacing 30% Co by Cu. In the first approximation, this decrease of the slope is most likely due to a reduction of the 3d susceptibility.

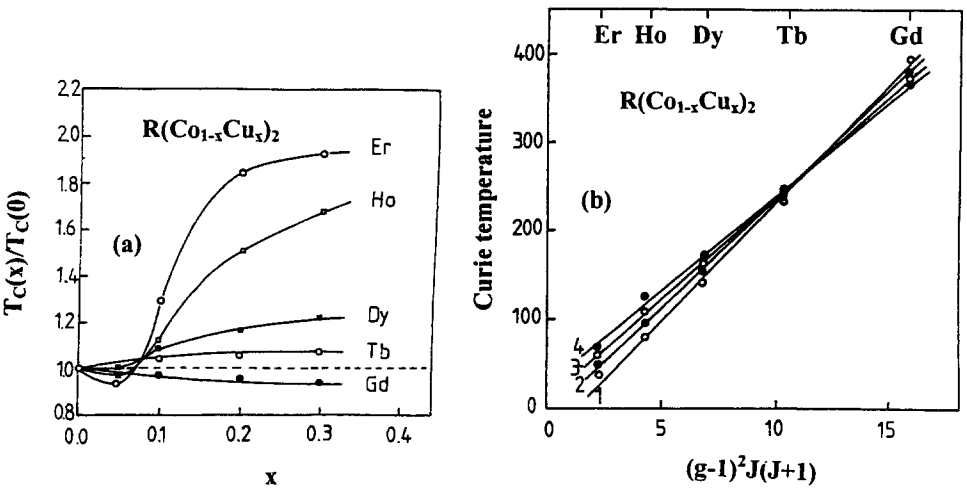


Fig. 98. (a) $T_c(x)/T_c(0)$ against x for $R(Co_{1-x}Cu_x)_2$; (b) T_c as a function of the De Gennes factor for $R(Co_{1-x}Cu_x)_2$. After Duc et al. (1988b).

4.3. Other R(Co,M)$_2$ compounds (M = Mn, Ni, and Rh)

Replacing Co by Mn causes T_c to increase sharply and then to reach a maximum when the Mn concentration exceeds about 25% in $R(Co_{1-x}Mn_x)_2$ (Ballou et al. 1992). For the $Gd(Co_{1-x}Mn_x)_2$ system, T_c increases up to its maximal value $T_c^{max} = 490$ K, i.e., the ratio $T_c^{max}/T_c(0)$ reaches 1.2. Moreover, this ratio essentially increases by going to lanthanides with a larger atomic number: it equals 1.45, 2.0, 2.76, 4.84, and 17.5, for R = Tb, Dy, Ho, Er, and Tm, respectively. This fact leads to the conclusion that the giant increase of T_c in RCo_2 for both Mn and Al substitutions has the same origin in spite of the quite different electronic structures of these dilutants. The lattice expansion, i.e., the "negative chemical pressure" when Mn replaces Co, has some contribution to the initial increase of T_c. However, the effect of the decrease in the number of d-electrons is the main cause of the observed phenomena.

Magnetic phase transitions in $Ho(Co_{1-x}Ni_x)_2$ were studied by Tari (1982). The FOT was indicated for $x \leqslant 0.1$ and the SOT for $x > 0.1$. The magnetic behavior can be simply understood by considering the band filling caused by substitution of Ni for Co. Since rhodium and cobalt are isoelectronic, the substitution of Rh for Co in $HoCo_2$ should provide a simpler system for the study of the magnetic phase transition. Because of the isoelectronic nature of Rh and Co, a large decrease in the paramagnetic susceptibility is not anticipated and, thus, the exchange field should be a more dominant interaction in determining the magnetic properties. Indeed, systematic magnetization and calorimetric studies have been carried out by Tari (1987) and Henry et al. (1991). The FOT was observed in the $Ho(Co_{1-x}Rh_x)_2$ compounds with $x \sim 0.08$. In this system, both the 3d susceptibility and Ho–Co exchange interactions were suggested to be reduced. Within the Inoue–Shimizu model, the change from FOT to SOT can be explained by taking these two factors into account.

5. 4f- and 3d-magnetism instability in $TmCo_2$-based compounds

Within the RCo_2 series, $TmCo_2$ takes an unique position between $ErCo_2$ having a Co moment of about 1 μ_B, and $LuCo_2$, which is an exchange-enhanced Pauli paramagnet. First magnetization and neutron diffraction measurements on $TmCo_2$ single crystals have shown that this compound, as well as other heavy-lanthanide–Co_2 compounds, has a collinear ferrimagnetic structure with Co- and Tm-magnetic moments equal to 0.8 and 5.4 μ_B/at., respectively, and an ordering temperature $T_c = 7$ K (Deportes et al. 1974; Gignoux et al. 1977a, 1977b). Dubenko et al. (1993) have deduced from their low-temperature thermal expansion measurements that the Co-magnetic moment in $TmCo_2$ is about 0.6 μ_B. This value of m_{Co} (lower than in other RCo_2 with magnetic R) was explained by the lower value of the (effective) molecular field exerted by the Tm-sublattice on the Co moment ($B_{mol}^{Co} = 60$ T), compared to the critical value $B_c = 70$ T of the d-electrons. The magnetic properties of $TmCo_2$ are, thus, expected to be similar to those of the isostructural $R_xY_{1-x}Co_2$ compounds in the concentration range with $x < x_c$ (the critical concentration), where they exhibit only a short range magnetic order and have no ordered Co-magnetic moment. The magnetic state of $TmCo_2$ is characterized by the presence of localized spin density fluctuations in the d-subsystem at low temperature. Gratz et al. (1995b) and Dubenko et al. (1995) have even found the absence of the Co moment in $TmCo_2$. Moreover, according to Dubenko et al. (1995), different single-phase $TmCo_2$ samples, prepared by a similar method with compositions close to stoichiometry, can exhibit different alignments of the Tm moments. The magnetic structure was found to vary from a collinear ferromagnetic state through a helical magnetic one to a "not fully ordered" one (Golosovsky et al. 1997). Some basic characteristics are listed in table 17 for the $TmCo_2$ samples numbered as N1–N5. As follows from this table, a clear correlation can be established between the magnetic type and the lattice parameter. The mechanism leading to the 4f-magnetism instability in $TmCo_2$ was assumed to depend on small variations in the stoichiometry within the homogeneous region. The crucial role of the lattice constant was confirmed by experiments under the pressure of 20.5 kbar on sample N2 (with a spiral magnetic structure): when applying pressure, T_c shifts up to 10 K corresponding roughly to $dT_c/dp \approx 0.3$ K/kbar. This enhancement of T_c was attributed to the pressure dependence of the Tm–Tm exchange coupling. Another mechanism providing a collinear magnetic alignment of the Tm moments in $TmCo_2$ is the 4f–3d intersublattice exchange energy. As discussed in section 4.2.1, partial Al substitution leads to a magnetic enhancement of the d-subsystem. The magnetic structure of $Tm(Co_{0.93}Al_{0.07})_2$ was studied. In this compound the Co atoms bear a magnetic moment. In the ordered state this compound is a collinear ferromagnet. With increasing temperature, the Tm moment decreases substantially, whereas the Co moment remains almost constant. In addition, one observes also a long tail in the $M_{Tm}(T)$ curve. This was attributed to a magnetic heterogeneity existing in the vicinity of T_c. A similar behavior was observed by X-ray diffraction measurement (Dubenko et al. 1993).

The magnetic state of Co in $TmCo_2$ manifests itself in the change of the resistivity behavior. The temperature dependencies of the electrical resistivity for $TmCo_2$ and $Tm(Co_{0.95}Al_{0.05})_2$ reported by Baranov et al. (1997) are shown in fig. 99. The $\rho(T)$ curve

TABLE 17

Characteristic parameters of different $TmCo_2$ and $Tm(Co_{0.93}Al_{0.07})_2$ cubic Laves phase samples: cell parameter at room temperature (a), occupation factor for the Co sites (δ), Tm-magnetic moment at 1.4 K (m_{Tm}) and magnetic structure. After Golosovsky et al. (1997).

Sample	a (Å)	δ	m_{Tm} (μ_B)	Magnetic structure
$TmCo_2$ (N3)	7.1334(3)	1.03(1)	6.4(1)	Collinear
$TmCo_2$ (N1)	7.1342(2)	1.04(1)	6.1(1)	Collinear
$TmCo_2$ (N4)	7.1355(3)	1.00(1)	6.8(1)	Helix + collinear
$TmCo_2$ (N2)	7.1360(3)	1.07(2)	4.9(1)	Helix
$TmCo_2$ (N5)	7.1366(3)	1.06(1)	1.5(2)	"Not fully ordered"
$Tm(Co_{0.93}Al_{0.07})_2$	7.1602(2)	—	5.6(4)	Ferrimagnetic

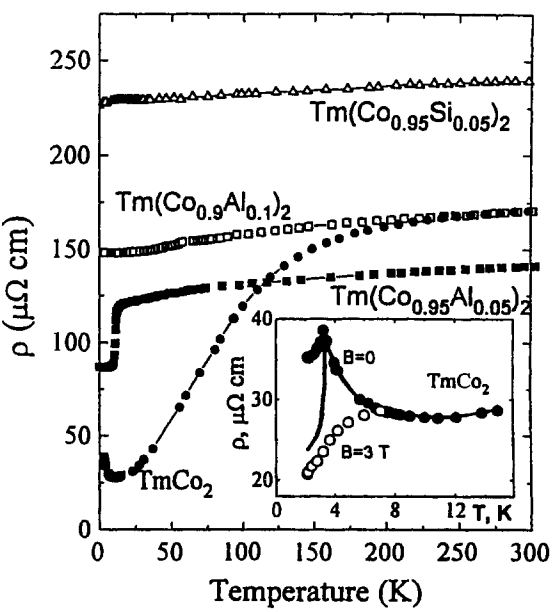


Fig. 99. Temperature dependence of the electrical resistivity for $TmCo_2$, $Tm(Co_{0.95}Si_{0.05})_2$, $Tm(Co_{0.9}Al_{0.1})_2$, and $Tm(Co_{0.95}Al_{0.05})_2$. The inset shows $\rho(T, B)$ for $TmCo_2$ in the vicinity of T_c. After Baranov et al. (1997).

for $TmCo_2$ at low temperature is characterized by the presence of the pronounced minimum at about 11 K (see inset of fig. 99). With decreasing temperature, $\rho(B = 0)$ increases and then decreases slowly below 3 K. Magnetoresistance data measured at 4.2 K are presented in fig. 100(a) for $TmCo_2$: $\rho(B)$ decreases by 35% in a magnetic field of 5 T. As a measurement of the contribution of the spin fluctuation scattering (see section 4.2), this magnetoresistivity result reflects rather a great effect of localized spin density fluctuations in the d-sublattice of $TmCo_2$. The substitution of 5 at.% Al for Co in $Tm(Co_{0.95}Al_{0.05})_2$ significantly changes the resistivity behavior: an abrupt decrease of ρ

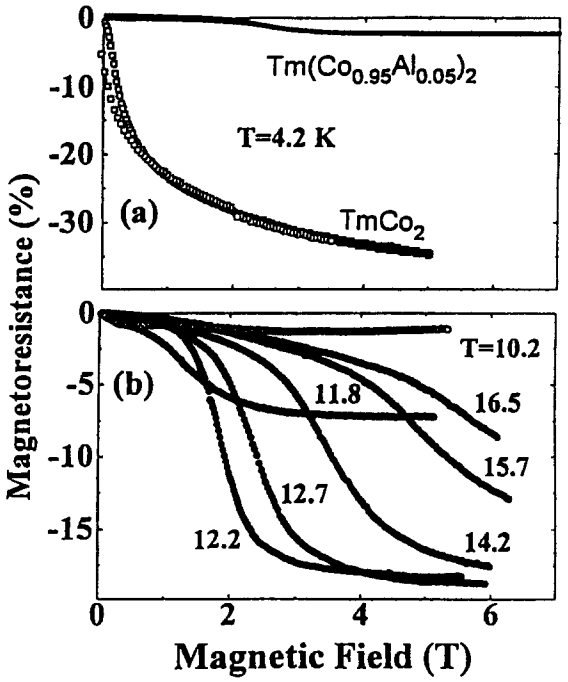


Fig. 100. (a) Magnetoresistance for $TmCo_2$ and $Tm(Co_{0.95}Al_{0.05})_2$ at 4.2 K; (b) Magnetoresistance for $Tm(Co_{0.95}Al_{0.05})_2$ at $T > T_c$.

with decreasing temperature below the FOT at 11.8 K was observed (see also fig. 99). As in other RCo_2 compounds this decrease of ρ in $Tm(Co_{0.95}Al_{0.05})_2$ can be connected with a quenching of spin fluctuations below T_c. Indeed, as can be seen in fig. 100(a), the magnetoresistance of $Tm(Co_{0.95}Al_{0.05})_2$ is rather weak at low temperature. However, at $T \geqslant T_c$, this compound shows a MMT which is accompanied by a sharp decrease in resistivity at the field-induced splitting of the d-band (fig. 100(b)). A similar electrical (and magnetic) behavior of $TmCo_2$-based compounds was observed for the isostructural $Ho_xY_{1-x}Co_2$ and $Er_xY_{1-x}Co_2$ compounds with lanthanide content near the critical value x_c (see fig. 101(a), (b)). For example, for $Er_{0.4}Y_{0.6}Co_2$ the substitution of 5 at.% Al for Co maintains the FOT in the $Er_{0.4}Y_{0.6}(Co_{0.95}Al_{0.05})_2$ compound (fig. 101(a)), and the MMT can also be observed at $T > T_c$ (fig. 101(b)).

For $TmCo_2$, a volume contraction with decreasing temperature was observed (Gratz et al. 1995b). The total volume change ω_s ($= 3\Delta l/l$) is about -6.5×10^{-4}. This result is completely different from that observed on the other magnetic RCo_2 compounds, in which a large positive volume expansion exceeding 1×10^{-3} arises due to a long-range magnetic order of the itinerant d-electrons. The absence of a positive magnetovolume effect in $TmCo_2$ has to be considered as convincing proof that at least down to 2.5 K there is no long-range magnetic order in the Co-sublattice. The substitution of Gd for Tm in the pseudobinary $Tm_{1-x}Gd_xCo_2$ system gives rise to a large positive volume anomaly at $x \geqslant 0.1$.

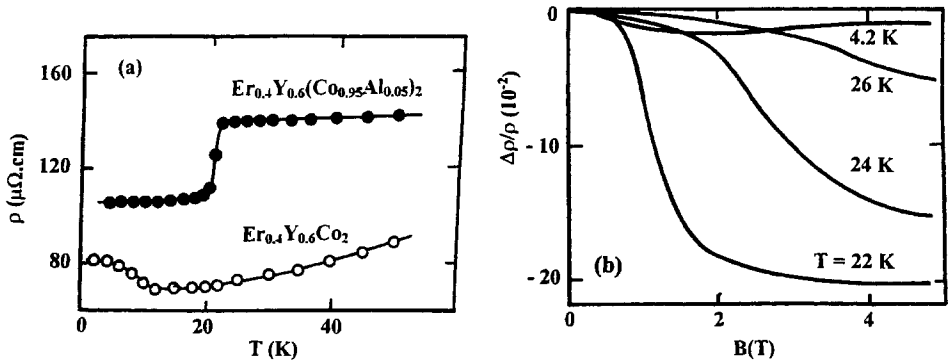


Fig. 101. (a) Temperature dependence of the electrical resistivity for $Er_{0.4}Y_{0.6}Co_2$ and $Er_{0.4}Y_{0.6}(Co_{0.95}Al_{0.05})_2$. (b) Magnetoresistance for $Er_{0.4}Y_{0.6}(Co_{0.95}Al_{0.05})_2$ at $T > T_c$. After Baranov et al. (1997).

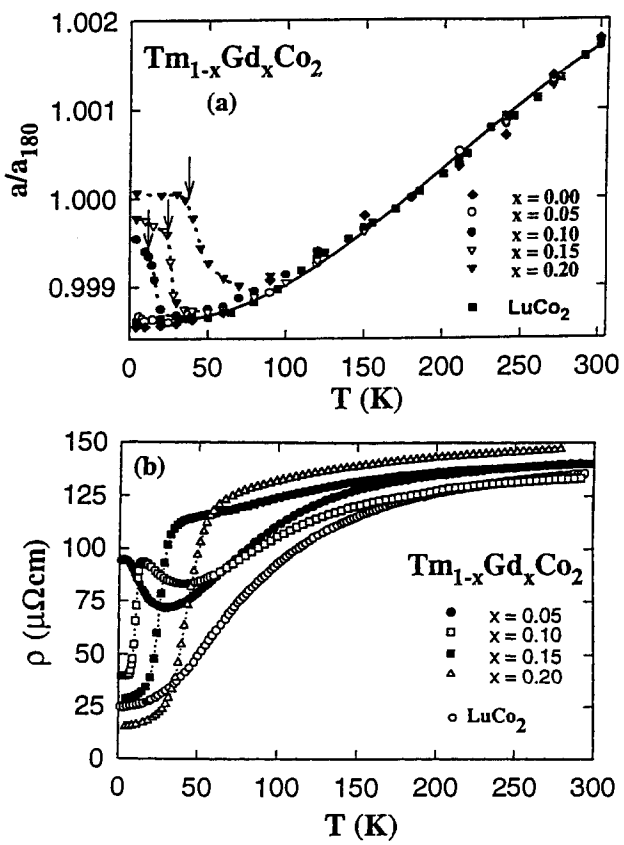


Fig. 102. (a) Temperature dependence of the thermal expansion for $Tm_{1-x}Gd_xCo_2$. (b) Temperature dependence of the resistivity of $Tm_{1-x}Gd_xCo_2$. Data for $LuCo_2$ are shown for comparison. After Gratz et al. (1995b).

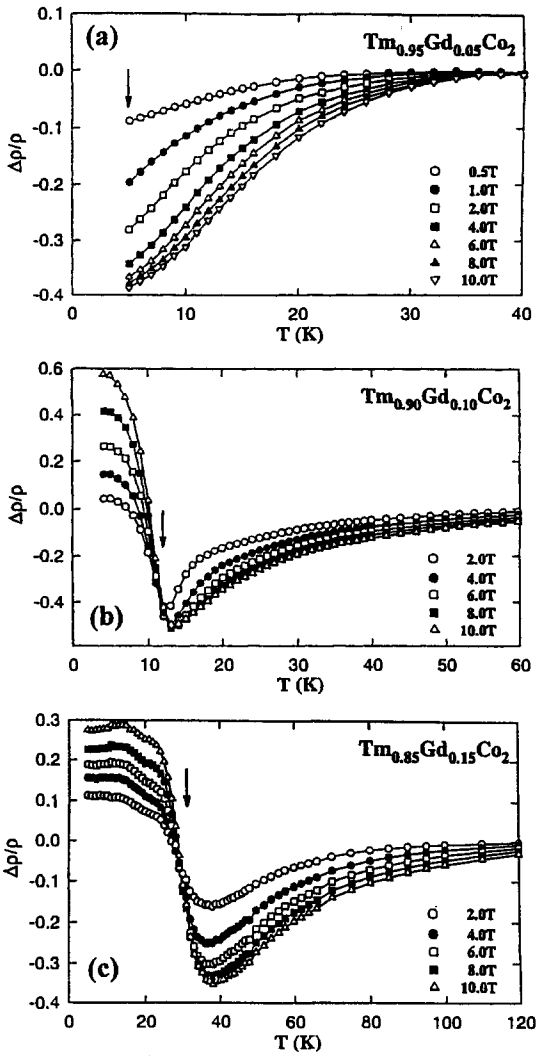


Fig. 103. Temperature dependence of the magnetoresistance ($\Delta\rho/\rho$) of $Tm_{1-x}Gd_xCo_2$ compounds, for a range of different magnetic fields, in the low temperature region: (a) $x = 0.05$, (b) $x = 0.1$, and (c) $x = 0.15$. After Gratz et al. (1996).

In addition, the result of the thermal-expansion study agrees well with that of the resistivity, in so far that a FOT appears to occur for the compounds with $x = 0.1$ and 0.15 (see figs 102(a), (b)).

The features of Co magnetism around the critical concentration of the $Tm_{1-x}Gd_xCo_2$ compounds are a good subject to study the origin of the positive contribution $\Delta R_V(B, T)$ to the magnetoresistance in eq. (56). For $x = 0.05$ (below the critical concentration), the

compound is paramagnetic and a very high negative magnetoresistance has been observed (fig. 103(a)). This is due to an enhanced spin-fluctuation mechanism as already discussed for the resistivity behavior above T_c for the ferrimagnetic RCo_2 compounds (see section 4). For $x = 0.1$ (the critical concentration) and $x = 0.15$ (above the critical concentration), $\Delta\rho/\rho(0)$ shows a minimum above T_c followed by a sharp increase towards positive values on cooling below T_c (figs 103(b), (c)). This behavior is more pronounced when the field is increased. Gratz et al. (1996) have related this positive magnetoresistivity to the fact that the external field reduces the effective field acting on the Co sublattice (and then brings the itinerant subsystem closer to the magnetic instability). We, however, consider that in the vicinity of T_c, the effect of the external magnetic field is to magnetize the Tm sublattice and then to strengthen the effective field acting on the Co subsystem rather than to reduce it. In this way, the external field enhances the formation of the 3d magnetism and gives rise to the contribution of $\Delta R_v(B, T)$ to the magnetoresistance as observed in the $R(Co,M)_2$ compounds.

6. Field-induced magnetic phase transitions in $R(Co,Al)_2$ Laves phase compounds

6.1. *Field-induced non-collinear magnetic structures in the Al-stabilized RCo_2 compounds*

The observation of field-induced non-collinear magnetic structures is a direct method of studying the intersublattice exchange interactions for a large number of collinear ferrimagnets including R–T intermetallics with heavy lanthanides. A non-collinear magnetic structure exists within a certain field interval between critical magnetic fields B_{t1} and B_{t2}. In the molecular-field approximation and without magnetic-anisotropy effects these critical fields are determined by (e.g., Tyablikov 1967; see also Duc 1997)

$$B_{t1} = -n_{RCo}|M_R - M_{Co}|, \tag{57a}$$

$$B_{t2} = -n_{RCo}(M_R + M_{Co}). \tag{57b}$$

In the non-collinear phase, the total magnetization or rather the magnetic moment per formula unit is proportional to the applied magnetic field:

$$\boldsymbol{M}_t = \boldsymbol{M}_R + \boldsymbol{M}_{Co} = \left|\frac{1}{n_{RCo}}\right| \boldsymbol{B}. \tag{58}$$

Here n_{RCo} (< 0) is the intersublattice molecular-field coefficient of the R–Co exchange interaction $- n_{RCo}\boldsymbol{M}_R\boldsymbol{M}_{Co}$. In this way, the slope yields the molecular-field parameter directly. Notice that, in the non-collinear phase, the effective molecular field acting on each subsystem is proportional to, and oriented along, the magnetization of that subsystem: indeed, from eq. (58) we derive that the effective molecular field, $\boldsymbol{B}^R_{mol}$, acting on the R-moments is given by

$$\boldsymbol{B}^R_{mol} = \boldsymbol{B} + n_{RCo}\boldsymbol{M}_{Co} = |n_{RCo}|\boldsymbol{M}_R. \tag{59}$$

Analogously, the field acting on the Co-subsystem equals

$$\boldsymbol{B}_{\mathrm{mol}}^{\mathrm{Co}} = |n_{\mathrm{RCo}}|\boldsymbol{M}_{\mathrm{Co}}. \tag{60}$$

Consequently, because in the non-collinear phase, for each subsystem, the magnitude of the magnetization does depend only on parameters specific for the subsystem itself (not on the applied field), it remains constant, i.e., during the process in which the sublattice moments are eventually forced to be parallel, the so-called "self-consistent" solution is maintained. The same conclusion is reached, when the exchange interactions between the lanthanide moments are taken into account explicitly, $\boldsymbol{B}_{\mathrm{mol}}^{\mathrm{R}}$ now being $(|n_{\mathrm{RCo}}| + n_{\mathrm{RR}})\boldsymbol{M}_{\mathrm{R}}$.

Experiments for the observation of the non-collinear state in RCo_2, however, meet with serious difficulties. These are connected with comparatively high values both of n_{RCo} and of the difference $M_{\mathrm{R}} - M_{\mathrm{Co}}$($M_{\mathrm{R}} > 5\,\mu_{\mathrm{B}}$/f.u., $M_{\mathrm{Co}} < 2\,\mu_{\mathrm{B}}$/f.u.). From eq. (57a) it can be shown that the first critical applied field B_{c1} is larger than 80 T (Brommer et al. 1993) even in the most favorable cases. A partial dilution of the magnetic lanthanide subsystem by non-magnetic yttrium or lutetium, often used in order to reduce the large difference $M_{\mathrm{R}} - M_{\mathrm{Co}}$, is not directly applicable to these compounds because of a simultaneous magnetic destabilization of the Co-subsystem. As already discussed in sections 4.1.2 and 4.1.3, such a destabilization leads to an inverse-like metamagnetic transition when the molecular field $B_{\mathrm{mol}}^{\mathrm{Co}}$ becomes lower than a critical value. A way to prevent the Co-subsystem in RCo_2 to become paramagnetic during the process of substituting Y or Lu for R is a partial replacement of Co by Al. It is known that a small amount of Al promotes a stabilization of the Co-subsystem: $Lu(Co_{1-x}Al_x)_2$ becomes ferromagnetic for $x > 0.07$ and $Y(Co_{1-x}Al_x)_2$ is ferromagnetic for $x > 0.12$ (see section 3.2). A typical example for this case is the high-field magnetization curve measured on free-powder samples of the $(Gd,Y)(Co,Al)_2$ compounds, where Co-magnetism is well established itself. The non-collinear phase starts to exist at the applied field of 42 T and the slope yields a R–Co molecular-field coefficient of 64 T/μ_{B} (Goto

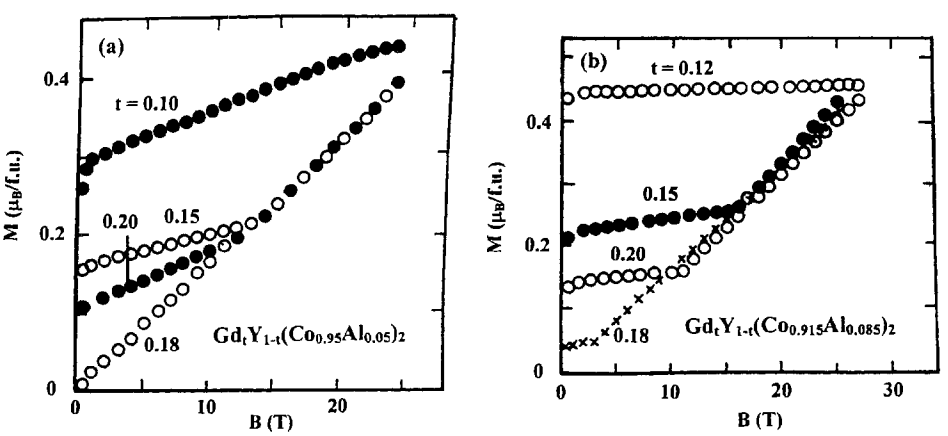


Fig. 104. Field-induced non-collinear magnetic structure in $(Gd_tY_{1-t})(Co_{0.95}Al_{0.05})_2$ (a) and $(Gd_tY_{1-t})(Co_{0.915}Al_{0.085})_2$. After Ballou et al. (1993a, 1993b).

et al. 1994a, 1994b). The non-collinear state can also be observed in those (R,Y)$(Co,Al)_2$ compounds in which the 3d-subsystem is magnetized by a molecular field created by the 4f moments. This is the case for the $Y_{1-t}Gd_t(Co_{0.95}Al_{0.05})_2$ and $Y_{1-t}Gd_t(Co_{0.915}Al_{0.085})_2$ systems (Ballou et al. 1993a, 1993b). The original $Y(Co_{1-x}Al_x)_2$ compounds for these systems are itinerant metamagnets with metamagnetic transition fields equal to 45 T and 2.25 T at 5% and 8.5% Al, respectively (Aleksandryan et al. 1985; Sakakibara et al. 1989). In these compounds, the molecular field exerted by the 4f moments can exceed the critical field of MMT of the 3d-subsystem, leading to the formation of the d-magnetic moment. In this way, kinks in the magnetization curves, which are characteristic of a transition from a collinear ferrimagnet to the non-collinear phase were observed (see fig. 104(a), (b)).

Non-collinear structures in $(Lu_{1-t}Tm_t)(Co_{0.88}Al_{0.12})_2$ are observed for the compounds with $t \leqslant 0.06$ (Brommer et al. 1993). In this system, the magnetization of the Co subsystem is assumed to be constant, whereas the Tm moment appears to exhibit an approximately constant (high-field) susceptibility. χ_{Tm} equals $6 \times 10^{-2}\ \mu_B$/T f.u. Taking into account, in eq. (57), the field dependence of the Tm magnetization, the critical fields B_{t1} and B_{t2} can be expressed as (Brommer et al. 1993)

$$B_{t1} = -\frac{n_{TmCo}|tM_{Tm} - M_{Co}|}{(1 + n_{TmCo}t\chi_{Tm})}, \tag{61a}$$

$$B_{t2} = -\frac{n_{TmCo}\{(1 + 2n_{TmCo}t\chi_{Tm})M_{Co} + tM_{Tm}\}}{(1 + n_{TmCo}t\chi_{Tm})}. \tag{61b}$$

The calculated phase diagram shows a satisfactory agreement with experimental data, i.e., with the observed lower and upper critical applied fields as a function of Tm content.

6.2. *Field-induced magnetic phase transitions in a ferrimagnet with one unstable magnetic sublattice.*

When one magnetic subsystem of a ferrimagnet exhibits a magnetic instability, i.e., undergoes a metamagnetic phase transition, the field-induced magnetic phase transitions are rather complicated. In section 4.13 we have already presented the induced MMT in the $Y_{1-t}Gd_t(Co_{0.915}Al_{0.085})_2$ compounds with $t < 0.04$, see fig. 56 (Ballou et al. 1993a, 1993b). We stressed there that the effect of the Gd moments is mainly to lower the critical field of MMT above which a stable collinear ferrimagnetic phase is formed. In this case, apparently, a stable non-collinear structure does not exist: due to the particular form of the magnetization curve of the (Co,Al) subsystem, a "self-consistent" solution mentioned in the preceding section is not possible. In a way, this observation elucidates the criterion for the existence of non-collinear structures as formulated by Cyrot and Lavagna (1979). In other cases, many different transitions can occur. A nice example is the sequence of phase transitions, different in their nature, which have been observed in $Y_{0.075}Tm_{0.25}(Co_{0.88}Al_{0.12})_2$ (Brommer et al. 1994, 1995). The experimental magnetization curve at 4.2 K is presented in fig. 105(a). This curve is characterized by two jump-like transitions at 6.5 T and 28 T and a region of a well pronounced peculiarity (a bend) between them. The corresponding Y-compound $Y(Co_{0.88}Al_{0.12})_2$ is a very weak ferromagnet

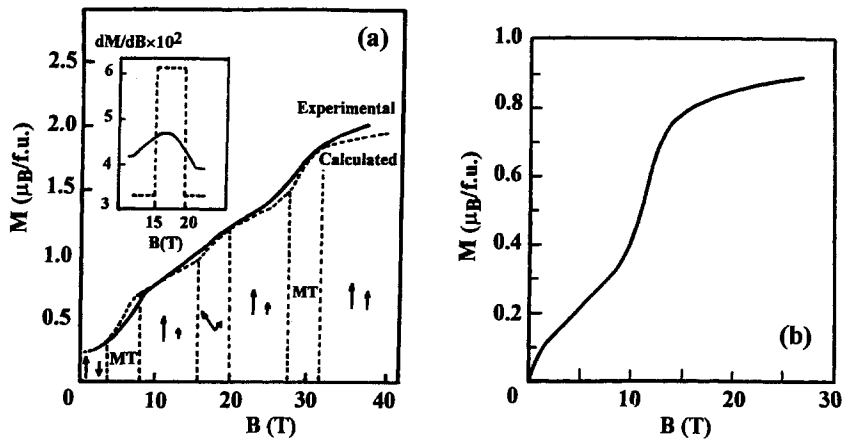


Fig. 105. Metamagnetic transitions in $Y_{0.75}Tm_{0.25}(Co_{0.88}Al_{0.12})_2$ (a), and $Y(Co_{0.88}Al_{0.12})_2$ (b). After Brommer et al. (1994).

(moment 0.08 μ_B/f.u.) with a MMT (at 12 T, moment about 0.5 μ_B/f.u.) to a strongly ferromagnetic state with a moment of more than 0.82 μ_B/f.u. (see fig. 105(b)). This was also taken to be the moment of the Co-subsystem in the corresponding $(Y,Tm)(Co_{0.88}Al_{0.12})_2$ powdered sample. From a fitting procedure, the molecular-field parameter was found to be -16.4 T/μ_B f.u. The Tm-moment was taken equal to 4.3 μ_B/Tm ion (Brommer et al. 1993). Thus, the Co-subsystem feels a molecular field $|n_{TmCo}|M_{Tm} = 17.6$ T, forcing it to be in the strongly ferromagnetic state. Upon application of a field, however, the effective field acting on the Co subsystem will decrease as long as the Co moment is pointing in the opposite direction. Consequently, the Co subsystem is driven, via the MMT, to the weakly ferromagnetic state. At still higher fields, a self-consistent solution for a non-collinear structure appears to be possible. After rotation to the ferromagnetic structure, further increase of the applied field forces the Co subsystem into the strongly ferromagnetic state again.

6.3. Field-induced magnetic structures of three coupled sublattices

In case two different kinds of lanthanides are placed on one sublattice, a three-subsystem model is necessary (Duc et al. 1993a; see also section 2.1.2.2). In the preceding sections, the three-sublattice model has been applied to explain the type of the magnetic phase transition for many $(R_1,R_2)Co_2$. For ferritic materials, the magnetic structures have been studied extensively in two- and three-sublattice models, including spontaneous breaking up of one sublattice into two (non-collinear) subsystems. Clark and Callen (1968) focus attention on the temperature dependence of the sublattice magnetizations. A three-sublattice model was applied in the description of the system $RMn_{6-x}Cr_xSn_6$ (Colpa and Brabers 1994), restricted to two equivalent Mn-sublattices. Here, we review the general treatment given by Brommer (1996a, 1996b). As before, we ignore magnetic anisotropy and reproduce linearized equations in a new form for the sublattice moments $\boldsymbol{M}_i$ ($i = 1, 2, 3$):

$$a_1 \boldsymbol{M}_1 - n_{12}\boldsymbol{M}_2 - n_{13}\boldsymbol{M}_3 = \boldsymbol{B}, \tag{62a}$$

$$-n_{12}\boldsymbol{M}_1 + a_2\boldsymbol{M}_2 - n_{23}\boldsymbol{M}_3 = \boldsymbol{B}, \tag{62b}$$

$$-n_{13}\boldsymbol{M}_1 - n_{23}\boldsymbol{M}_2 + a_3\boldsymbol{M}_3 = \boldsymbol{B}. \tag{62c}$$

Note that the coefficients a_j and the discriminant (determinant of the coefficient matrix of this set of equations) should be non-negative in order to have an energy minimum.

For a given collinear structure, the coefficients a_j can be calculated straightforwardly as a function of the applied field. Hence, the determinant (D) or any subdeterminant can also be calculated. In this way, for each collinear structure, the field range of its stability has been determined, for any combination of magnetic moments (of fixed magnitude) and molecular-field parameters. It turns out that without exception a smooth transition occurs to a non-collinear structure, i.e., all calculated magnetization curves are continuous and consist of horizontal portions (the collinear states) joined by straight lines (for the classes I and II below) or possibly by curved lines (see class III below). The total magnetic moment, $\boldsymbol{M}_t = \boldsymbol{M}_1 + \boldsymbol{M}_2 + \boldsymbol{M}_3$, always points in the direction of the applied field $\boldsymbol{B}$. We stress that this relation was not postulated, but has been derived from the stability conditions. In class I, the vectors $\boldsymbol{M}_j$ are allowed to be non-coplanar for a non-vanishing field. Then, eqs (62a), (62b), and (62c) must be identical. Hence, all molecular-field parameters are equal, and also a_j must be single-valued (equal), i.e., $-a_j = n_{12} = n_{23} = n_{13}$ [$= n$] for $j = 1, 2, 3$. Then we have $\boldsymbol{M}_t = \boldsymbol{B}/|n|$ in the region where a vector of length M_t can be constructed with three vectors, not necessarily coplanar, of length M_1, M_2, and M_3, respectively (if possible, down to $M_t = 0$ at zero applied field). Since for the non-vanishing determinant D all the components perpendicular to a non-zero field vanish, a vanishing determinant is then a necessary condition for the occurrence of a non-collinear structure. In fact, at the vanishing field B, the determinant vanishes always. A non-collinear structure may exist only in case all subdeterminants vanish, too (i.e., the three equations are dependent). This leads to

$$a_1 = \frac{-n_{12}n_{13}}{n_{23}}, \qquad a_2 = \frac{-n_{12}n_{23}}{n_{13}}, \qquad a_3 = \frac{-n_{13}n_{23}}{n_{12}}.$$

Consequently, since a_j should be positive (for any j), a non-collinear zero-field phase may exist only in case all molecular-field constants are negative (antiferromagnetic) or in case only one such constant is negative, the other two being positive (ferromagnetic).

For class II, $n_{12} \neq n_{23} = n_{13}$, the non-collinear states can either have collinear $\boldsymbol{M}_3$ and $\boldsymbol{B}$ (pointing in the same direction or in opposite directions) and non-collinear $\boldsymbol{M}_1$ and $\boldsymbol{M}_2$, or collinear $\boldsymbol{M}_1$ and $\boldsymbol{M}_2$, with, again, the corresponding two possibilities, both referred to as "pseudo-sublattice model". Typical examples of magnetization curves belonging to this class II are presented in fig. 106.

Finally, in case of class III, $n_{12} \neq n_{23} \neq n_{13} \neq n_{12}$, none of the particular non-collinear structures encountered in class II can occur. The vectors $\boldsymbol{M}_1$, $\boldsymbol{M}_2$, $\boldsymbol{M}_3$ and $\boldsymbol{B}$ are coplanar, but in a non-collinear structure all point in different directions. A computer program was developed to construct magnetization curves. One important feature is that curved lines

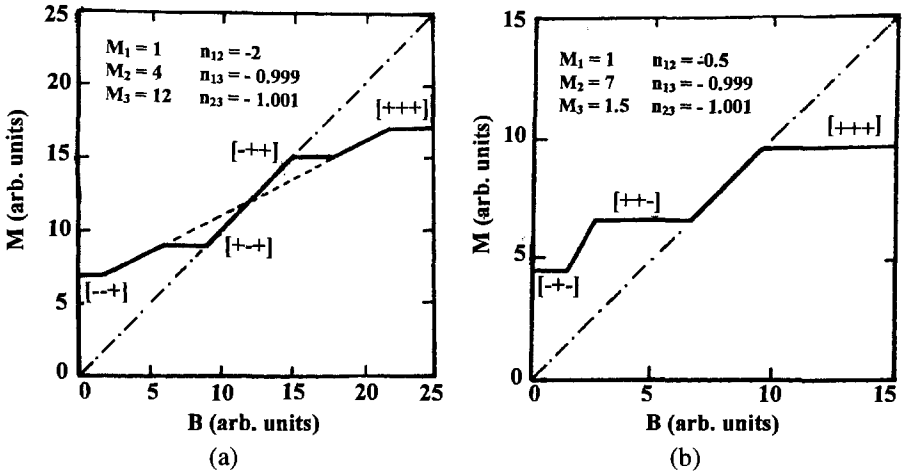


Fig. 106. Typical magnetization curves belonging to class II ($n_{13} = n_{23}$) in the three-sublattice model. After Brommer (1996a, 1996b).

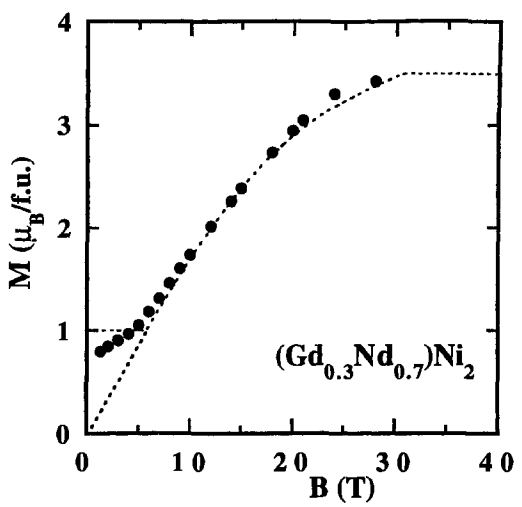


Fig. 107. High-field magnetization of $(Gd_{0.3}Nd_{0.7})Ni_2$. The dashed curve is calculated by the parameters listed in table 18.

can occur, which have some resemblance to the curves obtained in case anisotropy plays a role (Zhao 1994). Examples can be found in the study of high-field magnetization of the $(Gd,Nd)_mNi_n$ compounds by Duc et al. (1995a, 1995b). The results are presented in fig. 107 for $(Gd,Nd)Ni_2$. The magnetization curves were analyzed in an attempt to obtain direct information on the Gd–Nd exchange interactions. One should bear in mind, however, that a three-sublattice system can be described in the familiar two-sublattice model in case one of the subsystems exhibits a purely paramagnetic behavior, i.e., a linear response. This happens to be the case for the (Gd,Nd)Ni system. For $(Gd,Nd)Ni_2$ the curved

TABLE 18

Sublattice magnetic moments (M_{Gd}, M_{Nd} and M_{Ni}) and molecular-field coefficients n_{GdNd}, n_{GdNi} and n_{NdNi} for (Gd,Nd)–Ni compounds.

Compounds	M_{Gd} (μ_B/f.u.)	M_{Nd} (μ_B/f.u.)	M_{Ni} (μ_B/f.u.)	n_{GdNd} (T/μ_B)	n_{GdNi} (T/μ_B)	n_{NdNi} (T/μ_B)
$(Gd_{0.2}Nd_{0.8})Ni$	1.4	2.05	0	−6.8 (−10)[a]	—	—
$(Gd_{0.2}Nd_{0.8})Ni_2$	1.5	1.3	0.2	−4.0 (−3)[a]	−24	25
$(Gd_{0.3}Nd_{0.7})Ni_2$	2.25	1.05	0.2	−4.0	−21	42
$(Gd_{0.2}Nd_{0.8})Ni_3$	1.4	0.95	0.45	−2.7	−16	40
$(Gd_{0.15}Nd_{0.35}Y_{0.5})_2Ni_7$	2.1	1.3	0.8	−0.5	−15 (−21.8)[b]	12
$(Gd_{0.2}Nd_{0.8})Ni_5$	1.4	0.7	0.85	−1.0 (−1.8)[a]	−21.5 (−21)[b]	26
$(Gd_{0.6}Nd_{0.4})_2Ni_{17}$	8.4	1.7	5.5	0	−3.8 (−5.2)[b]	4

(a) n_{GdGd} deduced from T_N of the Gd–Cu system

(b) From high-field magnetization data for Gd–Ni compounds (Liu et al. 1994; Franse and Radwanski 1993)

lines (see fig. 107) are thought to be due to the existence of, presumably, an induced Ni moment, possible when the Ni subsystem exhibits a non-linear response. Although, in this general case, the induced moment is not necessarily constant (eq. (60b) must be modified, the resulting effective field acting on a subsystem now depending on the applied field), in the analysis, the Ni moment was taken constant (for simplicity). The obtained results for the molecular-field parameters are listed in table 18. Note that the value of n_{GdNd} is comparable with that of n_{GdGd} derived from the ordering temperature of the corresponding Gd–Cu compounds. Moreover, n_{GdNd} as well as n_{GdGd} decrease linearly with decreasing R-concentration.

6.4. Exchange interactions in RCo_2

The R–Co intersublattice exchange interaction can be determined directly in high-field free-powder measurements, but for the antiferromagnetic heavy rare earth HR–Co_2 only. An indirect determination, for the HR–Co_2 compounds, was systematically performed by Bloch and Lemaire (1970) from an analysis of the paramagnetic susceptibilities. A_{RCo} turns out to be ranging from 10.2×10^{-23} J to 13.5×10^{-23} J. In a description of the metamagnetic behavior of the Co subsystem in RCo_2, these values of A_{RCo} together with that of 25.6×10^{-23} J for $NdCo_2$ (Gignoux et al. 1975) were used by Duc et al. (1992a). In an analysis of the ordering temperatures, the A_{RCo} values can be reproduced, if the contribution of the R–R interaction is taken as estimated from RAl_2 compounds (Duc et al. 1993a). Neglect of this contribution of A_{RR}, leads to calculated A_{RCo} values up to 20×10^{-23} J (Duc et al. 1990; Duc 1991). We listed in table 19 the values of A_{RCo} deduced for RCo_2 using A_{RR} values derived from the ordering temperatures of RNi_2. In fact, neutron measurements performed on $HoCo_2$ (Castets et al. 1980) yield the value of 0.82×10^{-23} J, which is nearly half the value of 1.8×10^{-23} J deduced for $HoNi_2$. More recently, the value of A_{RR} of almost the same magnitude has also been used to explain the difference between exchange fields derived from inelastic-neutron scattering and high-field magnetization for $GdFe_2$ and $Gd_2Fe_{14}B$ (Liu et al. 1994). The A_{RR} value obtained from

TABLE 19
Values of the intersublattice exchange interaction parameter A_{RCo} for RCo_2 compounds.

Compounds	A_{RCo} (10^{-23} J)	
$GdCo_2$	18.8 [1][a]	19.2 [2][b]
$TbCo_2$	18.1 [1][a]	16.2 [3][b]
$DyCo_2$	18.0 [1][a]	—
$HoCo_2$	17.8 [1][a]	15.4 [3][b]
$ErCo_2$	16.0 [1][a]	14.6 [3][b]
$TmCo_2$	17.0 [1][a]	
$PrCo_2$	25.8 [1][a]	
$NdCo_2$	23.0 [1][a]	

(a) Data derived from T_c of RCo_2
(b) From high-field magnetization data on the $(R,Y)(Co,Al)_2$ compounds

References:

[1] Duc et al. (1993a) (data derived from T_c)
[2] Ballou et al. (1993a, 1993b)
[3] Duc, unpublished data

the magnetization measurements on the free powders of $(Gd,Nd)_mNi_n$ (see section 6.3) agrees with that deduced from the ordering temperature. Ballou et al. (1993a, 1993b) and Brommer et al. (1993) have derived a value of 19.2×10^{-23} J and 14.6×10^{-23} J for A_{RCo} in $(Gd,Y)(Co,Al)_2$ and $(Tm,Lu)(Co,Al)_2$, respectively, from high-field magnetization measurements. Note that these values are comparable with those listed in table 19. The same is true for the A_{RCo} values obtained for $(R,Y)(Co_{0.88}Al_{0.11})_2$ with R = Tb, Ho, Er (Duc, unpublished). The trend of the R-concentration dependence of A_{RCo} in all R–Co compounds (Duc 1997) is confirmed. Both the 3d magnetism and the 4f–3d exchange interactions in RCo_2, thus, are well described in terms of the hybridization of the 3d and 5d states. Finally, it is interesting to note that with this new set of A_{RCo} parameters, in order to maintain the results established in fig. 52, i.e., to describe the metamagnetic behavior of the 3d-subsystem in YCo_2 and RCo_2 with the same critical magnetic field (of 70 T), the value of $B_c[\sim x_c(g-1)J_R]$ must be scaled with the critical concentration determined from the specific-heat measurements (Hilscher 1988), i.e., x_c equals 0.125, 0.18, 0.3, 0.5, and 0.7 for R = Gd, Tb, Dy, Ho, and Er, respectively, see figs 81–83. Even so, in this estimation of the molecular field B_{mol}^{Co}, it is still necessary to introduce an experimentally observed value of J_R (which is, due to the effect of the crystalline field, always lower than their free ion value).

6.5. Concluding remarks on RCo_2 compounds

For a better understanding of 3d-magnetism in the RCo_2 compounds, it may be worthwhile to focus attention on some systematic trends in various observations. A systematic variation of the exchange parameter was already shown in the preceding section. Here, in fig. 108, we present the effective cobalt moment (p_{eff}) derived from the high-temperature susceptibility

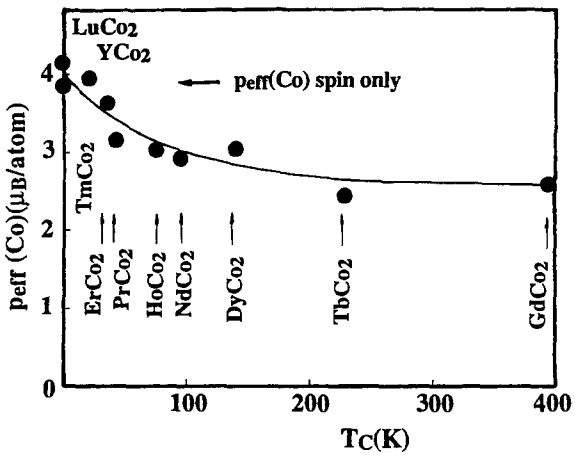


Fig. 108. p_{eff} as a function of Curie temperature in RCo_2. After Burzo and Lemaire (1992).

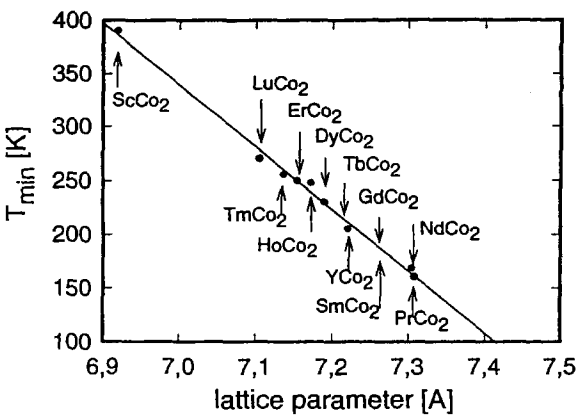


Fig. 109. T_{min}, the temperature at which the thermopower curve $S(T)$ shows a minimum (see text), as a function of the lattice parameter. After Gratz et al. (1995a).

(Burzo and Lemaire 1992). With increasing Curie temperature, p_{eff} appears to decrease steadily from $4\,\mu_B$ in YCo_2 and $LuCo_2$ (see also section 2.1.1) to about $2.6\,\mu_B$ in $GdCo_2$. Next, although for information on thermopower data we refer to the reviews written by Fournier and Gratz (1993) and Gratz et al. (1995a), we present here the relation between the position of the high temperature minimum in the $S(T)$ curve and the lattice parameter (at room temperature) (see fig. 109). This minimum is related to a local maximum of $N(\varepsilon)$ near the Fermi level. For YCo_2, the existence of such a peak in the DOS has been confirmed by band structure calculations (Yamada et al. 1984). For the RCo_2 compounds, however, the peak width varies with the lattice parameter. In this context, it is encouraging to recall here the variation of the Landau A_3-coefficient as a function of the Al concentration in

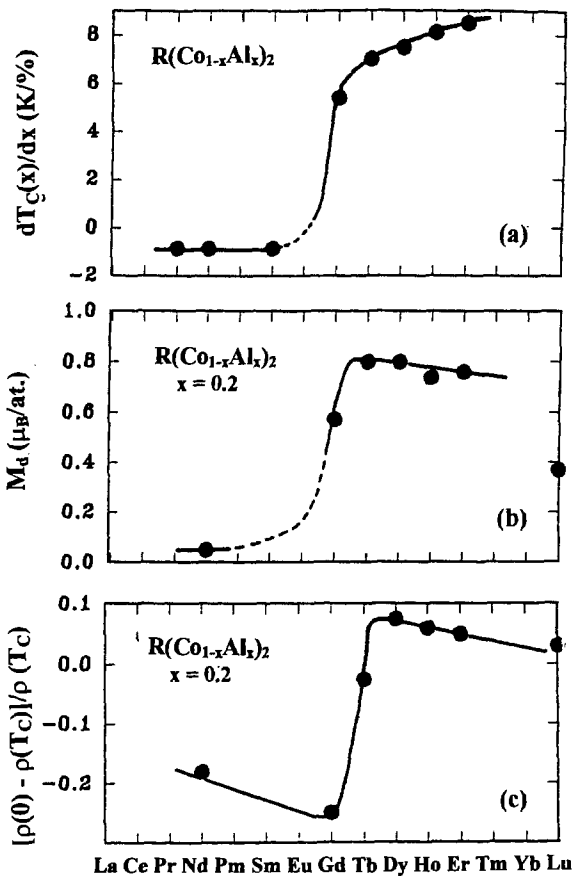


Fig. 110. Plots of dT_c/dx ($x \rightarrow 0$) (a), 3d-magnetic moment (b) and excess resistivity (c) as a function of lanthanide element in $R(Co_{1-x}Al_x)_2$.

$Y(Co_{1-x}Al_x)_2$ (see table 6, and also section 3). This decrease and the change of sign of A_3 was used as input in the discussion of various RCo_2 compounds with different lattice parameters, $R(Co_{1-x}M_x)_2$ (with M = Al, Si, Cu, ...) included. In fig. 110, we present for $R(Co_{1-x}Al_x)_2$ the dependence on the lanthanide element for dT_c/dx ($x \rightarrow 0$), the excess resistivity, and the 3d-magnetic moment. The initial increase of T_c becomes systematically lower when one goes from Tm to Gd, and then changes sign in the compounds with light lanthanides. As already discussed, the role of Al atoms in $R(Co,Al)_2$ is to increase the DOS of d-electrons at the Fermi level. However, due to the difference in the lattice parameter, $N(\varepsilon_F)$ is not the same in the "pure" RCo_2 compounds, which, thus, have different "starting positions", and also show a different variation at higher Al concentrations. This systematic change was observed by the measurements of the 3d-magnetic moment and the excess resistivity ($\Delta\rho$) (see section 4.2.1), not only for the $R(Co,Al)_2$ system, but also for the $R(Co,Si)_2$ and $R(Co,Cu)_2$ systems.

In conclusion, the sensitivity of the 3d-band near the Fermi level causes a wide variety in the magnetic and electronic behavior of different RCo_2 Laves phase compounds. This factor has to be taken into account in the search for a systematic description. The general behavior, shown in figs 108–110, may be considered as a proof for a systematic dependence on the atomic number, but, perhaps, also as a proof for the important role of the lattice parameter.

7. Other itinerant-electron metamagnetic systems

7.1. RCo_3-based compounds

The RCo_3 compounds crystallize in the rhombohedral $PuNi_3$-type of structure, space-group $R\bar{3}m$. This structure is obtained by systematic replacement of the Co ions by R ions in every second basal plane of RCo_5 (with $CaCu_5$ structure), according to the formula

$$2RCo_5 + R - Co \rightarrow 3RCo_3.$$

In the rhombohedral structure, the R atoms are situated at two different crystallographic sites, 3c(I) and 6c(II), whereas the 3d atoms are distributed over three different sites 3d(I), 6c(II), and 18h(III), see fig. 111. In a first approximation, the local arrangement of the R_I site is that of the hexagonal RCo_5 structure whereas the local arrangement of the R_{II} site

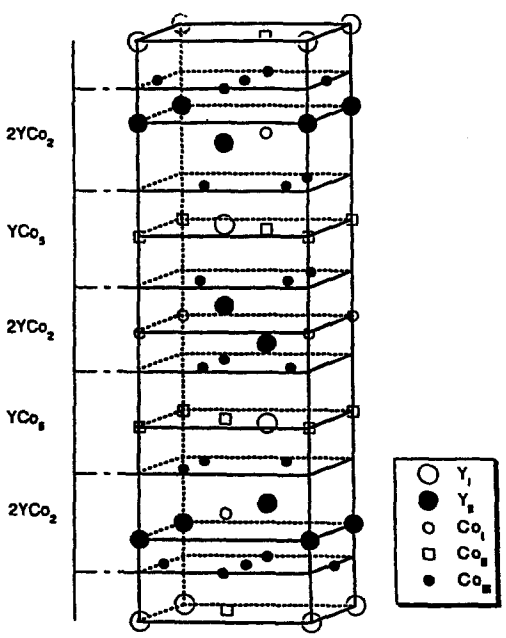


Fig. 111. Crystal structure of the RCo_3 compounds, viewed as the stacking of YCo_2 and YCo_5 cells.

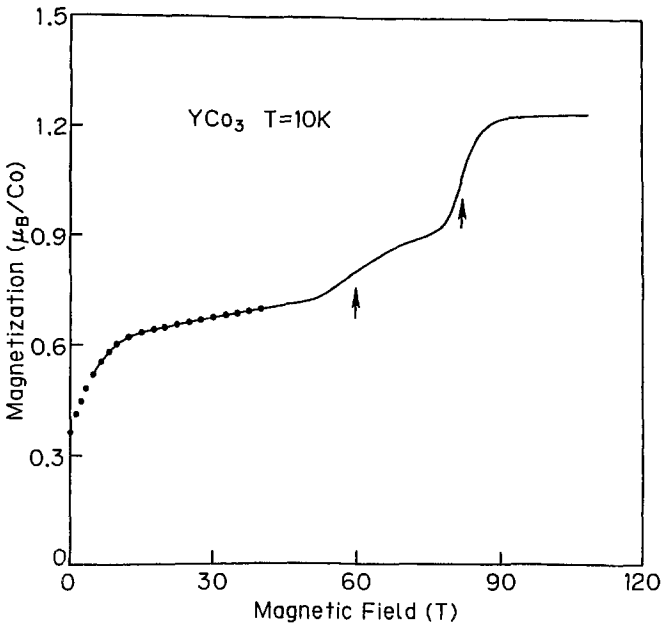


Fig. 112. Magnetization curve in the ultrahigh-magnetic field for YCo_3. After Goto et al. (1994a).

resembles that of the cubic RCo_2 Laves phase structure. In fact, for R ions placed at these sites the magnetic-anisotropy constants are found to have the opposite sign (and different magnitudes). Analogously, one might expect to find paramagnetic Co ions (as in YCo_2) and magnetic ones (as in YCo_5) with the occupancy ratio 1 to 2. Indeed, instabilities of the Co magnetism in RCo_3 have experimentally been observed by applying ultra-high magnetic fields or by the effect of the 4f–3d exchange interactions.

YCo_3 is an itinerant ferromagnet. According to data given in different studies, the Curie temperature of this compound ranges from 264 K to 320 K and the total magnetic moment ranges from 1.45 μ_B/f.u. to 1.8 μ_B/f.u. (Buschow 1980; Franse and Radwanski 1993). This wide spread in data of the basic magnetic characteristics may be caused by different deviations from stoichiometry for the samples studied in different experiments. Magnetization measurements of YCo_3 have been performed in ultra-high magnetic fields up to 110 T at 10 K (Goto et al. 1992). The observed magnetization curve of YCo_3 (see fig. 112) reveals two successive metamagnetic transitions at 60 T and 82 T, with magnetization changes from 0.72 μ_B/Co to 0.88 μ_B/Co and from 0.88 μ_B/Co to 1.23 μ_B/Co, respectively. Thus, the variations in magnetization due to these two transitions are 0.16 μ_B/Co and 0.35 μ_B/Co, respectively. It is interesting to note that the ratio of variation in the magnetization is about 1 : 2. Above 90 T, the magnetization is completely saturated with a spontaneous magnetization comparable to that of Y_2Co_7. In YCo_3, as mentioned above, Co atoms are on three different sites. All Co atoms are magnetic, but the (ferro)magnetic moments strongly depend on the sites, so that $m_{6c} > m_{3b} > m_{18h}$ (Kren et al. 1969). Since, in principle, the molecular field and the local DOS of Co depend on the site, it is

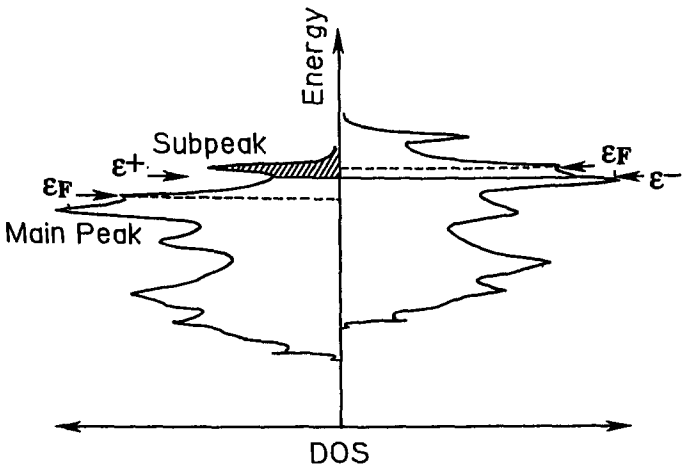


Fig. 113. 3d-DOS in YCo_3. ε_F: paramagnetic Fermi level; ε^+ and ε^-: Fermi level for the majority spins and minority spins, respectively. After Inoue and Shimizu (1985).

likely that the two MMTs occur successively on different sites. The fact that the increase of magnetization at the transition at 60 T is about half of the magnetization increase at 82 T suggests that the Co moment on the 3b and 6c sites exhibits a metamagnetic transition at 60 T and the Co_{18h} atoms at 82 T.

Band-structure calculations for YCo_3 have been performed by Inoue and Shimizu (1985), fig. 113. The DOS shows the existence of a sharp subpeak above the main peak and near the top of the 3d band. Accordingly, their magnetic properties are rather sensitive to a variation of the position of the Fermi level relative to the 3d band. For YCo_3, the Fermi level of the majority-spin states is located at the minimum of DOS between the main peak and the subpeak. In this case, YCo_3 is in a weakly ferromagnetic (WF) state (also referred to as an intermediate saturated ferromagnetic state). However, a MMT from the WF state to a strongly ferromagnetic (SF) state (i.e., a completely saturated ferromagnetic state) has been predicted for this compound if one can shift the Fermi level of the majority-spin state to the top of the 3d band, i.e., to the subpeak (fig. 113, the shaded area). This can be accomplished by the substitution of Fe for Co (Goto et al. 1991) or by the application of ultra high magnetic fields, as observed. In fact, this rigid band model has predicted that YCo_3 is in the WF state with an estimated magnetic moment of $0.8\,\mu_B$/Co and exhibits a transition to a SF state with a magnetization jump of $0.4\,\mu_B$/Co. It is in good agreement with the experimental observations. However, it does not explain the two metamagnetic transitions observed in YCo_3.

The YCo_3H_x compounds form two hydride phases: the β-phase ($1.0 \leqslant x \leqslant 1.9$) and the γ-phase ($3.4 \leqslant x \leqslant 4.0$). The β-phase has two modifications β_1 (or β_L) with $1.0 \leqslant x \leqslant 1.5$ and β_2 (or β_H) with $1.5 \leqslant x \leqslant 1.9$. The magnetic properties of YCo_3H_x are quite sensitive to the concentration x of absorbed hydrogen (Yamaguchi et al. 1985a, 1985b). The parent compound YCo_3 and the β_2-hydride are ferromagnetic with

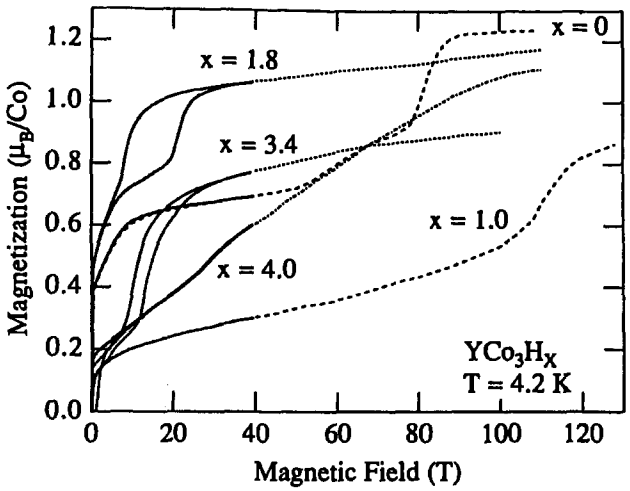


Fig. 114. Magnetization curve in the ultrahigh-magnetic field for YCo_3H_x at 4.2 K. After Bartashevich et al. (1994a, 1994b).

a WF ground state, whereas the spontaneous magnetization disappears in the β_1- and γ-hydrides. The MMT is still observed in the β-phase (Bartashevich et al. 1994a, 1994b). The γ-hydrides are antiferromagnetic (AF). In this phase, only a spin-flip transition from AF to F was observed at 14 T and at 29 T for $x = 3.4$ and 4.0, respectively (fig. 114). Additional electrons originating from the hydrogen atoms are primarily contained in the metal–hydrogen bonding band. The rest of them occupy the 3d band and upwards to the Fermi level (Yamaguchi et al. 1995). Hydrogen, however, has two effects. Firstly, it slightly modifies the DOS curve in the β-phase. The two magnetic groups of Co sites (i.e., the 3b, 6c sites on the one hand, and the 18h sites, on the other hand) then still exist and the two itinerant metamagnetic transitions occur in this hydride as in YCo_3. Secondly, it strongly modifies the DOS in the γ-phase and destroys the itinerant MMT in this phase. This difference in the modification of the DOS is related to the different site-occupation of hydrogen: hydrogen atoms are located on interstitial sites in the YCo_2 blocks for the β-phase, whereas they occupy lattice sites in the YCo_5 blocks for the γ-phase (Benham et al. 1989).

Due to the effective 4f–3d exchange interactions, the Co atoms in most of the RCo_3 phases are in the strongly ferromagnetic state. The 4f-moment is in antiparallel alignment to the Co moment in the heavy-lanthanide compounds, whereas both moments are parallel in the light-lanthanide compounds. For the former system, besides the inverse MMT of the Co sublattice from the SF state to the WF state, one also expects a field-induced transition from the ferrimagnetic collinear structure to a noncollinear structure.

The inverse MMT of the Co sublattice has not been observed in $GdCo_3$ since the exchange field acting on Co is too large (about 285 T). It can be demonstrated in the $Y_{1-t}Gd_tCo_3$ compounds (Aruga Katori et al. 1994). The Gd concentration dependence of the spontaneous Co-sublattice moment in $Y_{1-t}Gd_tCo_3$ is presented in fig. 115. The substitution of Gd for Y in YCo_3 leads to enhancement of the Co moment, with a clear step (the second MMT) of 0.27 μ_B/Co at $t_{c2} \approx 0.25$. These results reveal that the (complete) MMT

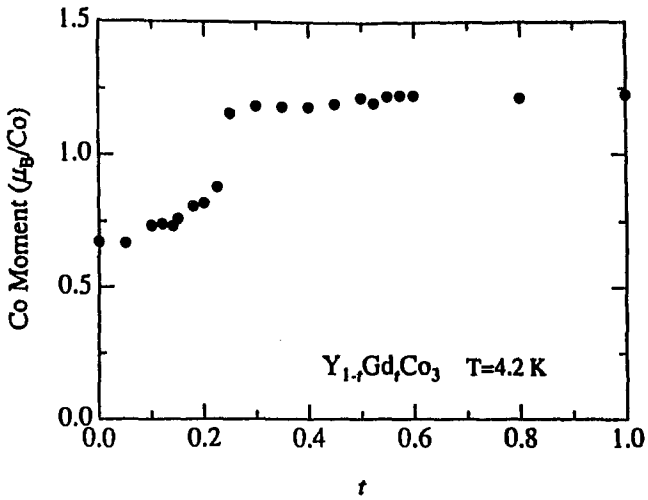


Fig. 115. Gd-concentration dependence of m_{Co} derived from saturation magnetization in $Y_{1-t}Gd_tCo_3$ compounds. After Aruga Katori et al. (1994).

of the Co sublattice, induced by the molecular field from the Gd sublattice, is stabilized even without an external field for $t > t_{c2}$. The expected first MMT of the Co sublattice, however, is not clearly visible as a step (according to later calculations to be expected at $t_{c1} \approx 0.1$, see fig. 117). The apparent broadening of the transition is ascribed to the inhomogeneous molecular field. Magnetization curves measured at 4.2 K are displayed in fig. 116(a), (b) for some characteristic $Y_{1-t}Gd_tCo_3$ compounds. Note that the magnetization of compounds with low Gd-concentration ($t \leqslant 0.22$) undergoes a diffuse (second) MMT (fig. 116(a)). In this concentration range, well below the compensation point, the Gd moments are oriented opposite to the applied field, so the molecular field acting on the Co moments is parallel to the applied field. Accordingly, $B_{c2}(t)$ decreases linearly with increasing t (see also fig. 117). For compounds close to the compensation concentration ($t_{com} \approx 0.525$), the magnetization increases almost linearly in fields above a critical value (fig. 116(b)). This is characteristic of a transition to a non-collinear ferrimagnetic phase. At the compensation point, the (critical) transition field B_{t1} should vanish. In practice, however, it remains above 10 T. In this case, the anisotropy of the Co sublattice (Co sites) may be important. From the experimental data, the strength of the 4f–3d exchange coupling was determined and a complete B–t phase diagram of $Y_{1-t}Gd_tCo_3$ compounds was constructed (fig. 117) (Levitin and Markosyan 1998).

The analysis of magnetization data is more straightforward in the case of the $Y_{1-x}Nd_xCo_3$ system, partly because the Nd and Co moments are ferromagnetically coupled. Substitution of Nd for Y in YCo_3 leads to enhancement of the spontaneous Co moment m_{Co} from $0.55\,\mu_B$/Co in YCo_3 to $1.17\,\mu_B$/Co in $NdCo_3$. The Nd-concentration dependence of the Co moment exhibits the two expected-steps as shown in fig. 118, at the critical concentrations $x = 0.35$ and 0.85, respectively (Goto et al. 1994b; Koui et al. 1994). In applied magnetic fields, several compounds do exhibit the two MMTs, as

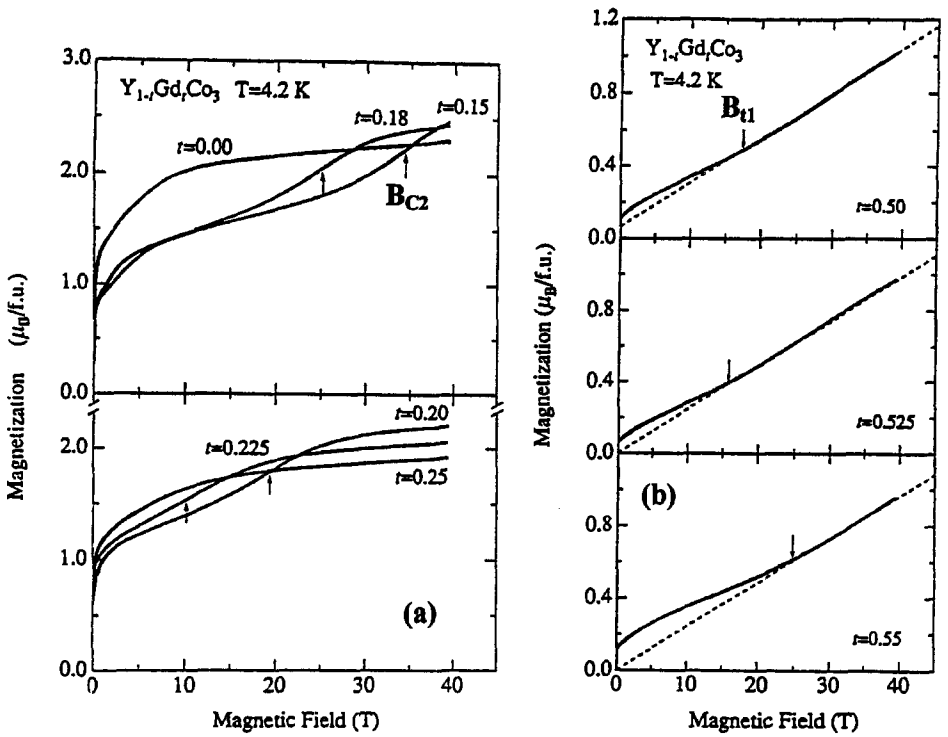


Fig. 116. Magnetization curves at 4.2 K for several characteristic $Y_{1-t}Gd_tCo_3$ compounds with MMT (a) and with field-induced collinear–noncollinear phase transition (b). After Aruga Katori et al. (1994).

illustrated in fig. 119 for $Y_{1-x}Nd_xCo_3$ with $x = 0.0$, 0.1 and 0.2. The critical fields of both transitions decrease linearly with increasing Nd concentration. Moreover, with increasing temperature, the critical fields do increase. This increase is ascribed to the weakening of the exchange field due to the decrease of the Nd magnetization. Since in YCo_3 the critical fields tend to decrease with increasing temperature, the influence of spin fluctuations appears to be negligibly small in these systems, in contradistinction to YCo_2, where the critical fields increase with a T^2-dependence ascribed to spin fluctuations.

$ErCo_3$ is a collinear ferrimagnet with uniaxial anisotropy in the whole magnetically ordered region (Yakinthods and Rossat-Mignod 1972). The high-spin moment of Co was estimated to be $1.3\,\mu_B$/Co. The magnetization along the c-axis exhibits two transitions, at 29.5 T and at 90 T (fig. 120) (Goto et al. 1995). The first transition corresponds to the (inverse) itinerant MMT at 80 T in YCo_3: the Co moment in the high-spin state is reduced due to the decrease of the effective field (sum of opposite exchange and external fields) acting on the Co sublattice. No transition corresponding to the MMT at 60 T of YCo_3 is clearly observed in $ErCo_3$ since the transition is rather broad. The transition at 90 T is a spin-flip one of the Co moment towards the direction of the applied field (and the direction of the Er moment). In contrast, the magnetization perpendicular to the c-axis (i.e., along the

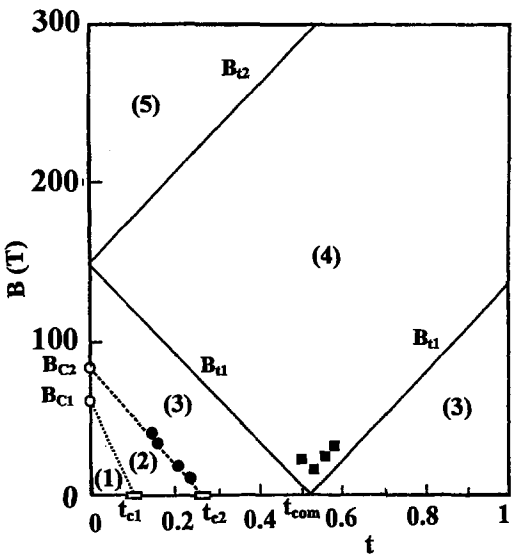


Fig. 117. Computed B–t magnetic phase diagram for $Y_{1-t}Gd_tCo_3$. The circles and squares represent the experimental data. (1) – weakly ferrimagnetic collinear phase, (2) – intermediate ferrimagnetic phase, (3) – strongly ferrimagnetic collinear phase, (4) – non-collinear phase and (5) – strongly ferromagnetic phase. After Levitin and Markosyan (1998).

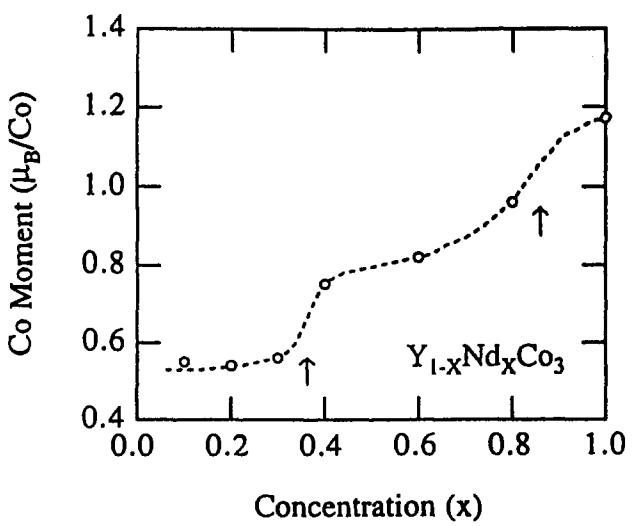


Fig. 118. Nd concentration dependence of m_{Co} derived from saturation magnetization in $Y_{1-x}Nd_xCo_3$ compounds. After Goto et al. (1994b).

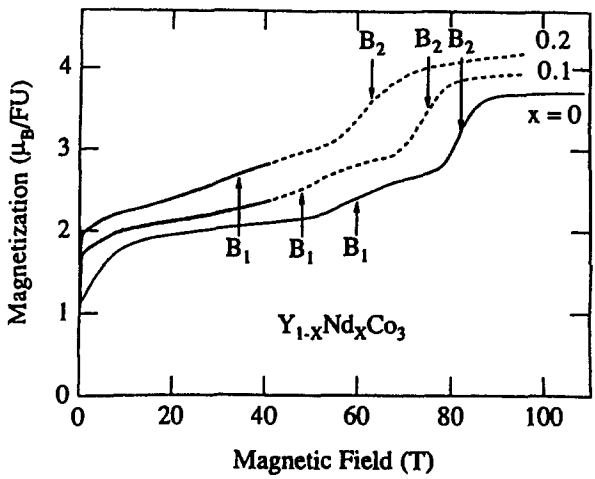


Fig. 119. Magnetization curves for $Y_{1-x}Nd_xCo_3$ compounds. After Goto et al. (1994b).

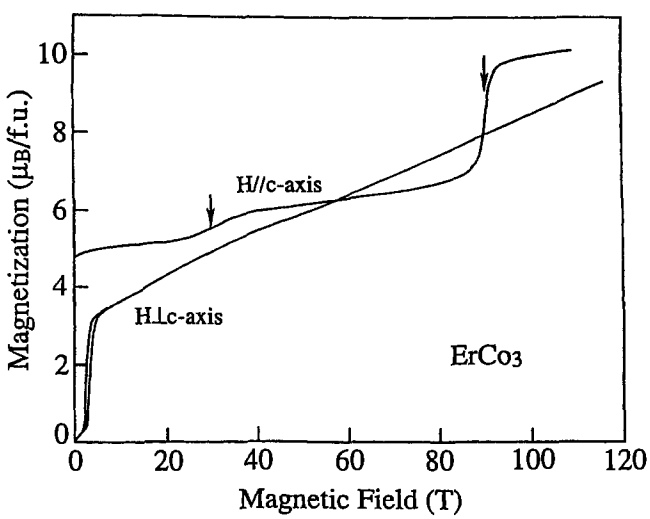


Fig. 120. Magnetization curves at 4.2 K for $ErCo_3$. After Goto et al. (1995).

b-axis), exhibits a collinear-noncollinear transition at about 3 T (due to the reorientation of the Er_{II} moments), and then increases gradually up to 110 T.

$HoCo_3$ is a collinear ferrimagnet with easy-plane type of anisotropy below 55 K (Shcherbakova and Ermolenko 1982). The magnetization in the basal plane shows an itinerant MMT of the Co sublattice at 66 T as in $ErCo_3$ (see fig. 121) (Goto et al. 1995). Meanwhile, the magnetization along the *c*-axis exhibits a collinear-noncollinear transition at about 5 T.

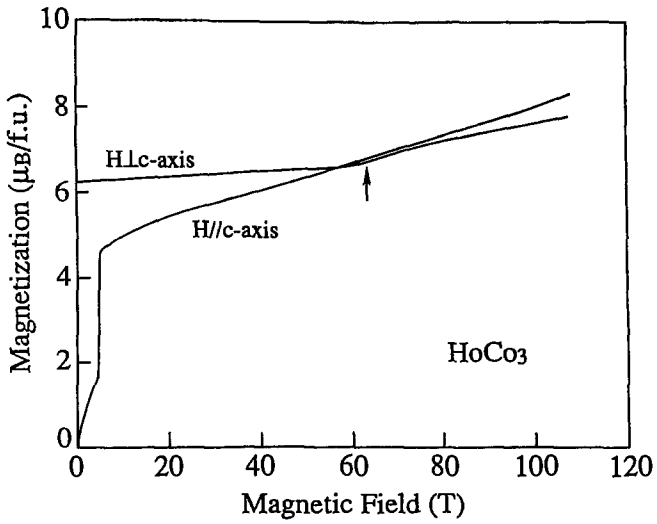


Fig. 121. Magnetization curves at 4.2 K for $HoCo_3$. After Goto et al. (1995).

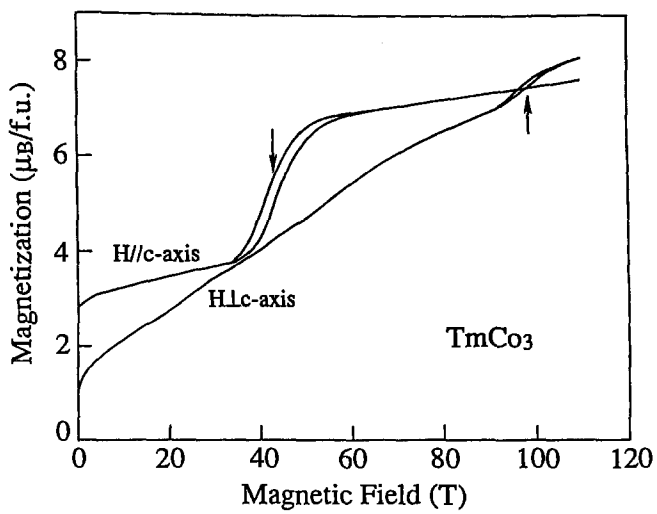


Fig. 122. Magnetization curves at 4.2 K for $TmCo_3$. After Goto et al. (1995).

$TmCo_3$ is considered to be a noncollinear ferromagnet with an easy-cone type of anisotropy below 30 K (Shcherbakova and Ermolenko 1982). The easy direction deviates from the c-axis by an angle of 13° at 4.2 K due to the local anisotropy energy of the Tm_{II} ion. In the zero field, Co is in the low-spin state with a magnetic moment of $0.76\,\mu_B$/Co (Ikonomou and Yakinthos 1976). Thus, a sharp transition at 43 T observed in the magnetization along the c-axis (see fig. 122) cannot be associated with the itiner-

ant MMT, but it is produced by a flip of the Co moment as in $ErCo_3$ and $HoCo_3$. In this case, however, the spin structure remains non-collinear. On the other hand, the magnetization perpendicular to the c-axis monotonically increases and exhibits a broad transition at 99 T. The corresponding magnetization jump of 1.1 μ_B/f.u. leads to the suggestion that this transition may be an itinerant MMT of the Co sublattice (Goto et al. 1995).

7.2. The RCo_5 compounds

With increasing R concentration, the transfer of lanthanide 5d electrons to the unfilled 3d band and the 3d–5d hybridization eventually lower the DOS at the Fermi level to such an extent that, beyond the critical concentration of rare-earth, the 3d atoms are no longer magnetic. With trivalent rare-earths, as mentioned before, the critical concentration is achieved in the RCo_2 compounds. For the systems with tetravalent rare-earth atoms, additional electrons shift ε_F even more rapidly to the region of higher energy with low DOS. In this case, the critical concentration is close to RCo_5. In practice, whereas Y_2Co_7 and YCo_3 with trivalent yttrium are ferromagnets, no spontaneous magnetization is observed down to 4.2 K in Th_2Co_7, $CeCo_3$, Ce_2Co_7, and Ce_5Co_{17} with tetravalent thorium and cerium (Givord et al. 1983). The susceptibility of these compounds shows a maximum around 160 K, but this maximum does not correspond to the magnetic phase transition. Below this temperature, the transition towards the state of a higher magnetic moment is induced by an applied field. In $ThCo_5$ and $CeCo_5$, however, the rare-earth concentration is lower, and these compounds exhibit a spontaneous magnetization at room temperature. $ThCo_5$ and $CeCo_5$ crystallize in the hexagonal $CaCu_5$-type structure. Co atoms occupy two sites, the 2c sites with a uniaxial symmetry and the 3g sites with an orthorhombic symmetry. The peculiar behavior of 3d magnetism in these compounds is associated with the difference of magnetic properties on different Co-sites. This is described below.

In the RCo_5 intermetallic compounds, there is an increasing tendency for the heavy lanthanides to form compounds richer in Co: RCo_{5+x}. Off-stoichiometric compounds have been found, such as $GdCo_{5.14}$, $TbCo_{5.1}$, $DyCo_{5.2}$, $HoCo_{5.5}$, and $ErCo_6$. The additional Co atoms are located at the lanthanide sites in the form of dumbbell-pairs (Schweizer and Tasset 1969). The same tendency is found for $ThCo_5$. The non-stoichiometric $Th_{1-\delta}Co_{5+2\delta}$ compounds exist within the range $0 \leqslant \delta \leqslant 0.08$ ($ThCo_5$ up to $Th_{0.92}Co_{5.16}$). Magnetic properties strongly depend on the substitution rate δ. The Curie temperature increases with increasing δ from 410 K for $ThCo_5$ up to 730 K for $Th_{0.92}Co_{5.16}$ (van der Goot and Buschow 1971). Furthermore, in the stoichiometric $ThCo_5$ compound Co remains in the low magnetic state and the MMT is not accessed experimentally, whereas in $Th_{0.95}Co_{5.10}$ the Co atoms are already in the high magnetic state at zero applied field (Givord et al. 1983; see fig. 123(c)). In the Co-poor compounds, the temperature dependence of the spontaneous magnetization and that of the superimposed susceptibility shows a maximum near 200 K (Ganapathy et al. 1974). Below 100 K, a transition towards the state of higher magnetization is induced by an applied field (fig. 123(a)). The polarized neutron diffraction study indicated that in the low-spin state the magnetization density is lower by about 20% on Co_{3g} atoms than on Co_{2c} ones, i.e., $m(Co_{2c}) = 1.21\,\mu_B$/Co and $m(Co_{3g}) = 0.96\,\mu_B$/Co for the $Th_{0.965}Co_{5.07}$ compound, whereas the magnetization densities on both Co sites are the same ($m(Co_{2c}) = m(Co_{3g}) = 1.58\,\mu_B$/Co) for the

$Th_{0.95}Co_{5.10}$ compound (Givord et al. 1977, 1979). The magnetic behavior at finite temperature also originates from the Co_{3g} atoms. These atoms exhibit a metamagnetic behavior analogous to that observed in Y(Lu)Co_2. The critical field in the present case, however, can be reached either by an applied magnetic field in the Co-poor compounds (figs 123(a), (b)) or by an increase of the exchange field on the Co_{3g} atoms in the Co-rich compounds caused by statistical substitution of Co dumbbells for Th atoms (fig. 123(c)). The effect due to the decrease of the internal field can be observed in the temperature dependence of spontaneous magnetization of the $Th_{1-\delta}Co_{5+2\delta}$ compounds. Since the magnetization of the 2c subsystem decreases as temperature increases, at some temperature in the compounds with $\delta = 0.04$ and 0.05, the Co_{2c}-exchange field acting on the 3g subsystem becomes less than B_c. This leads to a transition of the 3g subsystem into the paramagnetic state with a jump-like decrease in the magnetization. The discontinuity in the 3d-band splitting associated with metamagnetism in these compounds also results in an additional volume anomaly.

Magnetization measurements under pressure have been carried out for single crystalline $ThCo_5$ by Ballou et al. (1990). The magnetization curves are presented in fig. 124. Great effects of pressure on the magnetization are obtained in the low magnetic state whereas relatively slight effects are observed in the high magnetic state. Additionally, B_c is found to increase linearly with pressure at a rate of 2.8 T/kbar. The obtained results have been described by making use of a very simple model for the volume dependence of DOS and the molecular-field parameter.

$CeCo_5$ is a ferromagnet with a large uniaxial anisotropy, and belongs to a famous family of permanent-magnet materials. Within the homogeneity range, all the Co atoms in $CeCo_5$ are in the high-spin state with a moment of $1.42\,\mu_B$/Co (Ermolenko et al. 1980; Ermolenko et al. 1977; Bartashevich et al. 1994b). The substitution of Ni for Co supplies excess electrons in the d-band, and, thus, leads to the appearance of the low-spin state due to the decrease in the density of states at the Fermi level, as observed in the $Ce(Co_{1-x}Ni_x)_5$ compounds with $x \geqslant 0.075$ (together with the influence of the exchange field acting on the Co sublattice). A MMT to the high-spin state has been observed in an oriented powder $Ce(Co_{0.925}Ni_{0.075})_5$ sample (Givord et al. 1983). High-field magnetization studies on monocrystalline samples (Bartashevich et al. 1995) indicate for $Ce(Co_{0.9}Ni_{0.1})_5$ a MMT at a field $B_c = 21$ T applied along the (easy) c-axis. The critical field along the hard direction is estimated to be about 47 T (see fig. 125) As the temperature increases, the spontaneous magnetization of this compound exhibits a broad maximum around 200 K and the critical field of the transition increases monotonically. This metamagnetic behavior is similar to that of $Th_{0.965}Co_{5.07}$ (see above).

7.3. The $Ce_2Co_7B_3$ compounds

The structure of $R_{n+1}Co_{3n+5}B_{2n}$ compounds with $n = 1, 2, 3$ up to ∞ is closely related to that of the RCo_5 compounds, since it results from the stacking of one layer of RCo_5 and n layers of RCo_3B_2. In $R_2Co_7B_3$ ($n = 3$), magnetic investigations of pseudoternary $(Gd,Y)_2Co_7B_3$ compounds show a large induced Co moment due to the 4f–3d exchange interactions (Ballou et al. 1993a, 1993b). $Ce_2Co_7B_3$, however, exhibits a MMT in a wide temperature range (fig. 126) (Ido et al. 1995). In this compound, the MMT takes place from a low magnetization state to a higher magnetization state. At low temperatures, the

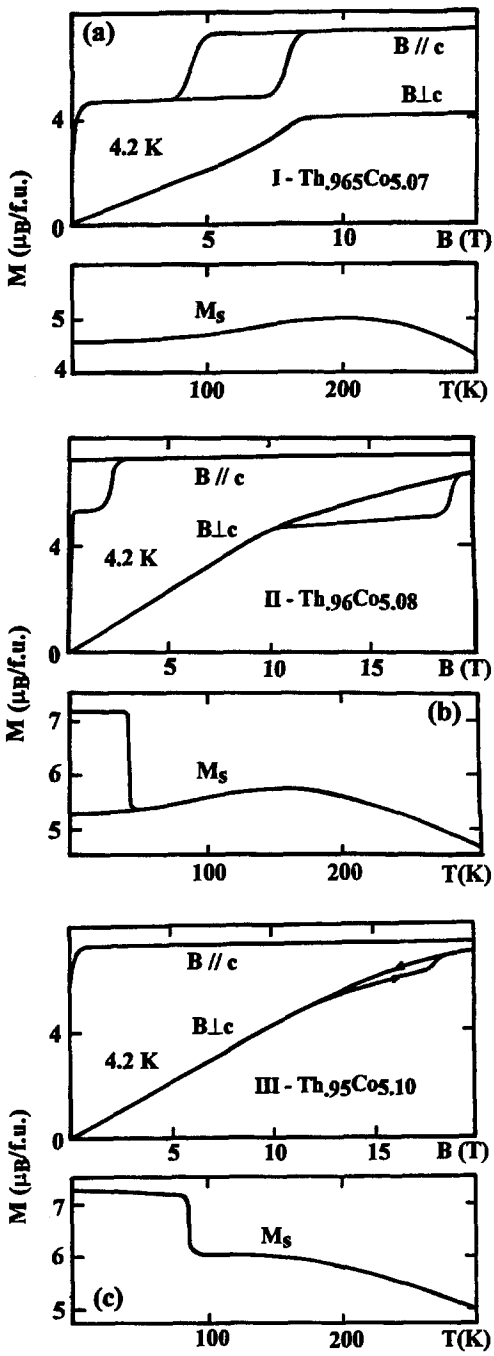


Fig. 123. Field variation of the magnetization at 4.2 K and temperature dependence of the spontaneous magnetization up to 300 K for three $Th_{1-\delta}Co_{5+2\delta}$ compounds. After Givord et al. (1983).

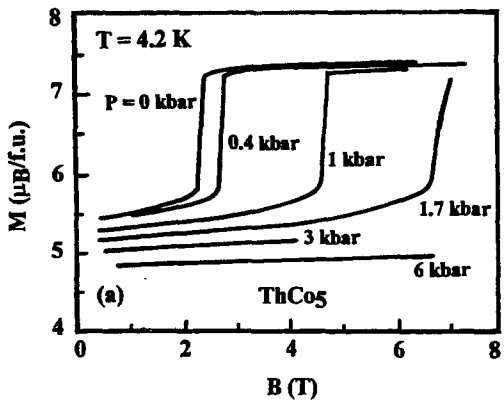


Fig. 124. The magnetization curves measured at 4.2 K along the c-axis in an increasing field at various pressures at 4.2 K in $ThCo_5$. After Ballou et al. (1990).

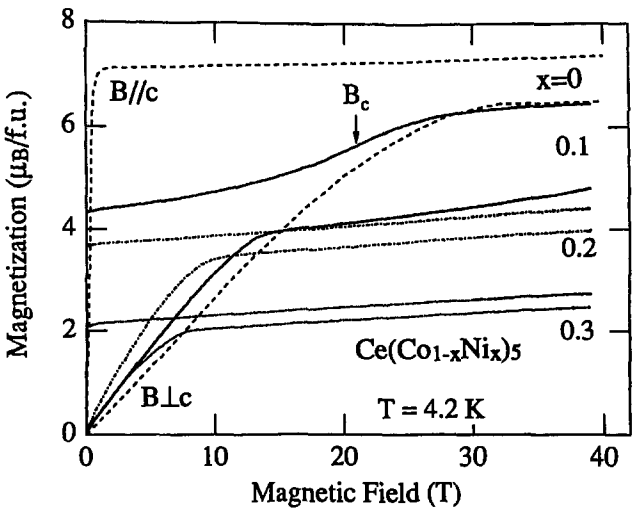


Fig. 125. Magnetization curves of single crystalline $Ce(Co_{1-x}Ni_x)_5$ along the c-axis and in the basal plane. The arrow indicates a MMT point. After Bartashevich et al. (1995).

metastable state exists in a wide magnetic field regime (i.e., the hysteresis with an up-critical field $B_{c2} = 8$ T and a down-critical field $B_{c1} = 2$ T). As the temperature increases, the hysteresis decreases. For $T = 150$ K, the hysteresis disappears ($B_{c1} = B_{c2} = B_c = 5.5$ T) and for $T > 150$ K, B_c starts decreasing with increasing temperature. The MMT of $Ce_2Co_7B_3$ has been suggested to be similar to that of $ThCo_5$. In the $R_{n+1}Co_{3n+5}B_{2n}$ compounds, the cobalt sites can be classified according to the number of adjacent "B-containing layers": Co(i) (with $i = 0, 1, 2$) has i adjacent B-containing layers (Ogata et al. 1993). The magnetic moments are $m_{Co(0)} = 1.2\,\mu_B$, $m_{Co(1)} = m_{Co(2)} = 0\,\mu_B$. In

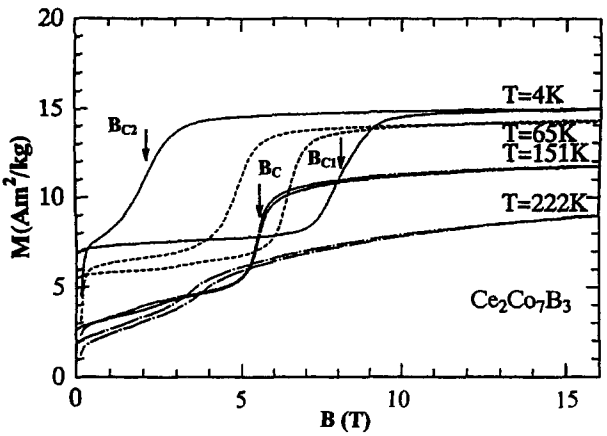


Fig. 126. Magnetization curves measured on free powders of $Ce_2Co_7B_3$ at various temperatures. After Ido et al. (1995).

$Ce_2Co_7B_3$, it is proposed that due to the strong 4f(Ce)–3d(Co) hybridization, the Co(1) sites are on the verge of satisfying the Stoner criterion (Ido et al. 1995). Accordingly, this metastable state is the origin of the MMT observed.

7.4. The $Co(S_{1-x}Se_x)_2$ compounds

The pyrite-type CoS_2 compound is known as an itinerant-electron ferromagnet. Its phase transition at $T_C = 124$ K is of second order. No MMT is observed in the paramagnetic temperature region (Adachi et al. 1979a). The application of high pressure changes the type of magnetic phase transition from SOT into FOT at $p = 0.4$ GPa (Hiraka and Endo 1996; Goto et al. 1997, 1998). In the pressure region where a FOT does occur, a MMT is observed just above T_C as shown in fig. 127. The $CoSe_2$ compound has the same pyrite structure. However, this compound is nonmagnetic at low temperatures. Its magnetic susceptibility shows a broad maximum at 40 K, indicating a strongly enhanced paramagnetic behavior. According to the electronic-structure calculations, the bandwidth of the anti-bonding 3p(S) states in CoS_2 is rather narrower than that of the 4p(Se) states in $CoSe_2$. Consequently, the DOS at ε_F for $CoSe_2$ becomes lower than that for CoS_2 (Yamada et al. 1998), with the result that CoS_2 is ferromagnetic, while $CoSe_2$ is not.

The substitution of Se for S causes T_C to decrease rapidly (Adachi et al. 1979a, 1979b). The $Co(S_{1-x}Se_x)_2$ compounds with $x \geqslant 0.12$ become exchange-enhanced Pauli paramagnets, where the MMT appears (Adachi et al. 1979a, 1979b; Takahashi and Tano 1982; Goto et al. 1998), see fig. 128. The critical field for the MMT increases linearly with the Se concentration x. With increasing temperature, the MMT in these paramagnetic compounds becomes broad, followed by the increase of the critical field B_c and, finally, disappears at a critical temperature T_0 (with 40 K $\leqslant T_0 \leqslant$ 75 K). In addition, one also observes a T^2-dependence in the variation of the critical field B_c. The critical concentration $x_c = 0.11$, at which ferromagnetism disappeared in the $Co(S_{1-x}Se_x)_2$ compounds at $T = 0$ K, was

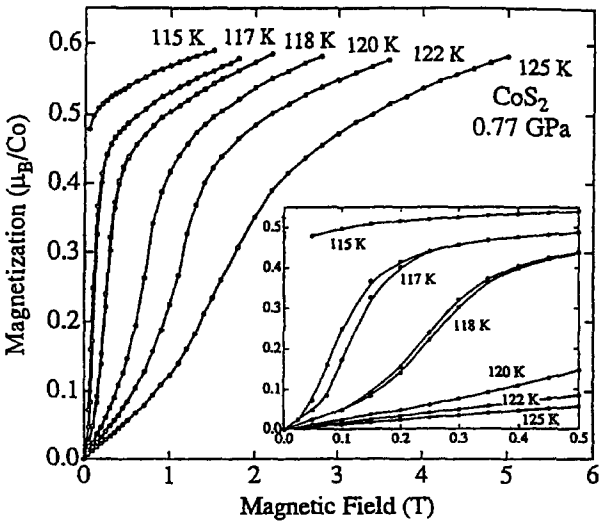


Fig. 127. Magnetization curves of CoS_2 at $p = 0.77$ GPa in the vicinity of T_C. The inset shows the magnetization curves on a finer scale. After Goto et al. (1998).

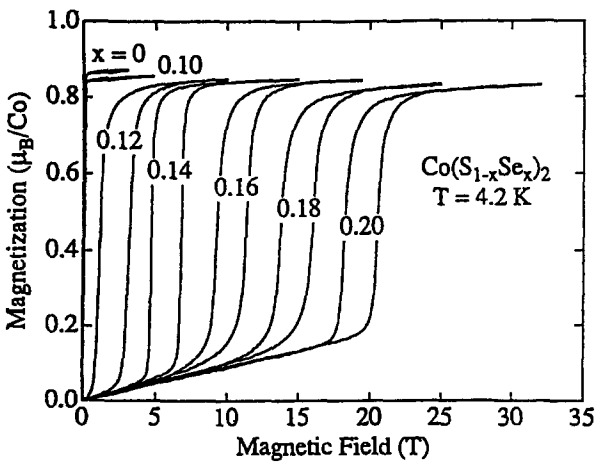


Fig. 128. Magnetization curves of several $Co(S_{1-x}Se_x)_2$ compounds measured at 4.2 K. After Goto et al. (1998).

estimated from the condition $B_c(x_c, T = 0) = 0$. The magnetic-phase diagram is plotted in fig. 129. In this figure, the concentration ($x = 0.01$) is also indicated at which the type of magnetic phase transition changes from second order to first order (Goto et al. 1998). For the compounds exhibiting a FOT, the MMT is also observed in the temperature range $T_C \leqslant T \leqslant T_0$. Upon the application of high pressure, T_C decreases. At the critical pressure p_c, the ferromagnetism disappears. Consequently, the magnetic properties under still

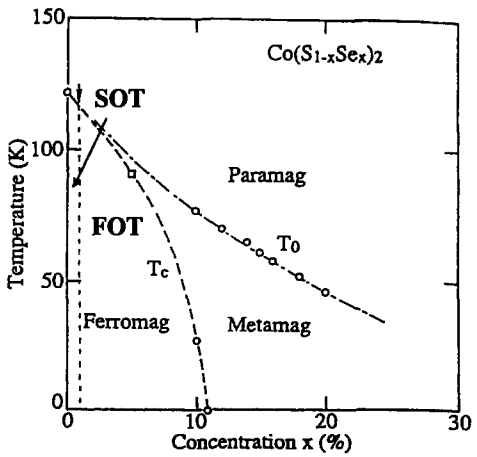


Fig. 129. Magnetic phase diagram of $Co(S_{1-x}Se_x)_2$. After Goto et al. (1998).

higher pressure ($p > p_c$), are observed to be quite similar to those of the paramagnetic compounds with $x \geqslant 0.12$.

7.5. Final remarks

In the last decade, crucial advances have been made in the studies of "itinerant-electron metamagnetism" (IEMM) in various materials. The finite-temperature magnetic properties of the Laves phase RCo_2 compounds can be understood in terms of a theory based on spin fluctuations. The same is true for the $Co(S_{1-x}Se_x)_2$ system. In some other (R,Co)-based systems, the MMT to a "high-spin state" starts from a (weakly) ferromagnetic state with rather a high ordering temperature. In this case, spin fluctuations may partly or completely be quenched. Nevertheless, in order to gain a better understanding of the mechanism, it is necessary to know more about the nature of the magnetic states. For this purpose, besides the magnetic measurements one needs other additional experiments. The quenching of spin fluctuations, in principle, can be effectively studied by means of specific-heat measurements under high-magnetic fields. However, due to the difficulties to build the calorimetric equipment for such a purpose, there are only few data on specific heat in the literature. Also magnetoresistance measurements are useful for the study of quenching of spin fluctuations. From such studies performed on the RCo_2-based compounds so far, one concludes that the MMT in these compounds can be well described as a transition from a "low-spin state" (or "spin fluctuation state") to the "high-spin state" (or "strongly ferromagnetic state"). For the itinerant-electron metamagnetic compounds mentioned in this section, unfortunately, data of this kind are still lacking.

Important theoretical progress has also been obtained for metamagnetism in multisublattice magnets. However, these improvements have been performed for multisublattice materials with different localized spin subsystems and a single (metamagnetic, or unstable) subsystem of the itinerant electrons. Again, this is sufficient for the Laves phase compounds,

but not for the Co-rich compounds. In order to solve this problem, band calculations have to be extended to describe separately the magnetic behavior for each d-subsystem. Finally, the magnetic instabilities in (R,Co) based compounds give rise to a variety of field induced multiphase transitions. The study of these phenomena, theoretical and experimental, gives the possibility of acquiring good knowledge not only of "itinerant-electron metamagnetism", but also of the important exchange coupling constants and the crystalline-field parameters.

Acknowledgements

We are grateful to Prof. Dr. T.D. Hien, Prof. Dr. J.J.M. Franse, Dr. T.N.H. Kim Ngan and all the colleagues of the Cryogenic Laboratory for collaboration and discussion over a number of years. We have also benefited by the fruitful cooperation between the Universities of Hanoi (Vietnam) and Amsterdam (The Netherlands), to which Dr. F.F. Bekker has attributed the most important contribution.

References

Acker, F., Z. Fisk, J.L. Smith and C.Y. Huang, 1981, J. Magn. Magn. Mater. **22**, 250.

Adachi, K., M. Matsui and M. Kawai, 1979a, J. Phys. Soc. Japan **46**, 1474.

Adachi, K., M. Matsui, M. Omata, J. Mollymoto, M. Motokawa and M. Date, 1979b, J. Phys. Soc. Japan **46**, 1474.

Aleksandryan, V.V., R.Z. Levitin and A.S. Markosyan, 1984a, Sov. Phys. Solid State **26**, 1165.

Aleksandryan, V.V., K.P. Belov, R.Z. Levitin, A.S. Markosyan and V.V. Snegirev, 1984b, JETP Lett. **40**, 815.

Aleksandryan, V.V., A.S. Lagutin, R.Z. Levitin, A.S. Markosyan and V.V. Snegirev, 1985, Zh. Eksp. Teor. Fiz. **89**, 271; Sov. Phys. JETP **62**, 153.

Aleksandryan, V.V., R.Z. Levitin, A.S. Markosyan, V.V. Snegirev and A.D. Shchurova, 1987, JETP **65**, 502.

Aleksandryan, V.V., N.V. Baranov, A.I. Kozlov and A.S. Markosyan, 1988, Phys. Met. Metallogr. **66**, 50.

Aoki, M., and H. Yamada, 1992, Physica B **177**, 259.

Appel, J., 1963, Philos. Mag. **8**, 1071.

Armitage, J.G.M., I.R.G. Graham, P.C. Riedi and J.S. Abell, 1990, J. Phys.: Condens. Matter **2**, 8779.

Aruga Katori, H., T. Goto, I.Yu. Gaidukova, R.Z. Levitin, A.S. Markosyan, I.S. Dubenko and A.Yu. Sokolov, 1994, J. Phys.: Condens. Matter **6**, 11119; 1994b, Sov. Phys. JETP **79**, 1994.

Ballou, R., M. Shimizu and J. Voiron, 1990, J. Magn. Magn. Mater. **84**, 23.

Ballou, R., A.S. Markosyan, I.S. Dubenko and R.Z. Levitin, 1992, J. Magn. Magn. Mater. **110**, 209.

Ballou, R., Z.M. Gamishidze, R. Lemaire, R.Z. Levitin, A.S. Markosyan and V.V. Snegirev, 1993a, Sov. Phys. JETP **75**, 1041.

Ballou, R., E. Burzo, V. Pop and A. Pentek, 1993b, J. Appl. Phys. **73**, 5693.

Baranov, N.V., and A.I. Kozlov, 1992, J. Alloys Comp. **190**, 83.

Baranov, N.V., M.I. Bartashevich, T. Goto, A.A. Yermakov, A.E. Karkin, A.N. Pirogov and A.E. Teplykh, 1997, J. Alloys Comp. **252**, 32.

Bartashevich, M.I., H. Aruga Katori, T. Goto, I. Yamamoto and M. Yamaguchi, 1994a, Physica B **201**, 135.

Bartashevich, M.I., T. Goto, R.J. Radwanski and A.V. Korolyov, 1994b, J. Magn. Magn. Mater. **131**, 61.

Bartashevich, M.I., T. Goto, A.V. Korolyov and A.S. Ermolenko, 1995, Technical Report of ISSP, University of Tokyo, No. 3088.

Bartashevich, M.I., H. Aruga Katori, T. Goto, H. Wada, T. Meada, T. Mori and M. Shiga, 1997, Physica B **229**, 315.

Béal-Monod, M.T., 1982, Physica B **109–110**, 1837.

Béal-Monod, M.T., S.-K. Ma and D.R. Fredkin, 1968, Phys. Rev. Lett. **20**, 929.

Benham, M.J., S.M. Bennington, D.K. Ross, N.F. Norens and M. Yamaguchi, 1989, Z. Phys. Chem. **163**, 283.

Berthier, Y., D. Gignoux, R. Kuentzler and A. Tari, 1986, J. Magn. Magn. Mater. **54–57**, 479.

Bloch, D., and R. Lemaire, 1970, Phys. Rev. B **2**, 2648.

Bloch, D., D.M. Edwards, M. Shimizu and J. Voiron, 1975, J. Phys. F.: Metal Phys. **5**, 1217.

Brommer, P.E., 1989, Physica B **154**, 197.

Brommer, P.E., 1991, Physica B **173**, 277.

Brommer, P.E., 1996a, J. Magn. Magn. Mater. **157/158**, 349.

Brommer, P.E., 1996b, Physica B **225**, 143.

Brommer, P.E., and J.J.M. Franse, 1990, in: Ferromagnetic Materials, Vol. 5, ed. E.P. Wohlfarth (North-Holland, Amsterdam) p. 323.

Brommer, P.E., I.S. Dubenko, J.J.M. Franse, R.Z. Levitin, A.S. Markosyan, R.J. Radwanski, V.V. Snegirev and A.Yu. Solokov, 1993, Physica B **183**, 363.

Brommer, P.E., I.S. Dubenko, J.J.M. Franse, F. Kayzel, N.P. Kolmakova, R.Z. Levitin, A.S. Markosyan and A.Yu. Sokolov, 1994, Physica A **189**, 253.

Brommer, P.E., I.S. Dubenko, J.J.M. Franse, F. Kayzel, N.P. Kolmakova, R.Z. Levitin, A.S. Markosyan and A.Yu. Sokolov, 1995, Physica B **211**, 155.

Brooks, M.S.S., and B. Johansson, 1993, in: Ferromagnetic Materials, Vol. 7, ed. K.H.J. Buschow (North-Holland, Amsterdam), Ch. 3.

Burkov, A.T., M.V. Vedernikov and E. Gratz, 1988, Solid State Commun. **67**, 1109.

Burkov, A.T., T. Nakama, T. Kohama, T. Shimogi, K. Shintani, R. Shimabukuro, K. Yagasaki and E. Gratz, 1998, J. Magn. Magn. Mater. **177–181**, 1069.

Burzo, E., and R. Lemaire, 1992, Solid State Commun. **84**, 1145.

Burzo, E., E. Gratz and V. Pop, 1994, J. Magn. Magn. Mater. **123**, 159.

Buschow, K.H.J., 1980, in: Ferromagnetic Materials, Vol. 7, ed. E.P. Wohlfarth (North-Holland, Amsterdam) p. 297.

Campbell, I.A., 1972, J. Phys. F **2**, L47.

Castets, A., D. Gignoux and B. Hennion, 1980, J. Magn. Magn. Mater. **15–18**, 375.

Clark, A., and E. Callen, 1968, J. Appl. Phys. **39**, 5972.

Colpa, J.H.P., and J.H.V.J. Brabers, 1994, Physica B **203**, 29.

Coqblin, B., J.R. Iglesias-Sicardi and R. Jullien, 1978, Contemp. Phys. **19**, 327.

Croft, M., R. Neifield, B. Qi, G. Liang, I. Perez, S. Gunapala, F. Lu, S.A. Shaheen, E.G. Spencer, N. Stoffel and M. de Boer, 1987, in: 5th Int. Conf. on Valence Fluctuations, eds S.K. Malik and L.C. Gupta (Plenum Press, New York) p. 217.

Cuong, T.D., L. Havela, V. Sechovski, A.V. Andreev, Z. Arnold, J. Kamarad and N.H. Duc, 1997, J. Alloys Comp. **262–263**, 141.

Cuong, T.D., L. Havela, V. Sechovski, Z. Arnold, J. Kamarad and N.H. Duc, 1998a, J. Magn. Magn. Mater. **177–181**, 597.

Cuong, T.D., N.H. Duc, P.E. Brommer, Z. Arnold, J. Kamarad and V. Sechovski, 1998b, J. Magn. Magn. Mater. **182**, 143.

Cyrot, M., and M. Lavagna, 1979, J. Phys. (Paris) **40**, 763.

De Chatel, P.F., and F.R. de Boer, 1970, Physica B **48**, 331.

Del Moral, A., and D. Melville, 1975, J. Phys. F.: Metal Phys. **5**, 1767.

Deportes, J., D. Gignoux and F. Givord, 1974, Phys. Status Solidi (b) **64**, 29.

Dubenko, I.S., R.Z. Levitin and A.S. Markosyan, 1992a, J. Magn. Magn. Mater. **111**, 146.

Dubenko, I.S., R.Z. Levitin, A.S. Markosyan and V.I. Silant'ev, 1992b, J. Magn. Magn. Mater. **94**, 287.

Dubenko, I.S., Gratz, E., R. Hauser, R.Z. Levitin, A. Lindbaum, A.S. Markosyan, R. Resel, V.V. Snegirev and A.Yu. Sokolov, 1993, in: Proc. Int. Meeting on Magnetoelastic Effects and Applications, Naples, Italy, 24–26 May, 1993; Elsevier Studies in Applied Electromagnetics in Materials, Vol. 4, p. 79.

Dubenko, I.S., R.Z. Levitin, A.S. Markosyan and H. Yamada, 1994a, J. Magn. Magn. Mater. **136**, 98.

Dubenko, I.S., R.Z. Levitin, A.S. Markosyan, V.V. Snegirev and A.Yu. Sokolov, 1994b, J. Magn. Magn. Mater. **135**, 326.

Dubenko, I.S., I.V. Golosovski, E. Gratz, R.Z. Levitin, A.S. Markosyan, I. Mirebeau and S.V. Sharygin, 1995, J. Magn. Magn. Mater. **150**, 304.

Duc, N.H., 1991, Phys. Status Solidi (b) **164**, 545.

Duc, N.H., 1994, J. Magn. Magn. Mater. **131**, 224.

Duc, N.H., 1996, J. Magn. Magn. Mater. **152**, 219.

Duc, N.H., 1997, in: Handbook of the Physics and Chemistry of Rare-Earths, Vol. 24, eds K.A.Gschneidner Jr. and L. Eyring (North-Holland, Amsterdam) p. 338.

Duc, N.H., and D. Givord, 1995, J. Magn. Magn. Mater. **151**, L13.

Duc, N.H., and T.K. Oanh, 1997, J. Phys.: Condens. Matter **9**, 1585.

Duc, N.H., and L.T. Tai, 1993, Phys. Status Solidi (a) **141**, K103.

Duc, N.H., T.D. Hien and J.J.M. Franse, 1985, Acta Phys. Pol. A **68**, 127.

Duc, N.H., T.D. Hien, P.E. Brommer and J.J.M. Franse, 1988a, J. Phys. F **18**, 275.

Duc, N.H., T.D. Hien and N.H. Chau, 1988b, Acta Phys. Pol. A **74**, 51.

Duc, N.H., T.D. Hien, P.E. Brommer and J.J.M. Franse, 1988c, Physica B **149**, 352.

Duc, N.H., T.D. Hien, P.P. Mai, N.H.K. Ngan, N.H. Sinh, P.E. Brommer and J.J.M. Franse, 1989, Physica B **160**, 199.

Duc, N.H., T.D. Hien and N.H. Chau, 1990, Acta Phys. Pol. A **78**, 119.

Duc, N.H., T.D. Hien, P.P. Mai and P.E. Brommer, 1991, Physica B **172**, 339.

Duc, N.H., T.D. Hien, P.E. Brommer and J.J.M. Franse, 1992a, J. Magn. Magn. Mater. **104–107**, 1252.

Duc, N.H., D. Givord, C. Lacroix and C. Pinettes, 1992b, Europhys. Lett. **20**, 47.

Duc, N.H., L.T. Tai, X. Li, F.R. de Boer and T. Goto, 1992c, in: Proc. Int. Conf. on Physics of Magnetic Materials, Beijing, p. 11.

Duc, N.H., T.D. Hien, R.Z. Levitin, A.S. Markosyan, P.E. Brommer and J.J.M. Franse, 1992d, Physica B **176**, 232.

Duc, N.H., V. Sechovski, D.T. Hung and N.H. Kim Ngan, 1992e, Physica B **179**, 111.

Duc, N.H., P.E. Brommer and J.J.M. Franse, 1993a, Physica B **191**, 239.

Duc, N.H., T.D. Hien, D. Givord, J.J.M. Franse and F.R. de Boer, 1993b, J. Magn. Magn. Mater. **124**, 305.

Duc, N.H., J. Voiron, S. Holtmeier, P. Haen and X. Li, 1993c, J. Magn. Magn. Mater. **125**, 323.

Duc, N.H., T.D. Hien, M.I. Bartashevich and T. Goto, 1994, in: Proc. Int. Conf. on Physics of Magnetic Materials, Japan, p. 363–366.

Duc, N.H., P.E. Brommer, X. Li, F.R. de Boer and J.J.M. Franse, 1995a, Physica B **212**, 83.

Duc, N.H., P.E. Brommer, F.R. Kayzel, C.V. Thang and J.J.M. Franse, 1995b, in: Proc. Int. Workshop on Materials Science, Hanoi, p. 137.

Doniach, S., 1967, Proc. Phys. Soc. **91**, 86.

Edwards, D.M., and E.P. Wohlfarth, 1968, Proc. Roy. Soc. A **303**, 127.

Endo, K., M. Iijima, A. Shinogi, T. Goto and T. Sakakibara, 1988, J. Phys. Colloq. (Paris) **49**, 265.

Ermolenko, A.S., A.V. Korolyov and A.F. Rozda, 1977, IEEE Trans. Magn. **13**, 1339.

Ermolenko, A.S., and Ye.V. Shcherbakova, 1980, Phys. Met. Metallogr. **48**, 39.

Farrell, J., and W.E. Wallace, 1966, Inorg. Chem. **5**, 105.

Franse, J.J.M., and R.J. Radwanski, 1993, in: Ferromagnetic Materials, Vol. 7, ed. K.H.J. Buschow (North-Holland, Amsterdam) p. 307.

Franse, J.J.M., T.D. Hien, N.H.K. Ngan and N.H. Duc, 1983, J. Magn. Magn. Mater. **39**, 275.

Fournier, J.M., and E. Gratz, 1993, in: Handbook of Physics and Chemistry of the Rare-Earths, Vol. 17, ed. K.A. Gschneidner Jr. (North-Holland, Amsterdam) p. 409.

Gabelko, I.L., R.Z. Levitin, A.S. Markosyan and V.V. Snegirev, 1987, Pis'ma Zh. Eksp. Teor. Fiz. **45**, 360 [JETP Lett. **45**, 459].

Ganapathy, E.V., W.E. Wallace and R.S. Craig, 1974, in: Proc. 11th Rare-Earth Conf., eds J.M. Haschke and H.A. Eick (USAEC, Oak Ridge) p. 430.

Gignoux, D., and F. Givord, 1979, J. Phys. F.: Metal Phys. **9**, 1409.

Gignoux, D., F. Givord and R. Lemaire, 1975, Phys. Rev. B **12**, 3878.

Gignoux, D., F. Givord and W.C. Koehler, 1977a, Physica B **86–88**, 165.

Gignoux, D., F. Givord and Schweizer, 1977b, J. Phys. F.: Metal Phys. **7**, 1823.

Gignoux, D., F. Givord, W.C. Koehler and R.M. Moon, 1977c, J. Magn. Magn. Mater. **5**, 1972.

Gignoux, D., F. Givord, R. Lemaire and N.V. Tinh, 1978, Inst. Phys. Conf. Ser. **37**, 300.

Givord, F., and R. Lemaire, 1971, Solid State Commun. **9**, 341.

Givord, F., and J.S. Shah, 1972, C. R. Acad. Sci. (Paris) B **274**, 923.

Givord, D., J. Laforest and R. Lemaire, 1977, Physica B **86–88**, 204.

Givord, D., J. Laforest and R. Lemaire, 1979, J. Appl. Phys. **50**, 7489.

Givord, D., J. Laforest, R. Lemaire and Q. Lu, 1983, J. Magn. Magn. Mater. **31–34**, 1991.

Golosovsky, I.V., B.E. Kvyatkovsky, S.V. Sharygin, I.S. Dubenko, R.Z. Levitin, A.S. Markosyan, E. Gratz, I. Mirebeau, I.N. Goncharenko and F. Bouree, 1997, J. Magn. Magn. Mater. **169**, 123.

Goot, A.S. van der, and K.H.J. Buschow, 1971, Phys. Status Solidi (a) **5**, 665.

Goto, T., and T. Sakakibara, 1993, Int. J. Mod. Phys. B **7**, 788.

Goto, T., K. Fukamichi, T. Sakakibara and H. Komatsu, 1989, Solid State Commun. **72**, 945.

Goto, T., T. Sakakibara, K. Murata, K. Komatsu and K. Fukamichi, 1990, J. Magn. Magn. Mater. **90–91**, 700.

Goto, T., M. Yamaguchi, T. Kobayashi and I. Yamamoto, 1991, Solid State Phys. **77**, 876.

Goto, T., H. Aruga Katori, T. Sakakibara and M. Yamaguchi, 1992, Physica B **177**, 225.

Goto, T., H. Aruga Katori, T. Sakakibara, H. Mitamura, K. Fukamichi and K. Murata, 1994a, J. Appl. Phys. **76**, 6682.

Goto, T., K. Koui, M.I. Bartashevich, H. Aruga Katori, M. Yamaguchi, I. Yamamoto and F. Sugaya, 1994b, Physica B **193**, 10.

Goto, T., M.I. Bartashevich, H. Aruga Katori, Ye.V. Shcherbakova and A.S. Ermolenko, 1995, Physica B **211**, 131.

Goto, T., Y. Shindo, S. Ogawa and T. Harada, 1997, Physica B **237–238**, 172.

Goto, T., Y. Shindo, S. Ogawa and T. Harada, 1998, J. Magn. Magn. Mater. **177–181**, 579.

Gratz, E., 1983, Solid State Commun. **48**, 825.

Gratz, E., 1992, unpublished data.

Gratz, E., and M.J. Zuckermann, 1982, in: Handbook of Physics and Chemistry of the Rare-Earths, Vol. 5, ed. K.A. Gschneidner Jr. (North-Holland, Amsterdam) p. 117.

Gratz, E., H. Sassik and H. Nowotny, 1981, J. Phys. F.: Metal Phys. **11**, 429.

Gratz, E., E. Bauer, V. Sechowsky and J. Churst, 1986, J. Magn. Magn. Mater. **54–57**, 517.

Gratz, E., N. Pillmayr, E. Bauer and G. Hilschen, 1987, J. Magn. Magn. Mater. **70**, 159.

Gratz, E., E. Bauer, R. Hauser, M. Maikis, P. Haen and A.S. Markosyan, 1993, Int. J. Mod. Phys. **7**, 366.

Gratz, E., A. Lindbaum, A.S. Markosyan, H. Mueller and A.Yu. Sokolov, 1994, J. Phys.: Condens. Matter **6**, 6699.

Gratz, E., R. Resel, A.T. Burkov, E. Bauer, A.S. Markosyan and A. Galatanu, 1995a, J. Phys.: Condens. Matter **7**, 6687.

Gratz, E., R. Hauser, A. Lindbaum, M. Maikis, R. Resel, G. Schaudy, R.Z. Levitin, A.S. Markosyan, I.S. Dubenko, A.Yu. Sokolov and S.W. Zochowski, 1995b, J. Phys.: Condens. Matter **7**, 597.

Gratz, E., R. Hauser, I.S. Dubenko and A.S. Markosyan, 1996, J. Phys.: Condens. Matter **8**, 11093.

Gschneidner Jr., K.A., and S.K. Dhar, 1984, in: Magnetic Excitations and Fluctuations, eds S.W. Lovesey, U. Balucani, F. Borsa and V. Tognetti (Springer-Verlag, Berlin) p. 177.

Gschneidner Jr., K.A., K. Ikeda, T.W.E. Tsang, O.D. McMasters, R.J. Stierman, S.S. Encker, S.E. Lambert, M.B. Maple and C. Buchal, 1985, Physica B&C **130**, 202.

Hathaway, K., and J. Cullen, 1991, J. Phys.: Condens. Matter **3**, 8911.

Hauser, R., E. Bauer, E. Gratz, M. Rotter, G. Hilscher, H. Michor and A.S. Markosyan, 1997a, Physica B **237–238**, 577.

Hauser, R., E. Bauer, E. Gratz, M. Rotter, H. Mueller, G. Hilscher, H. Michor and A.S. Markosyan, 1997b, Physica B **239**, 83.

Hauser, R., E. Bauer and E. Gratz, 1998, Phys. Rev. B **57**, 2904.

Hertel, P., J. Appel and D. Fay, 1980, Phys. Rev. B **22**, 534.

Henry, L.L., L.E. Wenger, G.D. Khattak and A. Tari, 1991, Phys. Rev. B **39**, 5972.

Hien, T.D., N.H. Duc and J.J.M. Franse, 1986, J. Magn. Magn. Mater. **54–57**, 471.

Hilscher, G., N. Pillmayr, C. Schmitzer and E. Gratz, 1988, Phys. Rev. B **37**, 3480.

Hiraka, T., and Y. Endo, 1996, J. Phys. Soc. Japan **65**, 3740.

Ho, S.C., I. Maartense and G. Williams, 1981, J. Phys. F **11**, 705.

Ido, H., H. Asano, G. Kito, N.M. Hong, G. Hilscher and R. Ballou, 1995, J. Magn. Magn. Mater. **140–144**, 955.

Iijima, M., K. Endo and G. Kido, 1989, Physica B **155**, 203.

Ikeda, K., and K.A. Gschneidner Jr., 1980, Phys. Rev. Lett. **45**, 134.

Ikeda, K., K.A. Gschneidner Jr., R.J. Steirman, T.W.E. Tsang and O.D. McMasters, 1984, Phys. Rev. B **29**, 5039.

Ikeda, K., S.K. Dhar, M. Yoshizawa and K.A. Gschneidner Jr., 1991, J. Magn. Magn. Mater. **100**, 292.

Ikonomou, P.F., and J.K. Yakinthos, 1976, Z. Phys. B **24**, 77.

Inoue, J., and M. Shimizu, 1982, J. Phys. F.: Metal Phys. **12**, 1811.

Inoue, J., and M. Shimizu, 1985, J. Phys. F.: Metal Phys. **14**, 2673.

Inoue, J., and M. Shimizu, 1988, J. Phys. F.: Metal Phys. **18**, 2487.

Ishiyama, K., K. Endo, T. Sakakibara, T. Goto, K. Sugiyama and M. Date, 1987, J. Phys. Soc. Japan **56**, 29.

Jarlborg, T., and A.J. Freeman, 1981, Phys. Rev. B **23**, 3577.

Kadowaki, K., and S.B. Woods, 1986, Solid State Commun. **58**, 507.

Klimker, H., and M. Rosen, 1976, J. Magn. Magn. Mater. **7**, 367.

Koui, K., M.I. Bartashevich, T. Goto, H. Aruga Katori and M. Yamaguchi, 1994, Physica B **201**, 143.

Kren, E., J. Schweizer and F. Tasset, 1969, Phys. Rev. B **186**, 476.

Kuentzler, R., and A. Tari, 1986, J. Magn. Magn. Mater. **61**, 29.

Lavagna, M., C. Lacroix and M. Cyrot, 1983, J. Phys. F **13**, 1007.

Lee, E.W., and F. Pourarian, 1976, Phys. Status Solidi (a) **33**, 483.

Lemaire, R., 1966, Cobalt **33**, 201.

Levitin, R.Z., and A.S. Markosyan, 1988, Sov. Phys. Usp. **31**, 730.

Levitin, R.Z., and A.S. Markosyan, 1998, J. Magn. Magn. Mater. **179–181**, 563.

Levitin, R.Z., A.S. Markosyan and V.V. Snegirev, 1982, JETP Lett. **36**, 445.

Levitin, R.Z., A.S. Markosyan and V.V. Snegirev, 1984a, Phys. Met. Metallogr. **57**, 274.

Levitin, R.Z., A.S. Markosyan and V.V. Snegirev, 1984b, Sov. Phys. Solid State **26**, 16.

Liu, J.P., F.R. de Boer, P.F. de Chatel, R. Coehoorn and K.H.J. Buschow, 1994, J. Magn. Magn. Mater. **134**, 159.

Luong, N.H., T.D. Hien and J.J.M. Franse, 1985, J. Phys. F.: Metal Phys. **15**, 1751.

Markosyan, A.S., R. Hauser, M. Galli, E. Bauer, E. Gratz, G. Hilscher, K. Kamushima and T. Goto, 1998, J. Magn. Magn. Mater. **185**, 235.

Michels, D., J. Timlin and T. Mihalisin, 1990, J. Appl. Phys. **67**, 5289.

Mills, D.L., and P. Lederer, 1966, J. Phys. Chem. Solids **27**, 1805.

Minakata, R., M. Shiga and Y. Nakamura, 1976, J. Phys. Soc. Japan **41**, 1435.

Misawa, S., 1988, Physica B **149**, 162.

Misawa, S., 1995, Physica B **211**, 158.

Mitamura, H., T. Sakakibara, T. Goto and H. Yamaguchi, 1995a, J. Magn. Magn. Mater. **140–144**, 821.

Mitamura, H., T. Sakakibara, G. Kido and T. Goto, 1995b, J. Phys. Soc. Japan **64**, 3459.

Moriya, T., 1979, J. Magn. Magn. Mater. **14**, 1.

Moriya, T., 1985, Spin Fluctuations in Itinerant Electron Magnetism, Springer Series in Solid State Sciences, Vol. 56 (Springer, Berlin).

Moriya, T., 1991, J. Magn. Magn. Mater. **100**, 261.

Muraoka, Y., M. Shiga and Y. Nakamura, 1977a, J. Phys. Soc. Japan **42**, 2067.

Muraoka, Y., M. Shiga and Y. Nakamura, 1977b, Phys. Status Solidi A **42**, 369.

Muraoka, Y., M. Shiga and Y. Nakamura, 1979, J. Phys. F **9**, 1889.

Murata, K., K. Fukamichi, T. Sakakibara, T. Goto and K. Suzuki, 1993, J. Phys.: Condens. Matter **5**, 1525 and 2583.

Murata, K., K. Fukamichi, T. Goto, H. Aruga Katori, T. Sakakibara and K. Suzuki, 1994a, Physica B **201**, 147.

Murata, K., K. Fukamichi, T. Goto, K. Suzuki and T. Sakakibara, 1994b, J. Phys.: Condens. Matter **6**, 6659.

Nordström, L., O. Eriksson, M.S.S. Brooks and B. Johansson, 1990, Phys. Rev. B **41**, 9111.

Nordström, L., M.S.S. Brooks and B. Johansson, 1992, J. Magn. Magn. Mater. **104–107**, 1378.

Ogata, H., H. Ido and H. Yamaguchi, 1993, J. Appl. Phys. **73**, 5911.

Ohkawa, F.J., 1989, Solid State Commun. **11**, 1767.

Pillmayr, N., C. Schmitzer, E. Gratz, G. Hilscher and V. Sechowsky, 1987, J. Magn. Magn. Mater. **70**, 162.

Pillmayr, N., G. Hilscher and E. Gratz, 1988, J. Phys. Colloq. (Paris) **C8**, 49 and **C49**, 273.

Pillmayr, N., G. Hilscher, M. Forsthuber and K. Yoshimura, 1990, J. Magn. Magn. Mater. **90–91**, 694.

Roeland, L.W., G.J. Cock, F.A. Muller, C.A. Moleman, K.A. McEwen, R.C. Jordan and D.W. Jones, 1975, J. Phys. F.: Metal Phys. **5**, L233.

Sakakibara, T., T. Goto, K. Yoshimura, M. Shiga and Y. Nakamura, 1986, Phys. Lett. A **117**, 243.

Sakakibara, T., T. Goto, K. Yoshimura, M. Shiga, Y. Nakamura and K. Fukamichi, 1987, J. Magn. Magn. Mater. **70**, 126.

Sakakibara, T., T. Goto and Y. Nishihara, 1988, J. Phys. Colloq. (Paris) **C8**, 263.

Sakakibara, T., T. Goto, K. Yoshimura and K. Fukamichi, 1989, Tech. Report of ISSP, Ser. A, No. 2208.

Sakakibara, T., T. Goto, K. Yoshimura and K. Fukamichi, 1990a, J. Phys. C **2**, 3381.

Sakakibara, T., T. Goto, K. Yoshimura, K. Murata and K. Fukamichi, 1990b, J. Magn. Magn. Mater. **90–91**, 131.

Sakakibara, T., H. Mitamura, G. Kido and T. Goto, 1992, Physica B **177**, 251.

Sakakibara, T., H. Mitamura and T. Goto, 1994, Physica B **201**, 127.

Sechovski, V., and L. Havela, 1988, in: Ferromagnetic Materials, Vol. 4, eds E.P. Wohlfarth and K.H.J. Buschow (North-Holland, Amsterdam) p. 309.

Schinkel, C.J., 1978, J. Phys. F.: Metal Phys. **8**, L87.

Schinkel, C.J., F.R. de Boer and B. de Hon, 1973, J. Phys. F.: Metal Phys. **3**, 1463.

Schrieffer, J.R., 1968, J. Appl. Phys. **39**, 642.

Schwarz, K., and P. Mohn, 1984, J. Phys. F.: Metal Phys. **14**, L129.

Schweiner, J., and F. Tasset, 1969, J. Less-Common Met. **18**, 245.

Shcherbakova, Y.V., and A.S. Ermolenko, 1982, Phys. Met. Metallogr. **54**, 53.

Shimizu, M., 1981, Rep. Prog. Phys. **44**, 329.

Shimizu, M., 1982, J. Phys. (Paris) **43**, 155.

Slater, J.C., and G. Koster, 1954, Phys. Rev. **94**, 1498.

Steiner, W., E. Gratz, H. Ortbauer and H.W. Cammen, 1978, J. Phys. F.: Metal Phys. **8**, 1525.

Swift, W.N., and W.E. Wallace, 1968, J. Chem. Phys. **49**, 154.

Takahashi, T., and M. Shimizu, 1965, J. Phys. Soc. Japan **20**, 26.

Takahashi, T., and M. Shimizu, 1966, J. Phys. Soc. Japan **21**, 681.

Takahashi, Y., and M. Tano, 1982, J. Phys. Soc. Japan **51**, 1792.

Tari, A., 1982, J. Magn. Magn. Mater. **30**, 209.

Tari, A., 1987, J. Magn. Magn. Mater. **69**, 247.

Terao, K., and H. Yamada, 1997, J. Phys. Soc. Japan **66**, 1063.

Tyablikov, S.V., 1967, Methods in the Quantum Theory of Magnetism (Plenum Press, New York, 1967).

Ueda, K., 1976, Solid State Commun. **19**, 965.

Voiron, J., 1973, Thesis (Grenoble).

Voiron, J., and D. Bloch, 1971, J. Phys. (Paris) **32**, 949.

Vonsovski, S., 1971, Magnetism (Nauka, Moscow).

Wada, H., K. Yoshimura, G. Kido, M. Shiga, M. Mekata and Y. Nakamura, 1988, Solid State Commun. **65**, 23.

Wada, H., M. Shiga and Y. Nakamura, 1990, J. Magn. Magn. Mater. **90–91**, 727.

Wada, H., T. Mori, M. Shiga, H. Aruga Katori, M.I. Bartashevich and T. Goto, 1994, Physica B **201**, 139.

Wohlfarth, E.P., and P. Rhodes, 1962, Philos. Mag. **7**, 1817.

Yakinthos, J.K., and J. Rossat-Mignod, 1972, Phys. Satus Solidi (b) **50**, 747.

Yamada, H., 1991, J. Phys.: Condens. Matter **3**, 4115.

Yamada, H., 1993, Phys. Rev. B **47**, 11211.

Yamada, H., and M. Aoki, 1993, in: Recent Advances in Magnetism of Transition Metal Compounds, eds A. Kotani and N. Suzuki (World-Scientific, Singapore) p. 42.

Yamada, H., and M. Shimizu, 1985, J. Phys. F: Metal Phys. **15**, L175.

Yamada, H., and M. Shimizu, 1990, J. Magn. Magn. Mater. **90–91**, 703.

Yamada, H., J. Inoue, K. Terao, S. Kanda and M. Shimizu, 1984, J. Phys. F: Metal Phys. **14**, 159.

Yamada, H., K. Terao and M. Aoki, 1998, J. Magn. Magn. Mater. **177–181**, 607.

Yamaguchi, M., H. Ikeda, T. Ohata, T. Katayama and T. Goto, 1985a, J. Less-Common Met. **106**, 165.

Yamaguchi, M., D.K. Ross, T. Goto and T. Ohta, 1985b, Z. Phys. Chem. N.F. **145**, 101.

Yamaguchi, M., T. Futakata, I. Yamamoto and T. Goto, 1992, J. Magn. Magn. Mater. **104–107**, 731.

Yamaguchi, M., I. Yamamoto, M.I. Bartashevich, H. Aruga Katori and T. Goto, 1995, J. Alloys Comp. **231**, 159.

Yoshie, H., and Y. Nakamura, 1988, J. Phys. Soc. Japan **57**, 3649.

Yoshimura, K., and Y. Nakamura, 1985, Solid State Commun. **56**, 767.

Yoshimura, K., and Y. Nakamura, 1990, J. Magn. Magn. Mater. **90–91**, 697.

Yoshimura, K., T. Shimizu, M. Takigawa, H. Yasuoka and Y. Nakamura, 1984a, J. Phys. Soc. Japan **53**, 503.

Yoshimura, K., S. Hirosawa and Y. Nakamura, 1984b, J. Phys. Soc. Japan **53**, 2120.

Yoshimura, Y., Y. Yoshimoto, M. Mekata, T. Sakakibara and T. Goto, 1987, J. Magn. Magn. Mater. **70**, 147.

Zhao, G.Z., 1994, Thesis (University of Amsterdam).

chapter 4

MAGNETOCALORIC EFFECT IN THE VICINITY OF PHASE TRANSITIONS

A.M. TISHIN

Faculty of Physics
M.V. Lomonosov Moscow State University
Moscow, 119899
Russia

Handbook of Magnetic Materials, Vol. 12
Edited by K.H.J. Buschow
© 1999 Elsevier Science B.V. All rights reserved

CONTENTS

1. Introduction 398
2. Elements of thermodynamic theory 400
   2.1. General thermodynamic formalism 400
   2.2. A simple model of a magnetic material 406
   2.3. Magnetic entropy, heat capacity and free energy 409
   2.4. Superpara- and ferromagnetic nanocomposite systems 418
   2.5. Inhomogeneous ferromagnet 422
   2.6. Magneto-elastocaloric effect 423
   2.7. MCE in the vicinity of magnetic phase transition 427
3. Methods of MCE measurements 429
   3.1. Direct methods 429
   3.2. Magnetization measurements 434
   3.3. Heat capacity measurements 435
   3.4. Other methods 436
4. Magnetocaloric effect in 3d metals, alloys and compounds 437
   4.1. Ferromagnetic 3d metals (Fe, Co, Ni) 437
   4.2. Alloys and compounds 442
   4.3. Thin films 445
5. Magnetocaloric effect in oxides 447
   5.1. Garnets 447
   5.2. Perovskites 453
   5.3. 3d oxide compounds 456
   5.4. Other oxides 459
6. Magnetocaloric effect in intermetallic compounds 460
   6.1. Rare earth–nonmagnetic element 460
   6.2. Rare earth–nickel 466
   6.3. Rare earth–iron 470
   6.4. Rare earth–cobalt 473
7. Magnetocaloric effect in rare earth metals and alloys 475
   7.1. Rare earth metals 475
   7.2. Rare earth alloys 494
8. Magnetocaloric effect in nanocomposite systems 501

9. Magnetocaloric effect in $Gd_5(Si_xGe_{1-x})_4$ alloys 504
10. Magnetocaloric effect in amorphous materials 506
11. Magnetic refrigeration 509
11.1. Passive magnetic regenerators 509
11.2. Magnetics refrigerators 510
11.3. Working materials for magnetic refrigerators 513
References 518

1. Introduction

During recent decades an essential interest in investigations of magnetothermal properties of materials was demonstrated due to their significance for the development of fundamental and applied magnetism on the whole. These phenomena have a strong influence on the character of the behavior of such fundamental physical quantities as the entropy, specific heat, and thermal conductivity, and could lead to a number of extra anomalies in the dependencies of the above mentioned material properties on temperature, magnetic field and some other external parameters.

Warburg (1881) first discovered the magnetocaloric effect (MCE) as an important manifestation of magnetothermal properties. About 120 years ago, he was the first of currently known scientists to observe heat evolution in iron under the application of a magnetic field. Soon after, Edison (1887) and Tesla (1890) suggested their thermomagnetic generators of electrical power, using materials with a sharp temperature dependence of magnetization. If the effect of the field takes place under adiabatic conditions, it can result in an increase or in a reduction of the original temperature of a magnetic material. This is a consequence of the variation, under the field, of the internal energy of the material possessing a magnetic structure.

Currently, the authors of most papers define the magnetocaloric effect as the change of the initial temperature of a magnetic material as an external magnetic field is applied under conditions of constant total entropy of the material (adiabatic magnetization). However, in our meaning the term MCE should be considered more widely. Thus, we will use it to describe processes of entropy variation of the magnetic subsystem.

MCE investigations were shown to yield the kind of information that is hard to obtain by other techniques. In recent years the interest in investigations of the MCE and the influence of the magnetic field on the entropy has become renewed for the following reasons: first, the possibility to obtain information on magnetic phase transitions, and, second, by the prospect of using some of the materials in magnetic cooling machines (magnetic refrigerators).

Up to the present, the MCE has not been reviewed completely enough anywhere. At the same time, in accordance with our estimation, about 400 papers about the MCE and related questions have been published. Some recent MCE data in lanthanide materials have been reviewed by Tishin (1997). A comprehensive review of the MCE properties of some transition metals and some alloys can be found in the papers of Kuz'min and Tishin (1991, 1993a).

This chapter presents the attempt of giving an overview of the investigations made in this field over the past years and mostly deals with MCE physics. The author gives special

emphasis to the character of the MCE behavior in different magnetic materials and comprehensively reviews the studies of this effect. This review will embrace materials with magnetic moments of either band or localized origin, and materials where the magnetic ordering can have collinear, as well as more complicated character, such as helical.

Since space does not permit to discuss the details of all questions of concern, we concentrate on the focal points giving the main theoretical concepts and experimental findings. The thermodynamic approach is the most elaborate one for understanding the observed phenomena. Also often used are Landau's theory of second-order phase transitions and mean-field approximation (MFA), proposed by Rosing (1892, 1896) and Weiss (1907). Both models well describe the behavior of a number of magnetic quantities, but are inapplicable in the vicinity of the transition point because of critical fluctuation effects. In the low temperature region the spin-wave theory is used to describe temperature dependencies of magnetization, MCE and specific heat in ferro- and antiferromagnets (Akhiezer 1961). Scaling theory is used in certain cases to describe the MCE in magnetic materials in the vicinity of the phase transition points (Mathon and Wohlfarth 1969; Stauffer 1970; and Kamilov and Aliev 1983).

A notable part of the chapter is dedicated to the description of experimental techniques used by various investigators to study MCE. Consideration is given to both quasi-stationary and pulse field setups.

For the first time a detailed discussion of experimental and theoretical studies of a great number of magnetic systems is given. The emphasis is put on understanding the physical essence of the observed phenomena. Results of calculations of the field effect on the entropy and specific heat are reported and systematized for a number of magnetic materials. Contributions to the entropy change from the exchange interaction and magnetic anisotropy are discussed. The problem of the maximum value of the effects under consideration is also addressed. It is shown, in particular, that in heavy rare earth metals the maximum MCE value at the magnetic phase transition from the ordered to the paramagnetic state can be as high as hundreds of Kelvins (e.g., in terbium it is 254 K under saturation field) and that it is proportional to the product of the transition temperature and the atomic magnetic moment (Tishin 1990a).

The magnetocaloric effect is utilized in magnetic refrigeration machines. At the beginning of the century Langevin (1905) demonstrated for the first time that the changing of a paramagnet magnetization would generally result in a reversible temperature change. The idea of utilizing reversible temperature changes in paramagnetic salts is well known to belong to Debye (1926) and Giauque (1927), over 20 years after Langevin's work appeared. The first experiments to put this idea into practice were carried out in 1933–1934 (Giauque and MacDougall 1933; de Haas et al. 1933; Kurti and Simon 1934). Investigation in the wide temperature region (from 4.2 K to room temperature and even higher) were encouraged by Brown (1976). Technologically the current interest in the MCE is connected with the real possibility to employ materials with large MCE values in the phase transition region in magnetic refrigerators (see, for example, Barclay 1994). The current extensive interest is to give birth to magnetic refrigeration as one of the most efficient methods of cooling at room temperatures and even higher. For instance, recently the Ames Laboratory (Iowa State University) and the Astronautics Corporation of America have been collaborating to create an advanced industrial prototype of a magnetic refrigerator operating in the

room temperature region (Zimm et al. 1998). In principle, such type of refrigerators could be used in hydrogen liquefiers, infrared detectors, high speed computers, SQUIDs, frozen food processing plants, large building air conditioning, motor vehicles, waste separation and treatment (see, for example, Gschneidner and Pecharsky 1997a). There is a number of surveys dealing with the problem of magnetic refrigeration. From the whole range of questions concerning this problem, we consider here only the aspect of working materials, leaving out most of the technical questions of refrigerator design and operation. Results are reported on a broad class of rare earth (and some other) materials promising from the viewpoint of magnetic refrigeration. In this part of the work the author puts accent primarily on the exploration of the physical mechanisms leading to the evolution of significant amounts of heat under a magnetic field.

2. Elements of thermodynamic theory

2.1. General thermodynamic formalism

Let us consider the general thermodynamic equations which can be used for description of magnetothermal effects in magnetic materials.

The internal energy U of the system can be written down as a function of the entropy S, the volume V and the magnetic field H:

$$U = U(S, V, H), \tag{2.1a}$$

or as a function of S, V and magnetic moment M:

$$U = U(S, V, M). \tag{2.1b}$$

Accordingly, the total differential of U can have the forms:

$$\mathrm{d}U = T\,\mathrm{d}S - p\,\mathrm{d}V - M\,\mathrm{d}H, \tag{2.2a}$$

$$\mathrm{d}U = T\,\mathrm{d}S - p\,\mathrm{d}V - H\,\mathrm{d}M, \tag{2.2b}$$

where p is the pressure, T is the absolute temperature.

Below, we will use the magnetic field H as mainly an external parameter in the free energy F and Gibbs free energy G.

The free energy F, which is a function of T, V and H is used for systems with constant volume and has the form:

$$F = U - TS \tag{2.3}$$

and its total differential has the form:

$$\mathrm{d}F = -S\,\mathrm{d}T - p\,\mathrm{d}V - M\,\mathrm{d}H. \tag{2.4}$$

The Gibbs free energy G is used for systems under constant pressure and is a function of T, p and H:

$$G = U - TS + pV - MH \tag{2.5}$$

with the total differential:

$$\mathrm{d}G = V\,\mathrm{d}p - S\,\mathrm{d}T - M\,\mathrm{d}H. \tag{2.6}$$

For F the internal parameters S, p and M (generalized thermodynamic quantities), conjugate to the external variables T, V and H, can be determined by the following equations of state:

$$S(T, H, V) = -(\partial F/\partial T)_{H,V}, \tag{2.7a}$$

$$M(T, H, V) = -(\partial F/\partial H)_{V,T}, \tag{2.7b}$$

$$p(T, H, V) = -(\partial F/\partial V)_{H,T}. \tag{2.7c}$$

Accordingly, for the Gibbs free energy the following equations are valid:

$$S(T, H, p) = -(\partial G/\partial T)_{H,p}, \tag{2.8a}$$

$$M(T, H, p) = -(\partial G/\partial H)_{T,p}, \tag{2.8b}$$

$$V(T, H, p) = -(\partial G/\partial p)_{T,H}. \tag{2.8c}$$

If the magnetic moment M is chosen in G as an external variable instead of the magnetic field H, then:

$$H = (\partial G/\partial M)_{T,p}. \tag{2.8d}$$

From eqs (2.8a) and (2.8b), (2.8a) and (2.8c) and (2.8a) and (2.8d) one can derive the Maxwell equations:

$$\left(\frac{\partial S}{\partial H}\right)_{T,p} = \left(\frac{\partial M}{\partial T}\right)_{H,p}, \tag{2.9a}$$

$$\left(\frac{\partial S}{\partial p}\right)_{T,H} = -\left(\frac{\partial V}{\partial T}\right)_{H,p}, \tag{2.9b}$$

$$\left(\frac{\partial S}{\partial M}\right)_{T,p} = -\left(\frac{\partial H}{\partial T}\right)_{M,p}. \tag{2.9c}$$

The heat capacity C at constant parameter x is defined as:

$$C_x = \left(\frac{\delta Q}{\mathrm{d}T}\right)_x. \tag{2.10}$$

When using the second law of thermodynamics

$$\mathrm{d}S = \left(\frac{\delta Q}{T}\right) \tag{2.11}$$

it can be given as:

$$C_x = T\left(\frac{\partial S}{\partial T}\right)_x. \tag{2.12}$$

The bulk thermal expansion coefficient $\alpha_T(T, H, p)$ can be defined as:

$$\alpha_T(T, H, p) = -\frac{1}{V}\left(\frac{\partial V}{\partial T}\right)_{H,p} \tag{2.13a}$$

or, using eq. (2.9b):

$$\alpha_T(T, H, p) = -\frac{1}{V}\left(\frac{\partial S}{\partial p}\right)_{T,H}. \tag{2.13b}$$

Let us consider the total entropy of the system $S(T, H, p)$. Its total differential can be written down as:

$$\mathrm{d}S = \left(\frac{\partial S}{\partial T}\right)_{H,p}\mathrm{d}T + \left(\frac{\partial S}{\partial H}\right)_{T,p}\mathrm{d}H + \left(\frac{\partial S}{\partial p}\right)_{T,H}\mathrm{d}p. \tag{2.14}$$

For an adiabatic process (where $\mathrm{d}S = 0$) one can obtain from eq. (2.14) using eqs (2.9a), (2.12) and (2.13b):

$$\frac{C_{H,p}}{T}\mathrm{d}T + \left(\frac{\partial M}{\partial T}\right)_{H,p}\mathrm{d}H - \alpha_T V\,\mathrm{d}p = 0, \tag{2.15}$$

where $C_{H,p}$ is the heat capacity under constant magnetic field and pressure.

For an adiabatic–isobaric process ($\mathrm{d}p = 0$), eq. (2.15) gives the following expression for the temperature change due to the change of the magnetic field (the magnetocaloric effect):

$$\mathrm{d}T = -\frac{T}{C_{H,p}}\left(\frac{\partial M}{\partial T}\right)_{H,p}\mathrm{d}H. \tag{2.16}$$

Let us consider the adiabatic–isochoric process ($dV = 0$). The total differential of $V(T, H, p)$ has the form:

$$dV = \alpha_T V\, dT + \left(\frac{\partial V}{\partial H}\right)_{T,p} dH - V\kappa^{-1}\, dp. \tag{2.17}$$

Here eq. (2.13b) and the expression for the bulk elastic modulus κ:

$$\frac{1}{\kappa} = -\frac{1}{V}\left(\frac{\partial V}{\partial p}\right)_{T,H} \tag{2.18}$$

were used. By means of eqs (2.15) and (2.17) the following equation can be derived for an adiabatic–isochoric process:

$$\left\{\frac{C_{H,p}}{T} - \alpha_T^2 \kappa V\right\} dT + \left[\left(\frac{\partial M}{\partial T}\right)_{H,p} - \alpha_T \kappa \left(\frac{\partial V}{\partial H}\right)_{T,p}\right] dH = 0. \tag{2.19}$$

The second term between the brackets is small and can be neglected, which leads to the equation (Kuz'min and Tishin 1992):

$$dT = -\frac{T}{C_{H,p}}\left[\left(\frac{\partial M}{\partial T}\right)_{H,p} - \alpha_T \kappa \left(\frac{\partial V}{\partial H}\right)_{T,p}\right] dH. \tag{2.20}$$

The second term in eq. (2.20) appears due to the internal magnetostriction tensions arising from the change in magnetic state of the system keeping the volume constant.

From eq. (2.14) the general expression for the temperature change dT of a magnetic material during adiabatic magnetization by a field dH under isobaric conditions can be obtained:

$$\frac{dT}{dH} = -\frac{(\partial S/\partial H)_{T,p}}{(\partial S/\partial T)_{H,p}}. \tag{2.21}$$

If the entropy change is considered as a function of T, M, and p, then its total differential can be written down as:

$$dS = \left(\frac{\partial S}{\partial T}\right)_{M,p} dT + \left(\frac{\partial S}{\partial M}\right)_{T,p} dM + \left(\frac{\partial S}{\partial p}\right)_{T,M} dp. \tag{2.22}$$

Using this equation and eqs (2.12) and (2.9c), one can obtain an expression for the temperature change caused by an adiabatic–isobaric change of magnetization:

$$dT = \frac{T}{C_{M,p}}\left(\frac{\partial H}{\partial T}\right)_{M,p} dM. \tag{2.23}$$

The finite temperature change $\Delta T = T_2 - T_1$ (where T_2 and T_1 are the final and the initial temperatures, respectively) under adiabatic magnetization can be obtained by integration of the corresponding equation eqs (2.23) or (2.16).

The thermodynamic equations obtained above are sufficiently general, since no assumptions as to the structure of the considered system were made. To obtain more concrete results one should know the form of the functions F or G of a specific system, which requires some model assumptions.

Let us consider the nonequilibrium thermodynamic potential $\Phi(T, H, M, p, V)$ in which the internal parameters M and V or p are regarded as independent variables. To obtain the equilibrium Gibbs free energy G or equilibrium free energy F one should minimize Φ with respect to M and V or M and p:

$$G(T, H, p) = \min_{M,V} \Phi(T, H, M, p, V), \tag{2.24a}$$

$$F(T, H, V) = \min_{M,p} \Phi(T, H, M, p, V). \tag{2.24b}$$

Then, with the help of the thermodynamic eqs (2.7) and (2.8) the equilibrium internal parameters of a system can be obtained. The form of the nonequilibrium potential Φ can be determined by symmetry and microscopic consideration.

It is known that in ferromagnets a second order phase transition takes place at the Curie point (T_C). Belov (1961a) adopted the Landau theory of second order phase transitions (Landau and Lifshitz 1958) to magnetic transitions. According to this theory, near the Curie point the potential Φ of a ferromagnet can be expanded in a power series of an order parameter, the latter becoming zero at the Curie point. In ferromagnets the order parameter is the magnetization and for a single domain, isotropic ferromagnet in the absence of magnetic field, the expansion takes the form:

$$\Phi = \Phi_0 + \frac{\alpha}{2} I^2 + \frac{\beta}{4} I^4 + \cdots, \tag{2.25}$$

where Φ_0 is a part of the potential not connected with the magnetization, I is the magnetization ($I = M/V$), α and β are thermodynamic coefficients.

At the Curie temperate α becomes zero and in the vicinity of the Curie temperature it can be presented as:

$$\alpha = \alpha_\Theta (T - T_C) + \cdots. \tag{2.26}$$

Above T_C $\alpha > 0$ and below T_C $\alpha < 0$. The coefficient β near T_C is not dependent on T: $\beta = \beta(T_C)$. Minimizing eq. (2.25) with respect to I, one can obtain from the equation $\partial\Phi/\partial I = 0$ the equilibrium value of spontaneous magnetization I_s:

$$I_s^2 = -\frac{\alpha}{\beta} = -\frac{\alpha_\Theta (T - T_C)}{\beta}. \tag{2.27}$$

By substitution of I_s into eq. (2.25) the equilibrium thermodynamic potential can be obtained.

For a ferromagnet in which the magnetoelastic interaction is taken into account, and which is brought into a magnetic field H, the potential Φ has the form:

$$\Phi = \Phi_0 + \frac{\alpha}{2} I^2 + \frac{\beta}{4} I^4 + \frac{1}{2} \gamma I^2 p - HI. \tag{2.28}$$

Minimization of eq. (2.28) with respect to I leads to the equation describing the magnetization near the Curie point (Belov 1961a):

$$(\alpha + \gamma p) I + \beta I^3 = H. \tag{2.29}$$

Since the condition of the Curie temperature implies vanishing of the coefficient in the first term of eq. (2.29), the displacement of T_C under pressure can be calculated by the equation:

$$\frac{\Delta T_C}{\Delta p} = -\frac{\gamma}{\alpha_\Theta}. \tag{2.30}$$

From eq. (2.29) we can calculate the derivative $(\partial H/\partial T)_I$, which after substitution into eq. (2.23) gives the values of the MCE near the Curie temperature:

$$\mathrm{d}T = \frac{\alpha_\Theta T}{C_{M,p}} \mathrm{d}I^2. \tag{2.31}$$

From eq. (2.31) it follows that the temperature change due to the change of magnetization is proportional to the squared magnetization: $\Delta T = kI^2$, where k is a coefficient of proportionality. Then from eq. (2.29) one can obtain an expression describing the MCE field dependence near the Curie temperature (Belov 1961a):

$$\frac{\alpha + \gamma p}{k^{1/2}} + \frac{\beta}{k^{3/2}} \Delta T = \frac{H}{\Delta T^{1/2}}. \tag{2.32}$$

Equations (2.16) and (2.23) obtained in this section are sufficiently general and include the contribution from paraprocesses and magnetocrystalline anisotropy. However, they are usually used for description of the MCE in the region of the paraprocess which is characterized by a simple relation between M and H. By paraprocess we mean the magnetization in the field region where the processes of domain wall displacement and magnetization vector rotation are completed and the field acts against thermal agitation and exchange interactions (in antiferromagnetic and ferrimagnetic materials). Other contributions to the MCE (such as the contribution from the magnetocrystalline anisotropy) will be discussed below.

Above we have considered the magnetocaloric effect in relation to a reversible process of magnetization. Nonreversible magnetothermal effects can arise due to such processes of magnetization as displacement of domain walls and nonreversible rotation of the saturation magnetization, or to first order magnetic phase transitions. These effects are characterized by a hysteresis in the magnetization cycle. The net magnetic work applied on the magnetic material in this case, proportional to $\oint H \, \mathrm{d}M$, is dissipated as heat which leads to the additional temperature rising.

Another source of additional heating is the Foucault currents which are induced in metals during applying of the magnetic field. According to the estimations made by Tishin (1988) in the case of rare earths this reason can give remarkable contribution (of about 0.1 K for rapid change of the field from 0 to 60 kOe) only in low temperature region. The nonreversible effects can decrease the sample cooling under adiabatic demagnetization.

2.2. *A simple model of a magnetic material*

According to the statistical theory, free energy of a system can be calculated as:

$$F = -k_B T \ln Z(x), \tag{2.33}$$

where k_B is the Boltzmann constant and $Z(x)$ is the statistical sum or partition function. Then, using eq. (2.7), one can obtain the internal parameters of the system. The partition function of the system is determined as (Smart 1966):

$$Z = \sum_n e^{-E_n/(k_B T)} = \mathrm{Sp}\left(e^{-\hat{\mathcal{H}}/(k_B T)}\right), \tag{2.34}$$

where $\hat{\mathcal{H}}$ is the Hamiltonian of the system and E_n are its eigenvalues.

Let us consider first a quantum mechanical case for a paramagnet. The Hamiltonian (for one atom) in this case has the form:

$$\hat{H} = -\hat{M}_J \vec{H}, \tag{2.35}$$

where $\vec{H}$ is the vector of magnetic field, $\hat{M}_J = g_J \mu_B \hat{J}$ the atom magnetic moment operator. The partition function for one atom is given by the equation (Smart 1966):

$$Z_J(x) = \sum_{m=-J}^{J} \exp\left[\frac{g_J \mu_B m H}{k_B T}\right] = \sum_{m=-J}^{J} \exp\left[\frac{mx}{J}\right], \tag{2.36}$$

where g_J is the g-factor of the atom, J is the total angular momentum quantum number, $m = J, J-1, \ldots, -J$, and x for a paramagnet has the form:

$$x = \frac{M_J H}{k_B T}, \tag{2.37}$$

$M_J = g\mu_B J$ is the magnetic moment of an atom.

After summation eq. (2.36) takes the form:

$$Z_J(x) = \sinh\left(\frac{2J+1}{2J}x\right) \Big/ \sinh\left(\frac{1}{2J}x\right). \tag{2.38}$$

For the system consisting of N atoms the free energy (its part related the magnetic subsystem) has the form:

$$F_M = -k_B T \ln\left(Z_J(x)\right)^N. \tag{2.39}$$

Then, the magnetic moment can be calculated by eq. (2.7b):

$$M = NM_J B_J(x), \tag{2.40}$$

where $B_J(x)$ is the Brillouin function:

$$B_J(x) = \frac{2J+1}{2J}\tanh\left(\frac{2J+1}{2J}x\right) - \frac{1}{2J}\tanh\left(\frac{x}{2J}\right). \tag{2.41}$$

For $k_B T \gg M_J H$ (or $x \ll 1$) (this case is usually realized in an experiment) $B_J(x)$ can be expanded as:

$$B_J(x) = \frac{J+1}{3J}x - \frac{[(J+1)^2 + J^2](J+1)}{90J^2}x^3 + \cdots. \tag{2.42}$$

So, in the case of $x \ll 1$, eq. (2.38) leads to the Curie law:

$$M = \frac{C_J}{T}H, \tag{2.43}$$

where $C_J = N\mu_B^2 g_J^2 J(J+1)/3k_B$ is the Curie constant.

From eq. (2.16) the MCE of a paramagnet can be obtained:

$$\mathrm{d}T = \frac{T}{2C_{H,p}C_J}\delta\left(M^2\right)_{T,p}, \tag{2.44}$$

where $\delta(M^2)_{T,p} = (\partial M^2/\partial H)_{T,p}\,\mathrm{d}H$ is the isothermobaric variation of squared magnetization.

The Hamiltonian of an isotropic ferromagnet has the form:

$$\hat{\mathcal{H}} = -\sum_{i>j}\mathcal{I}_{ij}\left(\hat{J}_i\hat{J}_j\right) - \sum_i \hat{M}_{i,j}\vec{H}, \tag{2.45}$$

where $\mathcal{I}_{ij}$ is the exchange integral for the interaction between the i and j ions, J_i is the total angular momentum operator of the ion. In the mean field approximation (MFA) eq. (2.45) becomes:

$$\hat{\mathcal{H}} = -\sum_j \mathcal{I}_{\mathrm{ex}} z J\left(\hat{J}_j\vec{n}\right) - \sum_i \hat{M}_{ji}\vec{H}, \tag{2.46}$$

where z is the number of the nearest neighbor magnetic ions, J is the quantum number of the total angular momentum, $\vec{n}$ is the unit vector determining the orientation of the total magnetic moment of the ion, $\mathcal{I}_{\mathrm{ex}}$ is the exchange integral (it is supposed in MFA that the exchange interaction for every pair of the nearest neighbors has the same value $\mathcal{I}_{\mathrm{ex}}$). In MFA the external magnetic field in eq. (2.36) should be replaced by the sum (Smart 1966):

$$H + H_{\mathrm{m}} = H + wM, \tag{2.47}$$

where $H_m = wM$ is the molecular field, w is the molecular field coefficient, related with the exchange integral. Equations (2.38)–(2.42) are valid in this case x takes the form:

$$x = \frac{M_J(H + wM)}{k_B T}. \tag{2.48}$$

The field and temperature dependences of M can be obtained by simultaneous solution of eqs (2.40) and (2.48).

In the absence of magnetic field for $T > T_C$ the equations have only one stable solution $M_s = 0$. When the temperature is less and/or close to the T_C a stable nonzero solution appears, corresponding to the spontaneous magnetic moment:

$$M_s^2 = M_{s0}^2 \frac{10(J+1)^2}{3((J+1)^2 + J^2)} \left(1 - \frac{T}{T_C}\right), \tag{2.49}$$

where $M_{s0} = NM_J$ is the spontaneous magnetic moment at $T = 0$ K.

In the paramagnetic region, where $x \ll 1$, only first term in eq. (2.42) may be taken into account and the magnetization equation takes the form of the Curie–Weiss law:

$$M = \frac{C_J H}{T - T_C}, \tag{2.50}$$

where T_C is the Curie temperature:

$$T_C = \frac{NM_{eff}^2 w}{3k_B} = \frac{2(J+1)}{3Jk_B} z\mathcal{I}_{ex}. \tag{2.51}$$

$M_{eff} = g_J(J(J+1))^{1/2}\mu_B$ is the effective magnetic moment of an atom. Using eq. (2.16), one can obtain for MCE of a ferromagnet in the paramagnetic region ($T > T_C$) the equation which has the same form as eq. (2.44).

For $T < T_C$ and nonzero magnetic field analysis of eqs (2.40) and (2.48) is substantially complicated. For $x \ll 1$ the following expression for MCE was obtained (Kuz'min and Tishin 1992):

$$dT = \frac{T_C}{2C_{H,p}C_J} \delta(M^2)_{T,p}. \tag{2.52}$$

In the classical case a magnetic material is regarded as consisting of particles with a magnetic moment μ, which can have an arbitrary orientation in space. The magnetic moment of such a system is given by the formula (Smart 1966):

$$M = N\mu L(x), \tag{2.53}$$

where

$$x = \mu H/(k_B T) \tag{2.54}$$

for paramagnets;

$$x = \mu(H + wM)/(k_B T) \tag{2.55}$$

for ferromagnets, and

$$L(x) = \coth x - \frac{1}{x} \tag{2.56}$$

is the Langevin function. For $x \ll 1$ $L(x)$ can be expanded as:

$$L(x) = \frac{x}{3} - \frac{x^3}{45} - \cdots . \tag{2.57}$$

Equations (2.43), (2.44), (2.50), (2.52) in this case are valid with the Curie constant:

$$C_J = \frac{N\mu^2}{3k_B} \tag{2.58}$$

and the Curie temperature:

$$T_C = \frac{N\mu^2 w}{3k_B}. \tag{2.59}$$

2.3. Magnetic entropy, heat capacity and free energy

An important characteristic of a magnetic material is the entropy of its magnetic subsystem S_M (magnetic entropy). It can be changed by variation of the magnetic field, temperature and others thermodynamic parameters. In the most of works available in literature and concerning magnetothermal properties, the isothermal variation of magnetic entropy, ΔS_M, induced by the magnetic field change is considered. S_M and ΔS_M are closely related with MCE value and magnetic contribution to the heat capacity. ΔS_M is also used to determine the characteristics of magnetic refrigerators, such as the refrigerant capacity (see section 11).

The total entropy of a magnetic material can be presented as (Tishin 1990a):

$$S(H, T, p) = S_M(H, T, p) + S_L(T, p) + S_e(T, p), \tag{2.60}$$

where S_M is the magnetic entropy, S_L is the entropy of the lattice subsystem and S_e is the entropy of conduction electron subsystem. This formula is correct for rare earth magnetic materials, but in the case of intermetallic and 3d magnetic materials 3d-electrons form the magnetic moment having an itinerant nature and their contribution to the conductivity is comparable with p- and s-electron contributions. Separation, for example, of the lattice entropy in this case is possible only if electron–phonon interaction is not taken into account. In eq. (2.60) it is assumed that S_e and S_L do not depend on a magnetic field.

The lattice entropy can be calculated by Debye interpolation formula:

$$S_{\mathrm{L}} = R\left[-3\ln\left(1 - \mathrm{e}^{T_{\mathrm{D}}/T}\right) + 12\left(\frac{T}{T_{\mathrm{D}}}\right)^3 \int_0^{T_{\mathrm{D}}/T} \frac{x^3\,\mathrm{d}x}{\mathrm{e}^x - 1}\right], \tag{2.61}$$

where R is the gas constant, T_{D} is the Debye temperature. The calculations by eq. (2.61) show that S_{L} decreases when T_{D} increases.

The electron entropy can be obtained by the standard relation:

$$S_{\mathrm{e}} = a_{\mathrm{e}} T, \tag{2.62}$$

where a_{e} is the electronic heat capacity coefficient.

As it follows from eq. (2.60), the total heat capacity of the magnetic material has the form:

$$C = C_M + C_{\mathrm{L}} + C_{\mathrm{e}}, \tag{2.63}$$

where C_M, C_{L} and C_{e} are the magnetic, lattice and electron contributions, respectively.

The heat capacity can be calculated using eq. (2.12). The lattice heat capacity under constant pressure C_{L} for temperatures substantially lower than T_{D} has the form:

$$C_{\mathrm{L}} = \frac{12\pi^4}{5} N k_{\mathrm{B}} \left(\frac{T}{T_{\mathrm{D}}}\right)^3. \tag{2.64}$$

It should be noted that difference between the heat capacity at constant pressure C_p and at constant volume C_V is given by the well known equation:

$$C_p - C_V = \frac{9\alpha_T^2}{\kappa} VT \tag{2.65}$$

and for solids below room temperature it is small and usually may be neglected.

The electronic heat capacity C_{e} at constant pressure is defined as:

$$C_{\mathrm{e}} = a_{\mathrm{e}} T. \tag{2.66}$$

As one can see from eq. (2.16), the contributions to the total heat capacity from the lattice and conduction electron subsystems act as an additional heat load, reducing MCE.

The magnetic entropy S_M of a spin subsystem is related to the free energy of the magnetic subsystem by eq. (7a). Using eq. (2.39) one can obtain (Smart 1966):

$$S_M(T, H) = N k_{\mathrm{B}} \left[\ln \frac{\sinh\left(\frac{2J+1}{2J} x\right)}{\sinh\left(\frac{1}{2J} x\right)} - x B_J(x) \right]. \tag{2.67}$$

For $x \ll 1$ (high temperature, low field) the statistical sum $(Z_J(x))^N$ in eq. (2.39) can be expanded in a power series of x, which leads to the following formula for S_M of a paramagnet (Vonsovskii 1974):

$$S_M(T, H) = Nk_B\left[\ln(2J+1) - \frac{1}{2}\frac{C_J H^2}{T^2}\right], \tag{2.68}$$

where C_J is the Curie constant.

For a ferromagnet above the Curie temperature the analogous equation is valid:

$$S_M(T, H) = Nk_B\left[\ln(2J+1) - \frac{1}{2}\frac{C_J H^2}{(T-T_C)^2}\right]. \tag{2.69}$$

In completely disordered state ($H = 0$, $T \to \infty$) the magnetic entropy in a system with localized magnetic moments reaches its maximum value which, according to eq. (2.68) and (2.69), is equal to:

$$S_M = Nk_B \ln(2J+1) \equiv R\ln(2J+1). \tag{2.70}$$

The magnitude of the magnetic entropy change ΔS_M (as well as the total entropy change ΔS) with the change of magnetic field $\Delta H = H_2 - H_1$ can be calculated from the Maxwell relation (2.9a) on the basis of magnetization data as:

$$\Delta S_M = S_M(H_2, T) - S_M(H_1, T) = \int_{H_1}^{H_2}\left(\frac{\partial M(H,T)}{\partial T}\right)_H \mathrm{d}H. \tag{2.71}$$

Equations (2.71), (2.43) and (2.50) give for a paramagnet and a ferromagnet above T_C, respectively:

$$\Delta S_M = -\frac{1}{2}\frac{C_J \Delta(H)^2}{T^2}, \tag{2.72}$$

$$\Delta S_M = -\frac{1}{2}\frac{C_J \Delta(H)^2}{(T-T_C)^2}, \tag{2.73}$$

where $\Delta(H)^2 = H_2^2 - H_1^2$. As one can see from eqs (2.72), (2.73) large heat values of ΔS_M are expected in magnetic materials with large M_{eff} and in a temperature range close to 0 K for paramagnets, and close to T_C for ferromagnets.

Oesterreicher and Parker (1984) in the framework of MFA obtained for the field dependence of ΔS_M of a ferromagnet in the vicinity of T_C the following expression:

$$\Delta S_M = -1.07\, R\left(\frac{g_J \mu_B J H}{k_B T_C}\right)^{2/3}, \tag{2.74}$$

where R is the gas constant. This equation yields the field dependence of the MCE near T_C as: $\Delta T \sim H^{2/3}$ (see eq. (2.77) below).

For the entropy change due to the field change from zero to H, we have:

$$\Delta S_M = S_M(H, T) - S_M(0, T) = S(H, T) - S(0, T) = \Delta S \tag{2.75}$$

with $H_1 = 0$ in eq. (2.71). In this formula the isothermal contributions ΔS_e and ΔS_L in the isothermal change of the total entropy ΔS are neglected.

The magnetic entropies $S_M(H, T)$ ($H \neq 0$) and $S_M(0, T)$ ($H = 0$) can be calculated on the basis of eq. (2.12) as:

$$S_M(H, T) = \int_0^T \frac{C_M(H, T)}{T} \, dT, \tag{2.76}$$

where $C_M(H, T)$ is the magnetic heat capacity which may be determined with the help of eqs (2.63), (2.64) and (2.66).

Another method for the evaluation of ΔS_M is based on the fact that the temperature dependence of the total entropy in the presence of a magnetic field $S(H, T)$ is shifted on the temperature axis relative to the zero-field total entropy $S(0, T)$ to the higher temperature region by the value of MCE for the magnetic material under adiabatic conditions. The $S(0, T)$ dependence can be determined on the basis of total heat capacity data by an equation analogous to (2.76). Then ΔS_M is calculated as the difference between $S(H, T)$ and $S(0, T)$ (other field-dependent contributions less than S_M contribution are not taken into account). The method requires experimentally measured $\Delta T(H, T)$ dependences and does not need experimental $C(H, T)$ dependences. It was used, for example, to evaluate ΔS_M in Gd (Brown 1976; Tishin 1990b).

Let us consider as an example the ferromagnetic compound EuS. Hashimoto et al. (1981) calculated the total temperature and field dependences of its entropy. First, on the basis of eq. (2.71) the magnetic entropy change ΔS_M, induced by various ΔH, was calculated. The necessary data on magnetization was determined by MFA for $T_C = 13$ K and $J = 7/2$. Then, using the heat capacity measurements of Moruzzi and Teaney (1963) and eq. (2.76), Hashimoto et al. (1981) calculated $S_M(0, T)$ and $S_M(H, T)$. The lattice entropy was determined by eq. (2.61), which allowed to evaluate the total entropy $S = S_M + S_L$. The results are shown in fig. 2.1. As one can see from fig. 2.1(b), $S_M(0, T)$ is saturated at high temperatures well above T_C.

The infinitesimal change dT of the sample induced by the adiabatic change of magnetic field is related with the infinitesimal total entropy change dS by the relation:

$$dT = -\frac{T \, dS_M}{C_{p,H}}. \tag{2.77a}$$

It can be derived with the help of eqs (2.12) and (2.14) for adiabatic–isobaric process. To obtain the magnetocaloric effect ΔT (the finite temperature change) one should integrate eq. (2.77a). This task is quite difficult because in general case all quantities are field and/or temperature dependent. In supposition that $C_{p,H}$ does not depend on magnetic field

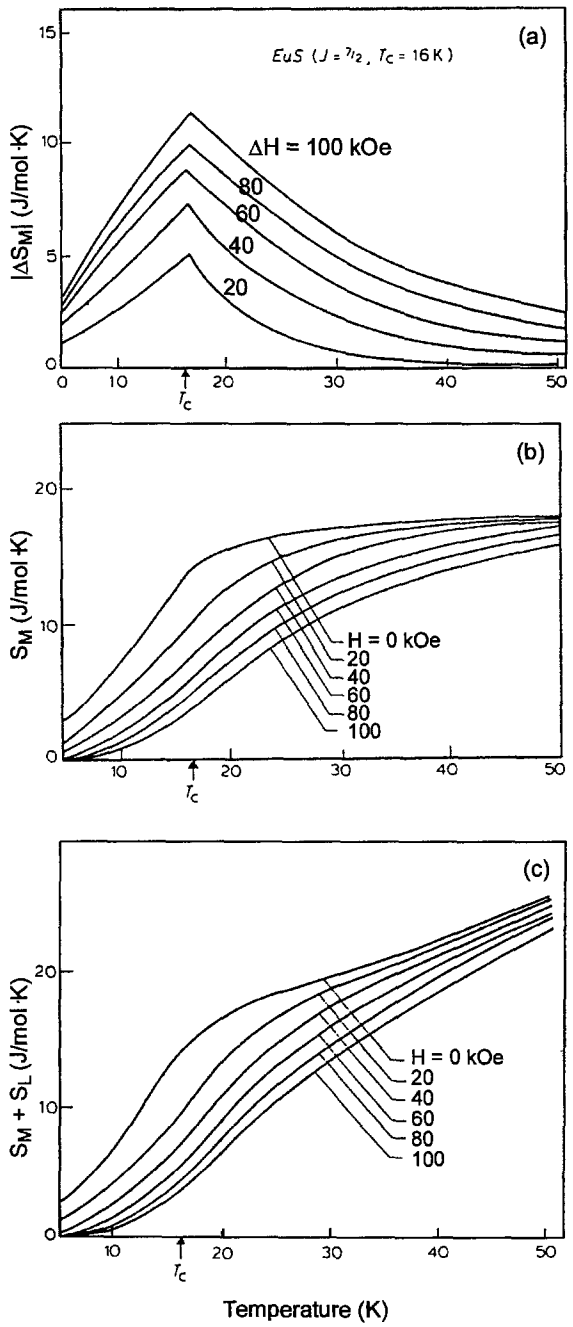


Fig. 2.1. The temperature dependences of: (a) the magnetic entropy change $\Delta S_M(T, H)$ induced by the magnetic field change ΔH; (b) the calculated magnetic entropy $S_M(T, H)$; (c) the total entropy $S(T, H) = S_M + S_L$ for EuS (Hashimoto et al. 1981).

and $\Delta S/C_{p,H}$ is small, the following equation relating ΔT and corresponding magnetic entropy change ΔS_M can be derived:

$$\Delta T = -\frac{T\Delta S_M}{C_{p,H}}. \tag{2.77b}$$

As was noted by Tishin (1997), the suppositions made above are valid only in the region far from the transition point and/or in relatively weak fields.

Druzhinin et al. (1975, 1977, 1979) took into account in Hamiltonian (2.45) the contribution from the one-ion hexagonal magnetocrystalline anisotropy in the form:

$$\hat{H}_a = -\sum_i \left(a\hat{J}_z^2 + b\hat{J}_z^4 + c\hat{J}_z^6 + \frac{d}{2}(\hat{J}_+^6 - \hat{J}_-^6) \right), \tag{2.78}$$

where the coefficients a, b, c, d are related to the crystal field coefficients A_l^m (Taylor and Darby 1972). The magnetic entropy S_M was determined by the Boltzmann equation:

$$S_M = -k_B N \sum_n \frac{\exp(-E_n/(k_B T))}{Z} \ln\left[\frac{\exp(-E_n/(k_B T))}{Z}\right]. \tag{2.79}$$

The $S_M(T)$ dependences were calculated for the case of $H = 0$ for Tb and Dy (Druzhinin et al. 1977). The results show some better agreement with experimental data in comparison with calculations made on the basis of isotropic MFA (see Hamiltonian (2.45)). The experimental $S_M(T)$ dependences were obtained from magnetization data by the equation:

$$S_M(T) = \int_0^{I_s(0)} \left(\frac{\partial H}{\partial T}\right)_I \mathrm{d}I - \int_0^{I_s(T)} \left(\frac{\partial H}{\partial T}\right)_I \mathrm{d}I, \tag{2.80}$$

where the first term is the magnetic contribution for $T > T_C$, equal to $k_B N \ln(2J + 1)$.

Bennett et al. (1993) considered theoretically the dependence of magnetic entropy of a ferromagnet with an axial anisotropy (the first term in the Hamiltonian (2.78)) on the magnetic field. The total Hamiltonian had the form:

$$\hat{\mathcal{H}} = -\sum_{i>j} \mathcal{I}_{ij}\hat{s}_i\hat{s}_j - \mu_B \sum_i (\hat{s}_i \vec{H} + a\hat{s}_{zi}^2), \tag{2.81}$$

where $\hat{s}_i$ is the spin angular momentum operator and the magnetic field is directed along the z axis.

In this case for $a > 0$ the preferred directions of the spins are $\pm z$ and for $a < 0$ they lie in the x–y plane. The magnetic moment was calculated by the Monte Carlo method for a $20 \times 20 \times 20$ fcc lattice using Hamiltonian (2.81), and ΔS_M was obtained by eq. (2.71) with $H_1 = 0$ and $H_2 = 10$ kOe. The calculations showed that for $a > 0$ increase of the anisotropy coefficient a lead to a sharpening and increase of ΔS_M peak height in the vicinity of T_C, but in the rest temperature range the curves were effectively identical. For

$a < 0$ ΔS_M essentially increased near T_C and decreased above T_C in the paramagnetic region with increasing of a in the absolute value.

For first-order magnetic phase transitions the magnetic Clausius–Clapeyron equation is valid:

$$\frac{dH}{dT} = -\frac{\Delta S_M}{\Delta M}, \tag{2.82}$$

where $\Delta S_M = S_{M(2)} - S_{M(1)}$ and $\Delta M = M_2 - M_1$ are the differences in magnetic part of the entropy and the magnetic moment between the magnetic states 2 and 1 at the temperature of the transition. This equation makes it possible to calculate the entropy change (and consequently, MCE) at the transition on the basis of magnetization data and the magnetic phase diagram H–T. From eqs (2.77), (2.82) one can obtain the formula for the magnetocaloric effect at the first-order transition (see, for example, Tishin 1994):

$$\Delta T = \frac{T}{C_{p,H}}\left(\frac{\partial H}{\partial T}\right)\Delta M. \tag{2.83}$$

In the classical limit the partition function, magnetic free energy and entropy of the system consisting of N particles with magnetic moments μ have the form (see McMichael et al. 1992):

$$Z_\infty(x) = 4\pi\,\frac{\sinh x}{x}, \tag{2.84}$$

$$F = -k_B T \ln\left(Z_\infty(x)\right)^N, \tag{2.85}$$

$$\begin{aligned} S_M &= Nk_B\left[\ln\left(4\pi\,\frac{\sinh x}{x}\right) - x\ln(x)\right] \\ &= Nk_B\left[1 - x\coth x + \ln\left(4\pi\,\frac{\sinh x}{x}\right)\right], \end{aligned} \tag{2.86}$$

where x is determined by eqs (2.54) and (2.55).

The magnetic entropy change under magnetization in magnetic fields from H_1 to H_2 can be calculated by the formulae, analogous to eqs (2.72) and (2.73) (see also eq. (2.58) for the Curie constant):

$$\Delta S_M = \int_{H_1}^{H_2}\left(\frac{\partial M}{\partial T}\right)_H dH = -\frac{N\mu^2}{6k_B}\,\frac{\Delta(H)^2}{T^2} \tag{2.87}$$

for a paramagnet; and

$$\Delta S_M = -\frac{N\mu^2}{6k_B}\,\frac{\Delta(H)^2}{(T - T_C)^2} \tag{2.88}$$

for a ferromagnet at $T > T_C$.

A more general expression for ΔS_M for a magnetic field increasing from zero to H in the classical limit has the form (see McMichael et al. 1992):

$$\Delta S_M = S_M(T, H) - S_M(T, 0) = Nk_B\left[1 - x\coth x + \ln\frac{\sinh x}{x}\right]. \tag{2.89}$$

In ferromagnets the magnetic entropy change due to the occurrence of the spontaneous magnetization below T_C in the absence of a magnetic field can be described in the framework of the Landau theory of the second-order phase transitions (Landau 1958). As it was shown in section 2.1, the spontaneous magnetization is determined by eq. (2.27). Substituting eq. (2.27) into eq. (2.25) one can obtain the equilibrium thermodynamic potential Φ and then, using equation $S = -\partial\Phi/\partial T$ the following formula (Belov 1961a):

$$\Delta S_M = -\frac{\alpha_\Theta}{2} I_s^2 = -\frac{(\alpha_\Theta)^2}{2\beta}(T - T_C). \tag{2.90}$$

The change in magnetic heat capacity, related to the change of magnetic entropy can be obtained by eq. (2.12), which gives:

$$\Delta C_M = T\frac{\partial \Delta S_M}{\partial T}. \tag{2.91}$$

From eqs (2.90), (2.91) it follows, that in the framework of the Landau theory the heat capacity anomaly ΔC_M at the Curie point in a ferromagnet has the form (Belov 1961a):

$$\Delta C_M = T\alpha_\Theta \frac{\partial(I_s^2)}{\partial T} = T\frac{(\alpha_\Theta)^2}{2\beta}. \tag{2.92}$$

The mean field approximation predicts the heat capacity anomaly as (Smart 1966):

$$\Delta C_M = -\frac{1}{2} w \frac{\mathrm{d}(I_s^2)}{\mathrm{d}T}. \tag{2.93}$$

Using eq. (2.49) for M_S, one can obtain:

$$\Delta C_M = k_B N \frac{5(J+1)}{J^2 + (J+1)^2}. \tag{2.94}$$

Calculations made by means of eq. (2.94) show that the maximum value of ΔC_M per atom is $5k_B/2$ (Foldeaki et al. 1995).

The heat capacity anomaly can also be calculated from the magnetization data by using the thermodynamic equation:

$$\Delta C_M = C_H - C_M = -T\left(\frac{\partial H}{\partial T}\right)_M\left(\frac{\partial M}{\partial T}\right)_H = T\left(\frac{\partial M}{\partial T}\right)_H^2\left(\frac{\partial H}{\partial M}\right)_T, \tag{2.95}$$

where C_H and C_M are the heat capacities at constant magnetic field and magnetic moment, respectively.

Kohlhaas et al. (1966) have shown, that the influence of magnetic field on the heat capacity can be determined by means of the relation:

$$C_H(T, H) = C_H(T_0, 0)\,\frac{T}{T_0}\left[1 - \frac{\partial \Delta T}{\partial T}\right], \tag{2.96a}$$

where $\Delta T = T - T_0$ is the MCE caused by the magnetic field change from H_0 to H. Equation (2.96a) allows to obtain the heat capacity in a magnetic field on the basis of zero-field heat capacity and MCE data. However, the formula presented by Kohlhaas et al. (1966) can not be used for real calculations due to the fact that the (H, T) coordinates of a point of calculation of the derivation of the MCE are unknown.

The approach, analogous to that proposed by Kohlhaas et al. (1966) (based on the consideration of reversible closed thermodynamic cycle), was used by Tishin et al. (1999) to investigate the magnetic-field and temperature dependences of ΔT in the vicinity of magnetic phase transitions. It was shown that in this region the MCE can be described by the following equation:

$$\Delta T(T_0, H) = -T_0\left[\Delta C(T, H) - \frac{\partial \Delta T(T_0, H)}{\partial T}\,\frac{C(T, H)}{C(T_0, H)}\right], \tag{2.96b}$$

where

$$\Delta C(T, H) = \frac{C(T_0, 0) - C(T, H)}{C(T_0, 0)},$$

and T_0 and T are the initial and final temperatures, respectively. It follows from eq. (2.96b) that at the temperature $T_M(H)$, where the peak (maximum or minimum) MCE occurs (here $\partial \Delta T/\partial T = 0$), the heat capacity of a magnetic material is not affected by the magnetic field. This temperature lies higher than the temperature of the zero magnetic field heat capacity peak and approaches the magnetic ordering temperature when the magnetic field decreases. According to the consideration of Tishin et al. (1999), one would also expect in a ferromagnet the caret-like shape of MCE temperature dependence with a single maximum near the magnetic ordering temperature. A simple antiferromagnetic material should exhibit a reverse caret-like behavior with a single minimum for weak magnetic fields not high enough to quench antiferromagnetism and convert it to a field induced ferromagnetism. The experimental measurements of the specific heat and MCE of high purity Gd, Dy, GdPd and $(Dy_{0.25}Er_{0.75})Al_2$ made in the work of Tishin et al. (1999) confirmed the conclusions derived from the theoretical model.

The magnetization data also can be used for the calculation of the free energy change arising from the magnetic ordering by the expression (Ponomarev and Moreva 1975):

$$\Delta F(T) = -\int_0^{T_c}\left[\int_0^{I_s(T')}\left(\frac{\mathrm{d}H}{\mathrm{d}T}\right)_I \mathrm{d}I\right]\mathrm{d}T'. \tag{2.97}$$

2.4. *Superpara- and ferromagnetic nanocomposite systems*

The enhancement of MCE in nanocomposite magnetic materials was discussed by Kokorin et al. (1984), Bennett et al. (1992), McMichael et al. (1992, 1993a, 1993b), Shull et al. (1993), Shull (1993a, 1993b), Shao et al. (1996a, 1996b), Chen et al. (1994, 1995).

In the works of McMichael et al. (1992) and Shull (1993a, 1993b) a superparamagnetic system was taken to consist of monodispersed and noninteracting magnetic clusters uniformly dispersed in a nonmagnetic matrix. Each cluster contains certain number of magnetic atoms. Such a system can be described by the mean field approximation in the classical limit.

The magnetic entropy change of a classical system due to the change of external magnetic field from zero to H can be calculated by eq. (2.89) and for weak fields and high temperatures ($x \ll 1$) by eq. (2.87):

$$\Delta S_M = -\frac{N\mu^2}{6k_B}\frac{H^2}{T^2}, \tag{2.98}$$

where N is the number of magnetic moments in the system and μ is the size of magnetic moment. As it is seen from eq. (2.98), ΔS_M (and consequently MCE) can be made larger if μ is made larger and N is simultaneously made smaller (to keep the saturation magnetic moment $M_0 = N\mu$ constant), because of the squared dependence of ΔS_M on μ and only a linear dependence on N. So, for a superparamagnet one can write (Shull 1993a):

$$\Delta S_M = -\frac{n((N/n)\mu)^2}{6k_B}\frac{H^2}{T^2}, \tag{2.99}$$

where n is the number of clusters and $(N/n)\mu = \mu_c$ is the magnetic moment of the cluster. The factor $n((N/n)\mu)^2$ in eq. (2.99) may be much larger than $N\mu^2$ in eq. (2.98).

The limit of the MCE enhancement follows from eq. (2.89), according to which ΔS_M will decrease at high x, and has a maximum at (McMichael et al. 1992):

$$x_{max} = \frac{\mu_c H}{k_B T} \approx 3.5, \tag{2.100}$$

where ΔS_M is given by:

$$\Delta S_M = -0.272\frac{M_0 H}{T}. \tag{2.101}$$

Equation (2.100) determines an optimum cluster size for given H and T.

By means of eq. (2.71), integrating from zero to H and from $T = 0$ to $T = \infty$ (where $M = 0$), McMichael et al. (1992) derived a sum rule:

$$\int_0^\infty \Delta S_M \, dT = -M_0 H. \tag{2.102}$$

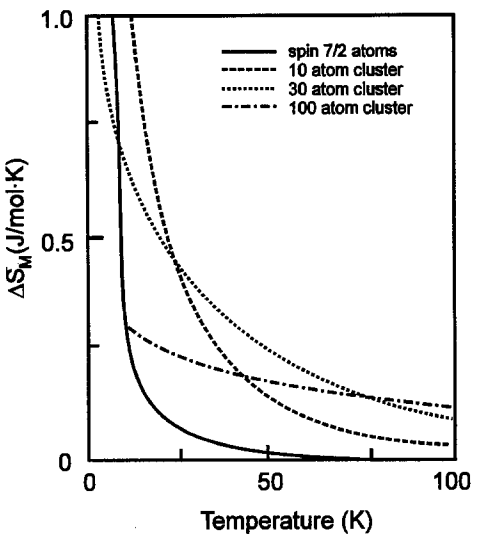


Fig. 2.2. Calculated magnetic entropy change induced by the removal of a magnetic field of 10 kOe for systems with different arrangements of 7/2 spin atoms (Shull et al. 1993).

Equation (2.102) determines the form of the $\Delta S_M(T)$ curve and implies that for materials with the same saturation magnetic moment M_0 those with higher ΔS_M at a particular temperature will have lower ΔS_M in the rest of the temperature range.

McMichael et al. (1992) calculated the magnetic entropy change due to removal of a magnetic field of 10 kOe for different arrangements of Gd atoms (spin equal to 7/2). For the calculations the mean field quantum mechanical expression (see eq. (2.67)) was used. In fig. 2.2 the results for systems consisting of individual atoms and of magnetic clusters of various sizes (10, 30, and 100 atoms) are presented. The accuracy of the calculations is confirmed by the closeness of the calculated curve for the individual atoms to the experimental one measured on a gadolinium gallium garnet (Shull et al. 1993). One can see an obvious enhancement of ΔS_M at high temperatures in clustered systems. The behavior of $\Delta S_M(T)$ is in accordance with the sum rule (2.102).

Equation (2.99) was obtained for the case of cluster magnetic moments independent of the temperature. If $\mu_c = \mu_c(T)$, eq. (2.99) becomes (Kokorin et al. 1984):

$$\Delta S_M = -\frac{n\mu_c^2 H^2}{6k_B T^2}\left(1 - \frac{T}{\mu_c}\frac{\partial \mu_c}{\partial T}\right). \tag{2.103}$$

The second term in the parentheses in eq. (2.103) can have a substantial value in the vicinity of the Curie point of magnetic cluster materials and lead to an additional contribution to ΔS_M in this region.

As follows from eq. (2.100) there is an optimum cluster size for a given H and T, which corresponds to a maximum value of ΔS_M. For the typical values $T = 300$ K and $H = 10$–50 kOe this size lies in the nanometer range (Chen et al. 1994). Chen et al. (1994) considered the process of nanocomposite system formation by deposition of magnetic and

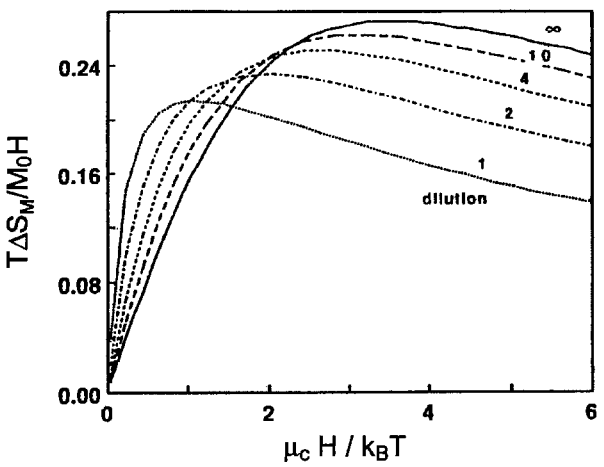


Fig. 2.3. Calculated reduced magnetic entropy change as a function of $x = \mu_C H/(k_B T)$ with dilution by nonmagnetic particles as a parameter (the field varies from H to 0). The numbers near the curves represent the values of the dilution (Chen et al. 1994).

nonmagnetic particles on a substrate. They took into account the possibility of formation of chains in the nonmagnetic matrix, consisting of magnetic particles (clusters) touching each other. These chains increase the effective magnetic cluster size, causing a deviation from the optimum value and a reduction of ΔS_M. The number and length of the chains forming in a nanocomposite during the random deposition process was numerically simulated by a simple computer model. These data were used for the calculation of the magnetic entropy change by means of the equation:

$$\frac{T\Delta S_M}{M_0 H} = \sum_i \frac{n_i}{n}\frac{1}{x}\left[1 - m_i x \coth(m_i x) + \ln\frac{\sinh(m_i x)}{m_i x}\right], \tag{2.104}$$

where m_i is the number of clusters per chain, n_i is the number of m_i type chains, $n = \sum_i n_i m_i$ is the total number of clusters.

It was shown, that the formation of chains reduces the magnetic entropy change. The value of this reduction depends on the dilution of the nanocomposite by the nonmagnetic particles, which is determined by the ratio of the number of nonmagnetic particles in the composite to the number of magnetic particles. The general dependence is such, that for large clusters ΔS_M increases with increasing dilution and the opposite situation takes place for small clusters. The cluster size (and the value of x), corresponding to the maximum magnetic entropy change increases with increasing dilution. These results are illustrated in fig. 2.3.

Later Chen et al. (1995) took into account the ability of particles to migrate on the substrate during the deposition and considered the influence of the substrate temperature on the chain formation. To simulate the process of nanocomposite fabrication the event driven Monte Carlo technique was used. It was shown that low substrate temperature presents difficulties to chain formation, thus leading to larger values of ΔS_M for a given

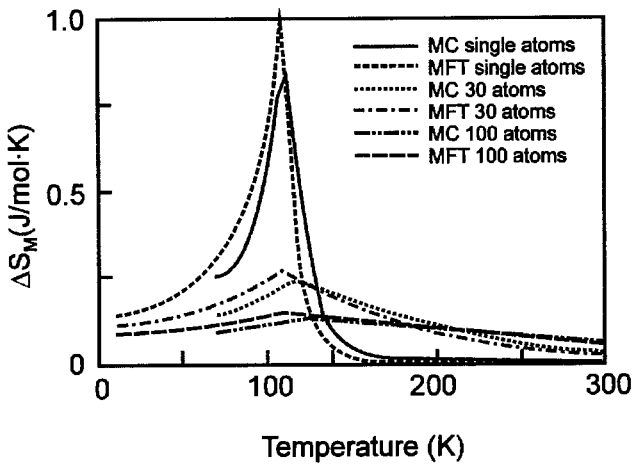


Fig. 2.4. Magnetic entropy change induced by the removal of a magnetic field of 10 kOe, calculated by the mean-field theory (MFT) and the Monte Carlo method (MC) for a ferromagnetic material, and for systems of interacting superparamagnetic clusters. The materials have the same ordering temperature of 108 K (Bennett et al. 1992).

value of dilution. Another way to reduce the effect of chain formation, proposed by Chen et al. (1995), was to use unipolar electrostatic charging of the magnetic particles. The results of calculations showed that this method can substantially reduce the decrease of ΔS_M due to chain formation.

Let us consider systems with interacting magnetic clusters. Such systems display behavior similar to that of ferromagnets, with an effective interaction temperature T_I, analogous to the Curie temperature T_C, and were called "superferromagnets" (Mørup et al. 1983). Above T_I the material is superparamagnetic and below T_I long-range order between the clusters occurs. In the superparamagnetic region, ΔS_M induced by a field change from 0 to H can be obtained, analogous to eq. (2.88) (Shull 1993), by the equation:

$$\Delta S_M = \frac{n((N/n)\mu)^2 H^2}{6k_B(T - T_I)^2}. \tag{2.105}$$

Analogous to the superparamagnetic case, the factor $n((N/n)\mu)^2$ in eq. (2.105) may become much larger than $N\mu^2$ in eq. (2.88). The latter is valid for a ferromagnet consisting of single magnetic atoms. This implies, that ΔS_M above T_I in a system with magnetically interacting clusters can become substantially larger than in a simple ferromagnet above T_C. The maximum value of ΔS_M is observed at $\mu_c H/(k_B T) \approx 3.5$, as in the case of a superparamagnet.

MFA calculations (Bennett et al. 1992; McMichael et al. 1993a, 1993b) show that, at $T = T_I$ and below T_I, ΔS_M is smaller in clustered systems than in simple ferromagnets. Bennett et al. (1992) made calculations in the framework of the Monte Carlo method, which is more correct near the Curie temperature than MFA. The theoretical results of ΔS_M induced by the removal of a magnetic field of 10 kOe are shown in fig. 2.4. $\Delta S_M(T)$

was calculated for a ferromagnetic system consisting of individual moments of $8\mu_B$ and for interacting magnetic clusters of 30 and 100 atoms. MFA and Monte Carlo results are in good agreement, although in MFA an adjusting of the ordering temperature was needed. The decrease of ΔS_M near the ordering temperature in the 100-atoms cluster system was about 3.6 times lower than for a simple ferromagnet. In the paramagnetic region ΔS_M in the clustered system was much larger than that in the ferromagnet, in accordance with the sum rule (2.102). A broader maximum in the $\Delta S_M(T)$ curve is observed for the systems with larger cluster sizes.

The magnetization measurements of ultrafine magnetic particles consisting of a metastable iron–mercury alloy in Hg have been used to calculate the $\Delta S_M(M, T)$ (Pedersen et al. 1997). It is shown that obtained values of ΔS_M are much larger than those theoretically calculated for a paramagnet system. Application of the model with interpartical magnetic interaction permitted authors to get better description of the experimental results. It is necessary to note that the investigations of the MCE in nano-scaled systems is promising direction which needs additional theoretical and experimental efforts.

2.5. *Inhomogeneous ferromagnet*

Belov (1961a) developed the Landau theory of the second order phase transitions (which was considered in section 2.1) for the case of spatially inhomogeneous ferromagnets. The inhomogeneity is one of the reasons of the appearance of magnetization "tails" above the Curie temperature.

The main idea in Belov's model was a spatially inhomogeneous distribution of the local Curie temperature $T_C(\vec{r})$. Using this model, Wagner et al. (1996) and Silin et al. (1995) calculated the mean magnetization $\langle I \rangle$ as a function of the field and temperature in the region of the magnetic phase transition. The maximum value of $T_C^{\max}(\vec{r}) = T_C$ was considered as the temperature of ferromagnetism arising and the minimum value $T_C^{\min}(\vec{r}) = T_C - \Delta T_C$ – as the temperature of the heat capacity peak.

The thermodynamic potential (its magnetic part) was chosen by Wagner et al. (1996) in the following form:

$$\Phi_M(T, M) = \int_0^1 \mathrm{d}s\, W(s)\left\{\frac{d_0}{2}\big(T - T_C(s)\big)M^2 + \frac{\beta}{4}M^4\right\}, \tag{2.106}$$

where s is the parameter responsible for the value of the local Curie temperature, $W(s)$ is the distribution function of the s parameter, I is the local magnetization and it was established, that $T_C(s) = T_C - s\Delta T_C$. The potential (2.106) yielded the equation for the local magnetization:

$$H = \alpha_\Theta(T - T_C - s\Delta T_C)I + \beta I^3, \tag{2.107}$$

which was then used to calculate the mean magnetization of the material:

$$\langle I \rangle = \int_0^1 \mathrm{d}s\, W(s)I(s). \tag{2.108}$$

Using the results of Wagner et al. (1996) for $\langle I \rangle$, Romanov and Silin (1997) calculated by eqs (2.71) and (2.77) (the dependence of heat capacity on H and T was neglected) the temperature and field dependences of MCE in the region of magnetic phase transition for an inhomogeneous ferromagnet. The equations obtained were rather complex. Therefore we only show in fig. 2.5 the results of numerical calculations, made under assumptions that $W(s) = 1$ and ΔT_C, characterizing the length of magnetization tails, is equal to $0.1\,T_C$. In fig. 2.5 the quantity $\Delta T\beta 10^2/(\alpha^2 T_C)$, characterizing the MCE, is plotted against T/T_C and the strength of magnetic field is characterized by the dimensionless parameter $t_0 = [3\beta/(\alpha\Delta T_C)](H/2\beta)^{2/3}$. The curves marked 1 were obtained for the simple Landau theory and the curves marked 2 for an inhomogeneous ferromagnet.

As one can see from fig. 2.5, the $\Delta T(T)$ dependences for an inhomogeneous ferromagnet are more gradual and the MCE is weaker than for a homogeneous one. In the first case the ΔT peak is observed in the temperature region of the magnetization tail $T_C - \Delta T_C < T < T_C$ and in the second case at $T = T_C - \Delta T_C$. An increase in magnetic field leads to a shift of the MCE maximum to higher temperatures and increases the difference in the $\Delta T(T)$ behavior. Calculations showed that the nature of the $W(s)$ function had only a slight effect on the $\Delta T(T)$ behavior for the case of strong fields but had a stronger effect for relatively weak fields.

2.6. *Magneto-elastocaloric effect*

The heat generation and absorption in magnetic materials during adiabatic processes (magneto- and elastocaloric effects) was discussed by Tishin (1998b). The general thermodynamic relations for the elastocaloric effect was derived, and numerical values for the rare earths Gd and Ho were calculated.

An elastocaloric effect (ECE) in magnets has not been introduced correctly enough in the available literature. In our opinion, the ECE is a heat emission or absorption at a constant applied magnetic field (in a simple case at zero field) and value changing external pressure, p (Tishin 1998b). If a pressure change takes place under adiabatic conditions then the ECE (like MCE) manifests itself as heating or cooling of a magnet by a temperature $\Delta T_{ECE}(p, T)$. In the case of ECE, eq. (2.14) for adiabatic processes takes the form:

$$\frac{C_{H,p}}{T}\,\mathrm{d}T - \left(\frac{\partial V}{\partial T}\right)_{H,p}\mathrm{d}p = 0, \tag{2.109}$$

where V is the volume. Thus, for the ECE we can write (Tishin 1998b):

$$\mathrm{d}T_{ECE} = \frac{T}{C_{H,p}}\left(\frac{\partial V}{\partial T}\right)_{H,p}\mathrm{d}p. \tag{2.110}$$

The general form of this formula is close to the thermodynamic equation for a temperature change of a gas in a reversible adiabatic expansion process. Because each real gas has a positive value for $(\partial V/\partial T)_p$, the gases may cool down under adiabatic expansion ($\mathrm{d}T < 0$ at $\mathrm{d}p < 0$). In thermodynamics this phenomenon, well known as the Joule–Thomson effect,

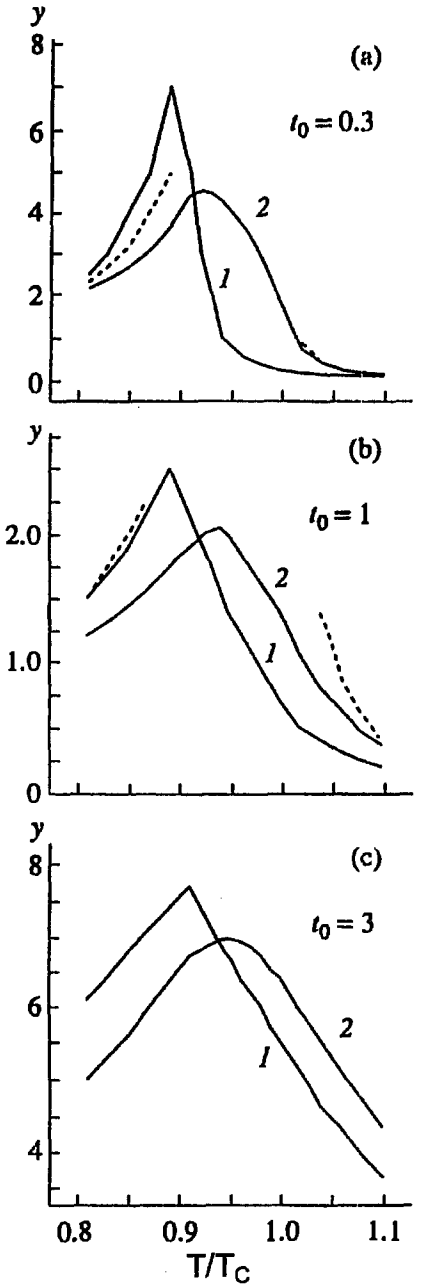


Fig. 2.5. Dependence of the dimensionless magnetocaloric effect $y = \Delta T \beta H \times 10^2/(\alpha^2 T_C)$ on reduced temperature T/T_C for different values of the parameter $t_0 = \frac{3\beta}{\alpha \Delta T_C}\left(\frac{H}{2\beta}\right)^{2/3}$ characterizing the strength of magnetic field: (a) $t_0 = 0.3$; (b) $t_0 = 1$; (c) $t_0 = 3$ (Romanov and Silin 1997).

is at present widely used to liquefy gases. Using the bulk thermal expansion coefficient, $\alpha_T(T, H, p)$, eq. (2.110) can be transformed into:

$$dT_{ECE} = \frac{\alpha_T V T}{C_{H,p}} dp. \tag{2.111}$$

The sign of the ECE is determined by the coefficient α_T. In regular solids the value of α_T is positive and lies in the range 10^{-3}–10^{-6} K^{-1}. A negative value of α_T occurs, for example, in water at temperatures up to 4°C. In accordance with eq. (2.111), it means that in this temperature interval water should cool down under adiabatic stress. For example, this effect, in principle, could lead to freezing of water in micro-pores of road surface under quick pressing of this water (at temperature close to zero) by vehicle tires.

As distinct from eq. (2.16) the ECE value is proportional to the temperature derivative of the volume, and to the pressure change. Thus, a nonzero value of the ECE could be found in any materials for which $(\partial V/\partial T)_p \neq 0$ (with the exception of a case when $T = 0$). From this viewpoint, the ECE could have a non-zero value in materials without any magnetic structure. This is the first and main difference between the ECE and the MCE.

The second distinction is the sign of the ECE. The volume of most materials increases with increasing temperature ($(\partial V/\partial T)_p > 0$). Thus, under the action of pressure ($dp > 0$) the sign of the ECE should be positive in most cases, in accordance with eq. (2.110). It is well known, that nonmagnetic solids without electronic or magnetic phase transitions have an almost constant value of $(\partial V/\partial T)_p$ in the temperature region above the Debye temperature, T_D. Therefore, at $T > T_D$ the value of the dT_{ECE} is proportional to the temperature T. Obviously, the ECE will have a small absolute value in temperature regions where $(\partial V/\partial T)_p$ is close to zero. In accordance with eq. (2.111), irregular behavior of the ECE could be found in the vicinity of temperatures where marked changes of $\alpha_T(T)$ and $C_{H,p}(T)$ take place. Near a phase transition the ECE could change its sign, for example, from negative to positive, which could result in a variation of the sign of the coefficient $\alpha_T(T)$ (Tishin 1998b).

Up to the present, the ECE has not been widely studied in different materials. However, simplified thermodynamic equations for the ECE in the case of a steel bar have been obtained by Sychev (1986). It is shown that in the first approximation the value of the ECE in the bar does not depend on its length and cross section. However, in a steel wire an ECE value of -0.16 K was reached under a rapidly applied stress up to 2×10^8 Pa (Sychev 1986).

An experimental investigation of the ECE has been made in the work of Annaorazov et al. (1996). The heat generation measurements in $Fe_{49}Rh_{51}$ occur under pulsed linear stress of the ingot applied by a couple of hawsers that were attached via two holes to the sample. It was shown that at the temperature of the antiferromagnetic (AFM)–ferromagnetic (FM) phase transition, $T_{AFM-FM} \sim 315$ K, the cooling of the ingot is about 5 K under a tensile stress of 5.29×10^8 Pa (Annaorazov et al. 1996). However, the nature of the negative sign of the ECE has not been interpreted. The duration of the stress pulses (adiabaticity of the process) and total accuracy of these measurements are unknown. The results of the work of Annaorazov et al. (1996) mostly have a fundamental meaning because the compound $Fe_{49}Rh_{51}$ can not be used in any commercial applications due to the

extremely high price of Rh. So, the search of other compounds with a large elastocaloric effect is a significant task. From this viewpoint, lanthanide metals and compounds are of great interest.

In rare earth metals the coefficient $\alpha_T(T)$ has large value in the vicinity of structural or magnetic phase transitions. In holmium the phase transition from the ferromagnetic conical phase to the antiferromagnetic spiral structure occurs at about 19 K. The specific volume change, dV/V, at this transition is equal to -2.2×10^{-4} in a temperature interval of $\sim$ 0.5 K (Steinitz et al. 1987). The atomic volume of La changes by 0.5% and 4% at the transitions from dhcp to fcc and from fcc to bcc, respectively. The thermal expansion coefficients of Eu^{2+} and Yb^{2+} are three times larger than in other rare earth elements (Taylor and Darby 1972). The fcc crystalline form of Sm transforms to dhcp by applying 7×10^8 Pa at room temperature. This structure transformation is accompanied by volume decrease of about 8% (Jayaraman 1991). The thermodynamic data for structural transitions of lanthanide metals are summarized in table 9.2 of the report of Jayaraman (1991). Thus, the rare earth elements could be considered as a favorable basis for creating materials with large ECE values (Tishin 1998b).

Let us estimate the ECE value in the rare earth metals gadolinium and holmium in the vicinity of magnetic phase transitions. According to the experimental data of Dan'kov et al. (1998) the transitions from the paramagnetic to the ferromagnetic phase occurs in Gd at $T_C = 294$ K. Below the spin reorientation temperature, $T_{SR} = 227$ K, the easy magnetization vector departs from the [0 0 0 1] crystallographic axis. The temperature dependence of the atomic volume in Gd has been studied by Finkel et al. (1971) and Finkel (1978). Near these magnetic phase transitions the value of bulk thermal expansion coefficient is close to zero. Thus, the ECE value at the Curie point T_C, as well as around T_{SR} should be approximately equal to zero. (It is necessary to note that the MCE reaches its maximum value at the Curie point of Gd.) At the same time, the gadolinium has a negative value of α_T (and, therefore, a negative ECE value) in the temperature region between T_C and T_{SR}. Based on the data of Dan'kov et al. (1998), Finkel et al. (1971) and Finkel (1978) it is possible to estimate that at $T = 285$ K and $dp = 10^8$ Pa the value of the ECE is negative and approximately close to -0.61 K (Tishin 1998b). Thus, the estimated dT_{ECE} value of Gd has the same order as the ECE value of $Fe_{49}Rh_{51}$, $dT_{ECE} \sim -1.7$ K, at pressure $\sim 10^8$ Pa (Annaorazov et al. 1996).

The experimental data concerning the heat capacity and bulk thermal expansivity at the ferromagnetic–antiferromagnetic phase transition at about 19.5 K can be found in the reports of Steinitz et al. (1987), Lounasmaa and Sundstrom (1966), Stewart and Collocott (1989) and White (1989). However, experimental values of the heat capacity presented by Lounasmaa and Sundstrom (1966), Stewart and Collocott (1989) and White (1989) are different at this phase transition. Taking $C_{H,p} \approx 14$ J/mol K and $\alpha_T \approx -4.4 \times 10^{-4}$ K^{-1}, we could obtain a value of the ECE close to -1.1×10^{-2} or -1.2 K at pressure values of 9.8×10^5 Pa ($\sim$10 bar) and 10^8 Pa ($\sim$1 kbar), respectively (Tishin 1998b). The pressure 1×10^8 Pa could be compared with pressure of a middle weight man on a magnetic material with a cross section about 7–8 mm^2. However, it is necessary to note that according to data of the work of Baazov and Manjavidze (1983), this pressure is close to the value of $\sim 1.7 \times 10^8$ Pa (17 kg/mm^2) which determines a limited durability of the rare earth metals under tensile strain.

For these estimations we neglected any influence of pressure on the values of α_T and $C_{H,p}$. Actually, due to the effect of pressure on the elastic and magnetic properties of the rare earth metals (see Jayaraman 1991), the above calculated ECE values should be considered as the first approximation only. In rare earth elements the shifts of magnetic phase transition temperatures reach a few K under pressure of 5×10^8 Pa (Jayaraman 1991). However, at present, experimental information about the values of α_T and $C_{H,p}$ at different pressures is unavailable and therefore, more accurate calculations of the ECE are impossible.

As shown above, in accordance with thermodynamics, a heat generation and/or absorption in magnets can arise at $dp = 0$ (MCE) as well as at $dH = 0$ (ECE). We have estimated the value of the ECE for the magnetic phase transitions in Gd and Ho. However, it is possible to reach large values of the ECE and MCE in cases where magnetic and structural phase transitions coexist. For example, the crystal structure of Dy transforms at about 90 K from the $P6_3/mmc$ to the Cmcm type. This transition involves large changes of the interatomic distances and accompanies the transition from a spiral antiferromagnet to a ferromagnet (Taylor and Darby 1972). If in an adiabatic process the pressure and the magnetic field change simultaneously, the total heat evolution can be written down as (Tishin 1998b):

$$dT = dT_{MCE} + dT_{ECE} = -\frac{T}{C_{H,p}}\left[\left(\frac{\partial I}{\partial T}\right)_{H,p} dH - \left(\frac{\partial V}{\partial T}\right)_{H,p} dp\right]. \tag{2.112}$$

The joint magneto-elastocaloric effect (MECE) has not previously been studied by experiment. The MCE and ECE can have positive as well as negative signs. So, the general behavior of the temperature dependencies of the MECE could be complicated. The nature of the MECE is close to the MCE in an adiabatic–isochoric process. The equations for the MCE under adiabatic–isochoric conditions have been derived by Kuz'min and Tishin (1992).

Currently, in the construction of magnetic refrigerators only the MCE (the first term of eq. (2.112)) is utilized. The second term (ECE) is neglected. In our opinion, the possibilities to use both effects at the same time under adiabatic and/or adiabatic–isochoric conditions should be analyzed. It is possible to propose, for example, a design of magnetic cryocooler in which a refrigerant is both affected by a magnetic field and also by a contraction or expansion of the refrigerant owing to the magnetostriction (Tishin and Kuz'min 1991; Tishin 1997). The benefit of a technical utilization of the ECE is that nonmagnetic materials with giant volume expansion or linear thermal expansion could be used.

2.7. MCE in the vicinity of magnetic phase transition

Tishin (1998a) discussed adiabatic magnetization processes (magnetocaloric effect) in the region of magnetic phase transitions. His discussion is based on the known experimental data about magnetic phase diagrams and magnetocaloric effects of the rare earth metals Gd and Dy. A correlation was assumed between the arrangement of the curves describing the magnetic phase transitions in H–T diagrams and the corresponding value of the magnetocaloric effect (Tishin 1998a).

The heavy rare earths are metals with well-studied magnetic properties (see, for example, the reviews of Jensen and Mackintosh (1991) and by McEwen (1991)). The magnetic

phase diagrams of these magnetic materials have been intensively studied by different techniques (see, for example, the reports of Bohr et al. (1986), Tindal et al. (1993), Gschneidner and Pecharsky (1997b)). The general form of the phase diagrams strongly depends on the used experimental techniques as well as on the method employed for the determination of the phase change point from the experimental curves. Most of currently practiced setups give different values of the phase transition points for the same sample. A comparison of the different procedures for determining the position of the phase transition point of gadolinium has been presented by Dan'kov et al. (1998).

Practically, experimentalists operate under either isothermal or adiabatic conditions when studying H–T magnetic phase diagrams of different magnetics materials. The isothermal conditions can be easily achieved by static and/or quasi-static magnetic field measurements. For example, this is the case for a very slowly increasing field in a situation where a material has the possibility to keep its zero field temperature due to heat exchange with the surrounding. At the same time, under adiabatic conditions, the temperature of the magnetic material under investigation could be changed by the magnetocaloric effect. For experimental measurements this situation is often observed when a sample is located inside a vacuum and/or in pulsed field studies. Up to the present, the experimental circumstances necessary for exact realization of the quasi-adiabatic conditions in non-vacuum are unknown. In accordance with the data published by Levitin et al. (1997) the transition between isothermal and quasi-adiabatic circumstances occurs in a range of fields increasing with rates from 200 kOe/s to 2 MOe/s (for situations where the sample is located in liquid nitrogen or helium). It is shown (Dan'kov et al. 1997) that in a nitrogen gas surrounding a field sweep rate of about 900 kOe/s clearly corresponds to the adiabatic condition.

Let us consider the H–T phase diagram of a magnetic material under atmospheric pressure. Under the isothermal conditions the concrete magnetic state in the H–T diagram is determined by the values of the zero field temperature and the applied magnetic field. In the adiabatic cases, when the initial temperature for a magnetization process can be changed due to MCE, the visualization of the H–T coordinates requires also the MCE value. In the case that an initial magnetic state of a sample under adiabatic conditions can be changed by applying a magnetic field (for example, from an antiferromagnetic to a ferromagnetic phase) the situation is more complicated. Especially, if the magnetic material can cross the curve of the first-order phase transition and/or if the rate of increasing field is too large (for example, 650 MOe/s as in the report of Nojiri et al. (1995)).

Tishin's (1998a) consideration refers directly to the MCE, since the measurement of the temperature change practically occurs when the magnetic field changes from zero to H. The analysis makes it possible to assume: first, the value of the MCE in the vicinity of the Curie point is limited by the shift of the Curie point as the field increases; second, under adiabatic conditions (without heat exchange with the surrounding) Gd can not change its initial magnetic state. Gd is a regular ferromagnet and, in our view, the above conclusions should also be applicable to other ferromagnets. Thus, the extent of heating of a ferromagnet during an adiabatic magnetizing process is determined by the behavior of the phase transition line.

The magnetic phase diagram of Dy is very complex. For example, Herz and Kronmüller (1978) and Nikitin et al. (1991b) denote the phase transition from the FM to the PM state, by the vertical line in the H–T diagram which starts from zero magnetic field and the

Néel temperature, $T_N \sim 180$ K. In other diagrams this line is shifted to the region of low (Gschneidner and Pecharsky 1997b) or high (Alkhafaji and Ali 1997) temperatures from the zero field transition point. Tishin's (1998a) scheme of the magnetic phase diagram of Dy is based on the experimental results described in these reports.

Tishin's (1998a) results were obtained under the assumption that in the vicinity of the zero field transition point the MCE in Gd and Dy could not lead to changes of the initial FM and/or AFM phases to other magnetic states. It may be stated for ferromagnetic Gd (based on the experimental results of Dan'kov et al. (1998)). In the case of Dy this result should be verified more thoroughly on the basis of new experimental measurements of the magnetic phase diagram and MCE on the same single crystalline sample of Dy.

The character of the behavior of the MCE in a magnetic field, when H becomes equal to the critical value, H_{cr}, could be explained in the framework of the thermodynamic relation for the magnetic entropy, S_M, which can be easily obtained from Maxwell's formula (see eq. (2.9a)) (Bailyn 1994).

In conclusion, Tishin (1998a) have assumed that the FM and/or AFM states of magnetic materials can not be changed under adiabatic magnetizing conditions due to the non-zero MCE value that leads to an additional shift of the initial temperature. The MCE can not exert any influence on the initial magnetic phase state. At atmospheric pressure the latter can be transformed just by applying a magnetic field of the corresponding value, $H \geqslant H_{cr}$. From the other side, it is known that the curves describing AFM–FM and FM–PM phase transitions of antiferro- and ferromagnets may become shifted with increasing field to the high and low temperature regions, corresponding to negative and positive signs of the derivative $dH_{cr}(T)/dT$, respectively. In our opinion, for fields close to the critical field, the sign of $dH_{cr}(T)/dT$ determines the MCE value. It is negative or close to zero MCE for the AFM state and positive for the FM phase.

The results obtained by Tishin (1998a) are especially important for experimental studies of magnetic materials with a large MCE value in the vicinity of the magnetic phase transition. It should be noted, however, that in the case of antiferromagnets these assumptions require further careful experimental verifications.

3. Methods of MCE measurements

3.1. Direct methods

3.1.1. Pulse techniques

The method of direct measurements of the change in material temperature during the application or removal of a magnetic field by an electromagnet (switch-on technique) was proposed by Weiss and Forer (1926). The first measurements in strong magnetic fields (up to 110 kOe) were made by this method on yttrium iron garnet by Clark and Callen (1969). The temperature of the sample was measured by a thermocouple.

Kurth et al. (1985) used a differential thermocouple, which gave more accurate result for the MCE measurements, see fig. 3.1. Here the differential thermocouple (3) measures the temperature difference between a massive copper body (2), (4) and the sample (6), which is the MCE value. Thermocouple (5) measures the average temperature of the sample.

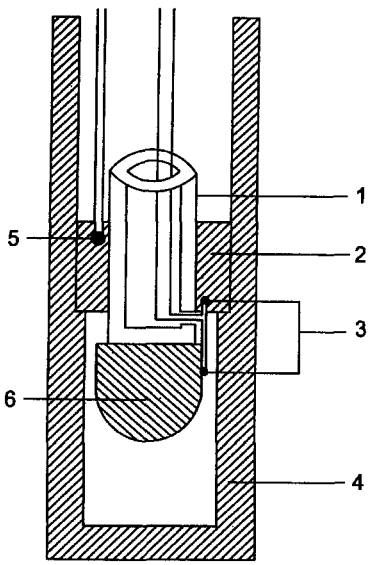


Fig. 3.1. Experimental setup for MCE measurements using a differential thermocouple: (1) insulating Plexiglas tube; (2) copper ring; (3) differential thermocouple for ΔT measurements; (4) copper screen; (5) thermocouple measuring the average sample temperature T; (6) the sample (Kuhrt et al. 1985).

MCE measurements in siderite $FeCO_3$ in pulsed magnetic fields were made by Borovikov et al. (1981). The samples were shaped as parallelepipeds with linear dimensions of several millimeters. A compact solenoid produced a pulsed magnetic field of 270 kOe with a pulse duration of 2 ms in a working space of 5.5 mm diameter and 20 mm long. The temperature change was measured by the thermocouple or by a magneto-optic technique allowing an instant temperature measurement (Litvinenko et al. 1973). The latter method is based on the observation of the absorption band series in the region of 24 000 cm^{-1} and can be used for measuring of the sample temperature above 21 K with an accuracy of 0.5 K.

A further development of the pulsed-field method was made by Ponomarev (1983, 1986). He studied the MCE in polycrystalline gadolinium in pulsed fields up to 80 kOe (with a total pulse length of 0.5 s) in the temperature range from 80 to 350 K. The copper–constantan thermocouple, made of strips $\sim$ 20 μm thick and 1 mm wide, was placed in the center of a sample that was 6 mm diameter wide and 15 mm long. The solenoid used had a length of 200 mm and a bore diameter of 50 mm. It was shown that for the given pulse duration, sample dimensions and thermocouple configuration any errors due to heat exchange between the sample, thermocouple and environment can be neglected.

Let us consider as an example the pulsed field setup, as described by Dan'kov et al. (1997). The principal scheme of this setup is shown in fig. 3.2 and the scheme of its low temperature part is displayed in fig. 3.3.

Changes of the sample temperature were measured by a copper-constantan thermocouple made of small diameter wires ($\approx$ 0.05 mm). This provide a small mass of thermocouple

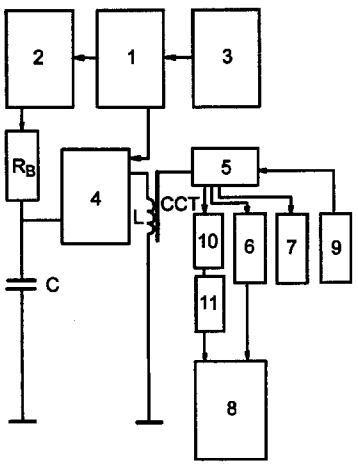


Fig. 3.2. Principal scheme of the experimental pulsed-field setup: (1) operation block; (2) high voltage source; (3) rectifier; (4) discharge block; (5) measurement block; (6) integrator; (7) microvoltmeter; (8) memory oscilloscope; (9) heat feeding block; (10) thermocouple signal amplifier; (11) compensation block; C – battery of capacitors; CCT – copper–constantan thermocouple; L – pulsed solenoid; R_B – ballast resistor (Dan'kov et al. 1997).

(typical weight of the sample is $\approx$ 1 g) and, consequently, a negligible heat load, which significantly reduces the heat leaks through the electrical wires.

The Gd sample, measured by Dan'kov et al. (1997) was shaped as a parallelepiped with dimensions 4 × 4 × 10 mm and cut into two equal parts along the long axes. The thermocouple was placed between the parts in the center of the sample. The experimental tests showed, that during the period of time required by the magnetic field to reach its maximum value (0.08 s) the heat exchange with environment lowers the sample temperature by less than 2%. That is why the sample was not insulated by a vacuum layer.

The low temperature insert (fig. 3.3) was assembled from thin-walled tubes made of non-magnetic stainless steel. The sample temperature was regulated by simultaneous operation of the electric heater (2) (fig. 3.3) controlled by feeding block (9) (fig. 3.2) and cooling by flowing of nitrogen or helium gas through the insert.

The magnetic field was created by the solenoid L under the discharge of a battery of capacitors C. The battery had a total capacity of 0.035 F and was charged up to 1000 V, which provided a total pulse duration of 0.2 s. A thyristor driven by the starting signal from the control desk 1 (fig. 3.2) was used as a power switch for the battery discharge. Simultaneously the starting signal triggered the pulse memory oscilloscope (8). The signal from thermocouple was fed into one channel of the oscilloscope. The signal from the field measuring coil (3) (fig. 3.3) after passing through the integrator (6) (fig. 3.2) was fed into the second channel. This technique made it possible to determine the sample temperature change due to the change of the magnetic field, i.e., the MCE at a given field and temperature. The measurements block (5) (fig. 3.2) was used for communication with other setup blocks.

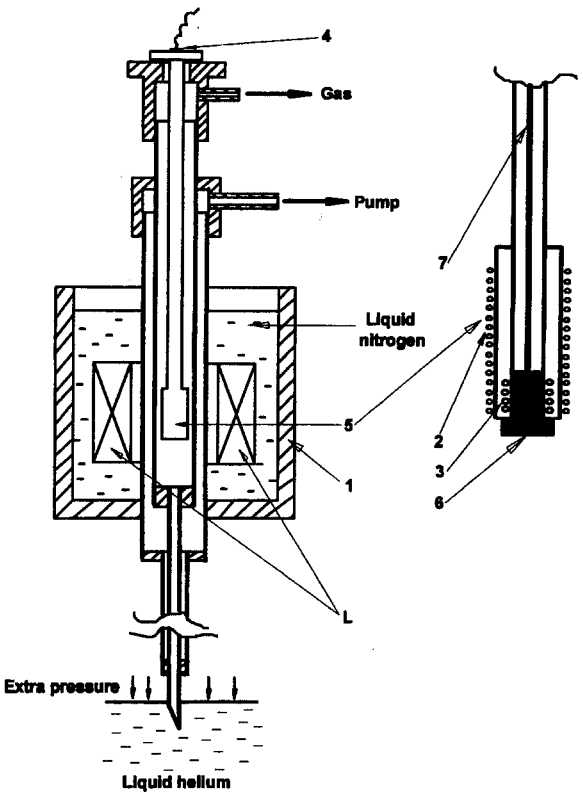


Fig. 3.3. Low temperature part of the experimental pulsed-field setup: (1) liquid nitrogen cryostat; (2) sample heater; (3) field measuring coil; (4) vacuum tight feed through connector; (5) sample holder; (6) sample inside the holder; (7) electrical wiring; L – pulsed solenoid (Dan'kov et al. 1997).

During the measurements a parasitic signal might be induced in the thermocouple wiring, which decreased the accuracy of measurements. To prevent the influence of this interference, a compensation scheme (11) (fig. 3.2) was employed, in which a signal from the field measuring coil (3) (fig. 3.3) was added as a compensation signal to the signal from thermocouple. Such a compensation scheme allowed to nearly completely exclude the influence of the interferences on the experimental results.

The solenoid L had a bore diameter of 23 mm and was wound from copper wire of a cross-sectional diameter of 1.3 mm. It was cooled by direct heat exchange with a liquid nitrogen bath, which made it possible to achieve a magnetic field up to 80 kOe. Tests showed that the solenoid possessed a small field inhomogeneity: the axial inhomogeneity was less than 5% within ± 1 cm from the solenoid center, and the radial inhomogeneity was one order of magnitude smaller.

Taking into account various sources of random and systematic errors (such as induced thermocouple interferences, various heat losses, eddy currents) Dan'kov et al. (1997) concluded that the apparatus permitted to measure the magnetocaloric effect with an accuracy of 8–15%, depending on the MCE value and the temperature range.

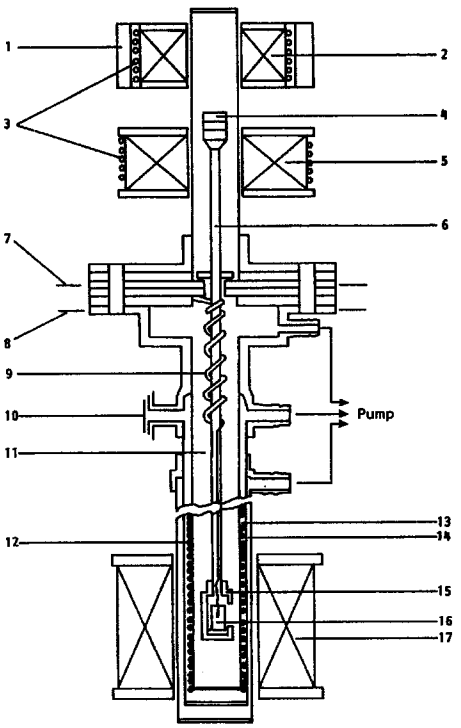


Fig. 3.4. Experimental setup for MCE measurements in a superconducting solenoid (see main text for details) (Tishin 1988).

3.1.2. Static apparatus

When the field is produced by an electromagnet the rise time has a maximum value of about a few seconds, while it can be several minutes for a superconducting solenoid. During the field rise a substantial dissipation of heat produced in the sample by the MCE can occur. Tishin (1988) considered this point and estimated, that the field rising time must not be greater than 10 s for temperatures above 30 K. In the temperature region of 10–20 K this time must be several times smaller because of the increase of the heat leak via the thermocouple. This implies that MCE measurements made by a switch-on technique are difficult in the case of a superconducting solenoid.

This is the reason why Nikitin et al. (1985a, 1985b) and Tishin (1988) used for MCE measurements in a superconducting solenoid a method in which the sample was brought quickly into the field. The measurement was done in the following sequence. First the sample was placed outside the solenoid. When the field strength in solenoid had reached a given value, the sample was brought as fast as possible ($\approx$ 1 s) inside the solenoid. When the sample was fixed in the center of solenoid, its temperature was measured.

The scheme of the experimental set-up is shown in fig. 3.4. The sample holder (15) made of teflon, containing the sample (16) was fixed at the end of a rod (6). To minimize the heat leak between the sample and the holder mica glued on to the bottom of the holder was used

as a gasket. The rod with the holder were placed into an evacuated tube (11) pumped to a pressure $\approx$ 1 Pa. Vacuum jackets (13) and (14) were used to reduce helium evaporation caused by sample heating by the electric heater (12). The heater through a connector (10) was connected to the temperature control circuit. The superconducting solenoid (17) made it possible to create magnetic fields up to 66 kOe. The whole apparatus was placed into liquid helium.

A special coil (5) was used to compensate the force pulling the sample into the solenoid. This force is the product of the field gradient and the sample magnetic moment. A permanent magnet made of $SmCo_5$ (4) and the special coil (5) prevented the sample from being pulled into the solenoid. The same coil is used to return the sample to its initial position. The sample is fixed in the upper position (out of the solenoid) by a ferrite permanent magnet (1) and begins to move after compensation of the field of the magnet (1) by another coil (2). A teflon gasket (7) on a flange (8) fixes the sample at the center of the solenoid during the measurement. When the sample reaches the center of the solenoid, the copper washer on the rod closes the contacts on the gasket (7), which leads to the turning off of the special coil (5). Coils (2) and (5) were water-cooled.

The switch-on technique for MCE measurements in a superconducting solenoid was used by Green et al. (1988). The apparatus of the latter authors employed a superconducting solenoid 12.13 cm in diameter, 25.4 cm long and 8.54 cm bore, which could produce a field up to 70 kOe. The temperature was measured after achieving the maximum field value by five thermocouples placed on the sample, which took 10 s. Together with the field rise time about 30 s the overall process had a duration of 40 s. This method was used to measure MCE in rare earth metals at the temperatures above 180 K.

3.2. Magnetization measurements

Experimental data on the magnetic field dependence of the magnetization at constant temperatures allow one to calculate the magnetic entropy change by means of eqs (2.71) and (2.75) and then the magnetocaloric effect by eq. (2.77b). Such calculations of ΔS_M in rare earth metals were made for instance by Foldeaki et al. (1995), Dan'kov et al. (1996) and other authors.

Equation (2.16) can be also used to calculate the value ΔT of the magnetocaloric effect from experimental data on magnetization and heat capacity (Tishin 1997):

$$\Delta T(T, H) = \int_{T(H=0)}^{T(H)} \mathrm{d}T = -\int_0^H \frac{T}{C(H, T)} \left(\frac{\partial I}{\partial T}(H, T)\right)_H \mathrm{d}H, \tag{3.1}$$

where $I = M/V$, $\Delta T(T, H) = T(H) - T(H = 0)$. In an experiment the field usually changes from $H = 0$ to H. However, in case if the values of the magnetic field are changed from a value of H_1 up to the H_2 than these values of the fields should be taken as the limits of the integration in the eq. (3.1).

Pecharsky and Gschneidner (1996) point to the difficulties of magnetization technique: (a) possible essential errors near the temperatures of magnetic phase transitions due to the MCE and poor thermal contact between the sample and thermocouple; (b) problems related with the presence of magnetic hysteresis in some materials at low temperatures.

Another method allowing to determine the MCE from pulsed field magnetization measurements was proposed by Levitin et al. (1997). It is based on the comparison of $I(H)$ dependences measured under isothermal and adiabatic conditions. Due to the magnetocaloric effect the initial temperature of ferro- and paramagnets increases during adiabatic magnetization. That is why the adiabatic magnetization curve will intersect the isothermal curves obtained at higher temperatures. The intersection points determine the field dependence of the sample temperature under adiabatic magnetization, i.e., the magnetocaloric effect.

It was concluded that the adiabatic conditions of magnetization are preserved for field rising rate of about 10^4 kOe/s or higher for the samples with dimensions of several mm. A decrease of the rate to 10–100 kOe/s leads practically to isothermal magnetization processes.

The possibility of the pulsed field method to measure the MCE was demonstrated on a paramagnetic $Gd_3Ga_5O_{12}$ single crystal in pulsed fields up to 400 kOe. As it was predicted, intersections between the adiabatic and isothermal curves were observed. The $\Delta T(H)$ curve obtained by this method gives $\Delta T = 46$ K for $\Delta H = 400$ kOe and $T = 4.2$ K in $Gd_3Ga_5O_{12}$. The adequacy of the obtained $\Delta T(H)$ curves was checked by MFA calculations.

3.3. Heat capacity measurements

This method was used to determine the MCE and ΔS_M by Brown (1976) and Gschneidner and coworkers (see, for example, Pecharsky and Gschneidner 1996). It allows to determine all parameters required for magnetic refrigeration design: heat capacity, ΔS_M, MCE and $S(T, H)$ dependences.

On the basis of eq. (2.12) the total entropies of the material in zero and nonzero magnetic field $S(T, 0)$ and $S(T, H)$ can be calculated by the equation

$$S(T, H) = \int_0^T \frac{C(T, H)}{T}\, dT, \tag{3.2}$$

if the experimental dependences of the total heat capacity $C(T, 0)$ and $C(T, H)$ are known. Then on the basis of these data the adiabatic temperature rise (i.e., MCE) ΔT for the field change from zero to H can be determined by

$$\Delta T = T(S, H) - T(S, 0), \tag{3.3}$$

where $T(S, H)$ and $T(S, 0)$ are the temperatures in the field H and $H = 0$ at constant total entropy S, respectively. For ΔS_M calculations the following formula can be used:

$$\Delta S_M = S(T, H) - S(T, 0), \tag{3.4}$$

where $S(T, H)$ and $S(T, 0)$ are the total entropies in magnetic field H and $H = 0$ at constant temperature, respectively. An analogous method was used by Tishin (1990a) to determine the $\Delta T(T)$ dependences of Gd on the basis of theoretically calculated entropies $S(T, 0)$ and $S(T, H)$. The method was tested on various magnetic materials such as RAl_2 (R = Er, Dy), $(Dy_{0.25}Er_{0.75})Al_2$, Gd–Pd, Gd and Dy. The data showed good accordance

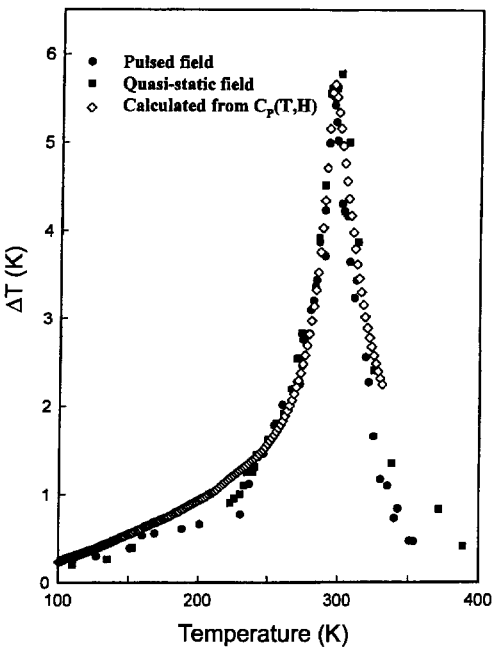


Fig. 3.5. The MCE temperature dependences of high purity polycrystalline Gd measured directly by quasistatic and pulsed techniques (filled symbols) compared with those determined from the heat capacity (opened symbols) for $\Delta H = 20$ kOe (Dan'kov et al. 1998).

with ΔS_M and ΔT results obtained by direct and magnetization measurements (Pecharsky and Gschneidner 1996).

The estimations of errors, made by Pecharsky and Gschneidner (1996), showed that the magnetocaloric parameters derived from the heat capacity method are characterized by sufficient accuracy: near room temperatures the uncertainty in ΔS_M is 100–300 mJ/mol K and the uncertainty in ΔT is 1–1.5 K. In the low temperature region the accuracy becomes substantially better.

Figure 3.5 shows the MCE temperature dependences measured on high purity polycrystalline Gd directly by pulsed-field and quasistatic (switch-on) techniques and determined from the heat capacity for a magnetic field change from 0 to 20 kOe. One can see quite good agreement between the results obtained by these three methods, especially in the temperature range from 220 to 330 K. The $\Delta S_M(T)$ curves of the single crystal Gd determined for ΔH up to 50 kOe from the magnetization measurements are also in good accordance with those calculated from the heat capacity data (Dan'kov et al. 1998).

3.4. Other methods

Bredy and Seyfert (1988) measured entropy changes in EuS induced by a magnetic field by means of a experimental set-up that consisted of a temperature control system, superconducting solenoid and thermal resistor.

The temperature control system, including carbon thermometer, electric heater and electronic system allowed to maintain the sample temperature at a constant value independently from the magnetic field variation. Magnetic fields up to 30 kOe were created by the superconducting magnet. A thermal resistor, made of brass, linked the sample holder to a liquid helium bath. The heat flux dQ/dt, flowing through the thermal resistor, determines the sample temperature. At constant magnetic field the flux is determined by the heat power W_0, generated by the sample heater. When the magnetic field is changed, additional heat Q_{magn} is realized in the sample due to the magnetization and the heater power W_x will be decreased or increased by the electronic system in order to compensate this heat and keep the temperature constant. The process can be described by the following system of equations:

$$\begin{cases} \dfrac{dQ(T)}{dt} = W_0, \\ \dfrac{dQ(T)}{dt} = W_x + \dfrac{dQ_{magn}}{dt}. \end{cases} \tag{3.5}$$

On the basis of this system one can, after integration, obtain the equation:

$$T\Delta S = T\big[S(H_2) - S(H_1)\big] = \int \left(\frac{dQ_{magn}}{dt}\right) dt = \int_{H_1}^{H_2} (W_x - W_0)\, dt, \tag{3.6}$$

where $H_2 = H(t_2)$; $H_1 = H(t_1)$. So, measuring W_0 and W_x and integrating these signals over time, one can determine the entropy change induced by the field change, mainly related to the magnetic entropy change.

4. Magnetocaloric effect in 3d metals, alloys and compounds

4.1. Ferromagnetic 3d metals (Fe, Co, Ni)

It follows from eq. (2.16), that in a ferromagnet the MCE must display a maximum in the vicinity of the Curie temperature. For the first time such a maximum was observed by Weiss and Piccard (1918). MCE studies made in Fe, Ni and Co in fields up to 30 kOe have shown that the magnitude of the MCE near T_C is well described by eq. (2.16) and is governed by the paraprocess (Weiss and Piccard 1918; Weiss and Forer 1924, 1926; Potter 1934; Hirschler and Rocker 1966; Kohlhaas et al. 1966; Kohlhaas 1967; Rocker and Kohlhaas 1967).

Equations (2.44) and (2.52) show that near the Curie temperature the value of the MCE in ferromagnets should be quadratic in the magnetization. This was used to determine the magnetization from the experimental data on the MCE (Weiss and Forrer 1926). For this purpose $\Delta T(I^2)$ curves linear in the region of the paraprocess were extrapolated to the I^2 axis. In the ferromagnetic region the intersection of I^2 axis corresponds to the value of I_s^2

TABLE 4.1

Parameters of 3d ferromagnets used in theoretical calculations, the results of the calculations of the maximum possible values of the MCE (ΔT_{max}) at $T = T_C$ and the values of the magnetic field H_{max} (the field varies from 0 to H_{max}), in which the MCE values are different from ΔT_{max} by at most 1% (Tishin 1990a).

3d ferromagnets	g_J	J	T_C, K	T_D, K	ΔT_{max}, K	H_{max}, $\times 10^4$ kOe
Fe	2	1.4	1043	420	350	6
Ni	3	0.3045	631	385	84	2.9
Co	2	0.95	1403	375	348	6.5

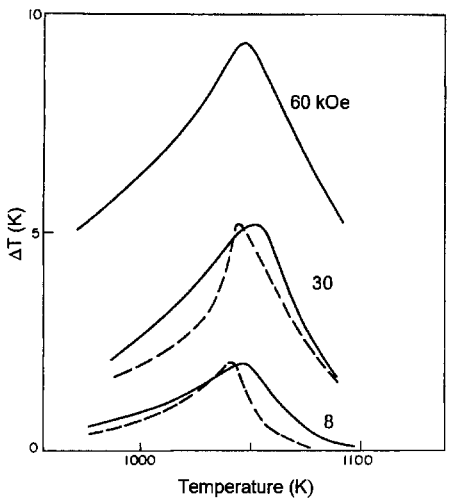


Fig. 4.1. Theoretical (solid lines) and experimental (dashed lines) temperature dependences of the MCE in Fe induced by the magnetic field changes ΔH specified near the curves (Tishin 1990a; Potter 1934).

at a given temperature. This method was used to determine the $I_s(T)$ dependence in Fe, Ni and Co by Weiss and Forrer (1926), Potter (1934) and Rocker and Kohlhaas (1967).

The Landau theory of the second order phase transitions gives eq. (2.32), which should be valid near T_C. The linear dependences of $H/\Delta T^{1/2}$ on ΔT was observed by Belov (1961a, 1961b) in Ni in the temperature range from 618 to 627 K.

The temperature dependence of the spontaneous magnetization in 3d ferromagnets is satisfactorily described by the mean field approximation. On the basis of this Tishin (1990a) used MFA to determine the magnetocaloric effect in Fe, Ni and Co. Equations (2.60)–(2.62), (2.67) were used to calculate the total temperature dependences of the entropy of a material in zero and nonzero magnetic fields and then by the method described in section 3.3 (see eq. (3.3)) the $\Delta T(T)$ dependences were obtained. In these calculations $g_J = 2$ was used and the values of J were determined by comparison of the experimental temperature dependences of the spontaneous magnetization in the vicinity of the Curie temperature with the results of the calculations made by MFA. The values of J, g_J, T_C and Debye temperature T_D are given in table 4.1.

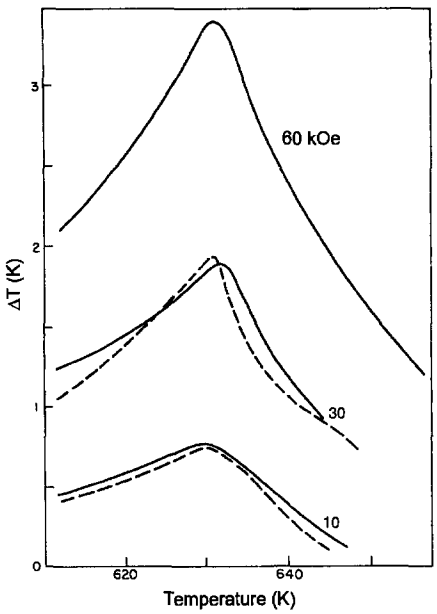


Fig. 4.2. Theoretical (solid lines) and experimental (dashed lines) temperature dependences of the MCE in Ni induced by the magnetic field changes ΔH specified near the curves (Tishin 1990a; Weiss and Forrer 1924).

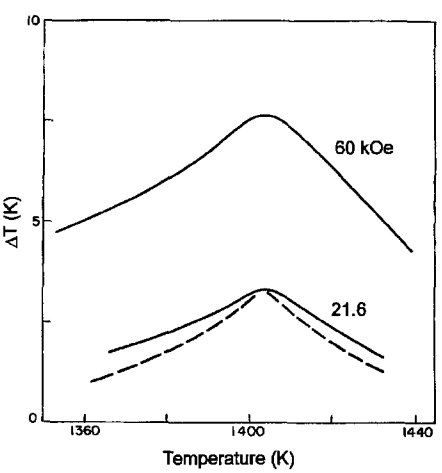


Fig. 4.3. Theoretical (solid lines) and experimental (dashed lines) temperature dependences of the MCE in Co induced by the magnetic fields specified near the curves (Tishin 1990a; Kohlhaas 1967).

Figures 4.1–4.3 present the results of theoretical calculations (solid lines) made by Tishin (1990a) together with experimental curves (dashed lines) of the MCE (Weiss and Forrer 1924; Potter 1934; Kohlhaas 1967). As one can see, they are in relatively good agreement. For $\Delta H = 60$ kOe near the Curie temperature the MCE value in Fe is 9.5 K. In

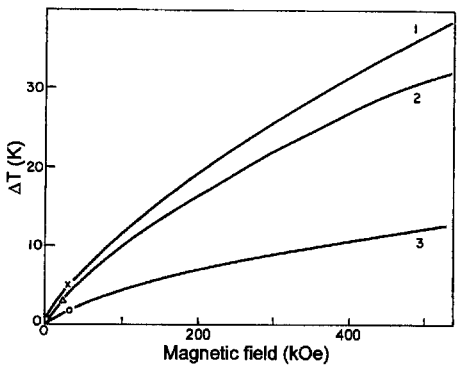


Fig. 4.4. Theoretical dependences of the MCE on the magnetic field (the magnetic field was changed from 0 to H) at $T = T_C$ for Fe (1), Co (2) and Ni (3) (Tishin 1990a). Experimental values are taken from the results published by Weiss and Piccard (1918), Potter (1934) and Kohlhaas (1967).

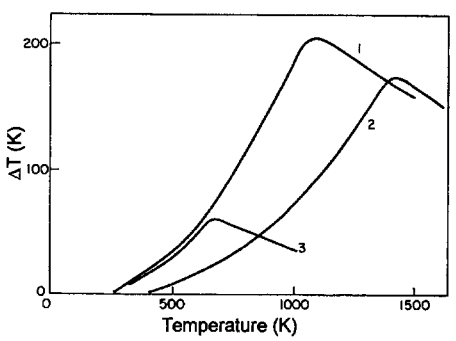


Fig. 4.5. Theoretical temperature dependences of the MCE induced by a field change of 6×10^3 kOe in Fe (1); Co (2) and Ni (3) (Tishin 1990a).

Gd and Tb, having the largest values of the MCE among the rare earth metals, the magnetocaloric effect is 12 and 10.5 K, respectively (Brown 1976; Nikitin et al. 1985a, 1985b).

Figure 4.4 shows the results of calculations of MCE field dependences in Fe, Ni and Co near the Curie temperature. It follows from fig. 4.4 that the linear increase of the MCE value with the field is observed in weak magnetic fields only. The experimental values of the MCE (see fig. 4.4) are well described by the calculated dependences.

Figure 4.5 presents the temperature dependences of the MCE in Fe, Ni and Co induced by a magnetic field of 6×10^3 kOe. Unlike rare earth metals, in 3d ferromagnets in this field the maximum of the MCE is fairly sharp. The MCE in Fe and Co exceeds that of Ni by several times. Tishin (1990a) calculated the maximum possible MCE in Fe, Co and Ni using eq. (2.77b). The maximum possible ΔS_M value was determined by eq. (2.70) for the corresponding J value. The values of $\Delta H_{max}(T_C)$ in which the MCE is different from ΔT_{max} by at most 1% were calculated in the framework of MFA. The results are shown in table 4.1. ΔT_{max} in Fe and Co is larger than in rare earth metals (see table 7.3).

Analogous mean field calculations of MCE were made by Hashimoto et al. (1981), which were found to be in good agreement with experimental results for Ni (Weiss and Forrer 1926). It was found that in Ni $\Delta T \approx 1.3$ K at $T_C = 628$ K and $\Delta H = 17.8$ kOe.

Noakes and Arrott (1973) studied the MCE of a nickel single crystal in the vicinity of T_C in weak fields up to 900 Oe. They found the maximum $\Delta T = 0.15$ K at $\Delta H = 900$ Oe.

The magnetocrystalline anisotropy contribution to the MCE can be found in the following way. In the general case the anisotropic part of the Gibbs energy can be written down as:

$$G_a = \sum_i K_i \psi_i, \tag{4.1}$$

where K_i is the anisotropy constant, ψ is a function of the orientation of the spontaneous magnetization vector. From eqs (2.8a), (2.77) and (4.1) the following formula for the MCE due to a rotation of the spontaneous magnetization can be obtained:

$$\Delta T_a = \frac{T}{C_{p,H}} \sum_i \left(\frac{\partial K_i}{\partial T}\right)_{p,H} \Delta\psi_i. \tag{4.2}$$

The MCE due to rotation of the spontaneous magnetization was investigated in Ni by Akulov and Kirensky (1940). To measure this effect a single crystal of nickel was placed in a field exceeding the value of technical saturation and then quickly turned with respect to the field. The value of temperature change was $\sim 10^{-3}$ K at 78 K. Under the conditions of measurement the energy of the magnetocrystalline anisotropy of a cubic crystal can be written down as:

$$G(T, H) \approx K_1(T) \sum_i \alpha_i^2 \alpha_j^2, \tag{4.3}$$

where $\alpha_i = H_i/|\vec{H}|$ are the direction cosines of the magnetic field $\vec{H}$ (or $\vec{I}_s$) with respect to the crystal axes, K_1 is the magnetocrystalline anisotropy constant. On the basis of eq. (4.3) the following expression can be derived (Akulov and Kirensky 1940):

$$\Delta T = \frac{T}{C_{p,H}} \left(\frac{\partial K_1}{\partial T}\right)_H \Delta \sum_{i \neq j} \alpha_i^2 \alpha_j^2. \tag{4.4}$$

The effect reaches its maximum value at low temperatures, where the derivative $(\partial K_1/\partial T)_H$ has high values. The results of experimental MCE measurements showed a fairly good agreement with calculations made by eq. (4.4).

The MCE due to rotation of the saturation magnetization in Co which has a hexagonal crystal structure and is characterized by an axial anisotropy was considered by Ivanovskii (1959), Ivanovskii and Denisov (1966a, 1966b). For a single crystal the following formula was obtained:

$$\Delta T = \frac{T}{C_{p,\Theta}} \left[\left(\frac{\partial K_1}{\partial T}\right)_\Theta \Delta \sin^2 \Theta + \left(\frac{\partial K_2}{\partial T}\right)_\Theta \Delta \sin^4 \Theta \right], \tag{4.5}$$

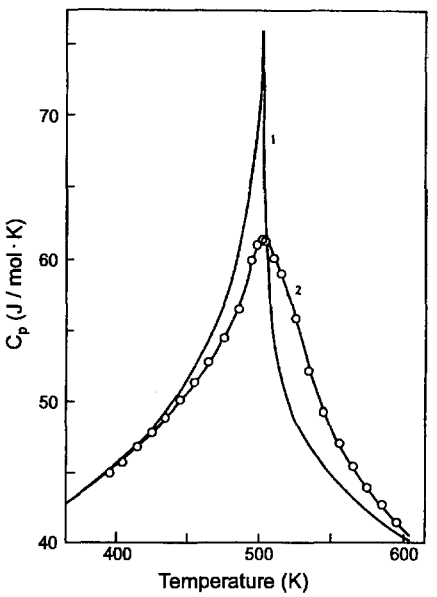


Fig. 4.6. Heat capacity of Fe in zero magnetic field (1) (experimental data) and $H = 30$ kOe (2) (calculated curve) (Kohlhaas et al. 1966).

where Θ is the angle between the c-axis and $\vec{I}_s$, and $C_{p,\Theta}$ is the heat capacity under constant pressure and Θ. On the basis of eq. (4.3) and the assumption of a random distribution of crystallite axes, Ivanovskii (1959) derived a formula for the MCE under magnetization of Co polycrystals. Experimental measurements showed that below 500 K the MCE caused by magnetic field increase had a negative sign ($\Delta T \approx 7 \times 10^{-2}$ K for $T = 504$ K and $\Delta H = 7$ kOe) and above 600 K ΔT was positive. The sign change of ΔT took place near 565 K. Ivanovskii (1959) related this behavior with the temperature dependence of K_1 in Co: near 535 K K_1 changed its sign from positive in lower temperature region to negative at higher temperatures.

To obtain the heat capacity of Fe in a magnetic field on the basis of the zero-field heat capacity and MCE measurements, eq. (2.96a) was used by Kohlhaas et al. (1966). As one can see from fig. 4.6, where the experimental results and the results of calculations are shown, the $C_{H,p}(T)$ curve near T_C becomes smooth and the maximum of $C_{H,p}$ becomes significantly lower under the influence of the magnetic field. Analogous behavior was observed in Ni, Co and Fe–Si alloys (Hirschler and Rocker 1966; Rocker and Kohlhaas 1967; Korn and Kohlhaas 1969).

4.2. Alloys and compounds

The MCE in ferromagnetic Cr_3Te_4 was investigated experimentally and theoretically using MFA by Hashimoto et al. (1981). The results are shown in fig. 4.7, where one can see a fairly good agreement between the calculations and experiment. At $T_C = 316$ K the MCE

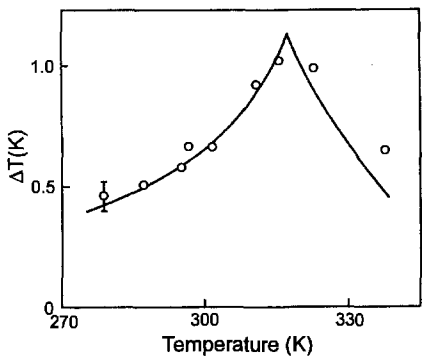


Fig. 4.7. The MCE in Cr_3Te_4 induced by a magnetic field of 20 kOe. Open circles are the experimental points and the solid curve is the MFA calculation (Hashimoto et al. 1981).

TABLE 4.2

Magnetic entropy change ΔS_M induced by a magnetic field change ΔH in some 3d metal based ferromagnets (Hashimoto et al. 1982).

Substance	T_C, K	$\lvert\Delta S_M\rvert$, $\times 10^{-3}$ J/g K	
		$\Delta H = 10$ kOe	$\Delta H = 8$ kOe
MnAs	318	2.9	11.4
MnP	298	2.9	11.4
CrTe	333	1.7	6.8

in Cr_3Te_4 reaches a value of $\approx$1.1 K for $\Delta H = 20$ kOe. The results on ΔS_M in the ferromagnets MnAs, MnP and CrTe, which have Curie points near room temperature are presented in table 4.2.

MFA was successfully used to describe the MCE in ferromagnetic compound Mn_5Ge_3, which had at $T_C = 298$ K $\Delta T \approx 1.7$ K for $\Delta H = 20$ kOe (Hashimoto et al. 1982).

Figure 4.8 shows the temperature dependence of the magnetic moment in a field of 4 kOe and ΔT for $\Delta H = 6.5$ kOe in the MnAs compound (Kuhrt et al. 1985). The temperature hysteresis accompanying the first-order transition from paramagnetism (PM) to ferromagnetism (FM) is also observed for the MCE.

In $MnAs_{1-x}P_x$ ($x = 0.08$; 0.09) compounds complex first-order field-induced transitions between different magnetic states (FM – spiral structure – FM) were observed below the magnetic ordering temperature (for $x = 0.08$ it was $\approx$ 220 K) (Kuhrt et al. 1985). The value of the MCE anomalies at these transitions was described by the Clausius–Clapeyron equation (2.82). For $x = 0.08$ at $T = 220$ K and $H = 70$ kOe $\Delta T \approx 1.2$ K. The temperature dependences of the heat capacity for $MnAs_{1-x}P_x$ ($0.03 \leqslant x \leqslant 0.13$) were measured by Krokozinski et al. (1982).

The MCE at the first-order transitions from ferri-(FI) or ferromagnetism to antiferromagnetism (AFM) was studied in FeRh (with Fe concentrations 0.48–0.50), $Mn_{2-x}Cr_xSb$ ($x = 0.03$; 0.05; 0.10; 0.16), Mn_3Ge_2, $CrS_{1.17}$ and $Mn_{0.95}V_{0.05}As$ (Selte et al. 1977; Flippen and Darnell 1963; Ponomarev 1972; Nikitin et al. 1990; Baranov et al. 1992).

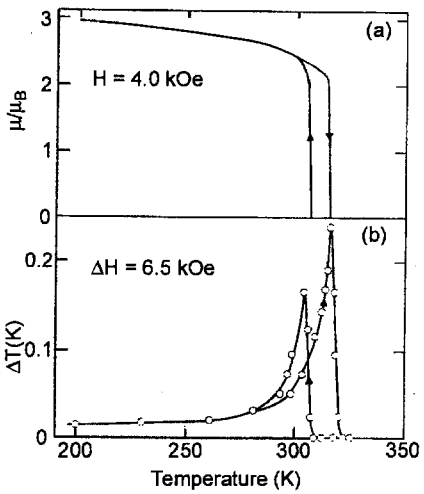


Fig. 4.8. Temperature dependence of the magnetic moment at $H = 4$ kOe (a) and MCE for $\Delta H = 6.5$ kOe (b) in the MnAs compound (Kuhrt et al. 1985).

In Fe–Rh alloys the AFM–FM phase transition takes place near room temperature within the concentration range 47–53% of Rh (Kouvel and Hartelius 1962; Zaharov et al. 1964). MCE measurements on quenched and annealed $Fe_{0.49}Rh_{0.51}$ were made by Nikitin et al. (1990) in magnetic fields up to 19.5 kOe. Magnetic fields induce the transition from the AFM structure, arising below the transition point $T_{\text{AFM–FM}} \approx 310$ K, to a ferromagnetic one. This is accompanied by sample cooling, reaching 13 K for the quenched sample at a field of 20 kOe (see fig. 4.9). It should be noted that the quenched and annealed samples display different values of the MCE and different temperature dependences of the MCE. Since the transition was of the first order, it had an irreversible character and $\approx$ 20–30 kOe was required to overcome the hysteresis effects.

Ponomarev (1972) studied the magnetization of $Fe_{0.58}Rh_{0.58}$ in pulsed fields up to 300 kOe in the temperature range from 77 to 330 K. He constructed the magnetic phase diagram $H_{\text{cr}}(T)$ (here H_{cr} is the field of the AFM structure destruction) and determine the specific magnetization change $\Delta\sigma$ ($\sigma = M/m$, where m is the mass) across the transition. On the basis of these data and the Clausius–Clapeyron equation (2.82) the magnetic entropy change ΔS_M at the transition temperature $T_{\text{AFM–FM}} = 333$ K was calculated ($\Delta S_M = 1.83 \times 10^5$ erg/g K), and then by eq. (2.77) the value $\Delta T \approx 20$ K was obtained.

Analogous calculations of ΔS_M were made by Baranov et al. (1992) for $Mn_{1.9}Cr_{0.1}Sb$ and by Flippen and Darnell (1963) for $Fe_{0.5}Rh_{0.5}$, $Mn_{2-x}Cr_xSb$, Mn_3Ge_2, $CrS_{1.17}$, $Li_{0.1}Mn_{0.9}Se$ on the basis of the data of Heikes et al. (1961). The results are shown in table 4.3. Direct measurements of the MCE in $Mn_{1.9}Cr_{0.1}Sb$ made by Baranov et al. (1992) gave $\Delta T = -2.7$ K for $\Delta H = 60$ kOe at $T \approx 245$ K in the vicinity of transition point.

Selte et al. (1977) studied the magnetocaloric effect in $Mn_{0.95}V_{0.05}As$ in pulsed magnetic fields up to 210 kOe and at the temperatures from 160 K to 260 K. At the transition from a helicoidal antiferromagnetic (HAFM) state with MnP crystal structure to a ferromagnetic state with NiAs structure near 200 K a positive MCE with a maximum value of about 5 K was induced by a field change of 210 kOe.

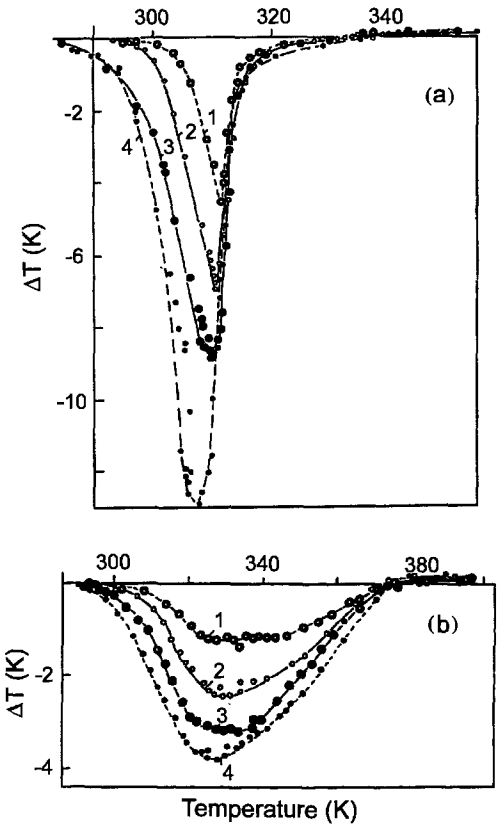


Fig. 4.9. Temperature dependences of the MCE for a quenched (a) and annealed (b) sample of $Fe_{0.49}Rh_{0.51}$ induced by a magnetic field: (1) $\Delta H = 6.5$ kOe; (2) 12.5 kOe; (3) 17 kOe; (4) 19.5 kOe (Nikitin et al. 1990).

Okazaki et al. (1993) investigated the MCE in ferromagnetic Ni–Mn alloys (66–83% Ni) characterized by partial atomic disorder in the crystalline structure. The degree of order was changed by annealing of the sample. The MCE peak was observed in the Curie temperature region and had a maximum value of about 0.5 K for $H = 6.4$ kOe in the ordered $Mn_{0.17}Ni_{0.83}$ alloy. Linear $\Delta T(I^2)$ dependences observed in this alloy system allowed to obtain the $I_s(T)$ curve. The MCE has also been studied by Sucksmith et al. (1953) in copper–nickel and by Znamenskii and Fakidov (1962) in copper–manganese alloys. An investigation of MCE in distorted triangular lattice antiferromagnet $RbMnBr_3$ has been done by Pérez et al. (1998).

4.3. Thin films

The MCE and magnetic entropy change induced by a magnetic field in thin films prepared on the basis of 3d elements was studied by Babkin and Urinov (1987, 1989) and Morelli et al. (1996). Babkin and Urinov (1989) considered the MCE due to the uniform rotation

TABLE 4.3

Change of the specific magnetization ($\Delta\sigma$) and magnetic entropy (ΔS_M), and temperature derivative ($\partial H_{cr}/\partial T$) of the critical field at the first order transition T_s in some magnetic substances based on 3d metals.

Substances	T_s, K	$\Delta\sigma$, emu/g	$-\partial H_{cr}/\partial T$, kOe/K	ΔS_M, $\times 10^4$ erg/g K	Ref.
$Mn_{1.97}Cr_{0.03}Sb$	127	39.6	1.08	4.28	[1]
$Mn_{1.95}Cr_{0.05}Sb$	211	32.8	1.97	6.5	[1]
$Mn_{1.90}Cr_{0.10}Sb$	305	24.3	2.43	5.9	[1]
	264	≈26	2.6	≈6.8	[2]
$Mn_{1.84}Cr_{0.16}Sb$	373	13.7	2.33	3.19	[1]
Mn_3Ge_2	164	3.5	2.08	0.72	[1]
$CrS_{1.17}$	160	1.85	2.29	0.42	[1]
$Fe_{0.5}Rh_{0.5}$	355	117	0.925	10.8	[1]
$Fe_{0.48}Rh_{0.52}$	333	104	1.75	18.3	[3]
$Li_{0.10}Mn_{0.90}Se$	72	26.4	5.3	14	[1]

References:

[1] Flippen and Darnell (1963)
[2] Baranov et al. (1992)
[3] Ponomarev (1972)

of the spontaneous magnetization vector in thin films. The magnetic free energy of the film was presented as:

$$F_M = K\sin^2\Theta - IH\cos(\phi - \Theta), \tag{4.6}$$

where K is the film anisotropy constant including the form anisotropy and induced magnetic anisotropy, ϕ and Θ are the angles between the film surface and the $\vec{H}$ and $\vec{I}$ vectors, respectively.

The value of the MCE was determined with the help of eqs (2.21), (2.7a) and the expression for equilibrium magnetic free energy obtained from eq. (4.6). The following formula for the MCE was derived (Babkin and Urinov 1989):

$$\left(\frac{\Delta T}{\Delta H}\right)_S = \left\{\frac{T}{C_H}\,\frac{K\sin^2 2\Theta}{IH[2K\cos 2\Theta + IH\cos(\phi - \Theta)]}\left[I\frac{\partial K}{\partial T} - K\frac{\partial I}{\partial T}\right] - \frac{T}{C_H}\,\frac{\partial I}{\partial H}\cos(\phi - \Theta)\right\}. \tag{4.7}$$

Depending on the relation between $K(T)$ and $I(T)$ the first term in eq. (4.7) gives a positive or negative contribution to the MCE. If the anisotropy is absent ($K = 0$, $\phi = 0$), eq. (4.7) transforms into eq. (2.16). If the film anisotropy is governed only by the form anisotropy ($K = 2\pi I^2$) the first term in eq. (4.7) is always negative. Figure 4.10(a) presents the results of calculations made by using eq. (4.7) for the case $H = 4\pi I$ and $K = 2\pi I^2$.

Experimental MCE measurements were made on polycrystalline ferromagnetic Ni and single crystalline ferrimagnetic dielectric γ-Fe_2O_3 films, 0.15–0.30 μm thick. A vanadium

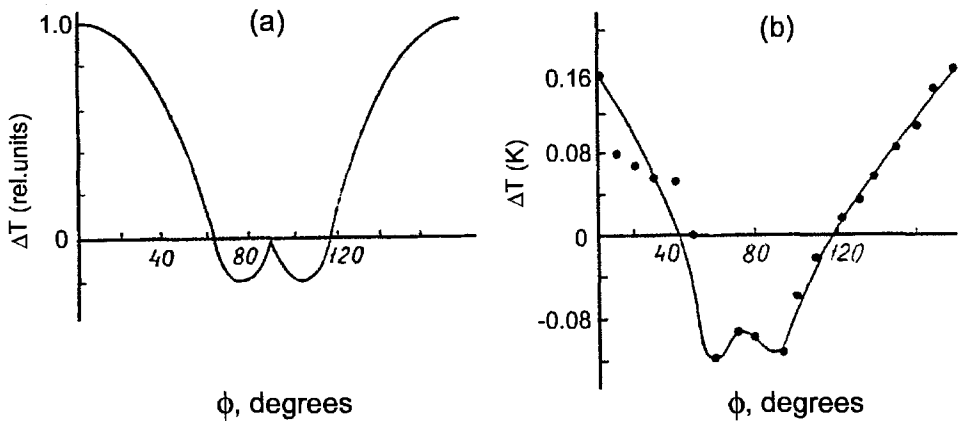


Fig. 4.10. Dependence of the MCE on the angle ϕ between the film surface and the magnetic field H: (a) theoretical calculation using eq. (4.7) for $H = 4\pi I$ and $K = 2\pi I^2$; (b) experimental data for the Ni film, $H = 3.4$ kOe (Babkin and Urinov 1989).

dioxide film 0.1–0.5 μm thick was used as a temperature-sensitive element (its resistance decreased drastically under heating near $\approx$ 330 K).

The experimental results for the Ni film for $H = 3.4$ kOe are shown in fig. 4.10(b) (analogous, but some more complicated behavior was displayed the γ-Fe_2O_3 film). With increasing magnetic field the maximum of the MCE near the hard magnetization axis ($\phi = 0$) disappears. The proposed theory contradicts the experimental results obtained for an orientation of the magnetic field near the hard axis (the region of negative MCE). The authors related such behavior to the presence of defects and surface anisotropy in the films, which broke the condition for uniform rotation of the magnetization vector.

Morelli et al. (1996) investigated the magnetic entropy change ΔS_M induced by the magnetic field in doped lanthanum manganite the 2.4 μm thick polycrystalline films of $La_{0.67}A_{0.33}MnO_3$ (A = Ca, Ba, or Sr) display FM–PM transition at 250, 300, and 350 K, respectively. The films were fabricated by a metalorganic deposition technique. The $\Delta S_M(T)$ dependences were calculated on the basis of magnetization data by using eq. (2.71). Near the Curie temperatures, wide maxima of ΔS_M were observed with the following values (for $H = 50$ kOe applied parallel to the film plane): 2×10^4 erg/g K for A = Ca, 1.4×10^4 erg/g K for Ba, and 1.5×10^4 erg/g K for Sr.

5. Magnetocaloric effect in oxides

5.1. Garnets

The MCE in polycrystalline rare earth garnets $R_3Fe_5O_{12}$ (R = Gd, Tb, Dy, Ho, Er, Tm, Yb, and Y) was studied by Belov et al. (1968, 1969, 1970, 1972), Belov and Nikitin (1970a, 1970b), Talalaeva et al. (1969) and Clark and Callen (1969).

Figure 5.1 shows the temperature dependences of MCE in $R_3Fe_5O_{12}$ polycrystals (R = Y, Gd, Tb, Dy, Ho, Er, Yb, Tm) induced by the magnetic field change of 16 kOe in the

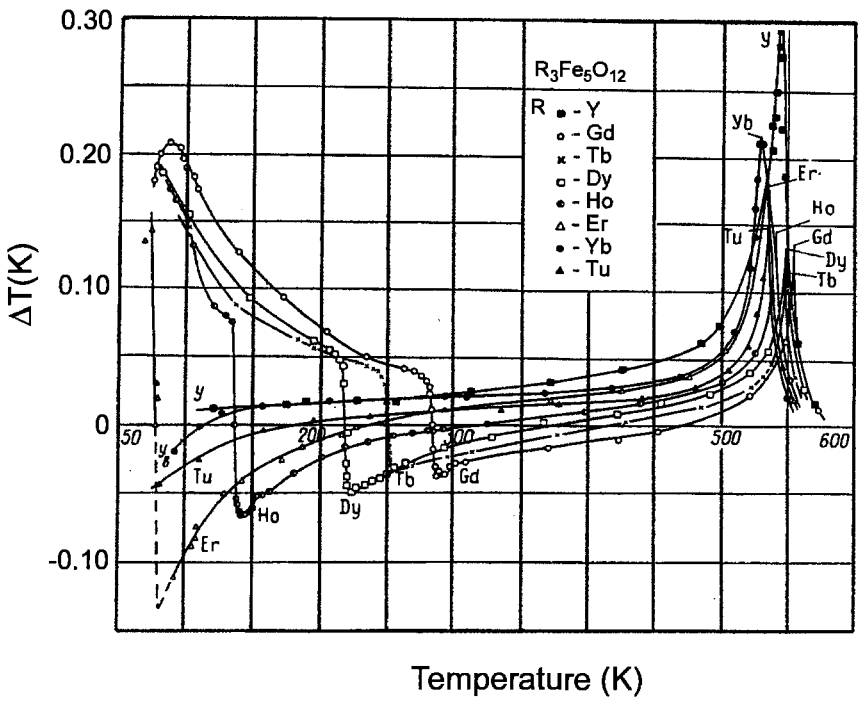


Fig. 5.1. Temperature dependences of the MCE induced by 16 kOe in $R_3Fe_5O_{12}$ (Belov et al. 1969).

temperature range from 78 to 600 K (Belov et al. 1969). One can see that for R = Y the MCE is positive in the whole temperature range and has a maximum near the Curie temperature. For R = Gd the $\Delta T(T)$ curve becomes more complicated. It also has a positive maximum near the Curie temperature, but then near 462 K, the MCE becomes negative. At $T = 285$ K the MCE suddenly changes its sign and in low temperature region another maximum appears. Analogous behavior was observed in other rare earth garnets. In the garnets with R = Tm and Yb the compensation points lie in the region of liquid helium temperatures. Clark and Callen (1969) measured the MCE in these compounds and found that the MCE induced by 110 kOe is negative near 4.2 K.

Such behavior is related with the ferrimagnetic structure of the rare earth iron garnets. According to the Néel model (Néel 1954) these materials have a magnetic structure consisting of three magnetic sublattices. The R^{3+} ions occupy dodecahedral sites (c-sublattice) and the Fe^{3+} ions occupy octahedral (a-sublattice) and tetragonal (d-sublattice) sites. The a- and d-sublattices are connected by strong antiferromagnetic exchange interactions. The weaker antiferromagnetic interaction takes place between d- and c-sublattices and the c–c and a–c interactions are weak and positive (Anderson 1964). Such exchange field distribution leads to a strong paraprocess in the c-sublattice in the whole temperature range below T_C, which displays itself in a strong temperature and field dependence of the c-sublattice magnetic moment. An intensive paraprocess in the a- and d-sublattices is pos-

sible only near T_C and the total magnetic moments of the d- and a-sublattices have weak field and temperature dependence at low temperatures.

Belov and Nikitin (1965, 1970a), in the framework of MFA, estimated the values of effective fields acting in the RE magnetic sublattice ($H_{2\text{eff}}$) and in the iron a–d magnetic sublattices ($H_{1\text{eff}}$) in rare earth iron garnets. It was shown that $H_{2\text{eff}} \approx 3 \times 10^5$ Oe and $H_{1\text{eff}} \approx 1.7 \times 10^6$ Oe, i.e., $H_{1\text{eff}} \gg H_{2\text{eff}}$.

Due to the difference in temperature dependences of the c- and a-, d-sublattice magnetizations, the compensation temperature T_{comp}, characteristic for ferrimagnets, appears in the garnets with heavy rare earth metals. Above T_{comp} the magnetic moment of the c-sublattice $\vec{M}_R$ is lower than the total magnetic moment of the a- and d-sublattices $\vec{M}_{Fe}$ and below T_{comp} the inverse situation takes place. The resultant magnetic moment of the rare earth iron garnet is $\vec{M} = \vec{M}_R + \vec{M}_{Fe}$ and it is oriented along the field direction. This leads to a change of the $\vec{M}_R$ and $\vec{M}_{Fe}$ orientations relative to the field at $T = T_{\text{comp}}$. Such behavior was observed by neutron diffraction measurements (Bertaut et al. 1956; Herpin and Meriel 1957; Prince 1957).

Belov and Nikitin (1970) considered the MCE and heat capacity near the compensation point of rare earth iron garnets in the framework of MFA using thermodynamic formulae (2.16) and (2.95), which were presented in vector form:

$$\mathrm{d}T = -\frac{T}{C_{H,p}}\left(\frac{\partial \vec{M}}{\partial T}\right)\mathrm{d}\vec{H}, \tag{5.1}$$

$$\Delta C = C_H - C_M = -T\left(\frac{\partial \vec{M}}{\partial T}\right)_H\left(\frac{\partial \vec{H}}{\partial T}\right)_M. \tag{5.2}$$

The total MCE was determined as the sum:

$$\Delta T = \Delta T_{Fe} + \Delta T_R. \tag{5.3}$$

Since $|\partial M_R/\partial T| \gg |\partial M_{Fe}/\partial T|$ and $|\partial M_R/\partial H| \gg |\partial M_{Fe}/\partial H|$ below T_C, the main contribution to the MCE in the low temperature region far enough from T_C is provided by the rare earth a-sublattice. On the basis of this the following equation for the MCE was obtained:

$$\Delta T = \frac{I_{20}}{C_{H,p}k_B T}\frac{\partial B_j(x_2)}{\partial x_2}\vec{H}\left(\frac{I_{20}}{2n\nu_2}\vec{H} + 2\mu_B s_2 \vec{H}_{2\text{eff}}\right), \tag{5.4}$$

where I_{20} is the magnetization of the RE sublattice at $T = 0$ K, ν_2 is the number of the RE atoms in the molecule, s_2 is the spin of the RE atom, n is the number of molecules in the unit volume, B_J is the Brillouin function. $\vec{H}_{2\text{eff}}$ is the molecular field acting on the RE sublattice due to the iron a–d sublattice:

$$H_{2\text{eff}} = \frac{z_{21}\mathcal{I}_{21}}{\mu_B}\frac{I_1}{I_{10}}, \tag{5.5}$$

where z_{21} is the number of the nearest neighbors of the a–d sublattice to an atom of the RE sublattice; $\mathcal{I}_{21}$ is the exchange integral describing the interactions between the RE and Fe sublattices; I_1 is the magnetization of the a–d sublattices, I_{10} equals I_1 at $T = 0$ K;

$$x_2 = \frac{I_{20}}{n\nu_2 k_B T} H + \frac{2\mu_B s_2}{k_B T} H_{2\text{eff}}. \tag{5.6}$$

If the directions of $\vec{H}$ and $\vec{H}_{2\text{eff}}$ coincides, then $\Delta T > 0$. In this case the external magnetic field increases the magnetic order in the c-sublattice, which leads to a decrease of the magnetic entropy and to sample heating. If $\vec{H}$ and $\vec{H}_{2\text{eff}}$ are aligned in opposite directions, then $\Delta T < 0$. The external magnetic field H in this case acts against $H_{2\text{eff}}$ and decreases the magnetic order in the c-sublattice. Such a process is accompanied by a magnetic entropy increase and a corresponding sample cooling. The paraprocesses of these two types were called ferromagnetic and antiferromagnetic ones, respectively (Belov 1968, Belov et al. 1968, 1969, 1972).

The ferro- and antiferromagnetic paraprocesses can be realized in the same magnetic sublattice at various temperature ranges, but in the rare earth iron garnets the MCE below T_C is determined by the paraprocess in the c-sublattice. Near T_C the ferromagnetic paraprocess in the iron a–d sublattice overcomes the antiferromagnetic one in c-sublattice and MCE becomes positive at some temperature, reaching a maximum near T_C.

The sign change of ΔT at T_{comp} is related with the change of the $\vec{M}_{\text{Fe}}$ orientation (and, consequently, the $\vec{H}_{2\text{eff}}$ orientation) relative to the magnetic field direction. The jump of ΔT observed at T_{comp} should be inversely proportional to T_{comp}, as it follows from eq. (5.4). This was confirmed experimentally in rare earth iron garnets by Belov et al. (1969). As it was noted by Belov and Nikitin (1970a, 1970b), the existence of ΔT jumps at T_{comp} points to the first-order character of this magnetic phase transition.

If the magnetic c-sublattice in the garnet is absent, as is in the case for R = Y, one can observe a $\Delta T(T)$ curve with one maximum near the Curie point, caused by the paraprocess in the a–d sublattice (although a- and d-sublattices are connected by negative exchange interaction, the ferromagnetic paraprocess in the d-sublattice prevails in the whole temperature range), see fig. 5.1.

Below T_{comp} at $T \approx 90$ K the MCE in $Gd_3Fe_5O_{12}$ displays an additional maximum which is higher than one near T_C. Also in the garnets with Ho, Dy and Tb an increase of the MCE below T_{comp} was observed (see fig. 5.1). Such behavior was related with a sharp change of the long range magnetic order, which took place in the RE sublattice in this temperature range (Belov 1961b; Belov and Nikitin 1970b). The low temperature of this ordering is due to the weakness of the effective field acting on the RE sublattice due to the a–d iron sublattice.

The replacement of Fe in the garnets by nonmagnetic ions can lead to a further decrease of the effective field $H_{2\text{eff}}$ and, consequently, to an increase of the RE sublattice paraprocess and the MCE in low temperature range. Such MCE increase was observed experimentally in $Gd_3Ga_xFe_{5-x}O_{12}$ ($0 \leqslant x \leqslant 1.5$) by Belov et al. (1972) (see fig. 5.2). The gadolinium gallium iron garnets (GGG) with $x > 1.5$ have superparamagnetic properties and will be considered in section 8.

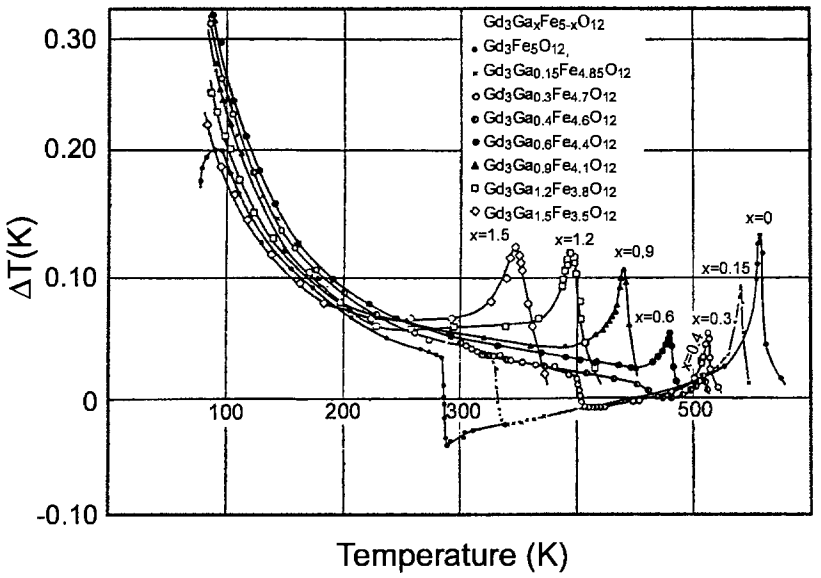


Fig. 5.2. Temperature dependences of the MCE induced by 16 kOe in $Gd_3Ga_xFe_{5-x}O_{12}$ ($0 \leqslant x \leqslant 1.5$) (Belov et al. 1972).

The magnetothermal properties of gadolinium gallium garnet $Gd_3Ga_5O_{12}$ (GGG), dysprosium gallium garnet $Dy_3Ga_5O_{12}$ (DGG) and dysprosium aluminum garnet $Dy_3Al_5O_{12}$ (DAG) were studied by Fisher et al. (1973), Filippi et al. (1977), Daudin et al. (1982), Hashimoto (1986), Li et al. (1986), Kimura et al. (1988), Kuz'min and Tishin (1991, 1993a, 1993b), Schiffer et al. (1994).

GGG and DGG have antiferromagnetic ordering below $T_N = 0.8$ K and 0.373 K, respectively. Above T_N they display simple paramagnetic behavior (Filippi et al. 1977; Yazawa et al. 1986). Figure 5.3 shows the temperature dependences of the magnetic entropy change for various ΔH for GGG and DAG (Hashimoto 1986; Li et al. 1986).

Below 20 K the population of all but the ground Kramers doublets of the Dy ions in DGG and DAG can be neglected, since the energy of the exited state is larger than the thermal agitation energy (Kuz'min and Tishin 1991). Therefore the value $J = 1/2$ can be used for the total angular momentum quantum number of these ions. For Gd^{3+} ion the crystal field splitting of the ground state with $J = 7/2$ (g-factor equals 2) is negligible for $T > 4.2$ K and this J value is thought to be the largest among the rare earth ions in the low temperature range. Figure 5.3 illustrates the ΔS_M increase for GGG in comparison with DAG in low temperature range caused by this effect.

Hashimoto (1986) by means of MFA studied the influence of the g-factor and J quantum number values on the temperature dependence of ΔS_M. The calculations were made for antiferromagnetic systems ($T_N = 1$ K) with $g_J = 2$ (J was being varied) and $J = 1/2$ (g_J was being varied) and for $\Delta H = 60$ kOe. It was found that ΔS_M increased with increasing J and g_J. For $J = 7/2$ and $g_J = 2$ the ΔS_M value was smaller than that for $J = 1/2$ and $g_J \geqslant 10$ at temperatures above 20 K.

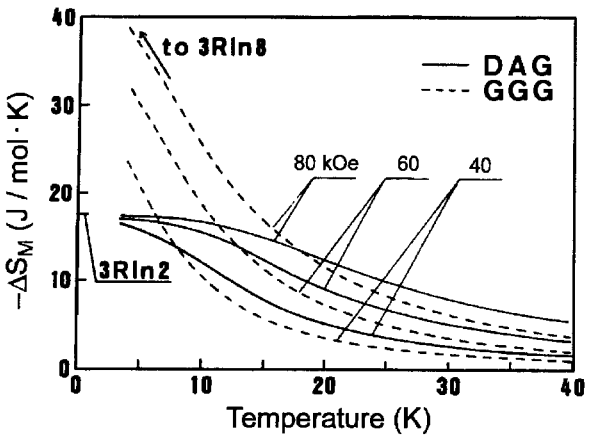


Fig. 5.3. Temperature dependences of ΔS_M in DAG and GGG induced by the magnetic field change $\Delta H = 40$, 60 and 80 kOe (Hashimoto 1986).

As it was shown by Numazawa et al. (1983), the thermal conductivity of GGG is ≈ 1 W/cm K at $T = 13$ K and ≈ 0.3 W/cm K at 4 K for DGG. The thermal conductivity of DAG is about twice of that in GGG (Hashimoto 1986).

The heat capacity of DGG and GGG was measured by Fisher et al. (1973), Filippi et al. (1977) and Schiffer et al. (1994). DGG displays a sharp λ-type heat capacity anomaly (with the height of $\approx 3R$) at $T_N = 0.35$ K. GGG shows a broad maximum with a value of about 2.4 R near $T_N = 0.8$ K. In an external magnetic field of 9 kOe the heat capacity maximum in GGG becomes sharp and shifts to 0.4 K. The heat capacity of $(Dy_{0.5}Gd_{0.5})_3Ga_5O_{12}$ was studied by Numazawa et al. (1996) in the temperature range from 0.65 to 4 K. At 0.65 K its heat capacity was about three times larger than that of GGG. The peak in $C(T)$ was expected to be below 0.65 K.

The field dependences of the MCE near the compensation point T_{comp} in $R_3Fe_5O_{12}$ (R = Gd, Dy and Ho) were studied by Belov et al. (1970). Tiablikov (1956), Pahomov and Gusev (1964) and Clark and Callen (1968) have shown, that in ferrimagnets in some field and temperature intervals ($H_{c1} < H < H_{c2}$, $T_{c1} < T < T_{c2}$) a noncollinear magnetic structure can appear as a result of competition between the external magnetic field and the negative intersublattice exchange interaction. H_{c1} and H_{c2} can achieve essential values, but near T_{comp} they should abruptly decrease (Clark and Callen 1968).

The noncollinear magnetic structure is characterized by a temperature independence of the total magnetic moment ($\partial M/\partial T = 0$) which, according to the eq. (2.16), gives $dT/dH = 0$. Consequently, the $\Delta T(H)$ dependence should have the following form in the noncollinear phase: an increase of ΔT with H for $H < H_{c1}$ with subsequent saturation for $H > H_{c1}$. This saturation behavior of $\Delta T(H)$ was observed near T_{comp} in $R_3Fe_5O_{12}$ (R = Gd, Dy, Ho) by Belov et al. (1970). Some field dependence of ΔT in the noncollinear phase revealed for R = Dy and Ho was related by the authors with the rare earth ion anisotropy.

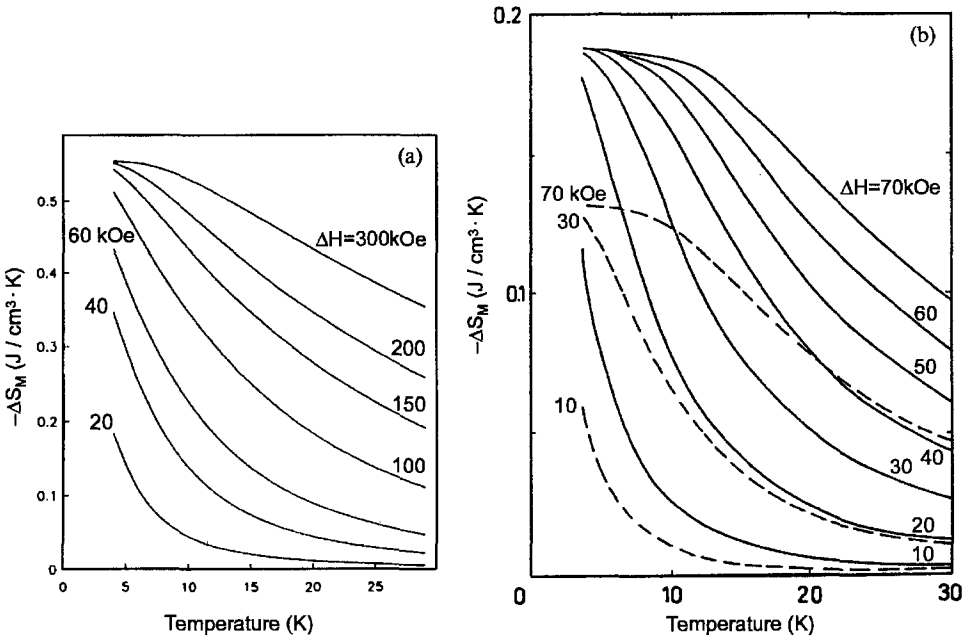


Fig. 5.4. Temperature dependences of the magnetic entropy change ΔS_M induced by a magnetic field in (a) $GdAlO_3$; (b) $DyAlO_3$ with H along the b-axis [0 1 0]. The dashed lines are the same for $Dy_3Al_5O_{12}$ with H along the [1 1 1] direction (Kuz'min and Tishin 1991, 1993b).

5.2. *Perovskites*

Rare earth orthoaluminates (REOA) $RAlO_3$ have an orthorhombically distorted perovskite structure (Geller and Bala 1956). REOA with R = Gd, Dy, Er display antiferromagnetic order below T_N = 3.875 K (Gd), 3.52 K (Dy) and 0.6 K (Er) and paramagnetism above T_N (Schuchert et al. 1969; Blazey et al. 1971; Sivardiere and Quezel-Ambrunaz 1971; Kimura et al. 1995). $DyAlO_3$ and $ErAlO_3$ are characterized by a substantial magnetic anisotropy (for $DyAlO_3$ $\mu_{eff} = 6.88\,\mu_B$ along the b-axis and $0.8\,\mu_B$ along the c-axis (Kolmakova et al. 1990)) and $GdAlO_3$ is almost magnetically isotropic. The magnetic entropy change ΔS_M induced by a field in $GdAlO_3$ and $DyAlO_3$ was calculated by Kuz'min and Tishin (1991, 1993a, 1993b) in the framework of MFA (J was taken to be 7/2 and 1/2, for Gd and Dy perovskites, respectively) (see fig. 5.4).

Kimura et al. (1995, 1997) determined ΔS_M for $RAlO_3$ (R = Dy, Ho, Er) on the basis of magnetization measurements along various crystal axes and eq. (2.71). It was established that in $ErAlO_3$ and $DyAlO_3$ magnetization decreased with temperature increasing for all crystal axes. The same behavior was observed in $HoAlO_3$ along a- and b-axes, but along c-axis its magnetization remained almost constant. The easy magnetization axis in $DyAlO_3$ and $ErAlO_3$ are b- and c-axis, respectively (see Kuz'min and Tishin 1991).

The experimental ΔS_M results are shown in fig. 5.5(a). As one can see a substantial dependence of ΔS_M character on the direction of a measurement is observed. The experimental results for $DyAlO_3$ and $ErAlO_3$ along the easy axes are in good agreement with

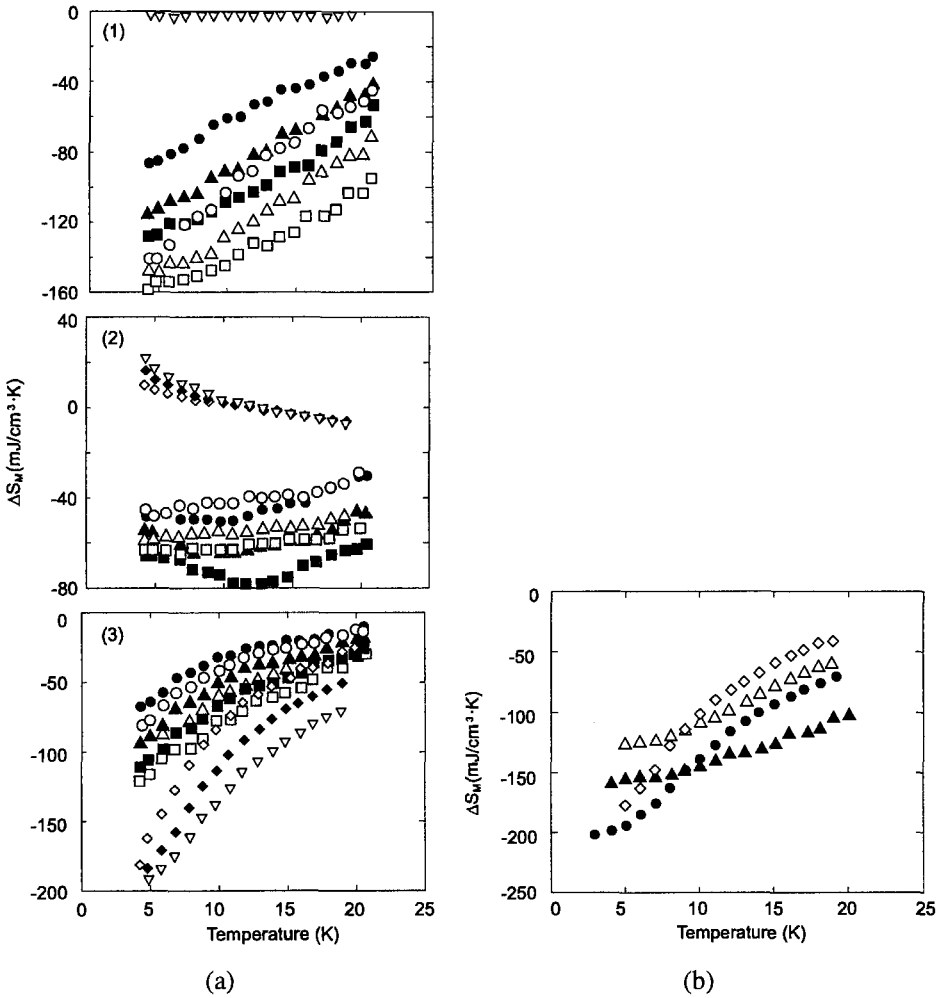


Fig. 5.5. (a) Temperature dependences of the magnetic entropy change ΔS_M induced by a various changes of a magnetic field, applied along *a*- (solid circles ($\Delta H = 30$ kOe), solid triangles (40 kOe), solid squares (50 kOe)), *b*- (open circles (30 kOe), open triangles (40 kOe), open squares (50 kOe)) and *c*-axis (open diamonds (30 kOe), solid diamonds (40 kOe), inverted open triangles (50 kOe)) in $DyAlO_3$ (1); $HoAlO_3$ (2); $ErAlO_3$ (3) single crystals, respectively. The ΔS_M is calculated on the basis of the experimental magnetization data. (b) Comparison of ΔS_M temperature dependences in $DyAlO_3$ (solid triangles) measured along *b*-axis and in $ErAlO_3$ (solid circles) along *c*-axis with that in $Gd_3Ga_5O_{12}$ (open diamonds) and $Dy_3Al_5O_{12}$ (open triangles) measured along [1 1 1] direction with a magnetic field change of 50 kOe (Kimura et al. 1997).

the calculations of Kuz'min and Tishin (1991). Kimura et al. (1995) made a comparison of ΔS_M induced by a field of 50 kOe for $ErAlO_3$ measured along c-axis, $DyAlO_3$ measured along *b*-axis and $Dy_3Al_5O_{12}$ and $Gd_3Ga_5O_{12}$ measured along [1 1 1] direction – see fig. 5.5(b). It is evident that ΔS_M for $ErAlO_3$ and $DyAlO_3$ is superior to that of $DyAl_5O_{12}$ and $Gd_3Ga_5O_{12}$. This is in agreement with the conclusion that $DyAlO_3$ and $ErAlO_3$ are

promising materials for magnetic refrigeration below 20 K, made by Kuz'min and Tishin (1991) on the basis of theoretical calculations.

Perovskite-type manganese oxides $R_{1-x}B_xMnO_3$ (R is a rare earth metal and B is a divalent alkali metal: Ca, Ba, Sr) are characterized by "colossal" magnetoresistance near the magnetic ordering temperature (Von Helmolt et al. 1993; Jin et al. 1994). In $La_{1-x}Ca_xMnO_3$ the colossal magnetoresistance takes place for $0.2 < x < 0.5$, where a transition from the paramagnetic insulating state to the ferromagnetic metallic state is observed. Samples with $0.5 < x < 1$ display the antiferromagnetic insulating state in the low temperature range. The magnetic phase diagram of $La_{1-x}Ca_xMnO_3$ system was constructed on the basis of the temperature dependences of the heat capacity by Ramirez et al. (1996). For $x > 0.5$, above T_N, an additional "charge ordering" transition occurs, which is accompanied by a maximum in the $C(T)$ curves.

Manganese perovskites are characterized by a considerable coupling between the magnetic and the lattice subsystems. This leads to an abrupt change of the magnetization, a discontinuous variation in the volume and softening of Young's modulus at the Curie temperature.

The sharp magnetization change should give a considerable magnetic entropy variation at the Curie point. The temperature dependences $\Delta S_M(T)$ in the $(La_{1-x}Ca_x)$ manganese oxide polycrystals were investigated by Zhang et al. (1996) and Guo et al. (1997a, 1997b). ΔS_M was determined on the basis of magnetization measurements. The results for $T = T_C$ are presented in table 5.1.

Zhang et al. (1996) studied ΔS_M in $La_{0.67}Ca_{0.33}MnO_\delta$. Substitution of Y reduces the saturation magnetization and consequently, ΔS_M (see table 5.1). The reduction was attributed by the authors to a decrease of the ferromagnetic coupling due to the contraction of the crystal lattice under substitution.

Guo et al. (1997a) determined ΔS_M in $La_{1-x}Ca_xMnO_3$ ($x = 0.20$; 0.33; 0.45). The $\Delta S_M(T)$ curves for $x = 0.20$ and 0.33 show a relatively narrow peak at T_C (see fig. 5.6). For $x = 0.45$ the maximum in the $\Delta S_M(T)$ curve is broader and smaller, which is consistent with a less sharp change of the magnetization at T_C in this sample compared with $x = 0.2$ and 0.33. $|\Delta S_M|$ at T_C for $x = 0.2$ is larger than that of gadolinium (≈ 4.2 J/kg K). It should be noted, that Zhang et al. (1996) obtained for $x = 0.33$ a $|\Delta S_M|$ value which is more than two times smaller than that measured by Guo et al. (1997a).

Polycrystalline $La_{0.75}Ca_{0.25}MnO_3$ samples with different average grain sizes were investigated by Guo et al. (1997b). T_C was found to be 177 K and 224 K for grain sizes of 120 and 300 nm, respectively. The lowering of T_C was accompanied by a broadening of the magnetic phase transition in the $M(T)$ curve. This leads to the broadening of the $\Delta S_M(T)$ peak and its decrease in the sample with 120 nm grain size. The values of ΔS_M at the Curie point are presented in table 5.1.

Recent MCE investigations of $La_{0.65}Ca_{0.35}Ti_{1-x}Mn_xO_{3-z}$ and $La_{0.5+x+y}Li_{0.5-3y}Ti_{1-3x}Mn_{3x}O_{3-z}$ conducted by Bohigas et al. (1998) suggest that the compounds are good candidates for working materials in enough wide temperature region.

The polycrystalline perovskite manganese oxide system $La_{1-x}Na_xMnO_3$ ($x = 0.075$, 0.10, 0.165, and 0.20) was studied by Zhong et al. (1998). The Curie temperature in this system varies from 193 K ($x = 0.075$) to 343 K ($x = 0.20$). $\Delta S_M(T)$ dependences were determined from magnetization measurements with the help of eq. (2.71) – ΔS_M maximum

TABLE 5.1

Magnetic entropy change ΔS_M induced by the magnetic field change ΔH at the Curie point for manganese oxides.*

Substance	T_C, K	$-\Delta S_M$, J/kg K	ΔH, kOe	Ref.
$La_{0.67}Ca_{0.33}MnO_\delta$	260	1.5	15	[1]
		2.5	30	
$La_{0.60}Y_{0.07}Ca_{0.33}MnO_\delta$	230	0.8	16	[1]
		2.5	30	
$La_{0.8}Ca_{0.2}MnO_3$	230	5.5	15	[2]
$La_{0.67}Ca_{0.33}MnO_3$	257	4.3	15	[2]
$La_{0.55}Ca_{0.45}MnO_3$	234	2	15	[2]
$La_{0.75}Sr_{0.15}Ca_{0.1}MnO_3$	327	2.8	15	[2]
$La_{0.75}Sr_{0.125}Ca_{0.125}MnO_3$	283	1.5	15	[2]
$La_{0.75}Ca_{0.25}MnO_3$ grains size 120 nm	177	2	15	[3]
$La_{0.75}Ca_{0.25}MnO_3$ grains size 300 nm	224	4.7	15	[3]

* See also data listed in work by Bohigas et al. (1998)

References:

[1] Zhang et al. (1996)
[2] Guo et al. (1997a)
[3] Guo et al. (1997b)

was observed near T_C and for $\Delta H = 10$ kOe was 1.32, 1.53, 2.11, and 1.96 J/kg K for $x = 0.075$, 0.10, 0.165, and 0.20, respectively.

5.3. 3d oxide compounds

Nikolaev et al. (1966) observed a change of sign of the MCE in nickel ferrite-chromite $NiFeCrO_4$ at the magnetic compensation point ($T_{comp} = 333$ K). This effect can be explained on the basis of the antiferromagnetic and ferromagnetic paraprocess conception (see section 5.1). The MCE in manganese spinel ferrites-chromites $MnFe_{2-x}Cr_xO_4$ ($0 \leqslant x \leqslant 1.6$) was measured by Belov et al. (1974). The maximum MCE value in $MnFe_2O_4$ is $\Delta T \sim 0.48$ K for $H = 16$ kOe near $T_C \approx 570$ K. The MCE studies made it possible to find a compensation point for the composition with $x = 1.085$. It appears because of the temperature dependence of the local slant angles of the Fe^{3+} and Cr^{3+} magnetic moments in the octahedral B-sublattice. For large Cr concentrations the presence of the slant angles gives an additional contribution to the ferromagnetic paraprocess in the B-sublattice near T_C and, consequently, to the total MCE.

The MCE in the spinel $Li_2Fe_5Cr_5O_{16}$ was measured by Belov et al. (1968). A sign change of the MCE was also observed at the compensation point (see fig. 5.7). In the low temperature region the MCE was not high and decreased with decreasing temperature (compare with low temperature MCE in $Gd_3Fe_5O_{12}$, figs 5.1 and 5.2). Such behavior was related with the low intensity of the paraprocess in the A- and B-sublattices due to the strong intersublattice exchange interactions.

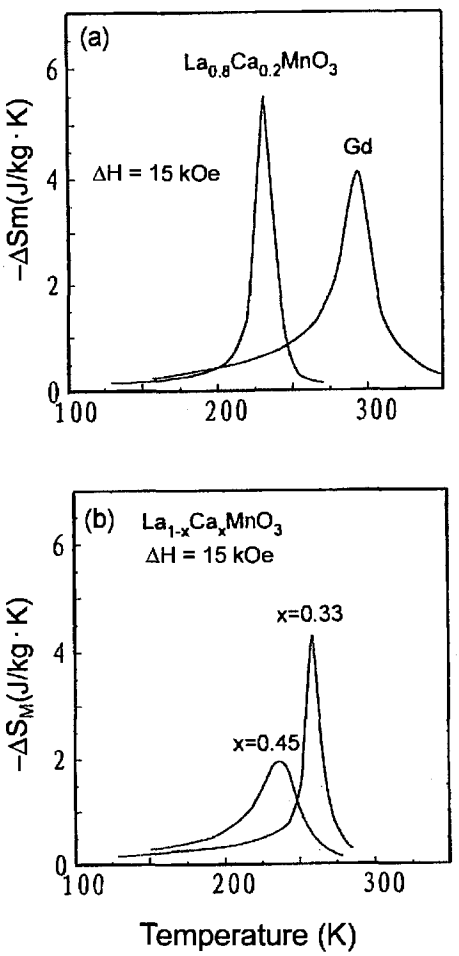


Fig. 5.6. Temperature dependences of the magnetic entropy change ΔS_M induced by a magnetic field of 15 kOe in $La_{1-x}Ca_xMnO_3$: (a) $x = 0.2$ and Gd; (b) $x = 0.33$ and 0.45 (Guo et al. 1997a).

Sucksmith et al. (1953) obtained the $I_s(T)$ curve of the mixed magnesium–zinc ferrite $MgOZnO \cdot 2Fe_2O_3$ from $\Delta T(I^2)$ measurements.

The MCE in hexagonal ferrites was investigated by Zhilyakov et al. (1993, 1994), Naiden and Zhilyakov (1997) and Belov et al. (1977). Zhilyakov et al. (1993) studied the MCE of polycrystalline $BaFe_{12-x}Co_xTi_xO_{19}$ (CoTi–M structure $x = 0$–3.0) and $BaCa_{2-x}Zn_xFe_{16}O_{27}$ (CoZn–W structure, $x = 0$–2.0) in the temperature range of 150–500 K (which is below T_C). In these ferrimagnets warming causes a set of spin-reorientation transitions from easy cone to easy plane (at the temperature T_1), from easy plane to easy cone (T_2) and from easy cone to easy axis (T_3). Measurements of the spontaneous MCE (at $H = 0$) revealed a peak ΔT value of about 0.1 K near 310 K where the spin reorientation transition from easy plane to easy cone takes place. In the presence

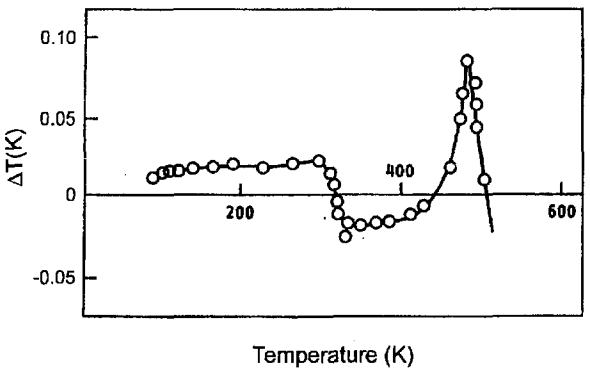


Fig. 5.7. Temperature dependence of the MCE in the spinel $Li_2Fe_5Cr_5O_{16}$ induced by a magnetic field of 16 kOe (Belov 1968).

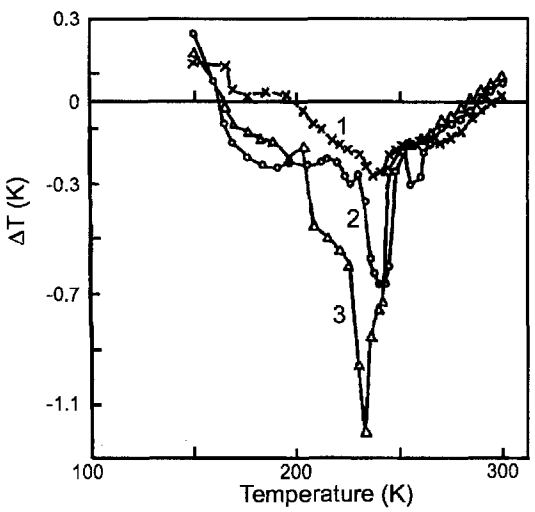


Fig. 5.8. Temperature dependence of the MCE in CoZn–W with $x = 1.3$ in various magnetic fields: (1) $\Delta H =$ 2 kOe; (2) 8 kOe; (3) 12 kOe (Zhilyakov et al. 1994).

of a magnetic field in CoTi–M ($x = 1.2$) and CoZn–W ($x = 1.0$) ferrites the maxima at the spin-reorientation transitions and sign changes of the MCE from negative to positive at $T \approx 300$ K and from positive to negative at $T \approx 420$ K were observed. The maximum absolute value of the negative MCE was about 0.2 K at $T \approx 150$ K in CoZn–W ferrite and the value for the positive MCE was about 0.1 K at $T \approx 340$ K in CoTi–M ($x = 1.2$) for ΔH of 7 kOe. The MCE temperature behavior was related by the authors with a competition between the anisotropy constants determining the magnetocrystalline anisotropy along the hexagonal axis.

Polycrystalline and basal plane textured samples of CoZn–W hexaferrites ($0 \leqslant x \leqslant 2.0$) were measured by Zhilyakov et al. (1994). For the samples with $x = 1.1$–1.5 the first-

order spin-reorientation transitions are observed in the presence of a magnetic field in the temperature interval from 77 to 250 K. Figure 5.8 shows the MCE at such a transition ($T_2 = 250$ K) in various magnetic fields. The value of the MCE is comparable with that observed in rare earth single crystals (see section 7). The estimations made by the authors showed that the main contribution to the MCE at $T = T_2$ is related with the field induced spin-reorientation transitions.

Naiden and Zhilyakov (1997) calculated the MCE in a CoZn–W ($x = 1.38$) hexaferrite single crystal along a hexagonal axis and in the basal plane on the basis of the equation similar to eq. (4.7) and experimental data on the temperature dependences of the magnetization, magnetocrystalline anisotropy constants and heat capacity. Peaks of negative (approximately -0.65 K) and positive ($\sim$1.5 K) MCE were observed in $H = 8$ kOe applied along the c-axis and in the basal plane at a temperature of about 210 K and 230 K, respectively (T_2 for this compound is equal to 220 K).

A $BaCo_{1.65}Fe^{2+}_{0.35}Fe^{3+}_{16}O_{27}$ single crystal was investigated by Belov et al. (1977). The anomalies corresponding to the second-order phase transition, at which the spins were turned from the basal plane and formed a cone with increasing temperature, were observed near 390–400 K in the temperature dependences of the MCE, measured in a field of 10 kOe aligned in the basal plane and the along c-axis. In the case of the basal plane measurements there was a maximum with a value of about 0.05 K, and in the case of the c-axis measurements there was a sign change of the MCE in the $\Delta T(T)$ curves. Near the Curie temperature ($\sim$750 K) a value of $\Delta T = 0.16$ K was observed for the both field directions. ΔT oscillations with sign changes were found when changing of the magnetic field orientation. The character of the oscillations was dependent on the measurement temperature, which was related with different values of the cone angle.

Druzhinin et al. (1979) calculated the temperature dependences $\Delta T(T)$ for various values of the angle formed by the field and the threefold crystal axis in corundum (Al_2O_3) with 0.13% V^{3+}. The calculations were made with allowance for uniaxial magnetic anisotropy and uniaxial g-tenser anisotropy on the basis of a spin Hamiltonian with the parameters known from the experiment. The sign and value of the MCE were shown to depend on the angle between the field and the threefold axis. Oscillations of ΔT in the angle dependence were observed in the temperature interval from 0 to 8 K.

Litvinenko et al. (1973) studied the MCE in an antiferromagnetic ($T_N = 32$ K) siderite $FeCO_3$ single crystal in pulsed fields up to 300 kOe. The sample displays essential field hysteresis at the metamagnetic transition from the antiferromagnetic to ferromagnetic state. The value of the MCE at $T = 4.2$ K in a field of 300 kOe was 24 K.

5.4. Other oxides

RXO_4 (R = rare earth, X = V, As, P) compounds display at low temperatures a crystallographic phase transition caused by the cooperative Jahn–Teller effect, which gives additional contribution to the entropy change. A magnetic field can also influence this transition. $DyVO_4$ exhibits the crystallographic transition at 14.3 K and an antiferromagnetic one at 3 K.

Figure 5.9 shows temperature dependences of the total entropy in $DyVO_4$ in various fields determined from the heat capacity measurements. The shoulders near 3 K and 15 K in the zero magnetic field entropy curve are related with antiferromagnetic and structural phase transition, respectively.

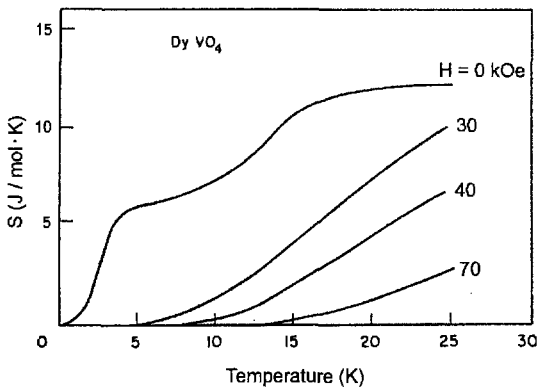


Fig. 5.9. Temperature dependences of the total entropy $DyVO_4$ in various magnetic fields (Daudin et al. 1982).

6. Magnetocaloric effect in intermetallic compounds

6.1. Rare earth–nonmagnetic element

The heat capacity of RAl_2 (R = Gd, Dy, Er, Ho) and $(Dy_{1-x}Er_x)Al_2$ (x = 0–1) alloys was measured by Gschneidner et al. (1994a, 1994b, 1996a, 1996b), Ranke et al. (1998a) and by Hashimoto (1991), Hashimoto et al. (1986). The RAl_2 compounds have the cubic Laves phase (Cu_2Mg-type) structure.

The saturation high temperature values of the magnetic entropy S_M (see section 2.3) were calculated by Gschneidner et al. (1994a, 1994b, 1996a, 1996b) on the basis of the magnetic heat capacity (C_M) data by eq. (2.76). The prorated zero-field heat capacities of $LaAl_2$ and $LuAl_2$ were used to evaluate the lattice contributions needed for the C_M calculations of $(Dy_{1-x}Er_x)Al_2$ system. The magnetic entropy change ΔS_M, induced by field changes was obtained from the heat capacity measured at various magnetic fields by the method described in section 3.3.

The experimental data on S_M, ΔS_M and ΔT are presented in table 6.1. The majority of the results on rare earth–nonmagnetic element alloys was already summarized earlier in the report of Gschneidner et al. (1996a, 1996b). The amount of magnetic entropy S_M utilized in the magnetic ordering process (column 6 of table 6.1) was determined on the basis of the values of the theoretically available maximum entropy, calculated by means of eq. (2.70) using J for the corresponding RE element (see table 6.2). The values of ΔS_M at $T = T_C$ are presented in column 8 of table 6.1 and their amounts relative to the theoretically available entropies are shown in column 9 of table 6.1. The values of ΔT are taken at the temperature T_{max} corresponding to the maximum of the temperature dependence of the MCE. The Curie temperatures were determined by Gschneidner et al. (1994a, 1994b, 1996a, 1996b) from the magnetic ac susceptibility measurements.

The heat capacity measurements of $(Dy_{1-x}Er_x)Al_2$ alloys made by Gschneidner et al. (1994a, 1994b, 1996a, 1996b) for x from 0.6 to 1.0 revealed a sharp peak below 14 K. Its height decreased with decreasing x. For x from 0 to 0.75 the heat capacity showed a broad λ-type anomaly at the Curie temperature. For x = 0.6, 0.75 and 0.9

TABLE 6.1

The Curie temperature (T_C), temperature of the maximum in the $\Delta T(T)$ curves (T_{max}), magnetic entropy S_M, magnetic entropy change ΔS_M induced by a magnetic field change ΔH at $T = T_C$, value of magnetocaloric effect ΔT induced by ΔH at $T = T_{max}$ of polycrystalline RE–nonmagnetic metal alloys. The values of S_M and ΔS_M are in the units of J/mol K per RE atom (J/(mol R K)). All measurements were made on polycrystals.

Compound	T_C, K	MCE			Magnetic entropy S_M		$-\Delta S_M$ at $T = T_C$		
		T_{max}, K	ΔT, K	ΔH, kOe	S_M, J/(mol R K)	% of theor. value	exper. value, J/(mol R K)	% of theor. value	ΔH, kOe
$GdAl_2$		167[a]	5.2[a]	75[a]	15.3[b]	91.4[b]	2.3[b]	13.3[b]	75[b]
$DyAl_2$	63.3[b]	63.9[a]	9.18[a]	75[a]	20.6[b]	89.4[b]	3.2[b]	13.9[b]	75[b]
	55.9[c]						4.1[c]		50[c]
$HoAl_2$	28.6[c]						6.3[c]		50[c]
$ErAl_2$	13[a]	13.6[a]	14.26[a]	75[a]	21.8[b]	94.6[b]	4[b]	17.4[b]	75[b]
	11.7[c]	22[c]	9[c]	50[c]			7.6[c]		50[c]
$Gd_{0.06}Er_{0.94}Al_2$	13[d]	30[d]	13[d]	80[d]					
$Gd_{0.14}Er_{0.86}Al_2$	40[e]	25[e]	8.8[e]	70[e]					
			4.5[e]	30[e]					
$(Dy_{0.85}Er_{0.15})Al_2$	54.4[a]	55.7[a]	9.59[a]	75[a]	21[b]	91.1[b]	4.0[b]	17.4[b]	75[b]
$(Dy_{0.70}Er_{0.30})Al_2$	45.5[a]	47.5[a]	9.83[a]	75[a]	21.3[b]	92.4[b]	4.4[b]	19.9[b]	75[b]
$(Dy_{0.55}Er_{0.45})Al_2$	39.3[a]	40.8[a]	10.54[a]	75[a]	20.7[b]	89.8[b]	6.5[b]	28.2[b]	75[b]
$(Dy_{0.50}Er_{0.50})Al_2$	37.8[a]	38.2[a]	10.46[a]	75[a]	21.0[b]	91.1[b]	6.4[b]	27.8[b]	75[b]
	46[c]						4.8[c]		50[c]
$(Dy_{0.40}Er_{0.60})Al_2$	32[a]	31.6[a]	10.4[a]	75[a]	21[b]	91.1[b]	6.4[b]	27.8[b]	75[b]
	32[f]		8.0[f]	50[f]					
$(Dy_{0.25}Er_{0.75})Al_2$	24[a,f]	24.4[a]	11[a]	75[a]	21.6[b]	93.7[b]	4.6[b]	20[b]	75[b]
			8.5[f]	50[f]					
$(Dy_{0.10}Er_{0.90})Al_2$	16.3[a]	17.7[a]	13.1[a]	75[a]	21.4[b]	92.8[b]	4.2[b]	18.2[b]	75[b]
Gd_3Al_2	281[f]						1.9[f]	11[f]	75[f]
	279.2[g]	273[g]	4.6[g]	55[g]					
GdPd	38[b]	38[e]	$\approx$ 8.7[e]	70[e]	13.8[b]	78.9[b]	3.4[b]	19.7[b]	75[b]
			$\approx$ 5.2[e]	30[e]					

TABLE 6.1 (Continued)

Compound	T_C, K	MCE			Magnetic entropy S_M		$-\Delta S_M$ at $T = T_C$		
		T_{max}, K	ΔT, K	ΔH, kOe	S_M, J/(mol R K)	% of theor. value	exper. value, J/(mol R K)	% of theor. value	ΔH, kOe
Gd_3Pd_4	$18(T_N)^h$				16.41^h	95^h	$\approx 1.3^h$		98.5^h
GdRh	19.93^i				17.4^i				
	20^j								
	24^j								
ErAlGa	3^k	6^l	$\approx 10.4^l$	75.3^l					
Er_3AlC	5.5^b	$\approx 5^l$	$\approx 12.8^l$	75.3^l			7.6^b	33^b	75^b
	2.8^m	$\approx 4.5^l$	$\approx 14.6^l$	98.5^l					
$Er_3AlC_{0.1}$		$\approx 9^l$	$\approx 6^l$	75.3^l					
$Er_3AlC_{0.25}$		$\approx 9^l$	$\approx 8^l$	75.3^l					
			$\approx 9.6^l$	98.5^l					
$Er_3AlC_{0.5}$		$\approx 7^l$	$\approx 9.2^l$	75.3^l					
			$\approx 11.6^l$	98.5^l					
$ErAl_{2.20}$	11^n						$\approx 6.2^n$		50^n
$HoAl_{2.24}$	25^n						$\approx 5^n$		50^n
$(Ho_{0.5}Dy_{0.5})Al_{2.25}$	34^n						$\approx 3.8^n$		50^n
$DyAl_{0.22}$	50^n						$\approx 4.3^n$		50^n

References:

(a) Gschneidner et al. (1996b)
(b) Gschneidner et al. (1996a)
(c) Hashimoto et al. (1986)
(d) Johanson et al. (1988)
(e) Zimm et al. (1992)
(f) Korte et al. (1998a)
(g) Nikitin et al. (1989a)
(h) Tanoue et al. (1992)
(i) Azhar et al. (1985)
(j) Buschow et al. (1975)
(k) Sill and Esau (1984)
(l) Pecharsky et al. (1996)
(m) Tokai et al. (1992a)
(n) Sahashi et al. (1987).

TABLE 6.2
Total angular momentum and maximum value of the magnetic entropy S_M in RE metals.

Element	La	Ce	Pr	Nd	Pm	Sm	Eu	Gd	Tb	Dy	Ho	Er	Tm	Yb	Lu
J	0	5/2	4	9/2	4	5/2	0	7/2	6	15/2	8	15/2	6	7/2	0
S_M, J/mol K	0	14.9	16.2	19.2	18.3	19.2	0	17.3	21.3	23.1	23.6	23.1	21.3	17.3	0

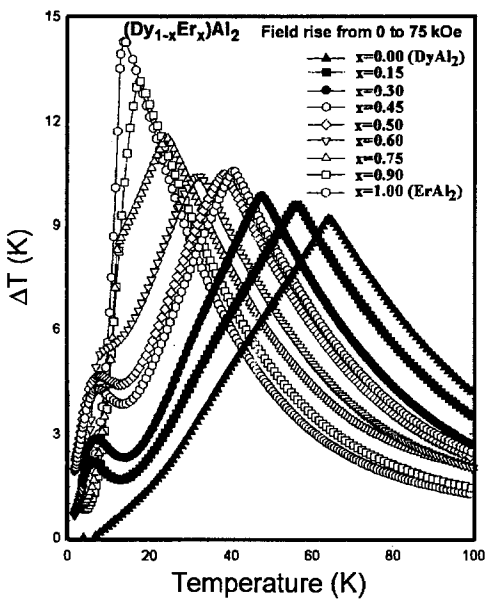


Fig. 6.1. Temperature dependences of the MCE induced by a magnetic field change from 0 to 75 kOe for $(Dy_{1-x}Er_x)Al_2$ alloys (Gschneidner et al. 1996b).

both anomalies were observed. The low temperature peak was related by the authors with Schottky anomaly due to the splitting of the ground states of the RE ions with $L \neq 0$ by the crystalline electric field. Earlier Schottky anomaly at about 23 K was found by Inoue et al. (1977) in the heat capacity of $ErAl_2$.

The temperature dependences of the MCE in the $(Dy_{1-x}Er_x)Al_2$ system are shown in fig. 6.1. The curves have caret-like character with broad maxima, which can be due to the possible spin-reorientation transitions. The maximum of ΔT was found in $ErAl_2$ and the lowest value was observed for $DyAl_2$. The low-temperature anomalies in the $\Delta T(T)$ curves were related by the authors with crystalline field effects. The magnetization measurements showed that the hysteresis in the $(Dy_{0.5}Er_{0.5})Al_2$ alloy was about 340 Oe at 2 K and became zero at 17 K (Gschneidner et al. 1994b).

Hashimoto et al. (1986, 1991) measured the heat capacity and the magnetization of the RAl_2 compounds with R = Er, Ho and Dy and of $(Gd_{0.1}Dy_{0.9})Al_2$ and $(Dy_{0.5}Ho_{0.5})Al_2$. The $\Delta S_M(T)$ curves, determined from the magnetization data are shown in fig. 6.2 and

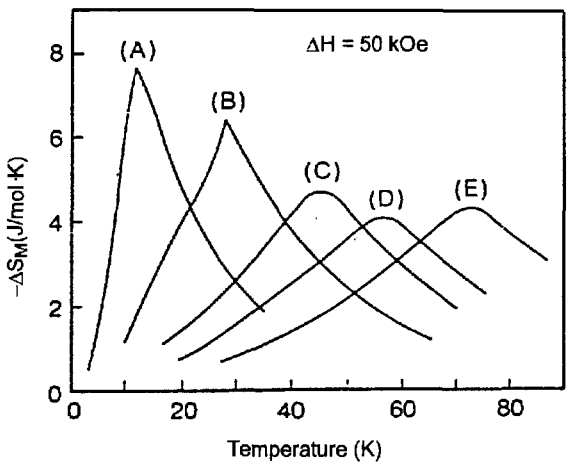


Fig. 6.2. Temperature dependences of ΔS_M induced by a magnetic field change of 50 kOe in RAl_2 alloys: (A) $ErAl_2$; (B) $HoAl_2$; (C) $(Ho_{0.5}Dy_{0.5})Al_2$; (D) $DyAl_2$; (E) $(Dy_{0.9}Gd_{0.1})Al_2$ (Hashimoto 1991).

ΔS_M at $T = T_C$ are presented in table 6.1. One can see, that the $\Delta S_M(T)$ values for $ErAl_2$ and $DyAl_2$ obtained by Hashimoto et al. (1986, 1991) are higher than those of Gschneidner et al. (1996b).

Zimm et al. (1992) studied the heat capacity and measured directly the MCE in $(Gd_{0.14}Er_{0.86})Al_2$ alloy (see table 6.1). The $\Delta T(T)$ curves of this material for various magnetic fields have broad maxima at $T_{max} \approx 25$ K, although the magnetic susceptibility measurements give $T_C \approx 40$ K. The authors related the broad ΔT maximum with random distribution of Er and Gd atoms on the rare earth sites, which leads to the variation of the local magnetic environments.

Johanson et al. (1988) measured the heat capacity of the $Gd_{0.06}Er_{0.94}Al_2$ alloy. The Curie temperature defined from the heat capacity anomaly was 13 K, and the MCE obtained from the temperature dependences of the heat capacity measured at various magnetic fields, was 13 K for $T = 30$ K for a field change of 80 kOe.

The MCE in Gd_3Al_2, which orders ferromagnetically below T_C and antiferromagnetically below 51 K (Gschneidner et al. 1996a), was measured by a direct method by Nikitin et al. (1989), see table 6.1. The Curie temperature was defined by Nikitin et al. (1989) from magnetization data with the help of Arrott plots.

The ErAgGa compound has the $CeCu_2$-type structure and, as it was shown by Sill and Esau (1984) to order ferromagnetically at about 3 K. The heat capacity measurements reveal two overlapping maxima at about 3 K and about 5 K. Ac susceptibility measurements showed a considerable frequency dependence below 8 K, which was explained by Pecharsky et al. (1996) by the existence of a spin-glass state. The additional maximum in the temperature dependences $C(T)$ measured in the zero field was related with the Schottky anomaly caused by the crystalline electric field splitting of low-lying energy levels of the Er ions.

The GdPd compound has the orthorhombic CrB-type structure and orders ferromagnetically below $T_C = 38$ K. The $\Delta T(T)$ curves measured directly by Zimm et al. (1992) for various ΔH have sharp peaks near T_C. The ΔT values are presented in table 6.1.

Tanoue et al. (1992) investigated the heat capacity, magnetic susceptibility and magnetization of the Gd_3Pd_4 compound that has the rhombohedral Pu_3Pd_4-type structure. It was found that Gd_3Pd_4 orders antiferromagnetically at 18 K. At about 6 K it displays another transition of ferromagnetic nature. In the presence of a magnetic field up to 98.5 kOe an additional heat capacity peak at about 13 K developed, which was attributed to a spin-reorientation transition. The entropy associated with the anomaly is about 2% of the total magnetic entropy S_M. The magnetic entropy S_M, calculated from heat capacity measurements by eq. (2.76) (for the temperature range from 0 to 40 K), was equal to 16.41 J/(mol Gd K), which is in good agreement with theoretical data on Gd (see table 6.2). The temperature dependences of the magnetic entropy change $-\Delta S_M(T)$ have maxima at about 20 K with the values of ≈ 0.17 J/(mol Gd K) for $\Delta H = 53.2$ kOe and ≈ 1.7 J/(mol Gd K) for $\Delta H = 98.5$ kOe ($-\Delta S_M$ values at $T = T_C$ are given in table 6.1).

The intermetallic compound GdRh has the cubic CsCl structure and orders ferromagnetically below the Curie temperature. Its heat capacity was studied by Azhar et al. (1985) and Buschow et al. (1975). Curie temperature values of 19.93 K and 20 K were defined from the temperature dependences of the heat capacity by Azhar et al. (1985) and Buschow et al. (1975), respectively. From magnetization measurements gave $T_C = 24$ K was found (Buschow et al. 1975). The magnetic entropy S_M, determined by eq. (2.76) (for $T \to \infty$) from the heat capacity data, was obtained to be 17.4 J/mol K, very close to the theoretical value for Gd (see table 6.2).

The heat capacity of the carbide alloys Er_3AlC_x ($x = 0.1$; 0.25; 0.5, and 1) was investigated by Pecharsky et al. (1996) and Gschneidner et al. (1996a, 1996b). Er_3AlC has an anti-perovskite-type crystal structure and, according to the measurements of Tokai et al. (1992a), orders magnetically at 2.8 K, showing λ-type heat capacity anomaly. An analogous anomaly was observed by Pecharsky et al. (1996) at 3.1 K. Ac susceptibility measurements of Pecharsky et al. (1996) revealed in the Er_3AlC alloy a small negative paramagnetic Curie temperature (−1.6 K), which was taken as evidence of antiferromagnetic ordering. As proposed by the latter authors, this antiferromagnetic state transforms to a ferromagnetic one by a magnetic field of about 24.6 kOe.

For the other carbide phases two heat capacity maxima were revealed: one at low temperature and another one at approximately 8 K. X-ray diffraction studies made by Pecharsky et al. (1996) on Er_3AlC_x ($x = 0.1$; 0.25; 0.5) showed that these compounds contain two phases: Er_3AlC and Er_2Al. The low-temperature heat capacity maximum in Er_3AlC_x was attributed by the authors to the antiferromagnetic ordering of Er_2Al (≈ 6 K).

The MCE of $ErAlC_x$ ($x = 0.1$; 0.25; 0.5), determined on the basis of heat capacity data, displays a wide maximum due to the presence of two phases with slightly different magnetic ordering temperatures. From table 6.1 one can see a gradual decrease of the MCE in Er_3AlC_x with increasing x. This was related by the authors with a reduction of Er_3AlC phase content and an increase of the amount of the antiferromagnetic Er_2Al phase.

Sahashi et al. (1987) studied the heat capacity of Al-rich RAl_2 (R = Dy, Ho, Er and $Ho_{0.5}Dy_{0.5}$) high density sintered compounds. To prepare the samples the powder metallurgical route was used. From the ingots of arc-melted RAl_2 (R = Dy, Ho, Er and

$Ho_{0.5}Er_{0.5}$) 3 μm sized powder was ball milled in ethanol. The milled powder was pressed under 10^3 kg/cm^2 and then sintered in an argon atmosphere for 1.5 hours at 1105°C. X-ray analyzes showed, that the Laves phase RAl_2 in the samples is surrounded by the RAl_3 phase with cubic Cu_3Au structure. The Curie temperatures of the $ErAl_{2.20}$, $HoAl_{2.24}$, $(Ho_{0.5}Dy_{0.5})Al_{2.25}$ and $DyAl_{2.22}$ alloys prepared in this way were obtained from $C(T)$ curves and are somewhat lower than in the corresponding stoichiometric compounds, see table 6.1. The $\Delta S_M(T)$ curves exhibit maxima near the Curie temperatures with values given in table 6.1. The ΔS_M maxima in the sintered compounds were broader than in the corresponding RAl_2 compounds, which have relatively sharp peaks.

6.2. Rare earth–nickel

In this section magnetothermal properties of R_3Ni, RNi_2, RNi, RNi_5 and RNiAl (R = rare earth element) compounds will be considered. According to magnetic investigations (Kirchmayr and Poldy 1978; Taylor and Darby 1972) Ni in these compounds has no magnetic moment.

The heat capacity of GdNi, HoNi and ErNi was measured by Sato et al. (1990). GdNi is a simple ferromagnet, while in HoNi and ErNi a noncollinear magnetic structure due to the crystalline field effects is observed. Heat capacity anomalies were revealed at the Curie temperature T_C: 70 K for GdNi and 10 K for ErNi. The heat capacity of HoNi displayed an anomaly at the temperature of the spin-reorientation transition equal to 13 K (T_C = 37 K according to the susceptibility measurements of Sato et al. (1982). The magnetic ordering entropy, determined by Sato et al. (1990) from the heat capacity data and eq. (2.76) in the temperature interval from 0 to 15 K, is equal to 15 J/mol K. This is inconsistent with the value calculated by eq. (2.70) for the Er^{3+} ionic state (see table 6.2). The authors attributed this difference to the crystalline field splitting of the Er ion ground state. The magnetic entropy due to the crystalline field effect estimated by Sato et al. (1990) on the basis of point charge model, was calculated to be 11 J/mol K at 15 K. Zimm et al. (1992) measured the temperature dependences of the MCE in GdNi directly. A relatively sharp peak was observed near T_C (the values of ΔT in various magnetic fields are given in table 6.3).

The heat capacity of the compounds RNi_2 (R = Tb, Dy, Ho, Er), $(Dy_{0.26}Er_{0.74})Ni_2$, $(Gd_{0.1}Dy_{0.9})Ni$ and $(Er_{1-x}Dy_x)Ni_2$ was studied by Gschneidner et al. (1996a), Tomokiyo et al. (1986), Hashimoto et al. (1992), Ranke et al. (1998a) and Yayama et al. (1987). The heat capacity measurements allowed Gschneidner et al. (1996a) to determine the temperature dependences of S_M and ΔS_M. As one can see from tables 6.2 and 6.3, in the Ni-based compounds approximately 60% of the theoretically available magnetic entropy is utilized in the magnetic ordering process, while in the Al-based compounds (RAl_2) this value is about 90%. The authors attributed this to crystalline field effects above T_C. The results of Tomokiyo et al. (1986) are shown in fig. 6.3. The ΔS_M for $DyNi_2$ and $ErNi_2$ was evaluated from the heat capacity data, and that of $HoNi_2$ was obtained from the magnetization data by eq. (2.71). As follows from table 6.3 the results of Tomokiyo et al. (1986) for $\Delta S_M(T_c)$ at ΔH = 50 kOe are about two times higher than those of Gschneidner et al. (1996a) at ΔH = 75 kOe.

Foldeaki et al. (1997) obtained $\Delta S_M(T)$ curves from magnetization measurements for $GdNi_2$ and $DyNi_2$. The maximum $-\Delta S_M$ values at $T = T_C$ were obtained to be $\approx$ 28 J/kg K for $DyNi_2$ and $\approx$ 14 J/kg K for $GdNi_2$ at ΔH = 70 kOe. As one can see,

TABLE 6.3

The Curie temperature (T_C), temperature of the maximum in the $\Delta T(T)$ curves (T_{max}), magnetic entropy S_M, magnetic entropy change ΔS_M induced by a magnetic field change ΔH at $T = T_C$, value of magnetocaloric effect ΔT induced by ΔH at $T = T_{max}$ of polycrystalline rare earth intermetallic alloys and compounds with Ni. The values of S_M and ΔS_M are in the units of J/mol K per RE atom (J/(mol R K)). All measurements were made on polycrystals.

Compound	T_C, K	MCE			Magnetic entropy S_M		$-\Delta S_M$ at $T = T_C$		
		T_{max}, K	ΔT, K	ΔH, kOe	S_M, J/(mol R K)	% of theor. value	exper. value J/(mol R K)	% of theor. value	ΔH, kOe
GdNi	70[a]	70[a]	7.5[a]	70[a]					
			4.2[a]	30[a]					
ErNi	10[b]				15[b]				
$GdNi_2$	75[a]	75[a]	5.9[a]	70[a]					
			3.2[a]	30[a]					
$TbNi_2$	37[c]	38[d]	11[d]	75.3[d]	12.1[c]	56.3[c]	3.55[c]	16.7[c]	75[c]
$DyNi_2$	20[c,e]				14.5[c]	62.9[c]	3.2[c]	13.9[c]	75[c]
							6.9[e]		50[e]
$HoNi_2$	13[e]						6.3[e]		50[e]
$ErNi_2$	6[c]				14.9[c]	64.6[c]	2.3[c]	10.0[c]	75[c]
	6.6[e]						6.9[e]		50[e]
$(Dy_{0.26}Er_{0.74})Ni_2$	9.5[c]				14.7[c]	63.8[c]	3.8[c]	16.5[c]	75[c]
$(Gd_{0.10}Dy_{0.90})Ni_2$	28[c]		≈ 10.8[d]	75.3[d]	15.3[c]	66.8[c]	4.8[c]	21.4[c]	75[c]
Pr_3Ni	$\approx 11(T_N)$[f]				4.5[f]				
Nd_3Ni	$\approx 6.5(T_N)$[f]				5.3[f]				
Er_3Ni	$\approx 7(T_N)$[f]				6.6[f]				
Gd_3NiGe_2	193[c]						2.97[c]	17.2[c]	75[c]
DyNiAl	29[c]	31[d]	≈ 6.3[d]	75.3[d]	15[c]	65.2[c]	2.15[c]	9.3[d]	75[c]
ErNiAl	$5.6(T_N)$[e]	8[g]	6[g]	50[g]					

TABLE 6.3 (Continued)

Compound	T_C, K	MCE			Magnetic entropy S_M		$-\Delta S_M$ at $T = T_C$		
		T_{max}, K	ΔT, K	ΔH, kOe	S_M, J/(mol R K)	% of theor. value	exper. value J/(mol R K)	% of theor. value	ΔH, kOe
$(Gd_{0.2}Er_{0.8})NiAl$	$11(T_l)^e$ $21(T_h)^e$	14[g]	6.8[g]	50[g]					
$(Gd_{0.4}Er_{0.6})NiAl$	$9(T_l)^e$ $32(T_h)^e$	22[g]	6.2[g]	50[g]					
$(Gd_{0.54}Er_{0.46})NiAl$	$13(T_l)^e$ $37(T_h)^e$	36[g]	5.2[g]	50[g]	17.4[c]	85.7[c]	5.5[c]	27.6[c]	75[c]
$(Gd_{0.7}Er_{0.3})NiAl$	$16(T_l)^e$ $47(T_h)^e$	42[g]	4.4[g]	50[g]					
GdNiAl	$23(T_l)^e$ $58(T_h)^e$	58[g]	4.1[g]	50[g]					

References:

(a) Zimm et al. (1992)
(b) Sato et al. (1990)
(c) Gschneidner et al. (1996a)
(d) Gschneidner et al. (1994b)
(e) Tomokiyo et al. (1986)
(f) Gschneidner et al. (1995), Korte et al. (1998a)

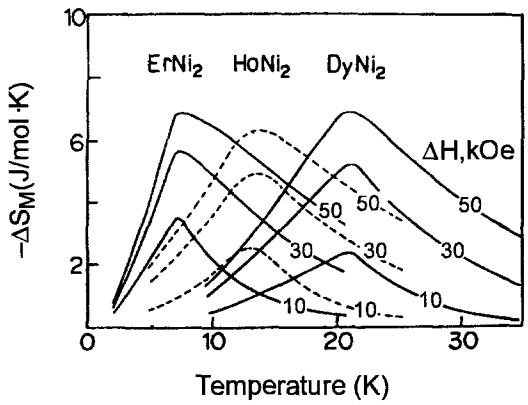


Fig. 6.3. Temperature dependences of ΔS_M of $DyNi_2$, $HoNi_2$ and $ErNi_2$ induced by the various magnetic field changes (Tomokiyo et al. 1986).

ΔS_M in $DyNi_2$ is two times larger than in $GdNi_2$. The low-field (100 Oe) temperature dependence of the magnetic susceptibility of the $DyNi_2$ displays irreversible character. There is a substantial hysteresis for the field-cooled and zero-field cooled curves. The Arrott plots of $DyNi_2$ compound, constructed in the temperature range from 5 to 50 K, did not display linear sections at any temperatures. The authors related this behavior to the complex nature of a magnetic transition at $T = T_C$ and a noncollinear magnetic structure below T_C due to the presence of crystalline field effects. The irreversible behavior described above was not observed for $GdNi_2$.

The temperature dependences of the MCE for $GdNi_2$ were obtained with the help of a direct method by Zimm et al. (1992) and for $TbNi_2$ from magnetization data by Gschneidner et al. (1995). MCE peaks were observed near T_C and the maximum ΔT values are presented in table 6.3.

Tishin (1990g) on the basis of MFA calculated the field dependences of magnetic entropy change $-\Delta S_M(H)$ (the magnetic field varied from 0 to H) at $T = T_C$ for GdNi, $GdNi_2$ and $GdNi_5$ (as in GdNi and $GdNi_2$, nickel in $GdNi_5$ is nonmagnetic). The nonlinear character of $-\Delta S_M(H)$ curves was observed for H below 50 kOe (the maximum magnetic field value was 100 kOe). At $H = 100$ kOe the value of $-\Delta S_M(H)$ was found to be about 2.7 J/mol K for GdNi, 1.7 J/mol K for $GdNi_2$ and 1.3 J/mol K for $GdNi_5$.

Based on theoretical investigations using Hamiltonian which includes both the crystalline electric field as well as exchange interaction, Ranke et al. (1998b) predicted an anomalous increase of S_M in paramagnetic $PrNi_5$. Their heat capacity measurements confirmed this result.

The heat capacity of Er_3Ni, ErNi, $Er_{1-x}Dy_xNi_2$, $Er(Ni_{1-x}Co_x)_2$ and $Er_{0.9}Yb_{0.1}Ni$ was investigated by Yayama et al. (1987), Li et al. (1988), Sahashi et al. (1990), Sato et al. (1990), Hashimoto et al. (1992), and Tokai et al. (1992a, 1992b). It was found that these compounds have substantial heat capacity values in the low temperature region. Er_3Ni has a broad heat capacity maximum near the ordering temperature at about 8 K, and above 15 K its heat capacity is comparable with that of Pb. The dilution of ErNi by Yb

led to a decrease of the magnetic transition temperature to about 4 K with preservation of the sharpness of the heat capacity peak. Gschneidner et al. (1995) measured the heat capacity of R_3Ni (R = Pr, Nd and Er) and Er_6Ni_2X (X = Sn, Pb and $Sn_{0.75}Ga_{0.25}$) alloys in a temperature interval from 1.5 to 40 K. The R_3Ni compounds order antiferromagnetically below the ordering temperatures determined from $C(T)$ curves and listed in table 6.3. The total heat capacity peak at the ordering temperature is of the λ-type. It is narrow in Nd_3Ni (with the maximum value of ≈ 0.7 J/K cm^3) and broader in Pr_3Ni (≈ 1.9 J/K cm^3) and Er_3Ni (≈ 0.42 J/K cm^3). The broad heat capacity maximum in the Er_3Ni compound was explained by a substantial contribution to the total heat capacity from the Schottky anomaly above T_N. The magnetic entropy determined by Gschneidner et al. (1995) from the heat capacity data are listed in table 6.3 (in J/mol K). They are in good agreement with the S_M value expected a ground state doublet of the Er ions ($J = 1/2$): $3R \ln 2 = 17.3$ J/mol K. This confirms the presence of strong crystalline electric field effects in the R_3Ni (R = Pr, Nd, Er) compounds. The Er_6Ni_2X alloys (X = Sn, Pb, and $Sn_{0.75}Ga_{0.25}$) ordered ferrimagnetically below about 18 K and had heat capacities essentially higher than that of Pb in this temperature range.

Korte et al. (1998a, 1998b) undertook a study of the magnetic properties, heat capacity and MCE in $(Gd_{1-x}Er_x)NiAl$ pseudo-ternary alloys ($x = 0$; 0.30; 0.46; 0.50; 0.55; 0.60; 0.80; 1.00). All these alloys have the ZrNiAl-type crystalline structure. By means of specific heat and magnetic susceptibility measurements it was shown that ErNiAl orders antiferromagnetically below 6 K. The temperature dependences of the heat capacity of other alloys displayed a series of peaks (for example $(Gd_{0.54}Er_{0.46})NiAl$ at $T = 23$, 28 and 58 K). The authors attributed the low-temperature heat capacity anomalies to antiferromagnetic transitions and the upper anomalies to ferromagnetic ordering. Magnetic susceptibility measurements confirmed these suppositions. The lowest (T_1) and highest (T_2) ordering temperatures obtained from the heat capacity measurements (for $(Gd_{0.2}Er_{0.8})NiAl$ from ac susceptibility data) are presented in table 6.3. The $\Delta S_M(T)$ curves (measured for $\Delta H = 50$ kOe) of ErNiAl and $(Gd_{0.2}Er_{0.8})NiAl$ have peaks near the antiferromagnetic ordering temperatures. In Gd-rich alloys a broad maximum due to the remaining contribution from the low-temperature antiferromagnetic ordering process was observed. The $\Delta T(T)$ curves show an analogous behavior, see fig. 6.4. $(Gd_{0.54}Er_{0.46})NiAl$ has a wide temperature range with almost flat $\Delta S_M(T)$ behavior. This was related by the authors with the existence of multiple ordering processes with entropy changes comparable in magnitude for both the AFM and the FM transitions. Similar $\Delta T(T)$ and $\Delta S_M(T)$ curves were observed for $x = 0.3$ and 0. Comparison of the maximum values of ΔS_M and ΔT for the $(Gd_{0.54}Er_{0.46})NiAl$, $(Dy_{0.25}Er_{0.75})Al_2$ and $(Dy_{0.40}Er_{0.60})Al_2$ alloys showed that although the value of ΔS_M in these three materials is comparable, the $\Delta T(T_{max})$ value is larger in the $(R'_xR_{1-x})Al_2$ compounds. This is connected with the large lattice heat capacity of the RNiAl compounds.

Table 6.3 contains also S_M, ΔS_M and MCE data obtained by Gschneidner et al. (1994a, 1994b, 1996a) from the heat capacity measurements.

6.3. Rare earth–iron

The MCE in the intermetallic compounds RFe_2 (R = Tb, Er, Y) and RFe_3 (R = Ho, Y) and $Tb_xY_{1-x}Fe_2$ ($x = 0$; 0.2; 0.33; 0.45; 0.8; 1.0) alloys was measured directly by Nikitin

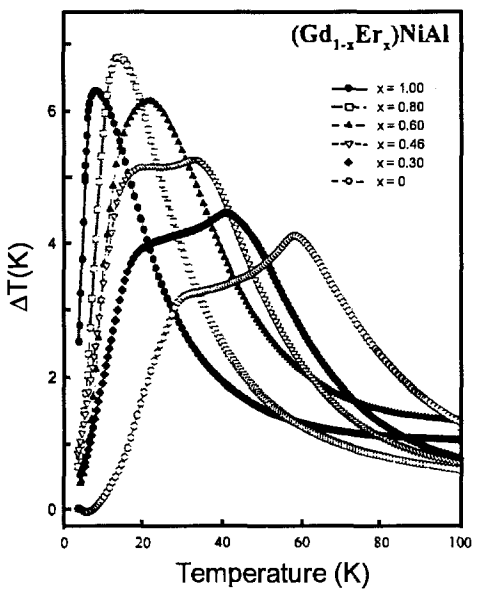


Fig. 6.4. Temperature dependences of the MCE induced by $\Delta H = 50$ kOe for the $(Gd_{1-x}Er_x)NiAl$ alloys (Korte et al. 1998a).

et al. (1973, 1975) in the temperature interval from 80 to 700 K. Since YFe_2 and YFe_3 have only one magnetic sublattice, they display $\Delta T(T)$ curves characteristic of a simple ferromagnet with one maximum near the Curie temperature T_C. $ErFe_2$ and $HoFe_3$ are ferrimagnets with two magnetic sublattices and compensation temperatures T_{comp} at 490 K and 389 K, respectively. Their $\Delta T(T)$ curves show a behavior analogous to that in gadolinium iron garnet: when increasing the temperature the MCE suddenly changes its sign from positive to negative near T_{comp} (see section 5.1 and fig. 5.1). The estimations made from MCE and Curie point data on the basis of MFA (Nikitin and Bisliev 1974) showed that the effective field H_{2eff} acting in the RE magnetic sublattice is about 1.6×10^6 Oe in $ErFe_2$ and about 10^6 Oe in $HoFe_3$ (Nikitin et al. 1973). This is considerably higher than H_{2eff} in rare earth iron garnets ($\sim 3 \times 10^5$ Oe) and leads to a weak paraprocess in the RE magnetic sublattice and to an MCE temperature behavior analogous to that observed in the $Li_2Fe_5Cr_5O_{16}$ spinel below T_{comp} (see fig. 5.7). In $Tb_xY_{1-x}Fe_2$ alloys the compensation behavior of the MCE was observed for $x = 0.33$ and 0.45. For the other compounds only one maximum at $T = T_C$ was observed in the $\Delta T(T)$ curves. The values of MCE at $T = T_C$ for the RFe_2 and RFe_3 compounds and $Tb_xY_{1-x}Fe_2$ alloys investigated by Nikitin et al. (1973, 1975) are presented in table 6.4. Minimum $\Delta T(T_C)$ value among $Tb_xY_{1-x}Fe_2$ alloys is observed for $x = 0.5$ (see table 6.4). For this composition T_{comp} coincides with T_C.

Jin et al. (1991) measured the MCE in as-cast $R_xCe_{2-x}Fe_{17}$ (R = Y or Pr and $x = 0$–2) alloys by a direct method at room temperature. Some of their results are listed in table 6.4 along with the Curie temperatures obtained by interpolation between the values for corresponding R_2Fe_{17} compounds. Annealing of the samples at 800–1000°C for several hours

TABLE 6.4

The Curie temperature T_C, and magnetocaloric effect ΔT induced by ΔH at $T = T_C$ of some polycrystalline rare earth–iron intermetallic alloys and compounds. All measurements were made on polycrystals.

Compound	T_C, K	MCE at $T = T_C$		MCE at the room temperature	
		ΔT, K	ΔH, kOe	ΔT, K	ΔH, kOe
YFe_3	535[a]	1.4[b]	15.8[b]		
$HoFe_3$	567[c]	≈ 0.55[b]	15.8[b]		
YFe_2	535[d]	≈ 1.25[d]	15.8[d]		
$Tb_{0.2}Y_{0.8}Fe_2$	≈ 570[d]	≈ 0.7[d]	15.8[d]		
$Tb_{0.33}Y_{0.67}Fe_2$	≈ 596[d]	≈ 0.4[d]	15.8[d]		
$Tb_{0.45}Y_{0.55}Fe_2$	≈ 610[d]	≈ 0.25[d]	15.8[d]		
$Tb_{0.8}Y_{0.2}Fe_2$	≈ 670[d]	≈ 0.5[d]	15.8[d]		
$TbFe_2$	695[d]	≈ 0.75[d]	15.8[d]		
$ErFe_2$	575[b]	0.2[b]	15.8[d]		
Y_2Fe_{17}	320[e]			≈ 1.4[f]	8[f]
$Y_{1.5}Ce_{0.5}Fe_{17}$	308			≈ 5[f]	8[f]
$Y_{1.2}Ce_{0.8}Fe_{17}$	300			≈ 6.9[f]	8[f]
$Y_{0.8}Ce_{1.2}Fe_{17}$	290			≈ 5[f]	8[f]
Ce_2Fe_{17}	≈ 270[a]			≈ 1.4[f]	8[f]
$Pr_{0.5}Ce_{1.5}Fe_{17}$				≈ 3.5*[f]	8[f]
				≈ 3.5**[f]	
$PrCeFe_{17}$	274			≈ 4.5*[f]	8[f]
				≈ 8**[f]	
$Pr_{1.2}Ce_{0.8}Fe_{17}$				≈ 7*[f]	8[f]
				≈ 13**[f]	
$Pr_{1.3}Ce_{0.7}Fe_{17}$				≈ 10*[f]	8[f]
				≈ 21.5**[f]	
Pr_2Fe_{17}	≈ 278[a]			≈ 5*[f]	8[f]
				≈ 8**[f]	

* Before annealing
** After annealing

References:

(a) Kirchmayr and Poldy (1978)
(b) Nikitin et al. (1973)
(c) Taylor and Darby (1972)
(d) Nikitin et al. (1975)
(e) Nikitin et al. (1991a)
(f) Jin et al. (1991)

did not affect ΔT in $Y_xCe_{2-x}Fe_{17}$ and led to its doubling for $x = 1.3$ in $Pr_xCe_{2-x}Fe_{17}$. The authors explained this by the Pr–Fe phase diagram: the Pr_2Fe_{17} phase is an incongruently melting compound and cannot be formed directly from the melt.

Wada et al. (1993) investigated the heat capacity and magnetic entropy of $Ce(Fe_{1-x}Co_x)_2$ ($x = 0$–0.3) alloys. The Laves phase compound $CeFe_2$ is an example of a system which is intermediate between localized magnetism and itinerant ferromagnetism. The magnetic measurements showed that $CeFe_2$ is a ferromagnet with $T_C = 230$ K and the magnetic moment per iron atom is about $1.15\,\mu_B$, which is lower than for other RFe_2 compounds (Deportes et al. 1981). The paramagnetic iron moment in $CeFe_2$ was found to be $0.5\,\mu_B$

at 300 K (Lindlay et al. 1988). Such a small magnetic moment in $CeFe_2$ was attributed to substantial hybridization of the iron 3d band states with the 4f band states of Ce (Eriksson et al. 1988). The substitution of small amount of Co ($0.04 < x < 0.3$) in $CeFe_2$ led to an antiferromagnetic phase at low temperatures, which upon heating turned into a ferromagnetic phase at the temperature T_{AFM-FM}. Electrical resistivity and lattice parameter measurements showed that the transition at T_{AFM-FM} was of the first order. Magnetization measurements made on the alloys with $x = 0.1$ and 0.2 at $T = 4.2$ K in fields up to 250 kOe revealed a metamagnetic transition (at ~ 80 kOe) with a considerable field hysteresis. The compounds with $x = 0$ and $x \geqslant 0.3$ showed usual ferromagnetic behavior.

Heat capacity measurements made on $CeFe_2$, $Ce(Fe_{0.9}Co_{0.1})_2$, $Ce(Fe_{0.8}Co_{0.2})_2$ and $Ce(Fe_{0.7}Co_{0.3})_2$ revealed anomalies at the Curie temperatures of 227 K, 180 K, 162 K, and 156 K, respectively. In the $Ce(Fe_{0.9}Co_{0.1})_2$ alloy an additional sharp peak was observed in the $C(T)$ curve at $T_{AFM-FM} = 80$ K. A less pronounced heat capacity anomaly at $T_{AFM-FM} = 68$ K was also observed in the $Ce(Fe_{0.8}Co_{0.2})_2$ alloy. Using eq. (2.76) and heat capacity data, Wada et al. (1993) calculated the temperature dependences of the magnetic entropy S_M of the $Ce(Fe_{1-x}Co_x)_2$ system for $x = 0$; 0.1; 0.2; 0.3. The data on paramagnetic $CeCo_2$ were used to evaluate the lattice and electronic contributions to the heat capacity. For $CeFe_2$, S_M started to increase at temperatures above 100 K and above T_C it reached a saturation value of 2.5 J/mol K. Analogous results were observed for $x = 0.3$ (the saturation S_M value was about 1 J/mol K). Equation (2.70), which is valid for magnetic systems with localized moments, gave the value $S_M = 11.5$ J/mol K for the two iron atoms ($J = 1/2$). This value is inconsistent with the value 2.5 J/mol K obtained for S_M in the $CeFe_2$ compound, which points to the intermediate character of magnetism in $CeFe_2$.

More complicated behavior was displayed by the $S_M(T)$ curves for $x = 0.1$ and 0.2. At $T = T_{AFM-FM}$ a sharp entropy change ΔS_{AFM-FM} ($\Delta S_{AFM-FM} = 1.2$ and 0.8 J/mol K for $x = 0.1$ and 0.2, respectively) was observed with subsequent gradual rise to the saturation value of 2.3 J/mol K for $x = 0.1$ and to 1.5 J/mol K for $x = 0.2$ above T_C. The authors regarded the entropy change ΔS_{AFM-FM} at T_{AFM-FM} as the magnetic entropy change. ΔS_{AFM-FM} was considered to consist of the following three contributions: the entropy change due to a difference in the degree of magnetic order in antiferromagnetic and ferromagnetic states, the lattice entropy change and the electronic entropy change. It was shown that the first two contributions in the considered alloys were close to zero. The main contribution to ΔS_{AFM-FM} is due to the electronic entropy change which arises from the difference between the values of the electronic heat capacity coefficient a_e for ferromagnetic and antiferromagnetic states (50 and 36.6 mJ/K^2 mol, respectively for $x = 0.1$) (see eq. (2.62)).

6.4. Rare earth–cobalt

The magnetic properties of the cubic Laves phase intermetallic compounds RCo_2 (R = rare earth) are well described by the s–d model in which the coexistence of localized spins and itinerant 3d electrons is assumed (Bloch and Lemaire 1970). According to this model the rare earth ions have localized magnetic moments and the 3d magnetic moment of Co is induced by the molecular field produced by the rare earth magnetic sublattice. $DyCo_2$, $HoCo_2$ and $ErCo_2$ exhibit the first-order transitions from paramagnetism to ferrimagnetism at the Curie points of 135, 77, and 33 K, respectively (Bloch et al. 1971; Voiron and

Bloch 1971; Kamarad et al. 1995). Bloch et al. (1975) explained the first- and second-order transitions in the RCo_2 compounds with the help of an s–d model and an expansion of the magnetic free energy as a power series of the d-electron magnetization. Dilution of the rare earth element in $HoCo_2$ compounds by Y led to a change from the first-order transition to the second-order type (Pillmayr et al. 1987).

Foldeaki et al. (1997) measured the magnetization of RCo_2 (R = Dy, Ho, Er) compounds and on the basis of these data calculated the magnetic entropy change ΔS_M induced by a field change of 70 kOe. Maxima were observed near the Curie point and the maximum values of $-\Delta S_M$ were about 14.5 J/kg K (at $T \approx 140$ K) for $DyCo_2$, about 22 J/kg K (at $T \approx 85$ K) for $HoCo_2$ and about 28 J/kg K (at $T \approx 42$ K) for $ErCo_2$. It should be noted that two $ErCo_2$ samples were studied: "good" and "wrong". The first, according to X-ray diffraction analysis, was a homogeneous one. The second had some distortions in crystalline structure and contained an oxide. The wrong $ErCo_2$ sample displayed ΔS_M values 30% smaller than the good one. The Arrott plots of the wrong $ErCo_2$ showed behavior, analogous to that observed in Dy–Zr nanocomposites. According to the authors opinion this indicates a multiphase nanosized crystalline structure in the wrong $ErCo_2$.

The heat capacity of $ErCo_2$ as a function of temperature was measured by Imay et al. (1995). A sharp anomaly associated with the first-order magnetic phase transition was found at 32 K. The magnetic contribution to the heat capacity, obtained by subtraction of the $LuCo_2$ heat capacity from the $ErCo_2$ experimental data, still persisted above T_C. This was explained by an interaction of the RE magnetic ions with a crystalline electric field. The temperature dependence of the magnetic entropy $S_M(T)$ calculated on the basis of the heat capacity data, displayed a discontinuous increase (from 5 to 17 J/mol K) at the Curie point, and at high temperatures (above 150 K) it reached its saturation value which is close to the value of 23.1 J/mol K calculated by eq. (2.70) for Er ions ($J = 15/2$, see table 6.2). The latter fact indicates that the Co magnetic moments have small contribution to the total S_M. The magnetic entropy discontinuity at T_C was explained by the authors by the change of the Er ion ground state degeneracy from a singlet in the magnetically ordered state to a quadruplet in the paramagnetic state.

Nikitin and Tishin (1991) measured directly the MCE in the $HoCo_2$ compound. The results are shown in fig. 6.5. The value of the MCE temperature profile is consistent with the sharp character of the first-order magnetic phase transition. The estimation of ΔS_M made by Nikitin and Tishin (1991) on the basis of heat capacity data of Voiron et al. (1974) gave the value of -6.4 J/mol K at $T = 82$ K and $\Delta H = 60$ kOe.

Pillmayr et al. (1987) and Hilscher et al. (1988) investigated the heat capacity of the $(R_xY_{1-x})Co_2$ (R = Ho, Dy) alloy systems. The magnetic ordering entropy S_M determined from these measurements dropped for $x < 0.2$ and for $x \geqslant 0.2$ it attained the theoretical values calculated on the basis of eq. (2.70) for Ho and Dy (see table 6.2). The magnetic entropy associated with the magnetic moment of Co (for $s = 1/2$ it is equal to 5.76 J/mol K) was not observed above T_C in both alloy systems. This was attributed to the itinerant character of the Co magnetic moment (Pillmayr et al. 1987). According to the authors opinion the magnetic entropy decrease observed for $x < 0.2$ may point to an instability of the RE magnetic moment in this concentration range (Pillmayr et al. 1987; Hilscher et al. 1988).

Saito et al. (1995) measured the heat capacity of the Er_3Co compound, which below $T_C = 13$ K exhibited a noncollinear magnetic structure. Above T_C a large magnetic con-

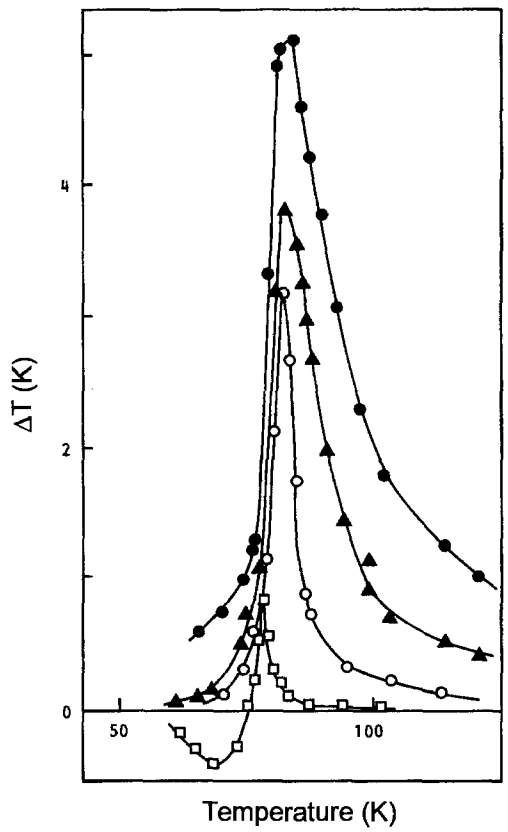


Fig. 6.5. Temperature dependences of the MCE induced by a magnetic field change ΔH: (•) 60 kOe; (△) 40 kOe; (○) 20 kOe; (□) 5 kOe (Nikitin and Tishin 1991).

tribution to the heat capacity was found. It was related with crystalline electric field effects (Schottky-type anomaly) and was interpreted in the framework of the point-charge model.

7. Magnetocaloric effect in rare earth metals and alloys

7.1. Rare earth metals

The heavy rare earth metals (REM) Gd–Lu (except Yb) and Y have hexagonal close-packed (hcp) crystalline structures. In the magnetically ordered state they display complex magnetic structures (except Gd) (Taylor and Darby 1972). In Tb, Dy and Ho a helicoidal antiferromagnetic (HAFM) structure occurs in a certain temperature interval from T_C to T_N. In the HAFM state, the magnetic moments within one and the same basal plane order ferromagnetically and are turned by some angle with respect to those in the neighboring basal plane. The axis of such antiferromagnetic spiral coincides with the six-fold crystallographic c-axis. The HAFM structure can be transformed by a field induced transition into the ferromagnetic state if the magnetic field exceeds some critical value H_{cr}. In the

magnetic phase diagram $H_{cr}(T)$ one can identifie the temperature T_K, which corresponds to the maximum value of H_{cr} ($\partial H_{cr}/\partial T = 0$ here). Below T_K the transition at $H = H_{cr}$ is of the first-order and above T_K it has the second-order character. The first-order transition is accompanied by "jumps" and some field hysteresis in the $I(H)$ curves at $H = H_{cr}$. Below T_C a ferromagnetic basal-plane phase was observed in Tb and Dy and in Ho a HAFM structure with a ferromagnetic component along the c-axis was found.

A more complicated magnetic structure was found in erbium. In the temperature range between $T_N = 85$ K and $T_{CY} = 53$ K a longitudinal spin wave along the c-axis occurs. Below T_{CY} the structure changed to a cycloid in which the spin wave was superimposed on a basal plane spiral structure. Below $T_C = 18$ K the c-axis component ordered ferromagnetically and the basal planes retained the spiral ordering forming a ferromagnetic cone (conical phase) (Cable et al. 1965; Atoji 1974; Habenshuss et al. 1974).

Thulium, below $T_N = 56$ K, displays an antiferromagnetic longitudinal spin wave phase. Below 32 K it turns into a ferromagnetic type structure composed of four basal plane layers with magnetic moments aligned parallel to the c-axis, followed by three layers with moments aligned antiparallel (Brun et al. 1970).

Neodymium has two double-hcp crystalline structure with two crystallographically inequivalent (hexagonal and cubic) sites and a complicated antiferromagnetic structure. The magnetic moments on the hexagonal sites order at $T_N = 19.2$ K and on the cubic sites below 7.8 K (Johansson et al. 1970).

7.1.1. Gadolinium

Neutron diffraction studies made by Cable and Wollan (1968) showed that Gd exhibits ferromagnetic ordering from liquid helium temperatures to the Curie temperature $T_C = 293$ K. The easy magnetization axis is directed along the c-axis from T_C down to the spin-reorientation temperature $T_{SR} \approx 230$ K below which the spontaneous magnetization vector departs from the c-axis and the easy cone arises.

The MCE, ΔS_M and heat capacity of single and polycrystalline gadolinium were studied by many authors (Brown 1976; Gschneidner and Pecharsky 1997a; Nikitin et al. 1978; Hashimoto et al. 1981; Maeda et al. 1983; Tishin 1990b, 1990c; Burkhanov et al. 1991; Dan'kov et al. 1992, 1996, 1998; Foldeaki et al. 1995). The temperature dependence of the MCE of Gd obtained by various methods displays a maximum near T_C (see figs 3.5 and 7.1). An additional small MCE anomaly was found in a Gd single crystal for H aligned along the c- and a-axis near T_{SR} by Nikitin et al. (1978).

Nikitin et al. (1978) studied the dependence of the MCE in a Gd single crystal on the magnetic field orientation. For a hexagonal crystal the anisotropic part of the Gibbs free energy can be expressed as follows:

$$G_A = K_1 \sin^2 \Theta + K_2 \sin^4 \Theta + K_3 \sin^6 \Theta + K_6^6 \sin^6 \Theta \cos 6\phi, \tag{7.1}$$

where Θ is the angle between the spontaneous magnetization vector $\vec{I}_s$ and the c-axis, ϕ is the angle between the basal-plane component of $\vec{I}_s$ and the a-axis, K_i are the anisotropy constants.

The last term in eq. (7.1) describes the basal-plane anisotropy which is usually small, and can be neglected. On the basis of eq. (7.1) and eq. (2.8a) the magnetic entropy change

ΔS_Θ arising during the variation of the $\vec{I}_s$ direction from the initial value of Θ_0 to the final value of Θ_H, which is the angle between the magnetic field and the c-axis, can be written down as:

$$\Delta S_{A\Theta} = -\left(\frac{\partial K_1}{\partial T}\right)_{H,p}\left(\sin^2\Theta_H - \sin^2\Theta_0\right) - \left(\frac{\partial K_2}{\partial T}\right)_{H,p}\left(\sin^4\Theta_H - \sin^4\Theta_0\right) - \left(\frac{\partial K_3}{\partial T}\right)_{H,p}\left(\sin^6\Theta_H - \sin^6\Theta_0\right). \tag{7.2}$$

The anisotropy constants K_i also depend on H, which leads to a magnetic entropy change $\Delta S_{A,H}$:

$$\Delta S_{A,H} = -\left[\left(\frac{\partial^2 K_1}{\partial H \partial T}\right)_p \sin^2\Theta_H + \left(\frac{\partial^2 K_1}{\partial H \partial T}\right)_p \sin^4\Theta_H + \left(\frac{\partial^2 K_3}{\partial H \partial T}\right)_p \sin^6\Theta_H\right]\Delta H. \tag{7.3}$$

The total magnetic entropy change $\Delta S_A = \Delta S_{A,\Theta} + \Delta S_{A,H}$ causes the anisotropic contribution to the MCE (Nikitin et al. 1978):

$$\Delta T_A = \Delta T_{A,\Theta} + \Delta T_{A,H} = -\frac{T}{C_p}\left(\Delta S_{A,\Theta} + \Delta S_{A,H}\right), \tag{7.4}$$

where the first term $\Delta T_{A,\Theta}$ is the contribution from the rotation of $\vec{I}_s$ against a magnetic anisotropy force and the second term $\Delta T_{A,H}$ is the contribution from the variation of the anisotropy constants in the applied field.

The total MCE was obtained as a sum of the MCE caused by a paraprocess (it was calculated by eq. (2.16)) and ΔT_A. The calculated $\Delta T(T)$ curve was in good agreement with the experimental one.

The ΔT_A values were determined from the experimental $\Delta T(H)$ dependences measured at various T as the intercepts on the ΔT axis by the extrapolation of the linear high field part of the $\Delta T(H)$ curves. It was shown that near T_C the main contribution to ΔT_A gave the second term in eq. (7.4). Below 230 K, the ΔT_A value is determined by the first term. As it follows from eqs (7.2) and (7.3), in this case $\Delta T_A = 0$ for $\Theta_H = \Theta_0$. This allowed to determine the temperature dependence of the Θ_0 (Nikitin et al. 1978), which was in good accordance with data obtained by other authors.

The magnetic entropy change ΔS_M induced by the field change in Gd, was determined from the magnetization data with the help of eq. (2.71) and from magnetocaloric effect by eq. (2.80). Good agreement was found between the experimental data and MFA calculations (Maeda et al. 1983; Tishin 1990a, 1990b, 1990c). Figure 7.1(a) and (b) present various contributions to the entropy of Gd in zero magnetic field and in a field of 70 kOe, calculated by eqs (2.60)–(2.62) and (2.67) by Tishin (1990a). The MCE in Gd for $\Delta H = 70$ kOe determined by the method described in section 4.1 is shown in fig. 7.1(c) (curve 1). This figure also presents experimental values of the MCE in Gd (curve 2) obtained by Brown

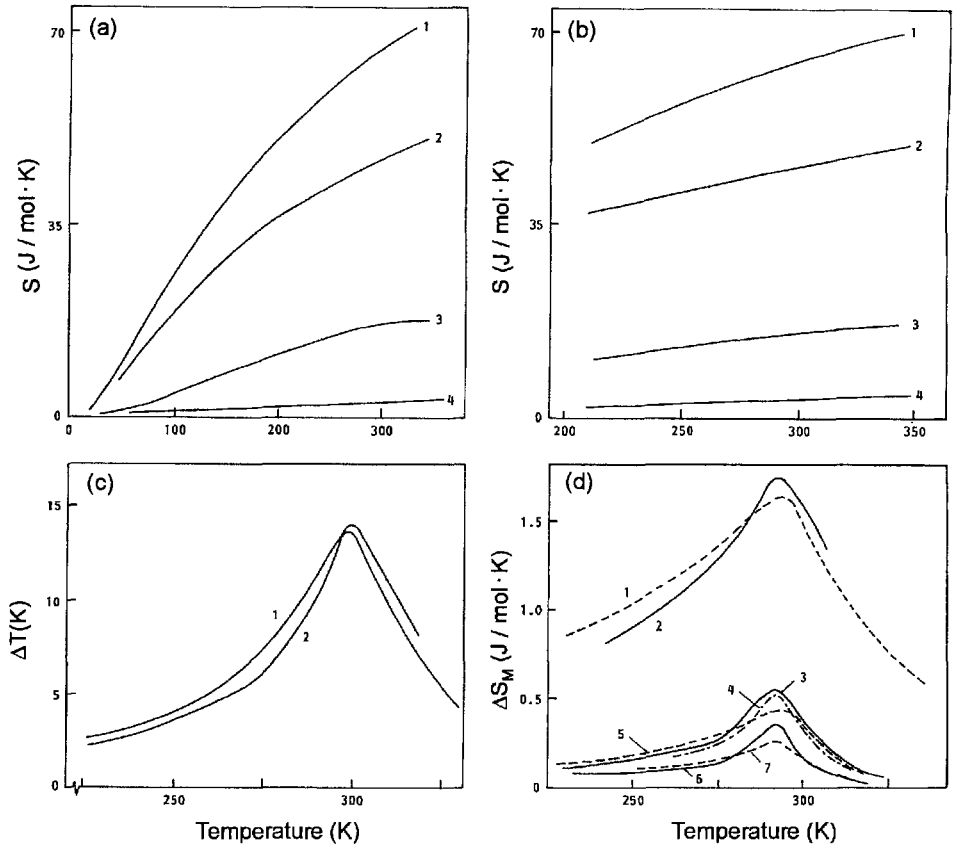


Fig. 7.1. Temperature dependences of calculated entropy and MCE for Gd. (a) $H = 0$; (b) $H = 70$ kOe: (1) total entropy; (2) lattice entropy; (3) magnetic entropy; (4) electronic entropy. (c) Experimental (curve 1) and calculated (curve 2) dependences of MCE in Gd for $\Delta H = 70$ kOe. (d) Temperature dependence of magnetic entropy ΔS_M in Gd for $\Delta H = 60$ kOe (curves 1, 2); $\Delta H = 10$ kOe (3, 4, 5); $\Delta H = 5$ kOe (6, 7) (calculated values – curves 1, 5, and 7; experimental values obtained from magnetization and MCE data – curves 2, 3, 6, and 4) (Tishin et al. 1990a).

(1976). It can be seen that the results of the calculations describe the experimental data quite well. The values of g_J, J, T_C, T_N and T_D used in the MFA calculations are presented in table 7.1. Figure 7.1(d) presents the theoretical and experimental ΔS_M curves for polycrystalline Gd. The values of ΔS_M determined by the results of magnetization and MCE measurements are quite close. The maximum ΔS_M and MCE values near the Curie temperature in Gd obtained by various authors are collected in table 7.2.

The heat capacity of polycrystalline Gd was measured from 15 to 335 K by Griffel et al. (1954), and on single-crystal samples near T_C by Lanchester et al. (1980) and Glorieux et al. (1995). Dan'kov et al. (1998) measured the heat capacity and magnetic field dependences of polycrystalline and single-crystal gadolinium. As it was noted earlier by Gschneidner (1993), the magnetic properties of RE metals are critically dependent on their purity. In all samples a pronounced λ-type anomaly was observed near T_C in

TABLE 7.1
Parameters of RE elements used by Tishin (1990a) in theoretical MFA calculations.

Parameter	Rare earth metal					
	Gd	Tb	Dy	Ho	Er	Tm
g_J	2	1,5	1.33	1.25	1.2	1.7
J	3.5	6	7.5	8	7.5	6
T_C, K	293	—	—	—	—	—
T_N, K	—	230	178	133	85	60
T_D, K	184	177	179	194	192	190

the temperature dependence of the zero-field heat capacity. The magnetic field effect on the λ-maximum was typical for ferromagnets: it was substantially broadened and shifted to higher temperatures with increasing magnetic field. A small zero-field heat capacity anomaly existed in the single-crystal sample at about 220–225 K (near T_{SR}), but was wiped out by the magnetic field above 20 kOe.

The significant reduction of the purity in the commercial Gd sample caused a sharp reduction of the maximum of the λ-type anomaly ($\sim 10\%$ as compared to high purity samples) and its temperature ($\sim 5\%$). An excess heat capacity in the commercial sample appeared in the temperature range between 70 and 286 K and above 300 K. The authors related these features with straining of the crystal lattice and weakening of the exchange interactions due to the interstitial impurities (such as carbon) dissolved in Gd. The interstitial impurities had also a distinct effect on the MCE measured in pulsed fields: the MCE value in the commercially pure Gd was about two times lower than in the high-purity samples (the maximum of ΔT was about 3.2 K at 288 K for $\Delta H = 20$ kOe in the commercial Gd).

7.1.2. Terbium

Terbium displays HAFM ordering in the temperature interval from $T_N = 230$ K to $T_C = 220.6$ K, which is characterized by weak critical fields: maximum $H_{cr} = 190$ Oe at $T_K = 228.5$ K (Bykhover et al. 1990). In fields above H_{cr} the HAFM structure in Tb and Dy is destroyed and a "fan" structure arises (in the given temperature interval), in which the magnetic moments in the basal planes form fan-type ordering around the field direction. Further increase of the field leads to complete ferromagnetic ordering at a field of about $2H_{cr}$ (Greenough and Hettiarachchi 1983; Drillat et al. 1984; Bagguley and Howe 1986).

When the HAFM structure is destroyed by a magnetic field, an MCE takes place because the entropies of the two phases (HAFM and fan or FM) are not equal. The MCE at the first-order transition at $H = H_{cr}$ applied in the basal plane of Dy and Tb_xY_{1-x} alloys was considered by Nikitin et al. (1977a, 1977b, 1979a), Nikitin and Andreenko (1981) and Nikitin et al. (1991b). It was shown that the transition is caused by changes in several interactions, namely the energy of exchange interaction between the basal planes the magnetoelastic energy, the Zeeman energy and the in-plane anisotropy energy. The first three contributions were shown to dominate.

TABLE 7.2

Ordering temperatures T_N or T_C, temperature of the maximum in the $\Delta T(T)$ curves (T^T_{max}), temperature of the maximum in the $\Delta S_M(T)$ curves (T^S_{max}) and maximum values of ΔS_M (at $T = T^S_{max}$) and ΔT (at $T = T^T_{max}$) induced by a magnetic field change ΔH for the heavy rare earth metals.

Element	T_C; T_N, K	MCE			$-\Delta S_M$		
		T^T_{max}, K	ΔT, K	ΔH, kOe	T^S_{max}, K	$-\Delta S_M$, J/mol K	ΔH, kOe
Gd	292[a]	296[b]	11.2[b]	50[b]	294[i]	1.75[i]	60[i]
	294[h]	296[b]	5.6[b]	20[b]	292[i]	0.55[i]	10[i]
		296[c]	18.8[c]	100[c]	295[j]	3.2*[j]	10[j]
		292[d]	10.8[d]	50[d]	295[k]	0.78**[k]($\|c$)	12[k]
		294[e]	4.8[e]	20[e]			
		293[f]	14[f]	70[f]			
		295[h]	5.8[h]	20[h]			
		296[h]	19.5**[h]($\|c$)	100[h]			
		294[g]	2.8**[g]($\|a$, $\|c$)	10[g]			
Tb	230[l]	227[m]	0.23**[m]($\|b$)	0.4[m]	230[p]	0.6**[k]($\|a$)	12[p]
		231[n]	5[n]	20[n]	230[q]	2.5[q]	60.2[q]
		233[n]	10.5[n]	60[n]			
		231[n]	10**[n]($\|b$)	60[n]			
		230[o]	60**[o](basal plane)	350[o]			
		230[o]	43**[o](basal plane)	150[o]			
Dy	180[l]	180[r]	2.2[r]	20[r]	178[q]	2.3[q]	60.2[q]
		179[n]	8.6[n]	60[n]	168[s]	2.2**[s]($\|a$)	60[s]
		177.5[s]	7.7**[s]($\|a$)	60[s]			
		≈178[s]	≈ 6.5**[s]($\|b$)	60[s]			
Ho	134[t]	132[u]	4.6[u]	60[u]	130[q]	1.8[q]	60.2[q]
		136[v]	6.1[v]	70[v]			
Er	85[w]	85[u]	3.2[v]	60[u]	85[q]	1.2[q]	60.2[q]
		86[x]	4.7[x]	75[x]			
Tm	56[y]	58[u]	1.5[u]	60[u]			
		58[z]	3.1[z]	70[z]			

* In J/kg K

** Measurements on single crystals (the direction of magnetic field is shown in parenthesis)

References:

(a) Nikitin et al. (1991d)
(b) Pecharsky and Gschneidner (1996)
(c) Gschneidner and Pecharsky (1997a)
(d) Benford and Brown (1981)
(e) Hashimoto et al. (1981)
(f) Brown (1976)
(g) Nikitin et al. (1978)
(h) Dankov et al. (1998)
(i) Tishin (1990b)
(j) Foldeaki et al. (1995)
(k) Dankov et al. (1992)
(l) Bykhover et al. (1990)
(m) Nikitin et al. (1989b)
(n) Tishin (1988)
(o) Druzhinin et al. (1977)
(p) Dan'kov et al. (1996)
(q) Nikitin and Tishin (1988)
(r) Hudgins and Pavlovic (1965)
(s) Nikitin et al. (1991a)
(t) Nikitin et al. (1991d)
(u) Tishin and Martinenko (1995)
(v) Green et al. (1988)
(w) Milton and Scott (1967)
(x) Zimm et al. (1988)
(y) Brun et al. (1970)

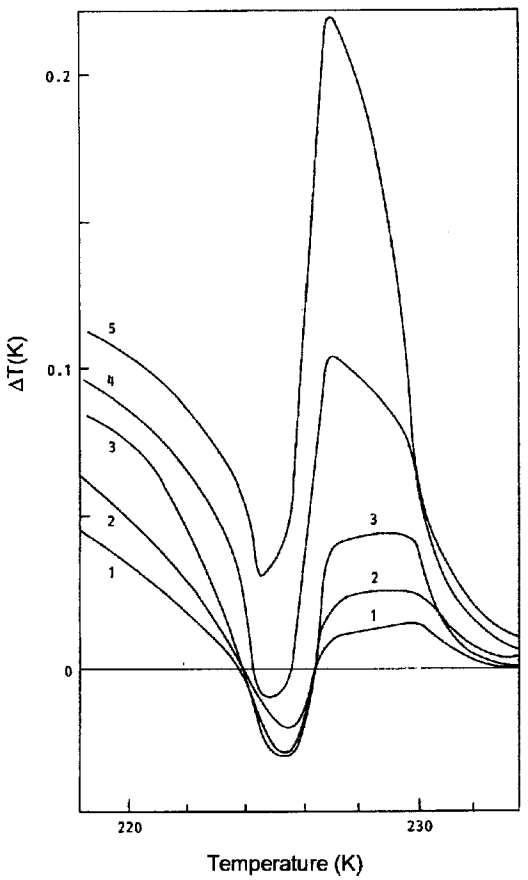


Fig. 7.2. Temperature dependences of the MCE for a Tb single crystal with the magnetic field applied along the b-axis: (1) $\Delta H = 200$ Oe; (2) 250 Oe; (3) 300 Oe; (4) 350 Oe; (5) 400 Oe (Nikitin et al. 1989b).

Nikitin et al. (1989) studied the MCE of Tb in fields up to 400 Oe applied along the easy magnetization direction (b-axis) in the temperature interval from T_C to T_N – see fig. 7.2. Between 220.5 and 223.4 K the MCE values are small and positive in weak fields and sharply increase above H_{cr}. For temperatures from 223.4 to 226 K the MCE is negative in fields $H < 350$ Oe. The negative MCE is characteristic of antiferromagnets, in which the external field reduces the magnetic order rather than enhances it, thus increasing the magnetic entropy (antiferromagnetic-type paraprocess). In the case of Tb the external field transforms the HAFM structure into the lower-symmetry fan structure. The magnetic phase diagram $H_{cr}(T)$ constructed on the basis of $\Delta T(H)$ curves (the magnetic field was changed from 0 to H) is in good accordance with that obtained from the magnetization measurements. H_{cr} was defined as the field of the maximum increase of ΔT.

Figure 7.3 shows the temperature dependences of the MCE in a single crystal of Tb induced by fields applied along the b-axis (Tishin 1988). The MCE maximum in Tb is

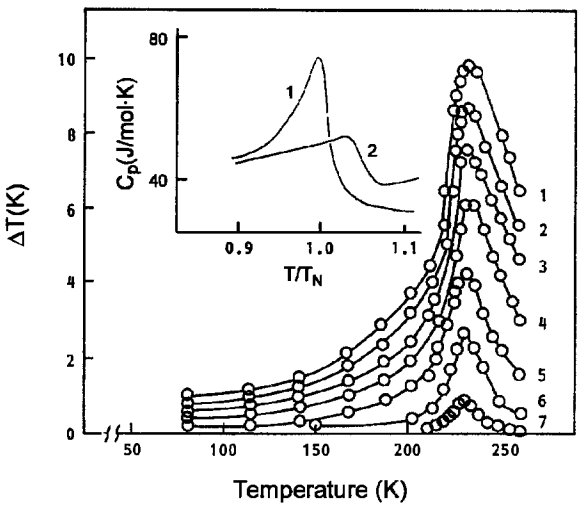


Fig. 7.3. Temperature dependences of the MCE for a Tb single crystal with the magnetic field applied along the *b*-axis: (1) $\Delta H = 60$ kOe; (2) 50 kOe; (3) 40 kOe; (4) 30 kOe; (5) 20 kOe; (6) 10 kOe; (7) 2.5 kOe. Inset: temperature dependences of the heat capacity of a Tb single crystal at: (1) $H = 0$; (2) $H = 60.2$ kOe (Tishin 1988; Nikitin et al. 1985a).

observed near T_N and is caused by a paraprocess, which is known to be the most strong near the temperature of the transition to a magnetically ordered state. Due to the complete destruction of the HAFM structure no MCE anomalies were observed near T_C for $\Delta H \geqslant 10$ kOe. The same results were obtained for measurements in the field applied along the *a*-axis (hard axis in Tb) which is related with a small magnetic anisotropy of Tb in basal plane at high temperatures.

Calculations of the MCE in Tb, made by Tishin (1990a) on the basis of the MFA, have shown relatively satisfactory agreement with the experimental data near T_N, see fig. 7.4: for $\Delta H = 20$ kOe the calculations leads to $\Delta T = 6$ K, while the experimental value is 5 K. The calculated MCE in strong magnetic fields is shown in the inset in fig. 7.4. As one can see, for $\Delta H > 2000$ kOe the maximum in the $\Delta T(T)$ curve disappears and for $T > T_N$ the MCE practically does not change. Note the disagreement of these results with the MCE value calculated earlier by Druzhinin et al. (1979) in the framework of MFA (the shape of the $\Delta T(T)$ curves was quite similar): $\Delta T = 120$ K for Tb at $T = T_N$ and $\Delta H = 1500$ kOe. According to Tishin (1990a), at $T = T_N$ the MCE value of 120 K can be reached only in a field of 2250 kOe, while for $\Delta H = 1500$ kOe the MCE amounts to 98 K.

Druzhinin et al. (1977) determined the MCE in a Tb single crystal in fields up to 350 kOe from the experimental adiabatic dependences of the magnetization in the basal plane obtained by the pulse method. The MCE was calculated by integration of eq. (2.23):

$$\Delta T = T - T_i = T_i \left\{ \exp\left[\int_{I_s(T)}^{I_T} \frac{1}{C_I} \left(\frac{\partial H}{\partial T} \right)_I \mathrm{d}I \right] - 1 \right\}, \tag{7.5}$$

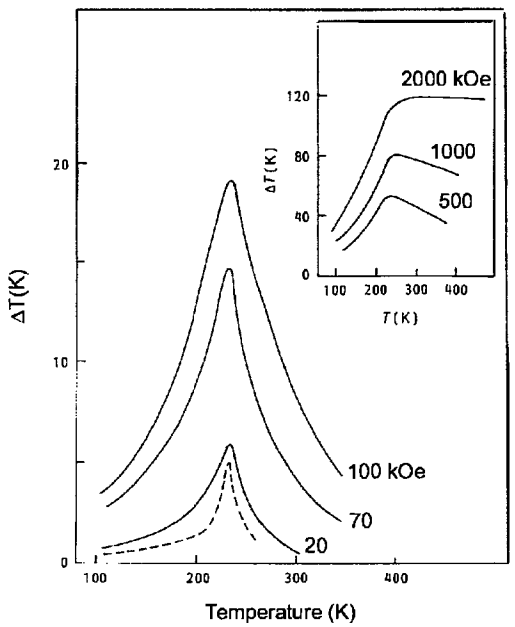


Fig. 7.4. Temperature dependences of the MCE in Tb: — theory; - - - experiment (Tishin 1990a).

where I and T are the final values of temperature and magnetization and $I_s(T_i)$ and T_i are the initial values of magnetization and temperature. A sharp MCE maximum with the value of 60 K was observed at $T = 230$ K.

The temperature dependences of the magnetic entropy change ΔS_M in Tb was evaluated from magnetization measurements by eq. (2.71) (Dan'kov et al. 1996) and from heat capacity and MCE data (Nikitin et al. 1985a). In the latter case, the results of zero-field heat capacity measurements made by Jennings et al. (1957) and eq. (2.77) were used for the $\Delta S_M(T)$ calculation (the field dependence of the heat capacity was not taken into account). Later, the ΔS_M values for the heavy rare-earths have been calculated more exactly by Tishin (1994). In these calculations the field dependence of the heat capacity was taken into account. The result for Tb is shown in fig. 7.5. As one can see, ΔS_M for $\Delta H = 60.2$ kOe has maximum near T_N.

The heat capacity of Tb in the presence of a magnetic field was calculated by Nikitin and Tishin (1987) and Tishin (1988) on the basis of the zero-field measurements of Jennings et al. (1957). First, $S(T, H)$ was calculated by eq. (2.76) and the MCE data, and then eq. (2.12) was used to calculate $C(T, H)$. The results for $H = 60.2$ kOe is shown in the inset in fig. 7.3. The heat capacity maximum becomes broader and lower in the field and shifts to the higher temperature region.

7.1.3. Dysprosium

The HAFM structure arises in Dy between $T_N \simeq 180$ K and $T_C \simeq 90$ K. Dy is characterized by much higher critical fields than Tb: the maximum H_{cr} value is about 11 kOe at $T_K = 165$ K (Bykhover et al. 1990).

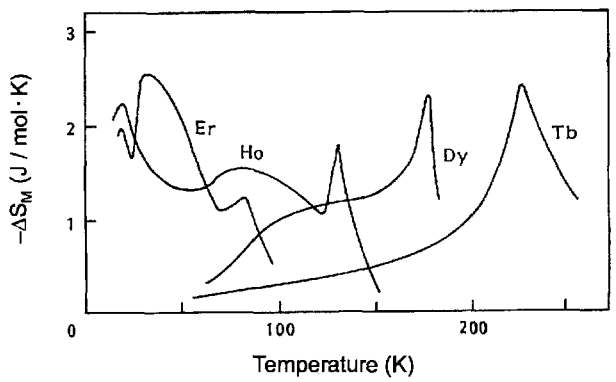


Fig. 7.5. Temperature dependences of the magnetic entropy change of Tb, Dy, Ho and Er induced by ΔH = 60.2 kOe (Tishin 1994).

Hudgins and Pavlovic (1965) performed detailed studies of the field and temperature dependences of the MCE in polycrystalline Dy in the fields up to 20 kOe and in the temperature interval from 77 to 320 K. The $\Delta T(H, T)$ curves were discussed in connection with the magnetic structure transformation. Later Tishin (1988) and Nikitin et al. (1985a) studied the MCE in polycrystalline Dy in fields up to 60 kOe.

Joint investigations of the MCE and magnetic properties of a Dy single crystal along the easy axis a were made by Nikitin et al. (1979a) in magnetic fields up to 13 kOe. It was found that a field induced HAFM–FM transition at H_{cr} causes a positive MCE ($\Delta T > 0$) within the temperature interval from 85 to 160 K. A change of sign of the MCE was found to take place at T_K, where H_{cr} had its maximum and $\partial H_{cr}/\partial T = 0$. According to the Clausius–Clapeyron equation (2.82) ΔS_M, and consequently ΔT, at this temperature should be equal to zero. It was concluded that T_K is a tricritical point in the magnetic phase diagram $H_{cr}(T)$ of Dy, where the first-order transition lines turn into the second-order transition line.

The MCE in Dy was also studied by Benford (1979) and Nikitin et al. (1991b). Figure 7.6 shows temperature dependences of the MCE in a Dy single crystal measured directly with the field applied along the a- and b-axis (Tishin 1988; Nikitin et al. 1991b). The MCE maximum observed for H applied along the a-axis at $T = 177.5$ K is associated with the HAFM–PM phase transition. The sharp increase of the MCE near $T \approx 90$ K corresponds to the FM–HAFM transition. In the region from 165 to 178 K the MCE is negative for $\Delta H = 10$ kOe. A substantial change of the $\Delta T(T)$ behavior is observed when the field is increased. The broad plateaus in the temperature interval from 90 to 135 K and $H < 20$ kOe are due to the destruction of the HAFM structure by fields $H > H_{cr}$. In stronger fields the plateaus gradually disappear and an additional MCE maximum appears around 155–165 K, the temperature of the maximum increasing as the field is increased. The minimum in high fields corresponds to the tricritical point $T_K = 165$ K. The general character of the MCE behavior in fields applied along the b-axis is similar to that measured along the a-axis. The differences in the low-temperature region was related by Nikitin et al. (1991b) with a contribution from the change of magnetic basal-plane anisotropy energy.

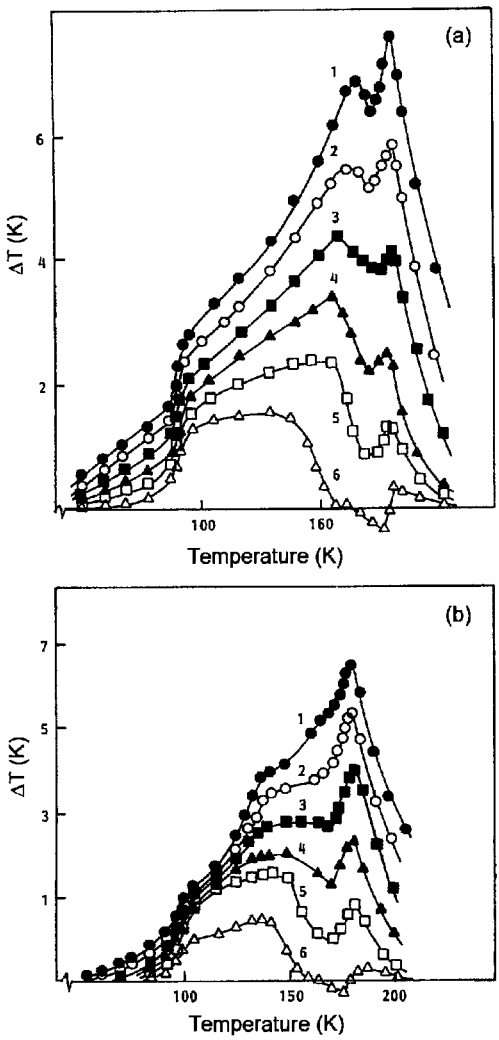


Fig. 7.6. (a) Temperature dependences of the MCE in a Dy single crystal in fields applied along a-axis: (1) $\Delta H = 60$ kOe; (2) 50 kOe; (3) 40 kOe; (4) 30 kOe; (5) 20 kOe; (6) 10 kOe. (b) Temperature dependences of MCE in a Dy single crystal with the magnetic field applied along b-axis: $\Delta H = 10$, 20, 30, 40, 50, and 60 kOe (curves 1–6, respectively) (Nikitin et al. 1991b).

Figure 7.7 shows the MCE in a Dy crystal obtained in various fields applied along the a-axis (Tishin 1988; Nikitin et al. 1991b). In the temperature interval from 85 to 165 K jumps in the $\Delta T(H)$ curves are observed. In the region from 165 to 178 K these jumps disappear and the MCE becomes negative in weak fields. Magnetization measurements showed that within the interval from 135 to 165 K the first-order transitions from HAFM to fan occurred (Nikitin et al. 1991b).

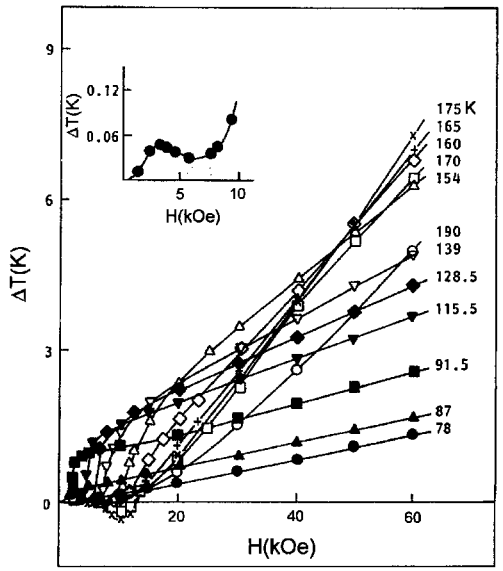


Fig. 7.7. The dependence of the MCE in a Dy single crystal on magnetic fields directed along the a-axis (the field was changed from 0 to H). The numbers near the curves are temperatures in Kelvin. Inset: initial part of the curve for $T = 78$ K (Tishin 1988; Nikitin et al. 1991b).

The second-order field induced transition HAFM–fan was observed from 165 K to T_N. In this case the field continuously deforms the HAFM structure until a fan structure is formed. This process is accompanied at an early stage by growth of the magnetic entropy due to lowering of the antiferromagnetic order. The maximum negative MCE (at $H \approx 10$ kOe) marks the point of maximum disorder in the magnetic structure.

Data on the magnetic entropy of Dy have been presented by Nikitin et al. (1985a, 1991b, 1991c), Nikitin and Tishin (1988) and Foldeaki et al. (1995). Figure 7.5 presents $\Delta S_M(T)$ curve for Dy for $\Delta H = 60.2$ kOe calculated on the basis of heat capacity and MCE data. The maximum of ΔS_M is observed near T_N. The $\Delta S_M(T)$ curve calculated for a Dy single crystal from MCE measurements leads to positive values in the temperature interval from 165 to 178 K. The temperature dependence of the magnetic entropy $S_M(0, T)$ of a high-purity Dy single crystal was determined by Nikitin et al. (1991c) by eq. (2.76) on the basis of heat capacity measurements. The saturation high-temperature S_M value obtained in this way equals 23 J/mol K, which is in good agreement with the theoretical value from table 6.2. Foldeaki et al. (1995) determined the temperature and field dependences of ΔS_M in polycrystalline Dy from the magnetization measurements by eq. (2.71). A positive magnetic entropy change was observed on the $\Delta S_M(H)$ curve at $T = 174$ K at low fields (below 1.5 kOe). The MCE and ΔS_M values obtained experimentally in Dy by various methods are presented in table 7.2.

The heat capacity of Dy was measured by Griffel et al. (1956), Lounasmaa and Sundstrom (1966), Ramji Rao and Narayama Mytry (1978) and Nikitin et al. (1991c). Maxima on the $C(T)$ curve were observed near T_N and T_C. The value of the maximum near the

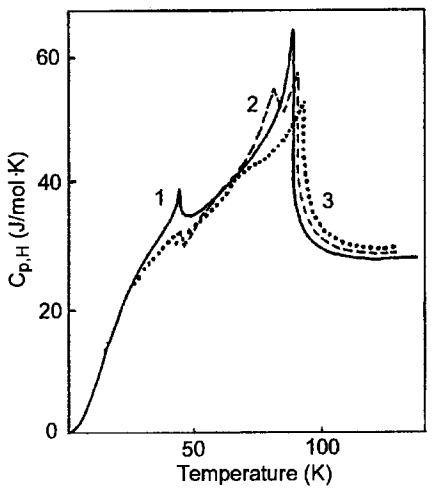


Fig. 7.8. Temperature dependences of the heat capacity Dy in various magnetic fields: (1) $H = 0$; (2) $H =$ 20 kOe; (3) 60 kOe (Nikitin and Tishin 1987).

HAFM–PM transition was shown to be in good agreement with the one calculated in the framework of MFA (Nikitin et al. 1991c).

Nikitin and Tishin (1987) using eq. (2.96) and MCE data calculated the heat capacity of Dy in magnetic fields up to 60 kOe from the zero-field heat capacity measurements of Griffel et al. (1956). The results are presented in fig. 7.8. The appearance of an additional maximum in the $C(T)$ curve for $H = 20$ kOe near $T = 160$ K was related by the authors with the occurrence of the fan structure. With increasing magnetic field the maximum disappears, which correlates with the transformation of the fan structure into the ferromagnetic one at high fields.

7.1.4. Holmium

The temperature dependences of the MCE of polycrystalline Ho measured directly for various ΔH are shown in fig. 7.9 (Nikitin et al. 1985a). MCE maxima are observed at $T_C = 20$ K ($\Delta T = 4.6$ K for $\Delta H = 60.2$ kOe) and at $T_N = 132$ K ($\Delta T = 4.5$ K for $\Delta H = 60.2$ kOe). The MCE is large in the temperature interval from 20 to 132 K with $\Delta T = 3.2$–4.6 K for $\Delta H = 60.2$ kOe. Small MCE maxima are observed in the region of 70–90 K for $\Delta H = 30.1$–60.2 kOe. They are due to a complex temperature dependence of the critical field H_{cr}, which destroys the HAFM structure. Green et al. (1988) found a MCE maximum in Ho near 136 K with the value of 6.1 K for $\Delta H = 70$ kOe.

The heat capacity of Ho was measured by Jayasuria et al. (1985), Lounasmaa and Sundstrom (1966). Nikitin and Tishin (1987) on the basis of zero-field heat capacity and MCE data calculated $C(H, T)$ curves of Ho by eq. (2.96). It was shown that a broad maximum appears in the $C(H, T)$ curve in the temperature range from 90 to 130 K for $H = 20$ kOe which is higher than H_{cr}. As the field is increased up to 60 kOe, this maximum disappears and only a plateau remains in the $C(H, T)$ curve. The maximum was related by the authors with the tricritical point in the magnetic phase diagram $H_{cr}(T)$.

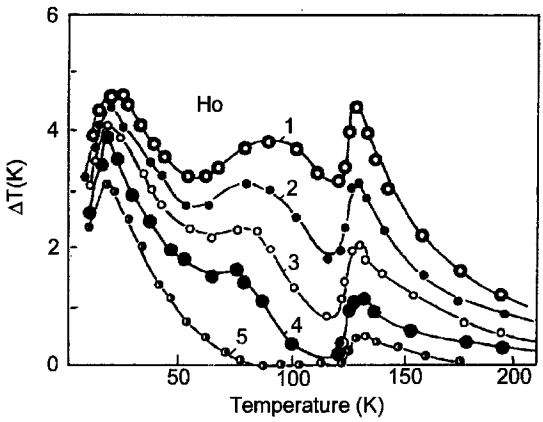


Fig. 7.9. Temperature dependences of the MCE of polycrystalline Ho for various ΔH: (1) 60.2 kOe; (2) 50.2 kOe; (3) 40.3 kOe; (4) 30.1 kOe; (5) 20.1 kOe (Nikitin et al. 1985a; Tishin 1988).

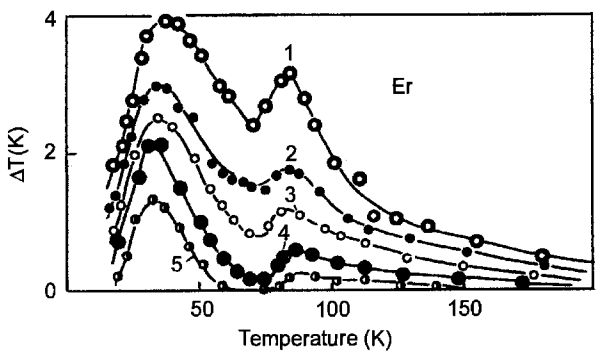


Fig. 7.10. Temperature dependences of the MCE of polycrystalline Er for various ΔH: (1) 60.2 kOe; (2) 50.2 kOe; (3) 40.3 kOe; (4) 30.1 kOe; (5) 20.1 kOe (Nikitin et al. 1985a; Tishin 1988).

The $\Delta S_M(T)$ curve for Ho, obtained from the MCE and heat capacity measurements, is shown in fig. 7.5. The sharp ΔS_M maximum occurs near T_N.

7.1.5. Erbium

The directly measured temperature dependence of the MCE of polycrystalline Er shows a maximum near the AFM–PM transition point T_N (Nikitin et al. 1985a) (see fig. 7.10). At $\Delta H = 60.2$ kOe the maximum MCE value was 3.2 K. An extra maximum, which was attributed to the destruction of the AFM structure by a magnetic field, was observed at $T = 35$ K. The maximum value $\Delta T = 3.8$ K exceeds that near T_N obtained for the same ΔH value. As well as Ho, Er shows a substantial MCE (about 3 K for $\Delta H = 60.2$ Oe) over a wide temperature interval from 30 to 85 K. Analogous $\Delta T(T)$ curves were obtained by Zimm et al. (1988) for polycrystalline Er. It was established that for $\Delta H = 75$ kOe the high-temperature (near T_N) and low-temperature MCE maxima

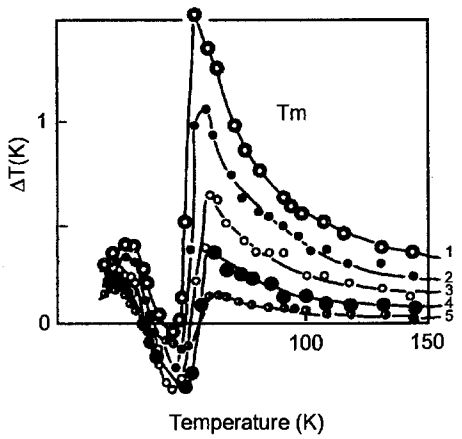


Fig. 7.11. Temperature dependences of the MCE of polycrystalline Tm for different values of ΔH: (1) 60.2 kOe; (2) 50.2 kOe; (3) 40.3 kOe; (4) 30.1 kOe; (5) 20.1 kOe (Nikitin et al. 1985a; Tishin 1988).

become almost equal and amount to 4.7 K. Zimm et al. (1988) found that below 20 K a magnetization–demagnetization cycle causes sample heating. This was explained by a fairly large magnetic hysteresis observed in this temperature range.

The $\Delta S_M(T)$ curve of Er for $\Delta H = 60.2$ kOe is presented in fig. 7.5. The ΔS_M maximum near T_N has a value of 1.2 J/mol K, while the low temperature maximum is much higher with $\Delta S_M = 2.5$ J/mol K.

The heat capacity of Er was studied by Skochdopole et al. (1955), Schmitzer et al. (1987), Dreyfus et al. (1961), Hill et al. (1984) and Krusius et al. (1974). The temperature dependence of the zero-field heat capacity of Er measured by Zimm et al. (1988) displayed a large step at 84 K corresponding to the AFM ordering along the c-axis. The broad shoulder from 30 to 80 K corresponds to the ordering in the basal plane and the sharp peak near 20 K is related with the first-order transition to a conical magnetic structure. A magnetic field of 10 kOe wiped out the peak at 20 K but had only a small effect on the high-temperature anomaly.

Heat capacity measurements in the absence of a magnetic field were made by Pecharsky et al. (1993) on high-purity polycrystalline Er in the temperature interval 1.5–80 K. Besides the peaks at 19 K (conical phase transition) and 51.4 K (AFM ordering in the basal plane), additional anomalies at 25.1, 27.5, 42, and 48.9 K were revealed. They were related by the authors with the spin-slip transitions between different commensurate AFM structures (Gibbs et al. 1986; Bohr 1991).

7.1.6. Thulium

The $\Delta T(T)$ curves of Tm measured by a direct method are shown in fig. 7.11 (Nikitin et al. 1985a). A MCE maximum with the value of 1.5 K for $\Delta H = 60.2$ kOe is observed near T_N at 58 K. At lower temperatures the MCE becomes negative which may be due to the deformation of the AFM structure by the magnetic field and which is accompanied by a

magnetic entropy increase. Analogous $\Delta T(T)$ curves were obtained by Zimm et al. (1989), although the maximum ΔT values in corresponding magnetic fields were somewhat higher.

The temperature dependence of the zero-field heat capacity of Tm showed a large step near T_N (Zimm et al. 1989). The application of 10 kOe did not have any noticeable influence on the $C(T)$ curve except rounding of the step at T_N.

7.1.7. Neodymium

The heat capacity and MCE of polycrystalline Nd were studied by Zimm et al. (1990) in the temperature range from 5 to 35 K and in fields up to 70 kOe. In the temperature dependences of the MCE measured by a direct method two maxima were found. The one near 20 K corresponds to magnetic ordering at the hexagonal sites, and the other, near 8 K, corresponds to ordering at the cubic sites. It should be noted that the latter maximum was much higher ($\Delta T \approx 2.5$ K at 10 K for $\Delta H = 70$ kOe) than the former ($\Delta T \approx 1.5$ K at 21 K for $\Delta H = 70$ kOe). The authors related this difference with a large magnetocrystalline anisotropy because of which only the basal plane component (the magnetic moments in the hexagonal sites order in the basal plane) of the external magnetic field in a crystallite can contribute to the magnetic ordering near T_N.

The relatively weak MCE in Nd (as compared with the heavy RE metals) was explained by the antiferromagnetic structure and crystalline field effects. The latter factor reduces the maximum available magnetic entropy from $R \ln 10$ ($J = 9/2$) in the absence of crystal field splitting to $R \ln 2$ ($J = 1/2$).

The heat capacity of Nd was measured by Lounasmaa and Sundstrom (1967) and Zimm et al. (1990). Two anomalies were observed at the corresponding magnetic phase transitions.

7.1.8. Theoretically available MCE in the heavy rare-earth metals

One of the fast developing areas of prospective applications of rare-earth metals is the design of new effective magnetic solid state refrigerators. The particular interest in magnetic refrigerators is associated with the possibility of their wide commercialization. Active prototypes of the latter are known by their high efficiency and notable life-in-service time. Hence, the practical use of the MCE has potentially a great future (see, for instance, Gschneidner and Pecharsky 1997a).

Nonetheless, the selection of magnetic materials that are good candidates for cooling media (magnetic refrigerant) is not straightforward, since a theory which could permit an accurate prediction of the magnetocaloric effect does not exist yet. Furthermore, modern experimental investigations in high magnetic fields up to 5 MOe and more are no longer something exotic. Since the MCE value in such fields can be extremely high, the possibility of its influence on the obtained experimental results needs to be accounted for.

Tishin's papers (1990a) and (1998c) describe the results of a computer simulation analysis of the magnetocaloric effect (MCE) in rare earth metals and rare earth based materials. The analysis of Tishin (1990a) was developed for calculating peak values of the MCE in rare earth magnets using a mean-field approximation. The study by Tishin (1998c) concentrates on the variation of the key thermodynamic parameters such as magnetic field, temperature, the Curie and Debye temperatures of the magnetic materials in wide range of values. Results of theoretical studies of the MCE in large magnetic fields were described.

TABLE 7.3

Results of calculations of maximum possible values of the maximum possible magnetic entropy change $-\Delta S_M^{max}$, magnetic entropy change ΔS_M^{theor} for $\Delta H = 6000$ and 10^4 kOe, maximum possible values of magnetocaloric effect ΔT_{max}, values of the field H_{max}, in which the MCE is different from ΔT_{max} by at most 1% and experimental maximum magnetic entropy change ΔS_M^{exp} near T_{ord} in the heavy RE metals (Tishin 1990a).

Parameter	Rare earth metal					
	Gd	Tb	Dy	Ho	Er	Tm
$-\Delta S_M^{max}$, J/mol K	17.3	21.3	23.1	23.6	23.1	21.3
$-\Delta S_M^{exp}$, J/mol K ($\Delta H = 60$ kOe)	2.1 $\Delta H = 70$ kOe	2.4	2.3	1.8	1.2	—
$-\Delta S_M^{theor}$, J/mol K ($\Delta H = 6000$ kOe)	15.8	19.4	21.4	22.3	22.6	21.0
$-\Delta S_M^{theor}$, J/mol K ($\Delta H = 10^4$ kOe)	16.8	20.6	22.5	23.1	22.7	21.0
ΔT_{max}, K	235	254	231	191	135	100
ΔH_{max}, $\times 10^4$ kOe	2.2	2.8	2.6	2.4	1.6	1.0
T_{ord}, K	293	230	178	135	85	60

The possible mechanisms of magnetic entropy change in a paraprocess region were discussed. Tishin's (1998c) study shows that there is a strong influence of the Debye temperature of the magnetic materials on the MCE value in a wide temperature region (from 4.2 K to 200–230 K).

Based on the molecular field theory, Tishin (1990a and 1998b) performed numerical simulations of the MCE value, ΔT, and the entropy, S, of heavy lanthanides. The used numerical approach was described in details by Tishin (1990a) and has been described also in section 3.3, the REM parameters used being listed in table 7.3. The magnetic fields considered were assumed to significantly exceed the critical magnetic fields necessary to destroy the antiferromagnetic state in the rare earth metals, and therefore, all calculations were performed for magnetic phase transition from the ferromagnetic to the paramagnetic state.

All results of the numerical simulation should agree quite well with the experimental data for the heavy lanthanides only for large magnetic fields, i.e., for fields in which the contribution of the AFM–FM phase transition to the magnetic entropy is rather small. During the simulation, the assumed values of the magnetic field ranged from 0 to 40 MOe and the initial temperature ranged from 10 K to 1000 K. It was found that the maximum value of magnetic field in our galaxy can reach about 10^{15} Oe (Kouveliotou et al. 1998). The energy spectrum can become extremely distorted in such high magnetic fields. Therefore, this naturally may affect the real field dependence of the magnetic entropy, S_M, and ΔT. Phenomena like crossover are considered by the author to yield staircase-like $\Delta T(H)$ and $S_M(H)$ curves. But Tishin (1998c) proposed that its contribution to the total value of the

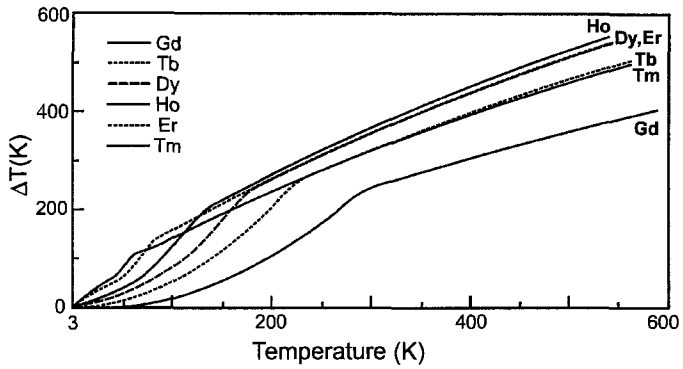


Fig. 7.12. Temperature dependences of the MCE in the heavy rare earth metals Gd, Tb, Dy, Ho, Er, and Tm for $\Delta H = 6$ MOe (Tishin 1990a).

overall MCE and the entropy should be relatively small. It should be noted that the results described can be applied to the real magnetic materials only outside the critical region. The calculations reveal the fact that if the temperature is high (near 1000 K), saturation of the MCE and magnetic entropy is absent even in the highest magnetic fields (up to 40 MOe), while near the temperature of the phase transition to the paramagnetic state the value of the magnetic entropy saturates in a field of about 10 MOe. In high fields ($H > 10$ MOe), the magnetic entropy practically equals zero up to the point $T \approx T_C$, i.e., there is no magnetic contribution to the entropy. This result leads to the following conclusion: in fields higher than 1 MOe the magnetic moments of the rare earth ions must be nearly completely aligned in a wide range of temperatures, up to the Curie temperature.

Tishin's calculations point to the fact that the general behavior of the MCE as a function of temperature is transformed significantly under the influence of a magnetic field. Anomalies in the MCE curves for $T > T_C$ are observed in magnetic fields up to 40 MOe, but the MCE increases with temperature, when $H > 5$ MOe and $T > T_C$. When $H > 5$ MOe, the MCE increases up to $T = T_C$ and then decreases smoothly when $T > T_C$. The temperature and field dependencies of the MCE in REM behave similarly. Figure 7.12 presents the temperature dependence of the maximum MCE for heavy lanthanides (in the saturation field). Gadolinium has the minimum MCE at all considered temperatures. Tishin's (1998c) analysis leads to the conclusion that at low temperatures the maximum MCE value (of heavy lanthanides) is determined by the Debye temperature, T_D, (i.e., by the small value of the lattice heat capacity). When the temperature exceeds 230 K the maximum MCE in all REM follows the total angular moments, J, and/or the effective magnetic moment, μ_{eff}. The calculations show, that Tb has the largest MCE in fields up to 2 MOe, while Er has the lowest. In higher fields Ho has the maximum value of MCE, and Gd the minimum. Furthermore, in high fields (although not in the saturation fields) the MCE is defined not only by the magnetic entropy, but also by a number of other parameters associated with the magnetic and crystal structures of the lanthanides.

The field dependences of the magnetic entropy in the vicinity of the phase transition to the paramagnetic state are found to be arranged in order of increasing Curie temperatures

of the lanthanides, except Gd. The calculations reveal that the MCE in REM continues to increase even when the magnetic entropy becomes almost equal to zero.

Calculations of the MCE value in the heavy RE metals as a function of the magnetic field at $T = T_{ord}$ (here $T_{ord} = T_C$ for Gd and T_N for the others RE metals) give satisfactory agreement with the experimental data for $\Delta H = 60$ kOe only for Gd, Tb and Dy (Tishin 1990a). This result is quite clear, since in Ho, Er and Tm the HAFM structure persists in much higher fields than in Tb and Dy. It follows from the experimental data that the behavior of the $\Delta T(T)$ curves is strongly influenced by these structures in fields up to 60 kOe (see above). One can suppose that in fields much higher than H_{cr} the MFA should describe the MCE sufficiently well.

The MFA calculations of $\Delta S_M(T, H)$ in heavy RE metals at $T = T_{ord}$ shown that a considerable rise in ΔS_M is observed only in fields below 2 MOe, whereas in fields of about 6 MOe the values of ΔS_M differ only slightly from their maximum values ΔS_M^{max}, calculated by eq. (2.70). Table 7.3 presents ΔS_M^{max}, the values of ΔS_M calculated for $\Delta H = 6$ MOe and 10 MOe, and maximum experimental ΔS_M values for $\Delta H = 60$ kOe near T_{ord} (Brown 1976; Nikitin and Tishin 1988; Tishin 1988).

Table 7.3 lists the maximum possible values of the magnetocaloric effect (ΔT_{max}) at $T = T_{ord}$, calculated by eq. (2.77) on the basis of ΔS_M^{max} values. Also listed are the calculated values of the fields $H_{max}(T_{ord})$, in which the MCE is different from ΔT_{max} by at most 1%. As one can see, an initial temperature rise of 100 K leads the MCE to increase by a factor 1.5–2. Such behavior of ΔT_{max} corresponds to the functional dependence $\Delta T \sim T$, as follows from eq. (2.77), since the factor $(\Delta S_M / C_{p,H})$ tends to a constant when H tends to infinity. The analysis made by Tishin (1990a) shows that the ΔT_{max} value in the series of heavy RE metals is directly proportional to the product $g_J J T_{ord}$.

From the classic point of view, the change of S_M value is usually related to the rotation of the magnetic moment vectors under influence of the magnetic field (i.e., the S_M decreases with increasing magnetization in classic magnetic materials). It has been experimentally established that the value of ΔS_M measured in 60 kOe in rare-earth metals and their alloys in the vicinity of their magnetic phase transition totals approximately 8 to 10% of ΔS_{max} (Tishin 1988). Moreover, the magnetization of Gd at the Curie point practically does not change in 100 to 300 kOe (Ponomarev 1986). The MCE value measured in 100 kOe in Gd equals 19 K (Dan'kov et al. 1998). But from Tishin's (1990a and 1998c) calculations it follows that ΔT_{max} in Gd is expected to be 234 K at $T = T_C$. Thus, it appears that for most of the sample's temperature increase one has to take account of paraprocesses (occurring in the region where the sample has already single domain structure and the atomic magnetic moments are mostly aligned parallel to the field). So the change of the MCE and the magnetic entropy is clearly determined not only by rotation of the magnetization vectors. This means that the experimental data can not be explained within the classic theory, which assumes the magnetic entropy decrease to occur at the expense of the rising order of the magnetic moments in the system. Thus, the use of a probability (quantum mechanical) approach to the entropy seems to be the right choice. This means that the magnetic entropy (and consequently the sample temperature) continues to change even in the region of the paraprocess, just because of the fact that the probability of atomic magnetic moment deflection from the field direction (due to the heat fluctuations) remains non-zero even in high magnetic fields. It is possible that the values of ΔS_M (which have been observed in

rare-earth intermetallic compounds by Gschneidner et al. (1994a, 1994b)) are large due to suppression of spin heat fluctuations in the low temperature region.

Since the influence of T_D on the MCE was not sufficiently studied yet, neither theoretically nor experimentally, it is of interest to define numerically the general rules of the phenomena. In general, the relation between the MCE and the entropy change is well known. To investigate the impact of the Debye temperature on the MCE we need to take into account the effect of the temperature on the lattice entropy (it is worth noting that the concept of total entropy as a sum of different parts can be used only for magnetic materials with localized magnetic moment, like REM). The entropy of a solid is known to increase significantly when the Debye temperature decreases. For instance, it is easy to show that at 300 K a decrease of the Debye temperature from 184 K (Gd) to 50 K leads to a lattice entropy (S_L) increase of about 33 J/mol K (70%). When the Debye temperature increases from 184 K to 500 K this leads to an S_L change of only approximately 23 J/mol K (50%). It is well known that the maximum possible value of the magnetic entropy change can be defined as $\Delta S_{max} = -R \ln(2J + 1)$ (see eq. (2.70)). So, from one point of view the maximum MCE is limited by the total quantum number and the measurement temperature. On the other hand, in general the MCE can vary due to the change of magnetic, lattice and electronic contributions to the heat capacity. The electronic part of the heat capacity gives a constant contribution to the heat capacity and does not change the MCE if T = const. The character of magnetic contributions to the heat capacity change (generally a decrease for ferromagnets) under exposure of a field is quite complicated and can be predicted only in general terms.

Tishin's (1998c) calculations show, that the change in T_D can significantly influence the magnetocaloric effect value. Consequently, a change in the Debye temperature has a different impact on the MCE value in the low- ($T < 200$–230 K) and high-temperature range. However, the problem of what are the ways and how the Debye temperature can be changed in real magnetic materials still remains quite insufficiently researched.

From the qualitative point of view, the Debye temperature can be treated as the rigidity of the crystal lattice. The rigidity of a lattice can be changed. For instance, one may change the fabrication process by making it amorphous or by the other processing means. Tishin (1998c) proposed that the Debye temperature can be effected significantly by addition of different elements to magnetic compounds. For example, additions of C, N or B are known to lead to a unit cell volume increase (swelling) of a magnetic material.

7.2. Rare earth alloys

7.2.1. Tb–Gd alloys

The MCE in Tb_xGd_{1-x} alloys was investigated by Nikitin et al. (1979b, 1980, 1981, 1988b). The alloys with $x > 0.94$ are examples of easy-plane ferromagnets with their hard magnetization direction along the c-axis (Nikitin et al. 1980). Such magnetic materials display a spin reorientation transition with the appearance of a magnetization component along the hard axis below some temperature.

The temperature dependences of the MCE measured in Tb_xGd_{1-x} alloys in fields applied in the basal plane (easy plane) have maxima near the Curie point (Nikitin et al. 1981). The MCE values measured along the b-axis are given in table 7.4.

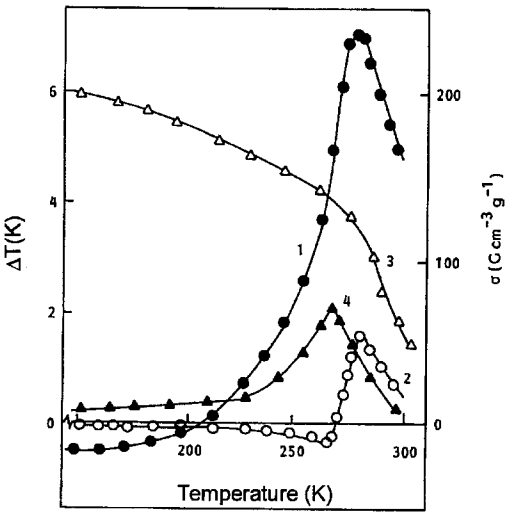


Fig. 7.13. Temperature dependences of the MCE in a $Tb_{0.2}Gd_{0.8}$ single crystal measured with the field applied along the c-axis with $\Delta H = 60$ kOe (curve 1) and 10 kOe (curve 2). Also shown are the temperature dependences of the specific magnetization in a field of 60 kOe (curve 3) and 10 kOe (curve 4) (Nikitin et al. 1988b).

The measurements along the hard c-axis revealed more complex MCE behavior. The temperature dependence of the MCE in the $Tb_{0.2}Gd_{0.8}$ alloy is shown in fig. 7.13 (curves 1 and 2). A maximum for the positive MCE can be observed near $T_C = 282$ K, as in the case of H directed along the b-axis. However, as the sample is cooled down, a sign change of the MCE takes place below T_C, where it becomes negative. The sign inversion temperature shifts towards lower temperatures in higher fields. Near T_C the MCE behavior is correlated with the temperature dependences of the magnetization (see fig. 7.13 and eq. (2.16)). For $H = 60$ kOe the $\sigma(T)$ curve has a form usually observed for ferromagnets and the MCE displays a maximum. For $H = 10$ kOe there is a maximum in the $\sigma(T)$ curve. The maximum appears due to the ordering of the magnetic moments in the basal plane in fields which are not high enough to orient them along the c-axis below T_C. The maximum in the $\Delta T(T)$ curve for $\Delta H = 10$ kOe is observed at the temperature where $\partial\sigma/\partial T$ is negative and has a maximum value (see curves 2 and 4 in fig. 7.13). The negative MCE corresponds to positive $\partial\sigma/\partial T$. The behavior of the temperature and field dependences of the MCE in $Tb_{0.2}Gd_{0.8}$ for magnetization along the c-axis near T_C were discussed by Nikitin et al. (1981) in the framework of the Landau theory of the second-order transitions.

The reasons for the appearance of a negative MCE in Tb–Gd alloys in the low temperature range in fields applied along the hard axis were considered by Nikitin et al. (1988b). The total MCE was presented as consisting of three contributions:

$$\Delta T \approx -\frac{T}{C_{H,p}}\left[\frac{\partial I_s}{\partial T} H\cos\Theta + \frac{\partial K_1}{\partial T}\left(\sin^2\Theta - 1\right)\right.$$
$$\left. + \mathcal{I}_{RR}\left(\frac{\partial I_{Tb}}{\partial T} I_{Gd} + \frac{\partial I_{Gd}}{\partial T} I_{Tb}\right)\left(\cos^2(\Theta_{Tb} - \Theta_{Gd}) - 1\right)\right], \qquad (7.6)$$

TABLE 7.4

Ordering temperatures T_N or T_C, temperature of the maximum in the $\Delta T(T)$ curves (T^T_{max}), temperature of the maximum in the $\Delta S_M(T)$ curves (T^S_{max}) and maximum values of ΔS_M (at $T = T^S_{max}$) and ΔT (at $T = T^T_{max}$) induced by a magnetic field change for the rare earth alloys.

Alloy	T_C; T_N, K	MCE			$-\Delta S_M$		
		T^T_{max}, K	ΔT, K	ΔH, kOe	T^S_{max}, K	$-\Delta S_M$, J/mol K	ΔH, kOe
$Gd_{0.3}Tb_{0.7}$	253[a]	252[b]	9.1*[b] ($\|b$)	60[b]			
		252[a]	0.4*[a] ($\|c$)	12[a]			
$Gd_{0.6}Tb_{0.4}$	271[a]	270[b]	8*[b] ($\|b$)	60[b]			
$Gd_{0.8}Tb_{0.2}$	282[a]	281[a]	2.2*[a] ($\|b$)	8[a]			
		282[b]	7.2*[b] ($\|c$)	60[b]			
		282[b]	$\approx$ 0.9*[c] ($\|c$)	9.1[c]			
$Gd_{0.2}Ho_{0.8}$	160[d]	160[d]	$\approx$ 7[d]	60.2[d]			
$Gd_{0.4}Ho_{0.6}$	194[d]	194[d]	$\approx$ 9[d]	60.2[d]			
$Gd_{0.6}Ho_{0.4}$	230[d]	230[d]	$\approx$ 9.5[d]	60.2[d]			
$Gd_{0.8}Ho_{0.2}$	268[d]	268[d]	$\approx$ 10[d]	60.2[d]	265[e]	$\approx$ 0.6[e]	10[e]
$Gd_{0.2}Er_{0.8}$	125[d]	125[d]	$\approx$ 4[d]	60.2[d]			
$Gd_{0.4}Er_{0.6}$	168[d]	168[d]	$\approx$ 7[d]	60.2[d]			
$Gd_{0.6}Er_{0.4}$	220[d]	220[d]	$\approx$ 8[d]	60.2[d]			
$Gd_{0.69}Er_{0.31}$					$\approx$ 232[f]	$\approx$ 15.8**[f]	90[f]
$Gd_{0.84}Er_{0.16}$					260[e]	$\approx$ 0.55[e]	10[e]
$Gd_{0.90}Er_{0.10}$					$\approx$ 274[f]	$\approx$ 14**[f]	$\approx$ 90[f]
$Gd_{0.3}Dy_{0.7}$					$\approx$ 208[g]	$\approx$ 16**[g]	70[g]
					$\approx$ 204[g]	$\approx$ 2.8**[g]	10[g]
$Gd_{0.51}Dy_{0.49}$					$\approx$ 248[g]	$\approx$ 10.4**[g]	70[g]
					$\approx$ 242[g]	$\approx$ 2**[g]	10[g]
$Gd_{0.7}Dy_{0.3}$					$\approx$ 254[h]	0.73[h]	16[h]
$Gd_{0.8}Dy_{0.2}$					$\approx$ 264[h]	0.72[h]	16[h]
$Gd_{0.88}Dy_{0.12}$					$\approx$ 280[g]	$\approx$ 14**[g]	70[g]
					$\approx$ 280[g]	$\approx$ 3.6**[g]	10[g]
$Gd_{0.9}Dy_{0.1}$					$\approx$ 276[h]	0.73[h]	16[h]
$Tb_{0.1}Y_{0.9}$	52[h]	55[i]	0.3*[i] ($\|b$)	60[i]			
		$\approx$ 50[i]	0.04*[i] ($\|c$)	60[i]			
$Tb_{0.63}Y_{0.37}$	176[h]	176[i]	5.6*[i] ($\|b$)	60[i]	$\approx$ 173[i]	5*[i] ($\|b$)	60[i]
$Tb_{0.865}Y_{0.135}$	205[h]	205[i]	$\approx$ 7*[i] ($\|b$)	60[i]			
$Dy_{0.7}Y_{0.3}$	135[j]	129[j]	3.7*[j] ($\|a$)	60[j]			
$Tb_{0.25}Dy_{0.75}$		194[k]	0.7[k]	13[k]			
$Tb_{0.5}Dy_{0.5}$		207[k]	1.7[k]	13[k]			
$Tb_{0.75}Dy_{0.25}$		218[k]	2.1[k]	13[k]			
$Er_{0.8}La_{0.2}$		45[l]	5.4[l]	70[l]			
		44[l]	0.8[l]	10[l]			

where Θ is the angle between the total spontaneous magnetization vector $\vec{I}_s$ and the c-axis, K_1 is the anisotropy constant, $\mathcal{I}_{RR}$ is the exchange integral for the indirect interaction between the Tb and Gd magnetic moments, I_{Tb} and I_{Gd} are the magnetizations of the Tb and Gd sublattices, respectively; Θ_{Tb} and Θ_{Gd} are the angles between the sublattice magnetization vectors $\vec{I}_{Tb}$ and $\vec{I}_{Gd}$ and the c-axis. The first term, calculated by eq. (2.16), is due to the variation of exchange interaction inside the Tb and Gd sublattices ($H \cos \Theta$ is the projection of the field on the magnetization vector $\vec{I}_s$), i.e., the paraprocess. The second term in eq. (7.6) is due to the rotation of $\vec{I}_s$ from the basal plane to the c-axis against anisotropy forces. The last term describes the variation of the exchange interaction between Tb and Gd magnetic sublattices, which leads to a change of the angle between $\vec{I}_{Tb}$ and $\vec{I}_{Gd}$ and the formation of a noncollinear magnetic structure.

The calculations by eq. (7.6) on the basis of experimental data for the $Tb_{0.2}Gd_{0.8}$ alloy showed that for $\Delta H = 60$ kOe the anisotropy contribution to the MCE (the second term in eq. (7.6)) is negative and its absolute value increases up to the temperature of the spin-reorientation transition near 223 K (where a magnetization component along the c-axis appears) and then remains constant (approximately -4 K). The contribution from the paraprocess is positive and has substantial values near the Curie temperature. At $T = 223$ K it reaches a value of about 4.3 K. The last term in eq. (7.6) is small and negative below 223 K. The total MCE calculated as a sum of these three contributions is in good accordance with experimentally measured negative MCE below 223 K for $\Delta H = 60$ kOe (Nikitin et al. 1988b).

7.2.2. Gd–Dy, Gd–Ho and Gd–Er alloys

The MCE in polycrystalline Gd–Ho and Gd–Er alloys was investigated by Nikitin et al. (1985b).

According to magnetization studies in Gd–Ho alloys a PM–FM transition at the Curie temperature T_C takes place if the Gd concentration exceeds 75 at.% and a HAFM structure exists between T_C and T_N, if the Gd concentration lies in the interval from 13 to 75 at.% (Fujii et al. 1976). In $Gd_{0.8}Ho_{0.2}$ a maximum in the $\Delta T(T)$ curve was found caused by the PM–FM transition. In the alloys with higher Ho concentrations a high-temperature MCE maximum related with the HAFM–PM transition at T_N was observed. In $Gd_{0.2}Ho_{0.8}$ a broad MCE maximum occurs in the temperature interval from 40 to 140 K (for $\Delta H = 20$ kOe), which is associated with the HAFM–FM transition. In fields $H > H_{cr}$ this maximum disappears. Tishin (1990d) determined $\Delta S_M(T)$ curves for the $Gd_{0.8}Ho_{0.2}$

TABLE 7.4 (Continued)

* Measurements on single crystals (the direction of magnetic field is shown in parenthesis)
** In J/kg K

References:

(a) Nikitin et al. (1981)
(b) Nikitin et al. (1988b)
(c) Nikitin et al. (1980)
(d) Nikitin et al. (1985b)
(e) Tishin (1990d)
(f) Smaili and Chahine (1996)
(g) Smaili and Chahine (1997)
(h) Nikitin (1989)
(i) Nikitin and Tishin (1989)
(j) Tishin (1988)
(k) Nikitin et al. (1989c)
(l) Zimm (1994)

alloy on the basis of magnetization measurements and eq. (2.71). The ΔS_M maximum was found near T_C for $\Delta H = 10$ kOe.

Gd–Er alloys exhibit more complex magnetic structures (Bozorth 1967; Millhouse and Koehler 1970; Fujii et al. 1976). Below T_N, AFM structures are observed if the Er concentration exceeds 30 at.%, but they are more complicated than simple helicoidal. As in Er, spin oscillations along the c-axis take place. The complex magnetic structures cause the appearance of maxima in the $\Delta T(T)$ curves at T_N and T_C, where a transitions from AFM to a ferromagnetic spiral-type structure occurs. In the $Gd_{0.8}Er_{0.2}$ alloy the MCE maximum is due to the PM–FM transition, and for the others investigated alloys it is due to an AFM–ferromagnetic spiral transition. The magnetic entropy change ΔS_M was calculated from the magnetization data for $Gd_{0.84}Er_{0.16}$ alloy by Tishin (1990d) and for $Gd_{0.9}Er_{0.1}$ and $Gd_{0.69}Er_{0.31}$ alloys by Smaili and Chahine (1996). The MCE and ΔS_M values for Gd–Ho and Gd–Er alloys are presented in table 7.4.

It was found that the maximum MCE value near T_N is proportional to T_N in Gd–Ho and Gd–Er alloys (Nikitin et al. 1985b). Since $T_N \sim G^{2/3}$, where $G = (g_J - 1)^2 J(J+1)$ is de Gennes factor, $\Delta T(T_N)$ should be approximately proportional to $G^{2/3}$. Such a dependence (for an average de Gennes factor) was observed in Gd–Ho and Gd–Er alloys.

The magnetic entropy change ΔS_M for Gd–Dy alloys was calculated by Burkhanov et al. (1991) and Smaili and Chahine (1997) from the magnetization data. Maxima of ΔS_M were observed near the temperatures of transition from the paramagnetic to the magnetically ordered state. Their values are presented in table 7.4.

7.2.3. Tb–Y, Dy–Y and Tb–Dy alloys

According to neutron diffraction measurements, heavy REM-yttrium alloys order below T_N in an antiferromagnetic structure of the same type that exists in the corresponding pure heavy REM (Koehler et al. 1963; Child et al. 1965). Magnetization measurements showed that in Tb_xY_{1-x} alloys a HAFM structure exists from helium temperatures to T_N for $x =$ 0.1–0.63. For $x \geqslant 0.835$ a HAFM–FM transition at T_C takes place (Nikitin 1989). The easy and hard magnetization directions in Tb_xY_{1-x} alloys are the crystallographic b- and c-axis, respectively.

MCE measurements in Tb_xY_{1-x} alloys with PM–HAFM and HAFM–FM transitions were carried out in fields up to 16 kOe by Nikitin et al. (1977a, 1977b), Nikitin (1978), Nikitin and Andreenko (1981), Nikitin and Tishin (1989). A tricritical point T_K was found in the phase diagram $H_{cr}(T)$ of the alloys. The $\Delta T(T)$ curves were analogous to those obtained for Dy (see fig. 7.7). Below T_K, jumps in the $\Delta T(H)$ curves were observed. The contributions to the MCE arising at the field-induced HAFM–FM transition at $H = H_{cr}$ were determined for $Tb_{0.835}Y_{0.135}$ alloy by Nikitin (1989). The MCE at the transition was obtained from the equation:

$$\frac{C_{p,H}\Delta T(H_{cr})}{T} = S_{HAFM} - S_{FM} = \left(\frac{\partial G_{FM}}{\partial T}\right)_p - \left(\frac{\partial G_{HAFM}}{\partial T}\right)_p, \tag{7.7}$$

where G_{HAFM} and G_{HAFM} are the Gibbs energy in the FM and HAFM states, respectively. The Gibbs energy in the corresponding magnetic phase was written down as:

$$G = F_{ex} + E_{me} + E_A^b - HI, \tag{7.8}$$

where F_{ex} is the free energy of the exchange interaction between the basal planes, E_{me} is the energy of the magnetoelastic interaction, E_A^b is the basal plane anisotropy energy, and I is the magnetization. From eqs (7.7) and (7.8) it follows that the MCE due to the HAFM–FM transition at $H = H_{cr}$ is:

$$\Delta T(H_{cr}) = \frac{T}{C_{p,H}} \left(\frac{\partial \Delta F_{ex}}{\partial T} + \frac{\partial \Delta E_{me}}{\partial T} + \frac{\partial \Delta E_A^b}{\partial T} - H_{cr} \frac{\partial \Delta I}{\partial T} \right), \tag{7.9}$$

where Δ denotes the change of the corresponding parameter across the transition ($\Delta I = I_{FM} - I_{HAFM}$). The calculations were made on the basis of experimental data on magnetostriction, anisotropy and magnetization and showed that for $T = 137$ K $> T_C$ in $Tb_{0.835}Y_{0.135}$ the main contribution to $\Delta T(H_{cr})$ comes from interplane exchange and magnetoelastic energy changes. The last contribution is due to the giant magnetostriction across the field induced HAFM–FM transition. As the temperature increases, the role of this contribution decreases and the negative exchange and positive Zeeman contributions become prevalent. Near the tricritical temperature $T_K = 190$ K these contributions compensate each other and $\Delta T(H_{cr}) = 0$. The results of calculations are confirmed by experimental $\Delta T(H)$ curves.

Nikitin and Tishin (1989) measured the MCE in Tb_xY_{1-x} alloys in fields up to 60 kOe. The temperature dependence of the MCE in the $Tb_{0.1}Y_{0.9}$ alloy measured along the b-axis shows a maximum near the magnetic ordering temperature T_N. Upon cooling the MCE changes sign and becomes negative. When the field was applied along the c-axis the maximum of positive MCE near T_N was broader than in the case of that H was applied along the b-axis. At $T = 30$ K a MCE minimum was observed with $\Delta T = -0.17$ K at $\Delta H = 60$ kOe. These data lead to the conclusion that application of a magnetic field along the c-axis results in a transformation of the magnetic structure. A ferromagnetic spiral seems to appear for the case that H is applied along the c-axis, when the magnetization has a ferromagnetic component along the c-axis and its basal plane component remains helicoidal.

Figure 7.14 shows the temperature dependences of the MCE in $Tb_{0.63}Y_{0.37}$ alloy for H applied along b-axis. When $\Delta H < 22$ kOe the MCE changes sign at low temperatures and displays a minimum with a value of -0.6 K at $T = 168$ K and $\Delta H = 15$ kOe. In stronger fields ($\Delta H > 22$ kOe), a negative MCE is not observed. This can be explained by the complicated temperature behavior of the MCE contribution arising from the destruction of the HAFM structure (see the magnetic phase diagram $H_{cr}(T)$ in the inset in fig. 7.14). Near T_N the MCE is mainly controlled by the paraprocess and has a sharp maximum. The negative MCE in $Tb_{0.1}Y_{0.9}$ and $Tb_{0.63}Y_{0.37}$ alloys was explained by the authors by the field-induced distortion of the HAFM structure which reduces, in the initial stage, the magnetic ordering and increases the magnetic entropy. The MCE maximum values near T_N in Tb_xY_{1-x} alloys are presented in table 7.4. The maximum ΔS_M values were calculated by eq. (2.77) on the basis of MCE and heat capacity data (Nikitin and Tishin 1989).

Tishin (1988) investigated the MCE in a $Dy_{0.7}Y_{0.3}$ single crystal in fields applied along the easy magnetization axis a. The MCE measurements made by a direct method for $\Delta H = 20$–50 kOe revealed two maxima: at $T = 70$ K and $T_N = 135$ K, which were explained by the complicated character of the temperature dependence of the critical field

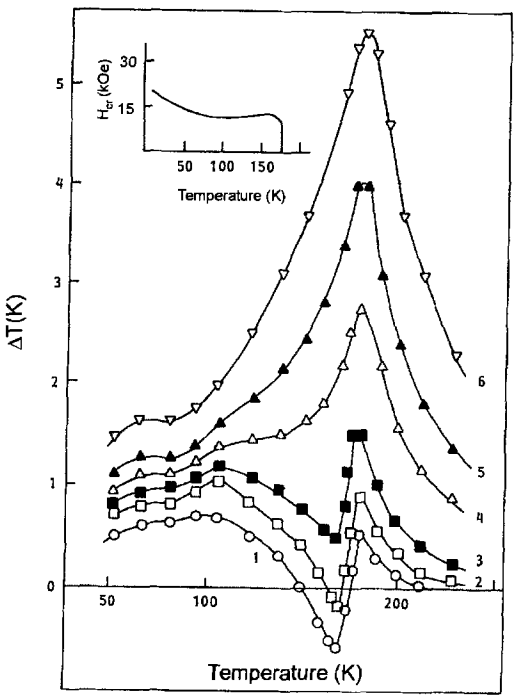


Fig. 7.14. Temperature dependences of the MCE in the $Tb_{0.63}Y_{0.37}$ alloy in fields applied along the b-axis: (1) $\Delta H = 15$ kOe; (2) 20 kOe; (3) 25 kOe; (4) 35 kOe; (5) 45 kOe; (6) 60 kOe. The insert shows the magnetic phase diagram $H_{cr}(T)$ (Nikitin and Tishin 1989).

$H_{cr}(T)$. For $\Delta H \leqslant 20$ kOe temperature dependence of the MCE displays one maximum near T_N. Negative MCE values are observed in the temperature interval from 90 to 110 K for $\Delta H < 25$ kOe. By analogy with Dy, this was explained by the formation of a fan structure. The $\Delta T(H)$ curves are similar to those for Dy and provide evidence that the HAFM–FM transition is of the first order in the interval from 4.2 to 110 K. In the region from 65 to 135 K this transition occurs via an intermediate fan structure. The HAFM–fan transition is of the first order in the interval from 65 to 110 K and of the second order above 110 K, where no jumps were observed in $\Delta T(H)$ curves. At the tricritical point $T_K = 110$ K the MCE due to the destruction of the HAFM structure is equal to zero and because of this a minimum in the $\Delta T(T)$ curve was observed.

Nikitin et al. (1989c) measured the MCE in polycrystalline Tb_xDy_{1-x} alloys with $x = 0.25$; 0.5 and 0.75 by a direct method. The temperature dependences of the MCE for $\Delta H = 13$ kOe (the maximum H_{cr} for Dy is about 10 kOe (Nikitin et al. 1991b)) in the alloys with $x \leqslant 0.5$ have two maxima and resemble those of the Gd–Ho alloys with high Ho content (see section 7.2.2). For $Tb_{0.5}Dy_{0.5}$ alloy the value of the high-temperature maximum at $T = 207$ K. For the latter, $\Delta T \approx 1.7$ K is larger than for the low-temperature maximum at $T = 175$ K ($\Delta T \approx 1.1$ K). For $x = 0.25$ the maxima are approximately equal. The authors related these maxima with the HAFM–FM and HAFM–PM transitions.

Field and temperature dependences of the magnetization characteristic of the presence of a HAFM structure were observed in a $Tb_{0.5}Dy_{0.5}$ single crystal by Bykhover et al. (1990). A minimum corresponding to the tricritical point T_K was observed in the $\Delta T(T)$ curves obtained with $\Delta H = 13$ kOe for $x = 0.25$ (at $T \approx 190$ K) and for $x = 0.5$ (at $T \approx 200$ K). A negative MCE appears for $x = 0.25$ near 190 K and was related with the formation of a fan structure. The low-temperature MCE maximum disappears in strong magnetic fields.

7.2.4. Er–La alloys

The temperature dependences of the heat capacity and the MCE of the polycrystalline $Er_{0.8}La_{0.2}$ alloy were measured by Zimm et al. (1994) in fields up to 70 kOe. Only one maximum and one anomaly, characteristic for ferromagnets, were observed in the $\Delta T(T)$ and $C(T)$ curves, respectively. Magnetization measurements confirmed the ferromagnetic ordering in $Er_{0.8}La_{0.2}$. The maximum ΔT value obtained in the $Er_{0.8}La_{0.2}$ alloy is not much larger than that of Er (see tables 7.2 and 7.4).

On the basis of heat capacity data a magnetic entropy value of 111 J/kg K was calculated by eq. (2.76) when the integration was made from 0 to 100 K. This value corresponds to $J = 7.8$, being close to $J = 15/2$ for Er.

8. Magnetocaloric effect in nanocomposite systems

In this section we shall consider the experimental investigations of the MCE in various nanocomposite systems which have attracted attention in recent years.

Shao et al. (1996a, 1996b) studied the MCE in nanocomposite ribbons prepared by a copper-sheated rolling technique from $Gd_{0.85}Tb_{0.15}$, $Gd_{0.85}Y_{0.15}$ and $Gd_{0.75}Zr_{0.25}$ alloys. The arc-melted and homogenized alloys were resolidified into amorphous particles about 20 nm in diameter by melt-spinning. Then these particles were milled within a sealed agate bowl containing agate balls. This method allowed it to obtain powder particles finer than mesh size 360 nm. X-ray analyzes showed that the milling led to the formation of nanocrystallites of 10–20 nm size within the original amorphous particles, although part of them remained amorphous. The powder was packed into an annealed copper tube, sealed at both ends and then rolled into the copper sheated nanocomposite ribbon. The powder density in the ribbon was about 80% of that of the corresponding bulk alloy. The samples cut from the composite ribbons had the dimensions of $5 \times 5 \times 0.8$ mm.

Heat capacity measurements made on the ribbons in the temperature range of 280–310 K revealed an increase with a maximum mean value of 57.9% for $Gd_{0.85}Y_{0.15}$. On the other hand, the Curie temperature was reduced in the ribbons. Shao et al. (1996a) related these experimental facts with the large proportion of interface atoms arranged in disorder, which changed the interatomic distances and lowered the number of the nearest neighbors.

The MCE (and ΔS_M) in nanosized $Gd_{0.85}Y_{0.15}$ ribbons was higher than in bulk material at temperatures above 240 K, see fig. 8.1. Such behavior is characteristic for superparamagnets (see fig. 2.4). At the same time no enhancement in the MCE was observed in the investigated $Gd_{0.85}Tb_{0.15}$ and $Gd_{0.75}Zn_{0.25}$ ribbons.

Investigation of magnetic and magnetocaloric properties of amorphous $Dy_{70}Zr_{30}$ and $Dy_{30}Zr_{70}$ allowed Giquere et al. (1999) to conclude that the materials can be considered as nanocomposites with interacting clusters.

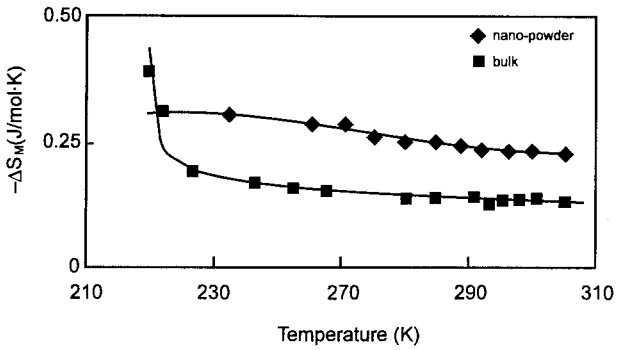


Fig. 8.1. Temperature dependences of the MCE induced by $\Delta H = 10$ kOe magnetic field in $Gd_{0.85}Y_{0.15}$ system in bulk and nanosized states (Shao et al. 1996a).

Many investigations were devoted to the studies of the MCE (or the corresponding magnetic entropy change) in the nanocomposite compound $Gd_3Ga_{5-x}Fe_xO_{12}$ ($x < 2.5$), also known as gadolinium gallium iron garnet (GGIG). Results have been presented by McMichael et al. (1993b), Shull et al. (1993), and Shull (1993a, 1993b). It is a magnetic nanocomposite present as a single crystallographic phase which according to X-ray data has the gadolinium gallium garnet ($Gd_3Ga_5O_{12}$ (GGG)) structure. The magnetic properties change considerably after addition of Fe relative to GGG which has simple paramagnetic behavior above 1 K (McMichael et al. 1993a, 1993b; Numazawa et al. 1996). Magnetization measurements reveal superparamagnetic behavior for $0 \leqslant x \leqslant 2.5$ and ferromagnetic behavior for $x \geqslant 2.5$. It is supposed that the formation of magnetic nano-scaled clusters is due to Gd–Gd interactions of the superexchange type realized via the Fe atoms (Shull 1993). Ferromagnetic resonance and Mössbauer spectroscopy data confirm that GGIG consists of nano-sized magnetic clusters.

Figure 8.2 shows the magnetic entropy change after removal of 9 kOe, calculated by eq. (2.71) for GGIG with $x = 0$, 1, 1.75, 2.5, and 5 on the basis of magnetization data. One can see an obvious increase of ΔS_M in the high-temperature region for increasing iron concentration. This is in qualitative agreement with theoretical results presented in fig. 2.2 under the assumption that higher iron concentration corresponds to larger cluster sizes. Extrapolation shows that samples with smaller x will have larger ΔS_M values below 6 K. The intersections of the ΔS_M curves for $x \neq 0$ with the GGG curve occur at higher temperatures when x increases, which was also predicted by theoretical calculations (see fig. 2.2). Measurements for $\Delta H = 50$ kOe showed that addition of iron to GGG did not cause such strong magnetic entropy changes as for $\Delta H = 9$ kOe, but the enhancement was still significant for temperatures above 9 K. It was established by Shull et al. (1993) that for $x = 1.75$ no hysteresis losses were observed.

McMichael et al. (1993a, 1993b) investigated $\Delta S_M(T)$ curves for rapidly solidified $Nd_{0.14}(Fe_{1-x}Al_x)_{0.8}B_{0.06}$ alloys ($x = 0$; 0.1; 0.2) for $\Delta H = 9$ kOe in the temperature range of 290–500 K. X-ray analyzes showed that the material, produced in the form of melt-spun ribbons, was structurally amorphous. $\Delta S_M(T)$ curves were calculated from magnetization data by eq. (2.71). Figure 8.3 shows that near the Curie temperatures (determined by differential scanning calorimetry) broad peaks of ΔS_M are observed. The

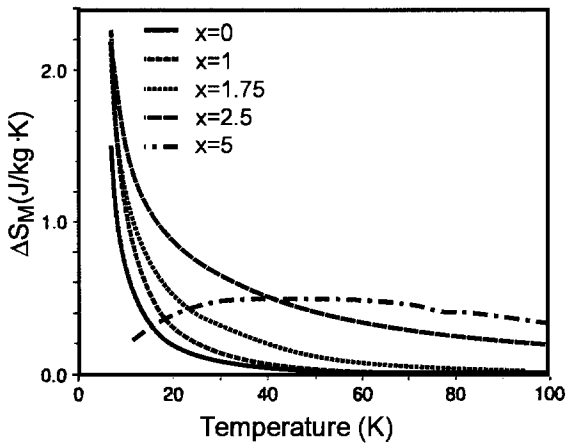


Fig. 8.2. Experimental temperature dependences of the magnetic entropy change $\Delta S_M(T)$ after removal of a magnetic field of 9 kOe in $Gd_3Ga_{5-x}Fe_xO_{12}$ ($0 \leqslant x \leqslant 5$) (McMichael et al. 1993b).

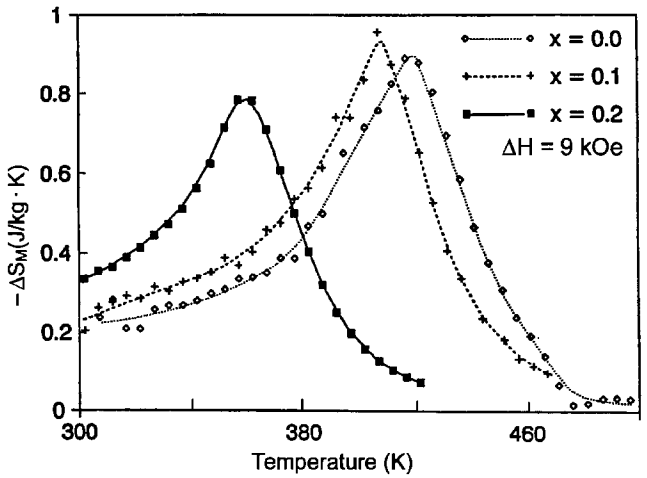


Fig. 8.3. Experimental temperature dependences of the magnetic entropy change $\Delta S_M(T)$ for $\Delta H = 9$ kOe in rapidly solidified $Nd_{0.14}(Fe_{1-x}Al_x)_{0.8}B_{0.06}$ alloys (McMichael et al. 1993a).

obtained results were interpreted in the framework of mean field calculations made for superferromagnets (see fig. 2.4). The experimental $\Delta S_M(T)$ curve for $x = 0.2$ was shown to be in good agreement with that calculated for cluster magnetic moments of about $20\mu_B$, corresponding to about 10 atoms of Fe. It was concluded that the magnetic structure of the alloy can be regarded as consisting of regions with local concentration fluctuations, rather than an assembly of distinct nanometersized magnetic particles dispersed in a nonmagnetic matrix. However, the magnetocaloric properties of these alloys display the characteristics predicted for superferromagnet nanocomposites.

Kokorin et al. (1984) studied the water quenched alloys $Cu_{0.783}Ni_{0.13}Fe_{0.087}$ and $Cu_{0.63}Ni_{0.22}Fe_{0.15}$. It was shown that the alloys were inhomogeneous solid solutions consisting of a nonmagnetic matrix with low concentration of Fe and Ni, and ferromagnetic inclusions rich in Fe and Ni, dispersed in the matrix. Mean dimension of the inclusions were 3–5 nm. Subsequent annealing of the samples at 773–973 K led to size increase of the inclusions. Also their number and the concentration of Ni and Fe in the inclusions increased.

According to magnetic susceptibility measurements $Cu_{0.783}Ni_{0.13}Fe_{0.87}$ displays at some temperature (at about 77 K for the as-quenched state and at about 300 K for the annealed state) a transition to a spin-glass like state due to the interactions between the magnetic clusters (Kokorin and Perekos 1978). At this transition no ΔT maximum was observed. At high temperatures, where the alloys displayed superparamagnetic behavior, a maximum of the MCE was found. This was attributed to the occurrence of ferromagnetic order inside the inclusions according to the second term in eq. (2.103). The maximum MCE value was $\Delta T \approx 10^{-2}$ for $\Delta H = 15$ kOe at $T \approx 750$ K for the annealed state. The temperature of the ΔT maximum corresponds to the Curie temperature of the magnetic particles in the material (628 K for the as-quenched state and 740 K for the annealed state).

The $Cu_{0.63}Ni_{0.25}Fe_{0.15}$ alloy is characterized by stronger interactions between the magnetic inclusions. It displays a superferromagnetic type of order, occurring at a temperature T_1, which is close to the Curie temperature of the inclusions in the material. That is why the observed MCE (with a maximum value about 0.015 K for $\Delta H = 15$ kOe near 700 K) and the magnetic susceptibility anomaly approximately coincide on the temperature scale (Kokorin et al. 1984).

9. Magnetocaloric effect in $Gd_5(Si_xGe_{1-x})_4$ alloys

The $Gd_5(Si_xGe_{1-x})_4$ alloys, some of which exhibit a large magnetocaloric effect, were investigated by Pecharsky and Gschneidner (1997a, 1997b, 1997c, 1997d). Three phase regions were found: the Gd_5Si_4-based solid solution for $0.5 < x \leqslant 1$, the Gd_5Si_4-based solid solution for $0 \leqslant x \leqslant 0.2$ (both these phases have an orthorhombic crystalline structure) and a ternary phase with the monoclinically distorted Gd_5Si_4 structure for $0.24 \leqslant x \leqslant 0.5$. Magnetic and heat capacity measurements allowed to construct a magnetic phase diagram. The alloys with $0.5 < x \leqslant 1$ have simple ferromagnetic structures with the Curie temperatures from 295 to 335 K. The alloys with $0 \leqslant x \leqslant 0.2$ order in two steps: ferrimagnetically at the upper transition temperature and ferromagnetically at the lower one. The upper transition temperature is almost independent of composition ($\sim$ 130 K), while the lower transition temperature decreases proportionally (down to 20 K) with decreasing x. The ternary solid solution phase alloys ($0.24 \leqslant x \leqslant 0.5$) also order magnetically in two steps. Upon cooling they initially order at T_{c1} to form a ferromagnetic structure 1 with a low net magnetic moment and later the second transition to a ferromagnetic structure 2 (at T_{c2}) occurs. The difference between T_{c1} and T_{c2} for $x = 0.24$–0.5 is about 40 K. For all the alloys with $x \leqslant 0.5$ the high-temperature magnetic transition is of the second-order type and the lower one is the first-order transition. Heat capacity measurements showed that the first-order nature of the lower magnetic transition was preserved even in high magnetic fields ($\sim$ 100 kOe).

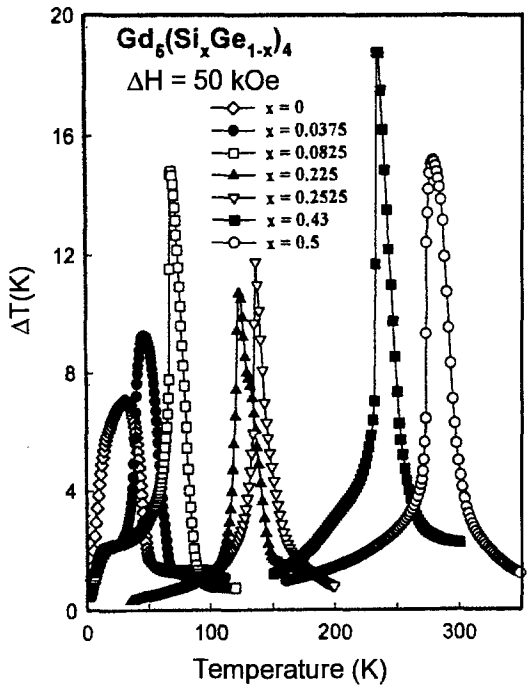


Fig. 9.1. Temperature dependence of the MCE induced by $\Delta H = 50$ kOe for the $Gd_5(Si_xGe_{1-x})_4$ alloys (Pecharsky and Gschneidner 1997b).

The magnetic entropy change $-\Delta S_M$ (for $\Delta H = 50$ kOe) of $Gd_5(Si_{1-x}Ge_{1-x})_4$ alloys with $x = 0$–0.5 was obtained by Pecharsky and Gschneidner (1997a) from the heat capacity and magnetization measurements. It was found that the main part of ΔS_M (about 90%) is associated with the lower temperature first-order magnetic transition which is due to the sharp change in magnetization at the transition temperature. Although the first-order transition is characterized by hysteresis, the magnetic structure changes back to ferromagnetic 1 (or ferrimagnetic) and remnant magnetization becomes zero after removing of the magnetic field. The comparison, made by Pecharsky and Gschneidner (1997a) with other known high-ΔS_M materials (such as $DyAl_2$, $GdAl_2$, $Gd_{0.73}Dy_{0.27}$, Gd) showed that ΔS_M is 2–10 times larger in these $Gd_5(Si_xGe_{1-x})_4$ alloys ($x = 0$–0.5). For the alloys with $x > 0.5$ a substantial decrease of ΔS_M (about three times) was observed. The authors related it with the second-order nature of the paramagnetic–ferromagnetic transition taking place in these alloys.

The MCE of the alloys with $x = 0$–0.5 determined on the basis of heat capacity data is shown in fig. 9.1. The MCE exhibits peaks near the temperature of the first-order transition and reaches the value ~18 K for $x = 0.43$.

Pecharsky and Gschneidner (1997c) investigated the effect of substituting small amounts (up to 0.6 at.%) of Fe, Co, Ni, Cu, Ga, Al and C on ΔS_M and MCE in $Gd_5(Si_2Ge_2)$. It was found that the substitution of Fe, Co, Ni and Cu led to the Curie temperature

increase with simultaneous $|\Delta S_M|$ decrease. The maximum value of $|\Delta S_M|$ found for $Gd_5(Si_{1.985}Ge_{1.985}Ni_{0.83})$ was $|\Delta S_M| \approx 12.4$ J/kg K for $\Delta H = 50$ kOe at $T \approx 296$ K. This was related by the authors with the loss of the first-order nature of the magnetic phase transition, which was confirmed by magnetization measurements. The addition of carbon and aluminum acted similarly as Fe, Co, Ni and Cu, leading to the elimination of the first-order transition and to conditions for the occurrence of a giant MCE. Addition of Ga in an amount of 0.33 at.% preserved the first-order nature of the lower magnetic transition in $Gd_5(Si_2Ge_2)$ and increased its temperature from $T_{c2} \approx 276$ K to about 286 K. The $-\Delta S_M$ value for $Gd_5(Si_{1.985}Ge_{1.985}Ga_{0.03})$ was $\approx$17.6 J/kg K at $T \approx 286$ K and the maximum ΔT value was about 14.8 K at $T \approx 292$ K for $\Delta H = 50$ kOe, which is almost the same as in $Gd_5(Si_2Ge_2)$ alloy. The substitution of 0.67 at.% Ga shifted the magnetic ordering temperature to higher temperatures of about 300 K, but led to the loss of the giant MCE (the maximum value of $|\Delta S_M|$ was about 9.5 J/kg K at $T \approx 300$ K). It should be noted that the heat capacity measurements of $Gd_5(Si_{1.985}Ge_{1.985}Ga_{0.03})$ showed that the lower and upper magnetic transitions merged between 50 and 75 kOe into the single second-order transition at temperatures above 320 K.

10. Magnetocaloric effect in amorphous materials

The magnetic properties and ΔS_M were examined in $R_{0.7}TM_{0.3}$ (R = Gd, Tb, Dy and Er; TM = Fe and Ni) and $Gd_{0.65}Co_{0.35}$ amorphous alloys by Liu et al. (1996a). The melt spanning was used to form ribbons 30–40 μm thick and 20 mm wide. The amorphism of the samples was confirmed by X-ray diffraction analysis. The heat capacity was measured for $Gd_{0.7}Ni_{0.3}$, $Er_{0.7}Fe_{0.3}$ and $Gd_{0.65}Co_{0.35}$ and used to calculate $\Delta S_M(T)$ and $\Delta T(T)$ curves by the method described in section 3.3. For other alloys ΔS_M was obtained on the basis of magnetization data.

Magnetic and the Mössbauer measurements showed, that below the Curie temperature the investigated alloys ordered ferromagnetically for R = Gd and displayed complex non-collinear magnetic structures for anisotropic R ions. The magnetic moment of the 3d ions was small or did not exist, so the magnetothermal properties were determined by the R magnetic subsystem. The coercivity near T_C was negligible even in the alloys with anisotropic R ions, although magnetic saturation was not achieved in these alloys in high magnetic fields. The Curie temperatures of the alloys, obtained from magnetization measurements, are shown in table 10.1.

The $\Delta S_M(T)$ and $\Delta T(T)$ curves for $Gd_{0.7}Ni_{0.3}$, $Er_{0.7}Fe_{0.3}$ and $Gd_{0.65}Co_{0.35}$ alloys are presented in fig. 10.1. One can see that the curves have broad maxima with relatively low heights near T_C. The zero-field heat capacity measurements showed that a λ-type anomaly at T_C is absent in these alloys. Such behavior in these amorphous materials was explained by the authors by the broad character of magnetic phase transition due to fluctuations of the exchange integrals resulting from the structural disorder. Calculations of the temperature dependences of the heat capacity made by the authors for various degrees of exchange integral fluctuations in the framework of MFA, confirmed this proposition.

Further investigations of the magnetothermal properties of amorphous R–TM alloys were made by Liu et al. (1996b) on $R_{0.7}(Fe_xNi_{1-x})_{0.3}$ (R = Gd and Dy) melt-spun ribbons. It was found that the addition of Fe led to an increase of T_C from 130 to 300 K for

TABLE 10.1

The Curie temperature T_C, temperature of the maximum in the $\Delta T(T)$ curves (T^T_{max}); temperature of the maximum in the $\Delta S_M(T)$ curves (T^S_{max}) and maximum values of ΔS_M (at $T = T^S_{max}$) and ΔT (at $T = T^T_{max}$) induced by a magnetic field change ΔH for some amorphous alloys.

Alloy	T_C, K	MCE			$-\Delta S_M$		
		T^T_{max}, K	ΔT, K	ΔH, kOe	T^S_{max}, K	$-\Delta S_M$, J/mol K	ΔH, kOe
$Dy_{0.7}Fe_{0.3}$	108[a]				≈ 108[a]	0.93[a]	10[a]
$Er_{0.7}Fe_{0.3}$	35[a]	≈ 40[a]	3.7[a]	80[a]	≈ 35[a]	12.2[a]	80[a]
		≈ 35[a]	2[a]	40[a]	≈ 35[a]	6.7[a]	40[a]
$Gd_{0.7}Ni_{0.3}$	130[a]	≈ 125[a]	3.3[a]	80[a]	≈ 110[a]	7.1[a]	80[a]
		≈ 125[a]	1.8[a]	40[a]	≈ 110[a]	3.2[a]	40[a]
		130[b]	6[b]	70[b]	130[b]	11[b]	70[b]
$Dy_{0.7}Ni_{0.3}$	35[b]	35[b]	3.5[b]	70[b]	≈ 48[b]	10[b]	70[b]
					≈ 48[b]	6.2[b]	40[b]
$Gd_{0.65}Co_{0.35}$	180[a]	≈ 210[a]	2.8[a]	80[a]	≈ 200[a]	3.6[a]	80[a]
		≈ 210[a]	2.1[a]	40[a]	≈ 200[b]	2.6[a]	40[a]
$Gd_{0.7}Fe_{0.12}Ni_{0.18}$	≈ 185[b]				130[b]	7.6[b]	70[b]
$Fe_{0.9}Zr_{0.1}$	≈ 237[e]				232[c]	10.5*[c]	14[c]
					227[c]	50*[c]	70[c]
$Fe_{0.891}Ni_{0.009}Zr_{0.1}$	≈ 255[c]				247[c]	11*[c]	14[c]
$Fe_{0.882}Ni_{0.018}Zr_{0.1}$	≈ 275[c]				263[c]	11.5*[c]	14[c]
$Fe_{0.873}Ni_{0.027}Zr_{0.1}$	≈ 288[c]				272[c]	12*[c]	14[c]
$Fe_{0.855}Al_{0.045}Zr_{0.1}$	≈ 286[c]				276[c]	12.5*[c]	14[c]
$Fe_{0.855}Si_{0.045}Zr_{0.1}$	≈ 303[c]				292[c]	12.5*[c]	14[c]
$Fe_{0.855}Ga_{0.045}Zr_{0.1}$	≈ 315[c]				300[c]	12.5*[c]	14[c]
$Fe_{0.855}Ge_{0.045}Zr_{0.1}$	≈ 310[c]				298[c]	12.5*[c]	14[c]
$Fe_{0.855}Sn_{0.045}Zr_{0.1}$	≈ 315[c]				307[c]	12.5*[c]	14[c]
$Fe_{0.05}Co_{0.7}Si_{0.15}B_{0.1}$	645[d]	645[d]	0.11[d]	10[d]			

* In kJ/m^3 K

References:

(a) Liu et al. (1996a)
(b) Liu et al. (1996b)
(c) Maeda et al. (1983)
(d) Belova et al. (1984)

$Gd_{0.7}(Fe_xNi_{1-x})_{0.3}$ alloys and from 35 to 110 K for $Dy_{0.7}(Fe_xNi_{1-x})_{0.3}$ alloys for x varied from 0 to 1. Gd-based alloys showed zero hysteresis in the whole temperature range, and in Dy-based alloys the coercive force decreased with increasing temperature and became zero near T_C. In the low temperature range, the $Dy_{0.7}Ni_{0.3}$ alloy displayed a peak in the temperature dependence of the magnetization in weak magnetic field. This is characteristic for spin glass behavior (the peak was located at $\sim$ 20 K for $H = 2$ kOe).

The magnetic entropy change ΔS_M was determined from the magnetization data and the MCE was estimated using ΔS_M and zero field heat capacity data in conjunction with eq. (2.77). Broad maxima were observed in the $\Delta S_M(T)$ curves near T_C for both the Gd- and the Dy-based alloys. The results for $Gd_{0.7}Fe_{0.12}Ni_{0.18}$ and $Gd_{0.7}Ni_{0.3}$ alloys are pre-

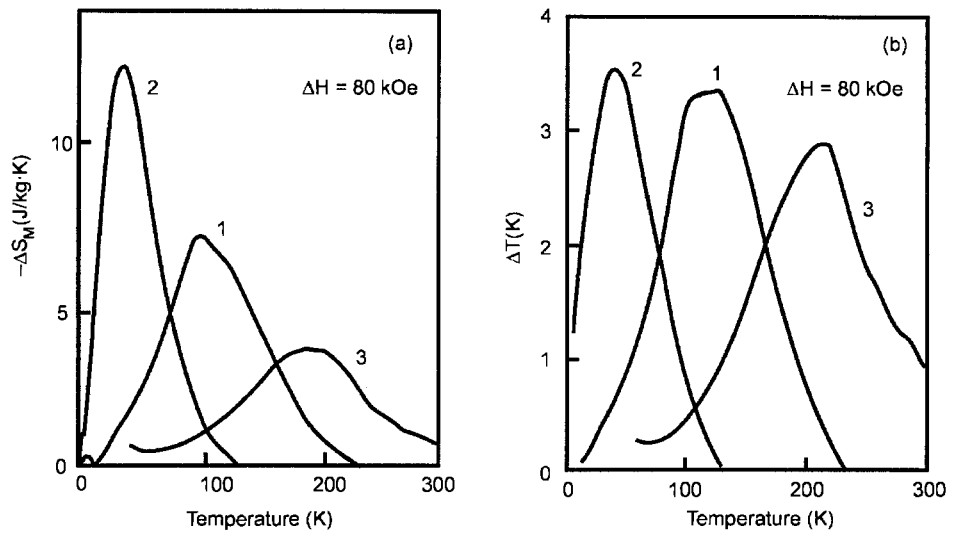


Fig. 10.1. Temperature dependence of $-\Delta S_M$ (a) and MCE (b) induced by $\Delta H = 80$ kOe in $Gd_{0.7}Ni_{0.3}$ (1), $Er_{0.7}Fe_{0.3}$ (2) and $Gd_{0.65}Co_{0.35}$ (3) amorphous alloys (Liu et al. 1996a).

sented in table 10.1. The substitution of Fe for part of the Ni led to broadening of the ΔS_M maximum with a simultaneous reduction of its value: 31% for $Gd_{0.7}(Fe_xNi_{1-x})_{0.3}$ and 12% for $Dy_{0.7}(Fe_xNi_{1-x})_{0.3}$ for a variation of x from 0 to 0.4 and $\Delta H = 70$ kOe. It should be noted, that in $Dy_{0.7}Ni_{0.3}$ below 10 K positive ΔS_M values were induced by the application of a magnetic field. The authors explained this as an artificial effect caused by spin-glass magnetization behavior in this temperature interval. The ΔS_M broadening was related with the additional concentration fluctuations and further broadening of the exchange integral distribution arising from the substitution of Fe for part of the Ni. The MCE in $Gd_{0.7}Ni_{0.3}$ was determined on the basis of ΔS_M calculated from magnetization data. It was larger than that calculated by Liu et al. (1996a) from the heat capacity measurements, see table 10.1.

Maeda et al. (1983) studied the magnetic properties of amorphous $(Fe_{1-x}Ni_x)_{0.9}Zr_{0.1}$ ($x = 0$, 0.01, 0.02, and 0.03) and $(Zr_{0.95}M_{0.05})_{0.9}Zr_{0.1}$ (M = Al, Si, Ga, Ge, and Sn) alloys, prepared by melt-spinning and piston anvil-quenching techniques. Magnetic fields up to 70 kOe were used. The $\Delta S_M(T)$ curves, obtained on the basis of these data, showed a broad maximum near the Curie temperature T_C. The maximum ΔS_M values and T_C are presented in table 10.1. The values of T_C and ΔS_M increased with increasing x. The atomic number of the M element in the $(Fe_{0.95}M_{0.05})Zr_{0.1}$ alloys had a small influence on the maximum ΔS_M value.

Belova et al. (1984) measured directly the MCE of a melt-spun ferromagnetic amorphous $Fe_{0.05}Co_{0.7}Si_{0.15}B_{0.10}$ ribbon. In the $\Delta T(T)$ curve a maximum with the value of $\Delta T = 0.11$ K was observed near $T_C = 645$ K for $\Delta H = 10$ kOe. In the temperature range from 390 to 465 K an additional ΔT anomaly was found, which was related by the authors with the temperature dependence of the local anisotropy constant.

Fuerst et al. (1994) prepared Gd_xAg_{1-x} ($x = 0.50$; 0.70; 0.75; 0.77; 0.80; 1) alloy ribbons by melt spinning in order to form a system containing small magnetic particles. X-ray diffraction and transmission electron microscopy analysis showed that the Gd ribbons consist of hexagonal Gd grains 0.5 μm in size. With decreasing x the amount of an amorphous Gd–Ag component increased. $Gd_{0.755}Ag_{0.225}$ ribbons contained 100 Å sized Gd grains embedded in an amorphous matrix with composition $Gd_{0.5}Ag_{0.5}$. A similar picture was observed for $x = 0.7$. In $Gd_{0.5}Ag_{0.5}$ ribbons crystalline GdAg grains (with a mean diameter of about 100 Å) but no gadolinium grains were found. From magnetization measurements $\Delta S_M(T)$ curves were calculated with the help of eq. (2.71) for $\Delta H = 9$ kOe. The Gd ribbon exhibited a $|\Delta S_M|$ maximum (with a value of about 2.5 J/kg K) near 290 K, which is lower than that for bulk Gd (about 3 J/kg K, as measured by the authors). For $0.7 \leqslant x \leqslant 0.8$ two broad $|\Delta S_M|$ maxima were observed, one near 280 K, and another in the interval 100–120 K. Their heights were 1.25, 0.75 and 0.1 J/kg K for the high-temperature maximum and 0.25, 0.6, 0.9 J/kg K for the low-temperature maximum for $x = 0.8$, 0.775, and 0.7, respectively. The authors related the former maximum with the T_C of the 100 Å sized particles of Gd and the latter maximum with the T_C of the ferromagnetic amorphous $Gd_{0.5}Ag_{0.5}$ alloy.

11. Magnetic refrigeration

In this section the possible utilization of magnetic materials in refrigeration technology will be briefly considered. At present only rare earth magnetic materials were recognized as appropriate for these purposes. According to Barclay (1994), the rare earth materials can be used in gas cycle refrigerators as passive regenerators. In magnetic refrigerators they can be applied as working materials (bodies) in externally regenerated or non-regenerative cycles. They can also serve as active magnetic regenerative refrigerators (AMRR). The main attention here will be paid to heavy rare earth metals and their alloys.

11.1. Passive magnetic regenerators

A regenerator serves to expand a refrigerator temperature span, since the temperature span produced by the adiabatic process itself is insufficient to achieve the desired temperature (especially in the case of magnetic materials). With the help of a regenerator the heat is absorbed from or returned to the working material at the various stages of a regenerative thermodynamical cycle.

In the low-temperature region the heat capacity of conventional regenerators in cryogenic refrigerators essentially decreases, since the lattice heat capacity of a solid is proportional to T^3 and the electronic heat capacity in metals is proportional to T (see eqs (2.64) and (2.66)). In the refrigerators used for cooling of helium gas this leads to a rapid decrease of the refrigerator effectiveness because below ≈10 K the volume heat capacity (the capacity per unit volume) of compressed helium increases. Buschow et al. (1975) proposed rare earth compounds as a possible solution of this problem. The statement of these authors was based on the fact that in rare earth compounds the low magnetic ordering temperatures and the associated heat capacity peaks can be combined with relatively high magnetic contributions to the volume heat capacity. Practical constructions of

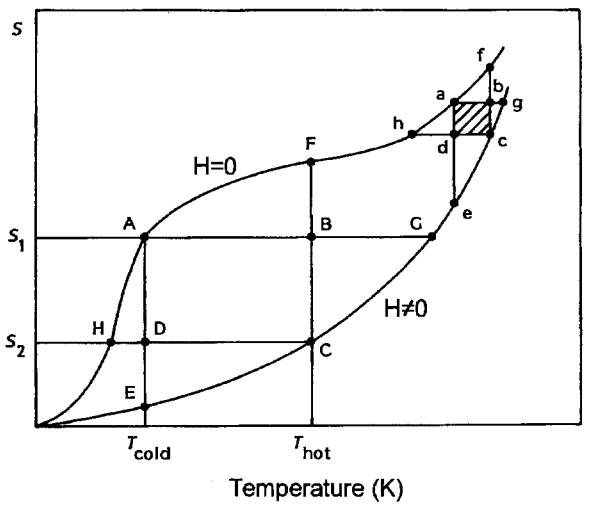


Fig. 11.1. *S–T* diagram of thermodynamic cycles used for magnetic refrigeration. Two isofield curves are shown: for $H = 0$ and $H \neq 0$ (Kuz'min and Tishin 1993a).

the passive magnetic regenerators using Er_3Ni compound appeared after investigations of heat capacity of various R–Ni compounds made in Japan by Hashimoto and coworkers (see section 6.2). Kuriyama et al. (1990) and Sahashi et al. (1990) used Er_3Ni in a two-stage Gifford–McMahon (G–M) refrigerator as the low-temperature stage regenerator. Later $ErNi_{0.9}Co_{0.1}$, $ErNi_{0.8}Co_{0.2}$, $Er_{0.9}Yb_{0.1}Ni$ alloys and their combinations with Er_3Ni were used as regenerators (Kuriyama 1994; Hashimoto et al. 1995; Satoh et al. 1996; Takashi et al. 1997). The use of passive magnetic regenerators allowed it to reach 4.2 K and to increase the cooling power in G–M refrigerators. Long et al. (1995a, 1995b) investigated heat capacity of the $Er_xDy_{1-x}Sb$ and RNiGe (R = Gd, Dy, Er and Y) compounds which can be suitable to regenerators in G–M refrigerators. The suggestion to use Nd (ordering temperature 20 K) as a regenerator was made by Chafe et al. (1997).

11.2. Magnetics refrigerators

In magnetic refrigerators nonregenerative Carnot cycle is used in conjunction with the magnetic type regenerative Brayton, Ericsson, and AMR (active magnetic regenerator) cycles (Barclay 1994).

The Carnot cycle with a temperature span from T_{cold} to T_{hot} is shown by the rectangle ABCD in the total entropy–temperature (*S–T*) diagram in fig. 11.1. The heat Q, corresponding to the load during one cycle of refrigeration, equals to $T_{cold}\Delta S_M$, where $\Delta S_M = S_2 - S_1$. Increasing the temperature span beyond a certain optimal value leads to a significant loss of efficiency as point C in fig. 11.1 tends to point G and the cycle becomes narrow. The temperature span of the Carnot cycle for a given T_{cold} and H is limited by the distance AG in fig. 11.1 (i.e., by the MCE at $T = T_{cold}$ and the field change from 0 to H), when Q becomes zero. At temperatures above 20 K the lattice entropy of

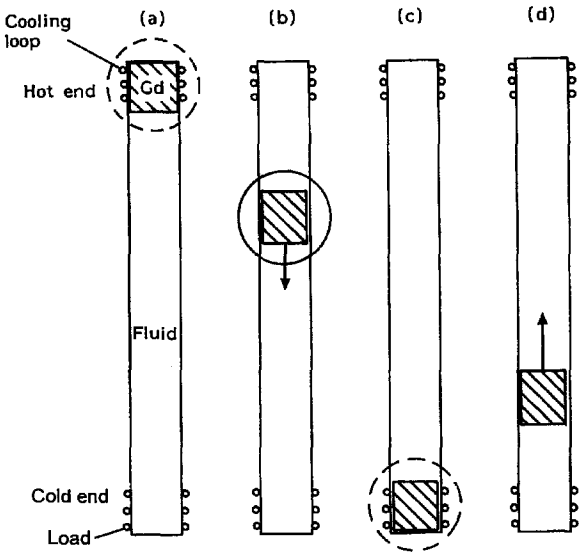


Fig. 11.2. Magnetic refrigerator using the Ericsson cycle. A solid circle indicates that the field is switched on (Brown 1976).

solids strongly increases, which leads to a decrease of the Carnot cycle area (see rectangle abcd in fig. 11.1). That is why applications of the Carnot-type refrigerators are restricted to temperatures region below 20 K.

Magnetic refrigerators operating at higher temperatures have to employ other thermodynamic cycles, including processes at constant magnetic field. Such cycles, as distinct from the Carnot cycle, allow to use the area between the curves $H = 0$ and $H \neq 0$ in the S–T diagram more fully. The rectangles AFCE and AGCH presents the Ericsson and Brayton cycles, respectively. The two cycles differ in the way the field change is accomplished, isothermally in the Ericsson cycle and adiabatically in the Brayton cycle. Realization of isofield processes in both of these cycles requires heat regeneration.

An example of magnetic refrigerator using the regenerative magnetic Ericsson cycle is the device proposed by Brown (1976), see fig. 11.2. The regenerator consists of a vertical column with fluid (0.4 dm^3, 80% water and 20% alcohol). The magnetic working material immersed in the regenerator consists of 1 mol of 1 mm thick Gd plates, separated by screen wire to allow the regeneration fluid to pass through in the vertical direction. The working material is held stationary in a water-cooled electromagnet while the tube containing the fluid oscillates up and down.

The first stage (fig. 11.2(a)) is isothermal magnetization, with the regenerator in its lowest position, so that the working material is at its top. Then, at constant field ($H = 70$ kOe), the regenerator tube is moved upwards (fig. 11.2(b)). The field is then reduced and cooling occurred (fig. 11.2(c)). At the last stage the working material passes back through the regenerator (fig. 11.2(d)). Then the cycle is repeated. If initially the regenerator fluid is at room temperature, after about 50 cycles the temperature at the top can reach +46°C and

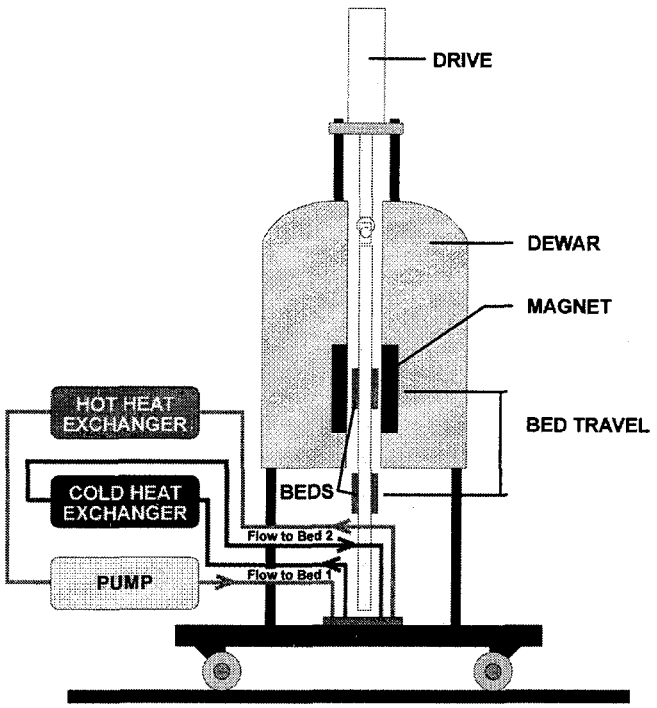


Fig. 11.3. Construction of an AMR refrigerator operating near room temperature (Zimm et al. 1998).

the temperature at the bottom can reach −1°C. The temperature gradient in this device is maintained in the regenerator column.

In the AMR refrigerator the magnetic working material and regenerator are joint in one unit. The idea of such device was proposed by Barclay and Steyert (1982a). In this case the temperature gradient exists inside the working material and such cycle cannot be described by a conventional gas cycle analogue (Hall et al. 1996). The theory of the AMR cycle was developed by Barclay and Steyert (1982a), DeGregoria (1992), Hall et al. (1996) and Johnson and Zimm (1996). Initially it was found that the reversible AMR cycle requires a linear increase of the MCE with increasing temperature in the working material (see Reid et al. 1994). Then it was argued that this requirement is not necessary and only definite boundary conditions should be fulfilled on the cold and hot ends of the regenerator (Hall et al. 1996). The AMR refrigerators were demonstrated to operate in cryogenic temperature regions (Wang et al. 1995) and near the room temperature (Green et al. 1990; Zimm et al. 1998).

Let us consider the AMRR construction created by Zimm et al. (1998), which is shown in fig. 11.3. A magnetic field up to 50 kOe was provided by a helium cooled superconducting solenoid working in the persistent mode. Two beds, each composed of 1.5 kg of Gd spheres, were used as the AMR. The spheres had a diameter between 150 and 300 μm and were made by a plasma-rotating electrode process. The beds were by turns moved in

and out of the dewar bore with a magnetic field. Water was used as a heat transfer fluid. The working cycle of the device started with water cooling by blowing it through the demagnetized bed located inside the magnetic area (bottom position in fig. 11.3). Then the water passed through the cold heat exchanger picking up the thermal load from the cooling object. After this the water was blown through the magnetized bed located in the magnetic field area where it absorbed the heat evolved due to the MCE. Next the water passed through the hot heat exchanger, giving up the heat absorbed from the magnetized bed. The cycle was finished by removing of the magnetized bed from the magnet and replacing it by the demagnetized one. During the movement of the beds the water flow was stopped. One cycle takes a minimum of 6 s (0.17 Hz). Such a device, working at 0.17 Hz with the field of 50 kOe in the room temperature range with the temperature span of 5 K, provided a cooling power of 600 watts (which is about 100 times better than in previous constructions) with a maximum efficiency of 60% that of the Carnot process.

11.3. Working materials for magnetic refrigerators

As was mentioned above, refrigerators without regeneration, working with a Carnot cycle can be used below 20 K. For these purposes, oxides with low magnetic ordering temperature temperatures such as $R_2Ga_5O_{12}$ and $RAlO_3$ were proposed (Barclay and Steyert 1982b; Hashimoto 1986; Kuz'min and Tishin 1991, 1993b). Barclay and Steyert (1982b) showed that among various gadolinium oxide compounds the gadolinium gallium garnet is the most suitable one as a working material for magnetic refrigerators in the temperature range between 2 and 20 K. Kuz'min and Tishin (1991, 1993b) and Kimura et al. (1995) have devoted their investigations to rare earth orthoaluminates with perovskite structure. From the MFA calculations made by Kuz'min and Tishin (1991) it was shown that $DyAlO_3$ and $GdAlO_3$ are the most advantageous compounds among the orthoaluminates. $DyAlO_3$ is more efficient in weak and moderate fields, while $GdAlO_3$ is better within the strong field region. An $ErAlO_3$ single crystal was found to be a promising material for temperatures below 20 K, as shown by magnetization measurements of Kimura et al. (1995). According to theoretical calculations made by Tishin and Bozkova (1997) some success can also be expected from the $Dy_xEr_{1-x}AlO_3$ orthoaluminates.

A possible construction of a magnetic refrigerator working below 20 K and utilizing the strong anisotropy of a $DyAlO_3$ single crystal was proposed by Kuz'min and Tishin (1991), see fig. 11.4. $DyAlO_3$ has $\mu_{\text{eff}} = 6.88\,\mu_B$ along [0 1 0] direction (b-axis) and $\mu_{\text{eff}} = 0.8\,\mu_B$ along [0 0 1] direction (c-axis) (Kolmakova et al. 1990). The working material, having the shape of a cylinder cut along the [1 0 0] direction (a-axis), rotates from the b-axis to the c-axis. The rotation of the single crystal with a volume of 10 cm^3 requires about 75 J. The rotation causes demagnetization and, consequently, cooling due to the MCE. The device allows the use of a short-circuited superconducting solenoid for producing the field, which can significantly reduce its weight. The advantages of this design is its simplicity and the possibility of miniaturization.

Daudin et al. (1982) suggested a solid solution between $DyVO_4$ and $Gd_3Ga_5O_{12}$ as a working material for use in an Ericsson cycle in the low-temperature range. Tomokiyo et al. (1985) proposed $Dy_3Ga_5O_{12}$ to be used in an Ericsson cycle below 20 K.

Initial studies in the room temperature range were carried out by Brown (1976), who used gadolinium as a working material in his magnetic refrigerator (see section 11.2). It

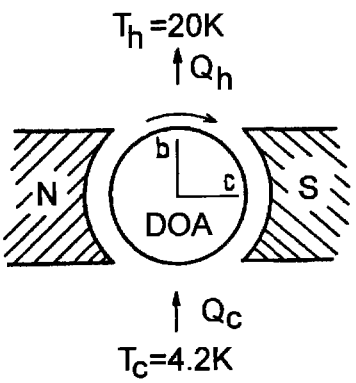


Fig. 11.4. Design of a magnetic refrigerator using $DyAlO_3$ as a working body. The axis of rotation is parallel to the crystal axis a (Kuz'min and Tishin 1991).

should be noted that in almost all of the earlier studies it was proposed to use Gd (T_C = 293 K) as a working material for room temperature refrigerators. However, in the case of Gd only the left part of the $\Delta S_M(T)$ curve is used. It is therefore desirable to search for working materials possessing performances as good as (or better than) Gd but having the Curie temperatures 15–20 K below 293 K. The suggestion to use binary and more complicated rare-earth alloys as a working bodies for the room temperature region was made by Tishin (1990d).

For the application in the ideal Ericsson magnetic regenerator cycle a magnetic working material should have a magnetic entropy change ΔS_M that is constant in the cycle temperature span. As a quantitative criterion of efficiency of the working material, the maximum refrigerant capacity $(\Delta S_M \Delta T_{cyc})_{max}$ with $\Delta T_{cyc} = T_{hot} - T_{cold}$ was used by Wood and Potter (1985). This corresponds to a cycle area in the S–T plane that is maximized for a given material, provided ΔS_M is constant over the whole cycle. In real cycles, however, the latter condition is usually violated. Irreversible processes in the real cycles are not taken into account in the proposed estimation. A reasonable value of the refrigerant capacity that might be realized in a real cycle of magnetic refrigerators is, according to Wood and Potter (1985), about half of the computed value.

The maximum refrigerant capacity as defined above apparently depends on the value of the magnetic field. To optimize refrigerator performance and cost by choosing the proper field value, one may use the specific maximum refrigerant capacity $(\Delta S_M \Delta T_{cyc})_{max}/H$ corresponding to a field change from 0 to H. Figure 11.5 shows the theoretical field dependences of the specific maximum refrigerant capacity for Tb–Gd alloys (Tishin 1990a). ΔS_M curves for the Tb–Gd alloys were calculated on the basis of MFA (Tb–Gd alloys with Gd contents higher than 6 at.% order ferromagnetically). It can be seen that with increasing Tb content, the specific maximum refrigerant capacity increases throughout the range of magnetic fields. A sharp decrease in the refrigerant capacity with the field decrease begins only for $H \leqslant 10$ kOe. Analysis of the data has led to two important conclusions (Tishin 1990a): (1) the use of Tb–Gd alloys as magnetic refrigerators near room temperature is more effective than the use of pure Gd; (2) Gd and its alloys with Tb have a high

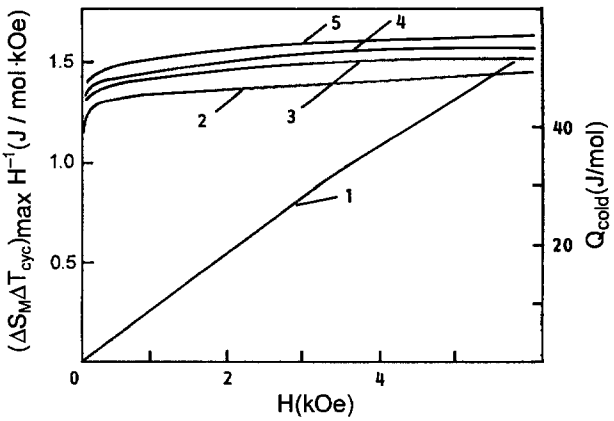


Fig. 11.5. Dependence of the specific maximum refrigerant capacity $(\Delta S_M \Delta T_{cyc})_{max}/H$ on the field for Tb_xGd_{1-x} alloys for: (2) $x = 0$; (3) 0.1; (4) 0.2; (5) 0.3. Curve (1) presents heat Q_{cold} transferred by Gd from load per cycle of refrigeration (Tishin et al. 1990a).

specific refrigerant capacity over a wide range of fields from 10 to 60 kOe, which enables one to construct magnetic refrigerators in which relatively weak fields are used.

Investigations in the room temperature region were continued by Tishin (1990d) with ferromagnetic alloys Gd–Tb, Gd–Dy, Gd–Er and Gd–Ho of high Gd concentration. Their $\Delta S_M(T)$ curves were measured and calculated on the basis of MFA. These binary alloys have the Curie temperatures close to room temperature. It was shown that Gd–Tb and Gd–Dy alloys are the most promising ones as working materials.

Further progress in optimizing magnetic refrigerators can be achieved using complex working bodies consisting of several parts, such as plates of foil, each prepared from a certain alloy. The specific weight of each of the required alloys can be changed by varying either the number of plates made from that alloy or the plate thickness. Roubeau, Steyert and Barclay put forward the idea of using a magnetic refrigerator in which the ordering temperature varies along the refrigeration column. Wood and Potter (1985) proposed the use of a porous ferromagnetic refrigerant with such an arrangement.

Tishin (1990d) showed that for a complex working material made from $Gd_{0.9}Tb_{0.1}$ and $Gd_{0.4}Tb_{0.6}$ in the ratio of 0.78 : 0.22 the value $\Delta S_M = 0.3$ J/mol K for $\Delta H = 10$ kOe can be achieved in the temperature interval from 255 to 295 K. Burkhanov et al. (1991) carried out an experimental study of Gd–Dy alloys and revealed that a complex working material consisting of 59% Gd and 41% $Gd_{0.9}Dy_{0.1}$ is the most promising refrigerant for the room temperature region. The effective Curie point of this complex material is below room temperature and ΔS_M reaches a value of 0.8 J/mol K at 10°C.

Rare earth alloys which can be used as working materials for magnetic refrigeration in the temperature interval from 20 to 250 K have also been extensively studied (Tishin 1990e, 1990f). A comparison of the refrigerant capacity of AFM rare earth metals and alloys with the results of Wood and Potter (1985) showed that the materials where the AFM structure was destroyed by a relatively small magnetic field were often more advantageous

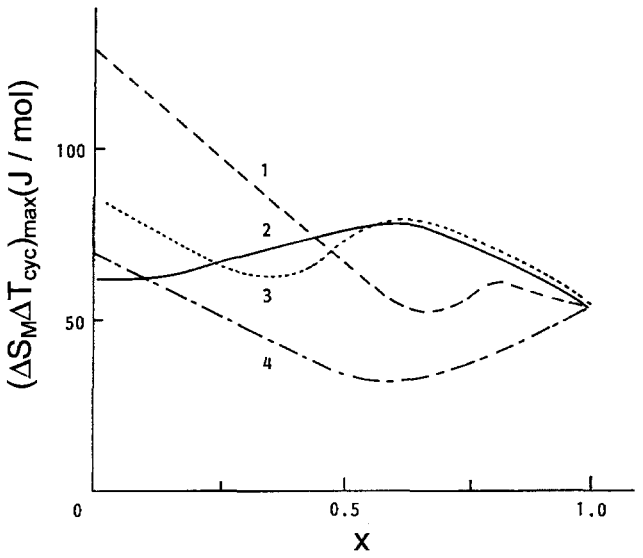


Fig. 11.6. Dependence of maximum refrigerant capacity of: (1) Gd_xHo_{1-x}; (2) Gd_xTb_{1-x}; (3) Gd_xDy_{1-x} and (4) Gd_xEr_{1-x} on Gd content x ($H = 60$ kOe) (Nikitin and Tishin 1988).

than ferromagnets. According to the temperature dependence of ΔS_M (see fig. 7.5) the rare earth metals are efficient within certain narrow temperature intervals. Thus, Ho is the most suitable for cycles from 20 to 135 K, where its refrigerant capacity reaches 129 J/mol for $H = 60$ kOe. Er is good enough for the range from 20 to 85 K, where its refrigerant capacity is 72 J/mol for $H = 60$ kOe. For Dy $(\Delta S_M \Delta T_{cyc})_{max} = 87.3$ J/mol in the temperature interval from 100 to 190 K. The specific maximum refrigeration capacity was considered by Tishin (1990f) who showed that Dy is a promising working material for refrigerators using relatively small ($\approx$ 10 kOe) magnetic fields, whereas Ho is advantageous for $H \geqslant 50$ kOe.

The results discussed above show that the problem of finding magnetic materials capable of working in a cycle with a wide temperature span can most advantageously be solved by using alloys of rare earth metals. With this end in view the Gd–Ho, Gd–Er, Gd–Tb and Gd–Dy alloys were studied by Nikitin and Tishin (1988). Figure 11.6 shows the maximum refrigeration capacity of these alloys for $H = 60$ kOe as a function of Gd content. Whereas Gd–Dy alloys were found to be best for the room temperature range (see above), Gd–Ho are preferable at lower temperatures. Thus, for fixed Ericsson cycle parameters, $T_{hot} = 300$ K, $T_{cold} = 20$ K and $H = 60$ kOe, a maximum refrigeration capacity of 60.5 J/mol is shown by $Gd_{0.8}Ho_{0.2}$ alloy. Therefore this alloy can be recommended as a working material for a magnetic refrigerator operating from room temperature down to 20 K.

Still better results in the range from 20 to 300 K can be achieved using a complex working body. The best results were achieved with Ho, $Tb_{0.5}Dy_{0.5}$ and $Gd_{0.6}Tb_{0.4}$, working in the intervals 20–135, 135–215, and 215–300 K, respectively. In this case $(\Delta S_M \Delta T_{cyc})_{max} = 269$ J/mol (Tishin 1990e, 1990f).

Hashimoto (1986, 1991) proposed for the magnetic Ericsson cycle with a temperature span from 10 to 80 K the use of complex magnetic materials consisting of RAl_2 intermetallic compounds (R = heavy rare earth metal). A layered material with the composition $ErAl_2$, $HoAl_2$ and $Ho_{0.5}Dy_{0.5}Al_2$ in a molar ratio of 0.312 : 0.198 : 0.490 had an almost constant ΔS_M value of about 3 J/mol K in the temperature range from 10 to 45 K for $\Delta H = 50$ kOe. A similar result was obtained for a complex sintered material of the same composition. ΔS_M in the complex sintered material composed of the $(Gd_{0.9}Dy_{0.1})_3Al_2$ and Gd_3Al_2 compounds which can be used near room temperatures was studied by Chang et al. (1998). A promising result was obtained below 35 K by Tomokiyo et al. (1986) using RNi_2 compounds (R = Dy, Ho, Er).

Pecharsky and Gschneidner (1997a, 1997b) proposed the use of the alloys $Gd_5(Si_xGe_{1-x})_4$ (see section 9) with large MCE as working materials for magnetic refrigerators. It was shown that the temperature of the MCE maximum can be easily tuned between 30 and 275 K by changing x. Adding Ga led to an increase of the MCE maximum temperature to about 290 K. A comparison of the refrigerant capacity of some of $Gd_5(Si_xGe_{1-x})_4$ alloys with other magnetic materials used as refrigerants showed that the former possesses 25–70% more capacity than the latter (Gschneidner et al. 1998). $(Gd_{1-x}Er_x)NiAl$ is another promising working material for temperatures below 60 K. It has table-like $\Delta T(T)$ and $\Delta S_M(T)$ curves in a wide interval as discussed in section 6.2 (Korte et al. 1998a).

Reid et al. (1994) considered the working body required for an AMR refrigerator with a temperature span from 100 to 300 K. As it was noted above, initially it was supposed that in an AMR refrigerator the working material should have a MCE increasing linearly with the rising temperature. To achieve this it was proposed to use a layered material consisting of Gd for the range 270–300 K, Tb for the range 220–240 K and Dy for the range of 170–185 K. No appropriate materials were suggested for the other temperature intervals. A possible physical mixing with a magnetic material diluted by aluminum particles to achieve the best $\Delta T(T)$ profile was also discussed.

Thus, we have considered the passive and active magnetic refrigerators and working materials which can be used for their operation. Concluding, it is evident that magnetic cooling is a promising technology for use in the refrigeration industry and will be one of the important markets for the rare earth industry in the near future. At the same time it is necessary to note that magnetic materials with large MCE value could be also utilized for the creation of novel types of heat pumps. These magnetic heat pumps could operate using thermodynamic cycles analogous to those used in magnetic refrigerators and could be, in some cases, more effective than conventional heat pumps. However, the works in this direction is currently practically absent.

Acknowledgements

The author wishes to thank S.Yu. Dan'kov, Prof. K.A. Gschneidner, Jr., Dr. M.D. Kuz'min, Associate Prof. V.K. Pecharsky, Dr. Yu.I. Spichkin and other co-authors of jointly made investigations of magnetocaloric effect for useful collaboration and helpful discussions, which led to a more deep understanding of the physics of magnetocaloric effect and permitted the author of this chapter to make a review of this matter. Author would like to thank Prof. K.A. Gschneidner for the support of my work in this direction for the recent years. The author thanks A.S. Chernyshov and M. Vinogradov for technical assistance.

References

Akhiezer, A.I., V.G. Bar'yakhtar and M.I. Kaganov, 1961, Sov. Phys. Usp. **7**, 567, 661.

Akulov, N.S., and L.W. Kirensky, 1940, J. Phys. **3**, 31.

Alkhafaji, M.T., and N. Ali, 1997, J. Alloys Comp. **250**, 659.

Anderson, E.E., 1964, in: Proc. Int. Conf. on Magnetics Nottingham, p. 660.

Annaorazov, M.P., S.A. Nikitin, A.L. Tyurin, K.A. Asatryan and A.Kh. Dovletov, 1996, J. Appl. Phys. **79**, 1689.

Atoji, M., 1974, Solid State Commun. **14**, 1074.

Azhar, A.A., C.D. Mitescu, W.R. Johanson, C.B. Zimm and J.A. Barclay, 1985, J. Appl. Phys. **57**, 3235.

Baazov, N.G., and A.G. Manjavidze, 1983, Investigation of Rare Earth Magnets by Neutron Methods (Metsniereba, Tbilisi).

Babkin, E.V., and H.O. Urinov, 1987, Sov. Phys. Solid State **29**, 133.

Babkin, E.V., and H.O. Urinov, 1989, Sov. Phys. J. **32**, 899.

Bagguley, D.M.S., and F.A. Howe, 1986, J. Magn. Magn. Mater. **58**, 191.

Bailyn, M., 1994, A Survey of Thermodynamics (AIP Press, New York) ch. 8.

Baranov, N.V., P.E. Markin and Yu.A. Hrulev, 1992, Pisma Zh. Tekh. Fiz. **18**, 20.

Barclay, J.A., 1994, J. Alloys Comp. **207/208**, 355.

Barclay, J.A., and W.A. Steyert, 1982b, Cryogenics **22**, 73.

Barclay, J.A., and W.A. Steyert, 1982a, in: Proc. 2nd Biennial Conf. on Refrigeration for Cryogenic Sensors and Electric Systems, Greenblet, MD, December 7–8.

Belov, K.P., 1961a, Magnetic Transformations (Consultant Bureau, NY).

Belov, K.P., 1961b, Zh. Eksp. Teor. Fiz. **41**, 692.

Belov, K.P., 1968, Helv. Phys. Acta **41**, 679.

Belov, K.P., and S.A. Nikitin, 1965, Phys. Status Solidi **12**, 453.

Belov, K.P., and S.A. Nikitin, 1970a, Izv. AN SSSR, Ser. Fiz. **34**, 957.

Belov, K.P., and S.A. Nikitin, 1970b, Zh. Eksp. Teor. Fiz. **58**, 937.

Belov, K.P., E.V. Talalaeva, L.A. Chernikova and V.I. Ivanovskii, 1968, JETP Lett. **7**, 331.

Belov, K.P., E.V. Talalaeva, L.A. Chernikova and V.I. Ivanovskii, 1969, Pisma JETP **9**, 671.

Belov, K.P., L.A. Chernikova, E.V. Talalaeva, R.Z. Levitin, T.V. Kudriavceva, S. Amadezi and V.I. Ivanovskii, 1970, Zh. Eksp. Teor. Fiz. **58**, 1923.

Belov, K.P., E.V. Talalaeva, L.A. Chernikova, T.V. Kudriavceva and V.I. Ivanovskii, 1972, Zh. Eksp. Teor. Fiz. **62**, 2183.

Belov, K.P., E.V. Talalaeva, L.A. Chernikova, A.S. Andreenko and V.I. Ivanovskii, 1974, Sov. Phys. JETP **39**, 316.

Belov, K.P., E.V. Talalaeva, L.A. Chernikova, T.I. Ivanova, V.I. Ivanovskii and G.V. Kozakov, 1977, Sov. Phys. JETP **45**, 307.

Belova, B.M., and V.L. Stoliarov, 1984, Fiz. Tverd. Tela **26**, 851.

Benford, S.M., 1979, J. Appl. Phys. **50**, 1868.

Benford, S.M., and G.V. Brown, 1981, J. Appl. Phys. **52**, 2110.

Bennett, L.H., R.D. McMichael, L.J. Swartzendruber, R.D. Shull and R.E. Watson, 1992, J. Magn. Magn. Mater. **104–107**, 1094.

Bennett, L.H., R.D. McMichael, R.D. Shull and L.J. Swartzendruber, 1993, J. Appl. Phys. **73**, 6507.

Bertran, E., V. Foriat, A. Herpin and P. Meriel, 1956, C.R. Acad. Sci. Paris **243**, 898.

Blazey, K.W., H. Rohrer and R. Webster, 1971, Phys. Rev. B **4**, 2287.

Bloch, D., and R. Lemaire, 1970, Phys. Rev. B **2**, 2648.

Bloch, D., F. Chaisse, F. Givord and J. Voiron, 1971, J. Physique **32**, 659.

Bloch, D., D.M. Edwards, M. Shimizu and J.Voiron, 1975, J. Phys. F: Metal Phys. **5**, 1217.

Bohigas, X., J. Tejada, E. del Barco, X.X. Zhang and M. Gales, 1998, Appl. Phys. Lett. **73**, 390.

Bohr, J., 1991, Surface Structures, Magnetic Structures and Small Inclusions, as Studied by X-ray Diffraction, Riso-R-585, p. 69.

Bohr, J., D. Gibbs, D.E. Moncton and K.L. D'Amico, 1986, Physica A **140**, 349.

Borovikov, V.S., N.E. Kaner, Yu.I. Litvinenko, A.M. Fishman and V.V. Shapiro, 1981, Zh. Eksp. Teor. Fiz. **53**, 816.

Bozorth, R.M., 1967, J. Appl. Phys. **38**, 1366.

Bredy, P., and P. Seyfert, 1988, Cryogenics **28**, 605.

Brown, G.V., 1976, J. Appl. Phys. **47**, 3673.

Brun, T., S. Sinha, N. Wakabayashi, G. Lander, L. Edwards and F. Spedding, 1970, Phys. Rev. B **1**, 1251.

Burkhanov, G.S., S.Yu. Dan'kov, S.A. Nikitin, A.M. Tishin and O.D. Chistiakov, 1991, Sov. Tech. Phys. Lett. **17**, 353.

Buschow, K.H.J., J.F. Olijhoek and A.R. Miedema, 1975, Cryogenics **15**, 261.

Bykhover, S.E., S.A. Nikitin, Yu.I. Spichkin, A.M. Tishin and Z.S. Umhaeva, 1990, Sov. Phys. JETP **70**, 1114.

Cable, J.W., and E.O. Wollan, 1968, Phys. Rev. **165**, 733.

Cable, J.W., E.O. Wollan, W.C. Koehler and M.K. Wilkinson, 1965, Phys. Rev. **140**, 1896.

Chafe, J.N., G.F. Green and J.B. Hendricks, 1997, Cryocoolers **9**, 653.

Chang, X., J. Yan, S. Zhou and Y. Long, 1998, Rare Metals, **17**, 76.

Chen, D.Y., S. Patel and D.T. Shaw, 1994, J. Magn. Magn. Mater. **134**, 75.

Chen, D.Y., S. Patel and D.T. Shaw, 1995, J. Magn. Magn. Mater. **146**, 175.

Child, H., W. Koehler, E. Wollan and I. Cable, 1965, Phys. Rev. A **138**, 1655.

Clark, A.E., and E. Callen, 1968, J. Appl. Phys. **39**, 5972.

Clark, A.E., and E. Callen, 1969, Phys. Rev. Lett. **23**, 307.

Dan'kov, S.Yu., T.I. Ivanova and A.M. Tishin, 1992, Pisma JTP **18**, 35.

Dan'kov, S.Yu., Yu.I. Spichkin and A.M. Tishin, 1996, J. Magn. Magn. Mater. **152**, 208.

Dan'kov, S.Yu., A.M. Tishin, V.K. Pecharsky and K.A. Gschneidner Jr., 1997, Rev. Sci. Instr. **68**, 2432.

Dan'kov, S.Yu., A.M. Tishin, V.K. Pecharsky and K.A. Gschneidner Jr., 1998, Phys. Rev. B **57**, 3478.

Daudin, B., A.A. Lacaze and B. Salce, 1982, Cryogenics **22**, 439.

Debye, P., 1926, Ann. Physik **81**, 1154.

DeGregoria, A.J., 1992, Adv. Cryog. Eng. **37**, 867.

de Haas, W.J., E.C. Wiersma and H.A. Kramers, 1933, Physica **1**, 1.

Déportes, J., D. Givord and K.R.A. Ziebeck, 1981, J. Appl. Phys. **52**, 2074.

Dreyfus, B., B.B. Goodman, A. Lacaze and G. Trolliet, 1961, C.R. Acad. Sci. **253**, 1764.

Drillat, A., J. Baruchel, S. Bates and S.B. Palmer, 1984, J. Magn. Magn. Mater. **44**, 232.

Druzhinin, V.V., S.P. Zapasski and V.M. Povishev, 1975, Fiz. Tverd. Tela **17**, 23.

Druzhinin, V.V., B.K. Ponomarev and S.P. Zapasski, 1977, Sov. Phys. Solid State **19**, 25.

Druzhinin, V.V., V.M. Melnikov and V.V. Shkarubski, 1979, Sov. Phys. Solid State **21**, 1002.

Edison, T.A., 1887, British patent 16 709.

Eriksson, O., L. Nordström, M.S.S. Brooks and B. Johansson, 1988, Phys. Rev. Lett. **60**, 2523.

Filippi, J., J.C. Lasjaunias, A. Ravex, F. Tcheou and J. Rossat-Mignold, 1977, Solid State Commun. **23**, 613.

Finkel, A.V., 1978, Structure of Rare Earth Metals (Metallurgiya, Moscow) (in Russian).

Finkel, A.V., V.V. Vorobev and M.I. Palatnik, 1971, Phys. Status Solidi (b) **47**, 53K.

Fisher, R.A., G.E. Brodale, E.W. Homung and W.F. Gianque, 1973, J. Chem. Phys. **59**, 4652.

Flippen, R.B., and F.J. Darnell, 1963, J. Appl. Phys. **34**, 1094.

Foldeaki, M., R. Chahine and T.K. Bose, 1995, J. Appl. Phys. **77**, 3528.

Foldeaki, M., A. Giguere, R. Chahine and T.K. Bose, 1997, Adv. Cryog. Eng. **43**.

Fuerst, C.D., J.F. Herbst, R.K. Mishra and R.D. McMichael, 1994, J. Appl. Phys. **76**, 6301.

Fujii, H., Y. Hashimoto and A. Meshima, 1976, J. Phys. Soc. Japan **41**, 1179.

Geller, S., and B. Bala, 1956, Acta Crystallogr. **9**, 1019.

Giauque, W.F., 1927, J. Amer. Chem. Soc. **49**, 1864.

Giauque, W.F., and D.P. MacDougall, 1933, Phys. Rev. **43**, 768.

Gibbs, D., J. Bohr, J.D. Axe, D.E. Moncton and K.L. D'Amico, 1986, Phys. Rev. B **34**, 8182.

Giquere, A., M. Foldeaki, R.A. Dunlop and R. Chahine, 1999, Phys. Rev. B **59**, 431.

Glorieux, G., J. Thoen, G. Bednarz, M.A. White and D.J.W. Geldart, 1995, Phys. Rev. B **52**, 12770.

Green, G., W. Patton and J. Stevens, 1988, Adv. Cryog. Eng. **33**, 777.

Green, G., J. Chafe, J. Stevens and J. Hamphrey, 1990, Adv. Cryog. Eng. **35**, 1165.

Greenough, R.D., and N.F. Hettiarachchi, 1983, J. Magn. Magn. Mater. **31–34**, 178.

Griffel, M., R.E. Skochdopole and F.H. Spedding, 1954, Phys. Rev. **93**, 657.

Griffel, M., R.E. Skochdopole and F.H. Spedding, 1956, J. Chem. Phys. **25**, 75.

Gschneidner Jr., K.A., 1993, J. Alloys Comp. **193**, 1.

Gschneidner Jr., K.A., and V.K. Pecharsky, 1997a, Magnetic Refrigeration, in: Rare Earths: Science, Technology and Applications III, eds R.G. Bautista, C.O. Bounds, T.W. Ellis and B.T. Kilbourn (The Minerals, Metals and Material Society, Pittsburg, PA) p. 209.

Gschneidner Jr., K.A., and V.K. Pecharsky, 1997b, private communication.

Gschneidner Jr., K.A., H. Takeya, J.O. Moorman and V.K. Pecharsky, 1994a, Appl. Phys. Lett. **64**, 253.

Gschneidner Jr., K.A., H. Takeya, J.O. Moorman, V.K. Pecharsky, S.K. Malik and C.B. Zimm, 1994b, Adv. Cryog. Eng. **39**, 1457.

Gschneidner Jr., K.A., V.K. Pecharsky and M.J. Gailloux, 1995, Cryocoolers **8**, 685.

Gschneidner Jr., K.A., V.K. Pecharsky, M.J. Gailloux and H. Takeya, 1996a, Adv. Cryog. Eng. **42**, 465.

Gschneidner Jr., K.A., V.K. Pecharsky and S.K. Malik, 1996b, Adv. Cryog. Eng. **42**, 475.

Gschneidner Jr., K.A., V.K. Pecharsky, A.O. Pecharsky and C.B. Zimm, 1998, in: Proc. Rare Earth Conf., Australia, October 25–30, to be published.

Guo, Z.B., Y.W. Du, J.S. Zhu, H. Huang, W.D. Ding and D. Feng, 1997a, Phys. Rev. Lett. **78**, 1142.

Guo, Z.B., J.R. Zhang, H. Huang, W.P. Ding and Y.W. Du, 1997b, Appl. Phys. Lett. **70**, 904.

Habenshuss, M.C., C. Stassis, S.K. Sinha, H.W. Deckman and F.H. Spedding, 1974, Phys. Rev. B **10**, 1020.

Hall, J.L., C.E. Reid, I.G. Spearing and J.A. Barclay, 1996, Adv. Cryog. Eng. **41**, 1653.

Hashimoto, T., 1986, Adv. Cryog. Eng. Mater. **32**, 261.

Hashimoto, T., 1991, in: Workshop on Magnetic Refrigeration and Convektive Refrigeration Techniques, 18th Int. Congress on Refrigerating, Montreal, August 15.

Hashimoto, T., T. Numazawa, M. Shino and T. Okada, 1981, Cryogenics **21**, 647.

Hashimoto, T., T. Numazawa, Y. Watanabe, A. Sato, H. Nakagome, O. Horigami, S. Takayama and M. Watanabe, 1982, Proc. ICEC 9, Butterworths, Guildford, UK, p. 26.

Hashimoto, T., K. Matsumoto, T. Kurihara, T. Numazawa, A. Tomokiyo, H. Yayama, T. Goto, S. Todo and M. Sahashi, 1986, Adv. Cryog. Eng. **32**, 279.

Hashimoto, T., M. Ogawa, A. Hayashi, M. Makino, R. Li and K. Aoki, 1992, Adv. Cryog. Eng. B **37**, 859.

Hashimoto, T., T. Tsukagoshi, H. Nitta, M. Yabuki, T. Kuriyama and H. Nakagome, 1995, Cryocoolers **8**, 677.

Heikes, R.R., T.R. McGuire and R.J. Happel, 1961, Phys. Rev. **121**, 1341.

Helmolt, R. von, J. Wecker, B. Holzapfel, L. Schultz and K. Samwer, 1993, Phys. Rev. Lett. **71**, 2331.

Herpin, A., and P. Meriel, 1957, J. Phys. Rad. **245**, 2033.

Herz, R., and H. Kronmüller, 1978, Phys. Status Solidi (a) **47**, 451.

Hill, R.W., J. Cosier and D.A. Hukin, 1984, J. Phys. F **14**, 1267.

Hilscher, G., N. Pillmayr, C. Schmitzer and E. Gratz, 1988, Phys. Rev. B **37**, 3480.

Hirschler, W., and W. Rocker, 1966, Z. ang. Phys. **21**, 368.

Hudgins, A.C., and A.S. Pavlovic, 1965, J. Appl. Phys. **36**, 3628.

Imai, H., H. Wada and M. Shiga, 1995, J. Magn. Magn. Mater. **140–144**, 835.

Inoue, T., S.G. Sankar, R.S. Craig, W.E. Wallace and K.A. Gschneidner Jr., 1977, in: Crystal Field Effects in Metals and Alloys, ed. A. Furrer (Plenum, New York) p. 143.

Ivanovskii, V.I., 1959, Fiz. Met. Metalloved. **7**, 29.

Ivanovskii, V.I., and P.P. Denisov, 1966a, Izv. Visch. Uchebn. Zaved., Fizika **3**, 135.

Ivanovskii, V.I., and P.P. Denisov, 1966b, Izv. Visch. Uchebn. Zaved., Fizika **6**, 147.

Jayaraman, A., 1991, High Pressure Studies: Metals, Alloys and Compounds, Handbook on the Physics and Chemestry of Rare Earths, 2nd edn, eds K.A. Gschneidner, Jr. and L. Eyring (Elsevier, Amsterdam) Vol. 1, ch. 9.

Jayasuriya, K.D., S.Y. Campbell and W.A. Stewart, 1985, J. Phys. F **15**, 225.

Jennings, L., R. Stanton and F. Spedding, 1957, J. Chem. Phys. **27**, 909.

Jensen, J., and A.R. Mackintosh, 1991, Rare Earth Magnetism, Structures and Excitations (Clarendon Press, Oxford).

Jin, S.G., L.M. Liu, Y.L. Wang and B.X. Chen, 1991, J. Appl. Phys. **70**, 6275.

Jin, S.G., T.H. Tiefel, M. McCormack, R.A. Fastnacht, S. Ramesh and L.H. Chen, 1994, Science **264**, 413.

Johanson, W.R., G. Pierce, C.B. Zimm and J.A. Barclay, 1988, J. Appl. Phys. **64**, 5892.

Johansson, J., B. Lebech, N. Nielsen, H. Bjerium-Moller and A. Mackintosh, 1970, Phys. Rev. Lett. **25**, 254.

Johnson, J.W., and C.B. Zimm, 1996, J. Appl. Phys. **79**, 2171.

Kamarad, J., Z. Arnold and M.R. Ibarra, 1995, J. Magn. Magn. Mater. **140–144**, Pt.2, 837.

Kamilov, I.K., and Kh.K. Aliev, 1983, Sov. Phys. Usp. **26**, 696.

Kimura, H., H. Maeda and M. Sato, 1988, J. Mater. Sci. **23**, 809.

Kimura, H., T. Numazawa, M. Sato, T. Ikeya and T. Fukuda, 1995, J. Appl. Phys. **77**, 432.

Kimura, H., T. Numazawa, M. Sato, T. Ikeya, T. Fukuda and K. Fujioka, 1997, in: Proc. 16th Cryogenic Engineering Conf./Intern. Cryogenic Materials Conf. (Elsevier Science, Oxford) p. 2069.

Kirchmayr, H.R., and C.A. Poldy, 1978, J. Magn. Magn. Mater. **8**, 1.

Koehler, W., H. Child, E. Wollan and J. Cable, 1963, J. Appl. Phys. **34**, 1335.

Kohlhaas, R., 1967, in: Magnetismus: Structur und Eigenschaften Magnetischer Festkorper VEB Deutscher Verlag für Grundstoffindustrie (Leipzig) p. 134.

Kohlhaas, R., W. Rocker and W. Hirschler, 1966, Z. Naturforsch A **21**, 183.

Kokorin, V.V., and A.E. Perekos, 1978, Pisma JETP **27**, 500.

Kokorin, V.V., A.V. Minkov and I.A. Osipenko, 1984, Fiz. Met. Metalloved. **57**(1), 197.

Kolmakova, N.P., I.B. Krynetskii, M.M. Lukina and A.A. Mukhin, 1990, Phys. Status Solidi (b) **159**, 845.

Korn, J., and R. Kohlhaas, 1969, Z. ang. Phys. **26**, 119.

Korte, B.J., V.K. Pecharsky and K.A. Gschneidner, Jr., 1998a, Advances in Cryogenics Engineering, Vol. 43, Ed. P. Kittel (Plenum, New York) p. 1737.

Korte, B.J., V.K. Pecharsky and K.A. Gschneidner, Jr., 1998b, J. Appl. Phys. **84**, 5677.

Kouvel, J.S., and C.C. Hartelius, 1962, J. Appl. Phys. **33** (Suppl.) 1343.

Kouveliotou, C., et al., 1998, Nature **393**, 235.

Krokoszinski, H.J., C. Santandrea, E. Gmelin and K. Barner, 1982, Phys. Status Solidi (b) **113**, 185.

Krusius, M., G.R. Pickett and M.C. Veuro, 1974, Solid State Commun. **14**, 191.

Kuhrt, C., T. Schittny and K. Barner, 1985, Phys. Status Solidi (a) **91**, 105.

Kuriyama, T., R. Hakamada, H. Nakagome, Y. Tokai, M. Sahashi, R. Li, O. Yoshida, K. Matsumoto and T. Hashimoto, 1990, Adv. Cryog. Eng. **35**, 1261.

Kuriyama, T., M. Takahashi, H. Nakagome, T. Hashimoto, H. Nitta and M. Yabuki, 1994, Adv. Cryog. Eng. **39**, 1335.

Kurti, N., and F. Simon, 1934, Nature **133**, 907.

Kuz'min, M.D., and A.M. Tishin, 1991, J. Phys. D: Appl. Phys. **24**, 2039.

Kuz'min, M.D., and A.M. Tishin, 1992, Cryogenics **32**, 545.

Kuz'min, M.D., and A.M. Tishin, 1993a, Cryogenics **33**, 868.

Kuz'min, M.D., and A.M. Tishin, 1993b, J. Appl. Phys. **73**, 4083.

Lanchester, P.C., K. Robinson, D.P. Baker, I.S. Williams, R. Street and E.S.R. Gopal, 1980, J. Magn. Magn. Mater. **15–18**, 461.

Landau, L.D., and E.M. Lifshitz, 1958, Statistical Physics (Pergamon Press, New York).

Langevin, P., 1905, Ann. Chim. Phys. **5**, 70.

Levitin, R.Z., V.V. Snegirev, A.V. Kopylov, A.S. Lagutin and A. Gerber, 1997, J. Magn. Magn. Mater. **170**, 223.

Li, R., T. Numazawa, T. Hashimoto, A. Tomokiyo, T. Goto and S. Todo, 1986, Adv. Cryog. Eng. **32**, 287.

Li, R., T. Hashimoto, M. Sahashi and Y. Tohkai, 1988, in: Proc. 12th Int. Cryogenic Engineering Conf., Butterworths, Guildorf, p. 423.

Lindley, E.J., B.D. Rainford and D.Mck. Paul, 1988, J. Phys. (Paris) **49**, C8.

Litvinenko, Y.G., V.V. Eremenko and V.I. Myatlik, 1973, Sov. Phys. Solid State **15**, 871.

Liu, X.Y., J.A. Barclay, R.B. Gopal, M. Foldeaki, R. Chahine, T.K. Bose, P.J. Schuler and J.L. LaCombe, 1996a, J. Appl. Phys. **79**, 1630.

Liu, X.Y., J.A. Barclay, M. Foldeaki, R.B. Gopal, R. Chahine and T.K. Bose, 1996b, Adv. Cryog. Eng. **42**, 431.

Long, Y., T. Hashiguchi, T. Hashimoto, M. Okamura and N. Sori, 1995a, J. Appl. Phys. **77**, 2214.

Long, Y., H. Fu, T. Hashimoto, K. Matsumoto, A. Onishi and T. Satoh, 1995b, J. Appl. Phys. **78**, 7410.

Lounasmaa, O.V., and L.J. Sundstrom, 1966, Phys. Rev. **150**, 399.

Lounasmaa, O.V., and L.J. Sundstrom, 1967, Phys. Rev. **158**, 591.

Maeda, H., M. Sato and M. Uehara, 1983, J. Japan Inst. Metals **47**, 688.

Mathon, J., and E.P. Wohlfarth, 1969, J. Phys. C **2**, 1647.

McEwen, K.A., 1991, Magnetic and transport properties of the rare earths, in: Handbook on the Physics and Chemistry of Rare Earths, Vol. 1, eds K.A. Gschneidner Jr. and L. Eyring (North-Holland, Amsterdam) p. 411.

McMichael, R.D., R.D. Shull, L.J. Swartzendruber and L.H. Bennett, 1992, J. Magn. Magn. Mater. **111**, 29.

McMichael, R.D., R.D. Shull, L.H. Bennett, C.D. Fuerst and J.F. Herbst, 1993a, Nanostruct. Mater. **2**, 277.

McMichael, R.D., J.J. Ritter and R.D. Shull, 1993b, J. Appl. Phys. **73**, 6946.

Millhouse, A., and W. Koehler, 1970, Colloq. Int. CNRS **102** (2), 213.

Milton, J.E., and T.A. Scott, 1967, Phys. Rev. **160**, 387.

Morelly, D.T., A.M. Mance, J.V. Mantese and A.L. Micheli, 1996, J. Appl. Phys. **79**, 373.

Mørup, M., M.B. Madsen, J. Franck, J. Villadsen and C.J.W. Koch, 1983, J. Magn. Magn. Mater. **40**, 163.

Moruzzi, V.L., and D.T. Teanly, 1963, Solid State Commun. **1**, 127.

Naiden, E.P., and S.M. Zhilyakov, 1997, Phys. Solid State **39**, 967.

Néel, L., 1954, Compt. Rend. **239**, 8.

Nikitin, S.A., 1978, Izv. Akad. Nauk SSSR, Ser. Fiz. **42**, 1707.

Nikitin, S.A., 1989, Magnetocaloric Properties of Rare Earth Metals and Their Alloys (MGU, Moscow) (in Russian).

Nikitin, S.A., and A.S. Andreenko, 1981, Phys. Met. Metallogr. **52** (1), 55.

Nikitin, S.A., and A.M. Bisliev, 1974, Fiz. Met. Metalloved. **37**, 81.

Nikitin, S.A., and A.M. Tishin, 1987, Sov. Phys. Solid State **29**, 1615.

Nikitin, S.A., and A.M. Tishin, 1988, Sov. Tech. Phys. Lett. **14**, 327.

Nikitin, S.A., and A.M. Tishin, 1989, Phys. Met. Metallogr. **67** (2), 59.

Nikitin, S.A., and A.M. Tishin, 1991, Cryogenics **31**, 166.

Nikitin, S.A., E.V. Talalaeva, L.A. Chernikova and A.S. Andreenko, 1973, Zh. Eksp. Teor. Fiz. **65**, 2058.

Nikitin, S.A., E.V. Talalaeva, L.A. Chernikova and A.S. Andreenko, 1975, Fiz. Met. Metalloved. **40**, 967.

Nikitin, S.A., A.S. Andreenko, G.E. Chuprikov and V.P. Posyado, 1977a, Sov. Phys. JETP **46**, 118.

Nikitin, S.A., A.S. Andreenko, G.E. Chuprikov and V.P. Posyado, 1977b, Zh. Eksp. Teor. Fiz. **73**, 228.

Nikitin, S.A., E.V. Talalaeva, L.A. Chernikova, G.E. Chuprikov, T.I. Ivanova, G.V. Kazakov and G.A. Yarkho, 1978, Sov. Phys. JETP **47**, 105.

Nikitin, S.A., A.S. Andreenko and V.A. Pronin, 1979a, Sov. Phys. Solid State **21**, 1616.

Nikitin, S.A., A.S. Andreenko, A.K. Zvezdin and A.F. Popkov, 1979b, Sov. Phys. JETP **49**, 1090.

Nikitin, S.A., A.S. Andreenko, A.K. Zvezdin and A.F. Popkov, 1980, Bull. Acad. Sci. USSR, Phys. Ser. **44** (7), 14.

Nikitin, S.A., A.S. Andreenko and G.E. Chuprikov, 1981, Vestnik Mosk. Univ. Ser. 3 **22**, 64.

Nikitin, S.A., A.S. Andreenko, A.M. Tishin, A.M. Arkharov and A.A. Zherdev, 1985a, Phys. Met. Metallogr. **60**, 56.

Nikitin, S.A., A.S. Andreenko, A.M. Tishin, A.M. Arkharov and A.A. Zherdev, 1985b, Phys. Met. Metallogr. **59** (2), 104.

Nikitin, S.A., A.M. Tishin, S.E. Bykhover and S.V. Redko, 1988a, Moscow Univ. Phys. Bull. **43**, 96.

Nikitin, S.A., A.M. Tishin and S.V. Redko, 1988b, Phys. Met. Metallogr. **66**, 77.

Nikitin, S.A., Yu.I. Spichkin and A.M. Tishin, 1989a, Fiz. Tverd. Tela **31**, 250.

Nikitin, S.A., A.M. Tishin and S.E. Bykhover, 1989b, Phys. Status Solidi (a) **114**, K99.

Nikitin, S.A., A.M. Tishin and P.I. Leontev, 1989c, Phys. Status Solidi (a) **113**, K117.

Nikitin, S.A., G. Myalikguliev, A.M. Tishin, M.P. Annorazov, K.A. Astaryan and A.L. Tyurin, 1990, Phys. Lett. A **148**, 363.

Nikitin, S.A., A.M. Tishin, M.D. Kuz'min and Yu.I. Spichkin, 1991a, Phys. Lett. A **153**, 155.

Nikitin, S.A., A.M. Tishin and P.I. Leontiev, 1991b, J. Magn. Magn. Mater. **92**, 405.

Nikitin, S.A., A.M. Tishin, S.F. Savchenkova, Yu.I. Spichkin, O.D. Chistyakov, S.V. Redko and Yu.A. Nesterov, 1991c, J. Magn. Magn. Mater. **96**, 26.

Nikitin, S.A., Yu.I. Spichkin, A.M. Tishin and O.D. Chistyakov, 1991d, Vestnik Mosk. Univ. Ser. 3 **32**, 90.

Nikolaev, V.I., I.A. Dubovcev, G.G. Ugodnikov and S.S. Yakimov, 1966, Izv. AN SSSR, Ser. Fiz. **30**, 949.

Noakes, J.E., and A.S. Arrott, 1973, in: Proc. 18th Ann. Conf. on Magnetics and Magnetic Materials, Vol. 2, p. 899.

Nojiri, N., Y. Shimamoto, N. Miura, M. Hase, K. Uchinokura, H. Kojima, I. Tanaka and Y. Shibuya, 1995, Phys. Rev. B **52**, 12749.

Numazawa, T., Y. Watanabe, T. Hashimoto, A. Sato, H. Nakagome, O. Horigami, S. Takayama and M. Watanabe, 1983, Proc. ICEC **9**, 30.

Numazawa, T., H. Kimura, A. Sato, H. Maeda, K. Shimamura and T. Fukuda, 1996, Adv. Cryog. Eng. **42**, 459.

Oesterreicher, H., and F.T. Parker, 1984, J. Appl. Phys. **55**, 4334.

Okazaki, T., R. Miyasawa and S. Takami, 1993, Mater. Trans. JIM **34**, 1.

Pahomov, A.S., and A.A. Gusev, 1964, Fiz. Met. Metalloved. **18**, 156.

Pedersen, M.S., S. Mørup, S. Linderoth, C. Johansson and M. Hanson, 1997, J. Phys. Condens. Matter **9**, 7173.

Pecharsky, V.K., and K.A. Gschneidner, Jr., 1996, Adv. Cryog. Eng. **42**, 423.

Pecharsky, V.K., and K.A. Gschneidner, Jr., 1997a, Appl. Phys. Lett. **70**, 3299.

Pecharsky, V.K., and K.A. Gschneidner, Jr., 1997b, Adv. Cryog. Eng. **43**, 1729.

Pecharsky, V.K., and K.A. Gschneidner, Jr., 1997c, J. Magn. Magn. Mater. **167**, L179.

Pecharsky, V.K., and K.A. Gschneidner, Jr., 1997d, Phys. Rev. Lett. **78**, 4494.

Pecharsky, V.K., K.A. Gschneidner, Jr. and D. Fort, 1993, Phys. Rev. B **47**, 5063.

Pecharsky, V.K., K.A. Gschneidner, Jr. and C.B. Zimm, 1996, Adv. Cryog. Eng. **42**, 451.

Pérez, F., T. Werner, J. Wosnitza, H.v. Löhneysen and H. Tanaka, 1998, Phys. Rev. B **58**, 9316.

Pillmayr, N., C. Schmitzer, E. Gratz, G. Hilscher and V. Sechovsky, 1987, J. Magn. Magn. Mater. **70**, 162.

Ponomarev, B.K., 1972, Zh. Eksp. Teor. Fiz. **63**, 199.

Ponomarev, B.K., 1983, Instr. Exp. Tech. **26**, 659.

Ponomarev, B.K., 1986, J. Magn. Magn. Mater. **61**, 129.

Ponomarev, B.K., and N.I. Moreva, 1975, Zh. Eksp. Teor. Fiz. **69**, 1352.
Potter, H.H., 1934, Proc. Roy. Soc. A **146**, 362.
Prince, E., 1957, Acta Crystallogr. **10**, 787.
Ramirez, A.P., P. Schiffer, S.W. Cheong, C.H. Chen, W. Bao, T.T.M. Palstra, P.L. Gammel, D.J. Bishop and B. Zegarski, 1996, Phys. Rev. Lett. **76**, 3188.
Ramji Rao, R., and J.V.S.S. Narayama Mytry, 1978, J. Low Temp. Phys. **33**, 413.
Ranke, von P.J., V.K. Pecharsky and K.A. Gschneidner, Jr., 1998a, Phys. Rev. B **58**, 12110.
Ranke, von P.J., V.K. Pecharsky and K.A. Gschneidner, Jr., 1998b, Phys. Rev. B **58**, 14436.
Reid, C.E., J.A. Barclay, J.L. Hall and S. Sarangi, 1994, J. Alloys Comp. **207/208**, 366.
Rocker, W., and R. Kohlhaas, 1967, Z. ang. Phys. **23**, 146.
Romanov, A.Y., and V.P. Silin, 1997, Phys. Met. Metallogr. **83**, 111.
Rosing, B.L., 1892, Zh. Russ. Fiz. Khim. Obshestva, Fiz. **24**, 105.
Rosing, B.L., 1896, Zh. Russ. Fiz. Khim. Obshestva, Fiz. **28**, 59.
Sahashi, M., H. Niu, Y. Tohkai, K. Inomata, T. Hashimoto, T. Kuzuhara, A. Tomokiyo and H. Yayama, 1987, IEEE Trans. Magn. **23**, 2853.
Sahashi, M., Y. Tokai, T. Kuriyama, H. Nakagome, R. Li, M. Ogawa and T. Hashimoto, 1990, Adv. Cryog. Eng. **35**, 1175.
Saito, A.T., A. Tutai, M. Sahashi and T. Hashimoto, 1995, Jpn. J. Appl. Phys. **34**, L171.
Sato, K., Y. Isikawa and K. Mori, 1982, J. Appl. Phys. **53**, 8222.
Sato, K., Y. Isikawa, K. Mori and T. Miyazaki, 1990, J. Appl. Phys. **67**, 5300.
Satoh, T., A. Onishi, R. Li, H. Asami and Y. Kanazava, 1996, Adv. Cryog. Eng. **41**, 1631.
Schiffer, P., A.M. Ramirez, D.A. Huse and A.J. Valentino, 1994, Phys. Rev. Lett. **73**, 2500.
Schmitzer, C., G. Hilscher, P. Vajda and J.N. Daou, 1987, J. Phys. F **17**, 865.
Schuchert, H., S. Hufner and R. Faulhaber, 1969, Z. Phys. **222**, 105.
Selte, K., A. Kjekshus, A.F. Andersen and A. Zieba, 1977, J. Phys. Chem. Solids **38**, 719.
Shao, Y., J. Zhang, J.K.L. Lai and C.H. Shek, 1996a, J. Appl. Phys. **80**, 76.
Shao, Y.Z., J.K.L. Lai and C.H. Shek, 1996b, J. Magn. Magn. Mater. **163**, 103.
Shull, R.D., 1993a, AIP Conf. Proc. **273**, 628.
Shull, R.D., 1993b, IEEE Trans. Magn. **29**, 2614.
Shull, R.D., R.D. McMichael and J.J. Ritter, 1993, Nanosruct. Mater. **2**, 205.
Silin, V.P., D. Wagner and V.M. Zverev, 1995, Phys. Lett. A **199**, 395.
Sill, R.L., and E.D. Esau, 1984, J. Appl. Phys. **55**, 1844.
Sivardiere, J., and S. Quezel-Ambrunaz, 1971, Compt. Rend. B **273**, 619.
Skochdopole, R.E., M. Griffel and F.H. Spedding, 1955, J. Chem. Phys. **23**, 2258.
Smaili, A., and R. Chahine, 1996, Adv. Cryog. Eng. **42**, 445.
Smaili, A., and R. Chahine, 1997, J. Appl. Phys. **81**, 824.
Smart, J.S., 1966, Effective Field Theories of Magnetism (W.B. Saunders, Philadelphia, London).
Stauffer, D., 1970, Phys. Status Solidi **2**, K41.
Steinitz, M.O., M. Kahrizi, D.A. Tindall, H.U. Astrom and G. Benediktsson, 1987, Phys. Rev. B **35**, 8747.
Stewart, A.M., and S.J. Collocott, 1989, J. Phys.: Cond. Matter **1**, 677.
Sucksmith, W., C.A. Clark, D.J. Oliver and J.E. Thompson, 1953, Rev. Mod. Phys. **25**, 34.
Sychev, V.V., 1986, Complex Thermodynamic Systems (Energoatomizdat, Moscow) (in Russian).
Takashi, I., N. Masashi, N. Kouki and Y. Hideto, 1997, Cryocoolers **9**, 617.
Talalaeva, E.V., L.A. Chernikova and V.I. Ivanovskii, 1969, Vestnik MGU, Ser. Fiz. Astron. **6**, 113.
Tanoue, S., K.A. Gschneidner, Jr. and R.W. McCallum, 1992, J. Magn. Magn. Mater. **103**, 129.
Taylor, K.N.R., and M.I. Darby, 1972, Physics of Rare Earth Solids (Chapman and Hall, London).
Tesla, N., 1890, US patent 428 057.
Tiablikov, S.V., 1956, Fiz. Met. Metalloved. **2**, 193.
Tindal, D.A., M.O. Steinitz and T.M. Holden, 1993, J. Appl. Phys. **73**, 6543.
Tishin, A.M., 1988, Magnetocaloric Effect in Heavy Rare Earth Metals and their Alloys, PhD thesis (Moscow State University).
Tishin, A.M., 1990a, Cryogenics **30**, 127.
Tishin, A.M., 1990b, Sov. Tech. Phys. Lett. **16**, 47.
Tishin, A.M., 1990c, J. Techn. Phys. **60**, 205.
Tishin, A.M., 1990d, Cryogenics **30**, 720.
Tishin, A.M., 1990e, Moscow Univ. Phys. Bull. **45** (2), 98.
Tishin, A.M., 1990f, J. Appl. Phys. **68**, 6480.
Tishin, A.M., 1990g, in: Proc. Int. Cryocooling Conf., Plymouth, MA, October 25–26, p. 247.
Tishin, A.M., 1994, Magnetic, Magnetothermal and Magnetoelastic Properties of Heavy Rare Earth Metals and Their Alloys in the Region of Magnetic Phase Transitions, DSc thesis (Moscow State University, Russia).
Tishin, A.M., 1997, J. Alloys Comp. **250**, 635.
Tishin, A.M., 1998a, J. Magn. Magn. Mater. **184**, 62.

Tishin, A.M., 1998b, to be published.
Tishin, A.M., 1998c, Adv. Cryog. Eng. **43**, 1549.
Tishin, A.M., and L.P. Bozkova, 1997, J. Appl. Phys. **81**, 1000.
Tishin, A.M., and M.D. Kuz'min, 1991, unpublished.
Tishin, A.M., and O.P. Martynenko, 1995, Physics of Rare Earth Metals in the Vicinity of Magnetic Phase Transitions (Nauka, Moscow) (in Russian).
Tishin, A.M., K.A. Gschneidner Jr. and V.K. Pecharsky, 1999, Phys. Rev. B **59**, 503.
Tokai, Y., A. Takahashi, M. Sahashi and T. Hashimoto, 1992a, in: Proc. 7th Int. Conf., Santa Fe, NM, November 17–19, p. 484.
Tokai, Y., A. Takahashi, M. Sahashi, T. Hashimoto, H. Yayama and A. Tomokiyo, 1992b, Jpn. J. Appl. Phys. **31**, 3332.
Tomokiyo, A., H. Yayama, T. Hashimoto, T. Aomine, M. Nishida and S. Sakaguchi, 1985, Cryogenics **25**, 271.
Tomokiyo, A., H. Yayama, H. Wakabayashi, T. Kuzuhara, T. Hashimoto, M. Sahashi and K. Inomata, 1986, Adv. Cryog. Eng. **32**, 295.
Voiron, J., and B. Bloch, 1971, J. Physique **32**, 949.
Voiron, J., A. Breton and I. Chaussy, 1974, Phys. Lett. A **50**, 17.
Vonsovskii, S.V., 1974, Magnetism (Israel Program Sci. Translations, Jerusalem).
Wada, H., M. Nishigori and M. Shiga, 1993, J. Phys. Soc. Japan **62**, 1337.
Wagner, D., A.Y. Romanov and V.P. Silin, 1996, Zh. Eksp. Teor. Fiz. **106**, 1753.
Wang, A.A., J.W. Johanson, R.W. Niemi, A.A. Sternberg and C.B. Zimm, 1995, in: Proc. 8th Int. Cryocooler Conf., p. 665.
Warburg, E., 1881, Ann. Phys. **13**, 141.
Weiss, P., 1907, J. Phys. Rad. **6**, 661.
Weiss, P., and R. Forrer, 1924, Compt. Rend. **178**, 1347.
Weiss, P., and R. Forrer, 1926, Ann. Phys. **5**, 153.
Weiss, P., and A. Piccard, 1918, Compt. Rend. **166**, 352.
White, G.K., 1989, J. Phys.: Cond. Matter **1**, 6987.
Wood, M.E., and W.H. Potter, 1985, Cryogenics **25**, 667.
Yayama, H., A. Tomokiyo, T. Hashimoto, T. Kuzuhara, R. Li, M. Sahashi and K. Inomata, 1987, IEEE Trans. Magn. **23**, 2850.
Yazawa, T., T. Numazawa and T. Hashimoto, 1986, in: Proc 11th Int. Cryogenic Engineering Conf., Berlin, Germany, p. 26.
Zaharov, A.I., A.M. Kadomceva, R.Z. Levitin and E.G. Poniatovski, 1964, Zh. Eksp. Teor. Fiz. **46**, 2003.
Zhang, X.X., J. Tejada, Y. Xin, G.F. Sun, K.W. Wong and X. Bohigas, 1996, Appl. Phys. Lett. **69**, 3596.
Zhilyakov, S.M., E.P. Naiden and G.I. Riabtsev, 1993, Izv. VUZov, Fizika **10**, 63.
Zhilyakov, S.M., G.I. Riabtsev and E.P. Naiden, 1994, Fiz. Tverd. Tela **36**, 2402.
Zhong, W., W. Chen, W. Ding, N. Zing, Y. Du and Q. Yan, 1998, Solid State Commun. **106**, 55.
Zimm, C.B., 1994, Adv. Cryog. Eng. **40**, 647.
Zimm, C.B., P.L. Kral, J.A. Barclay, G.F. Green and W.G. Patton, 1988, in: Proc. 5th Int. Cryocooler Conf., Monterey, CA, p. 49.
Zimm, C.B., J.A. Barclay, H.H. Harkness, G.F. Green and W.G. Patton, 1989, Cryogenics **29**, 937.
Zimm, C.B., P.M. Ratzmann, J.A. Barclay, G.F. Green and J.N. Chafe, 1990, Adv. Cryog. Eng. **36**, 763.
Zimm, C.B., E.M. Ludeman, M.C. Severson and T.A. Henning, 1992, Adv. Cryog. Eng. B **37**, 883.
Zimm, C., A. Jastrab, A. Sternberg, V. Pecharsky, K. Gschneidner, Jr., M. Osborn and I. Anderson, 1998, Adv. Cryog. Eng. **43**, 1759.
Znamenskii, B.V., and I.G. Fakidov, 1962, Phys. Met. Metallogr. **13**, 146.

Subject Index

ab initio models, 25
adiabatic process, 402
– for magnetic systems, 423
adiabatic–isobaric process, 402
adiabatic–isochoric process, 403
AMR cycle, 512
angular dependence, 57
– of GMR, 7
anisotropy, 205
anisotropy determined from NMR, 157
anisotropy in Co/Cu superlattices, 156
antiferromagnetic spiral structure, 426
axial anisotropy
– in magnetically ordered materials, 414

B_c (critical field at metamagnetic transition)
– concentration dependence, 296, 297, 306, 314, 315, 319, 321
– derivation, expressions, 269, 277
– in Laves phase compounds, 285, 292, 313, 317, 319, 358, 370
– temperature dependence, 288, 293, 307, 334
– volume or pressure dependence, 294, 299, 302
B_{t1} (critical field at collinear–noncollinear transition)
– derivation, expressions, 363, 365
basal-plane anisotropy
– in rare earth metals, 476
Boltzmann equation, 414
Brayton cycle, 511
Brillouin function
– in magnetic oxides, 449
– in magnetically ordered materials, 407
bulk elastic modulus, 403
bulk scattering spin asymmetry, 32, 36, 45
bulk thermal expansion coefficient, 402, 425

Carnot cycle, 511
channeling, 48
CIP geometry, 34, 49
Clausius–Clapeyron equation
– for magnetic systems, 415, 444, 484
cobalt films, 130
compensation thickness, 44, 47
CPP geometry, 11, 35, 51
critical field
– at collinear–noncollinear transition (see also B_{t1}), 363, 365
– at metamagnetic transition (see also B_c), 264, 269, 277, 285, 293, 312, 332, 345, 378, 383, 385, 386
critical pressure
– at the metamagnetic transition (see also B_c), 294
– at the onset of ferromagnetism, 304, 387
– concentration dependence, 304
– in Laves phase compounds, 330
crystal field coefficients, 414
^{63}Cu and ^{65}Cu NMR in thin films, 223
Curie constant, 407, 409, 411
Curie law
– of magnetic materials, 407
Curie temperature, 408
– concentration dependence, 344, 382
– derivation, expressions, 273
– in 3d metals, 437
– in intermetallic compounds, 466
– in Laves phase compounds, 340, 348, 356, 371
– in rare earth metals, 490
– in selected RT compounds, 374, 382
– resistivity change, 337
Curie–Weiss law, 408

3d magnetic materials, 409
de Gennes factor, 498
Debye interpolation formula, 410
Debye temperature, 410, 425
– in rare earth metals, 491

effective Co moment
– in Laves phase compounds, 281, 370
– volume or pressure dependence, 281
effective magnetic field, 107
effective magnetic moment, 408
EFG at Co nucleus, 128

EFG of hexagonal Co, 129
elastocaloric effects
– for magnetic systems, 423
electric field gradient (EFG), 120, 133
electrical resistivity
– concentration dependence, 350
– derivation, expressions, 280
– in Laves phase compounds, 287, 323, 337, 350, 372
– temperature dependence, 309, 323, 337, 348, 353, 354, 358, 361
electron–phonon interaction, 409
electronic specific heat constant
– derivation, expressions, 278
– magnetization or field dependence, 286
electronic thermal expansion coefficient
– derivation, expressions, 344
enhancement effect of the NMR, 123
enhancement factor, 206
entropy
– field induced, 409, 435
– in 3d metals, 409
– in intermetallic compounds, 473
– in magnetic materials, 402, 412, 420
– in magnetic systems, 409–412
– in magnetically ordered materials, 409
– in perovskites, 455
– in rare earth metals, 494
entropy change
– during adiabatic demagnetization, 403
– field induced, 412, 415
equation of state
– definition, description, 270, 295
– derivation, expressions, 270, 275, 277, 295
Ericsson cycle, 511, 516
exchange interaction
– in magnetic oxides, 450
– in magnetically ordered materials, 407

"fan" structure
– in rare earth metals, 479
ferromagnetic conical phase, 426
ferromagnetic resonance (FMR), 133
Foucault currents, 406
free energy
– definition, description, 267
– derivation, expressions, 268, 270, 272–275
– magnetization or field dependence, 269, 307
– of magnetic materials, 400, 404, 406
– of thin magnetic films, 446
– temperature dependence, 278
– volume or pressure dependence, 271
free induction decay (FID), 118, 119

gadolinium gallium garnet, 513
gadolinium gallium iron garnet, 450, 502
giant magnetostriction
– in rare earth metals, 499
Gibbs energy
– in 3d metals, 441
– in rare earth metals, 498
Gibbs free energy
– in rare earth metals, 476
– of magnetic materials, 401, 404
Gifford–McMahon (G–M) refrigerator, 510
granular systems, 17
grooved substrate, 15

Hamiltonian
– in magnetically ordered materials, 407, 414
heat capacity
– of amorphous materials, 506
– of 3d intermetallics, 410
– of intermetallic compounds, 460, 463, 465, 470, 473, 474
– of magnetic materials, 402, 410, 412, 416, 417, 435
– of magnetic systems, 410
– of magnetic oxides, 452
– of rare earth metals, 478, 483, 487
heat capacity anomaly
– in intermetallic compounds, 464
– in magnetic materials, 416
HFF (hyperfine field)
– of bulk material, 105, 109
– of Co alloys, 110
– of thin films, 113, 174
hybridization
– concentration dependence, 313
– in Laves phase compounds, 281, 312, 315, 318
– in selected RT compounds, 382, 386
– volume or pressure dependence, 284, 304

influence of interface roughness, 42
interface resistance, 29, 32
interface scattering spin asymmetry, 32, 36
interface spin asymmetry, 46
internal energy
– of magnetic materials, 400
intrinsic potential, 20, 48, 49
inverse GMR, 45, 47

Jahn–Teller effect
– in magnetic oxides, 459
Joule–Thomson effect, 423

Knight shift, 122, 224
Knight shift of hcp Co, 127
Kubo formalism, 24

Landau coefficients, 268
– concentration dependence, 295
– derivation, expressions, 274, 276, 306
Landau theory, 399, 416
Landau theory of second order phase transitions, 404, 422
Langevin function, 409
lattice expansion, 154
lattice sum
– of magnetic materials, 406, 411
Laves phase compounds, 281, 285, 373, 388
– definition, description, 264
lithography and microfabrication techniques, 14
longitudinal relaxation, 117

Mössbauer spectroscopy
– in nanocomposite systems, 502
magnetic anisotropy
– in Co–Cr thin films, 188
– in magnetic oxides, 459
magnetic cluster, 418, 420
magnetic entropy
– in intermetallic compounds, 465
– in magnetic oxides, 450
– in rare earth metals, 486
magnetic entropy change
– in intermetallic compounds, 460
magnetic field at a nucleus, 105
magnetic heat pumps, 517
magnetic moment
– in magnetically ordered materials, 407
magnetic recording media, 169
magnetic refrigeration, 455, 509
magnetic refrigerators, 399, 427, 510, 513, 515
– for magnetic systems, 513
magnetic regenerators, 509, 510
magnetic susceptibility
– in nanocomposite systems, 504
magnetization
– in intermetallic compounds, 463
– in magnetically ordered materials, 405, 434
– in thin magnetic films, 446
– of magnetic materials, 404
magneto-elastocaloric effect, 427
magnetocaloric effect (MCE), 405, 417, 423, 429, 430, 434, 435, 448
– during adiabatic demagnetization, 427
– in amorphous materials, 506, 508
– in 3d metals, 407, 437, 440
– in $Gd_5(Si_xGe_{1-x})_4$, 504
– in intermetallic compounds, 466, 469
– in magnetic materials, 398, 402
– in magnetic oxides, 449, 450, 456, 458
– in magnetically ordered materials, 405, 426, 434
– in nanocomposite systems, 501
– in rare earth metals, 477
– in thin magnetic films, 445
magnetocrystalline anisotropy, 405
– in 3d metals, 441
– in magnetically ordered materials, 414
magnetoelastic interaction
– in magnetically ordered materials, 405
magnetoresistance, 100, 154, 167
– at the metamagnetic transition (see also B_c), 337
– concentration dependence, 309, 340, 355
– derivation, expressions, 280, 356
– in Laves phase compounds, 264, 318, 352, 359, 363
– in perovskites, 455
– magnetization or field dependence, 290, 352, 356, 359
– temperature dependence, 280, 362
magnetostriction
– at the metamagnetic transition (see also B_c), 297, 337
– concentration dependence, 297
– magnetization or field dependence, 299, 319
magnetovolume coupling constant
– in Laves phase compounds, 298
magnetovolume effect
– in Laves phase compounds, 270, 360
Maxwell equations
– for magnetic systems, 401
Maxwell formula
– for magnetic systems, 429
Maxwell relation
– for magnetic systems, 411
MCE in hexagonal ferrites, 457
MCE in nanocomposite ribbons, 501
mean field approximation, 399, 407
mean free path, 49
mesoscopic models, 27
metamagnetic transition
– concentration dependence, 364
– definition, description, 263
– derivation, expressions, 277
– in Laves phase compounds, 317, 319, 321, 366
– in selected RT compounds, 374, 376
– resistivity change, 310
– volume or pressure dependence, 297
MFA
– in rare earth metals, 491
MMT
– derivation, expressions, 268, 270, 271, 277, 295, 306
– in Laves phase compounds, 285, 291, 292, 297, 304, 313–315, 317, 318, 334, 352, 360, 366
– in selected RT compounds, 375–377, 382, 383, 386

– resistivity change, 311, 337, 352, 356, 360
– specific-heat change, 307, 309
– volume or pressure dependence, 271, 301, 319, 320, 335
model of Valet and Fert, 31
molecular field
– concentration dependence, 317, 320, 340, 377
– definition, description, 363
– derivation, expressions, 267, 363
– in Laves phase compounds, 316, 340, 343, 358, 365, 366, 370
– in magnetically ordered materials, 408
molecular field coefficients, 408
– definition, description, 272
– derivation, expressions, 274, 363
– in Laves phase compounds, 364
molecular-field coefficients
molecular-field parameters
– in selected RT compounds, 369
– volume or pressure dependence, 383
Monte Carlo method, 420, 421
– for magnetic systems, 414

Néel model
– in magnetic oxides, 448
nanocomposite magnetic materials, 418
nanowires, 16, 37, 51, 56
neutron diffraction, 476
NMR (nuclear magnetic resonance), 114
– conventional, 114
– enhancement, 101, 188, 205
– enhancement effect, 157
– enhancement factors, 222
– of alloy thin films, 210, 215, 220
– of bcc Co, 137
– of Co-based thin films, 193
– of Co/Au multilayers, 193
– of Co/Cr multilayers, 191
– of Co–Cr thin films, 177
– of Co/Cu multilayers, 161, 166
– of Co/Cu superlattices, 141
– of Co/Fe multilayers, 208
– of Co/Ir multilayers, 221
– of Co/Mn multilayer, 210
– of Co/Ni multilayers, 215
– of Co/Pd multilayers, 200
– of Co/Pt multilayers, 199, 203
– of Co/Ru multilayers, 220
– of Co/Sb multilayers, 221
– of Co/Si multilayers, 223
– of Co/Sn multilayers, 222
– of Co/Zr multilayers, 222
– of ^{63}Cu and ^{65}Cu thin films, 223
– of Cu/Nb multilayers, 246
– of Fe/Cu multilayer films, 224
– of Fe/Mn multilayers, 235
– of Fe/V multilayers, 230
– of ferromagnetic materials, 123
– of Heusler alloy (Cu_2MnAl) films, 238
– of MnSb-based multilayers, 240
– of Ni/Cu multilayers, 224
– of NiFe films, 232
– of superconducting multilayers, 246
– of thin film rare earth elements, 250
– relaxation, 130
nonequilibrium thermodynamic potential, 404
nuclear relaxation, 122

orthoaluminates, 513

paramagnetic Curie temperature
– in Laves phase compounds, 281
paramagnetic susceptibility
– magnetization or field dependence, 276
– temperature dependence, 268, 276
paraprocess, 405
– in magnetic oxides, 450
partition function, 415
– of magnetic materials, 406
perovskites, 455
phase transitions
– field induced, 427
– in 3d intermetallics, 444
– in magnetic materials, 404, 415
– in magnetic oxides, 459
– in magnetically ordered materials, 426, 429
– in rare earth metals, 479
– in thin magnetic films, 447
pinning layer, 8

rare earth iron garnet, 449
rare earth magnetic materials, 409
recording media, 188
refrigerant capacity, 409, 514
regenerators, 510
resistor series model, 32

s–d model
– in intermetallic compounds, 473
scaling length, 49, 51
scattering potentials, 21, 48
Schottky anomaly
– in intermetallic compounds, 463
SDL (spin diffusion length), 30, 32, 37, 51, 52, 54
semi-classical models, 23
Slater–Pauling plot, 46
specific heat

– derivation, expressions, 278
– in Laves phase compounds, 264, 285
– magnetization or field dependence, 285
spin accumulation, 29–31
spin diffusion length (SDL), 29, 30
spin echoes, 119
spin electronics, 4
spin fluctuation scattering
– concentration dependence, 348, 359
– in Laves phase compounds, 287, 289
– temperature dependence, 280
spin fluctuation temperature
– derivation, expressions, 275
– in Laves phase compounds, 289, 337
spin fluctuations
– at metamagnetic transition (see also B_c), 285, 307
– concentration dependence, 340, 356
– definition, description, 275
– derivation, expressions, 275, 276
– in selected RT compounds, 378
– resistivity change, 280, 311, 337, 356
– specific-heat change, 278, 285, 307
– temperature dependence, 281, 303
– volume or pressure dependence, 344
spin mixing, 54
spin valve, 7, 11
spin-dependent scattering, 28
spin-glass state
– in nanocomposite systems, 504
spin-lattice relaxation, 54
strain, 100, 106, 141, 142, 153, 155, 198, 215
superparamagnet, 418, 421
susceptibility
– concentration dependence, 291, 295, 312, 313, 356
– derivation, expressions, 277, 279, 283, 337
– in Laves phase compounds, 279, 318, 370
– in selected RT compounds, 382, 386
– magnetization or field dependence, 270, 284, 365
– temperature dependence, 270, 277, 281–284, 293, 295, 303, 323, 337, 344, 382
– volume or pressure dependence, 291, 302, 303, 330, 332
symmetric spin valve, 11

temperature dependence, 55
thermal conductivity
– in magnetic oxides, 452
thermal expansion
– at the metamagnetic transition (see also B_c), 336
– at the onset of ferromagnetism, 325, 337
– concentration dependence, 345, 348, 362
– derivation, expressions, 343
– in Laves phase compounds, 358
thermal expansion coefficient, 426
thermodynamic coefficients, 404
thermodynamic potential
– for magnetic systems, 422
– in magnetically ordered materials, 416
thin films, 446
transverse relaxation time, 119
two-current model, 17

^{51}V NMR studies of multilayers, 230
volume magnetostriction
– at the onset of ferromagnetism, 332
– derivation, expressions, 299
– in Laves phase compounds, 298
– magnetization or field dependence, 319

Young's modulus
– in perovskites, 455

Materials Index

Ag/Co, 36
Ag/Fe, 27
Al_2O_3, 459
Au/Fe, 27

$BaCa_{2-x}Zn_xFe_{16}O_{27}$, 457
$BaCo_{1.65}Fe^{2+}_{0.35}Fe^{3+}_{16}O_{27}$, 459
$BaFe_{12-x}Co_xTi_xO_{19}$, 457

$CeCo_2$, 473
$CeCo_5$, 382, 383
$Ce_2Co_7B_3$, 383, 386
$Ce(Co_{0.9}Ni_{0.1})_5$, 383
$Ce(Co_{0.925}Ni_{0.075})_5$, 383
$Ce(Co_{1-x}Ni_x)_5$, 383, 385
$CeFe_2$, 472
$Ce(Fe_{0.7}Co_{0.3})_2$, 473
$Ce(Fe_{0.8}Co_{0.2})_2$, 473
$Ce(Fe_{0.9}Co_{0.1})_2$, 473
$Ce(Fe_{1-x}Co_x)_2$, 472
Co, 437, 474
– bcc, 109, 127, 134, 138
– fcc, 106, 109, 126, 127, 129–131
– hcp, 109, 126–128, 133
Co/Ag, 6, 36, 53, 197
Co/Au, 193, 194
Co/Au/Co, 8
Co–Cr, 169, 170
Co/Cr, 5, 179, 183, 186, 190
Co/Cu, 5, 12, 13, 16, 26, 36, 37, 40, 42, 50, 56, 141, 144, 158, 164, 168
$Co/Cu/Ni_{80}Fe_{20}$, 37
Co/Fe, 208, 209
Co/Ir, 217, 221
Co/Mn, 210, 211
Co/Ni, 215, 216
CoNiP, 216, 220
Co/Pd, 200, 201
Co/Pt, 201, 203
CoRu, 220
Co/Ru, 5, 217
CoS_2, 386, 387
$Co(S_{1-x}Se_x)_2$, 386–388
Co/Sb, 217, 221
$CoSe_2$, 386
Co/Si, 218, 223
Co/Sn, 218, 222
CoTi–M, 458
CoZn–W, 458
Co/Zr, 218, 222
$CrS_{1.17}$, 444
CrTe, 443
Cr_3Te_4, 442
Cu_2MnAl, 238
Cu/Nb, 246, 247
$Cu_{0.63}Ni_{0.22}Fe_{0.15}$, 504
$Cu_{0.783}Ni_{0.13}Fe_{0.087}$, 504

Dy, 417, 427, 428, 435, 475, 479, 483, 498, 516
$DyAl_2$, 463, 505
$DyAl_{2.22}$, 466
$DyAlO_3$, 453, 513
$Dy_3Al_5O_{12}$, 451, 454
$DyCo_2$, 326, 332, 336, 370, 473
$Dy(Co,Al)_2$, 346
$Dy(Co_{0.8}Al_{0.2})_2$, 350
$Dy(Co_{1-x}Al_x)_2$, 345
$Dy(Co_{1-x}Si_x)_2$, 354
$(Dy_{0.25}Er_{0.75})Al_2$, 417, 435, 470
$(Dy_{0.40}Er_{0.60})Al_2$, 470
$(Dy_{0.5}Er_{0.5})Al_2$, 463
$(Dy_{1-x}Er_x)Al_2$, 460
$Dy_xEr_{1-x}AlO_3$, 513
$(Dy_{0.26}Er_{0.74})Ni_2$, 466
$Dy_{0.7}(Fe_xNi_{1-x})_{0.3}$, 508
$Dy_3Ga_5O_{12}$, 451
$(Dy_{0.5}Gd_{0.5})_3Ga_5O_{12}$, 452
$(Dy_{0.5}Ho_{0.5})Al_2$, 463
$Dy_xLu_{1-x}Co_2$, 320
$Dy_xNd_{1-x}Co_2$, 331
$Dy_{0.7}Ni_{0.3}$, 507
$DyNi_2$, 466

$Dy_xPr_{1-x}Co_2$, 331
$DyVO_4$, 459, 513
$Dy_{0.7}Y_{0.3}$, 499
$(Dy,Y)Co_2$, 328, 337, 339, 340
$(Dy_xY_{1-x})Co_2$, 325
$Dy_{30}Zr_{70}$, 501
$Dy_{70}Zr_{30}$, 501
Dy–Zr nanocomposites, 474

Er, 488
ErAgGa, 464
$ErAl_2$, 463, 517
$ErAl_{2.20}$, 466
Er_2Al, 465
Er_3AlC, 465
Er_3AlC_x, 465
$ErAlO_3$, 453, 513
$ErCo_2$, 318, 319, 331, 332, 334, 344, 370, 473
$ErCo_3$, 378, 380
Er_3Co, 474
$Er(Co_{1-x}Al_x)_2$, 345
$Er(Co,Si)_2$, 352
$Er(Co_{0.9}Si_{0.1})_2$, 354
$Er(Co_{1-x}Si_x)_2$, 353–355
$Er_{1-x}Dy_xNi_2$, 466, 469
$Er_xDy_{1-x}Sb$, 510
$Er_{0.7}Fe_{0.3}$, 506
$ErFe_2$, 471
$Er_{0.8}La_{0.2}$, 501
Er–La alloys, 501
$(Er,Lu)Co_2$, 318
$Er_xLu_{1-x}Co_2$, 318, 320, 321
ErNi, 466, 469
$ErNi_2$, 466
Er_3Ni, 469, 470, 510
ErNiAl, 470
$ErNi_{0.8}Co_{0.2}$, 510
$ErNi_{0.9}Co_{0.1}$, 510
$Er(Ni_{1-x}Co_x)_2$, 469
Er_6Ni_2X, 470
$(Er,Y)Co_2$, 318, 329, 340
$Er_{0.4}Y_{0.6}Co_2$, 360, 361
$Er_{0.4}Y_{0.6}(Co_{0.95}Al_{0.05})_2$, 360, 361
$Er_{0.9}Yb_{0.1}Ni$, 469, 510
Eu, 426
EuS, 412, 436

Fe, 437
– bcc, 106
γ-Fe_2O_3 films, 446
$FeCO_3$, 430, 459
$Fe_{0.05}Co_{0.7}Si_{0.15}B_{0.10}$, 508
Fe/Cr, 5, 26, 34, 42
Fe/Cu, 224, 225, 228
Fe/Cu/Co, 26
Fe–Hg, 422
FeMn, 8
Fe/Mn, 235, 236
$Fe_{0.5}Ni_{0.5}$, 314
$(Fe_{1-x}Ni_x)_{0.9}Zr_{0.1}$, 508
$Fe_{0.49}Rh_{0.51}$, 444
$Fe_{0.5}Rh_{0.5}$, 444
$Fe_{0.58}Rh_{0.58}$, 444
$Fe_{49}Rh_{51}$, 425, 426
Fe/V, 230, 231

gadolinium gallium garnet, 419, 513
Gd, 412, 417, 419, 426–431, 435, 475, 505, 514, 517
$Gd_{0.5}Ag_{0.5}$, 509
$Gd_{0.755}Ag_{0.225}$, 509
Gd_xAg_{1-x}, 509
$GdAl_2$, 505
Gd_3Al_2, 464, 517
$GdAlO_3$, 453, 513
$Gd_{0.65}Co_{0.35}$, 506
$GdCo_2$, 316, 370, 371
$GdCo_3$, 376
$Gd(Co_{0.8}Al_{0.2})_2$, 350
$Gd(Co_{1-x}Cu_x)_2$, 356
$Gd(Co_{1-x}Mn_x)_2$, 357
Gd–Dy, 515
$Gd_{0.73}Dy_{0.27}$, 505
$(Gd_{0.1}Dy_{0.9})Al_2$, 463
$(Gd_{0.9}Dy_{0.1})_3Al_2$, 517
$(Gd_{0.1}Dy_{0.9})Ni$, 466
Gd–Er, 515
– alloys, 497
$Gd_{0.69}Er_{0.31}$, 498
$Gd_{0.8}Er_{0.2}$, 498
$Gd_{0.84}Er_{0.16}$, 498
$Gd_{0.9}Er_{0.1}$, 498
$Gd_{0.06}Er_{0.94}Al_2$, 464
$(Gd_{0.14}Er_{0.86})Al_2$, 464
$(Gd_{0.2}Er_{0.8})NiAl$, 470
$(Gd_{0.54}Er_{0.46})NiAl$, 470
$(Gd_{1-x}Er_x)NiAl$, 470, 517
$Gd_{0.7}Fe_{0.12}Ni_{0.18}$, 507
$Gd_{0.7}(Fe_xNi_{1-x})_{0.3}$, 507
$Gd_3Fe_5O_{12}$, 450, 456
$Gd_3Ga_{5-x}Fe_xO_{12}$, 502
$Gd_3Ga_xFe_{5-x}O_{12}$, 450
$Gd_3Ga_5O_{12}$, 435, 451, 454
$Gd_{0.8}Ho_{0.2}$, 497, 516
Gd–Ho, 515
– alloys, 497
(Gd,Nd)Ni, 368
$(Gd,Nd)Ni_2$, 368

$(Gd,Nd)_mNi_n$, 368, 370
$(Gd_{0.2}Nd_{0.8})Ni$, 369
$(Gd_{0.2}Nd_{0.8})Ni_2$, 369
$(Gd_{0.2}Nd_{0.8})Ni_3$, 369
$(Gd_{0.2}Nd_{0.8})Ni_5$, 369
$(Gd_{0.3}Nd_{0.7})Ni_2$, 368, 369
$(Gd_{0.6}Nd_{0.4})_2Ni_{17}$, 369
$(Gd_{0.15}Nd_{0.35}Y_{0.5})_2Ni_7$, 369
$Gd_{0.7}Ni_{0.3}$, 506, 508
GdNi, 466
$GdNi_2$, 466
$GdNi_5$, 469
GdPd, 417, 465
Gd–Pd, 435
Gd_3Pd_4, 465
GdRh, 465
Gd_5Si_4, 504
$Gd_5(Si_2Ge_2)$, 505, 506
$Gd_5(Si_xGe_{1-x})_4$, 504, 517
$Gd_5(Si_{1.985}Ge_{1.985}Ni_{0.83})$, 506
$Gd_{0.4}Tb_{0.6}$, 515
$Gd_{0.6}Tb_{0.4}$, 516
$Gd_{0.85}Tb_{0.15}$, 501
$Gd_{0.9}Tb_{0.1}$, 515
$Gd_{0.85}Y_{0.15}$, 501
$(Gd,Y)Co_2$, 318
$(Gd_xY_{1-x})Co_2$, 325
$(Gd_tY_{1-t})(Co_{0.95}Al_{0.05})_2$, 364
$(Gd_tY_{1-t})(Co_{0.915}Al_{0.085})_2$, 364
$(Gd,Y)_2Co_7B_3$, 383
$(Gd,Y)Cu_2$, 344
$Gd_{0.75}Zr_{0.25}$, 501

Heusler alloy, 238, 239
$HfCo_2$, 282
Ho, 427, 475, 487, 516
$HoAl_2$, 517
$HoAl_{2.24}$, 466
$HoAlO_3$, 453
$HoCo_2$, 318, 325, 332, 334, 336, 370, 473
$HoCo_3$, 380
$Ho(Co,Al)_2$, 347, 349
$Ho(Co_{1-x}Al_x)_2$, 345, 348
$Ho(Co_{1-x}Ni_x)_2$, 357
$Ho(Co_{1-x}Rh_x)_2$, 357
$Ho(Co,Si)_2$, 352
$Ho(Co_{1-x}Si_x)_2$, 354
$Ho_{0.05}Dy_{0.95}$, 250, 251
$Ho_{0.5}Dy_{0.5}Al_2$, 517
$(Ho_{0.5}Dy_{0.5})Al_{2.25}$, 466
$Ho_{0.5}Er_{0.5}$, 466
$HoFe_3$, 471
holmium, 426

HoNi, 466
$(Ho,Y)Co_2$, 328
$Ho_xY_{1-x}Co_2$, 325, 339

$La_{0.67}A_{0.33}MnO_3$ (A = Ca, Ba, Sr), 447
$La_{1-x}Ca_xMnO_3$, 455
$La_{1-x}Na_xMnO_3$, 455
$Li_2Fe_5Cr_5O_{16}$, 456, 471
$Li_{0.1}Mn_{0.9}Se$, 444
Lu, 475
$LuCo_2$, 264, 278, 281–289, 291–293, 371, 474
$Lu(Co,Al)_2$, 298, 345
$Lu(Co_{0.8}Al_{0.2})_2$, 350
$Lu(Co_{0.88}Al_{0.12})_2$, 348
$Lu(Co_{1-x}Al_x)_2$, 292, 293, 304, 305, 307, 308, 347, 364
$Lu(Co_{0.88}Ga_{0.12})_2$, 301, 303, 309
$Lu(Co_{0.91}Ga_{0.09})_2$, 308, 309
$Lu(Co_{1-x}Ga_x)_2$, 307
$Lu(Co_{1-x}Si_x)_2$, 312
$Lu(Co_{1-x}Sn_x)_2$, 301, 302
$LuNi_2$, 292
$(Lu_{1-t}Tm_t)(Co_{0.88}Al_{0.12})_2$, 365

$MgOZnO \cdot 2Fe_2O_3$, 457
MnAs, 443
$MnAs_{1-x}P_x$, 443
$Mn_{1.9}Cr_{0.1}Sb$, 444
$Mn_{2-x}Cr_xSb$, 443, 444
$MnFe_{2-x}Cr_xO_4$, 456
Mn_3Ge_2, 444
Mn_5Ge_3, 443
$Mn_{0.17}Ni_{0.83}$, 445
MnP, 443, 444
Mn/Sb, 240, 241
$Mn_{0.95}V_{0.05}As$, 444

Nd, 476, 490
$NdCo_2$, 370
$Nd(Co,Al)_2$, 350
$Nd(Co_{0.8}Al_{0.2})_2$, 350
$Nd(Co_{1-x}Al_x)_2$, 350
$(Nd,Dy)Co_2$, 330
$Nd_{0.14}(Fe_{1-x}Al_x)_{0.8}B_{0.06}$, 502
Nd_3Ni, 470
$Nd_xY_{1-x}Co_2$, 319, 322
Ni, 437, 466
– film, 447
NiAs, 444
Ni/Cu, 26, 224, 228
NiFe, 232
$Ni_{80}Fe_{20}$/Ag, 36
NiFe/Ag/Co/Ag, 58
$NiFeCrO_4$, 456

NiFe/Cu, 17
$Ni_{80}Fe_{20}$/Cu, 26, 36, 42
NiFe/Cu/Co/Cu, 58
$Ni_{80}Fe_{20}$/Cu/$Ni_{80}Fe_{20}$, 39
Ni–Mn alloys, 445
NiO, 8

orthoaluminates, 453

permalloy, 232, 234
$Pr_xCe_{2-x}Fe_{17}$, 472
(Pr,Dy)Co_2, 330
$PrCo_2$, 370
Pr_2Fe_{17}, 472
Pr_3Ni, 470

RAl_2, 460, 465
RAl_2 (R = Er, Dy), 435
RAl_3, 466
$RAlO_3$, 453, 513
rare earth garnets, 447
$R_{1-x}B_xMnO_3$, 455
$R_xCe_{2-x}Fe_{17}$, 471
RCo_2, 333, 473
RCo_3, 373
$R(Co,Al)_2$, 348
$R(Co_{0.8}Al_{0.2})_2$, 350, 351
$R(Co_{0.88}Al_{0.12})_2$, 349
$R(Co_{1-x}Al_x)_2$, 345, 372
$R_2Co_7B_3$, 383
$R_{n+1}Co_{3n+5}B_{2n}$, 385
$R(Co,Cu)_2$, 372
$R(Co_{1-x}Cu_x)_2$, 356, 357
$R(Co_{1-x}Mn_x)_2$, 357
$R(Co,Si)_2$, 351, 372
$R(Co_{1-x}Si_x)_2$, 312, 352, 353
RFe_2, 470
RFe_3, 470
R_2Fe_{17} compounds, 471
$R_{0.7}(Fe_xNi_{1-x})_{0.3}$, 506
$R_3Fe_5O_{12}$, 447, 452
$R_2Ga_5O_{12}$, 513
RNi, 466
RNi_2, 466, 517
R_3Ni, 466, 470
RNiAl, 470
RNiGe, 510
$R_{0.7}TM_{0.3}$, 506
RXO_4, 459
$(R_xY_{1-x})Co_2$, 474
$(R,Y)(Co_{0.88}Al_{0.11})_2$, 370
$R_xY_{1-x}Co_2$, 317, 329, 332
$RbMnBr_3$, 445

$ScCo_2$, 278, 281–283, 285, 287–289, 291–293
$Sc(Co_{1-x}Al_x)_2$, 292
Sm, 426
$SmCo_5$, 434
$Sn_{0.75}Ga_{0.25}$, 470
spinel, 471

Tb, 475, 479
$TbCo_2$, 325, 326, 370
$Tb(Co_{0.8}Al_{0.2})_2$, 350
$Tb_{0.5}Dy_{0.5}$, 500, 516
Tb_xDy_{1-x}, 500
$Tb_{0.2}Gd_{0.8}$, 495
Tb_xGd_{1-x}, 494
Tb–Gd alloys, 514
(Tb,Ho)Co_2, 327, 329
$Tb_xHo_{1-x}Co_2$, 325, 327
Tb–Y alloys, 252
(Tb,Y)Co_2, 325, 327, 337, 341
$Tb_{0.63}Y_{0.37}$, 499
$Tb_{0.835}Y_{0.135}$, 498
Tb_xY_{1-x}, 479, 498
$Tb_{1-x}Y_x$, 251
$Tb_xY_{1-x}Co_2$, 325, 326, 339
$Tb_xY_{1-x}Fe_2$, 470, 471
$Th_{0.92}Co_{5.16}$, 382
$Th_{0.95}Co_{5.10}$, 382, 383
$Th_{0.965}Co_{5.07}$, 382
$Th_{1-\delta}Co_{5+2\delta}$, 382, 384
$ThCo_5$, 382, 383, 385
Tm, 476, 490
$TmCo_2$, 358–360, 370
$TmCo_3$, 381
$Tm(Co_{0.9}Al_{0.1})_2$, 359
$Tm(Co_{0.93}Al_{0.07})_2$, 358, 359
$Tm(Co_{0.95}Al_{0.05})_2$, 358–360
$Tm(Co_{0.95}Si_{0.05})_2$, 359
$Tm_{1-x}Gd_xCo_2$, 360–362
$Tm_{1-t}Lu_t(Co_{0.88}Al_{0.12})_2$, 348

V/Ag, 231

Y, 475
YAl_2, 292
$Y_xCe_{2-x}Fe_{17}$, 472
YCo_2, 264, 271, 279, 281–288, 290–294, 318, 371
YCo_3, 374, 375
$Y(Co,Al)_2$, 345
$Y(Co_{0.855}Al_{0.145})_2$, 305
$Y(Co_{0.85}Al_{0.15})_2$, 304
$Y(Co_{0.88}Al_{0.12})_2$, 348, 365, 366
$Y(Co_{0.89}Al_{0.11})_2$, 309
$Y(Co_{0.90}Al_{0.10})_2$, 309

$Y(Co_{0.925}Al_{0.075})_2$, 313
$Y(Co_{1-x}Al_x)_2$, 291, 292, 294–301, 304, 307–312, 347, 364, 372
$Y(Co_xAl_yCu_z)_2$, 313, 314
$Y(Co_{1-x}Cu_x)_2$, 314, 356
$Y(Co,Fe)_2$, 315
$Y(Co_{1-x}Fe_x)_2$, 314
$Y(Co_{1-x}Ga_x)_2$, 309
YCo_3H_x, 375, 376
$Y(Co_{1-x}M_x)_2$, 314
$Y(Co,Ni)_2$, 315
$Y(Co_{1-x}Si_x)_2$, 312, 354
YFe_2, 286
YFe_3, 471
$Y_{1-t}Gd_tCo_3$, 376–379
$Y_{1-t}Gd_t(Co_{0.915}Al_{0.085})_2$, 319, 321, 365
$Y_{1-t}Gd_t(Co_{0.95}Al_{0.05})_2$, 365
$(Y_{1-x}La_x)Co_2$, 314
$(Y_{1-t}Lu_t)(Co_{0.88}Al_{0.12})_2$, 304, 306, 307
$(Y_{1-t}Lu_t)(Co_{1-x}Al_x)_2$, 311
$Y_{1-x}Nd_xCo_3$, 377, 379, 380
YNi_2, 286
$(Y,Tm)(Co_{0.88}Al_{0.12})_2$, 366
$Y_{0.075}Tm_{0.25}(Co_{0.88}Al_{0.12})_2$, 365
$Y_{0.75}Tm_{0.25}(Co_{0.88}Al_{0.12})_2$, 366
Yb, 426, 475

$ZrCo_2$, 282, 288
$(Zr_{0.95}M_{0.05})_{0.9}Zr_{0.1}$, 508